X-Ray Optics and Instrumentation

X-Ray Focusing: Techniques and Applications

Guest Editors: Ali Khounsary, Stephen L. O'Dell, and Gene Ice

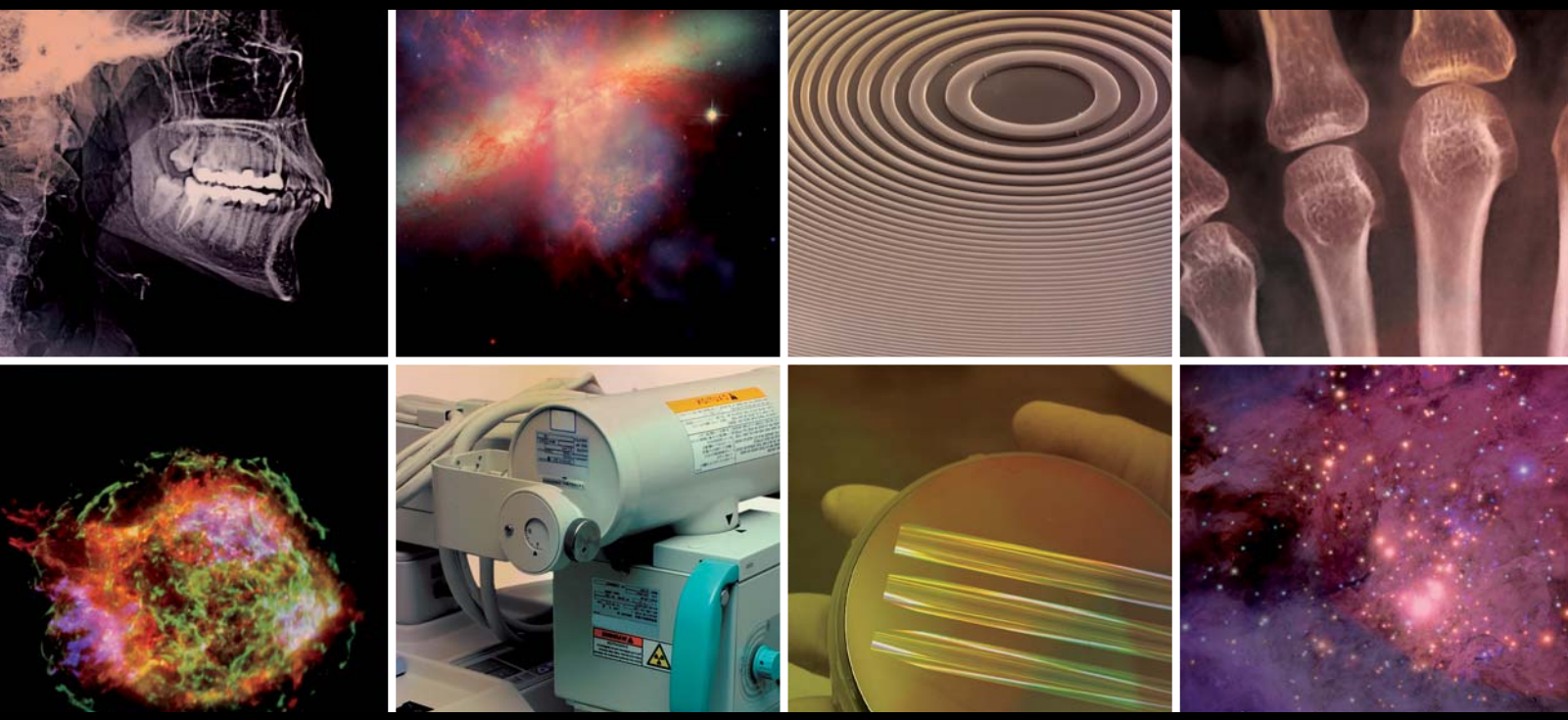

X-Ray Focusing: Techniques and Applications

X-Ray Focusing: Techniques and Applications

Guest Editors: Ali Khounsary, Stephen L. O'Dell, and Gene Ice

Contents

Hindawi Publishing Corporation
X-Ray Optics and Instrumentation
Volume 2010, Article ID 841391, 1 page
doi:10.1155/2010/841391

Editorial

X-Ray Focusing: Techniques and Applications

Ali Khounsary,[1] Stephen L. O'Dell,[2] and Gene Ice[3]

[1] *Argonne National Laboratory, Argonne, IL, USA*
[2] *NASA Marshal Space Flight Center, Huntsville, AL, USA*
[3] *Oak Ridge National Laboratory, Oak Ridge, TN, USA*

Correspondence should be addressed to Ali Khounsary, amk@aps.anl.gov

Received 31 December 2010; Accepted 31 December 2010

This Special Issue of *X-Ray Optics and Instrumentation* comprises ten review papers and six research articles, which collectively offer a broad overview of X-ray focusing techniques and applications in laboratory measurements, in synchrotron beamlines, and in X-ray astronomy. Focusing enables not only more intense illumination for reduced exposure time and higher signal-to-noise ratio, but higher spatial resolution through true imaging. Although X-ray focusing is accomplished through the application of some basic physical principles, such as reflection (mirrors), refraction (lenses), and diffraction (crystals or zone plates), stringent performance requirements coupled with physical, mechanical, environmental, and manufacturability imperatives or limitations make the task technically challenging. The diverse X-ray focusing techniques and applications covered in this Volume provide a glimpse into the scope, challenges, and future of this expanding field.

Acknowledgments

We wish to sincerely thank the authors who contributed to this volume and the numerous reviewers for their indispensible suggestions and comments. We also thank the Journal's Chief Editor, Professor. Carolyn MacDonald, for her support, and the staff at Hindawi Publications for their invaluable assistance in preparing this special issue.

Ali Khounsary
Stephen L. O'Dell
Gene Ice

Hindawi Publishing Corporation
X-Ray Optics and Instrumentation
Volume 2010, Article ID 109740, 19 pages
doi:10.1155/2010/109740

Review Article

Focusing X-Ray Optics for Astronomy

Paul Gorenstein

High Energy Astrophysics Division, Harvard-Smithsonian Center for Astrophysics, 60 Garden Street, MS-4, Cambridge, MA 02138, USA

Correspondence should be addressed to Paul Gorenstein, pgorenstein@cfa.harvard.edu

Received 28 February 2010; Accepted 12 October 2010

Academic Editor: Stephen L. O'Dell

Focusing X-ray telescopes have been the most important factor in X-ray astronomy's ascent to equality with optical and radio astronomy. They are the prime tool for studying thermal emission from very high temperature regions, non-thermal synchrotron radiation from very high energy particles in magnetic fields and inverse Compton scattering of lower energy photons into the X-ray band. Four missions with focusing grazing incidence X-ray telescopes based upon the Wolter 1 geometry are currently operating in space within the 0.2 to 10 keV band. Two observatory class missions have been operating since 1999 with both imaging capability and high resolution dispersive spectrometers. They are NASA's Chandra X-ray Observatory, which has an angular resolution of 0.5 arc seconds and an area of 0.1 m^2 and ESA's XMM-Newton which has 3 co-aligned telescopes with a combined effective area of 0.43 m^2 and a resolution of 15 arc seconds. The two others are Japan's Suzaku with lower spatial resolution and non-dispersive spectroscopy and the XRT of Swift which observes and precisely positions the X-ray afterglows of gamma-ray bursts. New missions include focusing telescopes with much broader bandwidth and telescopes that will perform a new sky survey. NASA, ESA, and Japan's space agency are collaborating in developing an observatory with very large effective area for very high energy resolution dispersive and non-dispersive spectroscopy. New technologies are required to improve upon the angular resolution of Chandra. Adaptive optics should provide modest improvement. However, orders of magnitude improvement can be achieved only by employing physical optics. Transmitting diffractive-refractive lenses are capable theoretically of achieving sub-milli arc second resolution. X-ray interferometry could in theory achieve 0.1 micro arc second resolution, which is sufficient to image the event horizon of super massive black holes at the center of nearby active galaxies. However, the physical optics systems have focal lengths in the range 10^3 to 10^4 km and cannot be realized until the technology for accurately positioned long distance formation flying between optics and detector is developed.

1. Introduction

Over the past decade focusing X-ray telescopes have had a very prominent role in astronomy, cosmology, and in positioning astrophysics at the frontier of fundamental physics. Currently (2010), four focusing X-ray telescopes are in space. The most notable are aboard two complementary missions. They are NASA's Chandra X-ray Observatory which has very high angular resolution and moderately high throughput, and the European Space Agency's XMM-Newton, which has high throughput and moderate angular resolution. There is also a Japanese led mission called Suzaku and the Swift mission, whose payload includes an X-ray telescope (XRT). NASA and ESA plus JAXA, the Japanese space agency, are collaborating on the development of the next major X-ray astronomy observatory mission, named the International X-Ray Observatory (IXO), whose telescope will have far more throughput than any other to date and whose X-ray spectrometers will be far more powerful in every respect than any currently in space. Information about all current and past X-ray astronomy missions in which NASA has participated is available at the website http://heasarc.nasa.gov/docs/observatories.html.

This paper provides background and general information about X-ray optics for astronomy and is an introduction to the more detailed descriptions of specific topics that appear in other articles in this issue.

The energy band where focusing X-ray telescopes currently are operating is 0.2 to 10 keV. These limits are not strict. Below the low-energy limit the interstellar medium is

Table 1: Various types of optics for X-ray telescopes.

Type	Best angular resolution (half power diam.)	Energy band	Status	Astronomical applications
Grazing incidence reflection	0.5 arcsec (actual)	0.15–10 keV	Currently operating***	Imaging and spectroscopy of all type objects
Grazing incidence reflection with ML coatings**	0.4 to 1 arcmin	5–>80 keV	Balloon experiments, NuSTAR in 2012	Broad band imaging of all type objects
Lobster-eye (grazing incidence)	Few arcmin	0.2–5 keV	Small payload prototypes	Wide Field monitoring and surveys
Laue Crystal Lens	~1 to 2 arcmin	Few % variable in 0.1–1 MeV band	Balloon and laboratory experiments	Hard X-ray, soft gamma-ray spectroscopy, nuclear lines
Normal incidence reflection with ML coatings**	<1 arcsec (actual)	<0.25 keV ~1% bandwidth	Recent missions, for example, TRACE	Imaging soft X-ray lines in the solar corona
Diffractive-refractive	10 to 100* microarcsec	>4 keV~ 10–20% bandwidth	Laboratory experiments	Central regions of galaxies + jets nearby stars
Interferometer	0.1* microarcsec	0.2 to 10 keV	Laboratory experiments	Imaging the environments of super massive black holes

* Expected resolution. ** multilayer coatings. *** In 2010, the Chandra X-Ray Observatory, XMM-Newton, Suzaku, and Swift XRT Total telescope areas at 1 keV are, respectively, 0.09 m^2, 0.43 m^2 (3 tel), 0.18 m^2 (4 tel), and 0.015 m^2.

opaque to extragalactic sources along all directions and to sources in the galactic plane more distant than 200 parsec (650 light-years, 6×10^{18} m). The upper limit has been determined in practice by the high-energy cutoff of grazing incidence optics. However, the employment of multilayer coatings plus longer focal lengths will extend the upper limit to nearly 80 keV starting with the launch of the NuSTAR mission, scheduled for 2012. Other papers in this issue describe how a structured array of Laue crystals will be able to concentrate hard X-rays and soft gamma-rays including some nuclear lines onto detectors with good energy resolution and low background.

The birth of X-ray astronomy, the initial discoveries, and even the work cited in the award of the 2002 Nobel Prize in physics to Riccardo Giacconi were all accomplished with mechanically collimated large area gas proportional counters. However, most of the progress of the past twenty-five years can be attributed to the large increase in detection sensitivity, positioning accuracy, high-resolution images, and spectra obtained with focusing telescopes. They have had a profound effect upon our understanding of stars, star formation, "normal" galaxies, active galaxies, clusters of galaxies, cosmology, and other aspects of astronomy. Focusing X-ray optics has also contributed greatly to our knowledge about the Sun and even provided some surprising results about comets and planets in our solar system. After nearly 30 years of observing gamma-ray bursts (GRBs) and debating their origin, a focusing X-ray telescope solved the mystery by providing precise positions of their longer lived X-ray afterglow that resulted in optical identifications and the knowledge that GRBs are extragalactic including some that are among the most distant and therefore the youngest objects ever detected in any band of the electromagnetic spectrum.

With IXO as the flagship, plans for future X-ray missions are centered upon focusing telescopes as highly sensitive imagers and concentrators for spectroscopy, polarimetry, and timing measurements. However, as shown by the RXTE, Swift BAT and INTEGRAL missions that are currently in orbit, very large area and very large field of view collimated or coded mask counters will continue to have important roles in fast X-ray timing measurements of intense sources, as all sky monitors of bursts and transient sources as well as surveying the hard X-ray sky.

Nearly all of the focusing telescopes that have observed sources more distant than the Sun have been based upon grazing incidence optics. The only other so far is a short observation of the Crab Nebula by a Laue crystal lens aboard a balloon [1]. The various types of focusing X-ray telescopes, which are in different stages of development, are listed in Table 1. The major international general user X-ray observatories will continue to be based upon grazing incidence optics indefinitely. The others are special purpose devices with a superior property for a limited range of objectives.

2. X-Ray Reflection and Resolution

Nearly all the telescopes to date that have been engaged in cosmic X-ray studies are based upon very low angle, that is, "grazing incidence" or "glancing angle" reflection. The reflective coatings are a very smooth, stable layer of a heavy metal, such as gold, platinum, or iridium, sometimes with a thin chromium sublayer bonding it to the substrate. In the absence of absorption edges the reflectivity of an elemental coating is high at small angles but declines slowly with angle up to its "critical angle" beyond which it drops precipitously. For a given X-ray energy the critical angle is determined by the decrement in the coating material's index of refraction with respect to vacuum. The decrement increases with density. The theoretical reflectivity of 30 nm of iridium, the thickness of the Chandra coatings, with an

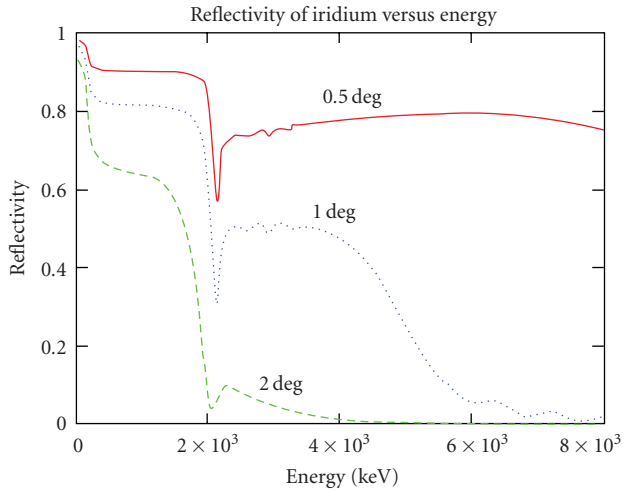

Figure 1: Reflectivity of 30 nm Iridium as a function of energy at three angles. The dips occur at the *M* absorption edges*.

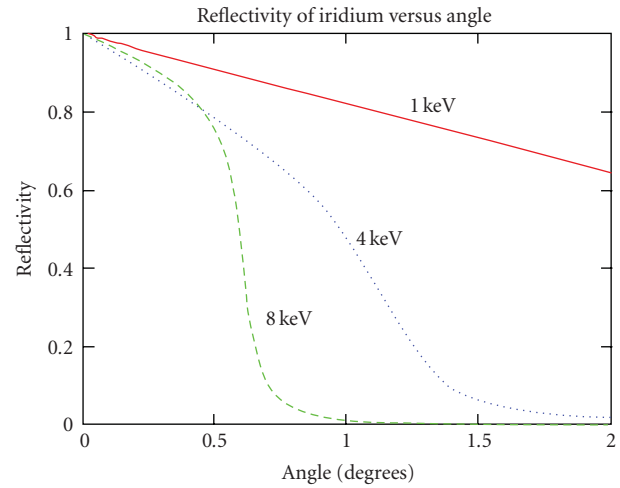

Figure 2: Reflectivity of 30 nm Iridium as a function of angle at three energies*.

rms surface roughness of 0.3 nm is shown as a function of angle for three energies and as a function of energy for three angles in Figures 1 and 2. (These results were obtained from the interactive CXRO web site of the Lawrence Berkley Laboratory, http://henke.lbl.gov/optical_constants/.) The abrupt changes in reflectivity that occur near 2 keV are due to iridium's M absorption edges. In the future this effect can be moderated but not totally eliminated by depositing a 10 nm carbon overcoat [2].

The point spread function (PSF), or resolution function of a grazing incidence telescope, consists of a core due mostly to local slope errors and a halo. The source of the halo is scattering by the irreducible small-scale surface roughness of the substrates and coatings. While smooth on the scale of visible light wavelengths the surface roughness of the most finely polished mirror is finite on the scale of X-ray wavelengths. Therefore the PSF is influenced by diffraction as well as by figure errors [9]. The fraction of photons in the halo increases with energy. The resolution is usually defined in the X-ray astronomy community as the diameter of the region that encompasses 50% of the total flux that accumulates with increasing angle and is called either the half power diameter (HPD) or the half energy width (HEW). Chandra's integral PSF on axis derived from a model that is based upon measurements at several energies in the large X-ray calibration facility at the Marshall Space Flight Center is shown in Figure 3. At 1 keV Chandra's on-axis HPD is about 0.5 arc seconds. At 9.7 keV Chandra's on-axis HPD is 1 arc second. With a Wolter 1 figure (Section 4.1) the angular resolution of the Chandra mirror degrades as the square of the angle off-axis. For example, at 8 arcminutes off-axis Chandra's HPD is 8 arcseconds at 1.5 keV. There is a more detailed description of grazing incidence X-ray reflection in a previous review by Aschenbach [10].

3. X-Ray Production in a Cosmic Setting

Many of the readers of this issue will have some degree of familiarity with X-ray detectors and optics but perhaps not with their astronomical applications. This section provides a brief description of several important objects in the X-ray sky that exemplify the broad range of topics that X-ray astronomy encompasses. More information about the science associated with X-ray astronomy can be found at several web sites including those of the following: Chandra X-Ray Observatory (http://cxc.harvard.edu/), NASA GSFC (http://imagine.gsfc.nasa.gov/docs/introduction/xray_information.html), Cambridge Institute of Astronomy (http://www-xray.ast.cam.ac.uk/xray_introduction/), and the 2nd edition of "Exploring the X-Ray Universe", F. D. Seward and P. Charles, Cambridge University Press, 2010.

The primary X-ray production processes include thermal radiation from a hot, that is, $\sim 10^6$ to 10^8 degrees, plasma that consists largely of H and He ions plus small quantities, that is, 10^{-4} or less of the number of H atoms, of ions of C, O, Ne, Mg, Si, S, Fe, and so forth. Although their relative abundances are small, line emissions from highly ionized heavier elements are very prominent components of a thermal spectrum, especially at a temperature below 20 million degrees. By imaging the flux upon a position sensitive cryogenic detector with very high pulse height resolution and low background and/or imaging the output of a dispersive grating, focusing X-ray telescopes are an essential component of a high-resolution spectrometer.

Synchrotron radiation from high-energy electrons traversing a magnetic field and Compton scattering of longer wavelength electromagnetic radiation by high-energy electrons that results in higher-energy photons, commonly called "inverse Compton scattering", are two other primary X-ray production mechanisms. Other processes include bremsstrahlung and fluorescence radiation resulting from the impact of high-energy particles or higher-energy X-rays upon cold material or a warm plasma and charge exchange between ions and cold gases. Charge exchange from solar wind ions to the H_2O and CO_2 in the halos of comets is the

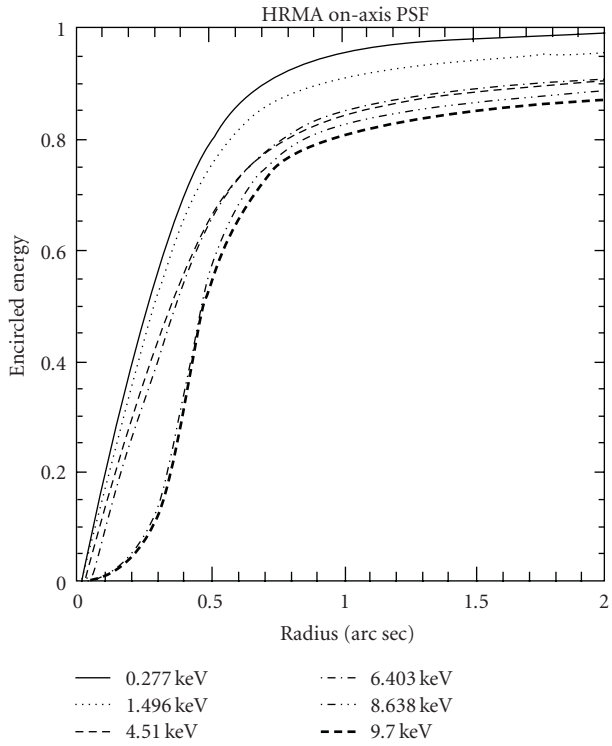

Figure 3: The integral point spread function of the Chandra X-ray telescope based upon measurements at several energies at the large MSFC X-ray calibration facility.

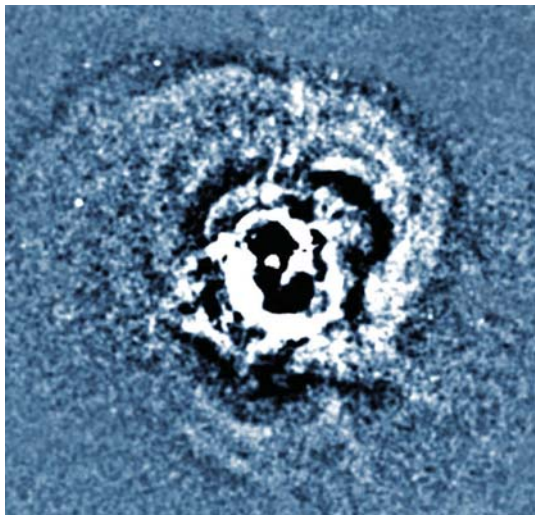

Figure 4: The Perseus cluster of galaxies has indications of episodic outbursts from the central galaxy, NGC 1275, very likely from the super massive black hole at its center. The size of the region is 400 arc seconds.

mechanism responsible for the surprisingly high-intensity and wide-spread X-ray emission from comets approaching the Sun.

There are environments where several processes are operating simultaneously. For example, the remnant of a young supernova remnant can emit thermal radiation as the

Figure 5: The Chandra X-ray image (pink) of the hot gas is superimposed on an optical image of two merging galaxies. The blue region shows the mass concentration as deduced from gravitational lensing. Field is 5.5 × 5.4 arc min.

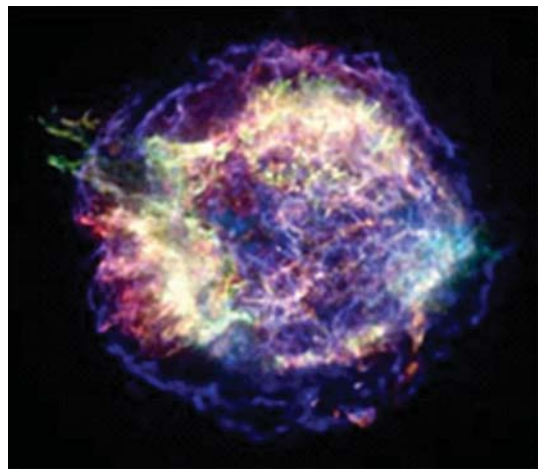

Figure 6: Chandra image of the over three-hundred-year-old supernova remnant, Cas A. The colors are "true" in that the higher energy X-rays are shown in blue and the lower energy X-rays in red. A point-like object near the center is not an ordinary star. It may be a neutron star remnant of a core collapse supernova explosion [3]. The size of the region is 7.3 × 6.4 arc minutes.

expanding ejecta collides with and shocks material in the interstellar medium or a shell of circumstellar matter shed during an earlier, milder eruptive phase in the life of the pre-supernova star. At the same time electrons may be accelerated to high energies by the shock waves and emit synchrotron radiation under the influence of a magnetic field.

The set of X-ray images that are shown illustrate the broad scope of X-ray astronomy. All images of cosmic X-rays sources were obtained by the Chandra X-Ray Observatory. They are available at http://chandra.harvard.edu/index.html. The principal sites of thermal radiation from hot plasmas include the hot gaseous medium within a cluster of galaxies. Figures 4 and 5 show two interesting examples of X-rays from galaxy clusters. While nearly all clusters of galaxies exhibit some structure or asymmetry in exposures with sufficiently high statistics, the very visible succession of waves shown in

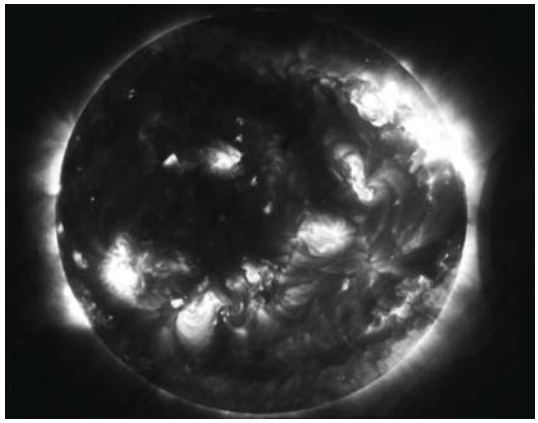

Figure 7: Image of the 6.35 nm Fe^{16} line of the Sun's corona taken from a sounding rocket with a multilayer coated normal incidence telescope [4]. An edge of the Moon appears on the right near the time of an eclipse. Image was provided by Leon Golub of CfA.

Figure 8: X-ray image of the Crab Nebula's neutron star pulsar and its wind nebula, which were created in a supernova explosion that occurred in 1054. They are near the center of the much larger optical image. The size of the region is 2.5 arc min.

Figure 4 is not typical of cluster emission but also not unique. They are evidence for a series of explosions emanating from the center of the central galaxy of the cluster, which houses a super massive black hole.

Figure 5 shows two clusters merging. The hot gaseous intracluster medium that each had contained (pink) previously has not yet settled into equilibrium with the new morphology of the gravitational field that was created by the merger. The mass concentration (blue) was determined by identifying gravitational lens effects. The significance of Figure 5 with respect to dark matter is discussed in Section 3.1. An X-ray image of a rich cluster of galaxies where the gas and galaxies have relaxed to an equilibrium state and are without an explosive center is an extended source of thermal emission from a relatively smooth distribution of hot (~50 million degrees) intracluster gas.

Figure 9: X-ray image of the remnant of a supernova that occurred in 1006. The spectrum of the blue regions at the perimeter is nonthermal and harder than the interior's and is believed to be sites of cosmic ray acceleration. The size of the image is 36 arc min.

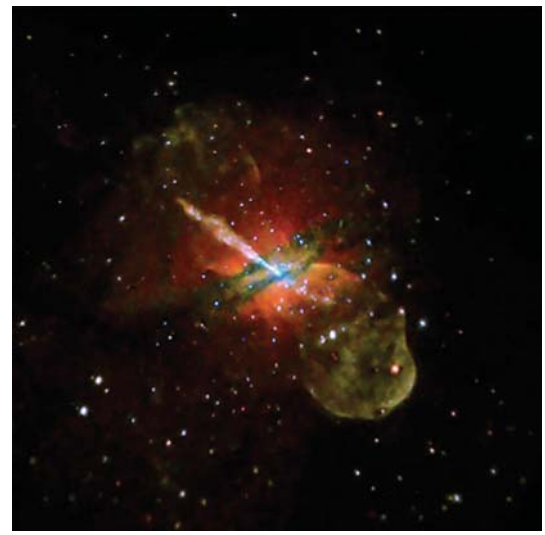

Figure 10: X-ray image of the radio galaxy Centaurus A. Opposing jets emanate from the center. The size of the image is 6.8 arc minutes.

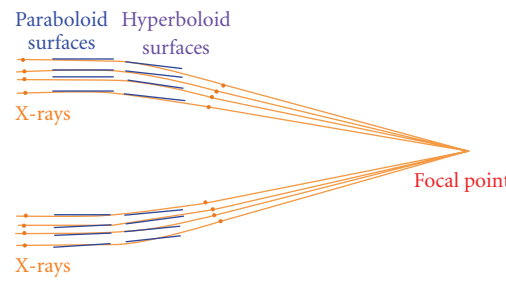

Figure 11: Focusing action of the Wolter 1 type grazing incidence telescope. Rays are reflected from the paraboloid to the hyperboloid and to the focus.

Figure 12: The Chandra telescope during integration of the four mirrors. The fourth mirror shell waits in the background.

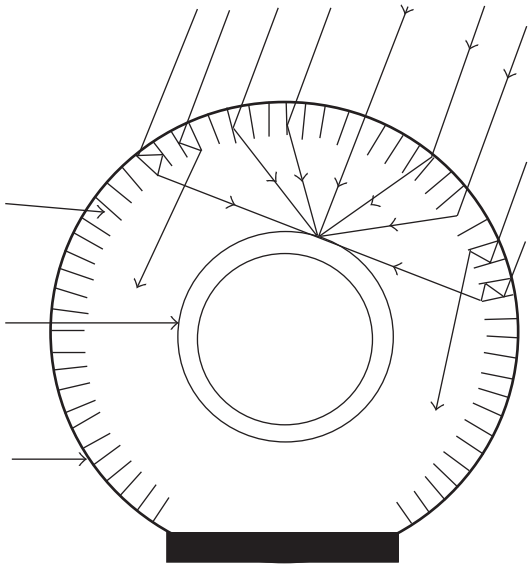

Figure 13: Lobster-eye optics are shown in one dimension. Except near the boundaries the focusing action is azimuthally symmetric. In the X-ray band the maximum graze angle is much smaller than shown in this sketch.

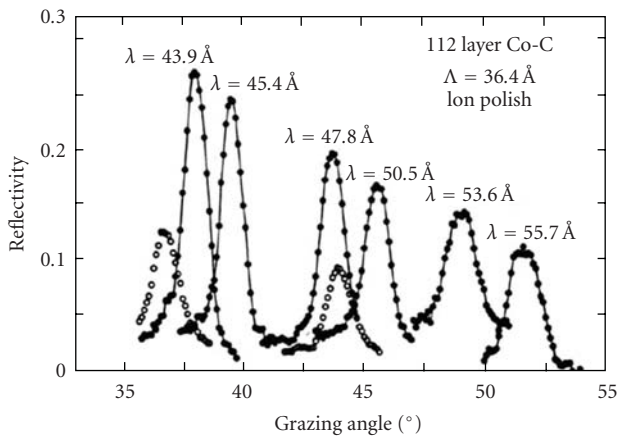

Figure 14: Soft X-ray reflectivity of a Co-C Multilayer coating [5, Figure 9.5].

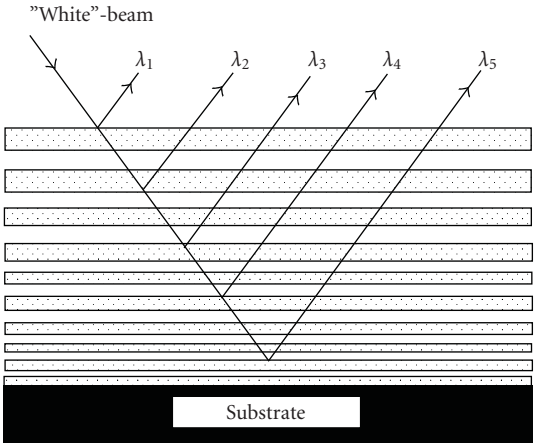

Figure 15: Reflection of hard X-rays by a multilayer whose period decreases with depth.

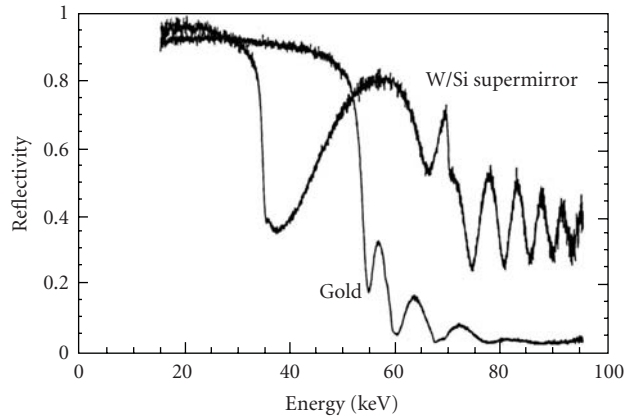

Figure 16: The observed X-ray reflectivities of gold and of a W/Si multilayer (oscillating line) at an angle of 3 mrad are shown [6].

The remnants of recent supernova explosions, Figure 6, are another source of thermal X-rays. Debris from the explosion expands and interacts with material from the interstellar medium. In many cases the supernova's environment is a circumstellar medium that was created when the pre-supernova star had experienced a previous, less disruptive mass ejection. In either case the surrounding medium is shocked by the rapidly expanding ejecta. In return, the ejecta themselves are shocked, that is, the "reverse shock", by the material it has encountered and add another, lower-temperature, thermal component to the total X-ray emission spectrum.

Thermal emission emanates from the few million degree coronas of the Sun (Figure 7) and stars. Stellar X-ray luminosities are only 10^{-11} to 10^{-7} that of the most luminous galactic X-ray sources. A base of more or less constant solar/stellar thermal X-ray emission underlies episodes of much higher-intensity transient nonthermal and thermal emission from dynamic active regions and flares. Thermal X-ray emission from plasmas with temperatures between 3 and 20 million degrees is characterized by very strong

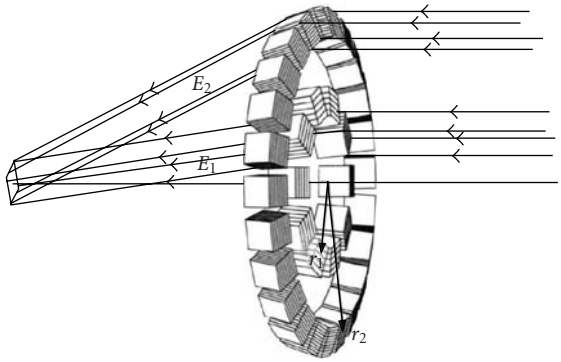

Figure 17: Laue crystal telescope illustrating that the energy that is concentrated varies with radius [7].

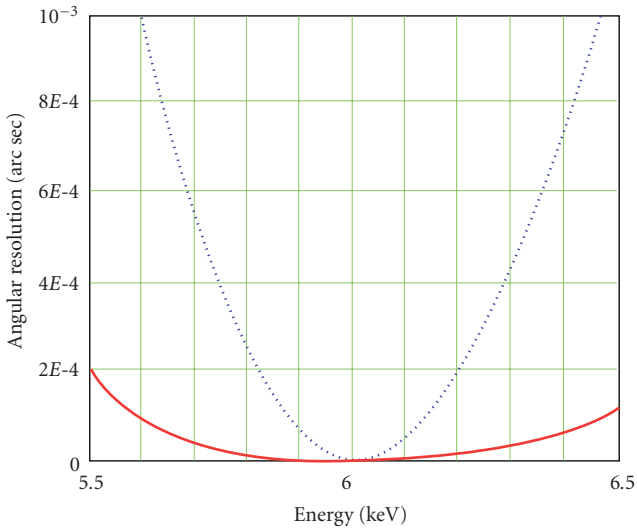

Figure 18: An example of the effect of chromatic aberration, in theory, upon the angular resolution of a diffractive-refractive pair is shown. The blue dotted line represents 1st order correction at 6 keV, the solid red line, correction to 2nd order [8].

emission lines from excitation and deexcitation of the heavier atoms. Both thermal and nonthermal processes account for the much higher than solar levels of X-ray emission and variability from members of star formation regions such as the Orion Nebula.

Rapidly rotating pulsars with high magnetic fields and their surrounding wind nebulae are sources of synchrotron X-ray radiation, the classic example being the Crab Nebula and its pulsar (Figure 8). Synchrotron X-rays are also a by-product of the acceleration of cosmic rays at the outer regions of expanding supernova remnant shells. A notable example of this process is the bright rims of SN 1006 (Figure 9).

Active galactic nuclei, that is, quasars, Seyfert galaxies, "BL Lac", and radio galaxies, are powered by accretion onto a super massive black hole (SMBH) at their centers. Figure 10 shows the relatively nearby radio galaxy Centaurus A, which is representative of many other radio galaxies. There is a central source at the SMBH and jets propagate outward from each side. Inverse Compton scattering is likely to be the mechanism responsible for the X-ray emission from the central source. Electrons are accelerated to high energy by mechanisms not thoroughly understood but probably involving the shock waves that are present. At the center the low-energy photon source for the inverse Compton scattering is the local environment of the accreting SMBH, such as a hot corona. There is no consensus on the mechanism powering the jets. According to Hardcastle et al. [11] and others the broadband spectral energy distribution and the X-ray spectrum imply a synchrotron origin for the X-rays. That would require electrons to be accelerated locally near the emission sites, not at the center. There is an alternative model based upon high-energy electrons experiencing inverse Compton scattering, the source of low-energy photons being the pervasive microwave background [12].

3.1. Dark Matter and Dark Energy. Observation of the X-ray emissions of clusters of galaxies has provided independent, corroborative evidence for the existence of dark matter and dark energy, two cosmological features that are not seen in fundamental particle experiments at accelerators. The indicator of dark matter is the presence of an extended, hot gaseous, X-ray emitting intracluster medium that pervades rich clusters of galaxies. Assuming that the galaxies have the same mass to light ratio as the Sun and nearby stars, the mass of the gas exceeds that of the visible portion of the galaxies significantly. However, the amount of mass that is needed to retain a gaseous halo with the observed temperature and spatial distribution is much greater than the mass of the gas. That proves that an additional component of mass exists, which is in fact the largest component. It is dark because it has not been seen in any band of the electromagnetic spectrum. The significance of Figure 5 is showing that the spatial distribution of the dark mass as inferred from gravitational lensing measurements is associated with the distribution of the galaxies, perhaps a surrounding dark halo, not the gas.

The existence of dark energy, which acts as a repulsive force that increases as the universe expands, is supported by two independent series of X-ray measurements. One is a standard candle approach based upon the premise that the gas-to-mass ratio in a rich cluster of galaxies is constant [13]. Its conclusion is in accordance with the earlier optical measurements that assume that type 1a supernova remnants are a standard candle. The other dark energy indicator is based upon observing the rate at which rich clusters of galaxies evolve. The evolution is influenced by a repulsive force that increases with time, which is the signature of dark energy [14].

4. Grazing Incidence Focusing X-Ray Telescopes

4.1. Introduction. The discovery of the first cosmic X-ray source occurred in 1962. That and the impressive amount of progress achieved in the subsequent 16 years, including the body of work that is cited in awarding the 2002 Nobel Prize in physics to Riccardo Giacconi, were all accomplished with

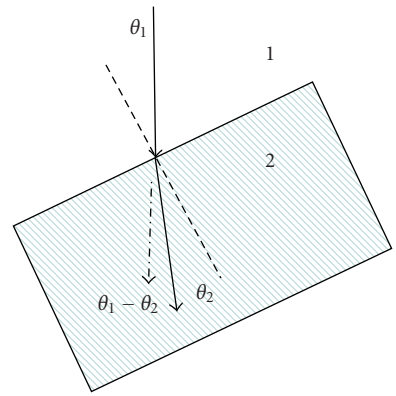

Figure 19: The left panel shows a ray (solid line) arriving at an interface between two media. The clear region "1" is a metal and the shaded region "2" is the vacuum, which has a larger index of refraction in the X-ray band. The dash-dot line is a continuation of the direction of the incident ray. We assume the interface should have been perpendicular to the incoming ray where it would have had no effect upon its direction. However, because of a slope error in the optic the interface is tilted at a finite angle of θ_1. The angle of the refracted ray (dash-dot line) is θ_2 so the error in the direction of the refracted ray is $\theta_1 - \theta_2$. Applying Snell's law relating the indices of refraction to the ray's directions the right panel calculates θ_2. All angles are small so the angle and its Sin are essentially the same. The error is proportional to the difference in the indices of refraction. In the X-ray band the difference between beryllium and vacuum is of the order 10^{-6} to 10^{-5}. Therefore the error is very small.

collimated gas proportional counters prior to the launch into orbit of the first focusing cosmic X-ray telescope. However, the potential power of focusing X-ray telescopes as a more sensitive and higher-resolution tool was recognized prior to all of those events in a 1960 paper by Giacconi and Rossi that described the increase in sensitivity that a parabolic concentrator would provide. In a paper appearing in a special issue of Experimental Astronomy, honoring the 400th anniversary of astronomical telescopes, Giacconi [15] reflects upon the history of the X-ray telescope from his unique perspective.

Although the focusing telescope concepts listed in Table 1 include several types, so far mostly one type, the grazing incidence telescope, has actually observed cosmic X-ray sources. The only exception is a brief balloon observation of the Crab Nebula with a Laue crystal telescope [1]. Furthermore, the figures of all of the grazing incidence telescopes that have been in orbit were fabricated in accordance with or approximating the Wolter1 geometry.

4.2. Wolter Type 1 Telescopes. Wolter [16] described several variations upon an imaging device consisting of two seemingly hollow cylinders in series with the diameter of each varying along the axis as a conic section curve. They were conceived as microscopes but the small dimensions and the high-resolution requirements made fabrication difficult and there are alternate approaches to X-ray microscopy [17]. However, the Wolter Type 1 geometry (Figure 11), sections of paraboloid and a hyperboloid in series, became the model for all of the cosmic X-ray telescopes that have been in orbit. Most of them consisted of several and in some cases many nested coaligned concentric Wolter 1 mirror pairs with a common focus.

The first Wolter 1 telescopes to be launched into orbit observed the Sun in 1973-1974 from the Apollo Telescope Mount (ATM) aboard the Skylab Space Station, the first mission to test the ability of humans to live and work in space for a substantial period of time. The Skylab ATM hosted two instruments, "S-O54" [18] and "S-O56" [19].

With a set of filters they recorded thousands of images on film over a period of nearly nine months. The film was returned to Earth by the Skylab astronauts.Van Speybroeck and Chase [20] provided a prescription for the Wolter 1 that high-resolution X-ray telescopes have followed or approximated. The high angular resolution telescope missions are the Einstein Observatory (1978–1981), ROSAT (1990–1999), and the Chandra X-Ray Observatory (launched in 1999), culminating in Chandra's 0.5 arc second resolution, half power diameter (HPD), on axis. In those three missions the optics consist of several, concentric integral, that is, full 360-degree cylinders, made of a thick, stiff, heavy material that can be accurately figured and finely polished without distortion. The Chandra telescope prior to final assembly is shown in Figure 12.

Wolter 1 telescopes with moderate or intermediate angular resolution and lower mass have been and are currently in space. Their optics have integral substrates, that is, whole cylinders, that are replicated from mandrels. The first of this type was EXOSAT (1983–1986) with epoxy-replicated Be backed mirror shells [21]. Next were electroformed nickel integral mirror shells [22]. This type of optic has achieved angular resolutions of 15 to 18 arc seconds and is probably capable of being improved. The first example was the focusing telescopes of the BeppoSAX mission (1996–2002). BeppoSAX obtained the first precise positions of gamma-ray bursts by imaging their X-ray afterglows. That led to identifying their optical counterpart and its extragalactic location [23]. At the beginning of 2010 the orbiting observatories with electroformed nickel telescopes are XMM-Newton (1999-) with three independent large area telescopes, each with 58 confocal parabola-hyperbola mirror shells and the much

smaller area single telescope Swift XRT (2004-) with 12 concentric mirror shells. The XRT, which Italy provided, is continuing the work of BeppoSAX by observing and accurately positioning the X-ray afterglows of gamma-ray bursts that are detected initially by the Swift Burst Alert Telescope, a large field of view position sensitive detector array with a coded aperture. Several of those positioned by the XRT are at cosmological distances. The XRT is addressing other objectives during the time between bursts that Swift detects at a rate of two per week. A new mission scheduled for launch in 2012 led by Russia includes an instrument named eRosita, being constructed in Germany, that contains a cluster of seven electroformed telescopes, each with 54 mirror shells. eRosita will extend the all-sky soft X-ray survey that was carried out by ROSAT to higher-energy X-rays. Many more AGNs are expected to appear because higher-energy X-rays will be able to penetrate the local absorbing matter surrounding a super massive black hole.

4.2.1. Segmented Telescopes. Lower angular resolution telescopes, specifically those built by the Goddard Space Flight Center for the Japanese ASCA (1993–2001) and Suzaku (2005-) missions, contained mirror shells made of much lighter, weaker aluminum foils that were segmented into several sections along the azimuth [24]. They approximated the parabola and hyperbola figures along the axis with straight lines; that is, they were double cones. Dipping the foils of ASCA in an acrylic lacquer solution under carefully controlled conditions followed by the deposition of a gold coating made their surfaces smooth and efficient X-ray reflectors. Because its substrates were flexible, the angular resolution of ASCA was about 3 arc minutes, limited by figure errors rather than the deviation of a double cone figure from the Wolter I paraboloid/hyperboloid. For Suzaku the foils were made smooth by an epoxy replication process that resulted in better than 2 arc minute resolution. Epoxy replication is also being used to coat the foils of telescopes for a future mission of the Japanese space agency [25]. Foil telescopes can accommodate a much higher packing density of mirror shells than the higher angular resolution telescopes and achieve a much better ratio of effective area to mass. They are well adapted for use with nondispersive spectrometer/detectors in the focal plane, such as solid state devices and (in the future) very high pulse height resolution cryogenic detectors. Foil mirrors are still an evolving technology [26].

Thermal forming of glass sheets whose thickness range is from 200 to 400 microns into telescope segments is another means of fabricating segmented X-ray telescopes [27, 28]. This technique is being used to manufacture the telescopes for the NuSTAR hard X-ray mission [29]. The thermal forming process is being refined at several institutions in the US and Europe for possible use in future missions including the International X-ray Observatory (IXO) [30–33].

Despite their angular resolution being relatively poor so far, segmented mirrors are the only practical option available to future very large area grazing incidence X-ray telescopes. The 3.3-meter diameter of the IXO telescope will be too large for the mirror shells to be integral structures. For the figure to be stable a complete cylinder of revolution with a 3.3-meter diameter would have to be very thick and therefore very massive. As described in other articles appearing in this issue in both Europe and the US there are currently major technology research projects devoted to improving the angular resolution of segmented mirrors for IXO. One approach is the aforementioned refinement of the process of thermal forming of glass segments. The other is assembling silicon mirror plates, known as "silicon pore optics" [34]. It is being developed under the supervision of ESTEC, the technology branch of ESA. While there is reason to expect significant improvement upon XMM-Newton, the 0.5 arc second angular resolution of the Chandra X-ray Observatory is not likely to be surpassed by any new grazing incidence telescope of its size or larger for a long time, if ever. Improvement upon Chandra on a significant scale will occur only with the development of a new technology.

In this issue, segmented optics are described in more detail in the article by Petre. A particular type of segmented X-ray telescope known as silicon pore optics is described in the article by Bavdaz et al.

4.3. The Wide Field X-Ray Telescope (WFXT). WFXT is a telescope concept that outwardly resembles the Wolter 1 but the figures of the front and rear sections are optimized polynomials instead of a parabola followed by a hyperbola. The field is "Wide" only in that the diameter where WFXT's angular resolution is less than 5 arc seconds is significantly larger than the Wolter 1's. The effective area as a function of angle off-axis is about the same for both. With polynomial figures the angular resolution of the telescope becomes much more uniform across the field of view and its average over the field of view is much superior to the Wolter 1. With current computer-controlled figuring and polishing techniques it is no more difficult to impart a polynomial figure to a mirror shell than a parabola or a hyperbola. Moreover, with the resolution not needing to be better than about 5 arc seconds it should be much less expensive to construct and less massive per unit area than the Chandra telescope. An early polynomial design was described by Burrows et al. [35]. Others have followed including a paper by Conconi and Compana [36]. The objective of WFXT is performing sensitive deep surveys that will discover and characterize extremely large populations of high redshift AGNs and observe the growth and development of clusters of galaxies. The WXFT concept and its scientific objectives are described in a "White Paper" [37] presented to the 2010 Decadal Astronomy Survey Committee of the US National Academies of Science.

4.4. Kirkpatrick-Baez Telescopes. Kirkpatrick and Baez [38] described a grazing incidence focusing device consisting of two orthogonal reflectors with each having the figure of a parabola in one dimension (KB). One-dimensional KB X-ray telescopes with several parabolic reflectors were constructed for sounding rocket experiments that scanned several older supernova remnants [39–41]. In a series of rocket flights

a 2D KB telescope imaged several clusters of galaxies [42]. A 2D KB telescope with a resolution of 35 arc seconds was constructed and tested as a prototype unit [43] for a large area modular array of telescopes that was selected as an "Attached Payload" on the International Space Station but the Attached Payload program was cancelled ultimately. A KB telescope has not been in orbit. However, it should be considered seriously as a candidate for the optics of IXO.

A KB telescope has certain advantages when the resolution requirement is not required to be better than several arc seconds. It is much less difficult and less costly to fabricate, especially with the availability of very thin, smooth, fairly flat glass from Schott AG. The thermal forming process used by X-ray that is being developed further in both the USA and Europe for possible use by IXO should apply very well to KB telescopes. In fact, the first use of heat slumping glass for X-ray telescopes was the construction of a KB telescope for the EUV/soft X-ray bands [44]. In addition the silicon pore optics technology being developed by ESA's ESTEC for IXO for a Wolter telescope is also applicable to the fabrication of KB telescopes [45]. A KB telescope can be divided conveniently into modules of almost any size. For each half of the telescope the figure of a reflector need be highly accurate in only one dimension. The alignment between the two orthogonal sections is not critical; so they can be made independently without experiencing much difficulty in the final assembly process. However, the optical axes of the KB modules have to be coaligned in direction very accurately. In contrast, front-rear section alignment is very critical in the Wolter 1 geometry but the coalignment of the optic axes is not as critical.

However, the KB geometry is inferior to the Wolter in the following respects. In part because the KB geometry is inherently a segmented telescope achieving very high angular resolution like that of the Chandra mirrors is not feasible. Up to about 10 arc minutes off axis, the theoretical angular resolution of the Wolter is superior. For small angles the off-axis resolution of the KB telescope varies linearly with angle whereas it varies as the square of the angle for the Wolter 1. At a fixed focal length the bandwidth of the Wolter mirror is larger because its two reflections occur in series whereas the two reflections of the KB are orthogonal. Consequently KB reflector graze angles are higher; so their reflectivity is generally lower at higher energies. On the other hand the aperture of a KB telescope is filled with a smaller number of reflectors and has therefore lower mass than a Wolter. However, the aperture efficiency of the KB geometry is less than the Wolter's because open area is lost due to the finite thickness of the reflectors in both dimensions. The loss occurs in just one dimension for the Wolter because the parabolic and hyperbolic sections of the telescope are aligned or, for electroformed telescopes, consist of a single continuous shell. This is a less important issue when the substrate material is very thin. The article by Hudec that appears in this issue discusses KB telescopes.

4.5. The Lobster-Eye Telescope. The lobster-eye telescope differs from all the others in that its area and resolution are essentially independent of angle. Its principal application is very broad sky surveying, monitoring, and positioning soft X-ray transient and variable sources including X-ray components of gamma-ray bursts, their X-ray afterglows, X-ray "flashes", and certain Type 2 supernovas as well as other known and any yet to be discovered soft X-ray time variable phenomena from random directions. Its function in the soft X-ray band would be similar to that of the coded mask BAT (Swift) in the hard X-ray band and that of Fermi in the gamma-ray band. As shown by the fortuitous discovery of a soft X-ray flare from a supernova while the Swift XRT was observing the X-ray afterglow of a gamma-ray burst [46] the variable soft X-ray sky contains sources that BAT and Fermi would not detect.

The concept for one dimension was introduced by Schmidt [47] and independently in a 2D geometry by Angel [48], who noting, its resemblance to crustacean eyes, gave it the memorable name. The geometry in one dimension is shown in Figure 13. A real instrument is unlikely to cover such a large angle.

This geometry is not suitable to imaging extended X-ray sources. Its intrinsic angular resolution is inferior to both Wolter and KB telescopes and its point response function is rather complex. It includes a considerable number of X-rays that are not reflected in either one or both dimensions. As a result nearly as much or more power appears in multiple side lobes as in the main image. A hybrid 1D lobster-eye plus an orthogonal 1D coded aperture concept was described by Gorenstein and Mauche [49]. The hybrid has significantly more area and greater bandwidth than the 2D optic but the background contained in a line is much higher than the background in a point-like image. A small 1D lobster-eye prototype was constructed by Gorenstein et al. [50] Hudec et al. [51] constructed both orthogonal 1-D halves of a small lobster-eye telescope. A very light weight 2-D lobster-eye telescope prototype was made from square channel plates by Fraser et al. [52] and is undergoing further development. Because the square cells are very small, the core angular resolution is potentially rather high although there will still be side lobes from rays that are not reflected or reflected more than once in either dimension.

Lobster-eye X-ray imaging systems are discussed in the article by Hudec in this issue.

4.6. Multilayer Coatings: Normal Incidence X-Ray Telescopes and Hard X-Ray Telescopes.

4.6.1. Multilayer Coatings. A multilayer coating consists of alternate layers of two materials with very different indices of refraction, that is, a heavy material and a light material. Examples of heavy materials used in multilayer coatings are cobalt, nickel, tungsten, and platinum. Low-density coating materials include carbon, boron carbide, and silicon. The virtuous property of multilayer coatings is that they reflect at angles of incidence larger than the critical angle of the densest materials. Spiller [5, Chapter 7] discusses multilayer structures and the equations governing their reflection properties. At every plane where there is an abrupt change

in the index of refraction, a fraction of the incoming beam is reflected. If the reflected beams from successive layers are in phase, the amplitude of the net-reflected beam is greatly enhanced. The action is very similar to that of a Bragg crystal but the wavelengths are longer. However, X-rays are still absorbed as usual by the materials; so the goal is to reflect the X-ray before it can be absorbed by the coating along its incoming and outgoing paths. The intensity of the reflected beam is less, considerably less, at very large angles of incidence than the incident beam. Multilayer coatings benefit focusing telescopes at both the low-energy and high-energy boundaries of the X-ray band. The reflectivity of a multilayer at angles much larger than the critical angle of grazing incidence is shown in Figure 14 [5, Figure 9.5].

On the low-energy end, that is, <0.25 keV they make normal incidence telescopes possible. At high energy grazing incidence telescopes with multilayer coatings can have significant effective area up to 80 keV, and even higher energy, under certain conditions, although with decreasing efficiency and smaller field of view.

Interface roughness is a much more critical factor in the reflection efficiency of a multilayer than of a single coating. It reduces the sharpness of the change in the index of refractions that exists at each boundary between the two materials. The result is lowering the reflection efficiency at each interface, which is particularly destructive because of the dependence upon coherence of reflection at several interfaces. Two factors influence the interface roughness. One is the physical roughness of the substrate. In most common deposition processes the substrate's roughness will propagate to every interface of the multilayer. The other factor is interdiffusion of the two materials. Both diminish the abruptness of the change in refractive index at the interface between the two materials and as a result diminish its contribution to the amplitude of the reflected rays.

4.6.2. Normal Incidence Soft X-Ray Telescopes

Angular Resolution and Bandwidth. With grazing angles of the order of a few degrees for each of two reflectors the physical area of the substrates of a grazing incidence telescope is the order of a hundred times larger than their projected area. Furthermore, the projected area of a Wolter mirror shell is a narrow annulus that occupies only a fraction of the aperture it encloses. Limited by the allowed mass and cost, the telescope will contain several or even many concentric Wolter pairs that have to be aligned coaxially to a common focus. In contrast the physical area of a normal incidence mirror and the projected area of the aperture are (almost) identical. Therefore a normal incidence telescope has comparatively very light weight. The amount of surface area that has to be machined and polished to an accurate figure is much smaller. There is no need to coalign multiple mirror shells. With those factors in its favor it is reasonable to expect that the angular resolution of a normal incidence telescope will be superior to that of a grazing incidence telescope and will be much less expensive. It should be possible to fabricate a normal incidence telescope that is diffraction limited with an angular resolution of a milliarcsecond or better while Chandra's half arc second resolution may be better than a large area grazing incidence telescope ever achieves.

However, normal incidence X-ray reflection occurs only with multilayer coatings with a constant period. The bandwidth is very small. The reflection efficiency is low and is significant only at very low energies. In fact, the Sun is the only target whose X-rays are currently being observed by a normal incidence telescope. Its three-million-degree thermal spectrum is populated with lines from highly ionized, C, O, Ne, Fe, and other ionic species whose intensity is enough to be imaged individually. Line intensities and their ratios are important plasma diagnostics. To image multiple solar lines a normal incidence telescope on the TRACE spacecraft is divided into several pie sectors, each coated according to a different multilayer prescription tuned to a specific line. A rotatable blocking aperture with an open pie section plus a detector that can accumulate and readout upon command allows the Sun to be imaged in several lines sequentially.

Figure 7 is an image of the 6.35 nm line of the solar corona taken by the Normal Incidence X-Ray Telescope (NIXT) from a sounding rocket in July 1991 near a time when the Sun was in total eclipse when viewed from the Big Island of Hawaii, Mexico, and Central America. The circular edge of the Moon can be seen at the right.

To counter the low efficiency for use in cosmic X-ray astronomy, Windt et al. [53] described a configuration consisting of an array of multiple normal incidence telescopes that can function either individually or in concert as an interferometer. They point out that the optics technology and manufacturing tools already exist. Normal incidence optics very similar to what they describe is being employed by the photolithography industry to image EUV patterns for the production of densely populated integrated circuits [54].

However, while normal incidence telescopes may be effective in a few observations involving very soft solar and stellar X-rays, their scope is very limited.

4.6.3. High-Energy Telescopes. Christensen et al. [55] showed that a multilayer coating consisting of alternate layers of a heavy and light material whose period decreases gradually with depth is able to reflect harder X-rays at angles significantly higher than its critical angle. The reflection mechanism is similar to what occurs in normal incidence reflection. However while the multilayer coatings of a normal incidence telescope have a uniform period and a very small bandwidth, the depth variable period of a hard X-ray multilayer reflector is effective over a broad bandwidth. A hard X-ray will penetrate the multilayer stack until it arrives at the depth where the Bragg condition is fulfilled sufficiently by a range of consecutive layers (Figure 15). There it will reflect with a significant fraction of the hard X-rays surviving absorption by the heavier material along the incoming and outgoing paths.

This method of broadening the bandwidth is not effective at low energies because the absorption is too strong.

Figure 16 is the reflectivity of a W/Si multilayer at an angle of incidence of 3.0 mrad as a function of energy and that of gold as measured in monochromatic X-ray beams at the European Synchrotron Radiation Facility [6]. In Figure 16 the reflectivity of gold begins to fall rapidly at 20 keV while the reflectivity of the multilayer which is declining at the critical angle resumes at higher energy when the coherent contribution of the multilayer becomes effective as the absorption diminishes. The reflectivity is significant up to the 68 keV K edge of tungsten. The oscillations in the reflectivity of the multilayer as a function of energy that is characteristic of monoenergetic X-rays are smoothed to a large extent in practice because the hard X-ray spectra of cosmic sources are generally continuous and the events are accumulated in energy channels of finite width. In addition a telescope is likely to contain multiple concentric reflectors with a range of graze angles, whose contribution in total also results in smoothing the effective area as a function of energy. However, small amplitude oscillations in effective area versus energy may still persist; so multilayer-coated telescopes require a much more detailed calibration than telescopes with single metal coatings.

Gold, platinum, and iridium have finite reflectivity at higher X-ray energies only for very small graze angles compared to multilayer coatings. The difference in effective area above 20 keV between Wolter telescopes with multiple mirror shells with gold (or platinum or iridium) and W/Si coatings is even larger than the impression given by Figure 16 because the mirrors at larger graze angles where gold does not reflect have more geometric area.

Several missions with multilayer-coated hard X-ray telescopes are in development or have been proposed that take advantage of the broader bandwidth. The first will be NuSTAR, a NASA Small Explorer mission with the Danish Technical University providing the multilayer coatings, that is scheduled for launch in 2012 (http://www.X-ray.caltech.edu/). The other missions are Astro-H of Japan (http://heasarc.gsfc.nasa.gov/docs/astroh/), a hard X-ray imaging/Polarimetry mission by Italy [56], and a hard X-ray telescope for the International X-Ray Observatory.

5. The Laue Crystal Telescope

At energies above 80 keV it becomes increasingly difficult and eventually impossible to focus X-rays by grazing reflection with any type of coating. However, the band from 150 keV to a few MeV includes both the continuum of AGN spectra and nuclear lines. The signals are faint and detector background per square centimeter is high. Bragg and Laue scattering are processes that can focus or more accurately concentrate very high-energy X-rays/gamma-rays onto a small area detector. The distinction between the two virtually vanishes at very high energies. Telescopes consisting of an array of mosaic crystals have been constructed to address this regime. The principal centers of activity are currently the University of Toulouse [7, 57] and the University of Ferrara [58, 59].

The orientation of each crystal is adjusted such that it diverts a narrow energy range of the incoming parallel beam to the focus. Each crystal is actually a mosaic of many smaller crystals whose orientation varies slightly. A gamma-ray entering the crystal will be reflected when it encounters a section of the crystal where the Bragg condition is fulfilled. The imperfections are beneficial because the mosaic arrangement of the crystallites results in a larger bandwidth.

The angular resolution of the optics is expected to be about an arc minute and the field of view, 5 to 10 arc minutes. Depending on the energy Laue crystal optics have longer focal lengths than grazing incidence optics. Therefore expandable optical benches or short distance formation flying between optics and detector are required. An international consortium has proposed to ESA to develop a major hard X-ray/gamma-ray mission based upon a Laue crystal telescope [60].

There was a successful balloon flight of this type of instrument, which detected soft gamma-rays from the Crab Nebula [1].

The paper entitled "Laue gamma-ray lenses for space astrophysics: status and prospects" by Frontera and Von Ballmoss that appears in this issue provides a more detailed description of this technique.

6. Diffractive and Refractive X-Ray Optics

6.1. Limitations on the Angular Resolution of Grazing Incidence Telescopes. Although Chandra's 0.5 arc second angular resolution is far short of its 1 keV diffraction limit of 14 milliarcseconds, it will be difficult for a sizable future generation grazing incidence X-ray telescope to improve upon it. The quantity of substrate area that was machined, polished, and iridium-coated for Chandra is about 250 times larger than its effective area, and this ratio would be about the same for a future high angular resolution grazing incidence telescope.

To avoid the intolerable problems of large mass and thicker substrates that larger integral mirror shells would require, the mirrors will almost certainly have to be segmented into smaller and thinner parts. While it reduces the telescope's mass, segmentation increases the number of substrates required to have the correct figure and be aligned. The only viable approach to better figure control is employing "active optics", which consists of attaching piezoelectric or other type controllers to the rear face of deformable substrates and working interactively to form the figure. This process is under study for the future Generation-X observatory, which has a resolution goal of 0.1 arc second [63]. Gen-X effective area goal is 50 m^2 at 1 keV, nearly three orders of magnitude larger than that of Chandra. This author's view is that larger size future grazing incidence telescopes will at best be able to achieve only a modest improvement upon Chandra's resolution. Significant improvement requires a technology that is not based upon grazing incidence optics. Normal incidence optics with multilayer coatings is an option that has been very successful in obtaining high-resolution X-ray images of the solar corona. However, as noted in Section 4.6.2 normal

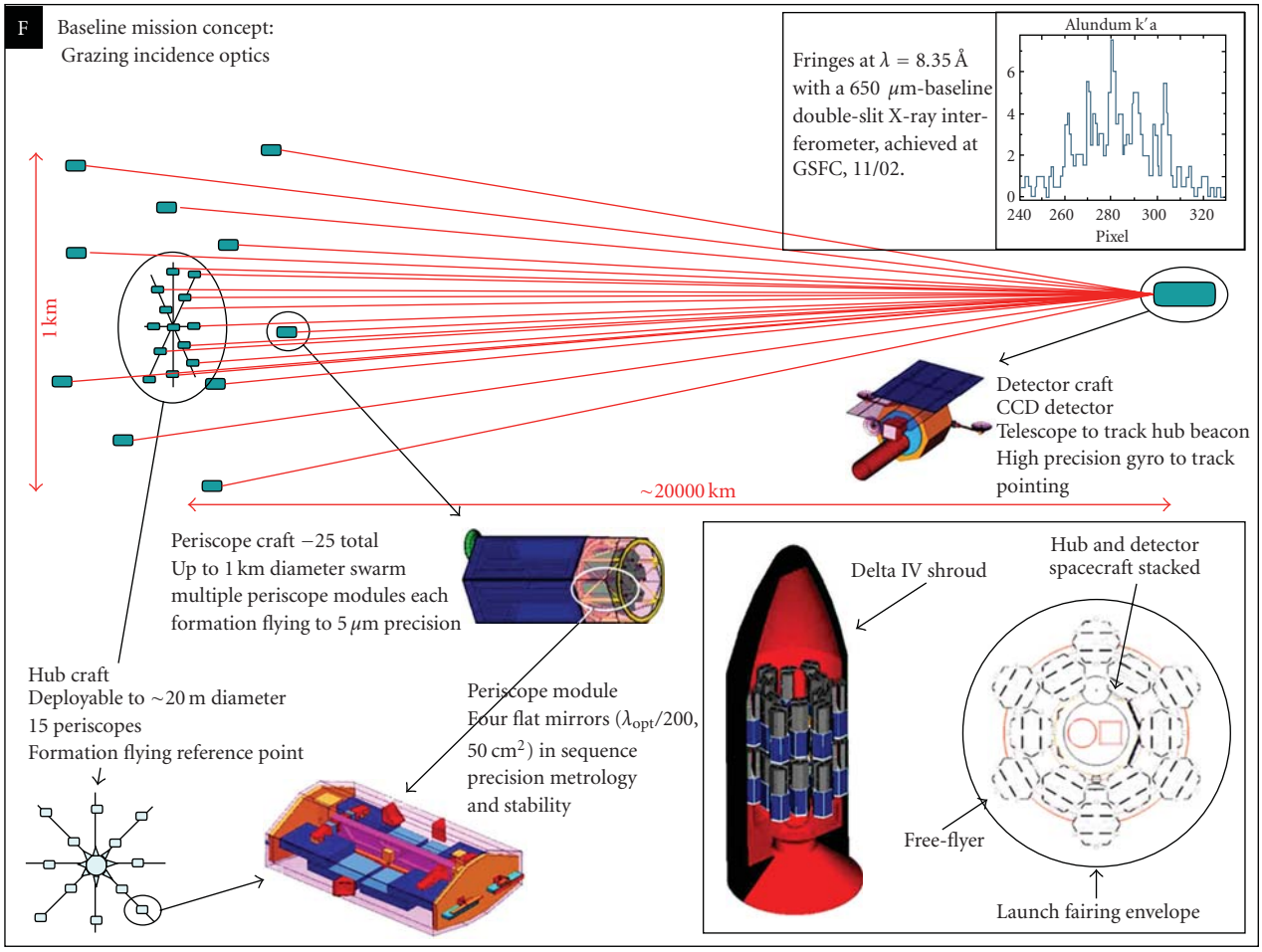

Figure 20: A possible configuration for an X-ray interferometer, Gendreau et al. [61]. In this example each of the collector optics are "periscopes" consisting of four grazing flat reflectors in series aligned such that the outgoing X-ray is insensitive to small angle rotations of the periscope [62].

incidence telescopes have low reflection efficiency and are effective only at long wavelengths and only over a very small bandwidth that must include a strong line to collect a sufficient number of photons. It is at best a special purpose device limited to imaging thermal X-ray lines with energies below one-quarter keV in nearby stars. Its scope is much too limited to be the technology for a future generation versatile high angular resolution cosmic X-ray observatory.

6.2. X-Ray Transmission: Diffraction and Refraction

6.2.1. Introduction. An alternative approach to higher angular resolution X-ray optics is based upon components that transmit rather than reflect X-rays. They include various levels of diffractive Fresnel zone plates (FZPs), which act as converging lenses, and refractive lenses [64], which can be either converging or diverging. Very small devices of both types are used routinely in experiments and microscopy at X-ray synchrotron radiation facilities. However with very intense, monochromatic beams at their disposal, laboratory scientists are not confronted with the problems of chromatic aberration, which is a characteristic of these devices. The sub-millimeter diameter of the laboratory devices frees them from the problems of very long focal lengths that are required by the meter and larger size components for astronomy.

Researchers at Tubingen University in Germany obtained images of the sun with very small Fresnel zone plates [65]. A few researchers have begun to consider diffractive-refractive optics as an option for high angular resolution X-ray astronomy [66–69]. However, a critical enabling technology, precision formation flying between widely separated spacecraft, does not yet exist. X-ray telescope missions will continue to be based exclusively upon grazing incidence optics as far one can foresee leaving ample time for better or worse to develop the formation flying capability and for the diffractive-refractive optics concepts to mature.

6.2.2. Chromatic Aberration and Resolution. The major issues for diffractive and refractive optics are that both are highly chromatic and that they have very low focusing power, resulting in the devices having extremely long focal lengths. The focal length of an FZP varies as the first power of

the energy, a lens as the second power. Skinner [66, 67] and at about the same time Van Speybroeck [70] in an unpublished memo described combinations of a FZP with an diverging refractive lens that correct chromatic aberration over a limited but significant range of bandwidth.

As described in the article by Skinner that appears in this issue, chromatic aberration can be corrected to first order when an optic consisting of a diffractive zone plate and a refractive lens is in direct contact. This occurs at the energy where the focal length of the lens is equal to minus twice that of the zone plate. That is the resolution and the first derivative of the combined focal length as a function of energy is zero. If the zone plate and lens are separated by the appropriate distance, a second-order correction can be achieved at a particular energy, that is, an energy where the resolution and its first and second derivatives as a function of the distance between the detector and optics are zero.

An example of the variation with energy of the resolution as a function of distance of the image from the optics is shown in Figure 18 for both cases. The average angular resolution as limited by chromatic aberration deteriorates as the bandwidth selected by utilizing the detector's energy resolution increases.

Figure 18 is a calculation of the contribution of chromatic aberration to the angular resolution of a diffractive-refractive pair whose focal lengths and separation satisfy the condition for a first-order correction (blue dotted line) and second order correction (red solid line). In both cases the prime energy is 6 keV and diffractive element is the basic Fresnel zone plate. For this calculation the diameter of the diffractive optic is 25 m and the focal length for the 1st order correction is 27,000 km. In the simulated 1st order correction the contribution of chromatic aberration to the resolution is less than 1 milliarcsecond from 5.7 to 6.5 keV. In the simulated 2nd order correction the contribution of chromatic aberration is less than 200 microarcseconds between 5.5 and 6.5 keV. However, the 2nd order system requires three spacecrafts to engage in precision formation flying and would not be considered until a later phase. The 6 keV diffraction limit as determined by the diameter of the components is not taken into account in Figure 17.

Transparency of the refractive lens is a major issue. It can be the most important factor driving the focal length to high values and it determines the lower limit on energy. The radius of curvature of the lens varies directly with the focal length. For a given diameter a larger radius of curvature results in a thinner lens. If a simple full body lens would be too opaque, its spherical or parabolic surface would be stepped back to a reference plane and become a Fresnel lens consisting of concentric zones, each zone with the same figure it had on the original parabolic surface. A refractive Fresnel lens configured like that made of a very light material such as beryllium can have very good transmission at 6 keV. If that is done for transparency without paying attention to maintaining phase coherence, each ring is essentially an independent lens. Their intensities will add. rather than amplitudes The diffraction limit will then be determined by the average width of the zone rings rather than the full lens diameter.

For a metal lens there is a small loss of efficiency due to large angle Laue scattering by the crystal planes of the metal.

6.2.3. Advantages of a Transmitting Optic. The most obvious advantage of a transmitting optic is that the areas of the aperture and the substrate are equal. The mass of a transmitting optic is a factor of 10^2 smaller than its grazing incidence counterpart. With essentially no depth other than a web of support structure for the FZP and lens, an optic (or several optics with different energy bands) can be stowed for launch and deployed in space. These favorable attributes are tempered by the fact that the product of the transmission and bandwidth is low. The efficiency of the simple zone plate with alternating open and closed zones is only 10% in the first-order image, with the rest being in the zero-order and fainter, higher-order images that mostly do not arrive at the detector. For comparison, the aperture efficiency of the 1.2 m diameter Chandra telescope is also only about 10%. As described by Skinner [66] FZPs with a surface that is contoured or blazed to maintain phase over the entire aperture can have much higher efficiency at several energy intervals within a limited range of bandwidth.

Figure errors have much more impact upon the resolution of reflective optics than upon that of refractive optics. If the local slope of a reflector has an error of θ, the direction of the reflected ray will have an error of $2 \cdot \theta$. When the ray is refracted at the interface between two media, the error is much smaller especially if there is only a small difference between the two indices of refraction. In the X-ray band the index of refraction of all materials is less than the vacuum's by a very small quantity, δ. It is shown in Appendix A that for small angles the relation between the slope error at the interface between the lens and vacuum, θ, and the direction of the refracted ray is $\delta \cdot \sin(\theta)$. For a refractive lens made of beryllium the values of δ at X-ray energies range from 10^{-5} to 10^{-6}.

Surface roughness has much less influence upon diffractive-refractive optics than it does upon grazing incidence optics. A surface roughness of 10 nm would be disastrous for the efficiency of grazing incidence reflection at X-ray energies. However, assuming that the effect of surface roughness of a transmitting optic is to vary the path length of an X-ray passing through the material, 10 nm variations in path length through beryllium will result in very small variations in the phase over the area of the incident beam. The coherence of a beam traversing the optic will not be disrupted significantly.

While the small difference in refractive indices between the optic and vacuum mitigates the effects of slope errors and surface roughness, it also results in focal lengths being extremely long. A refractive optic with a diameter of 1 m will have focal length of the order of 10^3 kilometers. Grazing incidence optics cannot benefit from very long focal lengths. The projected area of a mirror substrate would diminish and its mass would become larger as the length of the substrates increases to mitigate the reduction in projected area.

With less sensitivity to slope errors and surface roughness plus a much higher ratio of effective area to physical area diffractive and refractive optics should be much less

expensive to construct and have lower mass than grazing incidence telescopes.

However, it should be noted that although the angular resolution of diffractive-refractive telescopes may be very superior to Chandra's and the effective area larger within the energy band that is corrected for chromatic aberration, the sensitivity may not be superior. The very long focal length results in pixels with a large physical size that is more susceptible to cosmic ray-induced background. Also the detector is so far removed from the optics that the space between them cannot be enclosed to exclude background from diffuse cosmic X-rays and other sources. In any formation flying configuration the detector requires a local collimator, which is not nearly as effective in excluding diffuse X-ray background as the complete cover that exists over the space between a grazing incidence optic and a detector that are aboard the same spacecraft.

Diffractive-refractive X-ray optics including correcting chromatic aberration are described in more detail in the article by Skinner that appears in this issue.

7. X-Ray Interferometry

An X-ray interferometer is the ultimate tool for high angular resolution X-ray measurements and most likely for all of astronomy. The possibility of X-ray interferometry was demonstrated by Cash et al. [71] who observed interference fringes in the laboratory. There are many potential applications for an X-ray telescope with super high angular resolution. The crowning achievement would be an image of the event horizon of a super massive black hole (SMBH). A mission concept named the Black Hole Imager and its technical requirements were submitted as two "White Papers" to the U. S. National Academy of Science's Decadal Review of Astronomy and Astrophysics. One described the scientific significance of observing SMBHs at the centers of active galaxies [72, 73]. The other discusses the technology that would have to be developed to enable the measurements [61].

The resolution required to image a SMBH in an nearby external galaxy is about 0.1 microarcseconds. A few microarcsecond resolution would suffice for imaging the relatively small SMBH at the center of our galaxy, Sgr A*. However, the absorption along the line of sight in the galactic plane to Sgr A* may obscure important features of the event horizon and corona. Furthermore, several SMBH images are needed to obtain a consistent picture that not influenced by anomalous local conditions that is may exist at a single object.

For the diffraction limit to be below 0.1 microarcsecond at 6 keV, the diameter of the optics would have to exceed 500 m. Of necessity the Black Hole Imager would be a sparse aperture telescope, that is, an array of optics aboard separate spacecraft whose total area fills only a small fraction of the aperture. The system would resemble that of the optical/UV Stellar Imager concept [74], which consists of 30 static elements across 500 m. In a study for the NASA Institute for Advanced Concepts, Cash [75] estimated that an X-ray interferometer system would require a few dozen spacecraft to obtain a suitable image. As an alternative fewer elements can be used with changes in their alignments that create new baselines. The major differences are that the 10 km Stellar Imager focal lengths are much shorter than the Black Hole Imager's and the resolution in the optical/UV band is 0.1 milliarcsecond as compared to 0.1 microarcsecond at the X-ray energies. Also, the X-ray array has to be more stable and their relative positions known more accurate.

One of the outstanding issues is what the individual X-ray focusing or concentrating collectors should be. Currently the baseline collector is a "periscope" consisting of four flats in a grazing incidence configuration [62]. This geometry acts like a thin lens in that a slight tilt in direction does not affect the ray's outgoing direction. Appendix B shows a possible configuration for an X-ray interferometer with periscope collectors. However, the periscopes are massive and suffer from the shortcomings of grazing incidence reflection, such as sensitivity to local slope errors of the flats. Diffractive-refractive collectors would be much lighter, less expensive, and less sensitive to slope errors. However, the effect of chromatic aberration would have to be evaluated. For observing interference fringes a certain level of chromatic aberration may be tolerable when the detector is a cryogenic device with an energy resolution of 2 to 3 eV capable of recording interference patterns in narrow energy bands. More simulation studies are required to understand all the issues that affect X-ray interferometry, including whether or not a grazing incidence periscope or a diffractive-refractive pair is suitable collector.

8. Prospects for the Future

8.1. Current and Future X-Ray Missions with Focusing Telescopes. In 2010 four spacecrafts with focusing X-ray telescopes are operating. They are the Chandra X-Ray Observatory, XMM-Newton, Suzaku, and the Swift XRT. All appear to be in good health and have ample reserves of consumables, and the number of proposals from scientists hoping to utilize their capabilities remains high. In fact, the rate of oversubscription for observing time on the Chandra X-ray Observatory has not diminished after eleven years of operation. We can expect all of them to continue operations for an indefinite period. The Japanese space agency may possibly end support for Suzaku when a mission currently under development, Astro-H, is launched in a few years.

Table 2 lists the new missions which feature focusing X-ray telescopes that are in development plus three that have significant support from the astrophysics community but have not been approved. Those that have nominal launch dates have been approved or are likely to be approved. GEMS (http://heasarc.gsfc.nasa.gov/docs/gems/) is an X-ray polarimetry mission that has been selected for flight by NASA with the tentative launch date of 2014. The focusing telescope acts as a concentrator rather than as an imager; the targets are mostly point sources. eRosita [76] is the core instrument on the Russian Spektrum-Roentgen-Gamma (SRG) mission which is scheduled for launch in late 2012. The science driver is the detection of 50–100 thousand

clusters of galaxies up to redshift $z \sim 1.3$ in order to study the large-scale structure in the Universe and test cosmological models including Dark Energy.

NHXM and WFXT are included in Table 2 while other mission concepts have not because these two concepts are recognized as potential missions by the Italian Space Agency as well as from a team of astrophysicists. NHXM [56] consists of four identical telescopes with multilayer coatings. Three of the four telescopes will have at their focus identical spectral-imaging cameras while the fourth will have an imaging X-ray polarimeter. Other small-and medium-scale X-ray telescope missions are likely to be proposed in response to future announcements of opportunity from the space agencies.

While its launch date is very far off, the Generation-X mission concept [63] was the subject of a NASA-funded study and is generally recognized internationally as the successor to IXO.

In addition there may be other missions such as EXIST (http://exist.gsfc.nasa.gov/) where a focusing X-ray telescope is an important adjunct, not a component of the principal instrument.

IXO is the flagship mission of the major space agencies. Except for Gen-X, which is in the concept definition, phase IXO is the only observatory class mission of this group. Its major distinguishing capability is high-resolution spectroscopy from 0.15 to 10 keV with very high collecting area plus a hard X-ray telescope to measure the continuum up to ~80 keV. While its angular resolution cannot match Chandra's, it will be better than XMM-Newton's and is the best of this group (if Gen-X is not included). While Chandra is providing a library of high-resolution X-ray images, neither it nor XMM-Newton has the spectroscopic resolution and throughput required for a quantitative or in some cases even a qualitative understanding of the astrophysical processes occurring in those environments. IXO will provide that spectroscopic capability.

IXO will have a grating spectrometer (http://constellation.gsfc.nasa.gov/technology/xgs.html) that disperses X-rays. The final configuration has not yet been determined. Both of the two concepts under consideration by limiting the range of azimuth covered by the gratings and dispersing orthogonal to the plane of reflection make the spectral resolution less sensitive to the PSF of the telescope [77].

8.2. Developing New Technology for High Angular Resolution X-Ray Telescopes. Except for Gen-X (http://www.cfa.harvard.edu/hea/genx/) the essential technologies required by the missions appearing in Table 2 already exist even if they have not yet reached the state of development that fulfills NASA's and ESA's highest "Technology Readiness Levels" (TRLs). They need support for the final effort required to meet those goals.

The areas that are essentially still in the concept phase and require major technical development include the grazing incidence active optics for the Generation-X observatory, diffractive-refractive imaging, and X-ray interferometry. It is not possible to provide launch dates for missions based upon those concepts.

Gen-X's angular resolution goal is 0.1 arcsecond on axis, a factor of five better than Chandra's on-axis resolution. NASA supported an initial concept study of the optics for Gen-X. Given the very large collecting area and the characteristic feature of grazing incidence optics that the physical area of the substrates is some hundred times later than their effective collecting area the techniques used to create the figure and polish the substrates of Chandra cannot be applied to Gen-X. Also, whereas each mirror of Chandra is two integral cylinders in series whose thickness increases with shell radius, the many larger radii mirrors for Gen-X will have to be segmented into multiple, light-weight parts to keep the mass under control and innovative methods of figure formation need to be developed. It is expected that meeting Gen-X's angular resolution goals will require active optics. That is, the substrates will be furnished with controllers that allow the figure to be controlled interactively both on the ground and in orbit.

In contrast to Gen-X, fabricating the optics for a diffractive-refractive imaging telescope should not be difficult. High-accuracy machining should be sufficient, although lithography may be needed to create small-scale features for blazing. The enabling technology that is lacking is not related directly to the optics or detectors; it is mission operations, long distance formation flying between two spacecrafts (or possibly three at a later stage) in particular. Only one of the spacecrafts can be in true orbit. The other (others) would have to be powered, most likely by ion engines to maintain their alignment. The target, the optics, and the detector have to be aligned along a common axis with an accuracy of a centimeter in the two lateral dimensions in order for the image to land on the detector. The distance between the optics and detector, which is relatively easy to determine, has a much larger margin. An efficient means of finding and changing targets has to be developed. One efficiency booster would be employing two detector spacecrafts. While one is observing, the other is proceeding to the next target position. Although NASA and ESA are studying systems for measuring the positions of widely separated spacecraft accurately for LISA, a general relativity experiment, they are not addressing the issue of aligning them accurately.

The very long focal lengths required by diffractive and refractive X-ray optics preclude laboratory testing and calibration of a full size system in X-rays. Testing will have to be performed with centimeter size models rather than with actual, meter size optics. Some tests may be performed with visible light. Also, because the concepts are relatively new, more simulation studies have to be performed to resolve issues like how to best increase the bandwidth while dealing with chromatic aberration and to what degree it is possible or desirable to blaze the components to maximize the throughput and resolution in certain energy bands possibly at the expense of others.

X-ray interferometry has the most technology issues to resolve, for example, defining the nature and method of fabrication of the collector optics, establishing and maintaining accurate alignment of up to some thirty spacecraft distributed over a kilometer, as well as formation flying

Table 2: Future missions with focusing X-ray telescopes.

Mission or telescope	Agencies or countries	capabilities	Nominal launch date
International X-Ray Observatory (IXO)	NASA/ESA/JAXA	High-Resolution, High-Throughput X-ray Spectroscopy with Cryogenic Detectors and Dispersive GratingsSoft/Hard X-ray Imaging X-ray Polarimetry and Timing	202?
NuSTAR	NASA	Hard X-ray Imaging	2012
eRosita (SRG) [76]	Germany/Russia	X-ray Survey	2012
Astro-H	Japan (JAXA)	X-ray Spectroscopy with Cryogenic DetectorHard X-Ray Imaging	2013
GEMS	NASA	X-Pay Polarimetry	2014
New Hard X-ray Mission (NHXM)	Italy (with collaborators)	Soft/Hard X-rayImaging X-Ray Polarimetry	To be determined
Wide Field X-ray Telescope (WXFT)	Italy/US	Cluster Evolution Medium Deep Survey	To be determined
Generation-X	NASA (funded study)	High angular resolution active optics, Very large collecting area, High Res. Spectroscopy, Polarization, and Timing.	Concept, Requires New Technology

between all the optics spacecraft and a detector some 10^4 km distant. A great deal of effort has to be applied to quantitative simulations of the performance. An X-ray interferometer and Stellar Imager have several issues in common including formation flying, maintaining the stability of a cluster of spacecraft, and reforming the configuration when the target position is changed. The common need should motivate the space agencies to proceed with the development of formation flying technology.

Appendices

A. Error in the Direction of a Refracted Ray

See Figure 19.

B. Black Hole Imager/X-Ray Interferometer

See Figure 20.

References

[1] P. Von Ballmoos, H. Halloin, J. Evrard et al., "CLAIRE: first light for a gamma-ray lens," *Experimental Astronomy*, vol. 20, no. 1–3, pp. 253–267, 2006.

[2] D. H. Lumb, F. E. Christensen, C. P. Jensen, and M. Krumrey, "Influence of a carbon over-coat on the X-ray reflectance of XEUS mirrors," *Optics Communications*, vol. 279, no. 1, pp. 101–105, 2007.

[3] G. G. Pavlov and G. J. M. Luna, "A dedicated chandra acis observation of the central compact object in the cassiopeia a supernova remnant," *Astrophysical Journal*, vol. 703, no. 1, pp. 910–921, 2009.

[4] L. Golub, "The solar X-ray corona," *Astrophysics and Space Science*, vol. 237, no. 1-2, pp. 33–48, 1996.

[5] E. Spiller, *Soft X-Ray Optics*, chapter 8, SPIE Press, Bellingham, Wash, USA, 1994.

[6] K. Joensen, "Discovery of a Central X-Ray Object in the Cygnus Loop," Ph.D. thesis, Physics Department, University of Copenhagen, 1995.

[7] J. Rousselle, P. von Ballmoos, N. Barrière et al., "High-Z crystals for gamma-ray optics," in *Optics for EUV, X-Ray, and Gamma-Ray Astronomy IV*, vol. 7437 of *Proceedings of SPIE*, August 2009, 74370L.

[8] P. Gorenstein, W. Cash, N. Gehrels et al., "The future of high angular resolution X-ray astronomy," in *Space Telescopes and Instrumentation 2008: Ultraviolet to Gamma Ray*, vol. 7011 of *Proceedings of SPIE*, 2008, 70110U.

[9] B. Aschenbach, "Boundary between geometric and wave optical treatment of X-ray mirrors," in *Optics for EUV, X-Ray, and Gamma-Ray Astronomy II*, vol. 5900 of *Proceedings of SPIE*, pp. 1–7, August 2005, 59000D.

[10] B. Aschenbach, "X-ray telescopes," *Reports on Progress in Physics*, vol. 48, no. 5, pp. 579–629, 1985.

[11] M. J. Hardcastle, R. P. Kraft, G. R. Sivakoff et al., "New results on particle acceleration in the Centaurus A jet and counterjet from a deep Chandra observation," *The Astrophysical Journal*, vol. 670, no. 2, pp. L81–L84, 2007.

[12] J. Kataoka and Ł. Stawarz, "X-ray emission properties of large-scale jets, hot spots, and lobes in active galactic nuclei," *Astrophysical Journal*, vol. 622, no. 2, pp. 797–810, 2005.

[13] S. W. Allen, D. A. Rapetti, R. W. Schmidt, H. Ebeling, R. G. Morris, and A. C. Fabian, "Improved constraints on dark energy from Chandra X-ray observations of the largest relaxed galaxy clusters," *Monthly Notices of the Royal Astronomical Society*, vol. 383, no. 3, pp. 879–896, 2008.

[14] A. Vikhlinin, A. V. Kravtsov, R. A. Burenin et al., "Chandra cluster cosmology project iii: cosmological parameter constraints," *The Astrophysical Journal*, vol. 692, no. 2, p. 1060, 2009.

[15] R. Giacconi, "History of X-ray telescopes and astronomy," *Experimental Astronomy*, vol. 25, no. 1–3, pp. 143–156, 2009.

[16] H. Wolter, "Spiegelsysteme streifenden Einfalls als abbildende Optiken für Röntgenstrahlen," *Annalen der Physik*, vol. 10, p. 94, 1952.

[17] A. G. Michette, "X-ray microscopy," *Reports on Progress in Physics*, vol. 51, no. 12, pp. 1525–1606, 1988.

[18] M. V. Zombeck, G. S. Vaiana, R. Haggerty, A. S. Krieger, J. K. Silk, and A. Timothy, "An atlas of soft X-ray images of the solar corona from SKYLAB," *Astrophysical Journal Supplement Series*, vol. 38, pp. 69–85, 1978.

[19] J. H. Underwood, J. E. Milligan, A. C. deLoach, and R. B. Hoover, "S056 X-ray telescope experiment on the Skylab Apollo Telescope Mount," *Applied Optics*, vol. 16, no. 4, pp. 858–869, 1977.

[20] L. P. Van Speybroeck and R. C. Chase, "Design parameters of paraboloid- hyperboloid telescopes for X-ray astronomy," *Applied Optics*, vol. 11, no. 2, pp. 440–445, 1972.

[21] B. C. Taylor, R. D. Andresen, A. Peacock, and R. Zobl, "The Exosat mission," *Space Science Reviews*, vol. 30, no. 1–4, pp. 479–494, 1981.

[22] O. Citterio, G. Bonelli, G. Conti, E. Mattaini, and B. Sacco, "High-throughput optics for X-ray astronomy (*)(**)," *Il Nuovo Cimento C*, vol. 13, no. 2, pp. 375–389, 1990.

[23] E. Costa, F. Frontera, J. Heise et al., "Discovery of an X-ray afterglow associated with the γ-ray burst of 28 February 1997," *Nature*, vol. 387, no. 6635, pp. 783–785, 1997.

[24] P. J. Serlemitsos, L. Jalota, Y. Soong, H. Kunieda, Y. Tawara, and Y. Tsusaka, "The X-ray telescope on board ASCA," *Publications of the Astronomical Society of Japan*, vol. 47, no. 1, pp. 105–114, 1995.

[25] A. Furuzawa, T. Miyazawa, K. Yasufumi et al., "The current status of the reflector production for ASTRO-H/HXT," in *Space Telescopes and Instrumentation 2010: Ultraviolet to Gamma Ray*, vol. 7732 of *Proceedings of SPIE*, 2010, 77323F.

[26] P. J. Serlemitsos, Y. Soong, T. Okajima, and D. J. Hahne, "Foil X-ray mirrors for astronomical observations: still an evolving technology," in *Space Telescopes and Instrumentation 2010: Ultraviolet to Gamma Ray*, vol. 7732 of *Proceedings of SPIE*, 2010, 77320A.

[27] C. J. Hailey, S. Abdali, F. E. Christensen et al., "Investigation of substrates and mounting techniques for the High Energy Focusing Telescope (HEFT)," in *EUV, X-Ray, and Gamma-Ray Instrumentation for Astronomy VIII*, vol. 3114 of *Proceedings of SPIE*, pp. 535–543, August 1997.

[28] M. A. Jimenez-Garate, C. J. Hailey, W. W. Craig, and F. E. Christensen, "Thermal forming of glass microsheets for X-ray telescope mirror segments," *Applied Optics*, vol. 42, no. 4, pp. 724–735, 2003.

[29] W. W. Zhang, "Manufacture of mirror glass substrates for the NUSTAR mission," in *Optics for EUV, X-Ray, and Gamma-Ray Astronomy IV*, vol. 7437 of *Proceedings of SPIE*, 2009, 74370N.

[30] C. J. Hailey, F. E. Christensen, W. W. Craig et al., "Overview of segmented glass optics development for the Constellation-X Hard X-ray Telescope," in *X-Ray and Gamma-Ray Telescopes and Instruments for Astronomy*, vol. 4851 of *Proceedings of SPIE*, pp. 519–527, August 2002.

[31] P. Friedrich, B. Aschenbach, C. Braig et al., "Manufacturing of Wolter-I mirror segments with slumped glass," in *Space Telescopes and Instrumentation II: Ultraviolet to Gamma Ray*, vol. 6266 of *Proceedings of SPIE*, 2006, 62661G.

[32] M. Ghigo, S. Basso, R. Canestrari, and L. Proserpio, "Development of hot slumping technique and last optical performances obtained on a 500 mm diameter slumped segment prototype for adaptive optics," in *Astronomical and Space Optical Systems*, vol. 7439 of *Proceedings of SPIE*, August 2009, 74390M.

[33] R. Hudec, V. Marsikova, M. Mika et al., "Advanced X-ray optics with si wafers and slumped glass," in *Optics for EUV, X-Ray, and Gamma-Ray Astronomy IV*, vol. 7437 of *Proceedings of SPIE*, August 2009, 74370S.

[34] M. J. Collon, R. Günther, M. Ackermann et al., "Stacking of silicon pore optics for IXO," in *Optics for EUV, X-Ray, and Gamma-Ray Astronomy IV*, vol. 7437 of *Proceedings of SPIE*, 2009, 74371A.

[35] C. J. Burrows, R. Burg, and R. Giacconi, "Optimal grazing incidence optics and its application to wide-field X-ray imaging," *Astrophysical Journal*, vol. 392, no. 2, pp. 760–765, 1992.

[36] P. Conconi and S. Campana, "Optimization of grazing incidence mirrors and its application to surveying X-ray telescopes," *Astronomy and Astrophysics*, vol. 372, no. 3, pp. 1088–1094, 2001.

[37] S. Murray and The WFXT Team, "Wide field X-ray telescope mission," White Paper, NAS Decadel Survey Committee on Astronomy, 2009, http://wfxt.pha.jhu.edu/documents/white-papers/WFXT_RFI.pdf.

[38] P. Kirkpatrick and A. V. Baez, "Formation of optical images by X-rays," *Journal of the Optical Society of America*, vol. 38, p. 766, 1948.

[39] P. Gorenstein, B. Harris, H. Gursky, R. Giacconi, R. Novick, and P. Vanden Bout, "X-ray structure of the Cygnus Loop," *Science*, vol. 172, no. 3981, pp. 369–372, 1971.

[40] S. Rappaport, W. Cash, R. Doxsey, G. Moore, and R. Borken, "Discovery of a Central X-Ray Object in the Cygnus Loop," *Astrophysical Journal Letters*, vol. 186, p. L15, 1973.

[41] M. C. Weisskopf, H. Helava, and R. S. Wolff, "An upper limit to an X-ray point source at the center of the Cygnus Loop," *Astrophysical Journal*, vol. 194, pp. L71–L74, 1974.

[42] P. Gorenstein, D. Fabricant, K. Topka, F. R. Harnden Jr., and W. H. Tucker, "Soft X-ray structure of the Perseus cluster of galaxies," *Astrophysical Journal*, vol. 224, pp. 718–723, 1978.

[43] D. Fabricant, L. Cohen, and P. Gorenstein, "X-ray performance of the LAMAR protoflight mirror," *Applied Optics*, vol. 27, no. 8, pp. 1456–1464, 1988.

[44] S. Labov, "Figured grazing incidence mirrors from reheated float glass," *Applied Optics*, vol. 27, no. 8, pp. 1465–1469, 1988.

[45] R. Willingale and F. Spaan, "The design, manufacture and predicted performance of kirkpatrick-baez silicon stacks for the international X-ray observatory or similar applications," in *Optics for EUV, X-Ray, and Gamma-Ray Astronomy IV*, vol. 7437 of *Proceedings of SPIE*, 2009, 74370B.

[46] A. M. Soderberg, E. Berger, K. L. Page et al., "An extremely luminous X-ray outburst at the birth of a supernova," *Nature*, vol. 453, no. 7194, pp. 469–474, 2008.

[47] W. K. H. Schmidt, "A proposed X-ray focusing device with wide field of view for use in X-ray astronomy," *Nuclear Instruments and Methods*, vol. 127, no. 2, pp. 285–292, 1975.

[48] J. R. P. Angel, "Lobster eyes as X-ray telescopes," *Astrophysical Journal*, vol. 233, pp. 364–373, 1979.

[49] P. Gorenstein and C. W. Mauche, "All sky high resolution cameras for hard and soft X-rays," in *High Energy Transients in Astrophysics*, S. Woosley, Ed., AIP Conference Proceedings, no. 115, p. 694, 1984.

[50] P. Gorenstein, E. Whitbeck, G. K. Austin et al., "Lobster-eye X-ray telescope prototype," in *Multilayer and Grazing Incidence X-Ray/EUV Optics III*, vol. 2805 of *Proceedings of SPIE*, pp. 74–80, August 1996.

[51] R. Hudec, A. Inneman, L. Pina, V. Hudcova, L. Sveda, and H. Ticha, "Lobster eye X-ray telescopes: recent progress,"

in *X-Ray and Gamma-Ray Telescopes and Instruments for Astronomy*, vol. 4851 of *Proceedings of SPIE*, pp. 578–586, 2003.

[52] G. W. Fraser, A. N. Brunton, N. P. Bannister et al., "Lobster-ISS: an imaging X-ray all-sky monitor for the International Space Station," in *X-Ray and Gamma-Ray Instrumentation for Astronomy XII*, vol. 4497 of *Proceedings of SPIE*, pp. 115–126, August 2002.

[53] D. L. Windt, S. M. Kahn, and G. E. Sommargren, "Concepts: X-ray telescopes with high angular resolution and high throughput," in *Hyperspectral Remote Sensing of the Land and Atmosphere*, vol. 4151 of *Proceedings of SPIE*, p. 441, 2003.

[54] C. Wagner and N. Harned, "EUV lithography: lithography gets extreme," *Nature Photonics*, vol. 4, no. 1, pp. 24–26, 2010.

[55] F. E. Christensen, A. Hornstrup, N. J. Westergaard, H. W. Schnopper, J. Wood, and K. Parker, "Graded d-spacing multilayer telescope for high-energy X-ray astronomy," in *Multilayer and Grazing Incidence X-Ray/EUV Optics*, vol. 1546 of *Proceedings of SPIE*, pp. 160–167, 1992.

[56] G. Pareschi, G. Tagliaferri, A. Argan et al., "The new hard X-ray mission," in *X-Ray Astronomy 2009; Present Status, Multi-Wavelength Approach and Future Perspectives: Proceedings of the International Conference*, vol. 1248 of *AIP Conference Proceedings*, pp. 567–576, 2009.

[57] P. Von Ballmoos, H. Halloin, G. Skinner et al., "Max—a gamma-ray lens for nuclear astrophysics," in *Optics for EUV, X-Ray, and Gamma-Ray Astronomy*, vol. 5168 of *Proceedings of SPIE*, pp. 482–491, August 2004.

[58] F. Frontera, A. Pisa, V. Carassiti et al., "Gamma-ray lens development status for a European gamma-ray imager," in *Space Telescopes and Instrumentation II: Ultraviolet to Gamma Ray*, vol. 6266 of *Proceedings of SPIE*, 2006, 626627.

[59] F. Frontera, G. Loffredo, A. Pisa et al., "Focusing of gamma-rays with Laue lenses: first results," in *Space Telescopes and Instrumentation 2008: Ultraviolet to Gamma Ray*, vol. 7011 of *Proceedings of SPIE*, 2008, 70111R.

[60] J. Knödlseder, "GRI: the gamma-ray imager mission," *Advances in Space Research*, vol. 40, no. 8, pp. 1263–1267, 2007.

[61] K. Gendreau, Z. Arzoumanian, W. Cash et al., "Black Hole Imager: What Happens at the Edge of a Black Hole?" 2009, http://maxim.gsfc.nasa.gov/documents/Astro2010/Gendreau_BHI.pdf.

[62] A. Shipley, W. Cash, K. Gendreau, and D. Gallagher, "Maxim interferometer tolerances and tradeoffs," in *X-Ray and Gamma-Ray Telescopes and Instruments for Astronomy*, vol. 4851 of *Proceedings of SPIE*, pp. 568–577, August 2002.

[63] R. Brissenden and The Gen-X Team, "Generation-X technology development program," White Paper, NAS Decadel Survey Committee on Astronomy, 2009, http://www.cfa.harvard.edu/hea/genx/media/papers/astro2010/Astro2010-Brissenden-Gen-X.pdf.

[64] A. Snigirev, V. Kohn, I. Snigireva, and B. Lengeler, "A compound refractive lens for focusing high-energy X-rays," *Nature*, vol. 384, no. 6604, pp. 49–51, 1996.

[65] G. Elwert, "X-ray picture of the sun taken with Fresnel zone plates," in *Structure and Development of Solar Active Regions*, K. O. Kiepenheuer, Ed., IAU Symposium, no. 35, p. 439, 1968.

[66] G. K. Skinner, "Diffractive/refractive optics for high energy astronomy. I. Gamma-ray phase Fresnel lenses," *Astronomy and Astrophysics*, vol. 375, no. 2, pp. 691–700, 2001.

[67] G. K. Skinner, "Diffractive-refractive optics for high energy astronomy II. Variations on the theme," *Astronomy and Astrophysics*, vol. 383, no. 1, pp. 352–359, 2002.

[68] P. Gorenstein, "Design, Fabrication, and Characterization of Multilayers for Broad-band, Hard X-ray Astrophysics Instrumentation," in *X-Ray and Gamma-Ray Telescopes and Instruments for Astronomy*, vol. 4851 of *Proceedings of SPIE*, p. 598, 2003.

[69] C. Braig and P. Predehl, "Efficient Fresnel X-ray optics made simple," *Applied Optics*, vol. 46, no. 14, pp. 2586–2599, 2007.

[70] L. P. Van Speybroeck, Internal CfA Memorandum, 2000.

[71] W. Cash, A. Shipley, S. Osterman, and M. Joy, "Laboratory detection of X-ray fringes with a grazing-incidence interferometer," *Nature*, vol. 407, no. 6801, pp. 160–162, 2000.

[72] K. C. Gendreau, W. C. Cash, A. F. Shipley, and N. White, "The MAXIM pathfinder X-ray interferometry mission," in *X-Ray and Gamma-Ray Telescopes and Instruments for Astronomy*, vol. 4851 of *Proceedings of SPIE*, pp. 353–364, August 2002.

[73] K. C. Gendreau, W. C. Cash, P. Gorenstein, D. L. Windt, P. Kaaret, and C. Reynolds, "MAXIM: the black hole imager," *Proc. SPIE*, vol. 5488, no. 3, p. 394, 2004.

[74] K. G. Carpenter, R. G. Lyon, C. Schrijver, M. Karovska, and D. Mozurkewich, "Direct UV/optical imaging of stellar surfaces: the Stellar Imager (SI) vision mission," in *UV/Optical/IR Space Telescopes: Innovative Technologies and Concepts III*, vol. 6687 of *Proceedings of SPIE*, August 2008, 66870G.

[75] W. Cash, "X-ray interferometry ultimate astronomical imaging," Final Report, NIAC, 2001, http://www.niac.usra.edu/files/studies/final_report/389Cash.pdf.

[76] P. Predehl, R. Andritschke, H. Böhringer et al., "EROSITA on SRG," in *Space Telescopes and Instrumentation 2010: Ultraviolet to Gamma Ray*, vol. 7732 of *Proceedings of SPIE*, 2010, 77320U.

[77] W. Cash, "X-ray optics: a technique for high resolution imaging," *Applied Optics*, vol. 26, pp. 2915–2920, 1987.

Hindawi Publishing Corporation
X-Ray Optics and Instrumentation
Volume 2010, Article ID 687496, 9 pages
doi:10.1155/2010/687496

Review Article

Applications of Compact Laser-Driven EUV/XUV Plasma Sources

Armin Bayer, Frank Barkusky, Stefan Döring, Peter Großmann, and Klaus Mann

Laser-Laboratorium Göttingen e.V., Hans-Adolf-Krebs-Weg 1, 37077 Göttingen, Germany

Correspondence should be addressed to Armin Bayer, armin.bayer@llg-ev.de

Received 1 February 2010; Revised 25 August 2010; Accepted 25 September 2010

Academic Editor: Ali Khounsary

We present an overview on the EUV/XUV activities of the Laser-Laboratorium Göttingen based on table-top laser-produced plasma (LPP) sources. As target materials, gaseous jets of noble gases or solid Gold are employed. In order to obtain high EUV fluence, a Schwarzschild objective consisting of two spherical mirrors with Mo/Si multilayer coatings is adapted to the source. By demagnified (10x) imaging of the Au plasma, an EUV spot with a maximum energy density of $\sim$1.3 J/cm^2 is generated (3 μm diameter, pulse duration 8.8 ns). First applications of this system reveal its potential for high-resolution modification and direct structuring of solid surfaces. Additionally, an EUV/XUV setup for structural analysis was developed. Using a gas puff target combined with a grazing incidence optics (Kirkpatrick-Baez arrangement), it offers the possibility to perform angular resolved reflectivity, diffraction, and scattering experiments. For chemical analysis of various samples, an NEXAFS setup was built, based on gaseous Krypton as a broadband emitter in the water-window range around the carbon K-edge (4.4 nm). Here, proof-of-principle for NEXAFS with lab-scaled XUV sources is given on polyimide as a reference.

1. Introduction

The societal demand for ever faster electronic devices requires a change in the manufacturing processes within the next few years. Microstructures like transistors on silicon chips are currently produced with deep UV lithography which uses 193 nm laser radiation as light source. Expanded by liquid immersion, this technique is able to generate patterns with a resolution down to about 45 nm [1]. Since the resolution of an optical system is limited by the utilized wavelength, there is no way for further reduction of the structure sizes with common UV lithography.

In order to fulfill the roadmap of the semiconductor industry (Moore's Law), new techniques have to be invented. One of the leading candidates is extreme ultraviolet lithography (EUVL [2]). Using reflective imaging optics on the basis of multilayer mirrors, electronic devices with structure sizes well below 45 nm could be manufactured at a wavelength of 13.5 nm. For industrial lithographic systems, EUV radiation with high average power is required, which can be generated either by laser- or discharge-based plasma sources. Such EUV sources and corresponding beam steering optics are currently being developed with tremendous effort.

Besides semiconductor microlithography, there are also other applications of EUV radiation, which can strongly profit from the EUVL source and optics developments. Currently, the application of EUV radiation apart from microlithography comes more and more into focus. Main goal of our research is to utilize the unique interaction between EUV/XUV radiation and matter for probing, modifying, and structuring solid surfaces.

2. Laser-Produced Plasma Sources at the LLG

For EUV/XUV applications at the Laser Laboratorium Göttingen, a laser-produced EUV source was developed [3–5]. EUV radiation is generated by focusing an Nd:YAG laser (Innolas, fundamental wavelength 1064 nm, pulse energy 700 mJ, pulse duration 6–8 ns) onto a target. Currently, we are using gaseous (Oxygen, Nitrogen, Krypton, Xenon), liquid (Argon) and solid (Gold) target materials which are utilized for different applications.

For metrology purposes, we are using a gas puff target produced by a Proch-Trickl valve. The nozzle tip is located in the center of a vacuum chamber, which is evacuated below 10^{-3} mbar due to the low mean free path of EUV radiation at

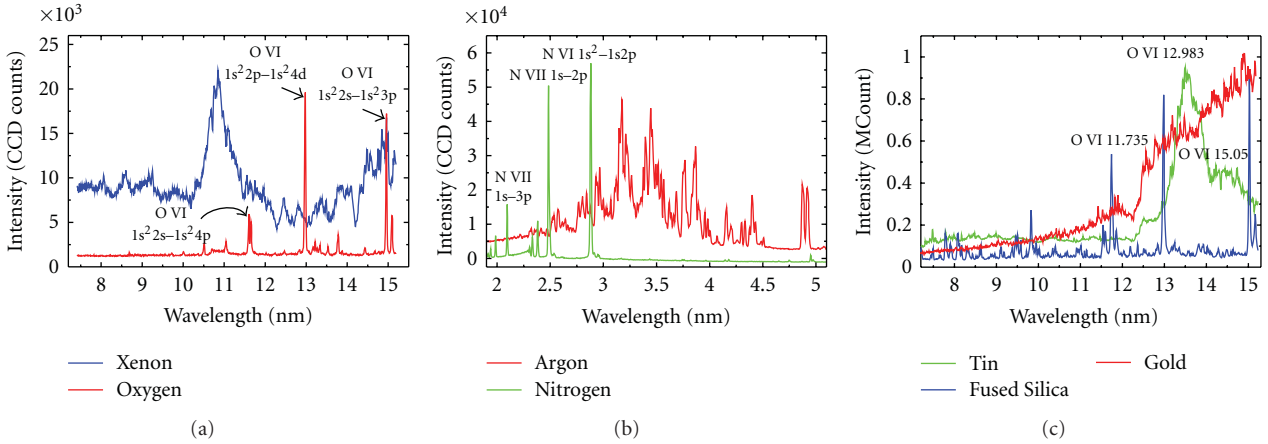

FIGURE 1: Spectra of the laser-produced plasma source developed at the LLG using different taget concepts and materials: gas puff targets in the EUV (a) and XUV (b) spectral region; solid state targets in the EUV spectral region (c). The employed target material defines the emission characteristics of the source.

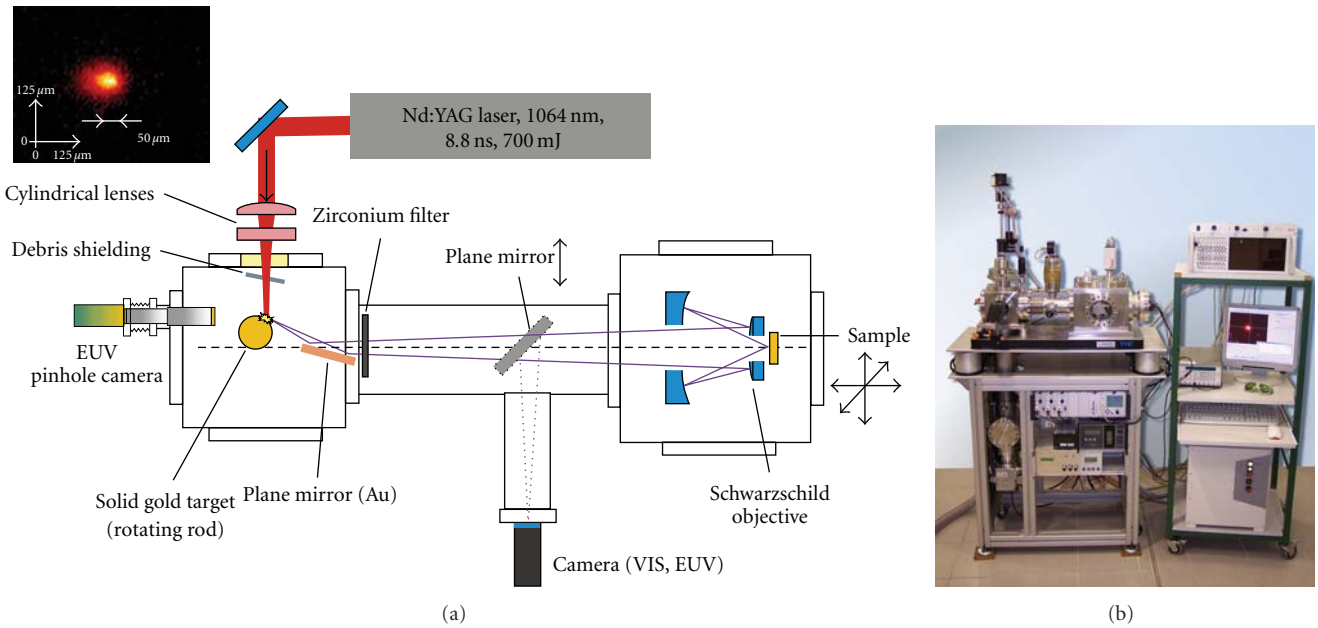

FIGURE 2: Schematic drawing of the integrated EUV source and optics system (a) and photo of the whole setup. The sample is mounted on a 3-axes translation stage. Sample adjustment is facilitated by an integrated video camera. A pinhole camera picture is shown in the upper left.

atmospheric pressure. For applications where higher source brilliances are needed, Argon (XUV spectral range) or Gold (EUV spectral range) targets were developed (cf. Figure 1 for spectra of different target materials).

The EUV/XUV plasma can be monitored with a pinhole camera, consisting of a CCD chip with an EUV-to-VIS quantum converter and a pinhole (diameter 30 μm) coated with a zirconium filter (thickness approximately 200 nm) for blocking out-of-band radiation (see also pinhole camera pictures in Figures 2 and 7).

3. Direct Structuring and Damage Tests with EUV Radiation

Laser ablation and photo-etching of polymers have been studied extensively especially in the visible and deep ultraviolet (DUV) spectral range [6–9]. For these wavelengths, ablation can be described in terms of thermal, photothermal, and photochemical models, or as a combination of these mechanisms [10]. A prerequisite for a preferable photochemical process without thermal load is short wavelength

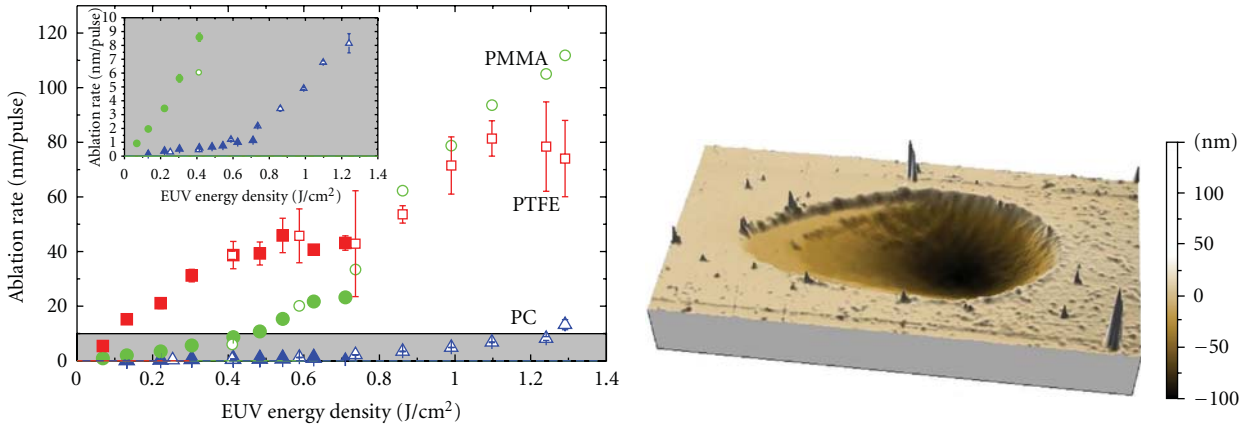

FIGURE 3: Ablation rates of various polymers, depending on the EUV energy density (a). (b) picture shows the AFM image of PMMA, irradiated with 1 EUV pulse at 1.3 J/cm^2.

radiation with photon energies that are high enough to directly break the polymer bonds [10]. Nevertheless, the interaction processes between polymers and radiation below a wavelength of 157 nm were investigated only in a few publications up to now. Examples are the structuring of PMMA using a capillary discharge Ne-like Ar laser (wavelength 46.9 nm, pulse duration 1.2 ns) [11], the free-electron laser (FEL) in Hamburg (FLASH) emitting 32 nm radiation at apulse duration of 25 fs [12], and a zinc X-ray laser (wavelength 21 nm, pulse duration 90 ps) [13]. In this context, it is interesting to note that at the FLASH light source, the ablation of PMMA is used also for spatial characterization of the FEL beam. Besides the EUV laser sources, also synchrotron radiation [14] and table-top EUV/XUV sources [15–17] were used for structuring of polymers. Usually the latter are capable to generate only relatively low energy densities. Using a laser-induced Ta plasma in combination with a grazing incident Au covered collector mirror, an energy density of up to 0.3 J/cm^2 was obtained that could be applied for ablation of silica glass [18]. Unfortunately, grazing incidence mirrors are not useful for mask-projection due to their inherently low numerical aperture and corresponding low spatial resolution. In this paper, we present a table-top EUV setup which is able to generate energy densities up to 1.3 J/cm^2 at pulse durations of 8.8 ns with high spectral purity. By removing the zirconium filter (T ~ 17%), the fluence can be increased to 6.6 J/cm^2. However, due to the increased spectral bandwidth (filtering only by Mo/Si mirrors of the objective), radiation in the visible and IR radiation might contribute to the observed damage morphologies.

3.1. Setup. The ambition of the designed EUV source and optics setup was to achieve a high energy density in the focus plane of an objective, combined with a high spatial resolution (several lines per micron) and a compact setup. For this reason, a solid Gold-based LPP source was adapted to a modified Schwarzschild objective [19]. By using additional beam-shaping techniques for the Nd:YAG laser, an energy density of 1.3 J/cm^2 of spectral filtered 13.5 nm radiation could be determined in the image plane of the Schwarzschild objective. This setup is currently used for various experiments, for example, the direct structuring of polymers or test of EUV optics and sensors.

3.2. Structuring of Polymers. For EUV lithography, photoresists based on PMMA are used. In this contribution, we have investigated the interaction between EUV radiation and polymers. Starting with ablation experiments on PMMA [20], we have expanded the study to PTFE and PC [21].

As an example, Figure 3 shows the ablation rates of the different polymers depending on the EUV energy density. Typical threshold behavior could be detected for PMMA and PC. Saturation occurs for PTFE due to the very high absorption and the resulting penetration depth of approximately 53 nm. Independent from polymer and fluences, roughness increases due to the structuring process by less than 30%, which makes this setup interesting for the generation of smooth profiles in polymers. In summary, the interaction process seems to be photochemical dominated, where the incidence EUV photons are able to break the polymer bonds until fragments can escape into vacuum.

3.3. Damage Tests on EUV Optics and Substrates. Additionally, the setup was used for determining damage thresholds for EUV optics and substrate materials [23]. As an example, results for fused silica (Suprasil 1 by Heraeus, 2 mm thickness) are displayed. The sample was cut into 1×1 cm^2 pieces and cleaned with ethanol before irradiation

In Figure 4(a), measured ablation depths are displayed as a function of the number of applied EUV pulses for selected energy densities. Obviously, a linear behaviour is observed for low intensities. However, at an energy density >5.4 J/cm^2, the crater depths for 10 pulses are deeper than expected from the linear fit for lower pulse numbers. This might be caused by a radiation-induced change of the material by

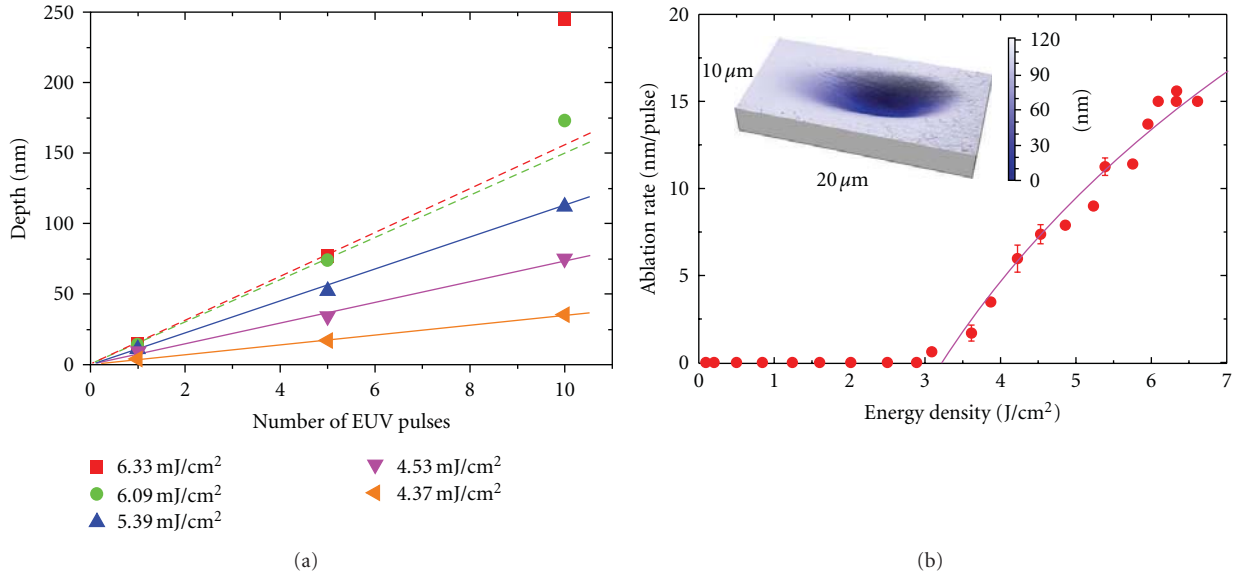

FIGURE 4: (a): Depths of EUV-generated ablation profiles in fused silica as a function of EUV pulse number for selected energy densities; (b): resulting ablation rates d as a function of the applied EUV energy density H; the solid line represents the fit curve according to an ablation rate $d = \alpha_{\text{eff}}^{-1} \ln(H/H_t)$ (α_{eff} = effective absorption coefficient, H_t = ablation threshold energy density); inset: AFM image of fused silica, irradiated with 5 pulses at highest intensity (6.6 J/cm²).

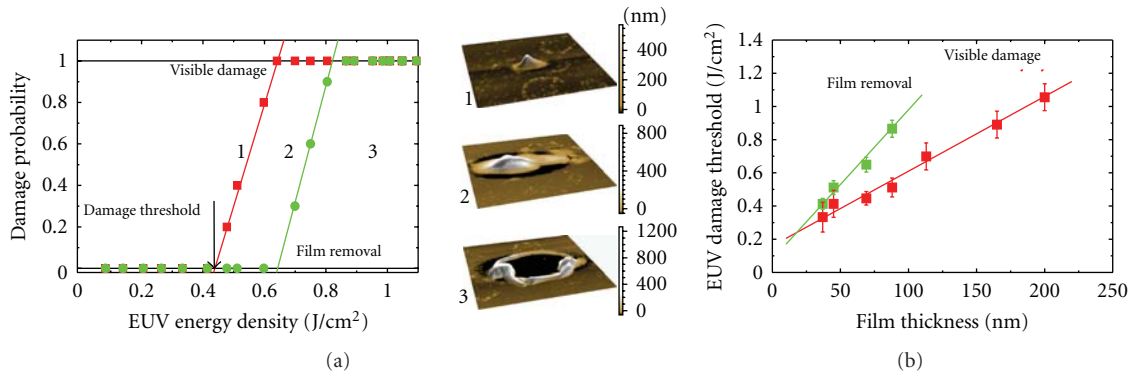

FIGURE 5: Damage threshold measurements on Gold layers. (a): Damage probability plot for a 70 nm thick Gold layer. Middle: corresponding AFM images. (b): film thickness dependence.

the first pulses (incubation effect). From the linear fit of the crater depths as measured with AFM, the ablation rate (depth per pulse) is determined (Figure 4(b)). The ablation rate d may be fitted by a logarithmic function according to $d = \alpha_{\text{eff}}^{-1} \ln(H/H_t)$. A corresponding best-fit yields an effective absorption coefficient $\alpha_{\text{eff}} = 0.0455\,\text{nm}^{-1}$ and an ablation threshold fluence $H_t = 3.22\,\text{J/cm}^2$.

It is important to note that the absolutely smooth crater profile (see AFM micrograph) is comparable to laser ablation reported for 157 nm radiation with nanosecond pulses [24]. As for 157 nm, this might be an indication for a photon-induced direct bond-breaking process, in contrast to a more thermally induced mechanism at wavelengths >190 nm.

For high reflectance, such fused silica substrates with for example, toroidal or ellipsoidal shapes are coated with a single (for grazing incidence reflectance) or multilayer structure (for reflectivity near to the surface normal). A commonly used material for single-layer optics is Gold.

In Figure 5, the damage probability was measured for Gold films of varying thicknesses. In the left, the damage probability is plotted for a 70 nm thick Gold layer performing a 1-on-1 damage experiment. For this, the sample was irradiated at 10 positions with 1 EUV pulse each at constant fluence. The number of damaged sites divided by 10 is the damage probability for this fluence. For this thin Gold layer, surface melting (1) starts at 420 mJ/cm² and complete film removal (2) at 650 mJ/cm². Repeating this experiment for different film thicknesses, (Figure 5(b)) yields a linear dependence between layer thickness and threshold energy density. This could be explained by a thermally dominated process.

Further damage experiments were performed on Mo/Si multilayer mirrors, silicon, and calcium fluoride. For each

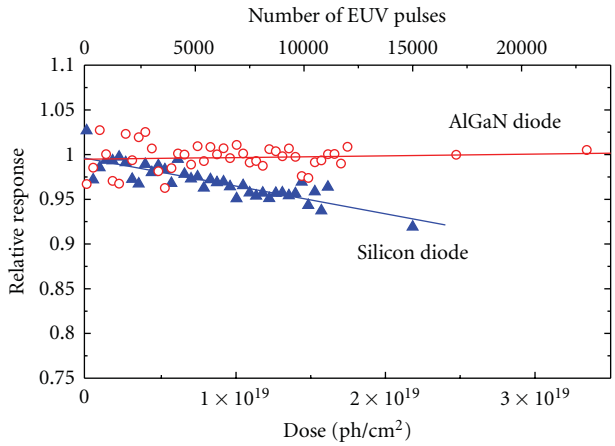

FIGURE 6: Radiation damage resistance of AlGaN diodes compared to standard silicon photodiodes.

material, damage thresholds were determined. A more detailed description of the experimental results can be found in [23].

3.4. Radiation Damage Resistance of EUV Diodes. Beside optics also damage resistance of sensors to radiation in the EUV/XUV spectral range is important, for example, in measuring absolute fluencies for EUV lithography. In this contribution, we have tested standard silicon photodiodes as well as AlGaN diodes. The latter was developed by the IMEC in Belgium and offered an intrinsically blindness to wavelengths above the UV spectral range [25]. For this kind of diode, responsivity and radiation damage resistance was measured at 13.5 nm wavelength. For this reason, the diodes were placed in the focus of the Schwarzschild objective. For measuring the damage resistance, the diodes were irradiated by high EUV pulse numbers. Plotting the measured responsivity against the EUV dose (EUV fluence times pulse number), the relative drop in responsivity can be displayed. The result is shown in Figure 6.

Here, a decrease in responsivity of 7% was measured for the silicon diode after $2 \cdot 10^{19}$ photons/cm^2. In contrast, for the AlGaN diode no change in responsivity was registered even after 3.3×10^{19} photons/cm^2. This makes it ideal for applications where high radiation stability is needed during extended exposure to short wavelength radiation.

4. EUV/XUV Surface Analysis Using a Reflectometry Setup

Since extreme-ultraviolet lithography (EUVL [2]) has emerged as a leading candidate for next generation lithography in the semiconductor industry, tremendous efforts have been made to develop and optimize EUV sources and optical elements needed for the task. For beam shaping and imaging, multilayer optics are needed which have to be thoroughly characterized with respect to figure error, surface roughness, and especially reflectivity. For the latter, one of the employed techniques is angular resolved EUV reflectometry. Lacking other EUV light sources, at first this task was done mainly at synchrotron facilities such as ALS at NBNL (Berkeley) and BESSY (Berlin) and it is done there until today. But with the availability of table-top EUV/XUV light sources (laser produced and gas discharge plasma sources), optics analysis is not limited to the synchrotron facilities any more.

Still the main focus for EUV reflectometry/scatterometry setups is the characterization of EUVL components like optics and masks [26–29]. Aside from that, only little work seems to be going on with the application of EUV reflectometry for surface analysis [30].

At the LLG, the developed plasma source is employed for EUV/XUV surface analysis in a reflectometry setup. With this setup, multiple types of measurements are possible: reflectometry (in θ-2θ-geometry), diffractometry (of nanoscale structures), and scatterometry. The wide range of measurement modes allows for analysis of a variety of sample parameters for example, refractive index, roughness, film thickness, density, and chemical composition.

4.1. Setup. The setup for EUV/XUV surface analysis is shown in Figure 7. The light emitted by the source passes through a 100 μm pinhole placed approximately 2 mm behind the plasma and a Zirconium filter which blocks higher wavelength components of the spectra. In the optics chamber, a Kirkpatrick-Baez arrangement (cf. Figure 8) images the pinhole onto the sample placed in the middle of the experimental chamber via an Mo/Si multilayer mirror. This mirror works as a spectral filter in the EUV spectral region and is adapted to the $1s^2 2p$–$1s^2 4d$ emission line of Oxygen at 12.98 nm (cf. Figure 1(a)). The reflectometer placed in the experimental chamber consists of two independent rotation stages for sample holder and detector diode, respectively. The beam diameter on the sample (perpendicular to the incident radiation) is approximately 300 μm in horizontal and 500 μm in vertical direction.

For monitoring of intensity fluctuations of the plasma source, a second EUV photodiode is used as a reference monitor. It is illuminated by a second filtering multilayer mirror with the same specifications as the main mirror.

4.2. Surface Analysis Measurements. Figure 9(a) shows a basic reflectivity measurement on a 100 nm carbon film on silicon. As the penetration depth of EUV radiation is in the range of some 10 nm, the curve shows quasibulk behavior. From such bulk measurements, the complex index of refraction can be calculated by line fitting the data with a mathematical model based on the Fresnel formulae.

To obtain structural information on the sample for example, film thickness and/or surface roughness, the fitting model must be expanded. For layered materials, either the Parratt Algorithm [31] or the Transfer Matrix Algorithm [32] is used and for fitting of surface roughness and/or interdiffusion thicknesses between layers commonly the Nevot-Croce Factor is used [33]. With this it is possible to obtain the film thickness of a sample fitting of the reflectometry data. Figure 9(b) shows the measurement of a 30 nm carbon layer on silicon. From the oscillations that are

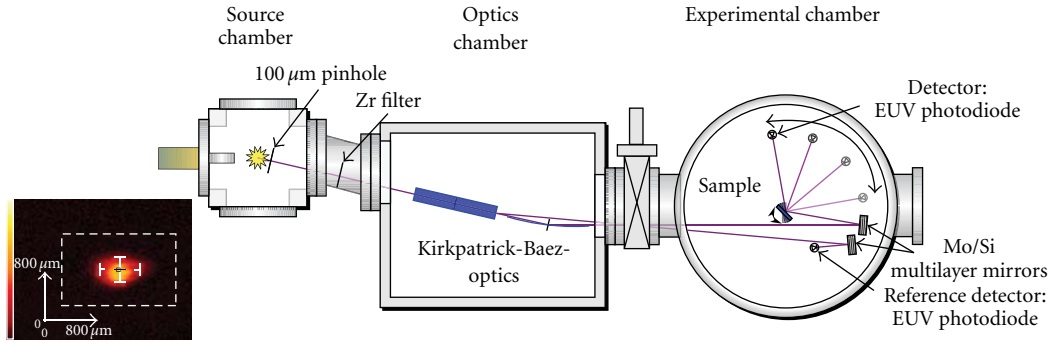

Figure 7: Schematic drawing of EUV/XUV surface analysis setup. It consists of an LPP source (Oxygen-target), an adaptable Kirkpatrick-Baez optics, and a reflectometer (cf. text). On the left, a pinhole camera image of the plasma is shown.

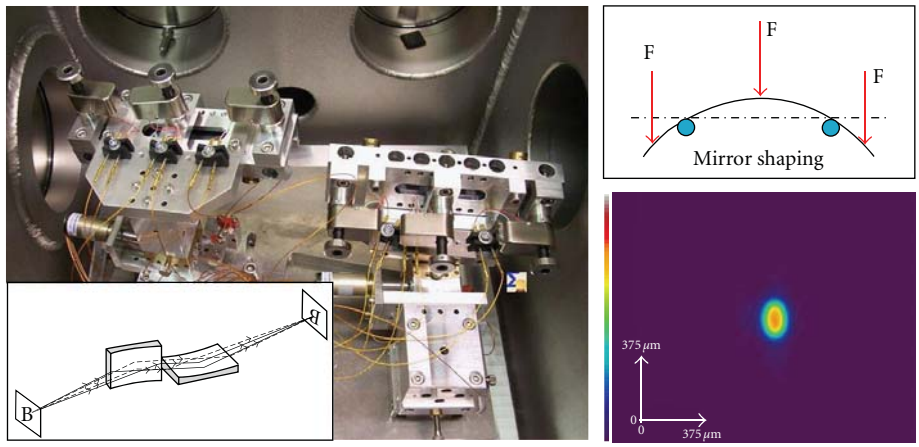

Figure 8: Adaptable Kirkpatrick-Baez optics used for beam shaping, based on two cylindrical bent mirrors. Left: photograph and working principle (inset). Right: principle of mirror shaping (top), using bendable silicon wafers with a high reflectivity carbon coating for beam shaping (collimating/focusing). The resulting intensity distribution (bottom) of the focused beam shows diameters of 300 μm $\times$ 500 μm (FWHM).

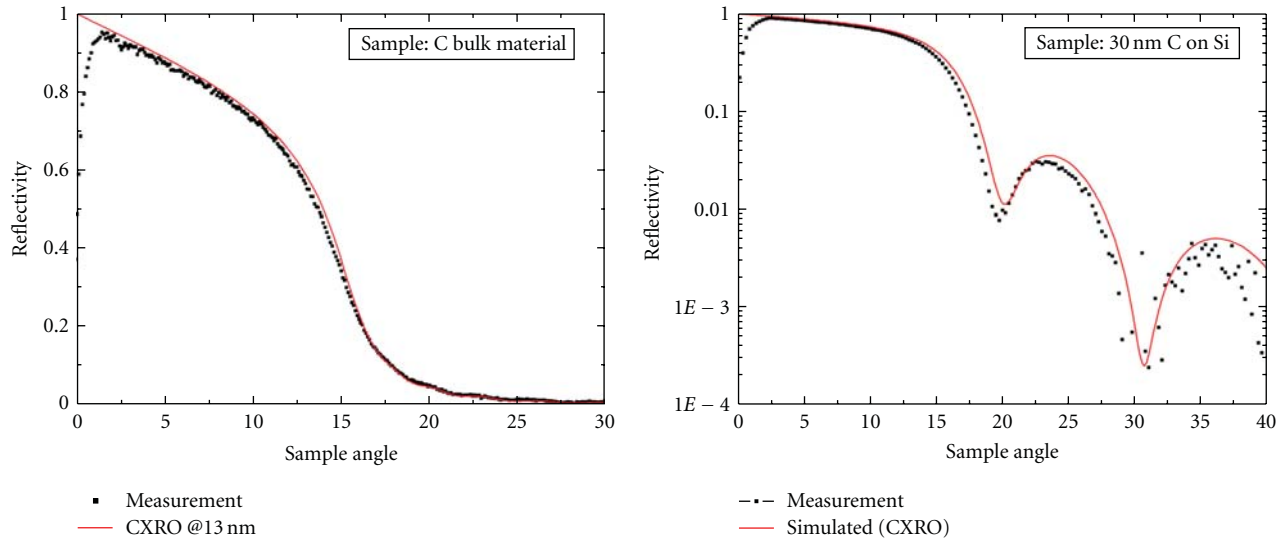

Figure 9: (a): Reflectivity of 100 nm carbon layer on silicon (black dots) compared to calculated values (red line) from the CXRO database [22]. (b): Reflectogram of a 30 nm carbon layer on silicon. From such measurements, the film thickness of the sample can be obtained.

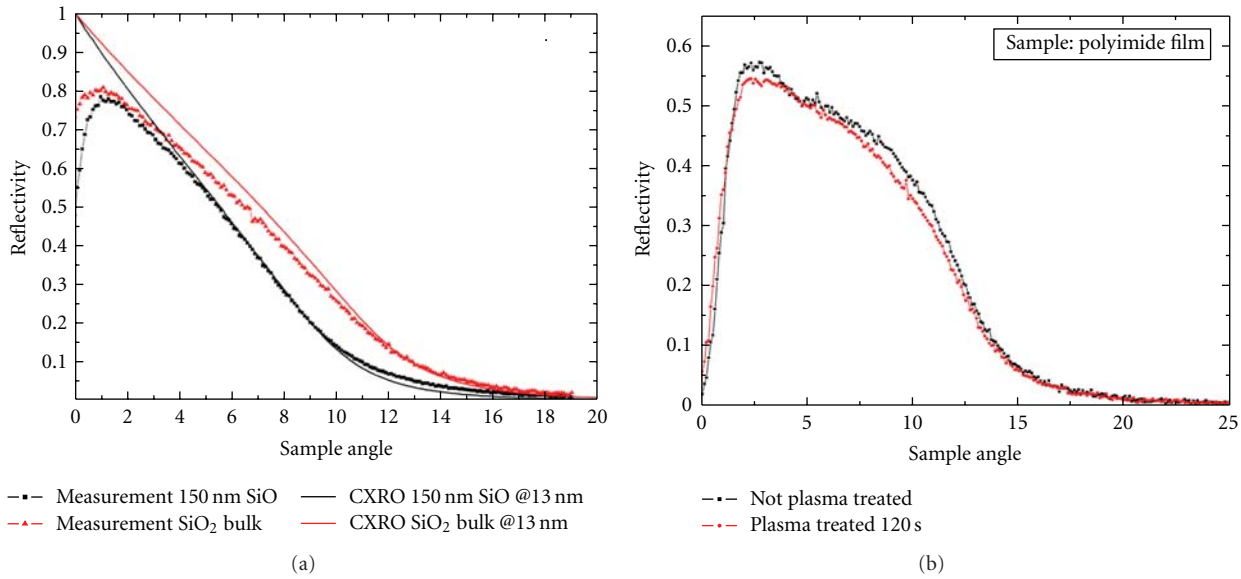

Figure 10: Material studies. (a): Reflectograms of different oxidation states of Si in SiO (black) and SiO_2 (red). (b): Comparison between plasma-treated (red) and untreated (black) Polyimide foils. In spite of the small penetration depth of the plasma treatment a difference in refractive index is measurable.

due to multiple reflections in the film, the layer thickness can be obtained.

Furthermore, as the complex refractive index varies with the relative mass densities of a compound material, it is possible to distinguish different oxidation states for example, in SiO_x. Figure 10(a) shows reflectograms of SiO and SiO_2 sample measurements as well as simulations.

Even the small influence of a surface plasma-treatment on a Polyimide foil could be detected. Figure 10(b) shows the reflectograms of the plasma treated (red) and the untreated (black) samples.

5. Near-Edge X-Ray Absorption Fine Structure (NEXAFS) Measurements

NEXAFS, formerly used mainly for surface- and interface-analysis [34], is being utilized more and more in other fields, such as X-ray microscopy [35], studies on the so-called "silent" sulphur [36], or studies on transient electronic structures of for example, rare earths [37, 38], to only name a few. As the interest in NEXAFS grew, so the importance to develop a table-top soft X-ray source became larger. Especially for the spectral range of the "water-window" ($\lambda = 2.2 \cdots 4.4$ nm) laser-driven plasma-sources have been developed in the last couple of years [39, 40].

In order to study the chemical structures of carbon-based specimen at the LLG, a compact setup for near edge X-ray absorption spectroscopy at the carbon K-edge based on a laser driven plasma source was built. Employing a Krypton gas puff-target, the required broad-band emission in the spectral range of the "water window" is generated. The table-top setup consists basically of the laser plasma source and a flat-field spectrometer (Figure 11) and can be used for

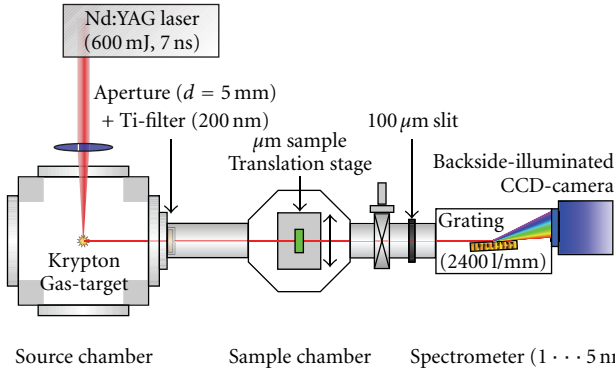

Figure 11: NEXAFS setup, consisting of an LPP-XUV source and an XUV flat field spectrometer.

NEXAFS experiments in transmission as well as in reflection under grazing incidence conditions (ReflEXAFS).

The latter method offers the advantage that thin film preparation is not necessary and the surface sensitivity is strongly enhanced.

In Figure 12, a measured NEXAFS spectrum of Polyimide is displayed, demonstrating the possibilities of this principle. Other applications are the determination of chemical changes in UV/EUV irradiated polymers [41] or the investigation of the transient electronic structure of PCMO.

6. Conclusions

The LLG table-top light source for EUV/XUV radiation is a very versatile tool for optical metrology as well as scientific applications such as surface analysis or NEXAFS. With the

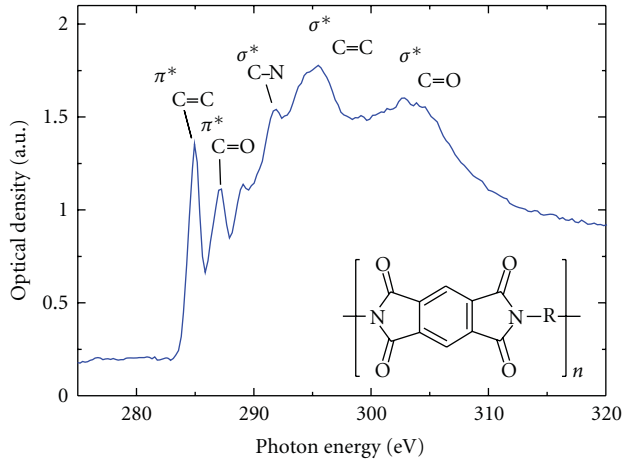

Figure 12: NEXAFS spectrum at the carbon K-edge of a Polyimide film ($d = 200$ nm) measured in transmission (average over 60 pulses). The data shows a deviation of less than 0.4 eV from corresponding synchrotron data.

help of various optical elements (Schwarzschild objective with multilayer coating for focusing, flexible Kirkpatrick-Baez arrangement for light guiding), the intensity distribution can be controlled, so that different experiments may be set up. The energy density within the focus of the Schwarzschild objective is sufficient to directly structure various materials such as polymers (PMMA, PC, PTFE), glasses (suprasil), crystals (Si, CaF_2), or metals (Au). From angular resolved reflectometry much information about material composition, density and surface roughness may be gained, whereas investigations on the near-edge X-ray absorption fine structure (NEXAFS) yield information about chemical bonding type and molecular orbitals.

Acknowledgments

The authors would like to thank Dr. A. Holländer (Fraunhofer IAP) for fabrication of plasma-treated polymer samples. Financial support by DFG (in the frame of SFB 755) and Federal Ministry for Economics & Technology (within InnoNet project XUV-Nano) is gratefully acknowledged.

References

[1] A. K. Raub, A. Frauenglass, S. R. J. Brueck et al., "Imaging capabilities of resist in deep ultraviolet liquid immersion interferometric lithography," *Journal of Vacuum Science and Technology B*, vol. 22, no. 6, pp. 3459–3464, 2004.

[2] B. Wu and A. Kumar, "Extreme ultraviolet lithography: a review," *Journal of Vacuum Science and Technology B*, vol. 25, no. 6, pp. 1743–1761, 2007.

[3] S. Kranzusch and K. Mann, "Spectral characterization of EUV radiation emitted from a laser-irradiated gas puff target," *Optics Communications*, vol. 200, no. 1–6, pp. 223–230, 2001.

[4] C. Peth, S. Kranzusch, K. Mann, and W. Viöl, "Characterization of gas targets for laser produced extreme ultraviolet plasmas with a Hartmann-Shack sensor," *Review of Scientific Instruments*, vol. 75, no. 10, pp. 3288–3293, 2004.

[5] S. Kranzusch, C. Peth, and K. Mann, "Spatial characterization of extreme ultraviolet plasmas generated by laser excitation of xenon gas targets," *Review of Scientific Instruments*, vol. 74, no. 2, pp. 969–974, 2003.

[6] R. Srinivasan and S. Lazare, "Modification of polymer surfaces by far-ultraviolet radiation of low and high (laser) intensities," *Polymer*, vol. 26, no. 9, pp. 1297–1300, 1985.

[7] S. Küper, S. Modaressi, and M. Stuke, "Photofragmentation pathways of a PMMA model compound under UV excimer laser ablation conditions," *Journal of Physical Chemistry*, vol. 94, no. 19, pp. 7514–7518, 1990.

[8] J. Ihlemann and K. Rubahn, "Excimer laser micro machining: fabrication and applications of dielectric masks," *Applied Surface Science*, vol. 154, pp. 587–592, 2000.

[9] T. Lippert and J. T. Dickinson, "Chemical and spectroscopic aspects of polymer ablation: special features and novel directions," *Chemical Reviews*, vol. 103, no. 2, pp. 453–485, 2003.

[10] T. Lippert, "Interaction of photons with polymers: from surface modification to ablation," *Plasma Processes and Polymers*, vol. 2, no. 7, pp. 525–546, 2005.

[11] L. Juha, M. Bittner, D. Chvostova et al., "Ablation of organic polymers by 46.9-nm-laser radiation," *Applied Physics Letters*, vol. 86, no. 3, Article ID 034109, 3 pages, 2005.

[12] J. Chalupský, L. Juha, J. Kuba et al., "Characteristics of focused soft X-ray free-electron laser beam determined by ablation of organic molecular solids," *Optics Express*, vol. 15, no. 10, pp. 6036–6043, 2007.

[13] T. Mocek, B. Rus, M. Stupka et al., "Focusing a multimillijoule soft X-ray laser at 21 nm," *Applied Physics Letters*, vol. 89, no. 5, Article ID 051501, 2006.

[14] Y. Zhang, T. Katoh, M. Washio, H. Yamada, and S. Hamada, "High aspect ratio micromachining Teflon by direct exposure to synchrotron radiation," *Applied Physics Letters*, vol. 67, p. 872, 1995.

[15] A. Bartnik, H. Fiedorowicz, R. Jarocki et al., "Strong temperature effect on X-ray photo-etching of polytetrafluoroethylene using a 10 Hz laser-plasma radiation source based on a gas puff target," *Applied Physics B*, vol. 82, no. 4, pp. 529–532, 2006.

[16] F. Barkusky, C. Peth, A. Bayer, and K. Mann, "Direct photoetching of poly(methyl methacrylate) using focused extreme ultraviolet radiation from a table-top laser-induced plasma source," *Journal of Applied Physics*, vol. 101, no. 12, Article ID 124908, 2007.

[17] H. Fiedorowicz, A. Bartnik, K. Jakubczak et al., "Application of laser plasma soft X-ray and EUV sources in micro- and nanotechnology," in *Laser Technology VIII: Applications of Lasers*, Proceedings of SPIE, September 2006.

[18] T. Makimura, H. Miyamoto, Y. Kenmotsu, K. Murakami, and H. Niino, "Direct micromachining of quartz glass plates using pulsed laser plasma soft X-rays," *Applied Physics Letters*, vol. 86, no. 10, Article ID 103111, 2 pages, 2005.

[19] F. Barkusky, C. Peth, K. Mann, T. Feigl, and N. Kaiser, "Formation and direct writing of color centers in LiF using a laser-induced extreme ultraviolet plasma in combination with a Schwarzschild objective," *Review of Scientific Instruments*, vol. 76, no. 10, Article ID 105102, 5 pages, 2005.

[20] F. Barkusky, C. Peth, A. Bayer, and K. Mann, "Direct photoetching of poly(methyl methacrylate) using focused extreme ultraviolet radiation from a table-top laser-induced plasma source," *Journal of Applied Physics*, vol. 101, no. 12, Article ID 124908, 2007.

[21] F. Barkusky, A. Bayer, C. Peth, and K. Mann, "Direct photoetching of polymers using radiation of high energy density

from a table-top extreme ultraviolet plasma source," *Journal of Applied Physics*, vol. 105, no. 1, Article ID 014906, 2009.

[22] Center for X-Ray Optics, Berkeley Lab, http://www-cxro.lbl.gov/.

[23] F. Barkusky, A. Bayer, S. Döring, P. Grossmann, and K. Mann, "Damage threshold measurements on EUV optics using focused radiation from a table-top laser produced plasma source," *Optics Express*, vol. 18, no. 5, pp. 4346–4355, 2010.

[24] J. Ihlemann, M. Schulz-Ruhtenberg, and T. Fricke-Begemann, "Micro patterning of fused silica by ArF- and F2-laser ablation," *Journal of Physics: Conference Series*, vol. 59, no. 1, pp. 206–209, 2007.

[25] F. Barkusky, C. Peth, A. Bayer, K. Mann, J. John, and P. E. Malinowski, "Radiation damage resistance of AlGaN detectors for applications in the extreme-ultraviolet spectral range," *Review of Scientific Instruments*, vol. 80, no. 9, Article ID 093102, 2009.

[26] J. Perlich, F.-M. Kamm, J. Rau, F. Scholze, and G. Ulm, "Characterization of extreme ultraviolet masks by extreme ultraviolet scatterometry," *Journal of Vacuum Science and Technology B*, vol. 22, no. 6, pp. 3059–3062, 2004.

[27] R. N. Watts, C. Tarrio, T. B. Lucatorto et al., "XUV optics characterization at the National Institute of Standards and Technology," *Nuclear Instruments and Methods in Physics Research Section B*, vol. 79, no. 1-4, pp. 244–246, 1993.

[28] L. Van Loyen, T. Böttger, S. Schädlich et al., "Laboratory LPP EUV reflectometer working with non-polarized radiation," *Applied Surface Science*, vol. 252, no. 1, pp. 57–60, 2005.

[29] S. Schröder, T. Herffurth, M. Trost, and A. Duparré, "Angle-resolved scattering and reflectance of extreme-ultraviolet multilayer coatings: measurement and analysis," *Applied Optics*, vol. 49, no. 9, pp. 1503–1512, 2010.

[30] M. Banyay and L. Juschkin, "Table-top reflectometer in the extreme ultraviolet for surface sensitive analysis," *Applied Physics Letters*, vol. 94, no. 6, Article ID 063507, 2009.

[31] L. G. Parratt, "Surface studies of solids by total reflection of X-rays," *Physical Review*, vol. 95, no. 2, pp. 359–369, 1954.

[32] C. C. Katsidis and D. I. Siapkas, "General transfer-matrix method for optical multilayer systems with coherent, partially coherent, and incoherent interference," *Applied Optics*, vol. 41, no. 19, pp. 3978–3987, 2002.

[33] P. Croce and L. Nevot, "Étude des couches minces et des surfaces par réflexion rasante, spéculaire ou diffuse, de rayons X," *Revue de Physique Appliquée*, vol. 11, no. 1, pp. 113–125, 1976.

[34] J. Stöhr, *NEXAFS Spectroscopy*, vol. 25 of *Springer Series in Surface Science*, Springer, New York, NY, USA, 2003.

[35] H. Ade and H. Stoll, "Near-edge X-ray absorption fine-structure microscopy of organic and magnetic materials," *Nature Materials*, vol. 8, no. 4, pp. 281–290, 2009.

[36] F. Jalilehvand, "Sulfur: not a "silent" element any more," *Chemical Society Reviews*, vol. 35, no. 12, pp. 1256–1268, 2006.

[37] M. Rini, Y. Zhu, S. Wall et al., "Transient electronic structure of the photoinduced phase of $Pr_{0.7}Ca_{0.3}MnO_3$ probed with soft X-ray pulses," *Physical Review B*, vol. 80, no. 15, Article ID 155113, 2009.

[38] M. V. Zimmermann, C. S. Nelson, J. P. Hill et al., "X-ray resonant scattering studies of orbital and charge ordering in $Pr_{1-x}Ca_xMnO_3$," *Physical Review B*, vol. 64, no. 19, Article ID 195133, pp. 1951331–19513317, 2001.

[39] M. Beck, U. Vogt, I. Will et al., "A pulse-train laser driven XUV source for picosecond pump-probe experiments in the water window," *Optics Communications*, vol. 190, no. 1–6, pp. 317–326, 2001.

[40] C. Peth, F. Barkusky, and K. Mann, "Near-edge X-ray absorption fine structure measurements using a laboratory-scale XUV source," *Journal of Physics D*, vol. 41, no. 10, Article ID 105202, 2008.

[41] B. Fuchs, F. Schlenkrich, S. Seyffarth et al., "Hardening of smooth pulsed laser deposited PMMA films by heating," *Applied Physics A*, vol. 98, no. 4, pp. 711–715, 2010.

Hindawi Publishing Corporation
X-Ray Optics and Instrumentation
Volume 2010, Article ID 784732, 9 pages
doi:10.1155/2010/784732

Research Article

Elliptically Bent X-Ray Mirrors with Active Temperature Stabilization

Sheng Yuan,[1] Matthew Church,[1] Valeriy V. Yashchuk,[1] Kenneth A. Goldberg,[2] Richard S. Celestre,[1] Wayne R. McKinney,[1] Jonathan Kirschman,[3] Gregory Morrison,[1] Tino Noll,[4] Tony Warwick,[1] and Howard A. Padmore[1]

[1] *Advanced Light Source, Lawrence Berkeley National Laboratory, Berkeley, CA 94720, USA*
[2] *Center for X-Ray Optics, Lawrence Berkeley National Laboratory, Berkeley, CA 94720, USA*
[3] *Ikawamachi Board of Education, Minamiakitagun, Akitaken 018-1516, Japan*
[4] *Helmholtz Zentrum Berlin für Materialien und Energie, Elektronenspeicherring BESSY-II, Albert-Einstein-Str. 15, 12489 Berlin, Germany*

Correspondence should be addressed to Sheng Yuan, syuan@lbl.gov

Received 30 January 2010; Accepted 9 July 2010

Academic Editor: Ali Khounsary

We present details of design of elliptically bent Kirkpatrick-Baez mirrors developed and successfully used at the advanced light source for submicron focusing. A distinctive feature of the mirror design is an active temperature stabilization based on a Peltier element attached directly to the mirror body. The design and materials have been carefully optimized to provide high heat conductance between the mirror body and substrate. We describe the experimental procedures used when assembling and precisely shaping the mirrors, with special attention paid to laboratory testing of the mirror-temperature stabilization. For this purpose, the temperature dependence of the surface slope profile of a specially fabricated test mirror placed inside a temperature-controlled container was measured. We demonstrate that with active mirror-temperature stabilization, a change of the surrounding temperature by more than 3 K does not noticeably affect the mirror figure. Without temperature stabilization, the rms slope error is changed by approximately 1.5 μrad (primarily defocus) under the same conditions.

1. Introduction

Beamlines at third- and fourth-generation synchrotron radiation light sources achieve unprecedented high-brightness and low emittance, producing coherent X-ray beams that demand X-ray optics suitable for micro- and nanofocusing and brightness preservation. The required quality of the corresponding reflecting optics is characterized with root-mean-square (rms) slope error tolerances below 0.3 μrad with significantly curved and sophisticated surface shapes [1, 2].

One of the most effective and widely used ways to achieve precise focusing is to use two, orthogonal, elliptically cylindrical reflecting elements at glancing incidence, the so-called Kirkpatrick-Baez (KB) pair [3], which focuses the beam separately in the tangential and sagittal directions. Recently, significant progress in the direct fabrication of elliptical surfaces has been achieved [4–6]. However, direct fabrication of tangential elliptical cylinders is often difficult due to the aspherical surface figure and sophisticated testing techniques needed during the polishing process [7, 8]. This is in contrast to flat optics, which are simpler to manufacture and easier to measure by conventional surface profilometry. In order to get the desired surface figure, a flat substrate, appropriately shaped in the sagittal direction, is precisely bent by applying torques (couples) at each end [9]. In addition, bendable optics allow more flexibility for tuning to different desired focal distances and are useful for adaptive (active feedback) applications.

The precision of the bender setting is limited by the metrology accuracy and fabrication tolerances, both are currently achievable of the level of 0.2 μrad. The best fabricated bendable optics had been set at the advanced light source (ALS) optical metrology laboratory (OML) to

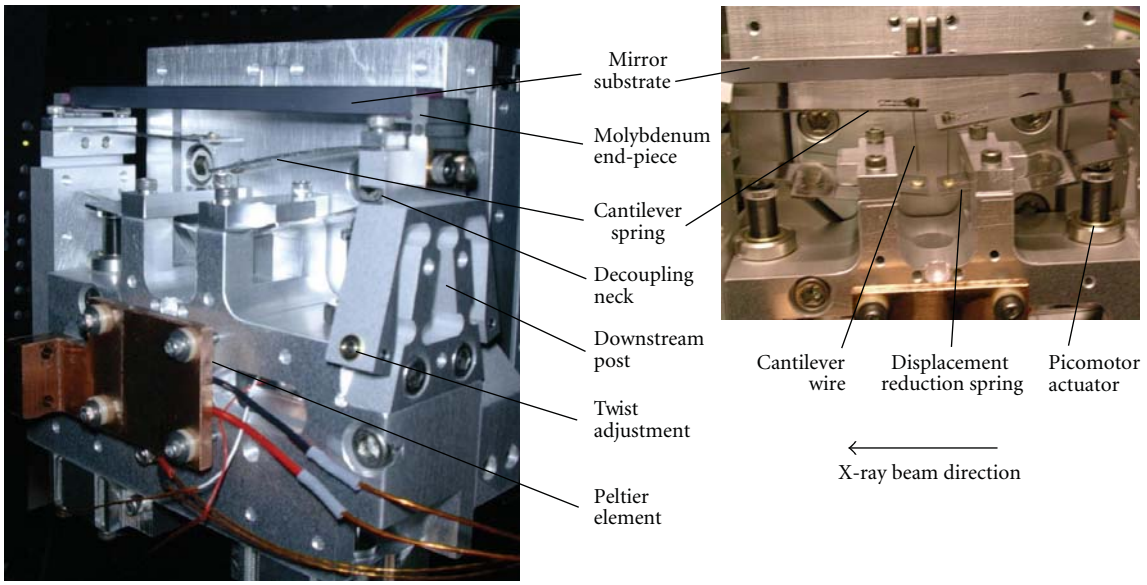

Figure 1: Bendable KB mirror used for the thermal investigations.

a residual slope error below 0.3 μrad (rms). The bent optics will relax over time due to the bending mechanics involved; however, optics can be in good shape for months, which is reasonable. Also, it is quite simple to recheck and rebend the mirror every few months, if there is noticeable degradation in optical performance.

The manufacture and use of high-quality X-ray optics requires surface metrology with an accuracy of better than 0.1 μrad [10]. While the accuracy of ex situ X-ray mirror metrology and tuning techniques has improved over time [11–17], the performance of optics on beamlines is still limited by environmental factors specific to their beamline applications [18–21]. Indeed, at beamlines, variations of the ambient temperature, vibration, temperature gradients due to X-ray absorption on the mirror's substrate, and so forth, are significantly different from that in an optical metrology lab. These factors require sophisticated environmental control of optical systems [22–24] and high-accuracy, at-wavelength, in situ metrology techniques for fine tuning and alignment of optics at beamlines [25–31]. The percentage of the impact of these environmental factors on actual beamlines, are currently under investigation at ALS beamline 5.3.1.

For the performance of bendable X-ray optics used for fine focusing at the beamline end-stations, thermal effects that depend on ambient temperature variation are especially troublesome. Mirror shape changes are induced by differences in the thermal expansion coefficients of the various materials used in the mirror-bending holder. In this paper, we present the design and laboratory testing of an elliptically bent KB mirror with active temperature stabilization. The same KB design is now used at BL 12.3.2 of the ALS, where focus spots around 1 μm are routinely achieved [32]. The smallest focus is limited by the alignment of the optics and the environmental control at the actual beamline.

2. Mirror Design

Figure 1 shows details of the mirror bender design. The bending mechanism of the mirror is based on two cantilever springs. With a wire, each cantilever spring is connected to a displacement-reduction spring that is driven with a Picomotor. The displacement of the Picomotor actuators is monitored with linear variable differential transformers (LVDT) with an accuracy of approximately 100 nm over the useful range. The bender design allows extremely fine control of the bending couples applied to the mirror substrate.

The mirror substrate is made of silicon. Most of the elements of the mirror bender assembly are made of aluminum which reduces the fabrication costs. Due to the large thermal expansion coefficients difference between Si ($\sim 2.6 \cdot 10^{-6}\,\mathrm{K}^{-1}$) and Al ($\sim 23.1 \cdot 10^{-6}\,\mathrm{K}^{-1}$), the mirror shape changes as the environmental temperature varies.

Another effect which worth mentioning is the thermal load from X-ray absorption on the mirror's substrate, when used at beamlines, which can lead to temperature gradients on the mirror. Dissipation of the absorbed power is important to provide good thermal conductivity between the Si substrate and the Al bender. The mirror design (Figure 1) and the materials used have been carefully optimized to provide a high heat conductance between the mirror body and the substrate. The Si mirror substrate is connected to the Al bender assembly by molybdenum end-pieces glued to the Si mirror substrate with special UHV compatible epoxy. The thermal conductivity of Mo (at room temperature) is approximately $138\,\mathrm{Wm}^{-1}\mathrm{K}^{-1}$, smaller than of Al ($\sim 237\,\mathrm{Wm}^{-1}\mathrm{K}^{-1}$) by a factor less than two, and larger than invar ($\sim 14\,\mathrm{Wm}^{-1}\mathrm{K}^{-1}$), which is commonly used in similar applications, by a factor of approximately ten. The mirror design and the selection of these materials allow efficient temperature stabilization of the mirror with a Peltier element attached directly to body of the mirror assembly (Figure 1).

Table 1: Original specifications of the KB test mirror.

Substrate material	Substrate thickness	Substrate length	Mirror center radius of curvature	Object distance	Image distance	Grazing angle
Si	5.08 mm	101.6 mm	57.14 m	2400 mm	120 mm	4.0 *m*rad

The mirror-bender design used in the present work is closely related to the design of KB mirrors fabricated for ALS beamline 12.3.2 [32]. Three similar mirrors are also used for micro-focusing at ALS beamline 10.3.2. In both cases, mirrors with active temperature stabilization based on a Peltier element have shown a significantly better X-ray focusing and stability performance than previous mirrors without temperature stabilization.

In this paper we present the results of ex situ visible-light shape measurement tests on a single KB mirror fabricated for use as a test X-ray optic at ALS beamline 5.3.1. The tests were conducted at the ALS OML. A new endstation on beamline 5.3.1, developed in the course of an LDRD (laboratory-directed research and development program) project [33, 34], is dedicated to the investigation of at-wavelength metrology of X-ray optics. The test mirror substrate (with a pre-shaped sagittal width profile [9]) and its intended surface figure profile, when bent, were designed for vertical focusing on ALS beamline 10.3.2, with optical specifications given in Table 1.

3. Assembly, Initial Alignment, and Adjustment of the Test Mirror

The assembly, preliminary alignment, and the setting of the mirror benders are performed by monitoring the mirror surface shape with a 6-inch ZYGO GPI interferometer at the OML.

First, with relaxed cantilever springs, the mirror substrate, which is an optical flat (the mid-spatial-frequency variation of the substrate slope is less than 0.2 μrad RMS, and the roughness is less than 1 Å RMS) with glued, Mo end-blocks, is attached to the bender mechanism (Figure 1). The downstream post is tightened to the mirror body, while the upstream post is loosened. Final positioning and tightening of the upstream post is made in such a way as to provide the smallest possible curvature of the installed substrate. The upstream post has two decoupling flexures that decrease the parasitic stress applied to the mirror substrate due to assembly error. The downstream post is equipped with an anti-twist mechanism and has one decoupling flexure. The flexures, which are 380-μm thick, do not provide complete stress decoupling apparently due to a small misalignment of the parts and a difference between the length of the substrate and the distance between the posts. The latter perturbation can cause a tension effect [9]. As a result, the mirror's radius of curvature due to residual stress begins at approximately 500 m (concave), with totally released cantilevers.

Second, the twist in the mirror substrate is removed using the dedicated downstream anti-twist adjustment shown in Figure 1. The anti-twist mechanism is designed with its axis of rotation on the reflecting surface of the mirror. Figure 2 shows normal-incidence interferograms of the mirror surface recorded before and after the twist correction.

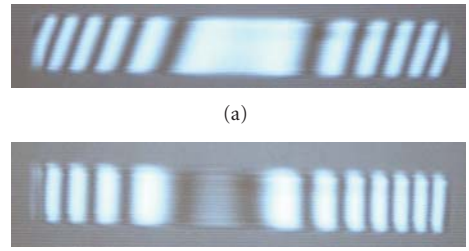

(a)

(b)

Figure 2: Mirror twist correction with the ZYGO GPI interferometer. The interferograms of the mirror surface before (a) and after (b) the twist correction are shown.

Third, a ZYGO GPI interferometer is used to measure the tangential radii of curvature from three sections of the mirror's clear aperture (upstream, central, and downstream). The mirror is iteratively bent to a shape close to the desired ellipse specified in Table 1 based on three local curvature values. The interferometer's measurements over the entire clear aperture of the mirror are limited to a relatively large radius of curvature, above ~200 m. Therefore, its measurements are only used to confirm that the benders have the required range of tuning.

Finally, the anti-twist correction process is repeated for the central part of the bent mirror. Later, a final, more precise anti-twist correction is performed using slope measuring profilers, including the upgraded ALS long trace profiler LTP-II [14] and the developmental long trace profiler (DLTP) [15], in the ALS OML. In this correction, the sagittal surface slope profile along the entire clear aperture of the mirror is measured, and the sagittal slope variation is minimized by manually tuning the twist adjustment screws (Figure 1). For illustration, Figure 3 shows the sagittal slope profiles of the mirror measured before and after twist correction. The twist correction removed a linear part of the sagittal slope variation that initially had peak-to-valley (PV) variation of 63 μrad. After the correction, the residual sagittal slope variation has a quadratic dependence on the tangential position with a PV variation of 24 μrad. We attribute the uncorrected sagittal slope variation to an asymmetrical stress of the substrate due to tolerances of the mirror assembly. Note that at glancing incidence, the effect of sagittal slope errors are reduced, relative to the tangential errors, by a factor that is on the order of the grazing incidence angle.

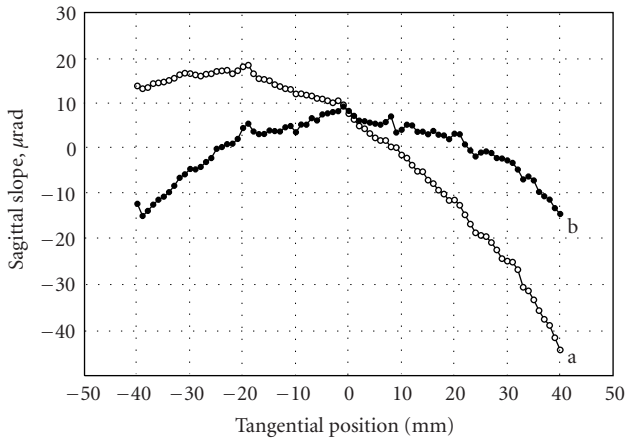

Figure 3: Mirror twist correction with the DLTP. The sagittal slope profiles of the mirror measured (a) before, and (b) after twist correction.

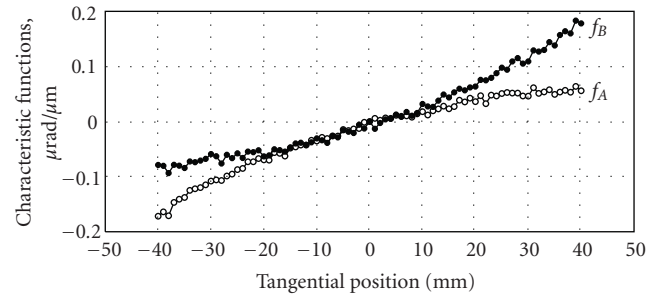

Figure 4: Characteristic functions of the test mirror benders measured with the DLTP: for the left-hand-side (upstream) bender (f_A) and for the right-hand-side (downstream) bender (f_B). Springs driven by Picomotors control the bending forces applied to the mirror. For convenience and linearity, we measure the Picomotor travel (in μm) directly, using an LVDT for feedback. Thus, the unit here is slope/μm of Picomotor travel.

For this reason, sagittal errors of this small magnitude, across the illuminated width of the mirror, will have little impact on focusing performance.

Note that when setting a set of KB mirrors for a beamline at the OML, the mutual perpendicularity of the mirror surfaces is aligned using the ZYGO GPI interferometer and a 90° optical reference cube.

4. Precision Setting and Characterization of the Mirror Benders

For optimally setting the mirror benders with a slope-measuring profiler, the DLTP [14] or the upgraded ALS LTP-II [15], we use an original procedure developed at the OML and described in Refs. [16, 17]. The procedure utilizes the near linearity of the bending problem. In this case, the minimum set of data necessary for characterization of one bender consists of three slope traces: (1) an initial measurement, $\alpha_1(x_i)$, (2) measurement after adjustment of the bending couple C_A by ΔC_A, $\alpha_2(x_i)$, and (3) measurement after adjustment of the second bending couple C_B by ΔC_B, performed at C_A, $\alpha_3(x_i)$. These three measurements, and their differences, provide a complete experimental characterization of the mirror benders, using the benders' characteristic functions

$$f_A(x_i) = \frac{\alpha_2(x_i) - \alpha_1(x_i)}{\Delta C_A},$$
$$f_B(x_i) = \frac{\alpha_3(x_i) - \alpha_1(x_i)}{\Delta C_B}. \quad (1)$$

Using a method of linear regression analysis with experimentally found characteristic functions of the benders, a prediction for a slope trace $\alpha_0(x_i)$, which is the best achievable approximation to the desired slope trace, and the corresponding optimal bending couplings, C_A^0 and C_B^0 are calculated. With this method [16, 17], the characteristic functions of the benders given by (1) can be used for retuning of the optics to a new desired shape without removal from the beamline and ex situ remeasuring with a slope profiler.

Figure 4 shows the characteristic functions of the test mirror, measured with the DLTP. As a measure of the bending couplings C_A and C_B, we use the readings from the LVDT sensors, measuring the displacements of the two Picomotor screws, in unit of μm. Note that the characteristic function of the upstream bender A (Figure 1) has a higher slope for the region closest to its bender; the opposite (downstream) side of the mirror surface is significantly less sensitive to the change of the bending coupling C_A. Similarly, the downstream bender B produces stronger curvature bending of its adjacent region of the mirror surface.

Once the predicted values of the optimal bending couplings (C_A^0 and C_B^0) are set, the mirror is measured once more to verify its shape. The inherent accuracy of the procedure is limited only by the current accuracy and precision of the OML slope measurements with the LTP-II and DLTP, which are close to 0.1 μrad.

Figure 5 shows the residual variation of the mirror tangential slope and height after subtraction of the desired elliptical shape. The variation, characterized with an rms slope variation of 0.5 μrad, is mostly due to the systematic, fourth-order, "bird-like" residual surface figure, with very little higher spatial frequency variation. There are a few sources potentially contributing to this figure error. As we have mentioned in Section 3, the current mirror assembly design does not allow for total compensation of the tension effect [9]. Fabrication errors of the sagittal shape and the thickness of the substrate are also possible.

Note that for the present investigation (unlike a beamline focusing application), the presence of the figure error is even useful for distinguishing a real change of the mirror shape from measurement errors.

From numerical simulations presented elsewhere [34], we also found the image distance may be slightly altered (then the mirror rebent according to the optimal bending techniques [16, 17]) to correct the residual fourth order aberration, thus resulting in a overall better mirror shape.

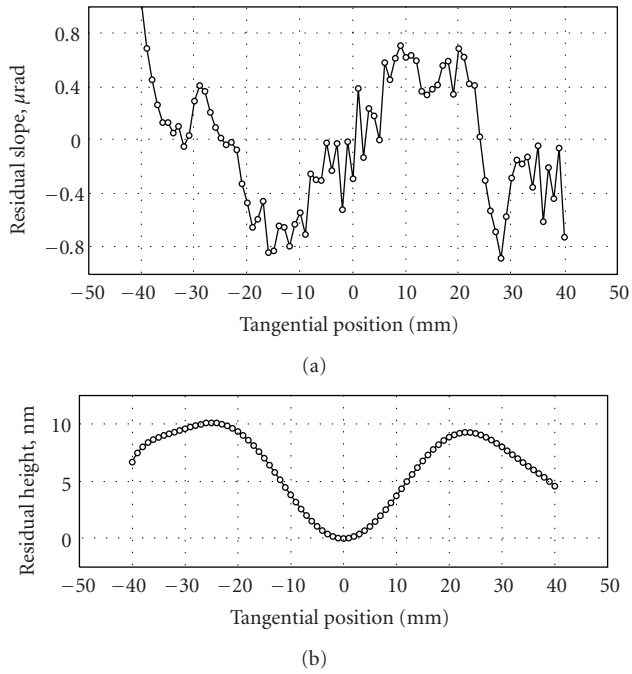

Figure 5: The residual variation of the mirror tangential slope after subtraction of (a) the desired shape. (b) The corresponding height trace obtained by a numerical integration of the slope trace.

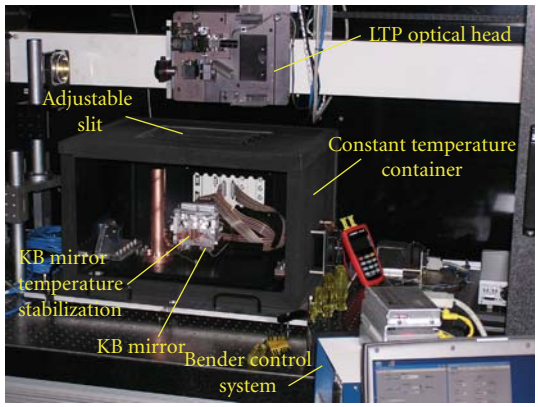

Figure 6: The container and the experimental arrangement for the LTP investigation of thermal effects with the bendable KB mirror. The mirror faces upward.

5. Experimental Setup for Thermal Tests

A special container with variable inside temperature was built for the LTP-II surface profile studies of the thermal dependence of X-ray optics. The container, with the KB mirror assembly inside, and the front side temporarily removed for inspection, is shown in Figure 6, as it was arranged for LTP-II measurements. The time constant for the current setup is about 35 minutes. For a longer mirror with larger bending mechanism, the time constant may vary.

The design of the container is based on a standard Thorlabs breadboard enclosure with plexiglass walls and feed-through panels on one of the sidewalls. For thermal isolation from the environment, the outside surface of the container is covered with self-adhesive thermal insulation material. The temperature inside the container is controlled with two actively stabilized Peltier elements. A temperature controller is utilized to supply current (5 A maximum) to the Peltier elements, connected in parallel, and to stabilize the temperature inside the container. A temperature transducer AD590, used as a feedback temperature sensor, is mounted on a bracket of one of the Peltier elements. One more temperature sensor, mounted in the center of the container breadboard, is used for monitoring temperature inside the container. A comparison of temperatures measured with the two sensors provides a measure of the temperature gradient. Test experiments with the container found that the uniformity of inside temperature variation is less than 0.3 C when the temperature range is within 4 C of room temperature.

For precise alignment of the upward-facing mirror with respect to the LTP-II light beam, there are four fine height adjusting screws placed at the corners of the container base plate (Figure 6). The LTP-II scans the mirror surface through an open, 200 mm (length) × 10 mm (width) slit, movable in the sagittal direction.

6. Thermal Effect on The Mirror Surface Shape

Mirror shape measurements at different stable, environmental temperatures were made with and without mirror-thermal stabilization.

After setting and characterization with the DLTP, the mirror was placed in the container mounted on the LTP-II optical table. The first set of LTP-II tests with the mirror were to investigate the mirror shape dependence on ambient temperature, without mirror temperature stabilization. Between shape measurements, a one hour time delay was given to reach thermal equilibrium inside the container.

A precise reference measurement at room temperature of 21 C was carried out after resetting of the mirror shape to the desired ellipse with the LTP. In order to suppress random noise and the error due to setup drift, a measurement run consisted of eight sequential scans performed according to the optimal scanning strategy suggested in [35]. At the best bent shape, the KB mirror's residual rms slope error was 0.55 μrad (Figure 7). While this is slightly larger than for the optimal bending obtained with the DLTP, the difference may be due to the increased systematic error of the LTP measurements due to the large distance between the LTP optical head and the mirror surface (Figure 1). See also a relevant discussion in [14].

Figure 7 summarizes the surface shape measurements performed at different temperatures inside the container, without mirror temperature stabilization. As the temperature within the container increases, the slope error of the originally best bent mirror increases.

The primary cause of the increase is the difference of thermal expansion of the mirror holder's aluminum body and the silicon mirror substrate (see Section 2). A simple estimation based on 100 mm substrate length gives a thermal

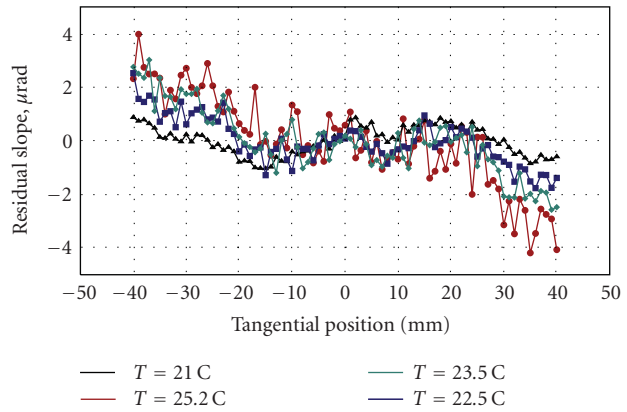

Figure 7: The residual variation of the mirror tangential slope measured at different temperatures inside the container and at the same setting of the benders. The traces correspond to the sagittal center of the mirror. The black, blue, green, and red curves are for $T = 21$ C, 22.5 C, 23.5 C and 25.2 C, respectively. The primary cause of the residual slope error increase is the temperature within the container.

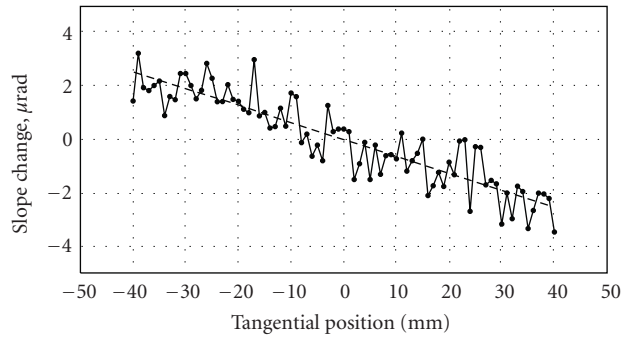

Figure 8: Temperature-induced surface slope change from a 4.2 C (25.2 C–21.0 C) temperature rise. The linear behavior represents a defocus with an effective convex radius of 15.7 km (dashed line).

expansion difference of 10 μm at $\Delta T = 5$C. The thermal expansion contributes to the tension the mirror assembly, leading to a change of the mirror shape.

Figure 8 shows the surface slope change due to thermal effects at the extreme temperature of $T = 25.2$ C within the measurement series. The slope change is obtained by subtracting the 21 C reference slope trace from the 25.2 C trace. The mirror slope change from the increased temperature has a linear form (cylindrical shape). Since the surface slope is the first order derivative of the surface height (sag), the linear difference slope term manifests as a focus error that will displace the focus longitudinally or blur the focal spot in a fixed image plane.

The measured curvature changes with changing temperature are given in Table 2. As in Figure 8, linear fitting to the slope trace differences are used for this measurement. The table also provides the corresponding values of the rms slope variation. To compensate the thermal effects, we can introduce defocus to the focal plane; the corresponding necessary

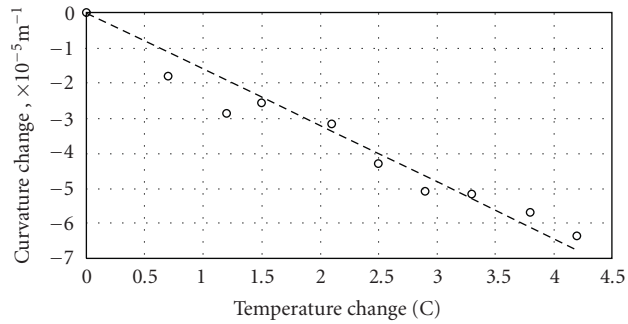

Figure 9: The mirror curvature change as a function of the container temperature. The dashed line shows a linear fit.

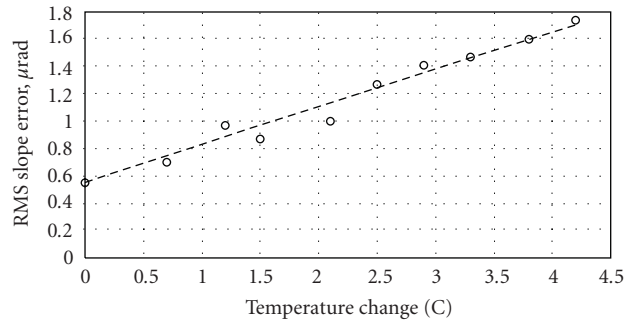

Figure 10: The rms slope error of the mirror surface shape as a function of the container temperature. The dashed line shows a linear fit.

defocus and the RMS slope error after the compensation are listed in Table 2 also.

Figures 9 and 10 present the data of the first two rows in Table 2 in a graphical form. The linear dependences in Figures 9 and 10 can be predicted based on the linearity of the temperature dependence of thermal expansion and on the linear character of the bending equation [9, 17]:

$$\frac{d^2y}{d^2x} = C_A g_A(x) + C_B g_B(x), \tag{2}$$

where

$$g_A(x) \equiv \left(\frac{1}{2} - \frac{x}{L}\right)\frac{1}{E\,I(x)}, \qquad g_B(x) \equiv \left(\frac{1}{2} + \frac{x}{L}\right)\frac{1}{E\,I(x)}, \tag{3}$$

and C_A and C_B are the bending couples, E is Young's modulus, and $I(x)$ is the moment of inertia of the substrate cross section. The best-fit linear approximations

$$\begin{aligned} \delta\text{Cur} &= -1.6(T - 21.0) \times 10^{-5}\text{m}^{-1}, \\ \delta\text{Slope} &= [0.28\ (T - 21.0) + 0.55]\,\mu\text{rad (rms)}, \end{aligned} \tag{4}$$

are shown in Figures 9 and 10 with the dashed lines.

In summary, without thermal stabilization, we observe a high sensitivity of the mirror shape to the ambient temperature. Temperature variations by a few degrees causes several micro-radians surface slope error: a magnitude that

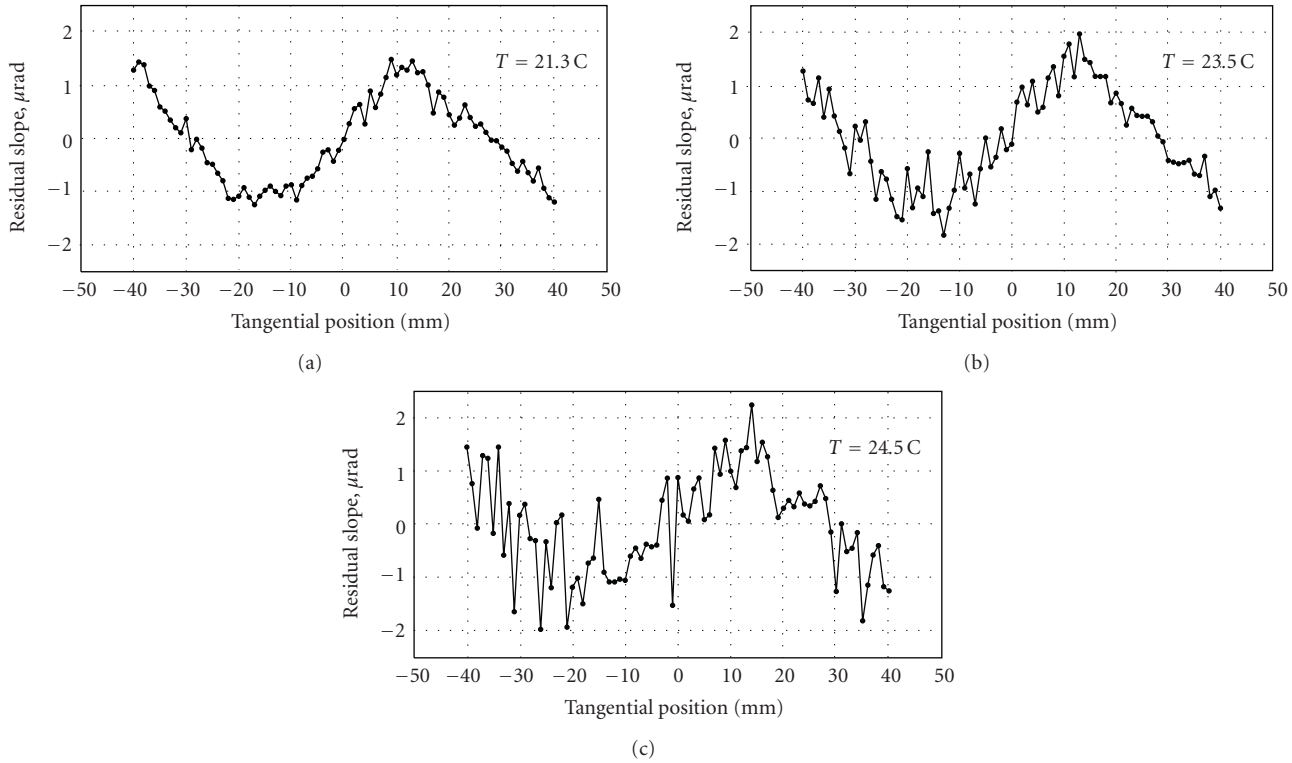

Figure 11: The residual variation of the mirror tangential slope measured at different temperatures inside the container without adjusting the bending couplings. The temperature controller attached to the bender body was set to constant 21.3°C. The traces correspond to the sagittal center of the mirror. Unlike the previous case, with no active temperature stabilization (Figure 7), the mirror figure remains constant. The increase of the random noise is due to the air convection that becomes stronger at higher temperature inside the container.

Table 2: Mirror curvature change and RMS slope error corresponding to different container temperatures, relative to the initial 21 C state. The corresponding focal change and residual RMS slope error (after compensation) are also given.

T (C)	21	21.7	22.2	22.5	23.1	23.5	23.9	24.3	24.8	25.2
curvature change (10^{-5} m^{-1})	0	−1.81	−2.87	−2.57	−3.17	−4.3	−5.09	−5.17	−5.69	−6.36
rms slope error (μrad)	0.55	0.70	0.97	0.87	1.00	1.27	1.41	1.47	1.60	1.74
required defocus compensation (mm)	0.00	0.10	0.17	0.20	0.25	0.26	0.28	0.30	0.35	0.40
rms slope error after defocus compensation (μrad)	0.55	0.56	0.68	0.65	0.71	0.78	0.76	0.87	0.83	0.87

would be unacceptable for most applications. The following section shows that the temperature sensitivity problem can be solved using an active temperature stabilization of the mirror body based on a Peltier element.

7. Effectiveness of the Mirror Temperature Stabilization

To investigate the effectiveness of the thermally stabilized KB mirror holder, a series of LTP measurements were conducted, in a similar manner to those described in the previous section. Using a dedicated Thorlabs temperature controller, the mirror body temperature was set to 21.3 C.

Figure 11 summarizes the slope measurements conducted at three different stable ambient temperatures. This time, while the temperature within the container increased, the slope error profile of the mirror remains unchanged. The observable increase of the random error is an artifact of the measurements associated with air convection along the LTP optical path [36]. The larger temperature inside the container, the stronger is the perturbation of the LTP light beam direction due to air convection.

Figure 12 shows a surface slope change at $T = 24.5$ C, relative to the 21.3 C slope trace. Compared with the earlier results, in Figure 8, the measurements with the thermally-stabilized mirror assembly show a significant suppression of the shape change effects.

8. Conclusions and Discussion

We have demonstrated that active temperature stabilization, based on a Peltier element attached directly to the body

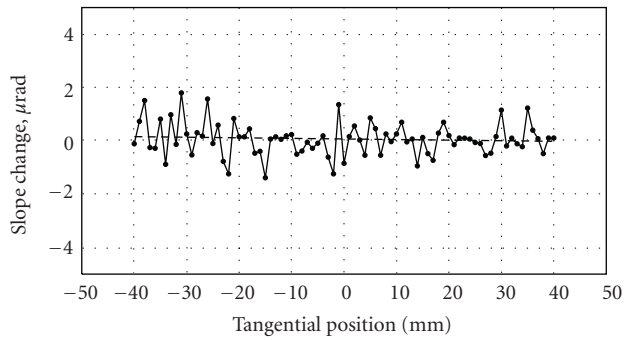

Figure 12: Temperature-induced surface slope change with a 3.2 C (24.5 C–21.3 C) increase in the ambient temperature. The dashed line is a linear fit. Unlike the previous case without temperature stabilization (Figure 8), here slope changes are not detectable within a measurement uncertainty of 3 *n*rad/mm that corresponds to a radius of curvature above 300 km.

of an elliptically bent KB mirror, provides mirror surface shape stability under several degrees of ambient temperature change. The design and the materials used in the mirror assembly have been carefully optimized to provide high heat conductance between the mirror body and its substrate.

Using a specially fabricated test mirror placed inside a temperature-controlled container, we investigated the thermal sensitivity of the mirror surface profile with and without active control of the mirror holder temperature. Without thermal stabilization, the rms variation of the mirror slope, measured with an LTP across an 80 mm clear aperture, changed by approximately 1.5 μrad (calculated from the RMS residual slope error before and after the maximum temperature change shown in Figure 7), under a 4.2 C temperature increase. However, with active thermal stabilization, in the presence of a 3.2 C temperature increase, the mirror slope did not noticeably change, within our measurement uncertainty, which is below 0.1 μrad.

The KB mirror, described throughout this work, is intended for use as a test X-ray optic at ALS beamline 5.3.1. The beamline endstation now under construction, is dedicated to at-wavelength, in situ metrology of X-ray optics [33, 34]. The test mirror's measured residual surface figure error of 0.5 μrad (rms) is relatively large when compared with the mirrors of the same design currently in use at the ALS beamline 10.3.2 and 12.3.2. We attribute this to the fact that this is an older, spare substrate with a significant sagittal width and/or thickness error. Contributions to the figure error may also come from the residual stress due to the imperfections of the mirror assembly. We are working on an upgrade of the mirror design that would allow us to significantly reduce the residual stress.

For the purposes of this investigation (separate from a beamline focusing application), the presence of the figure error is useful for distinguishing real changes of the mirror shape from measurement errors. Similarly, when using the mirror for testing at-wavelength metrology techniques, the known, residual figure error is a useful particularity that should be observable in the course of the metrology.

Disclaimer

Acknowledgment

This work was supported by the Director, Office of Science, of the U.S. Department of Energy under Contract no. DE-AC02-05CH11231.

References

[1] L. Assoufid, O. Hignette, M. Howells, S. Irick, H. Lammert, and P. Takacs, "Future metrology needs for synchrotron radiation grazing-incidence optics," *Nuclear Instruments and Methods in Physics Research Section A*, vol. 467-468, pp. 267–270, 2001.

[2] A. Erko, M. Idir, T. Krist, and A. G. Michette, Eds., *Modern Developments in X-ray and Neutral Optics*, Springer, Berlin, Germany, 2007.

[3] P. Kirkpatrick and A. V. Baez, "Formation of Optical Images by X-rays," *Journal of the Optical Society of America*, vol. 38, no. 9, pp. 766–774, 1948.

[4] C. Liu, L. Assoufid, R. Conley, A. T. Macrander, G. E. Ice, and J. Z. Tischler, "Profile coating and its application for Kirkpatrick-Baez mirrors," *Optical Engineering*, vol. 42, no. 12, pp. 3622–3628, 2003.

[5] H. Yumoto, H. Mimura, S. Matsuyama et al., "Fabrication of elliptically figured mirror for focusing hard X Rays to size less than 50 nm," *Review of Scientific Instruments*, vol. 76, no. 6, Article ID 063708, 5 pages, 2005.

[6] F. Siewert, H. Lammert, T. Noll et al., "Advanced metrology, an essential support for the surface finishing of high performance X-ray optics," in *Advances in Metrology for X-ray and EUV Optics*, vol. 5921 of *Proceedings of SPIE*, San Diego, Calif, USA, August 2005.

[7] S. Yuan and J. Sasian, "Aberrations of anamorphic optical systems. I: the first-order foundation and method for deriving the anamorphic primary aberration coefficients," *Applied Optics*, vol. 48, no. 13, pp. 2574–2584, 2009.

[8] S. Yuan and J. Sasian, "Aberrations of anamorphic optical systems. II. primary aberration theory for cylindrical anamorphic systems," *Applied Optics*, vol. 48, no. 15, pp. 2836–2841, 2009.

[9] M. R. Howells, D. Cambie, R. M. Duarte et al., "Theory and practice of elliptically bent X-ray mirrors," *Optical Engineering*, vol. 39, no. 10, pp. 2748–2762, 2000.

[10] P. Z. Takacs, "X-ray mirror metrology," in *Handbook of Optics*, M. Bass, Ed., vol. 5, chapter 46, McGraw–Hill, New York, NY, USA, 3rd edition, 2009.

[11] F. Siewert, H. Lammert, and T. Zeschke, "The nanometer optical component measuring machine," in *Modern Developments in X-ray and Neutron Optic*, A. Erko, M. Idir, T. Krist, and A. G. Michette, Eds., Springer, Berlin, Germany, 2008.

[12] R. D. Geckeler, "ESAD shearing deflectometry: potentials for synchrotron beamline metrology," in *Advances in X-ray/EUV Optics, Components, and Applications*, vol. 6317 of *Proceedings of SPIE*, San Diego, Calif, USA, August 2006.

[13] T. Kimura, H. Ohashi, H. Mimura, et al., "A stitching figure profiler of large X-ray mirrors using RADSI for sub-aperture data acquisition," *Nuclear Instruments and Methods in Physics Research Section A*, vol. 616, no. 2-3, pp. 229–232, 2010.

[14] J. L. Kirschman, E. E. Domning, W. R. McKinney, G. Y. Morrison, B. V. Smith, and V. V. Yashchuk, "Performance of the upgraded LTP-II at the ALS optical metrology laboratory," in *Advances in X-ray/EUV Optics and Components III*, vol. 7077 of *Proceedings of SPIE*, San Diego, Calif, USA, August 2008.

[15] V. V. Yashchuk, S. Barber, E. E. Domning et al., "Sub-microradian surface slope metrology with the ALS developmental long trace profiler," *Nuclear Instruments and Methods in Physics Research Section A*, vol. 616, no. 2-3, pp. 212–223, 2010.

[16] W. R. McKinney, S. C. Irick, J. L. Kirschman, A. A. MacDowell, T. Warwick, and V. V. Yashchuk, "New procedures for the adjustment of elliptic ally bent mirrors with the long trace profiler," in *Advances in Metrology for X-ray and EUV Optics II*, vol. 6704 of *Proceedings of SPIE*, San Diego, Calif, USA, August 2007.

[17] W. R. McKinney, S. C. Irick, J. L. Kirschman, A. A. MacDowell, T. Warwick, and V. V. Yashchuk, "Optimal tuning and calibration of bendabale mirrors with with slope measuring profilers," *Optical Engineering*, vol. 48, no. 8, Article ID 083601, 2009.

[18] S. Mourikis, W. Jark, E. E. Koch, and V. Saile, "Surface temperature and distortion of optical elements exposed to high power synchrotron radiation beams," *Review of Scientific Instruments*, vol. 60, no. 7, pp. 1474–1478, 1989.

[19] T. Warwick and S. Sharma, "Thermal effects and mirror surface figure requirements for a diagnostic beamline at the advanced light source," *Nuclear Instruments and Methods in Physics Research A*, vol. 319, no. 1–3, pp. 185–187, 1992.

[20] N. Kihara, K. Mashima, S. Miura et al., "Thermal and deformation analyses of side-cooled monochromator mirrors for the SPring-8/Figure-8 soft X-ray undulator," *Journal of Synchrotron Radiation*, vol. 5, no. 3, pp. 811–813, 1998.

[21] A. K. Freund, "Challenges for synchrotron X-ray optics," in *X-ray Mirrors, Crystals, and Multilayers II*, vol. 4782 of *Proceedings of SPIE*, Seattle, Wash, USA, July 2002.

[22] R. K. Smither, W. Lee, A. Macrander, D. Mills, and S. Rogers, "Recent experiments with liquid gallium cooling of crystal diffraction opticsa," *Review of Scientific Instruments*, vol. 63, no. 2, pp. 1746–1754, 1992.

[23] M. R. Howells, "Some fundamentals of cooled mirrors for synchrotron radiation beam lines," *Optical Engineering*, vol. 35, no. 4, pp. 1187–1197, 1996.

[24] H. R. Beguiristain, J. H. Underwood, M. Koike, et al., "haracterization of thermal distortion effects on beamline optics for EUV interferometry and soft X-ray microscopy," *Review of Scientific Instruments*, vol. 67, no. 9, pp. 1–9, 1996.

[25] K. A. Goldberg, H. R. Beguiristain, J. Bokor et al., "At-wavelength testing of optics for EUV," in *Electron-Beam, X-ray, EUV, and Ion-Beam Submicrometer Lithographies for Manufacturing V*, vol. 2437 of *Proceedings of SPIE*, Santa Clara, Calif, USA, February 1995.

[26] S. Qian, W. Jark, P. Z. Takacs, K. J. Randall, and W. Yun, "In situ surface profiler for high heat load mirror measurement," *Optical Engineering*, vol. 34, no. 2, pp. 396–402, 1995.

[27] S. Qian, W. Jark, G. Sostero, A. Gambitta, F. Mazzolini, and A. Savoia, "Precise measuring method for detecting the in situ distortion profile of a high-heat-load mirror for synchrotron radiation by use of a pentaprism long trace profiler," *Applied Optics*, vol. 36, no. 16, pp. 3769–3775, 1997.

[28] P. Z. Takacs, S. Qian, K. J. Randall, W. B. Yun, and H. Li, "Mirror distortion measurements with an In-Situ LTP," in *Advances in Mirror Technology for Synchrotron X-ray and Laser Applications*, vol. 3447 of *Proceedings of SPIE*, San Diego, Calif, USA, July 1998.

[29] O. Hignette, A. K. Freund, and E. Chinchio, "Incoherent X-ray mirror surface metrology," in *Materials, Manufacturing, and Measurement for Synchrotron Radiation Mirrors*, vol. 3152 of *Proceedings of SPIE*, San Diego, Calif, USA, July 1997.

[30] P. Revesz, A. Kazimirov, and I. Bazarov, "In situ visualization of thermal distortions of synchrotron radiation optics," *Nuclear Instruments and Methods in Physics Research Section A*, vol. 576, no. 2-3, pp. 422–429, 2007.

[31] T. Kimura, S. Handa, H. Mimura et al., "Development of adaptive mirror for wavefront correction of hard X-ray nanobeam," in *Advances in X-ray/EUV Optics and Components III*, vol. 7077 of *Proceedings of SPIE*, San Diego, Calif, USA, August 2008.

[32] M. Kunz, N. Tamura, K. Chen et al., "A dedicated superbend X-ray microdiffraction beamline for materials, geo-, and environmental sciences at the advanced light source," *Review of Scientific Instruments*, vol. 80, no. 3, Article ID 035108, 10 pages, 2009.

[33] S. Yuan, K. Goldberg, V. V. Yashchuk, et al., "At-wavelength and optical metrology of bendable X-ray optics for nanofocusing at the ALS," in *Frontiers in Optics 2009, Laser Science XXV, Special Symposium on Optics for Imaging at the Nanoscale and Beyond*, San Jose, Calif, USA, October 2009.

[34] S. Yuan, M. Church, R. Celestre, et al., "Surface slope metrology and interferometric wave front measurements on deformable soft X-ray mirrors performed in the laboratory and in-situ at-wavelength," in *Proceedings of the 10th International Conference on Synchrotron Radiation Instrumentation*, Melbourne, Australia, October 2009.

[35] V. V. Yashchuk, "Optimal measurement strategies for effective suppression of drift errors," *Review of Scientific Instruments*, vol. 80, no. 11, Article ID 115101, 10 pages, 2009.

[36] V. V. Yashchuk, S. C. Irick, A. A. MacDowell, W. R. McKinney, and P. Z. Takacs, "Air convection noise of pencil-beam interferometer for long-trace profiler," in *Advances in X-ray/EUV Optics, Components, and Applications*, vol. 6317 of *Proceedings of SPIE*, San Diego, Calif, USA, August 2006.

Hindawi Publishing Corporation
X-Ray Optics and Instrumentation
Volume 2010, Article ID 139148, 39 pages
doi:10.1155/2010/139148

Review Article

Kirkpatrick-Baez (KB) and Lobster Eye (LE) Optics for Astronomical and Laboratory Applications

René Hudec[1,2]

[1] *Astronomical Institute, Academy of Sciences of the Czech Republic, CZ-251 65 Ondřejov, Czech Republic*
[2] *Faculty of Electrical Engineering, Czech Technical University in Prague, Technicka 2, 160 00 Praha 6, Czech Republic*

Correspondence should be addressed to René Hudec, rene.hudec@gmail.com

Received 16 May 2010; Revised 26 November 2010; Accepted 22 December 2010

Academic Editor: Stephen L. O'Dell

Most of grazing incidence (reflective) X-ray imaging systems used in astronomy and in other (laboratory) applications are based on the Wolter 1 (or modified) arrangement. But there were proposed also other designs and configurations, which are considered for future applications for both in laboratory and (finitely) in space. The Kirkpatrick-Baez (KB) lenses as well as various types of Lobster-Eye (LE) optics and MCP/Micropore optics serve as an example. Analogously to Wolter lenses, the X-rays are mostly reflected twice in these systems to create focal images. The KB systems have already found wide usage in laboratory and synchrotron, both application are reviewed and discussed in detail in this paper. While this paper focuses on future possible applications of non-Wolter grazing incidence systems in space and astronomy, we also discuss in detail applications in other areas of science, where (in contrary to astronomy) some of these systems have demonstrated their advantages.

1. Introduction

X-ray astronomy represents an important part of recent astrophysics. Many scientific achievements of the last two decades of X-ray astronomy are closely related to the use of imaging X-ray telescopes. These telescopes achieve much better signal/noise ratio than X-ray experiments without optics—this allows, for example, the detection of faint sources. The use of X-ray optics further allows imaging, precise localization, photometry, spectroscopy, variability studies, and estimation of physical parameters of X-ray emitting regions (temperature, electron density, etc.). The space experiments with X-ray optics are also well suited for monitoring of X-ray sky for variable and transient objects including X-ray novae, X-ray transients, X-ray flares on stars and Active Galactic Nuclei (AGNs), galactic bulge sources, X-ray binaries, SGRs (Soft Gamma Ray Repeaters), and X-ray afterglows of GRBs (Gamma Ray Bursts). The X-ray optics represents an important part of numerous past, recent, and future space projects such as the European X-ray Observatory Satellite (EXOSAT), the Roentgen Satellite (ROSAT), Einstein, RT-4M Salyut 7, Fobos, the Advanced X-ray Astrophysics Facility AXAF/Chandra, the X-ray Multi-mirror Mission (XMM)/Newton, BeppoSAX, the Advanced Satellite for Cosmology and Astrophysics (ASCA), and the International X-Ray Observatory IXO.

In the laboratory, there are numerous applications of the X-ray optics for example, in plasma physics, laser plasma, synchrotron analyses, biology, crystallography, medicine, material and structure testing, X-ray lithography, and so forth. These applications will be reviewed in next sections of this paper, when the various application areas of the nonWolter X-ray optics will be described and discussed.

The alternative (to Wolter systems) X-ray imaging mirrors based on grazing incidence reflections were described in the literature and have found numerous applications in the laboratory, but their space and astronomy applications are still marginal. We review and discuss these systems, discuss their past and recent ground-based applications, and discuss their possible potential for future X-ray astronomy applications.

We give a brief introduction to the various types of grazing incidence X-ray optics in Section 2, with emphasis on the non-Wolter optical systems. In Section 3, the Kirkpatrick-Baez systems (consisting a set of two orthogonal parabolas of translation) are described and discussed in detail, for

both laboratory and space and astrophysical applications (yet limited but with promising potential for the future). In Section 4 the wide-field systems of Lobster Eye (LE) are in detail described and discussed, with emphasis on prototypes already designed, developed and tested. Both Schmidt and Angel optics are discussed, as well as MultiFoil (MFO) and MicroChannel Plate (MCP) approaches, including short comparison and recent published results demonstrating the measured performance. In Section 5 capillaries are introduced and described.

1.1. Why X-Ray Optics? There are numerous applications in space and in the laboratory where the X-rays imaging in is required. Very essential is the use of X-ray optics in X-ray astronomy and astrophysics since it improved the signal to noise ratio, and hence much fainter and more distant objects can be detected and investigated.

The grazing incidence reflecting X-ray lenses discussed in this work reflect typically soft X-rays from the optical region up to about 2–10 keV, depending on the surface material and on the angle of incidence. Since there were scientific requirements to enlarge the working range toward the higher energies, the recent efforts focus on various improvements and additional surface layers such as multilayer's to meet this [13, 14]).

In astronomy and astrophysics, it was the use of imaging X-ray telescopes based on grazing incidence X-ray optics that opened a completely new window to the Universe and has lead to great discoveries during the past decades. To acknowledge these achievements, the Nobel Prize for physics for the year 2002 was assigned to the Professor Riccardo Giacconi who significantly contributed to the construction of first astronomical X-ray telescopes in the 1960s and 1970s.

In this work, we focus on the non-Wolter grazing incidence X-ray imaging systems.

1.2. The History of X-Ray Imaging. The X-rays were discovered in 1895 by W. C. Roentgen. However, it took many years to establish the nature of X-rays as electromagnetic waves, and to find ways how to focus them. Essential was the discovery that the X-rays are diffracted when passing through a crystal (von Laue 1912 [16]). The second step for focusing of X-rays was the finding that the X-rays can be reflected from a polished surface at small (glancing, grazing incidence) angles (Compton 1923 [17] and Ehrenberg and Jentzsch 1929 [18]).

It is obvious that classical lenses and others optical telescope designs cannot be used for X-ray focusing and/or imaging, as X-rays are either absorbed or passed straight through lens or mirrors. In addition, any single mirror X-ray grazing incidence system suffers from severe astigmatism (Jentzsch 1929 [19]). The first design of X-ray optics was suggested by Kirkpatrick and Baez in 1948. The problem of astigmatism was overcome with the use of 2 orthogonally crossed mirrors, each providing 1D focusing. This led to the production of the first 2D X-ray image. In the same year, the experiment carried out by a V2 rocket discovered the Sun being a bright source of X-rays (Burnight 1949 [20]). The further important step came in 1951, when German physicist Hans Wolter (Wolter 1952 [1]) published his (different from Kirkpatrick and Baez) idea of grazing incidence X-ray mirrors. According to Wolter, a true X-ray image can be formed by two grazing reflections on three various parabolic/hyperbolic or parabolic/elliptic combinations of coaxial and confocal mirrors. The Wolter design is now the most widely one used in X-ray telescopes (e.g., EXOSAT, ROSAT, Chandra, Newton, IXO, etc.).

As already mentioned, the first celestial object seen in X-rays was Sun. However, the first X-ray image of the Sun was not taken by a mirror, but with the use of a simple pinhole camera (Chubb et al. 1961 [21], Byram et al. 1961 [22]). In 1962, a counter experiment on a sounding rocket discovered the first nonsolar celestial X-ray sources, namely, the diffuse X-ray background and the galactic source Scorpius X-1. In 1963, the first grazing incidence telescope of the Wolter type was used to record the X-ray images of the Sun on a photographic film (in the East, it was a similar experiment in 1978, also using sounding rocket, e.g., [23]). More advanced X-ray mirrors having sub-arcmin resolution came with the US space station Skylab in 1973. The station Skylab carried two solar X-ray telescopes S-054 (Underwood et al. 1977 [24]) and S-056 (Underwood and Attwood 1984 [25], Thiel et al. 1989 [26]) with fine angular resolution of a few arc seconds. The images were recorded on the X-ray film, taking the advantage of telescope being onboard of the manned space vehicle.

After Skylab telescopes, the interest moved towards the non-solar X-ray astronomy and astrophysics (e.g., [27]). The application of focusing X-ray optics to X-ray astronomy was first discussed by Giacconi and Rossi [28]. The most commonly used system since then consists of two successive conic sections of revolution (Magnus and Underwood, 1969 [29]).

The US Einstein observatory (HEAO-B) was launched in 1978, with a large nested (4 shells) X-ray imaging telescope of a Wolter type I configuration. The detectors of this telescope included the imaging proportional counter and a high-resolution microchannel plate device. The European EXOSAT satellite followed in 1983 with two identical mean-aperture Wolter-type I telescopes was produced by unique gold/epoxy replication. Also, the Soviet orbital station Salyut 7 carried similar imaging X-ray telescope RT-4M onboard, with an epoxy replicated X-ray mirrors produced by our group in the Czech Republic (Hudec et al., 1988 [30]). The aperture (24 cm) was similar to those of EXOSAT and the reflecting material was gold for the outer shell and nickel for the inner shell. The progress continued with German satellite ROSAT and recently with Chandra-AXAF and XMM-Newton (with unprecedented collecting area of XMM—the combined collecting area is 4,300 cm^2—and angular resolution of AXAF −0.5 arcsec). Nowadays, future large and advanced X-ray telescopes such as the IXO of the European Space Agency ESA, American agency NASA, and Japanese agency JAXA, or Astro-H by JAXA, are planned and considered. There are numerous and various efforts for these future technologies (e.g., Citterio et al. 2002 [31], Hudec et al. 2004 [32] and Hudec et al. 2006 [33]).

Apart from these Wolter type imaging systems, other types (non-Wolter) imaging elements based on grazing incidence were proposed and discussed. The Kirkpatrick-Baez mirror systems were flown several times on rockets; the Lobster Eye modules (e.g., Hudec et al., 2003 [34]) are still waiting for their space applications.

In parallel to space/astronomy oriented efforts, the X-ray optics has been developed for various laboratory and technology applications (e.g., sobelmen et al. 1990 [35]). Many of these efforts originated from astronomical X-ray optics developments and related techniques. More recently, as we will show in this paper, the future astronomical instrumentation can benefit from past developments of non-Wolter X-ray optics for laboratory and other non-astronomical applications. Recently available novel X-ray optics substrates such as improved silicon wafers can be favourably used in these systems, both laboratory and astronomical.

In the Czech Republic, the efforts on design and developments of X-ray lenses and X-ray telescopes started in late 60ies as a part of the Interkosmos program and focused on grazing incidence optics of various types (e.g., Hudec et al. 1981 [36], Hudec et al. 1984 [37], and Sobelman et al. 1990 [38]). Three main designs were investigated and supported, namely Wolter, Kirkpatrick-Baez (KB), and Lobster (Hudec et al. 1989 [39], Hudec et al. 1989 [40], Hudec et al. 1991 [41], Hudec et al. 1992 [42], Hudec et al. 1999 [43], Hudec et al. 2000 [44], Hudec et al. 2001 [45], Hudec et al. 2003 [46], Hudec et al. 2004 [32] and Hudec et al. 2004 [47]).

2. The Various Types of X-Ray Optics

According to the physical processes involved in the imaging process, one can divide the X-ray optics into the following groups:

(i) diffractive optics (Fresnel lenses + pinholes): not useful for space due to small apertures (albeit there are recent considerations of applications of analogues of refractive lenses based on mosaic crystals (Laue lenses) in space gamma-ray astronomy),

(ii) refractive optics: limited use, not useful for space,

(iii) reflective optics, based on total reflection (grazing incidence),

(iv) reflective optics, allowing normal incidence (multilayer's).

In this work, we will concentrate on reflective X-ray lenses (mirrors). The critical angle for total external reflection of X-rays from materials composed of heavy elements (Henke et al. 1993 [48], and Hubbell et al. 1975 [49], Hubbell et al. 1977 [49]) can be calculated as (Table 1)

$$\theta_c = 2.32 \times 10^3 \left(\frac{Z_\rho}{A}\right)^{1/2} \lambda, \quad (1)$$

Table 1: Critical angles θ_c (mrad) for selected materials frequently used to reflect X-rays in grazing incidence X-ray mirrors for two selected energies Cu K_α (8,0 keV) and Mo K_α (17.4 keV).

Material	Cu K_α	Mo K_α
Ni	7.37	3.40
Au	9.96	4.59
Ir	10.75	4.96
Glass	4.07	1.88

where Z, A and ρ are the atomic number, atomic mass and specific gravity, respectively, of the surface and λ is the X-ray wavelength in nm.

This gives a critical angle of about 1° for X-rays of a few keV. For larger incidence angles, the mirrors will absorb the X-rays. As already mentioned, the X-rays are reflected when they incident on very smooth surfaces at glancing angles less than the critical angle for total external reflection. However the decrease in reflectivity is not sharp because of inherent photoelectric absorption in the material as well as surface roughness of the surface.

Table 1 lists the critical angles for various materials for Cu K_α and Mo K_α radiation. Note that for example, the critical angles for Mo K_α are so small that it is very difficult to construct reflecting collimators for Mo K_α X-rays.

The critical angle, however, is in fact not sharply defined: the reflectivity R drops off slowly from near-unity at a very small glancing angle and the falloff is less sharp for heavy elements than for light ones. The decrease in the reflectivity is a function of the surface micro roughness; for the typical X-ray imaging purposes, the rms roughness must be less than 1…2 nm. Values of R as a function of θ, θ_c and σ have been computed using models of differing complexity (see Sinha et al., 1988 [38]; Kopecky, 1995 [50]). The effects can be computed by the Fresnel approximation (see Compton, 1935 [51]) and multiplied by a roughness factor $\gamma_\sigma = \exp -[(4\pi\sigma\theta/\lambda)^2]$. The requirement for grazing incidence reflections leads to telescope designs that are different from classical optical devices.

2.1. Wolter Optics. As seen in the previous sections, the X-rays can be reflected only on smooth surfaces at very small (typically less than 1 degree depending on surface material and the energy range) angles, that is, at grazing incidence. The suitable materials for the mirrors are the metals with high density, such as gold, nickel, and platinum. The reflection is nondispersive, that is, focusing of X-rays is over a broad energy range. The most common type of the grazing incidence optics is the Wolter optics (Wolter, 1952 [1]). Wolter designed an aplanatic system of X-ray grazing incidence mirrors free of both spherical aberration and coma, with the Abbe sine condition fulfilled (Figure 1).

As the Wolter optics is in detail described in other papers in this volume, as well as in many other papers (e.g., Aschenbach 1985 [52]) it will not be described and discussed in this paper. The Wolter optics constructed in the Czech Republic is shown on Figure 2.

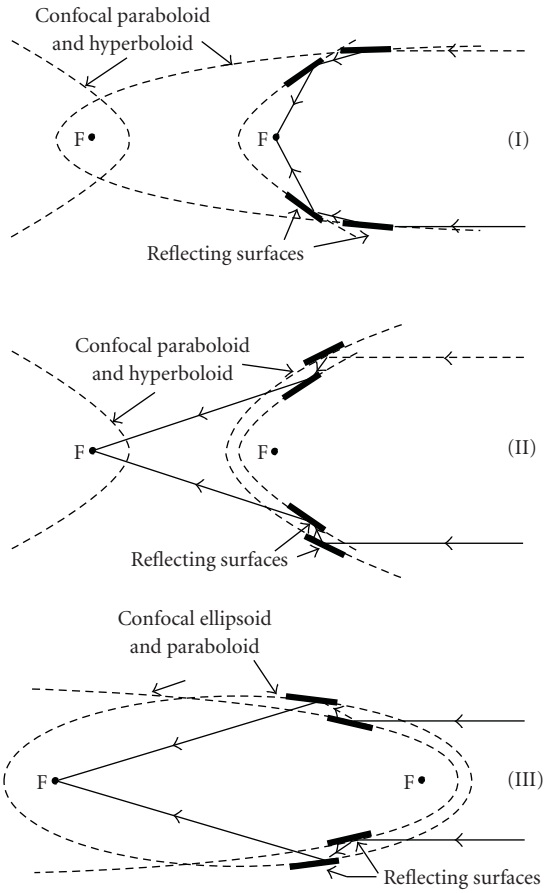

Figure 1: The schematics of Wolter X-ray lenses (according to Wolter 1952 [1]).

2.2. Double-Cone Approximation of Wolter Optics. For some applications, mostly those not requiring high angular resolution, the Wolter surfaces can be approximated by less laborious and hence less expensive conical profiles. The conical mirrors have lower imaging quality, but in many cases larger collecting area since the shells can be made very thin (Serlemitsos et al. 1997 [53]). These mirrors usually represent high-throughput systems, and can be preferably used in astronomical foil telescopes. The foil mirrors use thin foils instead of (thicker) grazing incidence reflecting surfaces. Examples of X-ray telescopes based on this approach are The Broad-Band X-Ray Telescope (BBXRT), Suzaku, and ASCA. In the case of ASCA, each of its 4 telescopes consists of 120 layers, while the Suzaku has about 180 shells in each of the 5 telescopes. The drawback of these and similar foil telescopes based on double conical arrangement is the spatial resolution limited to (in best cases) about 1 arcmin. This is also the case of the recent Astro-H telescope. More recently, multipore silicon wafer optics has been proposed (Bavdaz et al., 2004 [54]). It is based on conical approximation but with very special arrangement resulting in very short lengths of the surfaces and hence very small deviations from parabolic and hyperbolic surfaces. As a consequence, such systems could achieve fine angular resolution, of order of 10 arcsec.

Figure 2: Replicated grazing incidence X-ray optics (various technologies) designed and developed by our group in the Czech Republic. The replication technology has been modified several times to meet the dedicated requirements. The two black mirrors are produced by carbon fibre technology.

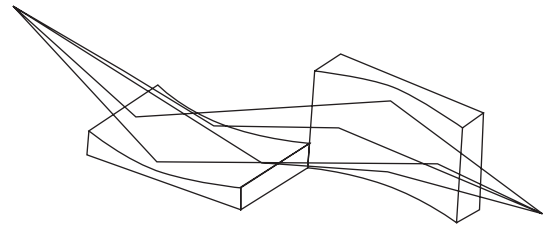

Figure 3: The arrangement of the Kirkpatrick-Baez X-ray objective (according to Kirkpatrick and Baez 1948 [2]).

2.3. Conical, Ellipsoidal, and Paraboloidal Optics. These mirrors with only one reflection find most of their applications in the laboratory either as collimating or focusing and/or imaging elements.

2.4. Kirkpatrick-Baez (KB) Optics. Although the Wolter systems are generally well known, Hans Wolter was not the first who proposed X-ray imaging systems based on reflection of X-rays. In fact, the first grazing incidence system to form a real image was proposed by Kirkpatrick and Baez 1948 [2]. This system consists of a set of two orthogonal parabolas of translation as shown in Figure 3. The first reflection focuses to a line, which is focused by the second surface to a point. This was necessary to avoid the extreme astigmatism suffered from a single mirror but still was not free of geometric aberrations. Nevertheless, the system is attractive for being easy to construct the reflecting surfaces. These surfaces can be produced as flat plates and then mechanically

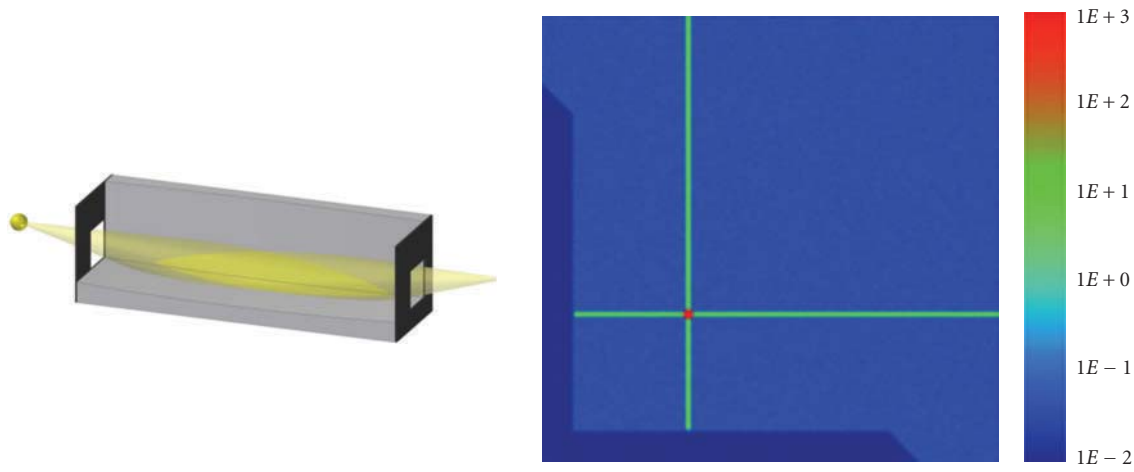

Figure 4: Principle of Montel optics (a) and simulated intensity distribution in the focal plane when no apertures are used (b): shadow of the mirrors (dark blue), direct rays (light blue), line foci (green) and focus point (red). Adopted from http://www.x-ray-optics.de/ [3].

bent to the required curvature. In order to increase the aperture a number of mirrors can be nested together, but it should be noted that such as nesting introduces additional aberrations.

This configuration is used mostly in experiments not requiring large collecting area (solar, laboratory). Recently, however, large modules of KB mirrors have been suggested also for stellar X-ray experiments.

2.5. Montel Optics. Montel optics (Montel 1957 [58]), also known as "side-by-side" optics, consist of two mirrors arranged perpendicular and side-by-side (Figure 4). The mirrors are shaped like elliptic cylinders. In the case of a very distant source or focal point, the incoming, respectively, out coming rays are nearly parallel to the optical axis leading to parabolic shaped cylinders as mirrors. Incoming rays hitting one of the mirrors first and then the other one will be redirected to the focus point. Some rays hit only one of the mirrors resulting in a horizontal or vertical line focus (Figure 4(b)). These rays, and the rays hitting none of the mirrors have to be blocked by suitable shaped apertures at the entrance and at the exit of the optics. This optics has laboratory applications only.

2.6. Normal Incidence Optics. There is one exception for the grazing incidence rule for reflecting X-rays mentioned before, and that is the multilayer normal incidence optics. This type of X-ray optics requires the multilayer deposition on the mirror surface allowing its use under normal incidence (e.g., Alford et al. 1995 [59]). The use of multilayer's results in narrow spectral range and in the past has been used mostly in solar experiments (TEREK Fobos, TEREK KORONAS...) as well as in laboratory applications (Schwarzschild microscopes, etc.). The normal incidence systems are limited to soft X-rays because of the limitation of multilayer's.

2.7. Lobster Eye (LE) Optics. This optic mimics the arrangements of eyes of lobsters and was suggested in the 1970s for a very wide field X-ray imaging but not yet used in space mostly due to severe manufacturing problems. Recently, the first test modules have been available for both the Schmidt and the alternative Angel configurations.

Images in the eye of a lobster are formed through reflections off the internal walls of a lattice of small square-sided tubes arranged over the surface of a sphere. This design can be used in the construction of a grazing incidence system to focus X-rays (Figure 5).

The X-ray objective based on the lobster eye was proposed by Angel (1979 [60]), following a similar design of a wide-field lens by Schmidt (1975 [53]). Each small channel is aligned along the radius of a sphere. A ray reflected twice off adjacent walls inside the channel is focused onto a spherical focal plane. Rays reflected only once are focused to a line causing background images to appear as a tapered cross. Some rays go through the lens with no reflections, contributing to diffuse background. The finite size of the tubes produces specific defocusing in the image, while the angle subtended by each tube at the focus limits the resolution of the system.

Despite these drawbacks, the great advantage of this design is an almost unlimited field of view (Gorenstein 1987 [61]). This makes it ideal for use as an all-sky X-ray monitor (Priedhorsky et al. 1996 [62], Priedhorsky et al. 2000 [62], Fraser 2002 [63], and Fraser 2003 [64],). Up to date, no X-ray telescopes have been launched using lobster-eye optics, mainly due to difficulty in manufacturing of the reflective tubes. However, improvements in multichannel plate technology has led to a proposal for a lobster-eye X-ray telescope could be placed on the International Space Station (Fraser et al. 2002 [65]) and to an application on BeppiColombo (Fraser et al., 2010 [66]), and the alternative glass foil technology developed in the Czech Republic has lead to the construction of several first telescopes

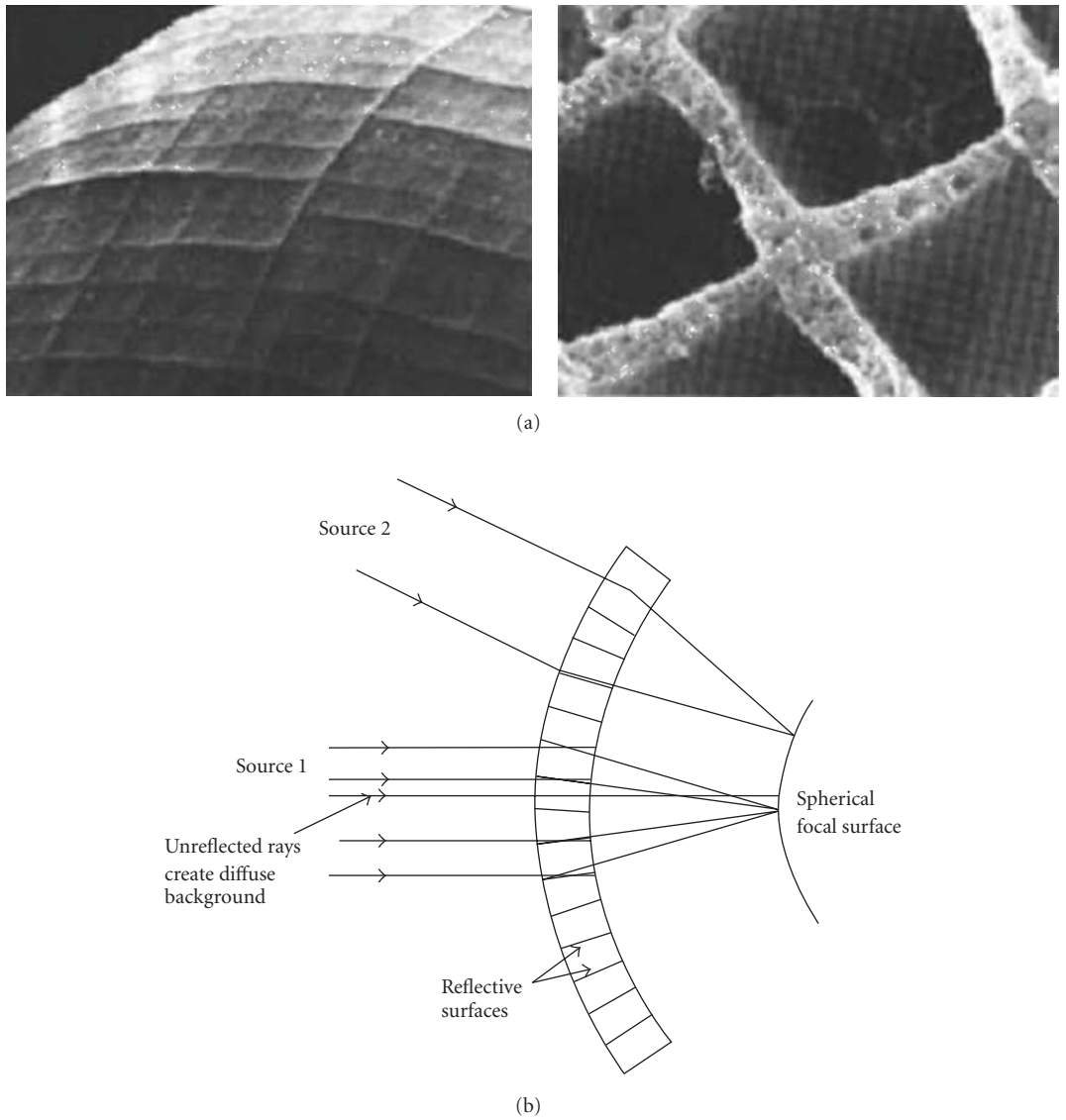

Figure 5: The Lobster-eye wide field X-ray imaging system (from http://www.src.le.ac.uk/lobster). (a) The real lobster eye, (b) the schema.

(Inneman et al. 1999 [67], Inneman et al. 2000 [68]). The related efforts in the Czech Republic have started soon after announcing the idea of lobster optics (Hudec et al., 1985 [69], Hudec et al., 2003 [70]).

2.8. Kumakhov (Polycapillary) X-Ray Optics. Another and fully different type of X-ray optics is based on the fact that the total external reflection also allows X-rays to be transmitted through single straight or tapered hollow glass tubes in analogy to visible light fibre optics (Thiel et al. 1989 [26]). This type of X-ray optic, based on an assembly of a large number of hollow capillary tubes stacked together was invented by Kumakhov (1990 [4]). In this type of X-ray lenses, the X-rays incident on the interior of the tubes at small angles (smaller than the critical angle for total external reflection) is guided down the tubes by total external reflection (Figure 6). Since the original proposal the technology to control X-rays using systematic arrangements of glass polycapillaries has developed significantly and depending on the specific arrangement and application, X-ray beams can be focused or divergent beams can be made quasiparallel.

Such arrays can control X-ray beams, such as collecting divergent radiation from a point source, collimating and focusing (Kumakhov, 1990 [4]). These X-ray optical systems can collect divergent radiation from a point source over a solid angle as large as one radian. Recently, capillary optics can be operated from 1 to 60 keV however, this range is expected to be further extended. These systems find applications in the laboratory but hardly in space telescopes because they do not represent true imaging devices.

2.9. MCP X-Ray Optics. The MicroChannel Plates (MCPs) also focus X-rays by reflection from the inside surfaces of the channels. This is easy to visualise in the simplest possible

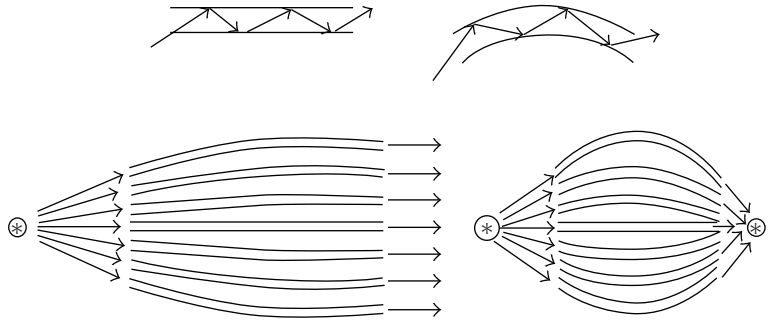

Figure 6: The Kumakhov X-ray lenses (polycapillary optics, Kumakhov, 1990 [4]) left arrangement for a quasiparallel beam, right arrangement for-point-to point focussing.

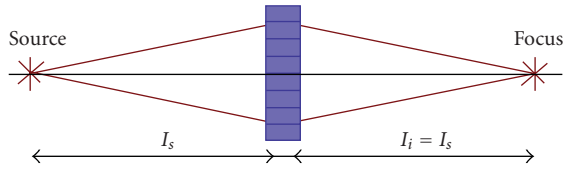

Figure 7: The principle of MCP X-ray Optics.

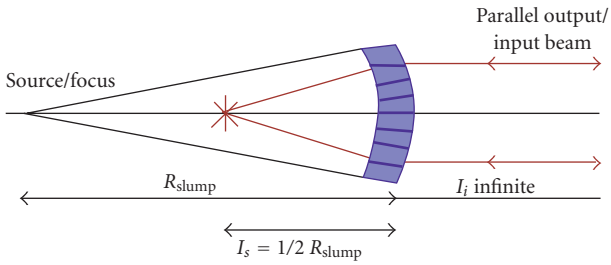

Figure 8: The MCP optics as Wolter lens.

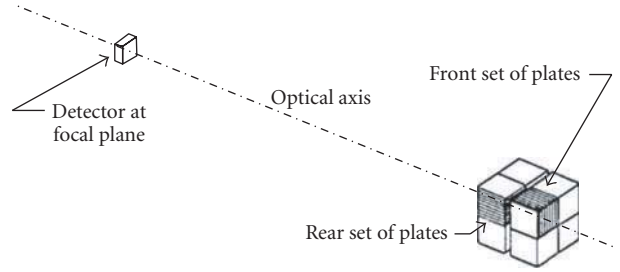

Figure 9: The KB optics design studied for HEAO-A (Kast 1975 [5]).

case of "point-to-point" focusing using an MCP with square cross-section channels (Figure 7). Recently, a modified MCP X-ray lens technology is called also X-ray MultiPore Optics.

The image is formed at the same distance from the plate as the source and the picture can be extended into two dimensions to allow focusing of a point source by an array of square channels such as an MCP, with the rays reflected twice. The MCP, however, focuses not every ray perfectly—a ray can go straight through a channel without reflection, so ending up either above or below the focus, causing a diffuse halo around the image, like in the lobster eye X-ray lens. Moreover, a ray can be reflected only once, so this ray will be focused in one-dimension only and consequently ending up somewhere along a line through the focus. This causes a cross-like image centred on the focus. About one quarter of the rays go into the "true" or point focus, one quarter into each line focus and one quarter into the diffuse halo.

An important modification occurs if the MCP is slumped to a spherical shape of radius R_{slump}, then it can be used to focus parallel rays to a point and/or to generate a parallel beam from a point source (Figure 8).

Two MCP-based designs have been suggested and exploited so far for the X-ray optics: the micro channel wolter optics and the lobster optics (Peele et al. 1996 [76]). In the first one, two MCPs are used as X-ray lenses, representing a conical approximation of a Wolter lens (Wallace et al. 1985 [77]).

3. Kirkpatrick-Baez X-Ray Optics

3.1. Kirkpatrick-Baez (KB) Telescopes. Two-dimensional X-ray image with grazing incidence reflection was taken by a Kirkpatrick-Baez system (Kirkpatrick and Baez 1948 [2]). It was the first two-dimensional X-ray image ever obtained in the laboratory. The configuration is shown in Figure 4. The incident rays are focused to a line image by a parabolic sheet mirror. If the rays are reflected a second time from a parabolic surface oriented at right angle to the first one, a point-like focus is achieved. This is correct for rays parallel to the centre line of the parabolas. In order to increase the collecting area, a stack of parabolas of translations constructed (Figure 9). Whereas in the case of only one double plate system a perfect focus for on-axis rays can be achieved, this is not possible for a multiple plate arrangement, where the focus remains perfect only along the projected direction of the surface normal of the primary. The exact solution for the intersection point with the focal plane of an arbitrary incident ray is given in the paper by Van Speybroeck et al. (1971 [78]). A detailed configurational analysis of the multiplate Kirkpatrick-Baez system has been carried out by Kast (1975 [5]).

As already mentioned, the Kirkpatrick-Baez (KB) X-ray optics was actually the first X-ray optics suggested for astronomical use.

Despite this fact, albeit some considerations and plans occurred, the astronomical X-ray telescopes flown so far on satellites mostly used the Wolter 1 type optics. However, it was used in several rocket experiments in the past, and in addition to that, it was proposed and discussed for several satellite experiments. Different situation is in the laboratory where KB systems are in frequent use, for example, at synchrotrons.

In contrast to the single double-plate system, the image of a point-like source starts to become increasingly extended in size as the number of plates involved increases. Wolter type I telescopes bend the incident ray direction two times in the same plane whereas the two bending in Kirkpatrick-Baez systems occur in two orthogonal planes, which for the same incidence angle on the primary mirror requires a longer telescope (Aschenbach, 2009 [79]).

3.2. KB-Early Stages. As already mentioned, Kirkpatrick and Baez (1948 [2]) have proposed an arrangement of concave mirrors to produce real images of extended objects with incidence at small grazing angles. They have considered both elliptical and parabolic profiles. The application in construction of an X-ray microscope was proposed, as well as focusing of electrons and other particles exhibiting external total reflection. It is worth to mention that their paper includes figures (and relevant discussion) with optics arrangement based on two reflectors/reflections but also on three of them.

The studies on focusing X-rays by mirror started already before the first published KB paper (Kirkpatrick and Baez, 1948 [2]), for example, one should mention the work of Ehrenberg (1947 [80]), who reported on efforts of formation of X-ray line images by reflection of X-rays from a point source at a gilded glass plate which had been bent to form an appropriate circular cylinder.

3.3. KB Systems in Astronomical Applications. Fisher and Meyerott (1966 [81]) have built another type of system with one-dimensional focusing which is composed of reflecting parabolas of translation that is, in a KB arrangement. A KB system of one-dimensional (1D) focusing was flown successfully in a sounding rocket by Gorenstein et al. (1971 [82]); during this flight, it was possible using the system to reconstruct an X-ray image of the Cygnus Loop based on the scans.

As an alternative to Wolter optics-based instruments, Van Speybroeck et al. [83] designed several telescope KB configurations that focus the X rays with sets of two orthogonal parabolas of translation. According to Van Speybroeck et al. [83] the crossed parabola systems should find application in astronomical observations such as high-sensitivity surveys, photometry, and certain kinds of spectroscopy where a large effective area is the most important factor rather than high angular resolution.

The design of a Kirkpatrick-Baez grazing-incidence X-ray telescope was proposed and discussed by Kast (1975 [5]) for using to scan the sky and to analyze the distribution of both properly reflected rays and spurious images over the field of view. He has shown that in order to obtain maximum effective area over the field of view, it is necessary to increase the spacing between plates for a scanning telescope in comparison to a pointing telescope. Spurious images are necessarily present in this type of lens, but they can be eliminated from the field of view by adding properly located baffles or collimators.

X-ray telescopes suggested by Kirkpatrick and Baez (1948 [2]) have several advantages over other types of X-ray telescopes for a general sky survey for low-energy X-ray sources. Although their angular resolution for axial rays is worse if compared with telescopes using successive concentric figures of revolution, they can be constructed more easily and have greater effective area [84], note that more recent papers give different observations, see [85]. The design of Kirkpatrick-Baez-type telescopes has been discussed by several authors (e.g., Van Speybroeck et al., 1971 [84],Gorenstein et al., 1973 [86], Weisskopf. 1973 [87]), and results have been reported from several experiments using one-dimensional focus from a single set of plates (Gorenstein et al., 1971 [82], Catura et al., 1972 [88], Borken et al., 1972 [89]).

These analyses were carried out during the (HEAO-A) study of the large-area collector experiment for the High Energy Astronomy Observatory, Mission A spacecraft. This analysis was not specific to the HEAO-A instrument but can be applied generally to any one- or two-dimensional telescope of the Kirkpatrick-Baez type. The HEAO-A telescope KB design consisted of four separate quadrants of nested plates with a total aperture of about 75×75 cm and a focal length of 6.55 m, giving a ratio of half-aperture to focal length of $Y_0/F = 0.057$. The plate length was 41 cm giving LIF = 0.063. The plate thickness t was 0.18 cm giving a ratio $t/L = 0.0044$. The detector had a square field of view of 20 by 20 mm (Kast 1975 [5]).

A method for optimizing the on-axis resolution of a KB reflecting element was presented and shown to be effective by Cohen (1981 [90]). Using the described procedure, the location of each of the 175 support points can be determined well by a computer assisted structural-optical software package before the actual assembly of each telescope unit. This automated procedure enabled to determine the optical characteristics of an entire telescope module consisting of seventy mirrors.

3.3.1. One-Dimensional KB System Used in Rocket Experiments. One-dimensional, and later two-dimensional (full), KB systems were flown in the past on several sounding rockets in order to achieve X-ray images of various celestial objects.

X-ray emission from the supernova remnant known as the Cygnus Loop or Veil Nebula was observed using a one-dimensional KB system in the energy range of 0.2 to 1 keV from an attitude controlled Aerobee 170 sounding rocket that was launched on 26 June 1970 from the White Sands Missile Range (Gorenstein et al., 1971 [6]).

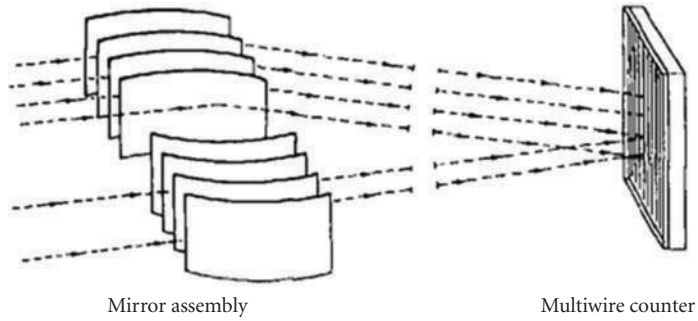

Figure 10: The one-dimensional KB optics used on rocket experiments (Gorenstein et al., 1971b [6]).

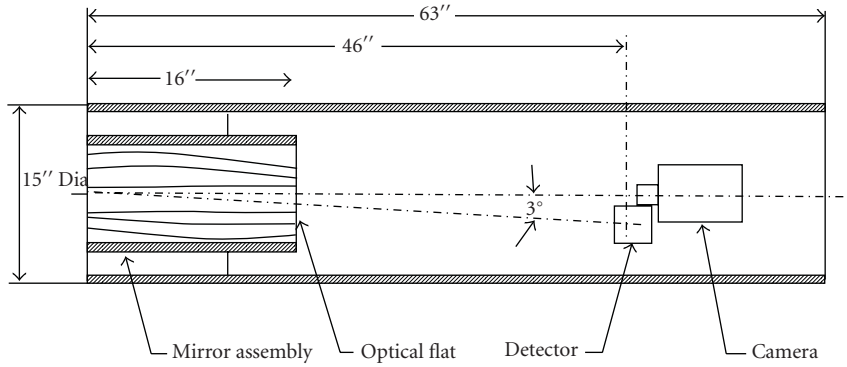

Figure 11: Schematic view of the KB telescope rocket payload (Gorenstein et al., 1971 [6]).

For that time, it was a rather unique instrument system, which focused X-rays by means of grazing incidence reflection, with the demonstration of advantages of focus compared to nonimaging systems used before, namely, better angular resolution and an improved ratio of signal to noise because the focused image is considerably smaller than the collecting area. Hence, the detector can be small and less influenced by cosmic ray effects.

The selection of KB optics was justified by the fact that the achievement of large sensitivity and a large field of view (FOV) was the main goal, not the angular resolution, due to the fact that the observational time available on sounding rockets in a scanning mode was very limited, to just few minutes.

The instrument consisted of a KB type collector that focused radiation in one dimension upon a multielement X-ray detector in the focal plane (Figure 10). The collector (KB module) had eight nested reflecting plates whose dimensions were 20 by 40 cm and was symmetric about the central plane. Each plate was curved slightly to approximate a parabola in one dimension and focused to a common line. The overall field of view of the instrument was 2 deg along the direction of focusing and 9 deg along the perpendicular direction. The eight reflecting surfaces were commercial 1-mm-thick float glass over coated with an evaporated layer of 150 nm of chromium for improved X-ray reflectivity at short wavelengths and were reinforced by a steel backing. The focal plane detector was a pair of four-wire proportional counters with a polypropylene entrance window of 1.3 microns.

Figure 11 shows a schematic view of the rocket payload (Gorenstein et al., 1971 [6]). The plates were fabricated from 0.040 inch sheets of commercial float glass measuring 8 × 16 inch. A 0.020 inch steel backing was bonded to the glass with RTV adhesive for mechanical strength. Following a procedure used by the Columbia University group in a different type of collector, a 150 nm layer of chromium was evaporated onto the glass surface by a commercial manufacturer. The resulting surface retains the original smoothness of the glass and has improved reflection properties at the shorter wavelengths. The reflecting plates were mounted inside of an aluminium box and constrained to follow the correct parabolic curves by a set of accurately placed contact pins at the top and bottom. A serious limitation to most commercial varieties of float glass available at that time was that although the surfaces are smooth, they were not free of ripples, but even then the instrument delivered valuable results.

3.3.2. Two-Dimensional KB Systems Used in Rocket Experiment. After initial rocket experiments with one-dimensional KB systems, a soft X-ray imaging system consisting of a large area focusing (full, i.e., for two-dimensional imaging) KB optics and a position sensitive proportional counter was constructed for cosmic X-ray observations from a sounding rocket (Gorenstein et al. 1975 [91]). It was the first instrument obtaining non-solar celestial X-ray images.

The focusing collector consisted of two successive arrays of reflecting plates shaped in the form of nested parabolas. The angular resolution of the system was 3′ over a field of 1.50 degrees. The detector was a two-dimensional device capable of a spatial resolution of about one millimetre for photon energies exceeding 0. 25 keV.

As already mentioned, Kirkpatrick and Baez first proposed the two successive orthogonal X-ray reflections from slightly curved plates, which could be used to form X-ray images. Van Speybroeck et al. [84] considered the optical properties of a nested array of orthogonal parabolas of translation that form images by this method. They derived some general geometric relations for achieving optimum resolution that are applicable to KB imaging devices. For radiation on the axis, the resolutions theoretically perfect in one dimension and only about a second of arc in the other. For radiation off axis the resolution degrades as the first power of the angle. In practice, alignment errors and imperfections in the reflecting plates themselves have in the reported KB case (Gorenstein et al., 1975 [91]) at least resulted in resolution of a few minutes of arc everywhere within the field of view.

One of the principal advantages of this design was that commercially available float glass without further polishing could be used as the reflecting surfaces. The fine polishing is usually the most time consuming and costly process in telescope construction if the float glass sheets are used, then the polishing of reflecting surfaces is achieved essentially without effort. Of course, considerable effort had to be applied to the problems of forming the reflecting surfaces into the correct geometry, but this was of a lesser magnitude. The active glass surfaces were coated with 50 nm of gold stabilized by a 50 nm undercoat of chromium.

The reflecting plates in this experiment were housed in a rectangular box 25 × 40 cm which was strengthened by four support rings. The effective collecting area of the device was determined by ray-tracing analysis using previously measured values of X-ray reflectivity versus angle of incidence. The angular resolution, about three minutes of arc in this case, was determined by the extent to which the authors succeeded in superimposing the images from the various plates. The system had a focal length of 180 cm and 25 front ($10'' \times 20'' \times 0.1''$) and 18 rear ($14.55'' \times 20'' \times 0.1''$) plates. The total geometric area was 1000 cm^2 and the effective area 264 cm^2 for 4.4 nm (Gorenstein et al., 1975 [91]).

3.4. KB as a Segmented Mirror. Segmentation can also be applied, to the Kirkpatrick-Baez (KB) array of stacked orthogonal parabolic reflectors (Figure 12). As shown in Figure 13, a large KB mirror can be segmented into rectangular modules of equal size and shape (Gorenstein et al., 1996 [7]). A segmented KB telescope has the advantage of being highly modular on several levels. All segments are rectangular boxes with the same outer dimensions. Along a column, the segments are nearly identical and many are interchangeable with each other. All reflectors deviate from flatness only slightly. On the other hand, the Wolter reflectors are highly curved in the azimuthal direction and the curvature varies over a wide range. Furthermore, within a segment, the KB reflectors themselves can be segmented along the direction of the optical axis (Gorenstein 1998 [92]).

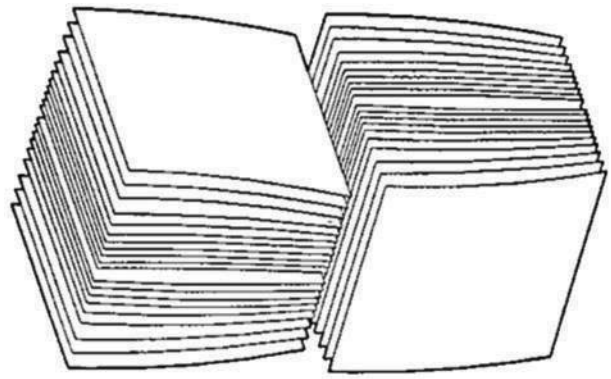

Figure 12: Kirkpatrick-Baez mirror consisting of orthogonal stacks of reflectors. Each reflector is a parabola in one dimension (Gorenstein et al., 1996 [7]).

3.5. KB in Astronomical Telescopes: Recent Status and Future Plans. First attempt to create an astronomical KB module with silicon wafers was reported by Joy et al. [93]. They have constructed a test KB module based on new material/substrate, namely, silicon wafers. The telescope module consisted of 94 silicon wafers with diameter of 150 mm, uncoated, with thickness of 0.72 mm. The device was tested both in optical and X-rays, with measured FWHM of 150 arcsecs, dominated by large-scale flatness. It should be noted that the surface quality and flatness of Si wafers improved essentially over the time.

The recent efforts in future larger and precise imaging astronomical X-ray telescopes require reconsidering both the technologies as well as designs. The future large X-ray telescopes require new light-weight and thin materials/substrates such as glass foils and/or silicon wafers. Their shaping to small radii, as required in Wolter designs, is not an easy task. While the KB arrangements represent a less laborious and hence less expensive alternative.

The use of KB arrangement for IXO project (the proposed joint NASA/ESA/JAXA International X-ray Observatory) was suggested and investigated by Marsikova et al. [8] and more recently by Willingale and Spaan, 2009 [85]. These investigations indicate that if superior quality reflecting plates are used and the focal length is large, angular resolution of order of a few arcsec can be achieved (Figure 16). Recent simulations further indicate that in comparison to Wolter arrangement, the KB optics exhibit reduced on axis collecting area but larger field of view, at comparable angular resolution (Willingale and Spaan, 2009 [85]).

Comparison of Wolter and KB optical arrangement in astronomical X-ray telescope is summarized in Table 2 (Marsikova et al., 2009 [8]). Note that in order to achieve the comparable effective area, the focal length of KB system

Table 2: Comparison of Wolter and KB optical arrangement in astronomical X-ray telescope (Marsikova, 2009 [8]).

	KB	W
Type of optics	Parabolic-parabolic planar	Parabolic-hyperbolic rotational
Number of reflections	2	2
Focal length aperture	20 m − 913 × 913 mm 40 m − 1826 × 1826 mm	10 m − dia 913 mm 20 m − dia 1826 mm
First mirror	134 mm from axis 268 mm from axis	134 mm from axis 268 mm from axis
Numbers of mirrors	420 840	394 788
Length of substrate	300 mm	300 mm
Material substrate	Silicon	Glass
Surface	Gold	Gold

Figure 13: A large KB mirror can be segmented into rectangular modules of equal size and shape (Gorenstein et al., 1996 [7]).

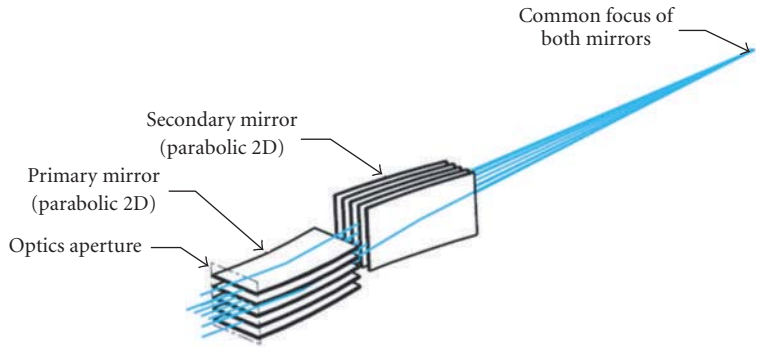

Figure 14: The principle of KB MFO telescope (Marsikova, 2009 [8]).

is required to be about twice of the focal length of Wolter system. The principle of MFO optics in KB arrangement is shown in Figure 14.

We note a very important factor and that is the ease (and hence, reduced cost) of constructing highly segmented modules based on multiply nested thin reflecting substrates if compared with Wolter design. While for example, the Wolter design for IXO requires the substrates to be precisely formed with curvatures as small as 0.25 m the alternative KB arrangement uses almost flat or only slightly bent sheets. Hence the feasibility to construct KB module with required 5 arcsec FWHM at a affordable cost is higher than those for Wolter arrangement.

The advanced KB telescopes based on MultiFoil Optics (MFO) approach (X-ray grazing incidence imaging optics based on numerous thin reflecting substrates/foils, for more details, see [33]. The distinction between MFO and other optics using packed or nested mirrors is that MFO is based

Table 3: Basic parameters of MFO KB modules assembled in 2009 (Marsikova, 2009 [8]).

	KB 001	KB 003	KB 004
Shape of substrates:	Elliptic	Parabolic	Elliptic
Focal length [m]:	16	20	16
Aperture [mm]:	100×50	100×50	100×50
Number of profiles:	2	11	2
Number of substrates:	6	33	6
Size of substrates [mm]:	$100 \times 100 \times 525$	$100 \times 100 \times 525$	$100 \times 100 \times 525$
Surface:	Au	Au	Au
Skeleton/house:	Al	Al	Al

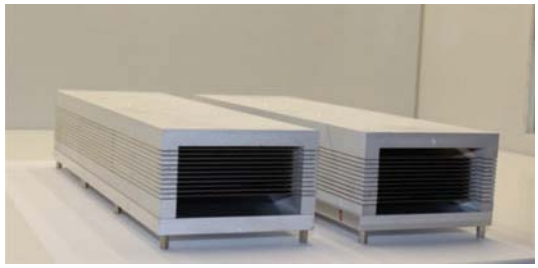

Figure 15: Laboratory samples of advanced KB MFO modules designed and developed at Rigaku Innovative Technologies Europe (RITE) in Prague (Marsikova, 2009 [8]). A summary of KB modules constructed so far is given in Table 3. The photograph shows the KB 003 module.

on numerous and very thin (typically less than 0.1 mm) substrates. The following KB test modules were recently designed and constructed at Rigaku Innovative Technologies Europe (RITE) in Prague.

(i) Advanced technologies of Si substrates shaping were investigated and developed. Suitable substrates for X-ray mirrors are supposed to be Si wafers because of their parameters.

(ii) Model based on raytracing (11 profiles)?.

(iii) Two sets of mirrors from Si chips $100 \times 100 \times 0.525$ mm (Figure 15).

(iv) Total optics length 600 mm, aperture 40×40 mm.

3.6. KB Microscopes. Apart from astronomical telescopes, there is a wide application of KB optics in various laboratory applications. The X-ray microscopy represents one of most important application.

McGee was the first who successfully demonstrated the use of crossed spherical reflectors in an X-ray microscope (McGee, 1957 [94]). Numerous applications and further improvements of KB systems in X-ray microscopes appeared in the following years. In this application, achievement of a very fine angular and spatial resolution is the most important goal.

3.6.1. Advanced KB Systems for X-Ray Microscopy. A full-field hard X-ray microscope has the potential to observe nanostructures inside relative thick samples that cannot be observed by a transmission electron microscope. Consequently, it promises to be a powerful tool in fields such as material science and biology. The spatial resolution of a full-field X-ray microscope with a Fresnel zone plate (FZP) reaches 30 nm in the hard X-ray region. However, chromatic aberration is an inevitable disadvantage of FZPs. To realize achromatic hard X-ray imaging, an imaging system with total-reflection X-ray mirrors is required. It is difficult to develop an X-ray mirror imaging system that can form an X-ray image with a sub-100 nm resolution. Wolter optics is a promising imaging system, but, on the other hand, Wolter optics that are sufficiently accurate to realize diffraction-limited resolution have yet to be fabricated because it is very challenging to figure an axially symmetric aspherical shape, even using ultra-precision machining and measurements. That is why Kirkpatrick-Baez (KB) optics was actively studied for hard X-ray nanofocusing. Figuring elliptical mirrors is comparatively easy because their shapes are nearly planar; therefore, elliptical mirrors with a figure accuracy of 2 nm are feasible even using existing techniques. However, it should be noted that an optical system containing only an elliptical mirror cannot satisfy the Abbe sine condition and it suffers from comatic aberration.

The KB system according to Kodama et al. [10], termed advanced Kirkpatrick-Baez (AK-B) optics, consists of two pairs of hyperbolic and elliptic mirrors as shown in Figure 18(a), which are called as the AK-B type I microscope. The two dimensional configuration shown in Figure 18(b) is similar to the Wolter type I microscope configuration. The horizontal image is formed by the first and the fourth mirrors, and the vertical image by the second and the third mirrors. The combination of the hyperbolic and elliptic mirrors corrects the astigmatism, and the two mirror pairs can reduce the obliquity. In another configuration of the AK-B (type II AK-B) the hyperbolic and elliptic mirrors were alternated, that is, the horizontal image is formed by the first and the third mirror and the vertical image by the second and the fourth mirror. However, the type II configuration generally has greater optical loss in the mirror assembly than type I. The spatial response of the microscope has been measured by X-ray backlighting a fine grid with laser-plasma X rays. A spatial resolution of better than 3 nm was reported with 2.5-keV X rays over the field of 800 nm at a magnification of 25. This microscope was applied for laser implosion experiments, resulting in high-resolution images of the compressed cores.

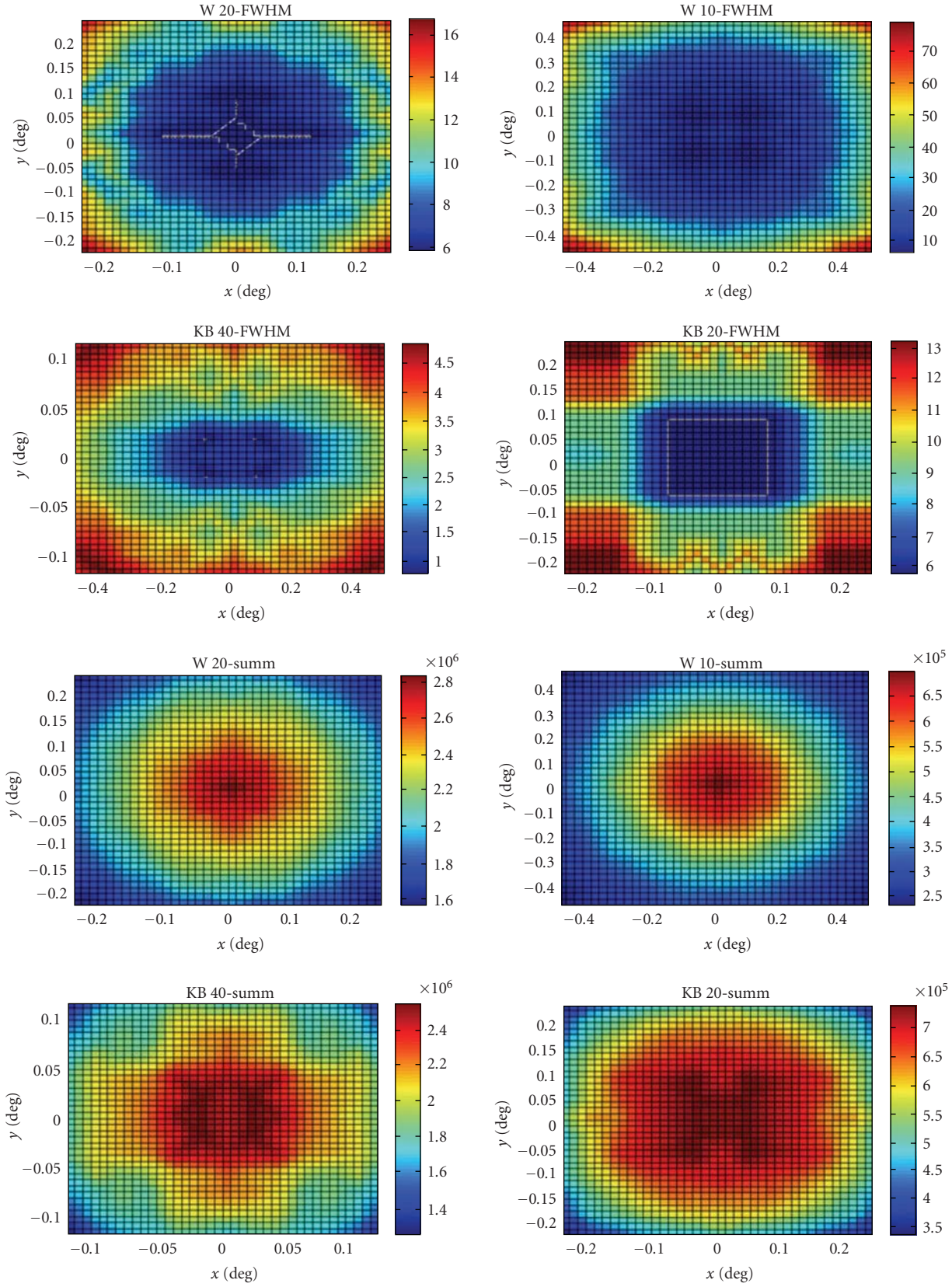

Figure 16: Comparison of focal images between KB and Wolter system (adopted from Marsikova, 2009 [8]). The upper 4 panels illustrate the FWHM in arcsecs, the bottom 4 panels the focal peak intensity.

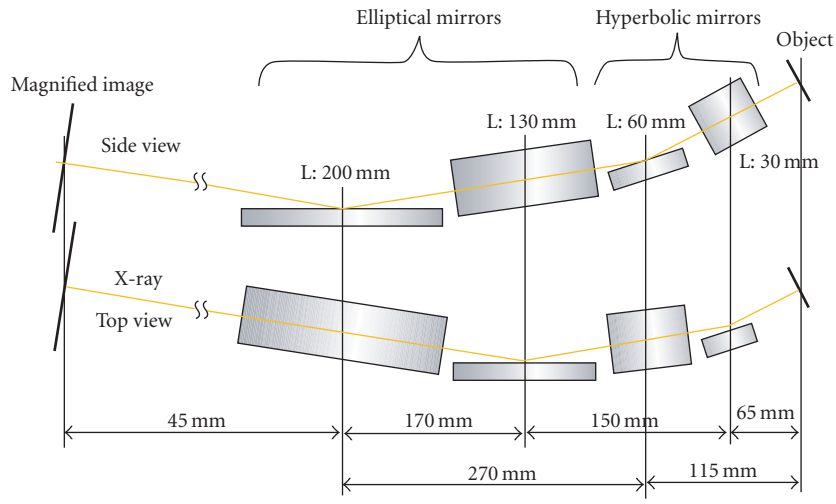

Figure 17: An Advanced KB system with 4 mirrors according to [9].

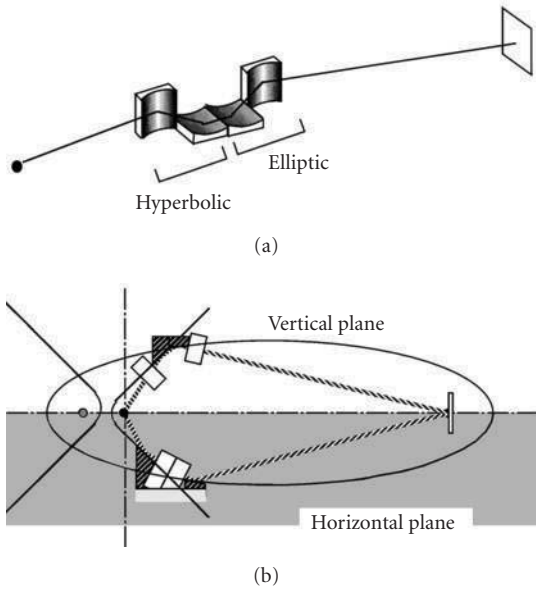

Figure 18: Schematic diagram of an AK-B microscope according to Kodama et al., 1996 [10]: (a) arrangement of the mirrors, (b) cross sections in the horizontal and the vertical planes.

However, AK-B optics containing four mirrors has to be aligned with high precision. This challenge needs to be overcome before AK-B optics can be utilized in practical applications. Matsuyama et al., 2009 [9], studied mirror alignment of AK-B optics with the goal of realizing a full-field hard X-ray microscope with a resolution of better than 100 nm. It is not currently known how accurately the four mirrors need to be aligned. In the study performed by Matsuyama et al., 2009 [9], the effect of one elliptical mirror and one hyperbolic mirror being misaligned on image quality was calculated using a wave-optics simulation. Based on these results, Matsuyama et al., 2009 [9], proposed a four-mirror alignment procedure for AK-B optics (Figure 17).

The mirrors for the AK-B microscope were made of fused-silica substrates. The surface figure of each mirror was measured with a Zygo interferometer. The deviation of the figure from a perfect surface (ether elliptic or parabolic) was less than 625 nm. Taking into account the measured deviations of all the mirrors in a ray-trace calculation, the spatial resolution of the AK-B was found to be degraded by less than 0.7 nm (the half-width of the point-spread function) at the centre of the field of view.

3.6.2. Scanning X-Ray Fluorescence KB Microscopes. A scanning X-ray fluorescence microscope (SXFM) is an imaging tool with which the element distribution of a sample can be visualized using X-ray fluorescence generated by the focused hard X-ray irradiation of the sample. Because the excitation beam consists of hard X rays, there is no need to install samples under vacuum. In this microscopy, spatial resolution and sensitivity depend on, respectively, beam size and photon flux. In the sensitivity point of view, the combination of a synchrotron radiation source, which can generate the brightest X-ray, and KB mirrors, which have high focusing efficiency, is one of the most powerful focusing systems for a SXFM. In terms of spatial resolution, the previous reports regarding hard X-ray nanofocusing suggested that KB mirrors enable us to obtain a nanobeam having a full width at half maximum FWHM of better than 40 nm. Owing to achromatic focusing using total reflection on a mirror surface, we can select the most efficient energy of X rays for various samples and experimental conditions.

An example of a high-spatial-resolution scanning X-ray fluorescence microscope (SXFM) using Kirkpatrick-Baez mirrors was developed and reported by Matsuyama et al., 2006 [8]. As a result of two-dimensional focusing tests, the full width at half maximum of the focused beam was achieved to be $50 \times 30\,\text{nm}^2$ under the best focusing conditions. The measured beam profiles were in good agreement with simulated results. Moreover, beam size was controllable within the wide range of 30–1400 nm by

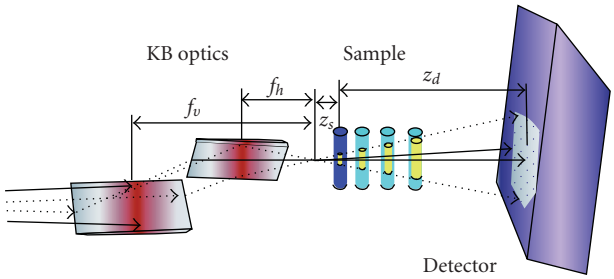

Figure 19: Scheme of the tomography setup using the divergent beam produced by Kirkpatrick-Baez optics (Mokso et al., 2007 [11]).

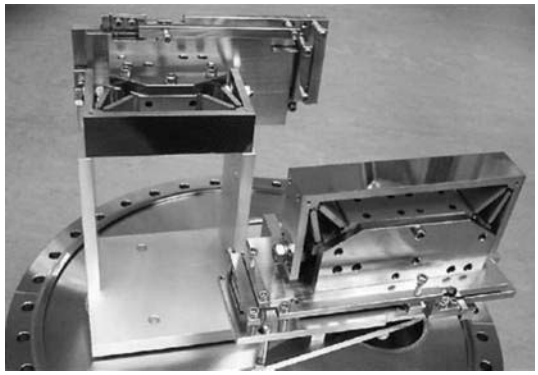

Figure 20: The modular K-B micro focusing mirror system is tested to mount on the 1400 rotatable CF flange (Chen et al., 2001 [12]).

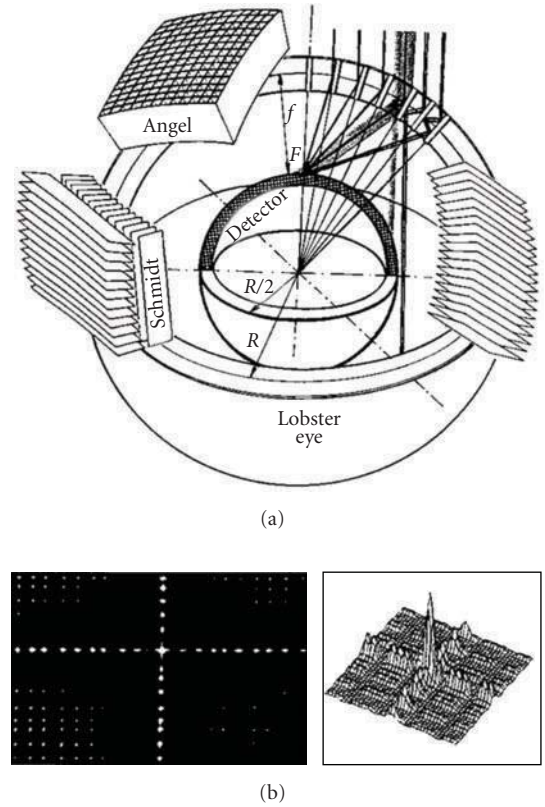

Figure 21: The schematic arrangement of the Lobster Eye type X-ray optics (a) with real image of the Schmidt objective prototype in optical light (b left) and distribution of intensity on the focal sphere for a point-line source (computer ray-tracing, b right).

changing the virtual source size, although photon flux and size were in a tradeoff relationship. To demonstrate SXFM performance, a fine test chart fabricated using focused ion beam system was observed to determine the best spatial resolution. The element distribution inside a logo mark of SPring-8 in the test chart, which has a minimum line width of approximately 50–60 nm, was visualized with a spatial resolution better than 30 nm using the smallest focused X-ray beam, demonstrating the superior performance of KB optics.

3.7. KB in X-Ray Tomography. The improvement of spatial resolution triggered by a broad spectrum of materials science and biological applications is one main driving force toward innovative designs and techniques in imaging technologies that provide three-dimensional 3D information about the sample in a nondestructive manner (Mokso et al. [11]). X-ray tomography is the oldest among them and still evolving. The use of Fresnel zone plates as objective lens has brought resolutions in the 100 nm range and is most applied in the soft X-ray regime for the study of thin and light materials such as single cells. The emerging field of coherent diffraction imaging, based on phasing a coherent Fraunhofer diffraction pattern, is expected, in the 3D imaging of tiny isolated objects, to overcome the resolution limit set by the X-ray optical devices. A drawback of the improved spatial resolution is the corresponding decrease in field of view and sample size. Larger, millimetre-sized samples can be

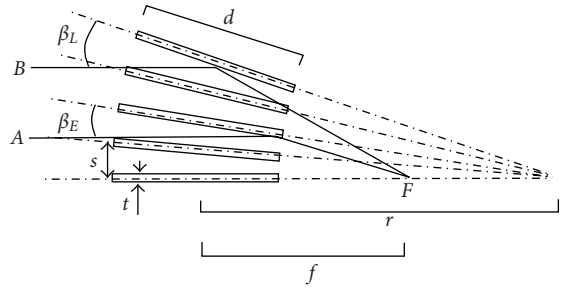

Figure 22: The schematic arrangement of the Lobster Eye type X-ray optics used for simple equations derivation (Sveda, 2003 [15]).

investigated in 3D with parallel beam synchrotron radiation micro tomography, but in this case, the resolution is limited by detector technology to slightly better than 1 nm.

A projection microscope that bridges the gap in terms of resolution and specimen size between these nanoscale and micro scale 3D imaging methods was suggested by Mokso et al., 2007 [11]. It is based on state-of-the-art focusing of hard X rays characterized by a large penetration power and depth of focus. This allows exploring nondestructively in a three-dimensional manner bulk material at the nanoscale. The high flux makes it adapted to fast imaging for dynamical studies. Further improvement of spatial resolution does not

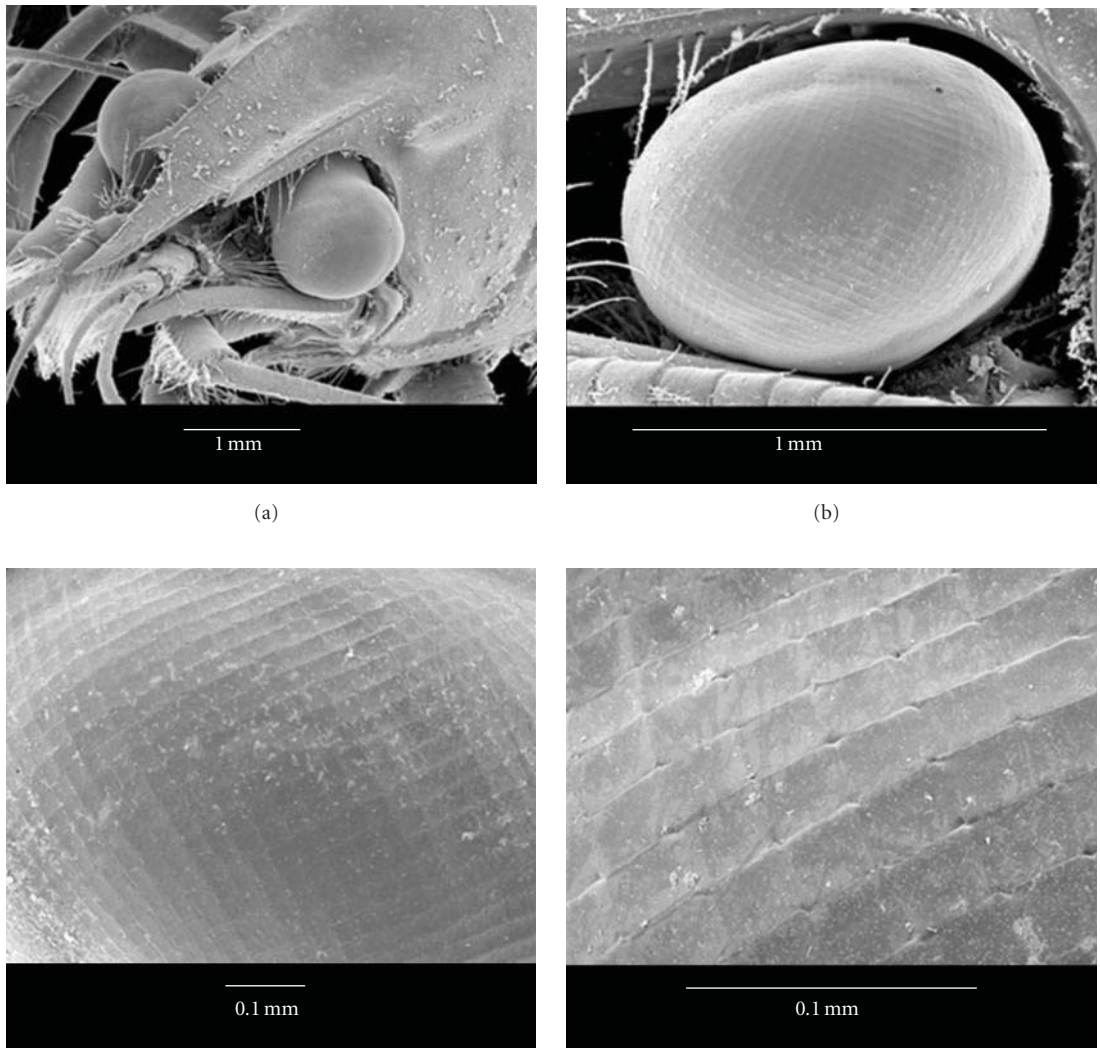

(a) (b)

(c) (d)

Figure 23: The d of a crayfish with eyes, the crayfish eye (a, b), and the surface details (c, d).

necessarily imply a reduced efficiency as it is the case for imaging with Fresnel zone plates and high-resolution detectors. In the original tomography setup sketched on Figure 19, bent-graded multilayer's set in the Kirkpatrick-Baez (KB) geometry focus undulator radiation to a spot below 90 nm in both directions. The focusing device generates a spherical wave illumination of the sample.

3.8. KB Systems for X-Ray Microprobes. A synchrotron X-ray microprobe having a submicron beam size based on the Kirkpatrick-Baez configuration was designed and constructed by using synchrotron radiation from a multiple wiggler for example, at the Photon Factory (Iida and Hirano, 1996 [95]). The described X-ray microprobe system is usable for spectroscopic and diffraction experiments. Though it is apparent that the X-ray microprobe technique will be more effectively developed using a third-generation low-emittance synchrotron light source, the described submicron system is practically useful for material characterization, considering the deep X-ray penetration depth and the difficulty in preparing extremely thin samples. Furthermore, the improved Kirkpatrick-Baez optics will attain the higher photon flux and the smaller beam size with the third-generation undulator radiation.

A K-B mirror system for microprobe was designed by Chena et al. [12], to achieve a spot size of $6.7 \times 2.9\,\text{mm}^2$ and a gain of 6.2×10^3 in the EPU beam line, based on the following considerations: gain, efficiency, and focal spot size. This mirror system, which contains a sixth order polynomial corrected cylindrical horizontal micro focusing mirror (HMFM) and an eight-order polynomial vertical micro-focusing mirror (VMFM) can accumulate and micro focus the undulator source into a nearly perfect point image. Two 17-4 PH stainless steel bent K-B mirrors with the monolithic flexure-hinge and modular mounting designs have the following features: (1) compact and modular fabrication, (2) stability of bending mechanism without

backlash, (3) appropriate for X-ray microfocusing system when mirrors have the central radii of curvature less than 10 m, and (4) modular and independent.

X-ray microbeam optics capable to achieve micron spatial resolution and high focusing gain has received considerable interest. Microfocusing photon beam of any wavelength mainly on free optical principles: reflectivity, refractivity, and diffraction. Fresnel zone plate accurately represents X-ray microbeam optics according to the diffraction. By applying lithography and deposition techniques, a feasible zone plate in which the outmost zone has a width of about 20 nm can microfocus the X-ray of synchrotron radiation into a beam spot size of few 10 nm with efficiency exceeding 10%. The compound refractive lenses that are fabricated from low-Z materials setup as a linear array of lenses have focal spots of few microns for a hard X-ray range.

Both K-B mirror system and tapered capillary optics can focus photon beams to achieve submicron spatial resolution based on the reflectivity. Selecting appropriate X-ray microbeam optics involves considering the focal spot size, photon energy range, photon flux density, efficiency, and divergent angle. For X-ray scanning experiments, the focal spot size must be as small as possible to achieve spatial resolution. However, transmission image experiments prefer the photon flux density to the spot size so that a few micron focal spots are acceptable. Microfocusing systems in the EPU beam line of Synchrotron Radiation Research Centre (SRRC) that exploit the merits of microbeams for transmission image experiments in soft X-ray range were designed according to the primary consideration: photon flux density (Chen et al., 2001 [12]). Therefore, K-B focusing mirror systems was adopted to achieve the microfocusing function and maintain their higher efficiency and no chromatic aberration in contrast to Fresnel zone plates (Chen et al., 2001 [12]). To satisfy the strict requirements of X-ray microbeam optics, two high order polynomial corrected cylindrical mirrors, HMFM and VMFM, based on the K-B design were designed to focus the X-ray beam with nearly no aberration and then demagnify it onto a micron image (Figure 20).

3.9. Application of KB for Neutron Focussing. As shown, for example, by Ice at al., 2005 [96], Kirkpatrick-Baez neutron supermirrors can efficiently focus neutron beams into small areas with a maximum divergence that is limited by the mirror critical angle. The size of the focal spot is primarily determined by geometrical demagnification of the source and by figure errors in the mirror shape. Ray-tracing calculations show that high-performance Kirkpatrick-Baez super mirrors can preserve neutron-source brilliance when focusing down to tens of microns and can focus approximately two orders of magnitude greater power into 100 microns than it is practical without focusing. The predicted performance is near the theoretical limit set by the source brilliance. Ice et al. [96], described the phase space arguments, ray-tracing calculations and actual performance of an M3 super mirror system designed to produce a focal spot below 100 microns. Although their design was optimized for neutron polychromatic micro diffraction, the design principles are certainly widely applicable to a range of neutron science.

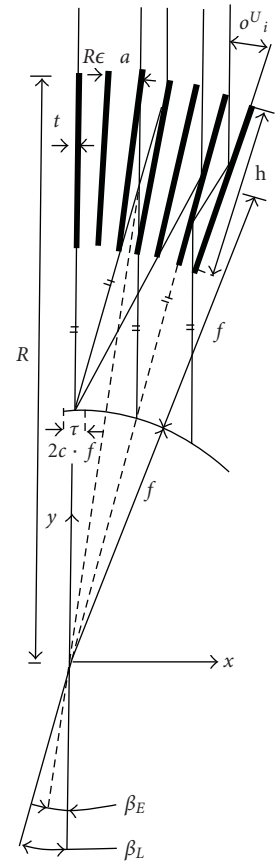

Figure 24: The X-ray reflections on the Schmidt X-ray lens.

4. Lobster-Eye Wide-Field X-Ray Optics

4.1. Introduction. The principle of lobster-eye type wide-field X-ray optics was published by Angel (Angel, 1979 [60]). The full lobster-eye optical grazing incidence X-ray objective consists of numerous tiny square cells located on the sphere and is similar to the reflective eyes of macruran crustaceans such as lobsters or crayfish (Figures 21 and 23). An alternative arrangement was proposed by Schmidt 1975 [97] (Figures 21 and 22). Both these arrangements will be discussed in detail later.

The wide-field mirror modules offer advantageous application in astrophysics. The major scientific achievements of the X-ray astronomy in the past are closely related to the use of large X-ray imaging telescopes based mostly on the Wolter 1 X-ray objectives. These systems usually achieve excellent angular resolution as well as very high sensitivity, but are quite limited in the field of view available, which is less than 1 degree in most cases. However, the future of X-ray astronomy and astrophysics requires not only detailed observations of particular triggers, but also precise and highly sensitive X-ray sky surveys, patrol and monitoring. The recently confirmed X-ray counterparts of Gamma Ray Bursters (GRBs) may serve as an excellent example. For recently in detail investigated GRB with precise localization accuracy, in almost all cases variable and/or fading X-ray

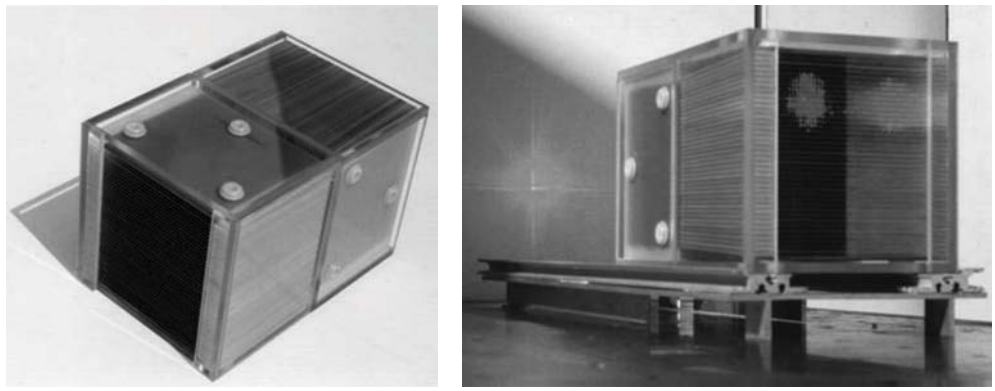

(a) (b)

Figure 25: (a) The Schmidt objective test module, 100×80 mm plates. (b) Optical tests of the Lobster eye objective from the (a).

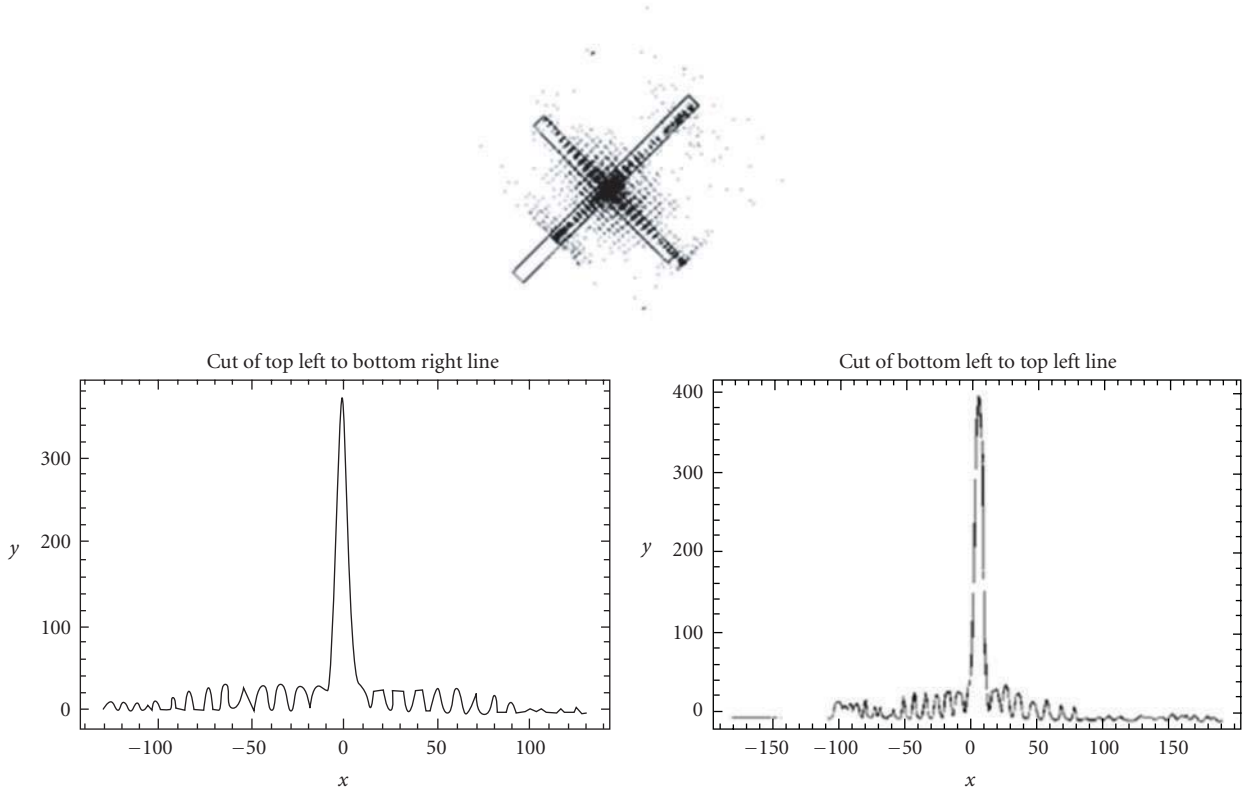

Figure 26: X-ray focal images of the Schmidt telescope prototype from Figure 25(a) at 1.5 nm taken in collaboration in the test facility of the X-ray astronomy group, University of Leicester, UK.

counterparts/afterglows have been identified. The X-ray identification of GRBs has lead to great improvements in study and understanding of these sources and especially has allowed identifications at other wavelengths due to better localization accuracy provided in X-rays if compared with gamma ray observations. Since most of GRBs seem to be accompanied by X-ray emissions, the future systematic monitoring of these X-ray transients/afterglows is extremely important. However, these counterparts are faint in most cases, hence powerful wide field telescopes are needed. An obvious alternative seems to be the use of wide field X-ray optics allowing the signal/noise ratio to be increased if compared with nonfocusing devices. The expected limiting sensitivity of lobster eye telescopes is roughly 10^{-12} erg^{-2} s^{-1} for daily observation in soft X-ray range. This is consistent with the fluxes detected for X-ray afterglows of GRBs. Furthermore, the wide field X-ray telescopes may play an important role in monitoring of faint variable X-ray sources to provide better statistics of such objects (note, e.g., the occurrence of two faint fading X-ray sources inside the

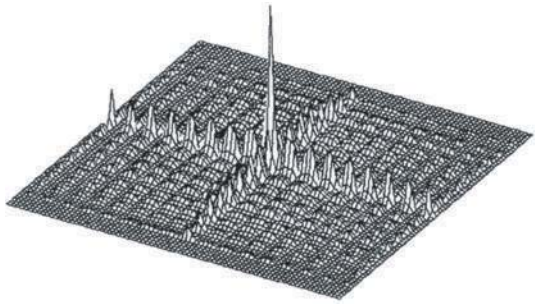

Figure 27: Intensity distribution in the focal plane (40×40 mm detector) according to mathematical ray-tracing for the identical test module and test arrangement as given above; the microroughness of reflecting surfaces are assumed to be 1 nm.

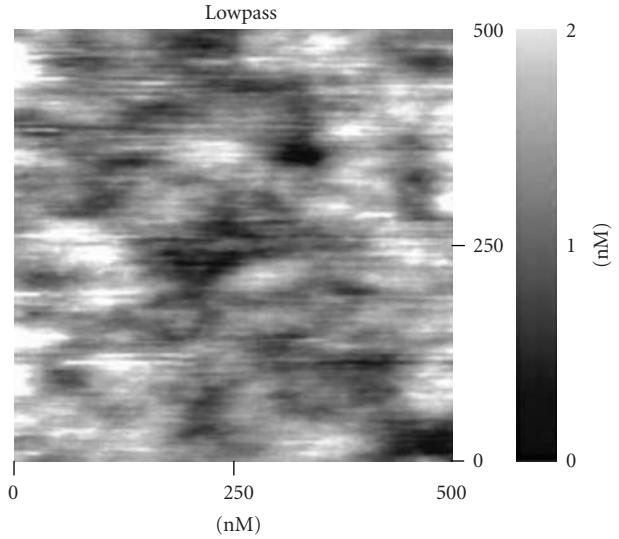

Figure 28: Tapping AFM images of the surface of the double-sided X-ray reflecting flats taken in collaboration in the test facility of the Astronomical Observatory in Brera, Italy—the resulting micro roughness RMS is 0.3 nm.

gamma ray box of GRB970616) as well as in other fields of X-ray astrophysics. The recent hunting for faint fading X-ray afterglows of GRBs has indicated that there is a large number of faint and/or variable X-ray sources worth of detailed study.

The wide field lobster eye telescopes are expected to play an important role in future X-ray astrophysics missions and analyses. The advanced prototypes of lobster eye optics modules of various sizes and various arrangements confirm the justification of space applications of these innovative devices. Both very small (3×3 mm based on 0.03 mm foils spaced at 0.07 mm) and large (300×300 mm based on 0.75 mm foils spaced at 10.8 mm) LE Schmidt prototypes have been designed, developed and tested. Advanced technologies for additional surface layers have been investigated as well.

There have been many attempts to increase slightly the available wide field coverage of Wolter and analogous X-ray telescopes. To avoid any confusion, we suggest restricting the term "wide-field X-ray optics" only for optical systems with field of view $\gg 1$ degree while to use the term "narrow-field system" for systems with FOV <1 degree.

The angular resolution is a function of spacing between the reflecting plates and focal length. In Schmidt arrangement, the Lobster Eye consists of plates of thickness t, depth d (Figure 22). Spacing between plate planes is s, focal length, radius r, focal point F, β the angle between optical axis and focused photons in time of detection. Beam A (Figure 22) shows the situation, where the plate is fully illuminated and the crossection of the plate is maximal (effective reflection). Beam B is the last beam that can be reflected into the focal point. Each beam, which is further from the optical axis, reflects more than once (critical reflection). If reflected twice from the same set of plates, photon does not reach the focal point and continues parallel to the incoming photon direction (Sveda 2003 [15]).

If $t \ll s \ll d \ll f$ we can derive the following simple equations (Sveda 2003 [15] Inneman 2001 [98]), where α is the estimate of the angular resolution

$$\begin{aligned} f &= \frac{r}{2}, \\ \beta_E &= \frac{a-t}{d}, \\ \beta_L &= 2bE, \\ \alpha &\sim \frac{2s}{r} = \frac{s}{f}. \end{aligned} \tag{2}$$

Detailed ray tracing simulations were performed for the LE modules designed and developed, for more details, see for, example, [15].

4.2. Schmidt Objectives. The lobster-eye geometry X-ray optics offers an excellent opportunity to achieve very wide fields of view. One-dimensional lobster-eye geometry was originally suggested by Schmidt (Schmidt, 1975 [53]), based upon flat reflectors. The device consists of a set of flat reflecting surfaces. The plane reflectors are arranged in an uniform radial pattern around the perimeter of a cylinder of radius R. X-rays from a given direction are focussed to a line on the surface of a cylinder of radius $R/2$ (Figure 24). The azimuthal angle is determined directly from the centroid of the focused image. At glancing angle of X-rays of wavelength 1 nm and longer, this device can be used for the focusing of a sizable portion of an intercepted beam of X-ray incident in parallel. Focussing is not perfect and the image size is finite. On the other hand, this type of focusing device offers a wide field of view, up to maximum of half sphere with the coded aperture. It appears practically possible to achieve an angular resolution of the order of one tenth of a degree or better. Two such systems in sequence, with orthogonal stacks of reflectors, form a double-focusing device. Such device should offer a field of view of up to 1000 square degrees at moderate angular resolution.

It is obvious that this type of X-ray wide field telescopes could play an important role in future X-ray astrophysics. The innovative very wide field X-ray telescopes have been suggested based on these optical elements but have not been

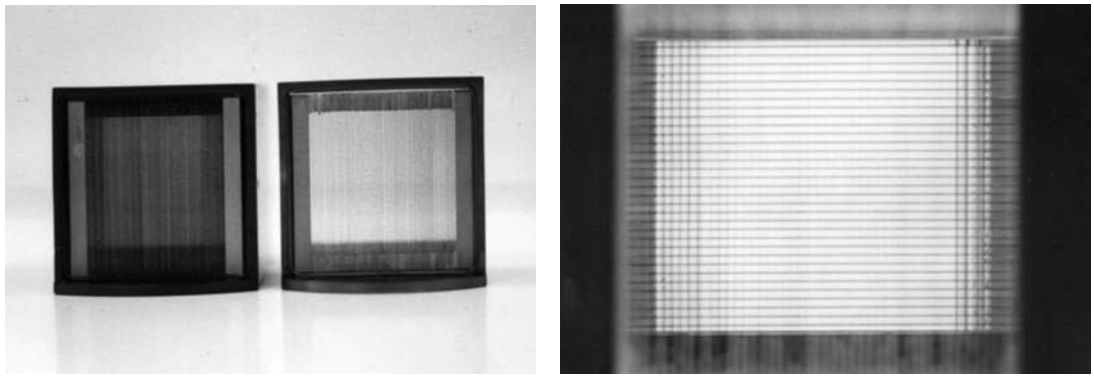

(a) (b)

Figure 29: (a) The mini-Schmidt objective test modules based on two sets of 60 23×23 mm flats, 0.1 mm thick used for X-ray tests illustrated on Figures 31(a)–37). (b) The front view of the mini-Schmidt objective test module from (a).

flown in space so far (e.g., Gorenstein 1979 [99]). One of the proposals is the All Sky Supernova and Transient Explorer (ASTRE). This proposal also includes a cylindrical coded aperture outside of the reflectors, which provide angular resolution along the cylinder axis (Gorenstein 1987 [61]). The coded aperture contains circumferential open slits 1 mm wide in a pseudorandom pattern. The line image is modulated along its length by the coded aperture. The image is cross-correlated with the coded aperture to determine the polar angle of one or more sources. The field of view of this system can be, in principle, up to 360 degree in the azimuthal direction and nearly 90% of the solid angle in the polar direction. To create this mirror system, a development of double-sided flats is necessary. There is also potential for possible extending the wide field imaging system to higher energy by the use of multilayer or other coatings in analogy to those described for flat reflectors in the Kirkpatrick-Baez geometry.

First lobster-eye X-ray Schmidt telescope prototype consisted of two perpendicular arrays of flats (36 and 42 double-sided flats 100 × 80 mm each). The flats are 0.3 mm thick and gold-coated (Inneman et al. 2002 [100], Inneman et al. 2002 [101]). The focal distance is 400 mm from the midplane. The FOV is about 6.5 degrees (Figures 25(a) and 25(b)). The results of optical and X-ray tests have indicated the performance close to those provided by mathematical modelling (ray-tracing). The X-ray test has been carried out in the test facility of the X-ray astronomy group, University of Leicester, UK (Figure 26). Another test modules of Schmidt geometry have been designed and developed, based on 0.1 mm thick gold-coated glass plates 23 × 23 mm at 0.3 mm spacing. The aperture/length ratio is 80. 60 such plates represent one module. Two analogous modules represent the 2D system for laboratory tests, providing focus to focus imaging with focal distances of 85 and 95 mm. The innovative gold coating technique has improved the final surface micro roughness rms to 0.2–0.5 nm (Figure 28). Various modifications of this arrangement have been designed both for imaging sources at finite distances (for laboratory tests) as well as of distant sources (the corresponding double-focusing array has $f = 250$ mm and FOV $= 2.5$ deg). In parallel, numerous ray-tracing simulations have been performed, allowing comparing theoretical and experimental results (Figures 27 and 29(b)).

Later on another test lobster eye modules have been constructed and tested both in visible light and in X-rays. As an example, we show X-ray test results for the mini-LE module. These results illustrate in detail the on-axis and off-axis imaging performance of the LE module tested.

The module is shown on Figure 29(a) and the test results including the experiment arrangement are in Figures 32(b) to 33, 34, 35, 36, and 37 Figure 31(b) and 32(a) show the X-ray measurement results of micro-LE X-ray module shown in Figure 45. For review of LE modules designed, constructed and tested see Table 4. The X-ray tests on coated flats used in LE modules as reflectors are illustrated in Figures 30 and 31(a). The largest LE module maxi is shown in Figure 42 and the example of optical imaging test is in Figure 43.

All test experiments of the mini-LE schmidt module (illustrated on Figure 29(a)) in 31(b)–36(b) were done with the microfocus X-ray tube (Bede microsource, Cu anode, 40 kV, 100 microamp) and the X-ray CCD Digital Camera (Reflex X16D3, 16 bit, DN > 30 000, 512 × 512 pixels, Back Illuminated CCD chip SITe, direct exposure).

4.3. Angel Objectives. Besides the Schmidt objectives described above, there is also an alternative based on slightly different arrangement, sometimes referred as two-dimensional lobster eye optics. The idea of two-dimensional lobster-eye type wide-field X-ray optics was first mentioned by Angel (Angel, 1979 [60]). The full lobster-eye optical grazing incidence X-ray objective consists of numerous tiny square cells located on the sphere and is similar to the reflective eyes of macruran crustaceans such as lobsters. The field of view can be made as large as desired and good efficiency can be obtained for photon energies up to 10 keV. Spatial resolution of a few seconds of arc over the full field is possible, in principle, if very small reflecting cells can be fabricated at long focal lengths.

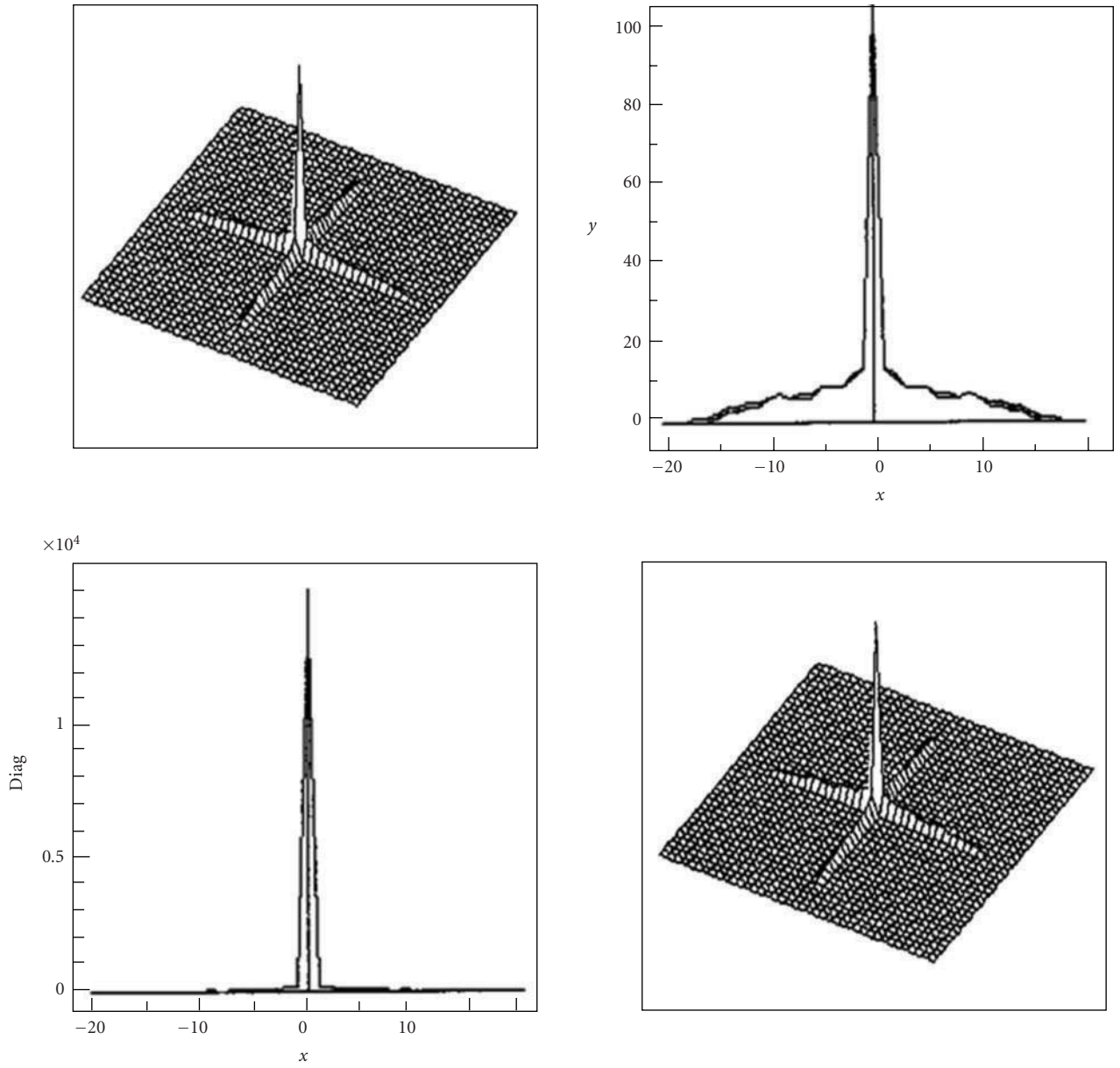

Figure 30: Intensity distribution in the focal plane (15 × 15 mm detector) for the 23 × 23 mm Schmidt objective, mathematical raytracing for micro roughness rms = 1 nm and wavelength = 1 nm.

The arrangement described above was, however, not been further developed for a long time because of difficulties with production of numerous polished square cells of very small size (about 1 × 1 mm or smaller at lengths of order of tens of mm).

The early feasibility studies have shown that this demand can be also solved by electroformed replication and first test cells as well as objective prototypes have been already successfully developed in this way. The recent approach is based on electroforming and composite material technology to produce identical triangular segments with square cells while these segments are aligned in quadrants onto a sphere.

The first Angel-developed telescope prototype consists of linear arrangement of 47 square cells of 2.5 × 2.5 mm, 120 mm long (i.e., length/size ratio of almost 50), with focal length of 1.3 m (Figures 38, 46(a), and 46(b)). The second Angel telescope prototype is represented by an array of 6 × 6 that is, 36 square cells, 2.5 × 2.5 mm each, 120 mm long, focus and length/size ratio as above. Both of these prototype modules have been produced and tested already. The microroughness of the inner reflecting surfaces is better than 1 nm. The third prototype was also finished, and consists of 2 × 18 perpendicular arranged cells 2.5 × 2.5 mm, 120 mm long (Figure 40(a)).

An innovative technique of production of 120 × 120 mm sized modules consisting of large number of 3 × 3 mm cells, 120 mm long, is also under development (for related possible arrangement, see Figure 39).

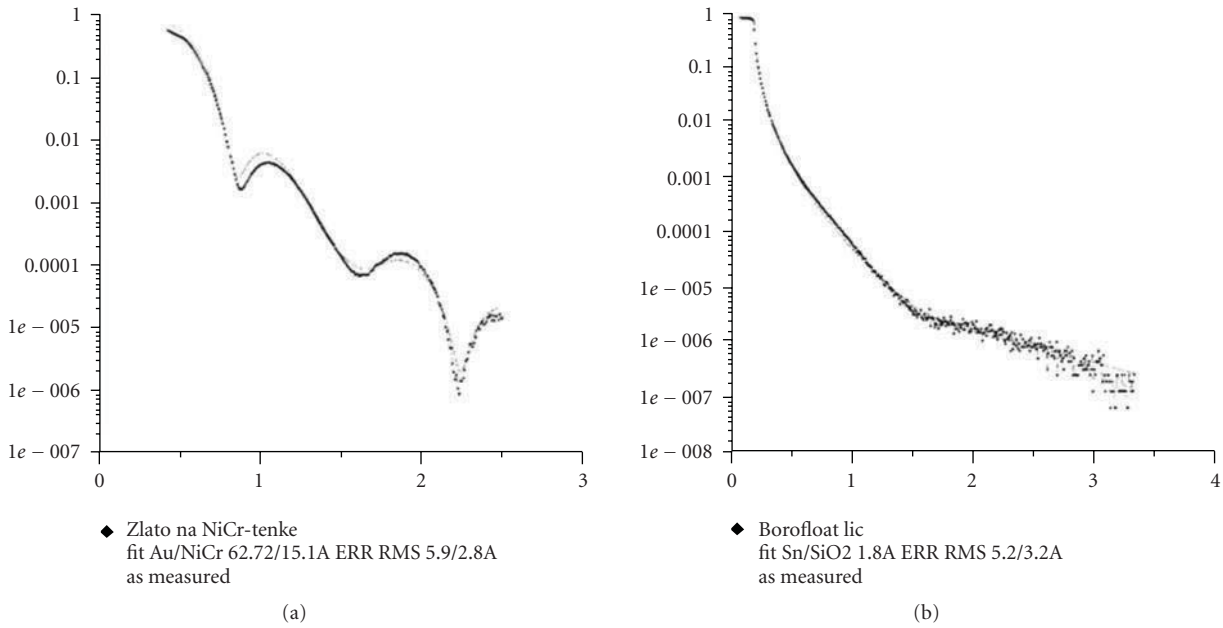

(a) (b)

Figure 31: (a) The X-ray reflectivity measurements of 0.1 mm float glass plate (used in the 23 × 23 mm Schmidt objective). Au/NiCr layers coated the reflecting surfaces. (b) The X-ray reflectivity measurements for BOROFLOAT 1.1 mm thick flat sample (with no additional layers).

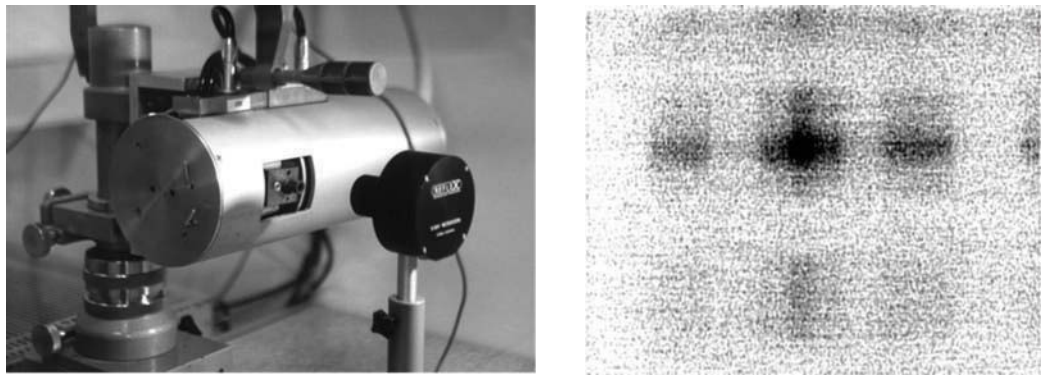

(a) (b)

Figure 32: The Micro source X-ray test facility at Rigaku, Prague (a) and the X-ray image of a 10 micron source at 8 keV detected by X-ray CCD camera (b) in the focal plane of the 3 × 3 mm micro Schmidt objective, the image area is 2.5 × 2.5 mm.

Table 4: Parameters of the LE Schmidt lenses designed and developed in the Czech Republic.

Modul	Size d (mm)	Plate thickness t (mm)	Distance a (mm)	Length l (mm)	Eff. angle a/l	Focal length f (mm)	Resolution r (arcmin)	Field of view (°)	Energy (keV)
macro	300	0.75	10.80	300	0.036	6000	7	16	3
midle	80	0.3	2	80	0.025	400	20	12	2
mini 1	24	0.1	0.3	30	0.01	900	2	5	5
mini 2	24	0.1	0.3	30	0.01	250	6	5	5
micro	3	0.03	0.07	14	0.005	80	4	3	10

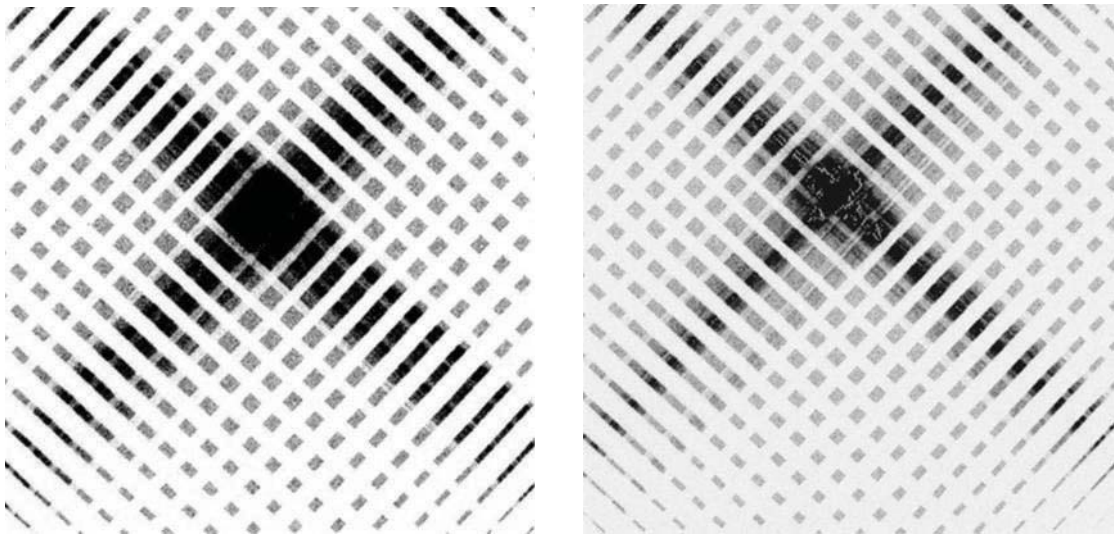

(a) (b)

Figure 33: (a) The focal image of the mini-LE Schmidt (see also Table 4) objective 23 × 23 mm, at 8 keV. X-ray tests were carried out at Rigaku, Prague. (b) The mini-LE Schmidt module X-ray focal spot image, another detector position angle.

4.4. Materials for Lobster Eye Lenses. In general, there is growing need for large segmented X-ray foil telescopes of various geometry and geometrical arrangements. This includes the large modules of the Wolter 1 geometry (e.g., assumed for the future ESA/NASA/JAXA X-ray astronomy mission IXO), the large Kirkpatrick-Baez (further referred as KB) modules (as they can play an important role in future X-ray astronomy projects as a promising and less laborious to produce alternative) as well as the large lobster eye modules in the Schmidt arrangements. Although these particular X-ray optics modules differ in the geometry of foils/shells arrangements, they do not differ much from the point of the view of the foils/shells production and assembly, and also share all the problems of calculations, design, development, weight constraints, manufacture, assembling, testing, and so forth. It is evident that these problems are common and rather important for majority of the large aperture X-ray astronomy space projects. All the space projects require light material alternative (e.g., Hudec et al. 2001 [45]).

We have developed the various prototypes of the above-mentioned X-ray optics modules based on high quality X-ray reflecting gold coated float glass foils (Figure 41, Hudec et al., 2000, [45]). Alternative substrates were also tested (Gorenstein et al. 1996 [7]). The glass represents a promising alternative to widely used electroformed nickel shells, the main advantage is much lower specific weight (typically 2.2 gcm^{-3} if compared with 8.8 gcm^{-3} for nickel). However, the technology needs to be further exploited and improved in order to achieve the required accuracy. For the large prototype modules of dimensions equal or exceeding 30 × 30 × 30 cm, mostly glass foils of thickness of 0.75 mm have been used for these large modules, although in future this thickness can be further reduced down to 0.3 mm and perhaps even less (we have successfully designed, developed and tested systems based on glass foils as thin as 30 microns, albeit for much smaller sizes of the modules, see Figure 45).

The requirement of minimizing the weight of future large X-ray space telescopes and at the same time achieving huge collecting areas means that the future large astronomical mirrors have to be based on thin X-ray reflecting foils that is, thin layers with low weight which can be easily multiply nested to form the precise high throughput systems (Figures 44(a), and 44(b)). Below, we discuss some of the analyzed techniques and approaches and related progress.

4.5. The Application and the Future of Lobster-Eye Telescopes. It is obvious that the first lobster-eye prototypes confirm the feasibility to design these telescopes with currently available innovative technologies (Figure 47). We propose the following steps to be undertaken for a real wide-field X-ray telescope: (1) to reduce further the microroughness as well as the slope errors of the reflecting surfaces in order to improve the angular resolution and the system reflectivity/efficiency. The recent development has already lead to significant microroughness improvement (to 0.2–0.5 nm), (2) to design and to construct larger or multiple modules in order to achieve larger fields of view (of order of 1000 square degrees and/or more) and enhanced collecting area, (3) to reduce further the aperture of the cells (for the Angel arrangement) and/or spacing and plate thickness (Schmidt arrangement) and to enhance the length/aperture ratio (recently nearly 50–80), and (4) to study the multilayer application on reflecting surfaces and/or other approaches in order to improve the energy coverage for higher energies.

The application of very wide field X-ray imaging systems could be without any doubt very valuable in many areas of X-ray and gamma ray astrophysics. Results of analyses and simulations of lobster-eye X-ray telescopes have indicated

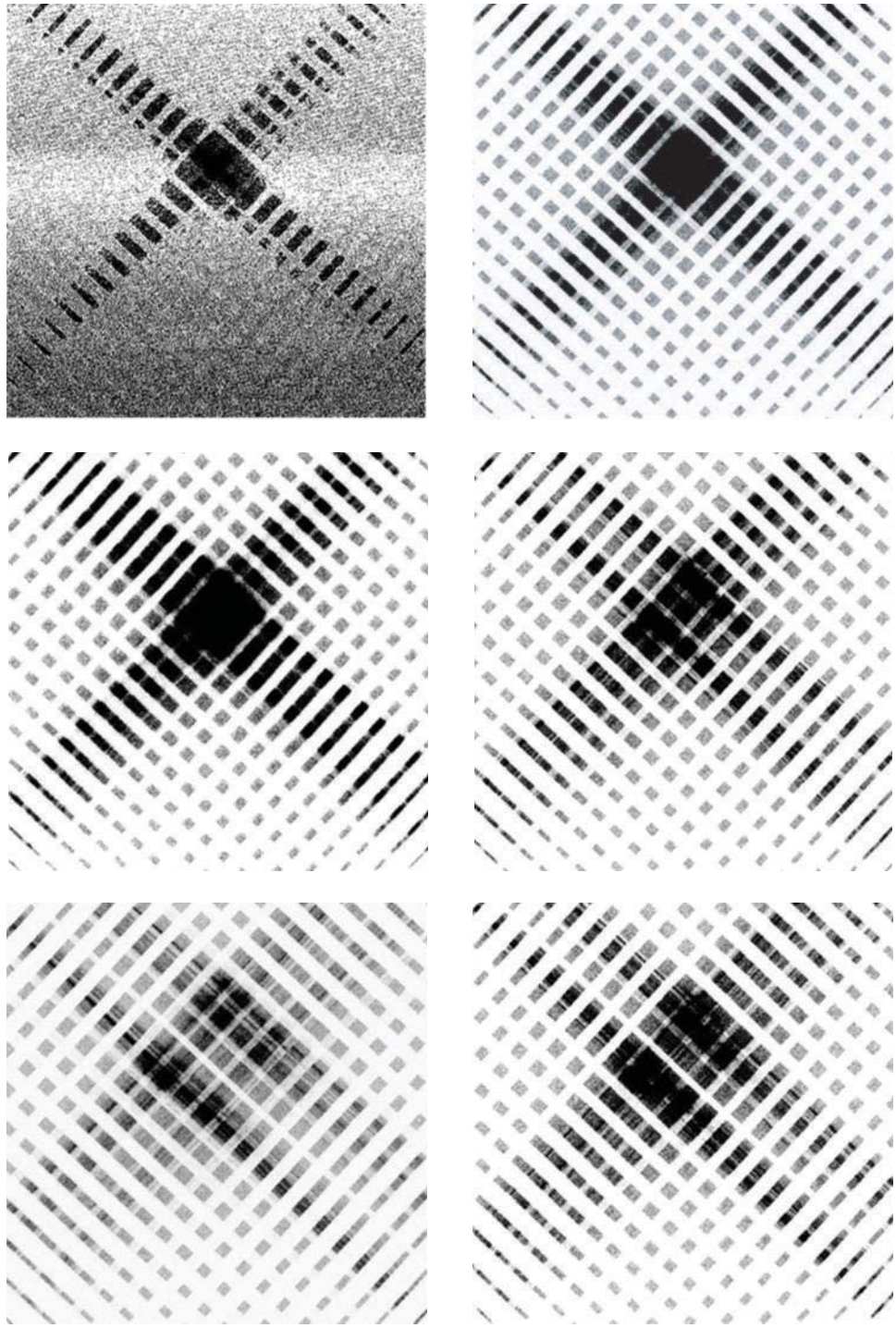

Figure 34: A sequence of X-ray focal spot images in front, in focus and behind the focal plane showing the defocusing behaviour of the mini LE Schmidt module (the distance between the detector position for first and the last image is 110 mm).

that they would be able to monitor the X-ray sky at an unprecedented level of sensitivity, an order of magnitude better than any previous X-ray all-sky monitor. Limits as faint as 10^{-12} erg cm^{-2} s^{-1} for daily observation in soft X-ray range are expected to be achieved, allowing monitoring of all classes of X-ray sources, not only X-ray binaries, but also fainter classes such as AGNs, coronal sources, cataclysmic variables, as well as fast X-ray transients including gamma-ray bursts and the nearby Type II supernovae. For pointed observations, limits better than 10^{-14} erg sec^{-1} cm^{-2} (0.5 to 3 keV) could be obtained, sufficient enough to detect X-ray afterglows to GRBs. As indicated by our preliminary results, the production of corresponding optical elements can be reasonably achieved by electroforming methods and

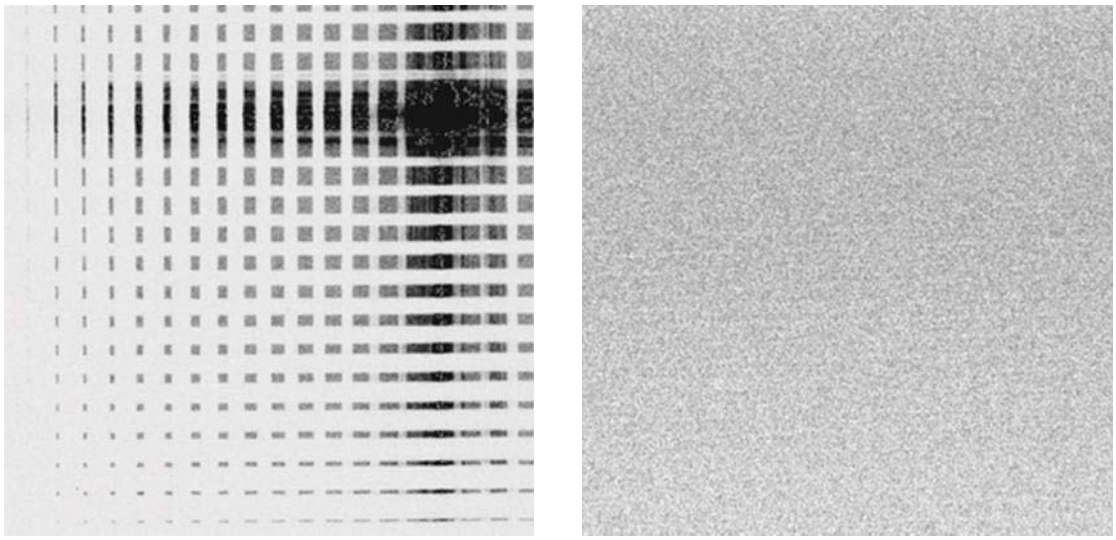

(a) (b)

Figure 35: The two X-ray images (signal exposure and dark-background image) exhibiting the focal spot of the LES module as well as the detection capability of the used X-ray CCD 16 bit detector. The average dark signal is 266 ADU at the exposure of 80 sec ADU, the rms noise is 2 ADU, that is, the achieved electronic dynamic range is more than 30 000. The measured intensity gain of this module is 420.

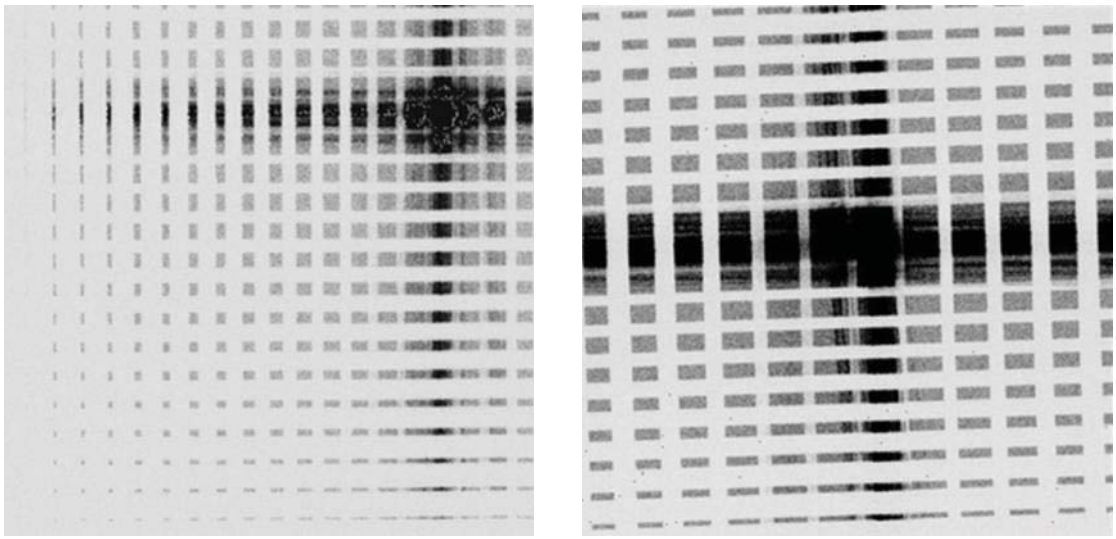

(a) (b)

Figure 36: (a) The X-ray focal image of the MINI LE SCHMIDT module showing the main intensity to be inside the main focal spot. The intensity gain achieved is 570 (for 8 keV X-ray tube and only part of the LE module active due to the high energy of X-ray photons—note that this module has been designed for energy of 2 keV). (b) The focal plane image for the LE test module. The measured gain is 500.

composite replication as the alternative to other methods. For the Schmidt objectives, the results obtained with the development of technology for production of large area and high-quality double-sided X-ray foils are very promising and together with composite material technologies represent an important input for the further development of this type of X-ray optics. The production of Angel lobster-eye cells is much more complicated, nevertheless the first prototypes of the lobster eye Angel cells have been also successfully designed and developed.

4.6. LE Laboratory Modifications. The lobster eye soft X-ray optics, originally proposed and designed for astronomical (space) applications, have potential for numerous laboratory applications.

As an example, LE optics can be modified for efficient collection of laser-plasma radiation for wavelengths longer than 8 nm (Bartnik et al., 2006 [55]). The optics for this application consists of two orthogonal stacks of ellipsoidal mirrors forming a double-focusing device (Bartnik et al., 2006 [55]). The ellipsoidal surfaces were covered by a layer

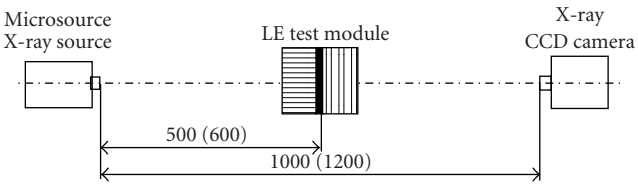

Figure 37: The arrangement of the X-ray tests of the LE modules.

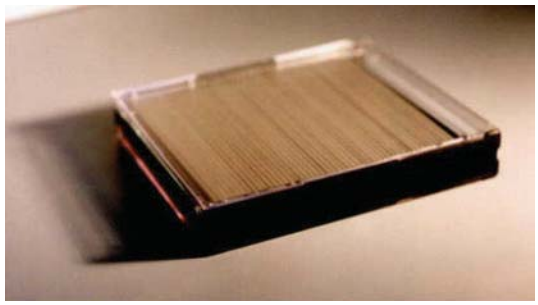

Figure 38: The unique linear Angel prototype produced by replication: 47 square channels, 120 mm long, and 2.5 × 2.5 mm. This picture illustrates the power of electroformed replication even for very long square cells which otherwise could not be polished inside. In this technology, the square mandrels were highly polished and then replicated, so the polished surface is now inside. This demonstrates that also other techniques as MCP can be considered for LE Angel arrangements.

of gold that has relatively high reflectivity at the wavelength range between 8–20 nm up to about 10 degrees of an incidence angle. A schematic view of half of the optics system together with a front view of the optic, are shown, respectively, in Figure 48. The mirrors forming the optics have the width of 40 mm. As can be noticed the spacing between adjacent mirrors rises with the distance from the axis. The curvature of the mirrors and the spacing between them were optimized by ray-tracing simulations to maximize an aperture of the optic and minimize the size of the focal spot.

The distances for the best focusing were found as 181 mm source—LE entrance, 183 mm LE rear cover—focus. The relative intensity distribution of the visible light at the focal spot is presented at Figure 48.

4.7. Hybrid LE. The lobster eye optics described in the previous section are wide field optics, but it is relatively complicated to achieve a better angular resolution with the given technological limitations of mirror thickness and spacing (Sveda et al. [56]).

One of possible solutions to this problem is induced by the typical use case of the standard lobster eye as an All Sky Monitor (ASM) for X-ray astronomy. The lobster eye will be used onboard the satellite and will scan the sky. If a certain point of the sky is outside the FOV of the optics at the moment, it will be inside the FOV sometime later because of scanning. Hence, in principle, we can accept smaller FOV in the scanning direction, if we can get some advantage as a trade-off, such as a better angular resolution. The desired optics would have a wide FOV and moderate angular resolution in one direction, and a smaller FOV and better angular resolution in another one.

It is necessary to use curved mirrors to achieve the better angular resolution with constraints on mirror dimensions. There is a relatively simple way to the final idea combining all these facts. A combination of the standard one-dimensional lobster eye in one direction and the Kirkpatrick-Baez parabolic mirror set in the other direction would fulfil all the requirements (Sveda et al., 2005 [56]), see Figure 49.

The preliminary results show that the hybrid lobster Eye can work as intended, that is, it increases the angular resolution in one direction while still having wide FOV in another. However, the blurring increases rapidly with the off-axis distance in the direction where focusing the parabolic mirrors are. Consequently, it is reasonable to think about such optics for point observations if the source and/or image are expected to be highly asymmetric. The effect of blurring is reduced for scanning observations, hence the increase in angular resolution is well achievable, but the decrease of gathered photons resulting in much worse limiting flux is so significant that, together with manufacturing difficulties, this optics is probably not usable for X-ray astronomy but may find usage in laboratory.

4.8. MCP as Alternative LE Optics. Alternative grazing incidence X-ray optics can use microchannel plate—MCP, in a Wolter-like or alternatively lobster-eye type, X-ray optic (for a detailed review, see, e.g., [57]). Depending on the application (laboratory or space) the MCP can be either flat or curved.

The MCP, when it is curved into a spherical geometry and square profile channels are used, becomes equivalent to the so-called lobster-eye telescope first proposed by Angel (1979 [60]) and is closely related to the orthogonal mirror proposed by Schmidt (1975 [53]). Chapman et al. [102] published an exhaustive theoretical treatment of the properties of square channel arrays (Figure 50) and detailed investigations and proposals based on application of MCP as LE lenses were reported, for example, by Priedhorsky et al. (1996 [62]), Fraser (1993 [71]) and Peele (2001 [103]), see also Figure 51.

The X-ray LE optic systems in Angel arrangement are based on slumped lead glass microchannel plates (MCPs). However, the spectral range of operation of existing MCP-based LE optics is limited to X-rays with energies of less than 4 keV. Harder X-rays with smaller critical grazing angles cannot be focused efficiently by glass MCPs because their walls are inaccessible for polishing and metallization. This energy range constraint of the MCP-based LE optics limits its application to vacuum chambers or open-space astronomical applications with infinite distance to the objects (such as celestial objects).

To reach their full capabilities, MCPs must be manufactured accurately to reduce figure error and have low surface roughness to reduce scattering. Their being manufactured from or coated in a material with high X-ray reflectivity is

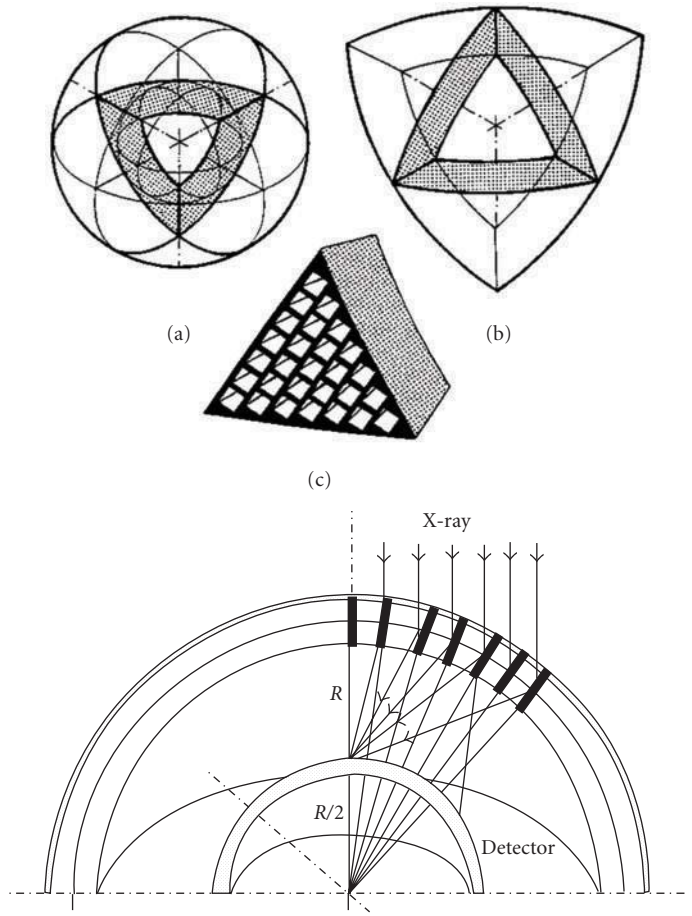

Figure 39: The schematic arrangement of the Angel lobster-eye objective (bottom) and the proposed construction based of electroformed triangular segments of this arrangement (top). The triangular segments represents parts of the sphere (a, b) and include square cells of Angel LE arrangement (c).

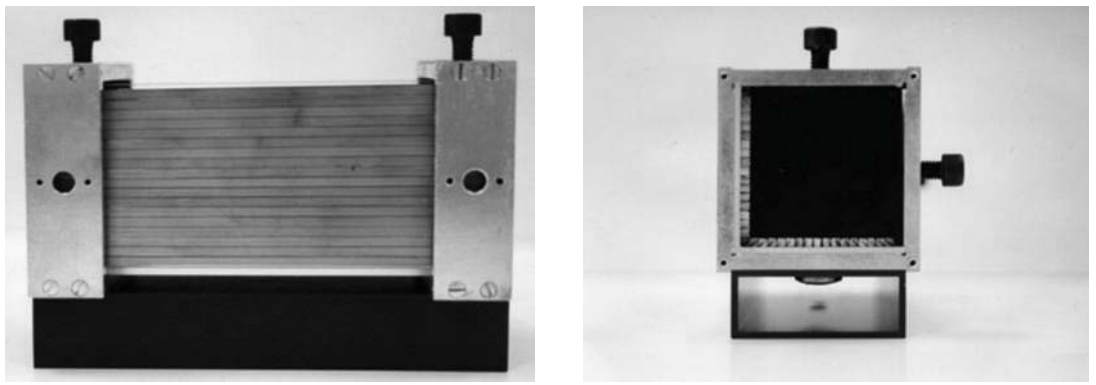

Figure 40: The Angel lobster eye test module, in L-shaped array of 2×18 cells, 2.5×2.5 mm, 120 mm long.

also desirable. Initial investigations of MCPs have used flat samples because figure error and surface roughness can be readily evaluated and samples are easier to prepare (Figure 52).

The cruciform structure of the focal spot for square profile channels was observed in the X-ray region for example, by Fraser et al. [71], though the focal spot itself was somewhat broader than it was expected because of imperfections in the MCP (Figure 53).

The focusing performance of the MCP may be effectively understood with the theoretical results published by Chapman et al. [102]. The MCP consists of an array of square

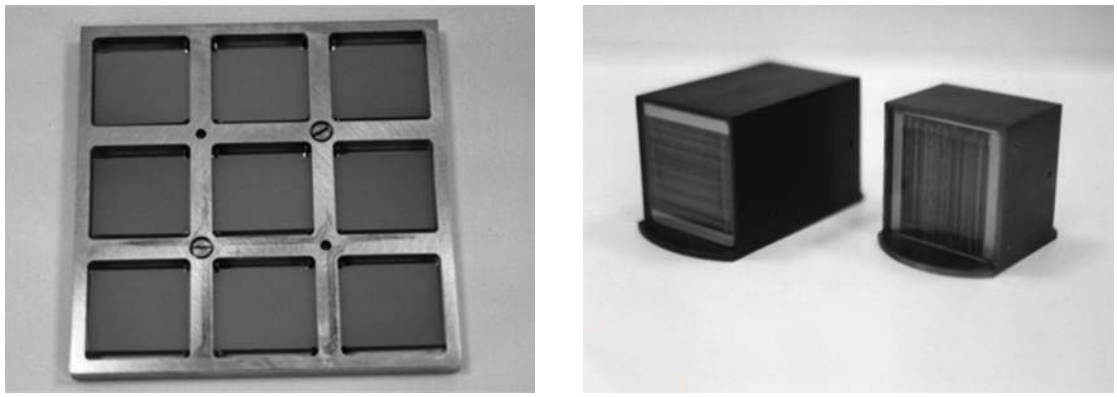

(a) (b)

Figure 41: The frame with 23 × 23 mm flats for the Schmidt objective prototype after gold coating (a) and the assembled modules (b).

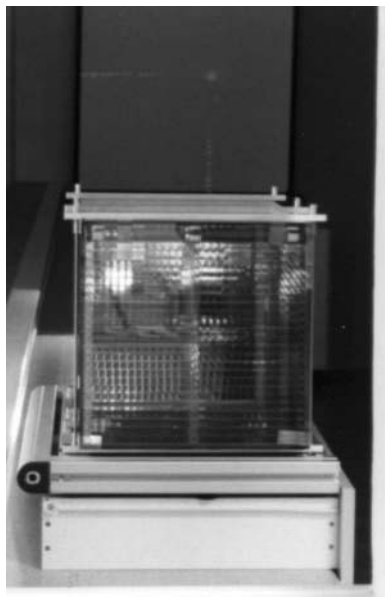

Figure 42: The large (30 × 30 cm) LE Schmidt lens during optical tests (with optical focal image).

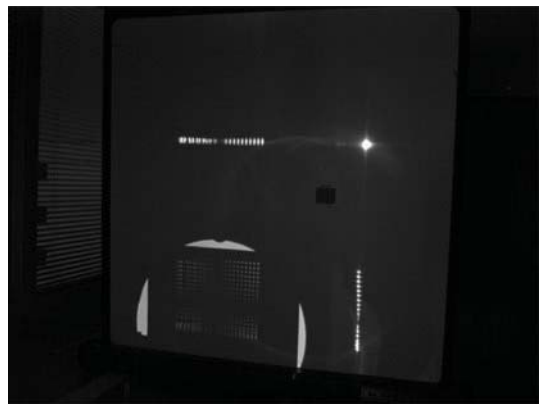

Figure 43: The focal plane image from the large (30 × 30 cm) LE 2D module (0.75 mm thick glass plates, optical light).

channels. X rays that strike the exterior walls on the face of the MCP are lost. Of the X-ray photons that enter a channel, a fraction that reflect once off two orthogonal walls are reflected into the focal spot, another fraction are reflected only from one wall and so are focused in one dimension to a line passing through the two-dimensional focus, and a third fraction pass straight through the array to form an unfocused background. Higher-order reflections are also possible, but the X-ray photons from such reflections strike a detector as if they were in one of the above mentioned classes. The resulting focal structure then consists of a bright focused spot with a fainter cross centred on this and a much less intense diffuse background. The relative number of photons in each of the above described structures depends on the ratio of the width of the channels to their length. At the optimal ratio for a lens with no axis of symmetry and with 100% reflectivity, 34.3% of the photons are focused into the central square, 24.3% end up in each of the one dimensional foci arms, and 17.2% end up in the unfocused background. The focusing efficiency in a given direction may be improved when a preferred axis is imposed on the device, but this is not consistent with a very-wide-field-of-view telescope. The X rays are brought to a focus with an angular resolution comparable with the angle that an individual channel subtends at the detector. In practice this implies that the MCP based lobster-eye telescope will always be limited in resolution by the physical size of the individual channels.

4.9. Comparison of MFO and MCP Design of LE Optics. Direct and reliable comparison of MFO and MCP designs of LE X-ray optics is difficult, as in both cases, the real optics performance deviates from theoretical one. For MCP design, the necessary slumping obviously introduces additional sources of errors (Bannister et al., 2007 [75]).

Some of the examples of the performance are shown below together with Table 5 comparing both approaches.

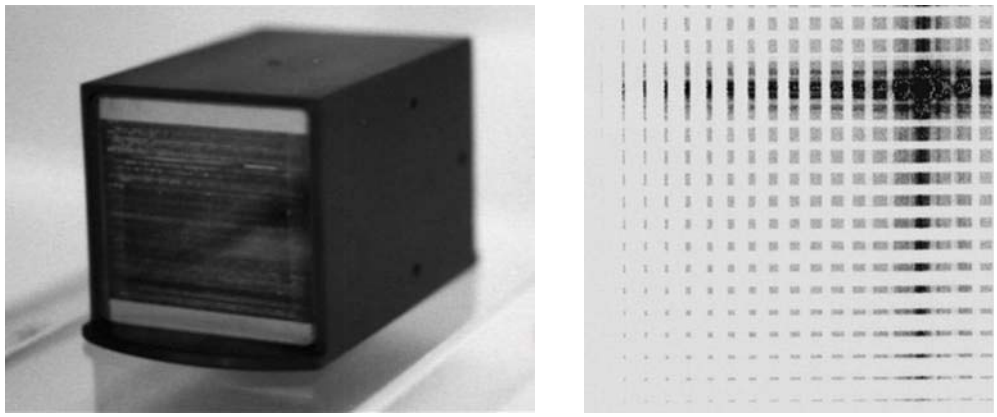

(a) (b)

Figure 44: (a) The mini (24 × 24 mm, 0.1 mm thick foils spaced at 0.3 mm) Schmidt LE module illuminated by the laser beam. (b) The mini Schmidt 2D prototype X-ray (8 keV) focal spot image (image area 12.3 × 12.3 mm). The measured gain was 680.

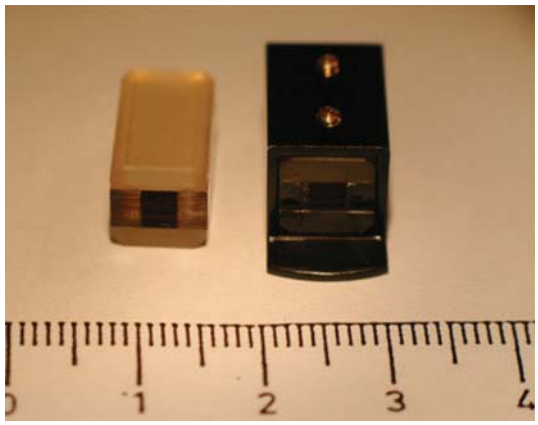

Figure 45: The micro LE Schmidt objectives, 3 × 3 mm. This figure illustrates that the MFO technology can be applied also for very small structures and very small Lobster Eye modules. In the devices illustrated, gold-coated float glass foils 30 micron thick are assembled with spacing of 70 microns. Small plate distances (together with long focal distance) represent condition for good angular resolution.

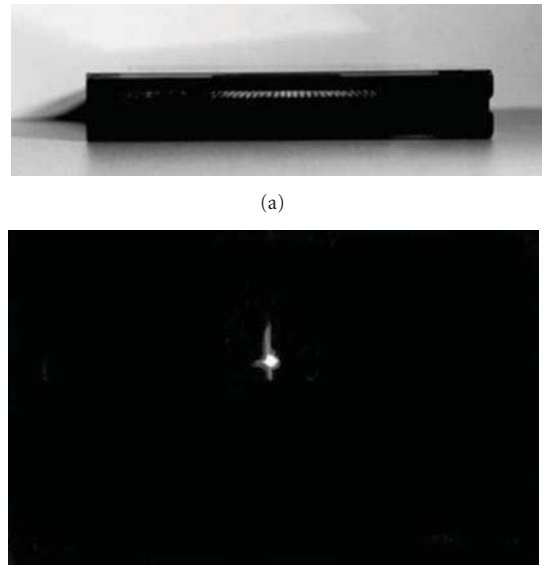

(a) (b)

Figure 46: (a) The Angel LE linear prototype (47 cells 2.5 × 2.5 mm, 120 mm long). (b) The optical focal image from the linear LE prototype in Angel arrangement.

Examples of recent measurement results for MFO LE design (Figures 54, 55, and 56) and MCP LE design (Figure 57) is shown below. For more details, see the given references.

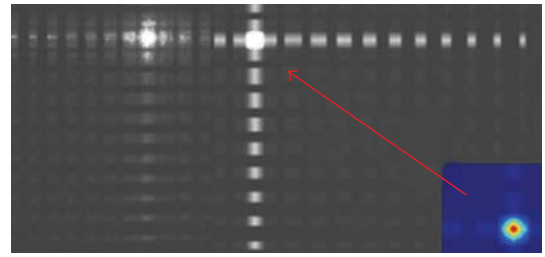

Figure 47: Experiment (left) and simulation (right) of a point-to-point focusing LE MFO test optic. 8 keV photons are used.

5. Capillaries

Although the capillaries represent collimating and not imaging elements, we note them here for completeness. Condensing an X-ray beam by using total external reflection along the interior surface of a hollow tapered glass capillary has been demonstrated by Stern et al. [104]. Tapered glass monocapillaries have been fabricated by many investigators (e.g., Engstrom et al., 1991 [105]). These capillaries condense X-ray beams by the use of geometrical reflection optics alone. X rays incident at glancing angles to the interior surface of the tapered capillary are reflected along its length toward an exit aperture of smaller dimensions than its entrance aperture. The decrease in the relative area of the apertures corresponds to an increase in flux per unit area (intensity) in the emerging

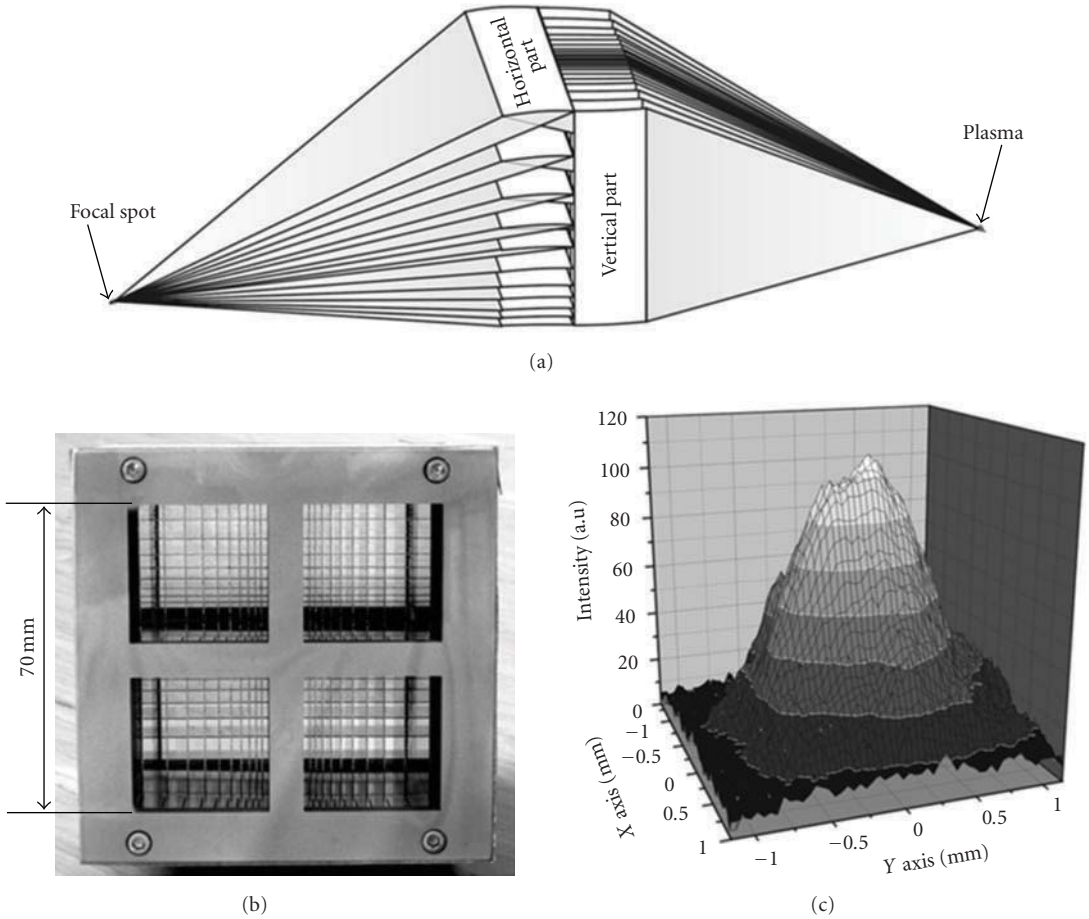

Figure 48: The lobster eye optic: (a) schematic view of half of the optic system, (b) front view of the optic (c) simulation of the intensity distribution at the lobster eye focus using 0.3 mm visible light source (Bartnik et al., 2006 [55]).

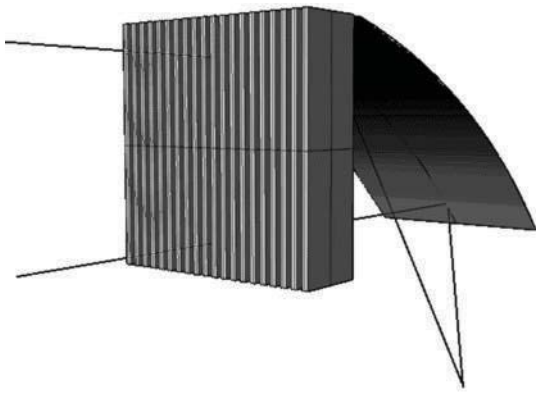

Figure 49: The sketch of the Hybrid Lobster Eye with two plotted rays. Only one parabolic mirror is schematically plotted here. In fact, a number of reflecting surfaces have to be used (Sveda et al., 2005 [56]).

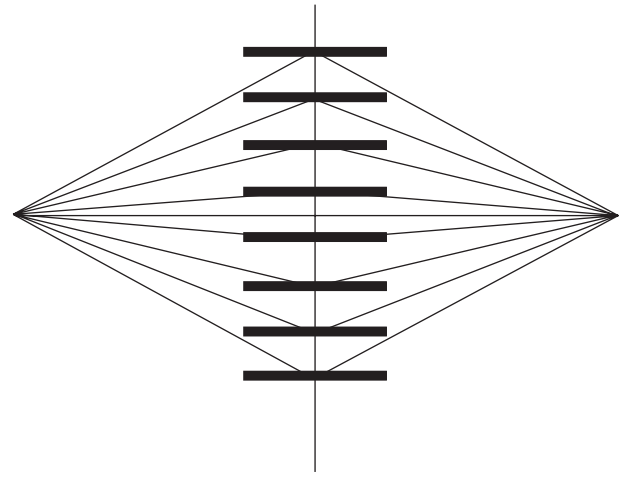

Figure 50: Focusing from a point source using a multichannel plate optic (MacDonald and Gibson, 2010 [57]).

beam. The reflection of X rays from the interior surface of the capillary is achieved through total external reflection from the glass surface. This specular reflection process occurs because the refractive index of the glass for X rays is less than unity. For an ideally flat surface one may characterize this reflectivity using the Fresnel reflectivity function for a given glass composition. For X rays with an energy of 6 keV or more, the reflectivity is often well described as a

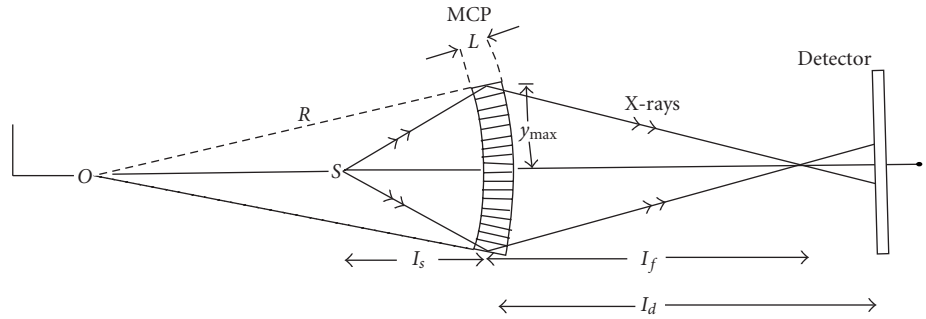

Figure 51: Creating a collimated beam with a slumped multichannel plate (Fraser et al. 1993 [71]).

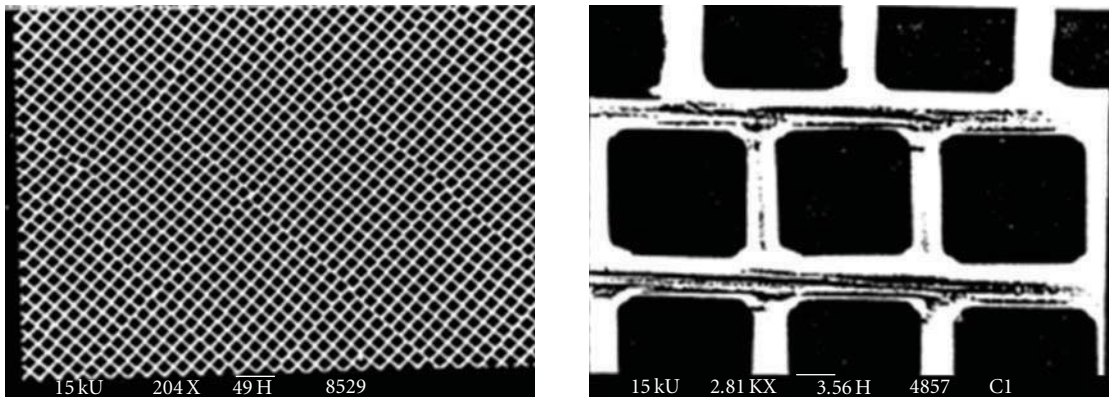

Figure 52: Square pore multichannel plate with 13.5-micron pore size, magnified at right (Brunton et al., 1995 [72]).

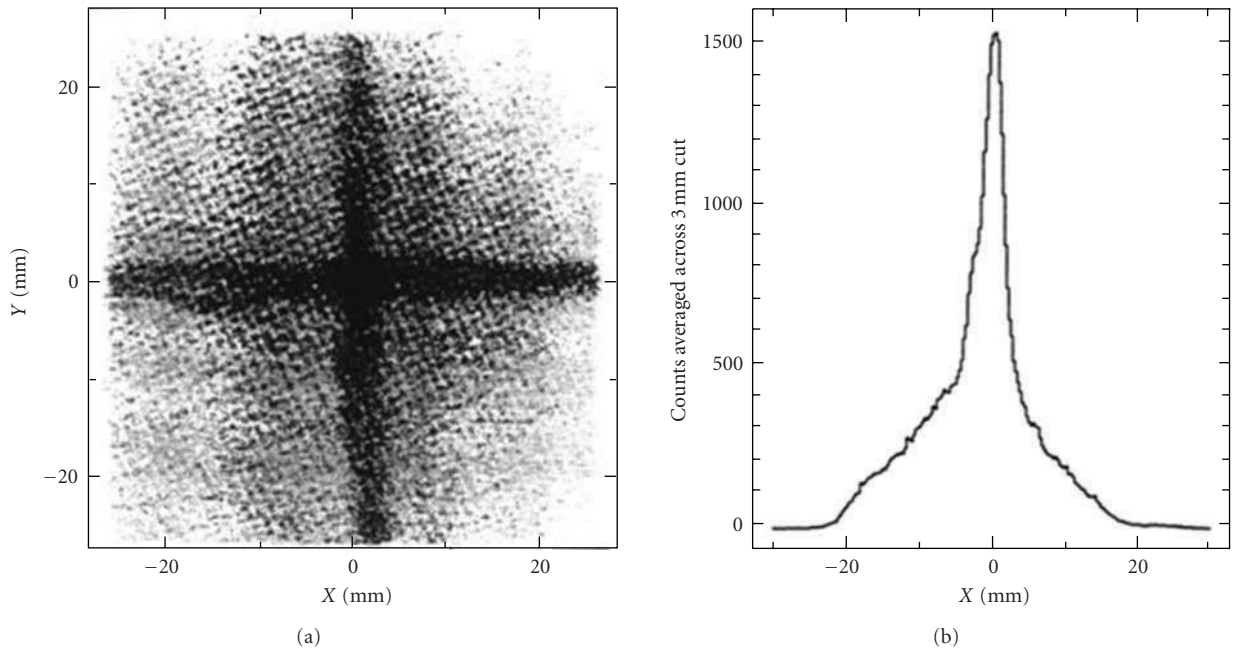

Figure 53: (a) Output image from MCP with 11 μm square pores and thickness to diameter ratio of 40 : 1 illuminated with 1.74 keV Si K X rays. (b) Scan of image with the same MCP, taken with 0.28 keV C K X rays (Brunton et al., 1995 [72]).

Table 5: Multifoil versus MCP approach to the Lobster ASM.

Property	MCP			Multi-foil
Surface microroughness	10–20 Å [54, 55, 90]	−	+	3–10 Å [57, 102]
Metal coating	More complicated, getting better	−	+	Simple, standard
Multilayers	Very difficult	−	+	Simple, standard [22]
Gain[1] (1 keV)	10–100 (30–40 derived from [54])	−	+	100–1000 (∼2500 simulation ∼1000 reality)
Gain[2] (8 keV)	Not documented	−	+	10–100 (300–400 [21], point-to-point focus)
Optics Weight[3]	∼0.1 kg [54]	+	−	∼1.0 kg
Optics dimensions[4]	$70.0 \times 70.0 \times 0.3$ mm [54]	+	−	$78 \times 78 \times 23$ mm
FOV	Unlimited in principle	+	−	Wide but limited
Energy range	<3 keV [54]	−	+	<10 keV[5]
ASM module FOV[6]	$\sim 20 \times 20$ deg [54]	+	−	6×6 deg
Daily limiting flux [10^{-13} erg s^{-1} cm^{-2}]	∼20 [54]	−	+	∼5–10[7]
Angular resolution	∼4 arcmin	+	+	∼4 arcmin
Detector shape	Curved [54]	−	+	Planar

[1] Defined as a ratio of photons gathered inside the FWHM with and without optics.
[2] Defined as a ratio of photons gathered inside the FWHM with and without optics.
[3] 6×6 deg FOV, $f = 37.5$ cm, both approaches scaled to fit these criteria.
[4] 6×6 deg FOV, $f = 37.5$ cm, both approaches scaled to fit these criteria.
[5] Au coated, microroughness $\sigma \sim 10$ Å.
[6] The rating of this property is disputatious: larger FOV results in smaller number of modules to build and test, on the other hand, if anything goes wrong, larger part of the sky will be uncovered and higher costs for insitu repair is demanded.
[7] Depends on the PSF blurring by distortions, backgroung estimates. . ..

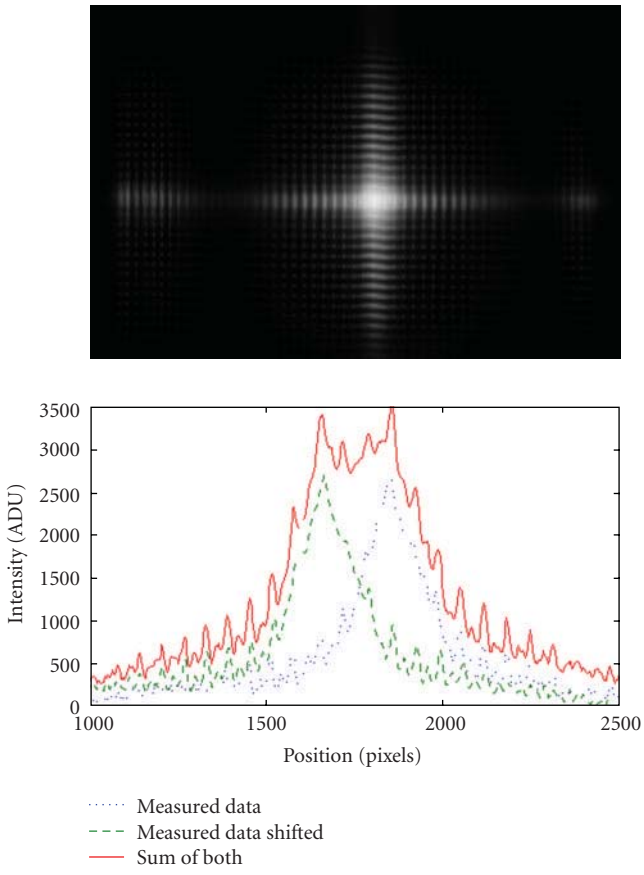

Figure 54: Measurements of MFO LE optics with $f = 25$ cm in 8 keV with Medipix2 detector with measured FWHM of 8 arcmin (Tichy et al., 2010a [73]).

step function with respect to the grazing angle of X rays to the surface, with the position of the step termed the critical angle. Approximately 90% of the ray's incident below this critical angle reflects specularly from the surface (Balaic and Nugent, 1995 [106]). The electroformed micromirrors represent another alternative to single capillaries (Arndt et al. 1998 [107], Pina et al. 1996 [103], and Pina et al. 2000 [108]).

Several factors conspire to degrade the gain in intensity expected in the emerging beam from the capillary. These include poor interior-surface quality of the glass (roughness), the absorption of X rays by the ambient gases present within the capillary, and limitations in the capacity of the capillary to accept the range of incident X-ray angles available from the source (Balaic and Nugent, 1995 [106]). The latter constraint is determined by the angular limits of total external reflection for the type of glass and X-ray energies used.

Systems involving the use of a large number of capillary channels for shaping X-ray beams were first suggested by Arkdev and his collaborators in 1986 (Arkadev et al., 1989 [109]) The development and study of polycapillary optics and its applications in X-ray lithography (Klotzko et al., 1995 [110]), X-ray astronomy (Russell et al., 1997 [111], and Russell et al. 1999 [97]) diffraction analysis (Owens et al., 1997 [76], Kardiawarman et al. 1995 [112]), X-ray fluorescence (Gao et al., 1996 [113]) and medicine (Kruger et al., 1996 [114]) have been reported.

Like multichannel plates, they differ from single-bore capillaries in that the focusing or collecting effects come from the overlap of the beams from hundreds of thousands of channels, rather than from the action within a single tube (MacDonald and Gibson, 2010 [57]). X rays can be transmitted down a curved fibre as long as the fibre is

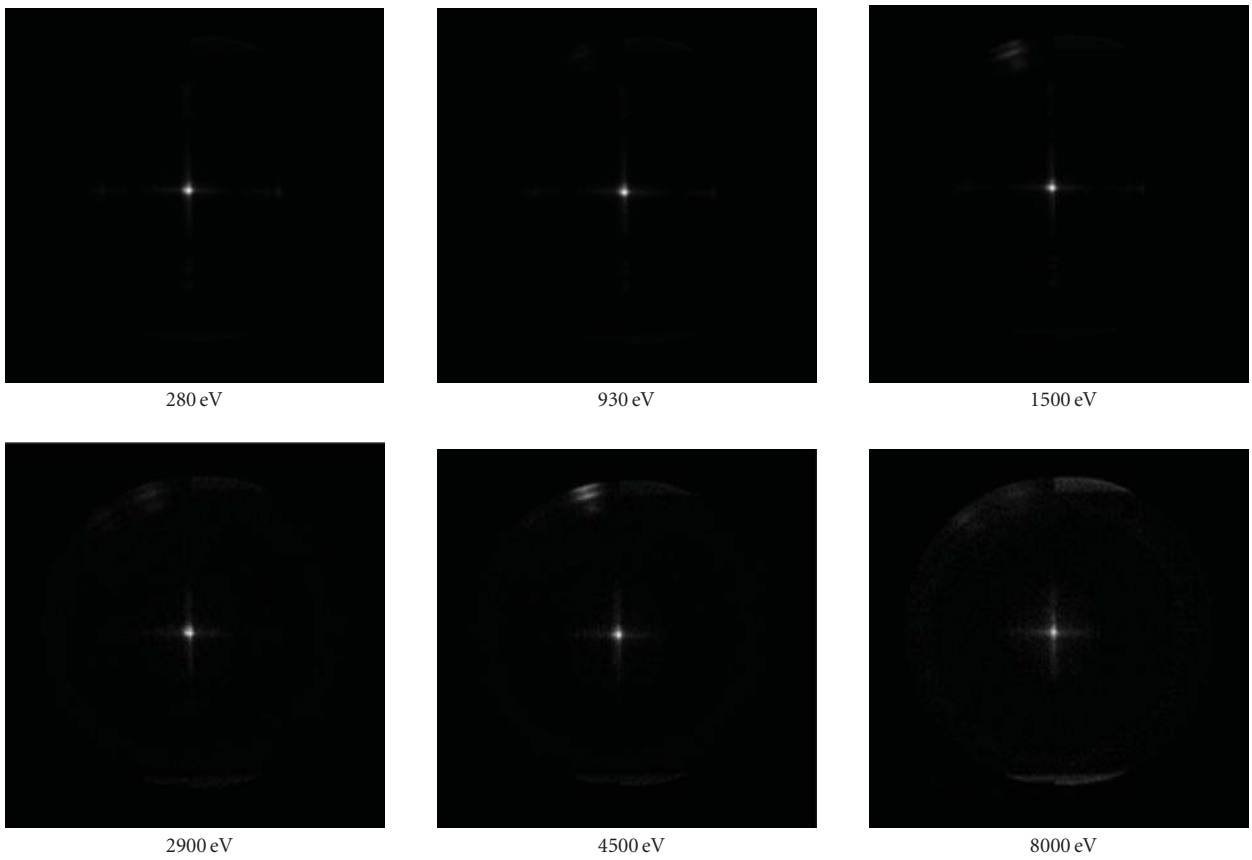

Figure 55: X-ray images from MFO LE, $f = 25$ cm, Palermo test facility (Tichy et al., 2010b [74]).

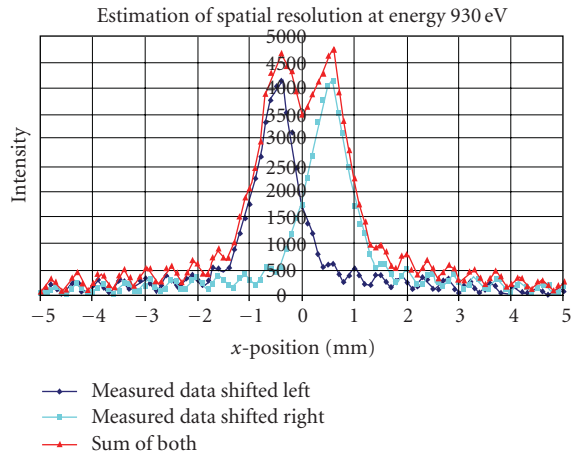

Figure 56: Measurements of MFO LE optics with $f = 25$ cm in the Palermo X-ray facility (measured FWHM of about 10 arcmin between 0.28 and 8 keV (Tichy et al., 2010b [74]).

small enough and bent gently enough to keep the angles of incidence less than the critical angle. The angle of incidence for the ray near one edge increases with tube diameter. The requirement that the incident angles remain less than the critical angle necessitates the use of tiny tube diameters. However, mechanical limitations prohibit the manufacture of capillary tubes with outer diameters smaller than about 300 microns. For this reason, polycapillary fibres are employed. Typical channel sizes are between 2 and 12 microns. Thousands of such fibres are strung through lithographically produced metal grids to produce a multifibre lens. Alternatively, a larger-diameter polycapillary fibre can be shaped into a monolithic optic.

Polycapillary X-ray optics is a powerful, relatively new control technology for X-ray beams (MacDonald and Gibson, 2010 [57]). Using polycapillary optics to collimate the output from a point source provides in most cases much higher intensity than pinhole collimation, particularly if 2-dimensional collimation is required. Collimating optics that collect from 0.7 to 3 millisteradian of a divergent beam has an output diameter range from 1 to 6 mm for a monolithic optic to ≥3 cm for a multifibre collimating optic. Output divergence varies inversely with the photon energy, and is around 3 mrad at 8 keV. Focusing the beam yields even higher-intensity gains. Measured focused beam gains for sample sizes from 0.3 to 0.5 mm are about a factor of 100, and agree well with computations (MacDonald and Gibson, 2010 [57], and references therein). Computed gains for smaller samples are even higher. Polycapillary optics can also be used to perform low pass spectral filtering, which allows the use of increased source voltage. Further, the optics also removes the connection between source size and resolution, which allows the use of increased source current. Increasing the voltage

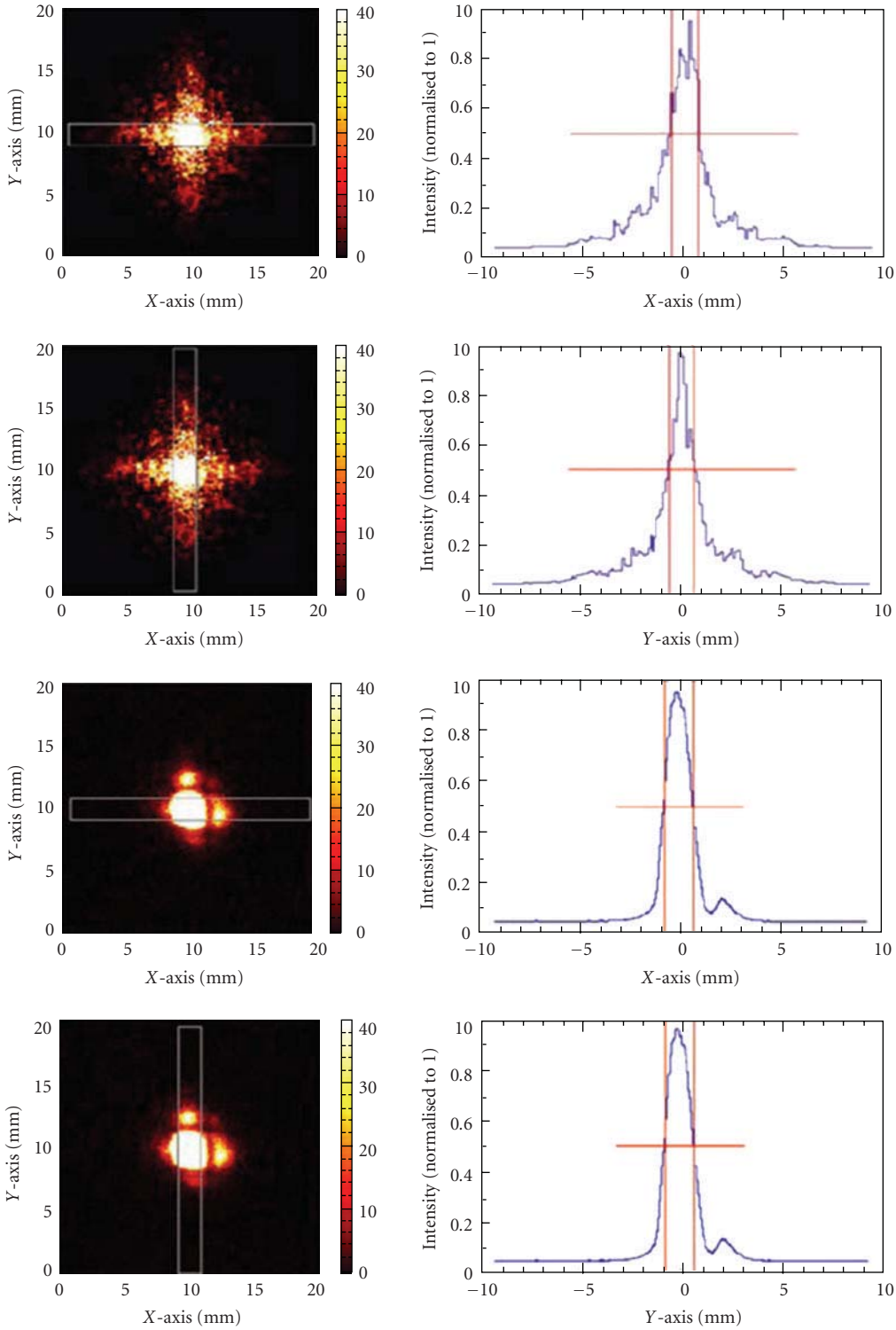

FIGURE 57: *Upper panel*: simulated LE MCP $f = 3.8$ cm optic performance at a wavelength of 121.6 misalignments have been modelled by introducing an additional tilt to each and direction of each tilt is taken from a Gaussian distribution with a FWHM X-axis and 1.70° in the y-axis. The resulting focal spot has a FWHM (horizontal) and 2.64° ± 0.2° (vertical). *Lower panel*: laboratory measurements. Cross-arm structures characteristic of a square-pore MCP optic are clearly visible. The FWHM of the central focus is 2.38 deg (horizontal) ×2.70 deg (vertical) (Bannister et al., 2007 [75]).

and current of the source increases the useful intensity. While not true imaging optics, polycapillary fibres can transmit an image in the same manner as a coherent fibre bundle. Polycapillary optics can be used to magnify and demagnify images and to remove the high-angle Compton scattering which can otherwise result in substantive image degradation.

6. Summary

The grazing incidence X-ray optical elements of non-Wolter type, mainly Kirkpatrick-Baez and lobster-eye optical systems, offer alternative solution for many various future goals both in space and in laboratory. They can offer cheaper, and/or lighter alternatives as well as a larger field of view. At the same time, new computer-based systems allow to consider alternative and arrangements which were impossible before.

Some of these systems, such as KB optics, have already found wide applications in laboratory at synchrotron, demonstrated their performance and advantages. This includes also further modifications and improvements of these systems. It is obvious that for example, KB systems have fully demonstrated their superior imaging performance and accuracy.

The KB microscopes have found wide application in many laboratory areas. Different situation is in the field of telescope applications: here the KB telescopes were used in the past on sounding rockets in the 1970s, and discussed for satellite applications after, but eventually have never flown on a satellite. This situation can however change with introduction of new type of substrates, new and better alignment control. Furthermore, funding pressures may lead to serious consideration of KB optics as an alternative to Wolter-1 optics for large-area X-ray telescopes, owing to the lower cost of the former systems.

The drawback of KB systems if compared to Wolter 1 system that is, the longer focal length to achieve the same effective area and performance can be solved by some kind of novel advanced deployable techniques.

While the historical KB telescope applications were based on thin sheets of float glass, the recently available improved Silicon wafers represent an even more promising alternative, especially for segmented telescopes, as they have better optical surfaces and a very low microroughness (due to chemical-mechanical polishing). In our understanding, the early KB stacks based on Si wafers were unable to demonstrate the full capacity of KB imaging as the early substrates were of inadequate quality for X-ray optics applications. Si wafers with considerably improved parameters and flatness have been available recently. There are also novel methods how to improve further the quality of thin float glass (e.g., by thermal forming on precise flat mandrels).

The results obtained in the field of very wide field X-ray telescopes of lobster-eye type seem to be promising very much. The prototypes developed and tested confirm that these telescopes are fully feasible and can achieve fine angular resolutions of 4 arcmin or better over a wide field of view, as well as high gain to up to 3 keV and still reasonable gain up to 10 keV of the Schmidt arrangement and MFO technology is used. The modular concept allows using the detector techniques recently available and also allows modifying the telescope design for a dedicated experiment. The low weight of both optic as well as detector allows considering LE monitors to be flown on a small satellites, in extreme case even picosatellites. These new devices are ready for X-ray astronomy applications and are expected to help to solve various questions of recent X-ray astrophysics. In addition to that, there are also wide application possibilities in laboratory.

Acknowledgments

The works performed in the Czech Republic partly described here are based on a wide collaboration of several Czech Institutions, namely the teams from Czech Technical University, Faculty of Nuclear Science, Prague, Institute of Chemical Technology in Prague, RITE Rigaku Innovative Technologies Europe, Prague, ON Semiconductor Czech Republic, Astronomical Institute of the Academy of Sciences of the Czech Republic, Ondrejov, and many others. The investigations of lobster (crayfish eyes) have been supported recently by the involvement of Faculty of natural science of the Charles University in Prague, Dr. Adam Petrusek and Petr Jan Juracka. The development of X-ray optics in the Czech Republic is also supported by several grants and projects. The design and development of innovative X-ray telescopes was supported by the grants 106/97/1223 and 102/99/1546 provided by the Grant Agency of the Czech Republic. The authors also acknowledges the support from the Ministry of Industry and Trade of the Czech Republic, Projects nos. FB-C3/29/00 and FD-K3/052. More recently, the authors acknowledges the support provided by the Grant Agency of the Academy of Science of the Czech Republic, Grant nos. IAAX01220701, by the Ministry of Education and Youth of the Czech Republic, Projects nos. ME918 and ME09028 and by Ministry of Industry and Trade of the Czech Republic, FD-K3/052. The investigations related to the ESA IXO project are supported by the ESA PECS Project no. 98039. M.S. was supported by the junior grant by the Grant Agency of the Czech Republic, Grant no. 202/07/P510. The KB optics development is supported by the Ministry of Education and Youth of the Czech Republic, Project no. ME09004.

References

[1] H. Wolter, "Spiegelsysteme streifenden Einfalls als abbildende Optiken für Röntgenstrahlen," *Annalen der Physik*, vol. 10, pp. 94–114, 1952.

[2] P. Kirkpatrick and A. V. Baez, "Formation of optical images by X-rays," *Journal of the Optical Society of America*, vol. 38, no. 9, pp. 766–773, 1948.

[3] 2010, http://www.X-ray-optics.de/.

[4] M. A. Kumakhov, "Channeling of photons and new X-ray optics," *Nuclear Inst. and Methods in Physics Research, B*, vol. 48, no. 1–4, pp. 283–286, 1990.

[5] J. W. Kast, "Scanning kirkpatrick-baez x-ray telescope to maximize effective area and eliminate spurious images; design," *Applied Optics*, vol. 14, no. 2, pp. 537–545, 1975.

[6] P. Gorenstein, B. Harris, H. Gursky, and R. Giacconi, "A rocket payload using focusing X-ray optics for the observations of soft cosmic X-rays," *Nuclear Instruments and Methods*, vol. 91, pp. 451–459, 1971.

[7] P. Gorenstein, E. Whitbeck, K. Gerald et al., "Lobster-eye X-ray telescope prototype," in *Multilayer and Grazing Incidence X-Ray/EUV Optics III*, vol. 2805 of *Proceedings of SPIE*, p. 74, 1996.

[8] V. Marsikova, "X-ray optics: wolter," in *Proceedings of the International Workshop on Astronomical X-Ray Optics*, Prague, Czech Republic, December 2009.

[9] H. Sabet, K. Ishii, S. Matsuyama et al., "A method to modify coordinates of detectors in positron emission tomography systems," *Nuclear Instruments and Methods in Physics Research A*, vol. 600, no. 3, pp. 678–682, 2009.

[10] R. Kodama, N. Ikeda, Y. Kato, Y. Katori, T. Iwai, and K. Takeshi, "Development of an advanced Kirkpatrick-Baez microscope," *Optics Letters*, vol. 21, no. 17, pp. 1321–1323, 1996.

[11] R. Mokso, P. Cloetens, E. Maire, W. Ludwig, and J.-Y. Buffière, "Nanoscale zoom tomography with hard X rays using Kirkpatrick-Baez optics," *Applied Physics Letters*, vol. 90, no. 14, Article ID 144104, 3 pages, 2007.

[12] S. J. Chen, S. Y. Perng, P. C. Tseng, C. K. Kuan, D. J. Wang, and C. T. Chen, "K-B microfocusing system using monolithic flexure-hinge mirrors for synchrotron X-rays," *Nuclear Instruments and Methods in Physics Research A*, vol. 467-468, pp. 283–286, 2001.

[13] A. Ivan, R. J. Bruni, S. B. Cenko, P. Gorenstein, and S. E. Romaine, "High-energy characterization of multilayers for hard X-ray astronomy," in *X-Ray Optics for Astronomy: Telescopes, Multilayers, Spectrometers, and Missions*, vol. 4496 of *Proceedings of SPIE*, pp. 134–139, July 2001.

[14] K. D. Joensen, P. Gorenstein, J. L. Wood, F. E. Christensen, and P. Hoghoj, "Preliminary results of a feasibility study for a hard X-ray Kirkpatrick-Baez telescope," in *Advances in Multilayer and Grazing Incidence X-Ray/EUV/FUV Optics*, vol. 2297 of *Proceedings of SPIE*, pp. 180–189, July 1994.

[15] L. Sveda, *Astrophysical aspects of lobster eye X-ray telescopes*, Ph.D. thesis, Charles University Prague, Faculty of Mathematics and Physics, Prague, Czech Republic, 2003.

[16] M. von Laue, "Eine quantitative Prüfung der Theorie für die Interferenzerscheinungen bei Röntgenstrahle," *Proceedings of the Bavarian Academy of Sciences*, vol. 72, no. 5, pp. 303–322, 1912.

[17] H. Compton, "The spectrum of scattered X-rays," *Physical Review*, vol. 22, no. 5, pp. 409–413, 1923.

[18] W. Ehrenberg and F. Jentzsch, "Über die Auslösung von photoelektronen durch röntgenstrahlen aus metallspiegeln an der grenze der totalreflexion," *Zeitschrift für Physik*, vol. 54, no. 3-4, pp. 227–235, 1929.

[19] F. Jentzch, "Optische versuche mit rontgenstrahlen," *Zeitschrift für Physik*, vol. 30, p. 1268, 1929.

[20] T. R. Burnight, "Soft X-radiation in the upper atmosphere," *Physical Review*, vol. 76, p. 165, 1949.

[21] T. A. Chubb, H. Friedman, R. W. Kreplin, R. L. Blake, and A. E. Unzicker, *Mémoires de la Société Royale des Sciences de Liège*, vol. 4, p. 235, 1961.

[22] E. T. Byram, T. A. Chubb, and H. Friedman, "Ultraviolet light from celestial sources," *Universite de Liege, Institute of Astrophysics College*, vol. 8, no. 418, pp. 469–475, 1961.

[23] R. Hudec, B. Valnicek, V. Hudcova, J. Sylwester, and Z. Kordylewski, "-ray pictures of the sun taken from Vertical 8," *Astronomical Institutes of Czechoslovakia, Bulletin*, vol. 35, no. 3, pp. 153–158, 1984.

[24] J. H. Underwood, J. E. Milligan, A. C. deLoach, and R. B. Hoover, "S056 X-ray telescope experiment on the Skylab Apollo Telescope Mount," *Applied Optics*, vol. 16, no. 4, pp. 858–869, 1977.

[25] J. H. Underwood and D. T. Attwood, "The renaissance of x-ray optics," *Physics Today*, vol. 34, p. 44, 1984.

[26] D. J. Thiel, E. A. Stern, D. H. Bilderback, and A. Lewis, "Focusing of synchrotron radiation using tapered glass capillaries," *Physica B*, vol. 158, no. 1-3, pp. 314–316, 1989.

[27] J. Underwood and T. W. Barbee, "Layered synthetic microstructures as Bragg diffractors for X rays and extreme ultraviolet: theory and predicted performance," *Applied Optics*, vol. 20, no. 17, pp. 3027–3034, 1981.

[28] R. Giacconi and B. Rossi, "A 'telescope' for soft X-ray astronomy," *Journal of Geophysical Research*, vol. 65, p. 773, 1960.

[29] J. D. Mangus and J. H. Underwood, "Optical design of a glancing incidence X-ray telescope," *Applied Optics*, vol. 76, no. 6, pp. 95–102, 1969.

[30] R. Hudec, B. Valnicek, B. Aschenbach, H. Brauninger, and W. Burkert, "Grazing incidence replica optics for astronomical and laboratory applications," *Applied Optics*, vol. 27, no. 8, pp. 1453–1455, 1988.

[31] O. Citterio, M. Ghigo, F. Mazzoleni et al., "Development of soft and hard X-ray optics for astronomy: progress report II and considerations on material properties for large diameter segmented optics of future missions," in *X-Ray Optics for Astronomy: Telescopes, Multilayers, Spectrometers, and Missions*, vol. 4496 of *Proceedings of SPIE*, pp. 23–40, July 2001.

[32] R. Hudec, L. Pina, A. Inneman et al., "Innovative technologies for future astronomical X-ray mirrors," in *UV and Gamma-Ray Space Telescope Systems*, vol. 5488 of *Proceedings of SPIE*, pp. 875–885, June 2004.

[33] R. Hudec, L. Pina, A. Inneman et al., "Novel technologies for X-ray multi-foil optics," in *Optics for EUV, X-Ray, and Gamma-Ray Astronomy II*, O. Citterio and S. L. O'Dell, Eds., vol. 5900 of *Proceedings of the SPIE*, pp. 276–287, 2005.

[34] R. Hudec, A. V. Inneman, L. Pina, V. Hudcova, H. Sveda, and L. Ticha, "Lobster-eye X-ray telescopes: recent progress," in *X-Ray and Gamma-Ray Telescopes and Instruments for Astronomy*, J. E. Truemper and H. D. Tananbaum, Eds., vol. 4851 of *Proceedings of the SPIE*, pp. 578–586, 2003.

[35] I. Sobelman, I. A. Zhitnik, B. Valnicek et al., "Images of the sun obtained with the TEREK X-ray telescope on Phobos-1," *Pis'ma v Astronomicheskii Zhurnal*, vol. 16, pp. 323–329, 1990.

[36] R. Hudec, B. Valnicek, V. Prazak, and I. Solc, "Properties of galvanoplastic grazing incidence mirrors for astronomical applications," *Astronomical Institutes of Czechoslovakia, Bulletin*, vol. 31, no. 3, pp. 188–191, 1981.

[37] R. Hudec and B. Valníček, "Development of X-ray mirrors for high-energy astrophysics in czechoslovakia," *Advances in Space Research*, vol. 3, no. 10–12, pp. 545–547, 1984.

[38] S. K. Sinha, E. B. Sirota, S. Garoff, and H. B. Stanley, "X-ray and neutron scattering from rough surfaces," *Physical Review B*, vol. 38, no. 4, pp. 2297–2311, 1988.

[39] R. Hudec, B. Valnicek, L. Svatek, and V. Landa, "Development and production of ultrathin X-ray mirrors," in *EUV, X-Ray, and Gamma-Ray Instrumentation for Astronomy and Atomic Physics*, Proceedings of SPIE, pp. 617–624, Society of Photo-ptical Instrumentation Engineers, San Diego, Calif, USA, August 1989.

[40] R. Hudec, B. Valnicek, L. Svatek, and V. Landa, "New developments in replica X-ray grazing incidence optics," in *X-Ray Instrumentation in Medicine and Biology, Plasma Physics, Astrophysics, and Synchrotron Radiation*, R. Benattar, Ed., vol. 1140 of *Proceedings of SPIE*, 1989.

[41] R. Hudec, B. Valnicek, J. Cervencl et al., "Recent developments in production of thin X-ray reflecting foils," in *X-Ray/EUV Optics for Astronomy, Microscopy, Polarimetry, and Projection Lithography*, vol. 1343 of *Proceedings of SPIE*, pp. 162–163, July 1990.

[42] R. Hudec, A. Inneman, U. Arndt, and L. Pina, "Compact laboratory X-ray Beam Line with focusing microoptics," in *Proceedings of the International Congress of X-Ray Optics and Microanalysis*, Institute of Physics Conference Series, chapter 7, Manchester, UK, 1992.

[43] R. Hudec, A. Inneman, U. W. Arndt, and L. Pina, "Replicated X-ray micromirrors," in *Proceedings of the l3th International Conference on X-Ray Opticsand Microanalysis*, IOP Conference Series, Manchester, UK, 1992.

[44] R. Hudec, L. Pina, and A. Inneman, "Replicated grazing incidence X-ray optics: past, present, and future," in *X-Ray Optics, Instruments, and Missions II*, vol. 3766 of *Proceedings of SPIE*, p. 62, July 1999.

[45] R. Hudec, "Innovative technologies for future X-ray telescopes," in *Proceedings of the Astronomical Society of the Pacific*, H. Inoue and H. Kunieda, Eds., vol. 251 of *New Century of X-ray Astronomy*, p. 44, Astronomical Society of the Pacific, San Francisco, Calif, USA, 2001.

[46] R. Hudec, "Wide-field sky monitoring—optical and X-rays," *Memorie della Societa Astronomic Ataliana*, vol. 74, p. 973, 2003.

[47] R. Hudec, L. Sveda, A. Inneman, and L. Pina, "Astronomical lobster eye telescopes," in *UV and Gamma-Ray Space Telescope Systems*, vol. 5488 of *Proceedings of SPIE*, pp. 449–459, June 2004.

[48] B. L. Henke, E. M. Gullikson, and J. C. Davis, "X-ray interactions: photoabsorption, scattering, transmission, and reflection at E = 50-30,000 eV, Z = 1-92," *Atomic Data and Nuclear Data Tables*, vol. 54, no. 2, pp. 181–342, 1993.

[49] J. H. Hubbell, W. M. J. Veigele, E. A. Briggs, R. T. Brown, D. T. Cromer, and R. J. Howerton, "Atomic form factors, incoherent scattering functions, and photon scattering cross sections," *Journal of Physical and Chemical Reference Data*, vol. 4, no. 3, pp. 471–538, 1975.

[50] M. Kopecký, "Diffuse scattering of x rays from nonideal layered structures," *Journal of Applied Physics*, vol. 77, no. 6, pp. 2380–2387, 1995.

[51] A. H. Compton, "Incoherent scattering and the concept of discrete electrons," *Physical Review*, vol. 47, no. 5, pp. 367–370, 1935.

[52] B. Aschenbach, "X-ray telescopes," *Reports on Progress in Physics*, vol. 48, no. 5, pp. 579–629, 1985.

[53] W. K. H. Schmidt, "A proposed X-ray focusing device with wide field of view for use in X-ray astronomy," *Nuclear Instruments and Methods*, vol. 127, no. 2, pp. 285–292, 1975.

[54] M. Bavdaz, D. H. Lumb, A. Peacock, M. Beijersbergen, and S. Kraft, "Development of X-ray optics for the XEUS mission," in *X-Ray Sources and Optics*, C. A. MacDonald, A. T. Macrander, T. Ishikawa, C. Morawe, and J. L. Wood, Eds., vol. 5539 of *Proceedings of the SPIE*, pp. 95–103, 2004.

[55] A. Bartnik, H. Fiedorowicz, R. Jarocki et al., "Lobster eye optics for collecting radiation of a laser-plasma soft X-ray source based on a gas puff target," *Advances in X-Ray Analysis*, vol. 49, p. 395, 2006.

[56] L. Sveda, V. Semencova, A. Inneman, L. Pina, and R. Hudec, "Hybrid lobster optic," in *RenePublication: Laser-Generated, Synchrotron, and Other Laboratory X-Ray and EUV Sources, Optics, and Applications II*, G. A. Kyrala, J.-C. J. Gauthier, C. A. MacDonald, and A. M. Khounsary, Eds., vol. 5918 of *Proceedings of SPIE*, pp. 22–30, 2005.

[57] C. A. MacDonald and W. M. Gibson, "Polycapillary and multichannel plate X-ray optics," in *Handbook of Optics*, vol. 5 of *Atmospheric Optics, Modulators, Fiber Optics, X-Ray and Neutron Optics*, 3rd edition, 2010.

[58] M. Montel, *X-Ray Microscopy with Catamegonic Roof Mirrors, X-Ray Microscopy and Microradiography*, Academic Press, New York, NY, USA, 1957.

[59] C. S. Alford, R. M. Bionta, D. M. Makowiecki et al., "Molybdenum/beryllium multilayer mirrors for normal incidence in the extreme ultraviolet," *Applied Optics*, vol. 34, no. 19, pp. 3727–3730, 1995.

[60] J. R. P. Angel, "Lobster eyes X-ray telescopes," *The Astrophysical Journal*, vol. 233, p. 364, 1979.

[61] P. Gorenstein, "All sky supernova and transient explorer (ASTRE)," in *Variability of Galactic and Extragalactic X-Ray Sources*, A. Treves, Ed., Associazione per L'Avanzamento dell'Astronomia, Milano, Italy, 1987.

[62] W. C. Priedhorsky, A. G. Peele, and K. A. Nugent, "An X-ray all-sky monitor with extraordinary sensitivity," *Monthly Notices of the Royal Astronomical Society*, vol. 279, no. 3, pp. 733–750, 1996.

[63] G. Fraser, 2002, http://www.src.le.ac.uk/lobster.

[64] G. W. Fraser, "An imaging All-sky monitor (ASM) based on Lobster Eye X-ray optics. An international space station (ISS) attached payload submitted in response to the ESA call for mission proposals for the flexi-missions F2 and F3," *Bulletin of the American Astronomical Society*, vol. 35, p. 865, 2003.

[65] G. W. Fraser, A. N. Brunton, N. P. Bannister et al., "Lobster-ISS: an imaging X-ray all-sky monitor for the International Space Station," in *X-Ray and Gamma-Ray Instrumentation for Astronomy XII*, Proceedings of SPIE, pp. 115–126, August 2001.

[66] G. W. Fraser, J. D. Carpenter, D. A. Rothery et al., "The mercury imaging X-ray spectrometer (MIXS) on bepicolombo," *Planetary and Space Science*, vol. 58, no. 1-2, pp. 79–95, 2010.

[67] A. Inneman, R. Hudec, L. Pina, and P. Gorenstein, "Lobster—eye X-ray optics," in *X-Ray Optics, Instruments, and Missions II*, vol. 3766 of *Proceedings of SPIE*, pp. 72–79, July 1999.

[68] A. Inneman, R. Hudec, and L. Pina, "Progress in Lobster-eye X-ray optics development," in *X-Ray Optics, Instrumants, and Missions IV*, vol. 4138 of *Proceedings of SPIE*, pp. 94–104, July 2000.

[69] R. Hudec, B. Valnicek, I. Solc et al., "Wolter 1 type X-ray mirror system with mean resolution and maximum effective collecting area for the spectral region of 1–10 nm, In its Publ. of the Astron," *Institute of Mathematics of the Academy of Sciences of the Czech*, no. 61, pp. 1–4, 1985.

[70] R. Hudec, L. Pina, A. V. Inneman et al., "Lightweight X-ray optics for future space missions," in *X-Ray and Gamma-Ray Telescopes and Instruments for Astronomy*, J. E. Truemper and H. D. Tananbaum, Eds., vol. 4851 of *Proceedings of the SPIE*, pp. 656–665, 2003.

[71] G. W. Fraser, A. N. Brunton, J. E. Lees et al., "Development of micro channel plate MCP X-ray optics," in *Multilayer and Grazing Incidence X-Ray/EUV Optics III*, vol. 2011 of *Proceedings of SPIE*, pp. 215–226, 1993.

[72] A. N. Brunton, G. W. Fraser, J. E. Lees, W. B. Feller, and P. L. White, "X-ray focusing with 11 μm square porte microchannel plates," in *X-Ray and Ultraviolet Sensors and Applications*, vol. 2519 of *Proceedings of the SPIE*, 1995.

[73] V. Tichý, L. Švéda, J. Maršík et al., "Tests of imaging with lobster-eye X-ray optics and medipix2 detector," *Baltic Astronomy*, vol. 18, no. 3-4, pp. 369–373, 2009.

[74] V. Tichý, M. Hromčík, R. Hudec et al., "Tests of lobster-eye optics for a small X-ray telescope," *Baltic Astronomy*, vol. 18, no. 3-4, pp. 362–368, 2009.

[75] N. P. Bannister, E. J. Bunce, S. W. H. Cowley et al., "A wide field auroral imager (WFAI) for low earth orbit missions," *Annales Geophysicae*, vol. 25, no. 2, pp. 519–532, 2007.

[76] S. M. Owens, F. A. Hoffman, C. A. MacDonald, and W. M. Gibson, "Microdiffraction using collimating and convergent beam polycapillary optics," in *Proceedings of the 46th Annual Denver X-Ray Conference*, vol. 41 of *Advances in X-Ray Analysis*, pp. 314–318, Steamboat Springs, Colo, USA, August 1997.

[77] K. Wallace, M. Bavdaz, M. Collon et al., "X-ray pore optic developments," *Reports on Progress in Physics*, vol. 48, pp. 579–629, 1985.

[78] G. S. Vaiana, L. Van Speybroeck, M. V. Zombeck, A. S. Krieger, J. K. Silk, and A. Timothy, "The S-054 X-ray telescope experiment on SKYLAB," *Space Science Instrumentation*, vol. 3, no. 1, pp. 19–76, 1977.

[79] B. Aschenbach, "Realization of X-ray telescopes-from design to performance," *Experimental Astronomy*, vol. 26, no. 1–3, pp. 95–109, 2009.

[80] W. Ehrenberg, "X-ray optics," *Nature*, vol. 160, no. 4062, pp. 330–331, 1947.

[81] P. C. Fisher and A. J. Meyerott, "High sensitivity detectors for few-kev x-rays," *IEEE Transactions on Nuclear Science*, vol. NS-13, p. 580, 1966.

[82] P. Gorenstein, B. Harris, H. Gursky, R. Giacconi, R. Novick, and P. Vanden Bout, "X-ray structure of the Cygnus Loop," *Science*, vol. 172, no. 3981, pp. 369–372, 1971.

[83] L. P. Van Speybroeck, R. C. Chase, and T. F. Zehnpfennig, "Orthogonal mirror telescopes for X-ray astronomy," *Applied Optics*, vol. 10, p. 537, 1971.

[84] L. P. Van Speybroeck, R. C. Chase, and T. F. Zehnpfennig, "Orthogonal mirror telescopes for X-ray astronomy," *Applied Optics*, vol. 10, no. 4, pp. 945–949, 1971.

[85] R. Willingale and F. H. P. spaan, "The design, manufacture and predicted performance of kirkpatrick-baez silicon stacks for the international X-ray observatory or similar applications," in *Optics for EUV, X-Ray, and Gamma-Ray Astronomy IV*, vol. 7437 of *Proceedings of SPIE*, August 2009.

[86] P. Gorenstein, A. DeCaprio, R. Chase, and B. Harris, "Large area focusing collector for the observation of cosmic X rays," *Review of Scientific Instruments*, vol. 44, no. 5, pp. 539–545, 1973.

[87] M. C. Weisskopf, "Design of grazing-incidence X-ray telescopes. 1," *Applied Optics*, vol. 12, no. 7, pp. 1436–1439, 1973.

[88] R. C. Catura, P. C. Fisher, H. M. Johnson, and A. J. Meyerott, "Asymmetry of soft x-ray emission near M87," *The Astrophysical Journal*, vol. 177, p. L1, 1972.

[89] R. Borken, R. Doxsey, and S. Rappaport, "A soft x-ray survey of the galactic plane from Cygnus to norma," *The Astrophysical Journal*, vol. 178, p. L115, 1972.

[90] L. M. Cohen, "Optimum shape of a Kirkpatrick-Baez X-ray reflector supported at discrete points for on-axis performance," *Applied Optics*, vol. 20, no. 9, pp. 1545–1549, 1981.

[91] P. Gorenstein, H. Gursky, F. R. Harnden Jr., A. Decaprio, and P. Bjorkholm, "Large area soft X-ray imaging system for cosmic X-ray studies from rockets," *IEEE Transaction on Nuclear Science*, vol. NS-22, pp. 616–619, 1975.

[92] P. Gorenstein, "Deployable ultrahigh-throughput X-ray telescope: concept ," in *X-Ray Optics, Instruments, and Missions*, vol. 3444 of *Proceedings of SPIE*, p. 382, 1998.

[93] M. K. Joy, J. J. Kolodziejczak, M. C. Weisskopf, S. B. Fair, and B. D. Ramsey, "Imaging properties of a silicon wafer X-ray telescope," in *Advances in Multilayer and Grazing Incidence X-Ray/EUV/FUV Optics*, vol. 2297 of *Proceedings of SPIE*, pp. 283–286, July 1994.

[94] J. F. McGee, "A long-wavelength X-ray reflection microscope," in *X-Ray Microscopy and Microradiography*, V. E. Cosslett, A. Engstrom, and H. H. Patte, Eds., p. 164, Academic Press, New York, NY, USA, 1957.

[95] A. Iida and K. Hirano, "Kirkpatrick-Baez optics for a sub-μm synchrotron X-ray microbeam and its applications to X-ray analysis," *Nuclear Instruments and Methods in Physics Research B*, vol. 114, no. 1-2, pp. 149–153, 1996.

[96] G. E. Ice, C. R. Hubbard, B. C. Larson et al., "Kirkpatrick-Baez microfocusing optics for thermal neutrons," *Nuclear Instruments and Methods in Physics Research A*, vol. 539, no. 1-2, pp. 312–320, 2005.

[97] H. Russell, M. Gubarev, J. Kolodziejczak, M. Joy, C. A. MacDonald, and W. M. Gibson, "Polycapillary X-ray optics for X-ray astronomy," in *Proceedings of the 48th Denver X-Ray Conference*, vol. 43 of *Advances in X-Ray Analysis*, 1999.

[98] A. Inneman, *Technological aspects of the development and construction of optical elements for X-rays*, Ph.D. thesis, Czech Technical University in Prague, Faculty of Mechanical Engineering, Prague, Czech Republic, 2001.

[99] P. Gorenstein, "X-ray optics for the LAMAR facility, an overview," *Proceedings of the Society of Photo-Optical Instrumentation Engineers*, vol. 184, pp. 63–72, 1979.

[100] A. Inneman, L. Pina, and R. Hudec, "Development of foil segments for large astronomical X-ray telescopes," in *X-Ray Optics for Astronomy: Telescopes, Multilayers, Spectrometers, and Missions*, P. Gorenstein and R. B. Hoover, Eds., vol. 4496 of *Proceedings of SPIE*, 2002.

[101] A. Inneman, L. Pina, R. Hudec, H. Ticha, and V. Brozek, "Innovative X-ray optics for astrophysics," in *Design and Microfabrication of Novel X-Ray Optic*, D. C. Mancini, Ed., vol. 4783 of *Proceedings of SPIE*, pp. 156–164, 2002.

[102] H. N. Chapman, K. A. Nugent, and S. W. Wilkins, "X-ray focusing using square channel-capillary arrays," *Review of Scientific Instruments*, vol. 62, no. 6, pp. 1542–1561, 1991.

[103] A. G. Peele, "Deconvolution of an extended object viewed by a lobster-eye telescope," *Nuclear Instruments and Methods in Physics Research A*, vol. 459, no. 1-2, pp. 354–364, 2001.

[104] E. A. Stern, Z. Kalman, A. Lewis, and K. Lieberman, "Simple method for focusing x rays using tapered capillaries," *Applied Optics*, vol. 27, pp. 5135–5139, 1988.

[105] P. Engström, S. Larsson, A. Rindby et al., "A submicron synchrotron X-ray beam generated by capillary optics," *Nuclear Instruments and Methods A*, vol. 302, no. 3, pp. 547–552, 1991.

[106] D. X. Balaic and K. A. Nugent, "X-ray optics of tapered capillaries," *Applied Optics*, vol. 34, no. 31, pp. 7263–7272, 1995.

[107] U. W. Arndt, P. Duncumb, J. V. P. Long, L. Pina, and A. Inneman, "Focusing mirrors for use with microfocus X-ray tubes," *Journal of Applied Crystallography*, vol. 31, no. 5, pp. 733–741, 1998.

[108] L. Pina, A. Inneman, and R. Hudec, "Optics for X-ray and laser plasma soft X-ray radiation," in *High Power Lasers-Science and Engineering*, R. Kossowsky, M. Jelinek, and R. F. Walter, Eds., NATO ASI Series, pp. 373–380, Kluwer Academic, Dodrecht, The Netherlands, 1996.

[109] V. A. Arkd'ev, A. I. Kolomitsev, M. A. Kumakhov et al., "Wide-band X-ray optics with a large angular aperture," *Soviet Physics—Uspekhi*, vol. 32, no. 3, p. 271, 1989.

[110] Q. Klotzko, Q. F. Xiao, D. M. Gibson et al., "Investigation of glass polycapillaries for use in proximity X-ray lithography," in *Applications of Laser Plasma Radiation II*, vol. 2523 of *Proceedings of SPIE*, pp. 175–182, 1995.

[111] H. Russell, W. M. Gibson, M. V. Gubarev et al., "Application of polycapillary optics for hard X-ray astronomy," in *Grazing Incidence and Multilayer X-Ray Optical Systems*, R. B. Hoover and A. B. C. Walker II, Eds., vol. 3113 of *Proceedings of SPIE*, pp. 369–377, 1997.

[112] R. Kardiawarman, R. York, X.-W. Qian, Q.-F. Xiao, C. A. MacDonald, and W. M. Gibson, "Application of a multifiber collimating lens to thin film structure analysis," in *X-Ray and Ultraviolet Sensors and Applications*, R. B. Hoover and M. B. Williams, Eds., vol. 2519 of *Proceedings of SPIE*, pp. 197–206, July 1995.

[113] N. Gao et al., "Monolithic polycapillary focussing optics and their applications in microbeam X-ray fluorescence," *Applied Physics Letters*, vol. 69, no. 11, pp. 1529–1531, 1996.

[114] D. G. Kruger, C. C. Abreu, E. G. Hendee et al., "Imaging characteristics of X-ray capillary optics in digital mammography," *Medical Physics*, vol. 23, no. 2, pp. 187–196, 1996.

Hindawi Publishing Corporation
X-Ray Optics and Instrumentation
Volume 2010, Article ID 479631, 8 pages
doi:10.1155/2010/479631

Review Article

Hard X-Ray Focusing with Curved Reflective Multilayers

Christian Morawe[1] and Markus Osterhoff[1,2]

[1] *X-Ray Optics Group, European Synchrotron Radiation Facility, 6 rue Jules Horowitz, 38043 Grenoble, France*
[2] *Institute for X-Ray Physics, University of Göttingen, Friedrich-Hund-Platz 1, 37077 Göttingen, Germany*

Correspondence should be addressed to Christian Morawe, morawe@esrf.fr

Received 24 March 2010; Accepted 21 July 2010

Academic Editor: Ali Khounsary

This paper provides a comprehensive overview on the utilization of curved graded multilayer coatings as focusing elements for hard X-rays. It concentrates on the Kirkpatrick-Baez (KB) focusing setup that has been developed at 3rd generation synchrotron sources worldwide. The optical performance of these devices is evaluated applying analytical and numerical approaches. The essential role of the multilayer coating and its meridional d-spacing gradient are discussed as well as important technological issues. Experimental data and examples of operational KB focusing devices and applications complement the work.

1. Introduction

Over the last decade, hard X-ray optics has evolved rapidly, accelerated by the intense use of extremely brilliant 3rd generation synchrotron radiation sources. The use of smaller samples, the study of local areas, or the need to scan an object with high spatial resolution pushed the development of focusing devises. At present, X-ray beams can be focused down to spots below 50 nm using various optical elements such as Fresnel Zone Plates (FZPs) [1], Compound Refractive Lenses (CRLs) [2], Wave Guides (WGs) [3], capillary optics [4], curved Total Reflection Mirrors (TRMs) [5, 6], transmission Multilayer Laue Lenses (MLLs) [7, 8], and Reflective Multilayers (RMLs) [9, 10]. Several theoretical studies, mainly numerical wave optical calculations, were published treating the cases of FZPs [11], CRLs [12], TRMs [13, 14], and MLLs [15, 16]. Advanced numerical ray tracing calculations have been applied to RMLs [17, 18]. Alternatively, a purely analytical approach was proposed [19, 20]. The topic of this publication is the application of curved graded RMLs to KB focusing devices [21]. The KB geometry consists of two perpendicularly oriented curved mirrors and is particularly useful on synchrotron beamlines since it can transform the elongated synchrotron source into a nearly circular spot (Figure 1). Being an off-axis system the device produces a clean spot with low background and does not require beam stops or protecting apertures. A single focusing mirror per dimension operating under grazing incidence, as outlined in chapter 2, is not suitable for imaging applications since the Abbé sine condition [22] is not fulfilled. However, two successive mirrors (elliptic/hyperbolic), the so called Wolter geometry [23], can overcome this limitation.

2. Basic Optics Considerations

2.1. Resolution Limits. As in visible light optics the diffraction limited resolution (Full Width at Half Maximum, FWHM) of an X-ray optical element with a flat rectangular aperture is given by

$$D_{\text{diff}} = \frac{0.44 \cdot \lambda}{\text{NA}}, \tag{1}$$

where $\text{NA} = n \cdot \sin\varepsilon$ is the numerical aperture with the opening angle 2ε and the optical index n and λ the wavelength of the radiation. The minimum achievable spot size, however, is also limited by the demagnified image of the source of size S

$$D_{\text{source}} = \frac{q}{p} \cdot S, \tag{2}$$

where p is the source distance and q the image distance with respect to the optics. The phenomenon can also be treated in

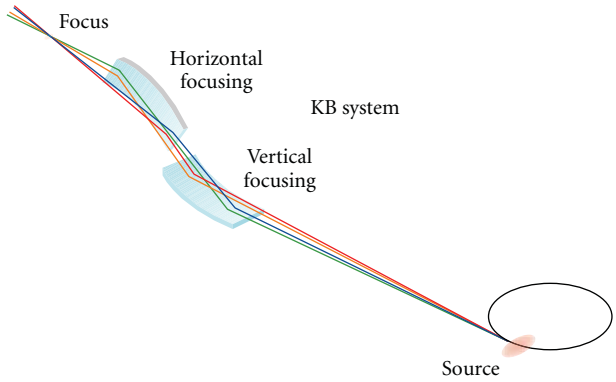

Figure 1: Schematic view of a KB focusing setup for a synchrotron source. By proper choice of the respective image distances the elongated source can be focused to a circular spot.

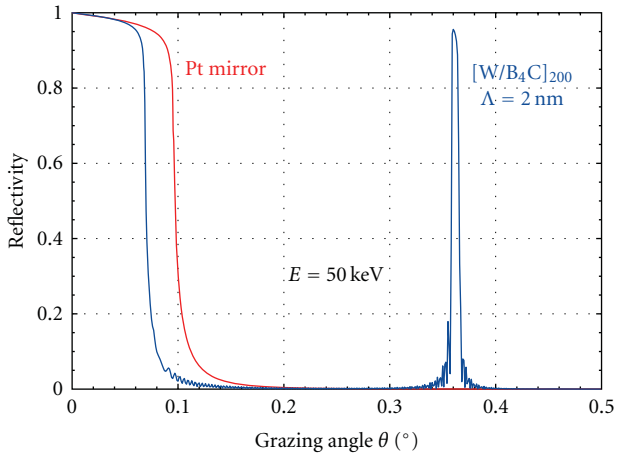

Figure 2: Comparison of the simulated reflectivity of a Pt TRM and a W/B_4C RML with a d-spacing of 2.0 nm at a photon energy of 50 keV.

terms of the coherence properties of the beam. With a source-size limited transversal coherence length [24]

$$L_T \approx \frac{\lambda}{2} \cdot \frac{p}{S}, \tag{3}$$

and assuming that the optical aperture selects only the coherent section of the incoming beam, the diffraction limited spot size becomes

$$D_{\text{diff}}(L_T) \approx 1.76 \cdot \frac{q}{p} \cdot S \approx D_{\text{source}}. \tag{4}$$

This means that, apart from a geometrical factor, the diffraction limited spot size of a coherently illuminated optical element is of the order of the size of the source image. Additional performance limiting effects of real optics are figure errors, scattering from defects or nonuniform areas, and further experimental obstacles like alignment, vibration, or drift.

Whilst the short wavelength of hard X-rays alone would principally allow for a spot size far below the nm scale, the main drawback in X-ray optics remains the low achievable numerical aperture. The latter is caused by the weak interaction of high-energy photons with matter, as given by the complex optical index

$$n = 1 - \delta + i\beta \approx 1, \tag{5}$$

where δ describes the dispersion and β the absorption in the material. Most development efforts in focusing optics for hard X-rays are therefore dedicated to increasing the numerical aperture.

In the case of reflecting optical elements and neglecting phase shifts upon reflection, the ideal geometry for a point-to-point focusing setup would be an ellipsoid. Since this work deals with KB setups operated at very small grazing angles, the scheme can be very well approximated by perpendicular projections on two elliptic cylinders. Thus, the treatment can be reduced to two individual ellipses.

2.2. Total Reflection Mirrors. In the case of a single elliptic TRM the range of grazing angles is limited to the upper side by the critical angle of total external reflection θ_C (Figure 2) given by

$$\sin\theta_C = \sqrt{2 \cdot \delta} \tag{6}$$

and to the lower side only by the physical mirror length when approaching the minimum angle of incidence at the intersection point with the semiminor axis of the ellipse. Since δ is a small quantity for hard X-rays, the achievable opening 2ε is very limited. A quantitative estimate can be made assuming a full opening of up to half of the critical angle [9].

$$4 \cdot \varepsilon \leq \theta_C \tag{7}$$

leading to a diffraction limit of

$$D_{\text{diff}}(\text{TRM}) \approx \frac{1.76 \cdot \lambda}{\sqrt{2 \cdot \delta}} = 1.76\sqrt{\frac{\pi}{r_0 \cdot \rho_e}}, \tag{8}$$

where r_0 is the classical electron radius and ρ_e the electron density of the material. This means that the focusing power of a TRM is entirely limited by material properties. For a Pt mirror one obtains a minimum spot size of about 25 nm FWHM. It should be noted that, in contrast to other techniques, TRM focusing has the advantage of being nondispersive.

2.3. Reflective Multilayers. Considerable improvement can be obtained by the use of RMLs where a stack of periodic bilayers reflects the incoming wave field. Provided the ML d-spacing Λ matches the modified Bragg equation

$$\Lambda = \frac{\lambda}{2\sqrt{n^2 - \cos^2\theta}}, \tag{9}$$

at any point along the mirror, constructive interference enhances the reflectivity up to values that can reach 90% or more. The Bragg angle of a RML can be several times

bigger than the critical angle of a TRM. Figure 2 shows a comparison of the simulated reflectivity between a Pt TRM and a 200-period W/B_4C RML at a photon energy of 50 keV.

The typical number of bilayers in RMLs is of the order of 100, leading to an energy resolution in the percent range. In conjunction with high peak reflectivity, this means that RMLs can provide an integrated reflectivity exceeding those of perfect crystals by two orders of magnitude. Flat RMLs are well understood and have been used as X-ray optical elements for many years [25, 26]. Thanks to the flexible d-spacing and the choice of suited material pairs the optical performance of RMLs can be optimized according to photon energy, incidence angle, and further experimental parameters. This choice is also affected by properties like interface diffusion, stress, and chemical stability.

Instead of periodic RMLs, nonperiodic layered structures can be deposited to obtain broader reflectivity profiles [27]. In combination with meridional thickness gradients they can also be applied to KB setups [28].

To focus X-rays an RML has to be curved in accordance with the angular dependence

$$\sin\theta = \frac{b}{\sqrt{p \cdot q}} \tag{10}$$

of the ellipse where b is its semiminor axis.

As for TRMs, the achievable resolution of curved RMLs can be estimated analytically [9]. Applying the Bragg law without refraction correction

$$\sin\theta \approx \frac{\lambda}{2 \cdot \Lambda}, \tag{11}$$

which is a good approximation for small d-spacings and low wavelengths, respectively, the diffraction limit can be calculated as

$$D_{\text{diff}}(\text{RML}) \approx \frac{0.88}{1/\Lambda_2 - 1/\Lambda_1}. \tag{12}$$

Here, $\Lambda_{1,2}$ indicate the ML d-spacings at the respective edges of the mirror. The resolution is therefore limited only by the lateral d-spacing gradient of the RML. For a short period RML with strong gradient ($\Lambda = 2, \ldots, 3$ nm) focal spots of about 5 nm FWHM appear realistic. Equation (12) can be compared with the corresponding formula for a linear Fresnel Zone Plate (FZP)

$$D_{\text{diff}}(\text{FZP}) = 0.88 \cdot \Delta R \tag{13}$$

with outermost zone width ΔR. Considering a RML as an equivalent to half of a linear zone plate (1/2 FZP) with outermost repetition period $\Lambda_2 = 2 \cdot \Delta R$ and setting the largest ML d-spacing Λ_1 to infinity (half of central FZP zone) one obtains

$$D_{\text{diff}}\left(\frac{1}{2}\text{FZP}\right) = 0.88 \cdot \Lambda_2 = D_{\text{diff}}(\text{RML}). \tag{14}$$

Equation (14) shows that, within the given approximation, both optical elements are different representations of the same focusing configuration (Figure 3).

For applications it is interesting to note that none of the above equations (8) or (12) contains any explicit energy dependence.

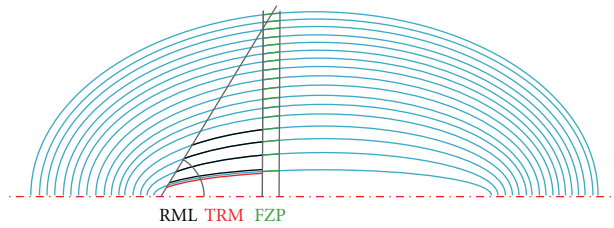

Figure 3: TRM, RML, and FZP in the same focusing configuration.

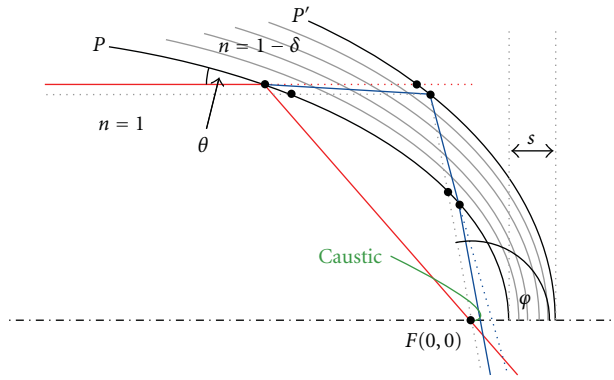

Figure 4: Ray propagation through a curved layered structure. Rays reflected from the upper RML surface P reach the ideal focus F. Rays reflected at P' are refracted when crossing P.

3. Models and Simulations

3.1. Ray Tracing Calculations. So far the RML was treated as a single reflecting surface. In order to investigate the impact of the beam penetration into the ML structure, both numerical and analytical ray tracing simulations were developed [18–20]. An analytical approach is shown in Figure 4 for the case of a parabolic RML. It can be shown that the elliptic case is virtually identical for the high ellipse eccentricities that occur in synchrotron applications. The RML stack is approximated by a single thick layer of average optical index $n = 1 - \delta$. Multiple reflections and refractions within the stack are neglected, and refraction at the surface P is treated in linear approximation. The aim is to calculate the principal intersection points of rays that penetrate into the structure and that are reflected by the second interface P'. An ensemble of parallel incoming beams forms an envelope curve of enhanced intensity (caustic) near the ideal focus F.

The analytical derivation is carried out to first order in δ, which is a small quantity for hard X-rays. The resulting intersection points of the outgoing beams with the optical axis X on the one hand and with the focal plane Y on the other can be written as

$$\begin{aligned} X(y = 0) &\approx \delta \cdot s \cdot t^4, \\ Y(x = 0) &\approx 2 \cdot \delta \cdot s \cdot t^3 \end{aligned} \tag{15}$$

with

$$t = \tan\frac{\varphi}{2} \tag{16}$$

Table 1: Comparison of the transmitted energy bandwidth of different optical elements.

	FZP	CRL	RML
dE/E	$D^2/(1.76 \cdot f \cdot \lambda)$	$D^2/(3.52 \cdot f \cdot \lambda)$	$D^2/(3.52 \cdot \Delta f \cdot \lambda)$

and s being as indicated in Figure 4. Rays impinging at lower grazing angles θ produce stronger aberrations in both x and y directions. Both the layer thickness and the refracting power of the medium amplify the effect. The situation is illustrated in Figure 5 for a source distance $p = 150\,\text{m}$, an image distance $q = 0.077\,\text{m}$, and a photon energy $E = 24550\,\text{eV}$.

Figure 6 shows the intersection points Y with the focal plane given in Figure 5 as a function of the grazing angle θ. The purple line represents a calculation using the approximation (15) while the red line was obtained by exact numerical ray tracing on the same structure. Both curves are in good agreement for higher angles. Closer to the critical angle θ_C, where the linear approximation of Snell's law fails, the curves diverge. The solid circles are independent calculations made at Osaka University using a different ray tracing code. There is a reasonably good agreement between the two methods [29]. The examples in Figures 5 and 6 were calculated for a parameter set corresponding to realistic focusing setups at a 3rd generation synchrotron beamline. The expected aberrations in the focal plane would be lower than 10 nm for a typical grazing angle of 0.3°.

The analytical approach has the benefit that equations (15) allow for an estimate of chromatic aberrations and for a comparison with other types of focusing elements. Chromaticity enters through the energy dependent refractive decrement

$$\delta \propto \frac{1}{E^2}. \tag{17}$$

It can be shown that [20], for a given optical element, the tolerated bandwidth dE/E for a given focal spot size D (FWHM) takes the form summarized in Table 1. It has to be underlined that, in contrast to FZPs and CRLs, where the macroscopic focal length f appears in the denominator, only the small aberration $\Delta f \cong X$ enters the formula for the RML, which makes this element nearly achromatic. The physical background of the different impact on the chromaticity is clearly visible. For FZPs and CRLs the phase shift induced by the optical elements is at the origin of their focusing properties, and chromaticity is therefore unavoidable. In the case of RMLs, however, it is rather a parasitic effect that should be suppressed as much as possible.

It has to be emphasized that the above analysis is based on ideal elliptically or parabolically shaped RMLs. It is known, however, that the optimum shapes of focusing RMLs differ from these perfect mathematical curves. It is a general practice to assume that RMLs have to fulfill Bragg's law (9) locally [30, 31] in order to provide constructive interference at the same photon energy and at any point along the optical surface. The ML d-spacings and consequently the interface positions in space change as the optical indices differ from unity. There is strong evidence that this refraction correction implicitly leads to the optimum RML shape [18]. Full wave optical computations will be required to derive structures that minimize or suppress aberrations. They will also have to include effects caused by figure errors and by the finite source size.

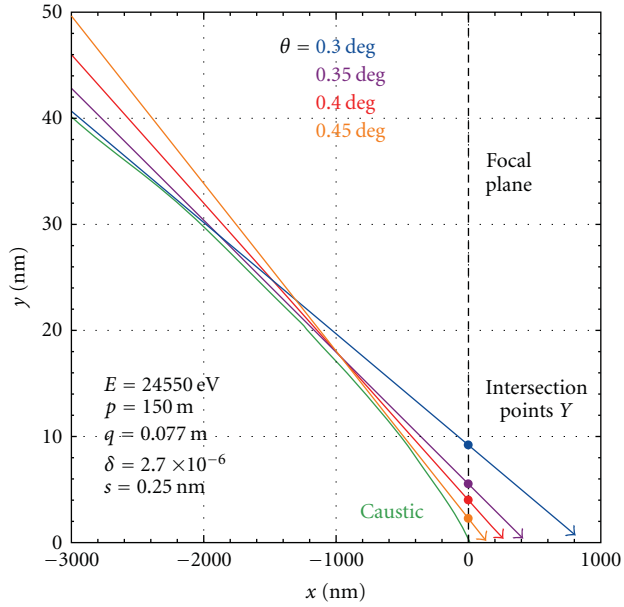

Figure 5: Ensemble of rays (straight arrows) emerging from a RML under variable grazing angles and constant s. The lower thick curve indicates the corresponding caustic.

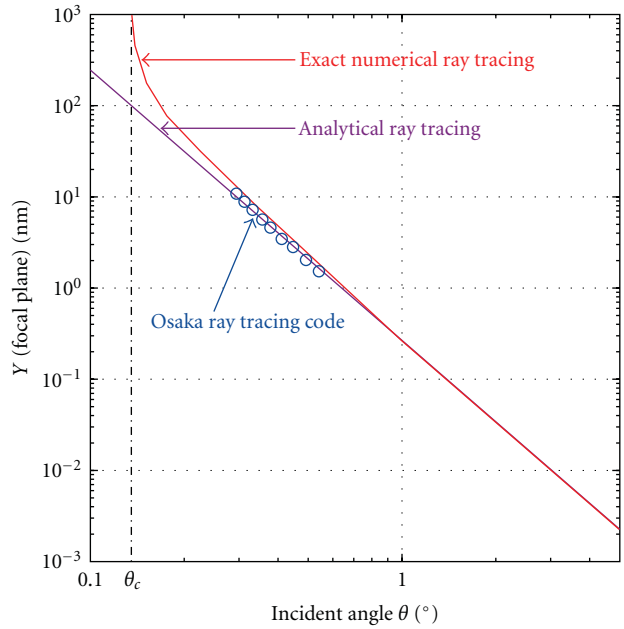

Figure 6: Intersection points of the rays with the focal plane as a function of the grazing angle. The purple line was derived from (15), the red curve shows exact ray tracing calculations. Blue circles indicate simulated data from Osaka University.

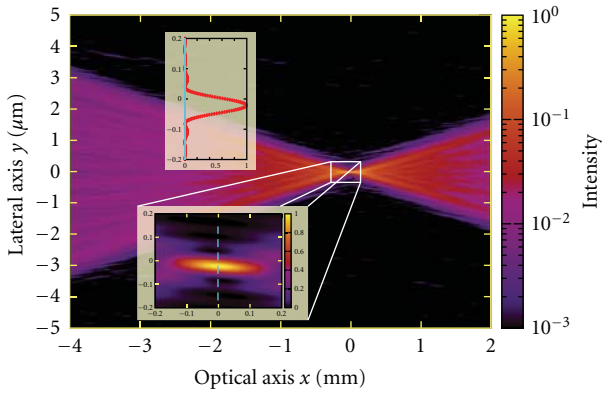

FIGURE 7: Field intensity of a point source focused by an ideal elliptic Pd mirror (logarithmic scale).

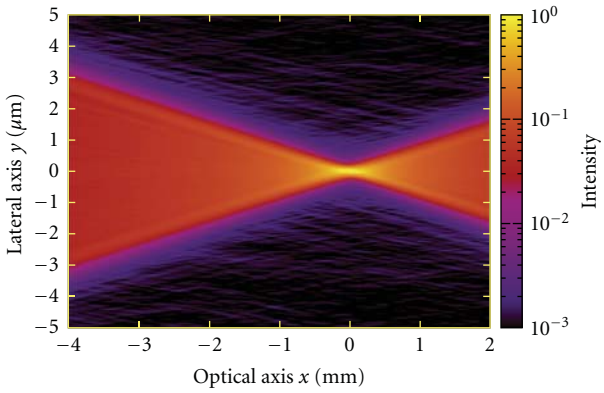

FIGURE 8: Partially coherent superposition of the focused fields of different point sources representing a spatially extended source (logarithmic scale). Figure errors on the Pd mirror are included.

3.2. Wave Optical Calculations. A first step to minimize the aberration of RMLs is wave optical calculations for a single reflecting surface and the related wave propagation in free space from the source to the mirror and further to the focal plane. An isotropic and monochromatic point source emits a number of rays (typically ten thousands), which are traced onto the mirror's surface S, where they are reflected. The amplitude is multiplied by the corresponding Fresnel coefficient, so the outgoing field $A(s)$ is known in amplitude and phase. In a region around the nominal focus point the intensity distribution is calculated by a numerical solution of Kirchhoff's integral of diffraction, treated here in two dimensions corresponding to the plane of incidence (x, y):

$$I(x,y) = \left| \frac{1}{\sqrt{\lambda}} \int_S A(s) \cdot \frac{e^{ikr}}{\sqrt{r}} \cdot ds \right|^2. \quad (18)$$

Figure 7 shows the field intensity emitted by an isotropic point source and focused by an ideal elliptic Pd mirror at a photon energy of 8 keV. Source and image distances are $p = 85$ m and $q = 0.2$ m, respectively. The angle of incidence at the mirror center was set to 4 mrad = 0.23°.

The geometrical cone of the converging beam, the diffraction waist, as well as interference features from the finite aperture are clearly visible. In the present case, a diffraction limited spot size of 71 nm FWHM was obtained. The model was refined to treat extended sources as well as figure errors on the mirror surface. Figure 8 shows the performance of the same Pd mirror as in Figure 7, this time assuming a Gaussian source of 85 μm FWHM and a figure error of about 5 nm peak-to-valley (PV). The simulation was made for an ensemble of partially coherent point sources representing a spatially extended source. The focal spot size has increased to 190 nm. The blurring and the disappearance of the interference fringes are mainly due to the finite and only partially coherent source.

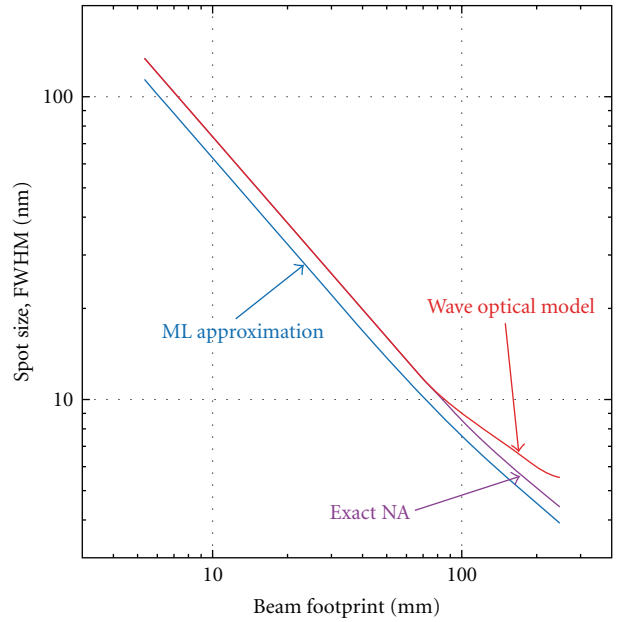

FIGURE 9: Diffraction limited focal spot size (FWHM) versus beam footprint on an elliptic RML, calculated from equation (12) (blue curve), from the exact NA (purple curve), and using a wave optical code for a single surface (red curve).

It is of interest to compare wave optical results with those that can be obtained by purely geometrical considerations as outlined in Section 2. Figure 9 shows the diffraction limited focal spot size versus the illuminated footprint along a mirror, calculated from (12) (blue curve), from the exact NA (purple curve), and using a wave optical code (red curve). The parameters used in the calculations correspond to those given in Figure 5. The incoming beam aperture is increased while remaining centered at $\theta = 0.35°$.

It can be seen that the geometrical approach assuming a flat numerical aperture NA (thin lens approximation) agrees well with the wave optical calculations for short mirror sections. As the length of the footprint becomes comparable with the image distance, the geometrical approach underestimates the spot size. In the latter case, the strongly asymmetric aperture can no longer be approximated by a thin lens. Equation (12) returns systematically lower values than the other methods, mainly due to the neglected refraction correction. Despite the observed differences, all

Table 2: Comparison of the experimental performance of various X-ray optical elements.

Type	Reflecting			Diffracting		Refracting
Element	TRM	RML	WG	FZP	MLL	CRL
D [nm]	25	7	<50	15	16	<50
E [keV]	<20	<60	<20	<10	<20	<100
$\Delta E/E$	—	1%–10%	—	0.1%	0.01%–0.1%	—
Geometry	Deflecting KB	Deflecting KB	In-line KB	In-line KB	In-line KB	In-line KB
Preference	Focusing	Focusing	Holography	Imaging	Imaging	Imaging

three descriptions return values that are consistent within the given degree of simplification.

4. Technological Options

4.1. Overview. At present, three alternative approaches have been developed to produce curved RMLs for applications at 3rd generation synchrotron sources. APS (USA) investigated profile coatings to provide optical surfaces with the required fixed focus elliptic curvature [6], essentially without ML coatings. Work at the ESRF (France) concentrated on ML coated flat mirrors integrated into dynamical benders to approach the optimum curvature [32]. SPring-8 and the University of Osaka (Japan) developed deterministic polishing techniques [33] and differential deposition to obtain ultra precise surfaces and the required ML coatings [34]. KB focusing systems for X-rays, though mainly based on TRMs, are commercially available from various suppliers. A nonexhaustive list is given in [35–41].

4.2. ML Deposition. The principal challenge in the fabrication of an RML is the accurate deposition of the d-spacing gradient that fulfills (9). In order to guarantee both uniform reflectivity and phase the tolerated thickness errors of the individual layers must be far below the width of the ML Bragg peak. In practice, the accuracy must be of the order of 0.5% or better. Today, the most common deposition method is magnetron sputtering. It combines high deposition rates (0.1–1.0 nm/s) with reasonably stable operation over a full coating cycle. The high kinetic energy of sputtered particles favors the formation of smooth and dense thin layers. Relative motion between sputter source and substrate, sometimes complemented by the insertion of masks, is the method of choice to produce the correct thickness gradient. This technique is also known as differential deposition.

4.3. Alternative Solutions. An interesting alternative focusing scheme was proposed by Montel [42] where the two perpendicular reflecting surfaces are positioned side by side. This approach offers a more compact arrangement and enables equal demagnification in both directions. The critical issue is the corner line where both mirrors are in contact. Single reflection optics with ellipsoidal shape is attractive thanks to its higher transmission and potentially larger collection angle. The fabrication is particularly challenging in terms of both figuring and polishing. Both types of optics are commercially available [43–46] and are mainly used in combination with laboratory X-ray sources.

5. Experimental Progress

With Pt coated mirrors diffraction limited spot sizes of about 25 nm were measured [47]. More recently, this value could be significantly improved by the use of Pt/C RMLs. During experiments at Spring-8, a line focus of 7 nm could be obtained with a monochromatic beam at 20 keV [10]. This remarkable performance was achieved by inserting an online wave front correction mirror to account for residual figure errors on the focusing element itself [48]. An example of a line profile is given in Figure 10, containing both experimental data and a numerical simulation (courtesy H. Mimura). It is important to note that these experimental findings are in line with the theoretical estimates made in Sections 2 and 3.

The main drawback of fixed focus KBs is their lack of flexibility required for operation at variable energies. Dynamical setups based on bent RMLs, that offer the possibility to switch the photon energy, have achieved best results of about 45 nm [49]. So far, figure errors and mechanical vibrations were identified as principal obstacles to reach smaller spots.

6. Comparison with Other Focusing Elements

It is not within the scope of this paper to provide a full comparison of the various optical elements presently used to focus hard X-rays. Nevertheless, Table 2 gives a brief overview on the typical experimental performance along some key parameters such as the smallest achieved spot size D, typical energy range E, intrinsic bandwidth $\Delta E/E$, and practical aspects concerning geometry and preferred mode of operation. It is not exhaustive and subject to ongoing evolution. The corresponding references and abbreviations were introduced in Section 1. A similar summary was published in [50]. A comprehensive overview on the different types of X-ray optics can be found in [51].

7. Applications

Over the last 10 years, at ESRF, more than 20 RML based KB focusing devices were delivered to different beamlines.

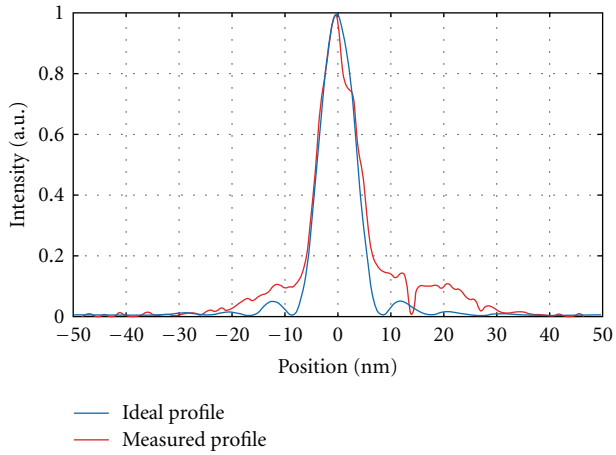

Figure 10: Experimental intensity profile (red curve) through the focal line of a curved RML fabricated at Osaka University and measured at Spring-8. The blue curve shows the ideal shape of the diffraction limited case (courtesy H. Mimura).

They provide focal spots from 100 μm down to less than 100 nm to the user community. In contrast to crystal optics the high reflectivity and the broad bandwidth of the ML elements allow for high intensity, making them the system of choice for flux limited experiments. The most brilliant ESRF KB nanofocusing setups provide flux densities of about $3 \cdot 10^5$ ph/s/mA/nm^2. Novel techniques like projection tomography [52] and fluorescence imaging [53] on the nanometer scale have evolved thanks to the excellent performance of this optical system. They provide new opportunities for various scientific and engineering disciplines.

8. Summary and Outlook

KB focusing devices based on graded RML coatings play a major role in present day X-ray optics, in particular on 3rd generation synchrotron beamlines. Thanks to their ML coating their numerical aperture can be increased by a factor of about 5 compared with TRMs. They are widely used and have generated diffraction limited focal spots down to 7 nm FWHM. While both design and fabrication of curved RMLs have developed rapidly over the last decade, a full wave optical description is still lacking.

Several approaches to further reduce the spot size might be considered. The use of higher-order Bragg peaks would increase the numerical aperture, on the expense of reflectivity and flux. A real technological breakthrough would be the use of two coherently illuminated curved RMLs facing each other. A rough estimate shows [9] that such a setup would reduce the diffraction limit by a factor 4 compared to a single element. If one adds a second RML on each side, leading to two successive reflections (Wolter geometry), the gain in aperture would be about 8.

From a fundamental point of view the 1 nm limit seems to be within reach. The task to align several optical elements to within atomic distances, however, represents a major technological challenge.

Acknowledgments

The authors would like to thank the members of the Department of Precision Science and Technology, Graduate School of Engineering, Osaka University (Japan) for their kind support. The research leading to these results has received funding from the European Community's Seventh Framework Programme (FP7/2007–2013) under grant agreement no. 226716.

References

[1] W. Chao, B. D. Harteneck, J. A. Liddle, E. H. Anderson, and D. T. Attwood, "Soft X-ray microscopy at a spatial resolution better than 15 nm," *Nature*, vol. 435, no. 7046, pp. 1210–1213, 2005.

[2] C. G. Schroer, O. Kurapova, J. Patommel et al., "Hard x-ray nanoprobe based on refractive x-ray lenses," *Applied Physics Letters*, vol. 87, no. 12, Article ID 124103, pp. 1–3, 2005.

[3] A. Jarre, C. Fuhse, C. Ollinger, J. Seeger, R. Tucoulou, and T. Salditt, "Two-dimensional hard x-ray beam compression by combined focusing and waveguide optics," *Physical Review Letters*, vol. 94, no. 7, Article ID 074801, 2005.

[4] D. H. Bilderback, S. A. Hoffman, and D. J. Thiel, "Nanometer spatial resolution achieved in hard x-ray imaging and Laue diffraction experiments," *Science*, vol. 263, no. 5144, pp. 201–203, 1994.

[5] H. Mimura, S. Matsuyama, H. Yumoto et al., "Hard X-ray diffraction-limited nanofocusing with Kirkpatrick-Baez mirrors," *Japanese Journal of Applied Physics*, vol. 44, no. 16–19, pp. L539–L542, 2005.

[6] W. Liu, G. E. Ice, J. Z. Tischler et al., "Short focal length Kirkpatrick-Baez mirrors for a hard x-ray nanoprobe," *Review of Scientific Instruments*, vol. 76, no. 11, Article ID 113701, pp. 1–6, 2005.

[7] H. C. Kang, J. Maser, G. B. Stephenson et al., "Nanometer linear focusing of hard X rays by a multilayer Laue lens," *Physical Review Letters*, vol. 96, no. 12, Article ID 127401, pp. 1–4, 2006.

[8] H. C. Kang, H. Yan, R. P. Winarski et al., "Focusing of hard X-rays to 16 nanometers with a multilayer Laue lens," *Applied Physics Letters*, vol. 92, no. 22, Article ID 221114, 2008.

[9] Ch. Morawe, O. Hignette, P. Cloetens et al., "Graded multilayers for focusing hard X rays below 50nm," in *Advances in X-Ray/EUV Optics, Components, and Applications*, vol. 6317 of *Proceedings of SPIE*, 63170F.

[10] H. Mimura, S. Handa, T. Kimura et al., "Breaking the 10 nm barrier in hard-X-ray focusing," *Nature Physics*, vol. 6, pp. 122–125, 2009.

[11] F. Pfeiffer, C. David, J. F. van der Veen, and C. Bergemann, "Nanometer focusing properties of Fresnel zone plates described by dynamical diffraction theory," *Physical Review B*, vol. 73, no. 24, Article ID 245331, 2006.

[12] C. G. Schroer and B. Lengeler, "Focusing hard X rays to nanometer dimensions by adiabatically focusing lenses," *Physical Review Letters*, vol. 94, no. 5, Article ID 054802, 2005.

[13] K. Yamauchi, K. Yamamura, H. Mimura et al., "Nearly diffraction-limited line focusing of a hard-X-ray beam with an elliptically figured mirror," *Journal of Synchrotron Radiation*, vol. 9, no. 5, pp. 313–316, 2002.

[14] C. M. Kewish, L. Assoufid, A. T. Macrander, and J. Qian, "Wave-optical simulation of hard-x-ray nanofocusing by precisely figured elliptical mirrors," *Applied Optics*, vol. 46, no. 11, pp. 2010–2021, 2007.

[15] C. G. Schroer, "Focusing hard X rays to nanometer dimensions using Fresnel zone plates," *Physical Review B*, vol. 74, no. 3, Article ID 033405, 2006.

[16] H. Yan, J. Maser, A. Macrander et al., "Takagi-Taupin description of X-ray dynamical diffraction from diffractive optics with large numerical aperture," *Physical Review B*, vol. 76, no. 11, Article ID 115438, 2007.

[17] H. Mimura, S. Matsuyama, H. Yumoto et al., "Reflective optics for sub-10 nm hard X-ray focusing," in *Advances in X-Ray/EUV Optics and Components II*, vol. 6705 of *Proceedings of SPIE*, 67050L.

[18] H. Mimura, S. Handa, Ch. Morawe et al., "Ray-tracing analysis in aberration of a laterally- graded multilayer mirror," *Nuclear Instruments and Methods in Physics Research A*, vol. 616, no. 2-3, pp. 251–254, 2010.

[19] J.-P. Guigay, Ch. Morawe, V. Mocella, and C. Ferrero, "An analytical approach to estimating aberrations in curved multilayer optics for hard x-rays: 1. Derivation of caustic shapes," *Optics Express*, vol. 16, no. 16, pp. 12050–12059, 2008.

[20] Ch. Morawe, J.-P. Guigay, V. Mocella, and C. Ferrero, "An analytical approach to estimating aberrations in curved multilayer optics for hard x-rays: 2. Interpretation and application to focusing experiments," *Optics Express*, vol. 16, no. 20, pp. 16138–16150, 2008.

[21] P. Kirkpatrick and A.V. Baez, "Formation of optical images by X-rays," *Journal of the Optical Society of America*, vol. 38, p. 766, 1984.

[22] E. Abbe, "über die Bedingungen des Aplanatismus der Linsensysteme," *Jenaisch. Ges. Med. Naturw.*, vol. 129, 1879.

[23] H. Wolter,, "Spiegelsysteme streifenden Einfalls als abbildende Optiken für Röntgenstrahlen," *Annals of Physics*, vol. 445, p. 94, 1952.

[24] J.-A. Nielsen and D. McMorrow, *Elements of Modern X-Ray Physics*, John Wiley & Sons, London, UK, 2001.

[25] J. Underwood and T. W. Barbee Jr., "Layered synthetic microstructures as Bragg diffractors for X rays and extreme ultraviolet: theory and predicted performance," *Applied Optics*, vol. 20, no. 17, pp. 3027–3034, 1981.

[26] Ch. Morawe, "Graded multilayers for synchrotron optics," in *Proceedings of the 9th International Conference on Synchrotron Radiation Instrumentation*, vol. 879, pp. 764–769, January 2007.

[27] Ch. Morawe, E. Ziegler, J.-C. Peffen, and I. V. Kozhevnikov, "Design and fabrication of depth-graded X-ray multilayers," *Nuclear Instruments and Methods in Physics Research A*, vol. 493, no. 3, pp. 189–198, 2002.

[28] Ch. Morawe, C. Borel, E. Ziegler, and J.-C. Peffen, "Application of double gradient multilayers for focusing," in *X-Ray Sources and Optics*, vol. 5537 of *Proceedings of SPIE*, pp. 115–126, November 2004.

[29] Ch. Morawe, J.-P. Guigay, V. Mocella et al., "Aberrations in curved x-ray multilayers," in *Advances in X-Ray/EUV Optics and Components III*, vol. 7077 of *Proceedings of SPIE*, September 2008, 70770T.

[30] M. Schuster and H. Göbel, "Parallel beam coupling into channel-cut monochromators using curved graded multilayers," *Journal of Physics D: Applied Physics*, vol. 28, p. A270, 1995.

[31] Ch. Morawe, P. Pecci, J.-C. Peffen, and E. Ziegler, "Design and performance of graded multilayers as focusing elements for X-ray optics," *Review of Scientific Instruments*, vol. 70, no. 8, pp. 3227–3232, 1999.

[32] O. Hignette, P. Cloetens, G. Rostaing, P. Bernard, and Ch. Morawe, "Efficient sub 100 nm focusing of hard X rays," *Review of Scientific Instruments*, vol. 76, no. 6, pp. 1–5, 2005.

[33] Y. Mori, K. Yamauchi, K. Yamamura et al., "Development of plasma chemical vaporization machining and elastic emission machining systems for coherent X-ray optics," in *X-Ray Mirrors, Crystals, and Multilayers*, vol. 4501 of *Proceedings of SPIE*, pp. 30–42, July 2001.

[34] H. Mimura, S. Matsuyama, H. Yumoto et al., "Reflective optics for sub-10 nm hard X-ray focusing," in *Advances in X-Ray/EUV Optics and Components II*, vol. 6705 of *Proceedings of SPIE*, August 2007, 67050L.

[35] http://www.crystal-scientific.com/?KBfocus=.

[36] http://www.idtnet.co.uk.

[37] http://www.irelec.fr/en/produit.asp?idproduit=39.

[38] http://www.j-tec.co.jp/english/focusing/index.html.

[39] http://www.seso.com/uk/index.htm.

[40] http://www.zeiss.de/en.

[41] http://www.winlightx.com.

[42] M. Montel, "X-ray microscopy with catamegonic roof mirrors," in *X-Ray Microscopy and Microradiography*, pp. 177–185, Academic Pres, New York, NY, USA, 1957.

[43] http://www.axo-dresden.de/index1.html.

[44] http://www.incoatec.de.

[45] http://www.rigaku.com/optics.

[46] http://www.xenocs.com/accueil.htm.

[47] H. Mimura, H. Yumoto, S. Matsuyama et al., "Efficient focusing of hard x rays to 25 nm by a total reflection mirror," *Applied Physics Letters*, vol. 90, no. 5, Article ID 051903, 2007.

[48] T. Kimura, S. Handa, H. Mimura et al., "Wavefront control system for phase compensation in hard X-ray optics," *Japanese Journal of Applied Physics*, vol. 48, no. 7, Article ID 072503, 2009.

[49] O. Hignette, P. Cloetens, Ch. Morawe et al., "Nanofocusing at ESRF using graded multilayer mirrors," in *Proceedings of the 9th International Conference on Synchrotron Radiation Instrumentation (SRI '07)*, vol. 879, pp. 792–795, January 2007.

[50] A. Snigirev and I. Snigireva, "Hard X-ray microoptics," in *Modern Developments in X-Ray and Neutron Optics*, A. Erko, M. Idir, T. Krist, and A. G. Michette, Eds., pp. 255–285, Springer, Berlin, Germany, 2008.

[51] http://www.x-ray-optics.com.

[52] R. Mokso, P. Cloetens, E. Maire, W. Ludwig, and J.-Y. Buffire, "Nanoscale zoom tomography with hard x rays using Kirkpatrick-Baez optics," *Applied Physics Letters*, vol. 90, no. 14, Article ID 144104, 2007.

[53] P. Bleuet, A. Simionovici, L. Lemelle et al., "Hard X-rays nanoscale fluorescence imaging of Earth and Planetary science samples," *Applied Physics Letters*, vol. 92, no. 21, Article ID 213111, 2008.

Hindawi Publishing Corporation
X-Ray Optics and Instrumentation
Volume 2010, Article ID 317909, 5 pages
doi:10.1155/2010/317909

Research Article

High-Energy X-Ray Microprobe System with Submicron Resolution for X-Ray Fluorescence Analysis of Uranium in Biological Specimens

Yasuko Terada,[1] Shino Homma-Takeda,[2] Akihisa Takeuchi,[1] and Yoshio Suzuki[1]

[1] *Japan Synchrotron Radiation Research Institute, SPring-8, 1-1-1 Kouto, Sayo, Hyogo 679-5198, Japan*
[2] *Research Center for Radiation Protection, National Institute of Radiological Sciences, 4-9-1 Anagawa, Inage-ku, Chiba 263-8555, Japan*

Correspondence should be addressed to Yasuko Terada, yterada@spring8.or.jp

Received 3 November 2009; Accepted 21 May 2010

Academic Editor: Gene Ice

Total-external-reflection Kirkpatrick-Baez mirror optics for high-energy X-rays have been applied to the X-ray microprobe at beamline 37XU of SPring-8. A focused beam size of 1.0 μm (V) $\times$ 0.83 μm (H) has been achieved at an X-ray energy of 30 keV, and a total photon flux of the focused beam was about 5×10^9 photons/s. Micro-X-ray fluorescence (μ-XRF) analysis of the uranium distribution in rat kidneys has been performed with the mirror-focused beam. The sensitivity of uranium was evaluated from the XRF intensity of thin standard samples, and the minimum detection limit was estimated at 10 μg/g. The high-spatial-resolution analysis revealed that uranium was concentrated in the epithelium of the proximal tubules in the inner cortex. The maximum concentration of uranium in the tubule was estimated to be 503 μg/g using a semiquantitative evaluation.

1. Introduction

X-ray microscopy with a total-external-reflection mirror optics is an attractive technique for X-ray fluorescence (XRF) analysis using synchrotron radiation because mirrors are achromatic and give relatively high-brilliance beams compared to other focusing elements. Suzuki et al. have successfully developed a total-external-reflection mirror system for microfocusing in the X-ray energy range of 30–100 keV at SPring-8 [1]. They have obtained a focused spot of less than 1 μm below X-ray energies of 90 keV using a 200 m long beamline. Further focusing tests have proved that the mirror system had excellent performance in the high-energy X-ray region and enables not only microscopy but also spectroscopic analysis with sub-micron resolution for high-Z elements.

The need for heavy element analysis has been greatly increasing by the importance of heavy metal accumulation in living organisms. High-energy X-rays (>20 keV) enable direct detection of K lines from high-Z elements. Nakai et al. have carried out XRF analysis of trace rare-earth and heavy elements using 116 keV X-rays at SPring-8 [2]. They pointed out the advantage of high-energy X-rays for bulk analysis and confirmed that the minimum detection limit (MDL) of the heavy elements was at the sub-ppm level. More recently, microbeam analysis is required for sub-cellular-level measurements of elemental distributions with high-energy X-rays. Among the problems of the greatest interest are health effects of uranium on populations. For example, environmental contamination in uranium-polluted areas is continuing to rise and uranium can have serious health impacts, such as renal toxicity. Total-external-reflection mirror optics developed by Suzuki et al. [1] is one of the most appropriate focusing systems to enable the analysis of trace heavy elements. In this study, the application of a high-energy scanning X-ray microprobe to evaluate the uranium distribution in rat kidneys is described.

2. Experimental

2.1. X-Ray Focusing Optics. The basic design of elliptic Kirkpatrick-Baez optics is essentially the same as that

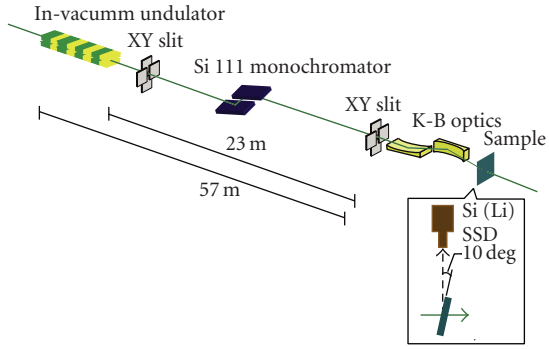

Figure 1: Schematic diagram of experimental setup at BL37XU of SPring-8.

described in our previous study [1]. Parabolic mirrors were fabricated by the bent-polished method at Cannon Co. Ltd., Japan [3, 4]. The mirror material was fused quartz with a thickness of 13 mm. The reflective surface was coated by platinum with a thickness of 1000 Å, and the average glancing angle was 0.8 mrad. The focal length was 250 mm for the vertical focusing mirror and 100 mm for the horizontal focusing mirror.

The experiments were carried out on undulator beamline 37XU of SPring-8 [5]. A schematic diagram of micro-focusing optics is illustrated in Figure 1. X-rays from an undulator were monochromatized by a Si 111 double-crystal monochromator with a rotated-inclined crystal geometry [6]. The first crystal employed a pin-post design to enhance the water cooling efficiency. The focusing optics was located 57 m from the light source. The effective length of each mirror was about 80% of full length for focal length of 250 mm and about 65% for focal length of 100 mm, respectively. It is thought that these effective lengths were limited by the relatively large figure errors at the either end of the mirrors. The illuminating beam size was determined by an aperture size of an XY slit in front of the mirror (slit size: 64 μm $\times$ 52 μm), and only the center area of the mirror was illuminated.

2.2. Scanning X-Ray Microprobe and Application for Biological Specimen. The K-B microfocusing optics was used for a scanning fluorescence X-ray microprobe system. Samples were mounted on an X-Y translation stage, and a takeoff angle of 10° was usually used for detecting fluorescence X-rays from the samples. The fluorescence X-rays were measured by Si(Li) solid state detector which was placed perpendicular to the incident beams to minimize the scattered X-rays. Figure 1 also shows this geometry.

Calibration standards with various known concentrations of uranium (20–100 μg/g) were used to determine sensitivities and to calibrate intensity levels. These standards were prepared by mixing standard solutions with a polyvinyl alcohol solution. The mixed sample solutions were frozen and then were cut into 20 μm sections with a cryomicrotome. Thin sections of kidneys of adult rats were prepared by using the procedure described in [7]. The rats were exposed to uranium (1.4 mg/kg) by subcutaneous injection. The animals were treated and handled in accordance with the guidelines of the "Guide for the Care and Use of Laboratory Animals at the National Institute of Radiological Sciences". Two days after the administration of uranium, the kidneys were removed and then embedded in an optimal cutting temperature compound to prepare dried sections with 20 μm thickness. All sections placed on polypropylene film were fixed on an acrylic holder.

3. Results and Discussion

3.1. Performance Test of X-Ray Focusing Elements. The evaluation of focused beam profiles was out with a dark-field knife-edge scan [8] to obtain more accurate beam profiles than with a conventional knife-edge scan. The intensity of the incident and transmitted X-rays were measured by ionization chambers. A tantalum blade with a thickness of 3 mm was used as the knife edge. To satisfy the dark-field condition, a blade placed between focal point and the detector blocks the direct beam. The detector can feel only the scattered X-rays from the knife edge. The focused profiles at an X-ray energy of 30 keV are shown in Figure 2. The focused beam size of 1.0 μm (V) $\times$ 0.83 μm (H) full width at half maximum (FWHM) is obtained. Here, it is useful to consider the theoretical focused beam size to evaluate the experimentally measured beam size. The actual source size in vertical direction can assume same size of electron beam, which is 15.8 μm. The horizontal source size is defined by an XY slit placed at 34 m from the light source, and the slit width is set to be 200 μm. Using the focal length of the mirrors, the distance between the light source and the mirrors, and the actual source size, the geometrical focused beam size is calculated to be 0.096 μm (V) $\times$ 0.87 μm (H). On the other hand, according to the literature [1], the diffraction-limited spot size was 0.13 μm (V) $\times$ 0.04 μm (H) at 30 keV. The measured beam size in the horizontal direction is near the geometrical beam size (0.87 μm). However, the beam size in the vertical direction is significantly larger than the geometrical beam size (0.096 μm). This difference is believed to arise from the spread of the beam size in the vertical direction due mainly to the vibration and distortion of the monochrometer crystals. The total photon flux of the focused beam is about 5×10^9 photons/s at 30 keV.

3.2. Uranium Distribution of a Rat Kidney. Using the focused beam described in the previous section, the quantitative determination of uranium is considered by a calibration curve technique. The obtained calibration curve measured at 30 keV X-rays is shown in Figure 3. The data shows good linearity between a uranium concentration of 100 and 20 μg/g. This technique using thin standards has been discussed and validated as the quantitative analysis with microbeam for biological specimens [9]. The MDL is expressed as

$$\mathrm{MDL} = 3 * \left(\frac{C}{I_N}\right) * \left(\frac{I_B}{t}\right)^{1/2}, \quad (1)$$

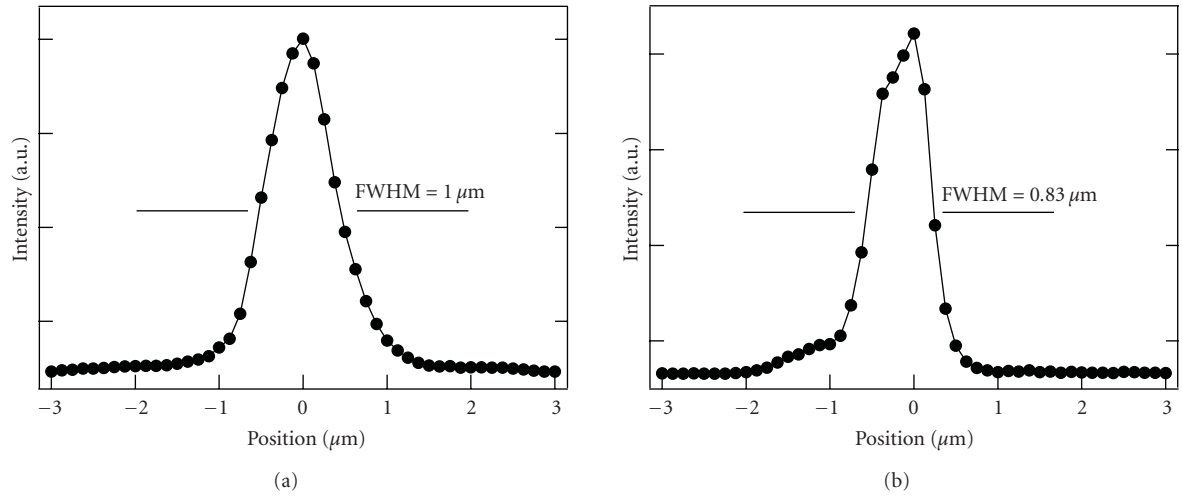

Figure 2: Measured profiles of focused beam at an X-ray energy of 30 keV using dark-field knife-edge scan. (a) Beam profile in the vertical direction (focal length = 250 mm) and (b) beam profile in the horizontal direction (focal length = 100 mm).

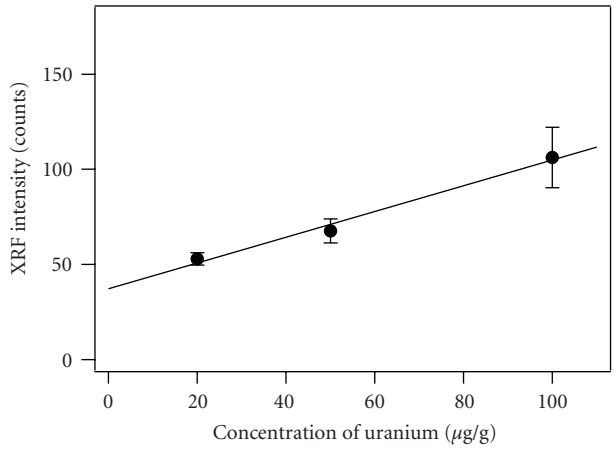

Figure 3: Calibration curve for the determination of uranium. The XRF intensity was plotted against the uranium concentration.

where C is the concentration of uranium (μg/g), I_N is the net intensity (number of counts), I_B is the background intensity (number of counts) and t is the counting time (10 s) [10]. To quantitatively evaluate the uranium concentration, 5×5 raster scans of the each standards were performed. For example, relative standard deviation, which is calculated by dividing the standard deviation by the mean value, of the total XRF intensity of uranium was 12% at concentration of 20 μg/g. According to (1), the estimated MDL value at the lowest end is 10 μg/g. These results suggest that the system allows us to quantitatively analyze heavy trace elements in biological samples even with microbeam resolution.

Prior to the μ-XRF imaging of the samples, XRF imaging with beam size of 200 μm $\times$ 200 μm was performed to determine the overall elemental distribution in the renal sections at X-ray energy of 30 keV. Figure 4 shows the distribution of iron, zinc, and uranium in the kidney. The intensity of the XRF images is shown as the color scale from blue to white, which corresponds to the XRF intensity from lowest to highest. Although an XRF image of uranium is usually measured by detecting an $U\ L_\alpha$ line (13.6 keV), here, $U\ L_\beta$ lines ($L_{\beta 1}$: 17.2 keV, $L_{\beta 2}$: 16.4 keV) are measured to avoid overlapping by rubidium K_α line (13.4 keV) because of the existence of rubidium in the rat kidney [11]. Iron was localized to the inner stripe of the outer medulla (Figure 4(b)), while the zinc was distributed equally in the cortex and in the outer stripe of the outer medulla than the inner stripe of the outer medulla (Figure 4(c)). In contrast to the normal elements, uranium shows a completely different distribution. The uranium was localized only in the outer stripe of the outer medulla (Figure 4(d)). To get more detailed information about uranium distributions, high resolution μ-XRF imaging in the highly localizing area marked in Figure 4(d) was carried out at the X-ray energy of 37 keV. The two-dimensional distribution of uranium is shown in Figure 5(a). The shape of the proximal tubule is obviously visualized by the uranium distribution. Figure 5(b) represents an XRF spectrum measured at the point indicated by an arrow head in Figure 5(a). It is observed that the uranium L_β lines can be clearly detected without interference from other elements. Uranium concentrations for the image were calculated using the calibration curve showed in Figure 3. However, a corrected calibration curve was used for estimating the uranium concentration because of different excitation energy between Figure 3 (30 keV) and Figure 5 (37 keV). Assuming the matrix density and thickness between the samples and standards have approximately the same value, we considered only the correction for the linear absorption coefficients of 30 and 37 keV X-rays. The model linear absorption coefficients of uranium were 763 cm^{-1} at 30 keV, and 442 cm^{-1} at 37 keV, respectively. These coefficients were provided from the NIST physical reference data [12]. Though this correction is only approximately, it is expected that the calculated values give a semiquantitative map of the uranium concentration.

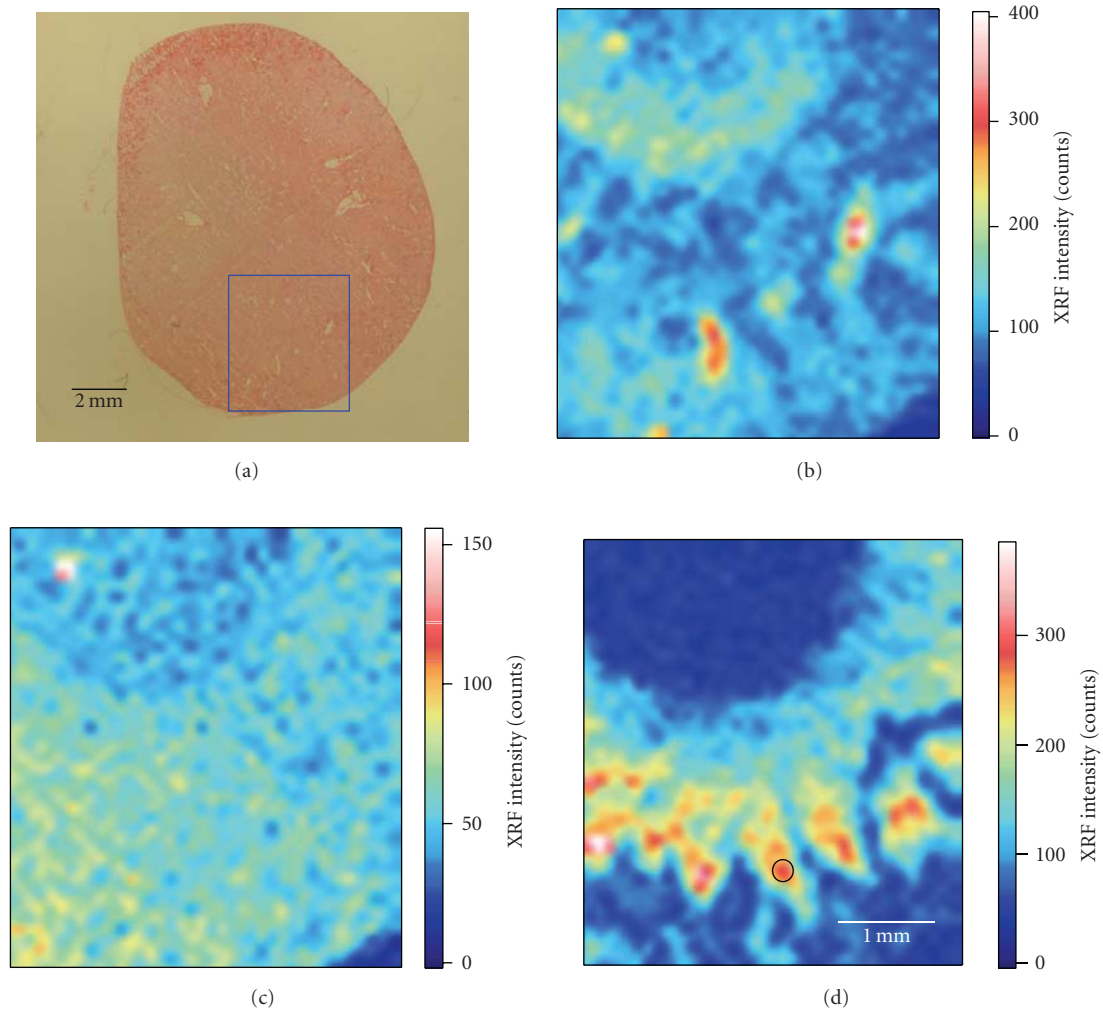

Figure 4: XRF imaging of a renal cross section. (a) photograph of a serial section showing the imaging area. The two-dimensional distribution of (b) iron, (c) zinc, and (d) uranium. Beam size: 200 μm (V) $\times$ 200 μm (H), imaging area: 4.5 mm (V) $\times$ 4 mm (H), pixel size: 100 μm, and dwell time: 5 s.

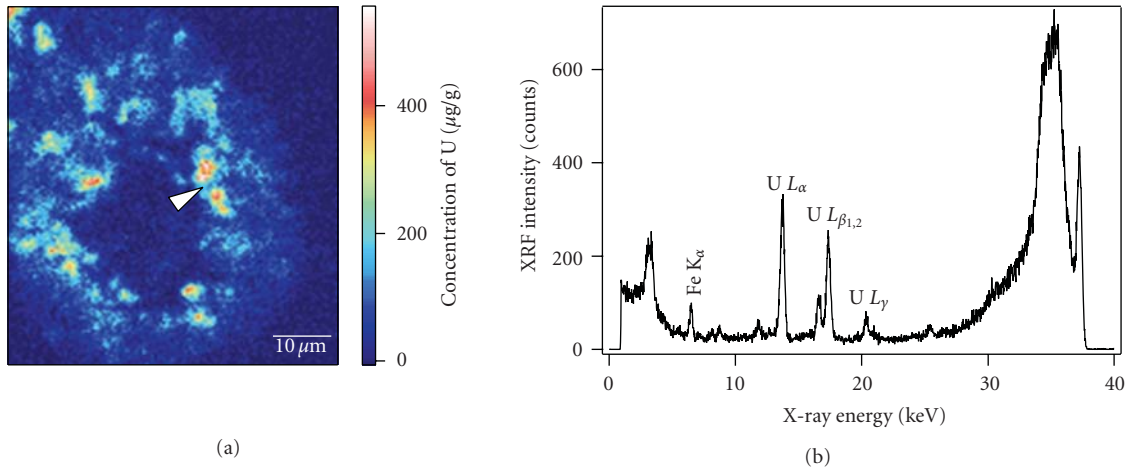

Figure 5: High resolution μ-XRF image of the marked area in Figure 4(d) measured at 37 keV X-rays. (a) The two-dimensional distribution of uranium. The XRF intensities are estimated to the concentration of uranium. Beam size: 1.2 μm (V) $\times$ 1.4 μm (H), imaging area: 75 μm (V) $\times$ 57 μm (H), pixel size: 0.5 μm, and dwell time: 5 s. (b) X-ray fluorescence spectrum at arrow head in Figure 5(a). Measurement time is 600 s.

The maximum concentration of uranium in the tubule was estimated to be 503 μg/g by using the assumptions above. The quantified value is about 23 times higher than the mean concentration in the kidney (22.3 μg/g wet weight at 2 days measured by inductively-coupled plasma mass spectrometry). This intense localization is in good agreement with a previous study [7]. The elemental imaging indicated that uranium is selectively distributed in the proximal tubules and highly concentrated in the epithelium of the tubules.

4. Conclusion

A scanning fluorescence X-ray microprobe with sub-micron transverse spatial resolution was achieved at beamline 37XU of SPring-8 using total-external-reflection K-B mirror optics. A focused beam size of 1.0 μm (V) $\times$ 0.83 μm (H) FWHM at the X-ray energy of 30 keV was achieved. The mirror optics provides sufficient spatial resolution to examine μ-XRF analysis of high-Z elements even with high-energy X-rays. The quantitative evaluation of μ-XRF analysis was performed by a calibration-curve method. The MDL with a beam size of around 1 μm^2 was 10 μg/g. The X-ray microprobe was also utilized to map the uranium distribution in the kidneys of rats exposed to uranium acetate. It was revealed that uranium localized in the proximal tubule with a 23 times higher concentration compared to the whole kidney. These results provide useful information to understanding the chemical and radiological toxicity of uranium in the kidney. This technique will contribute greatly to understand dynamic mechanism of trace high-Z elements with sub-micron resolution and will open new application for a variety of fields using XRF analysis.

Acknowledgments

This study has been performed under the approval of Japan Synchrotron Radiation Research Institute (JASRI) as Nanotechnology Support Project of the Ministry of Education, Culture, Sports, Science, and Technology (Proposal no. 2008A1662/BL37XU). A part of the experiments also has been carried out under the approval of SPring-8 Proposal Review Committee (Proposal no. 2007A1392).

References

[1] Y. Suzuki, A. Takeuchi, and Y. Terada, "High-energy X-ray microbeam with total-reflection mirror optics," *Review of Scientific Instruments*, vol. 78, no. 5, Article ID 053713, 3 pages, 2007.

[2] I. Nakai, Y. Terada, M. Itou, and Y. Sakurai, "Use of highly energetic (116 keV) synchrotron radiation for X-ray fluorescence analysis of trace rare-earth and heavy elements," *Journal of Synchrotron Radiation*, vol. 8, no. 4, pp. 1078–1081, 2001.

[3] A. Takeuchi, Y. Suzuki, H. Takano, and Y. Terada, "Kirkpatrick-Baez type X-ray focusing mirror fabricated by the bent-polishing method," *Review of Scientific Instruments*, vol. 76, no. 9, Article ID 093708, 4 pages, 2005.

[4] A. Takeuchi, Y. Suzuki, and H. Takano, "X-ray focusing mirror fabricated with bent-polishing method," in *Proceedings of the 18th International Conference on Synchrotron Radiation Instrumentation*, vol. 705 of *AIP Conference Proceedings*, pp. 760–763, San Francisco, USA, 2004.

[5] Y. Terada, S. Goto, N. Takimoto, et al., "Construction and commissioning of BL37XU at SPring-8," in *Proceedings of the 18th International Conference on Synchrotron Radiation Instrumentation*, vol. 705 of *AIP Conference Proceedings*, pp. 376–379, San Francisco, USA, 2004.

[6] M. Yabashi, H. Yamazaki, K. Tamasaku et al., "SPring-8 standard X-ray monochromators," in *X-Ray Optics Design, Performance, and Applications*, vol. 3773 of *Proceedings of SPIE*, pp. 2–13, Denver, Colo, USA, July 1999.

[7] S. Homma-Takeda, Y. Terada, A. Nakata et al., "Elemental imaging of kidneys of adult rats exposed to uranium acetate," *Nuclear Instruments and Methods in Physics Research Section B*, vol. 267, no. 12-13, pp. 2167–2170, 2009.

[8] Y. Suzuki, A. Takeuchi, H. Takano, and H. Takenaka, "Performance test of fresnel zone plate with 50 nm outermost zone width in hard X-ray region," *Japanese Journal of Applied Physics*, vol. 44, no. 4A, pp. 1994–1998, 2005.

[9] S. Homma-Takeda, Y. Nishimura, H. Iso, T. Ishikawa, H. Imaseki, and M. Yukawa, "A new approach for standard preparation in microbeam analysis: development and validation," *Journal of Radioanalytical and Nuclear Chemistry*, vol. 279, no. 2, pp. 627–631, 2009.

[10] C. J. Sparks, "X-ray fluorescence microprobe for chemical analysis," in *Synchrotron Radiation Research*, H. Winick and S. Doniach, Eds., pp. 459–512, Plenum Press, New York, NY, USA, 1980.

[11] S. Homma-Takeda, Y. Terada, H. Iso, et al., "Rubidium distribution in kidneys of immature rats," *International Journal of PIXE*, vol. 19, no. 1-2, pp. 39–45, 2005.

[12] "X-ray Form Factor, Attenuation, and Scattering Tables database," http://physics.nist.gov/PhysRefData/FFast/html/form.html.

Hindawi Publishing Corporation
X-Ray Optics and Instrumentation
Volume 2010, Article ID 412323, 16 pages
doi:10.1155/2010/412323

Review Article

Thin Shell, Segmented X-Ray Mirrors

R. Petre

X-ray Astrophysics Laboratory, NASA Goddard Space Flight Center, Greenbelt, MD 20771, USA

Correspondence should be addressed to R. Petre, robert.petre-1@nasa.gov

Received 14 May 2010; Accepted 29 November 2010

Academic Editor: Stephen L. O'Dell

Thin foil mirrors were introduced as a means of achieving high throughput in an X-ray astronomical imaging system in applications for which high angular resolution was not necessary. Since their introduction, their high filling factor, modest mass, relative ease of construction, and modest cost have led to their use in numerous X-ray observatories, including the Broad Band X-ray Telescope, ASCA, and Suzaku. The introduction of key innovations, including epoxy replicated surfaces, multilayer coatings, and glass mirror substrates, has led to performance improvements and in their becoming widely used for X-ray astronomical imaging at energies above 10 keV. The use of glass substrates has also led to substantial improvement in angular resolution and thus their incorporation into the NASA concept for the International X-ray Observatory with a planned 3 m diameter aperture. This paper traces the development of foil mirrors from their inception in the 1970s through their current and anticipated future applications.

1. Introduction

The thin foil X-ray mirror was invented to fulfill a particular observational objective. In the 1970's, with the introduction into X-ray astronomy of high resolution imaging through the Wolter I mirrors on the Einstein Observatory, it became recognized that not all applications for which imaging is desired require high angular resolution (<1 arcmin). High angular resolution comes at a cost: mirrors must be accurately figured and held rigidly. These requirements lead to a thick substrate, high mass, and large expense. Since X-ray imaging above ~0.02 keV requires grazing incidence mirrors, the need for thick substrate material leads to inefficient aperture utilization (i.e., low throughput), and thus limited sensitivity. For some astronomical measurements it is desirable to take advantage of the increased sensitivity afforded by imaging but where high throughput is preferred over angular resolution. This is especially true in situations in which the detection of a large number of photons is required to perform the measurement of interest; examples include spectroscopy of relatively isolated sources and polarimetry. For such applications, replacing a small number of thick, massive, expensive mirror shells with a large number of thin, low mass, low cost shells offers the desired improvement in throughput with sufficient angular resolution to resolve most sources. Thus the driving idea behind the foil mirror was to provide a low cost, low mass, high throughput alternative to high-resolution mirrors.

Since its inception, the foil mirror has shown itself to be versatile and adaptable to a wide range of applications. It has become the starting point for virtually all applications requiring low cost, lightweight mirrors, with moderate imaging applications. Because of its efficient aperture utilization, it has evolved into the baseline design of choice for imaging above 10 keV. Important innovations have been introduced, most importantly the substitution of glass for aluminum foil as the mirror segment substrate. Over time, as demand has increased for improved angular resolution, the design has undergone steady improvement. The principles leading to its invention are the basis for its most ambitious manifestation, the mirror for the International X-Ray Observatory (IXO).

This paper traces the development of the foil mirror. It describes the innovations that have led to its evolution from a simple light bucket to a high-resolution imaging system with applications across a broad energy band.

It should be noted that the many conceptual and implementation innovations leading to the first foil mirrors

Figure 1: Close-up view of entrance aperture of a foil mirror. The large number of nested shells plus the use of thin foil substrates combine to provide a large filling factor. The average distance between foils is approximately 1 mm.

were due to Peter Serlemitsos at NASA's Goddard Space Flight Center (GSFC). Not only has he pioneered the concept [1], but he is also responsible for many of the improvements over the past 30 years. He has also led the team that constructed every such mirror that has flown in space thus far. While others are responsible for recent parallel developments towards higher angular resolution (e.g., introduction of glass as a substrate material), it is the work of Serlemitsos that made this type of mirror viable. His contribution to astrophysics through the invention of the thin foil mirror was recognized by his being awarded the 2009 Joseph Weber prize by the American Astronomical Society.

2. Basic Principles

The basic design and principles of the conical foil mirror are described in Serlemitsos [2] and Petre and Serlemitsos [3]. In its pure form, the thin foil mirror is a Wolter I design in which many thin shells are nested to fill the available aperture. A high filling factor (ratio of usable to total aperture) is obtained when the substrate thickness is small compared with the gap between adjacent shells (in contrast to the thick substrates in the high resolution imaging mirrors to date, such as Einstein, ROSAT, and Chandra). Since emphasis is on low cost and high collecting area rather than image quality, the paraboloidal and hyperboloidal surfaces are approximated by conic frusta, thus the term "conical approximation." For large focal ratios (focal length to aperture diameter), the conical approximation introduces only an intrinsic blur of a few to a few tens of arc seconds, depending on the axial length of the mirror segment. The degree of simplification offered by introducing this approximation far outweighs the reduced intrinsic imaging performance, which in actual implementations tends to be small compared with the overall mirror angular resolution.

The optical design of foil mirrors follows a common template (see, e.g., [3]). The mirror shells are nested to maximize the on-axis effective area (Figure 1). This is accomplished by leaving no radial gap between the outer diameter of the front of one shell and the rear of the next shell outward: viewing from the front of the mirror on axis, the entire aperture is covered by either a reflecting surface or the front edge of one. This maximum filling approach leads to a linear off-axis vignetting function. The vignetting with off-axis angle is a function of incident energy, steeper at higher energy. A practical approximation of the diameter of the field of view is given by the average graze angle of the mirror. At radii beyond half the graze angle, the effective area is typically less than half the on-axis area. The angular resolution, if characterized by half power diameter (HPD), is essentially constant across the field of view: off-axis aberrations are small compared with the blur introduced by the conical approximation within the field of view of a typical focal plane instrument. The image of a point source changes from circularly symmetric to elongated perpendicular to the off-axis shift direction, however. Outside the nominal field of view, aberrations (particularly coma and oblique spherical aberrations) degrade the HPD.

The conical design has several practical attributes that simplify construction. First, it can be shown by simple geometric arguments that all the many nested mirror surfaces in each of the two reflection stages (paraboloid analog, usually referred to as the primary surface and hyperboloid analog, referred to as the secondary), when flattened onto a plane, all describe a segment of the same annulus. This means that the substrates can be mass produced, with only two cutting fixtures needed to shape substrates. Second, since no axial curvature is imparted to the reflecting surfaces, surface preparation can be kept simple (e.g., forming the overall shape of a relatively smooth substrate). The only requirement on the preparation technique is that it produces or preserves a surface that is smooth on spatial scales larger than approximately 1 mm. Various coating techniques can then provide the necessary smoothness on smaller spatial scales. Third, the design lends itself to modularity and mass production. The mirror is usually divided into angular segments, quadrants, or thirds, with a separate housing for each.

The introduction of the conical approximation greatly reduces the precision requirements on the substrate. A number of substrate materials have been tried, but the best-suited material is aluminum. Aluminum has low density, the right balance between stiffness, and ductility to allow forming and can be found in large, thin rolls or sheets with high gloss finish.

The method used for shaping aluminum into the conical form has changed minimally since its first use. If the raw stock comes from a roll, it was first flattened by compression between two glass plates under heat. The aluminum is cut approximately to shape and then given its basic shape (a segment of a cone frustum) by pressing it against a mandrel and thermally cycling it. The aluminum is formed so that global surface structure such as roll marks runs along the direction of incidence of the radiation to minimize scatter off surface features that remain after coating. (This means that stock from a roll needs to be flattened so that curvature can be introduced in the opposite direction.) Refinements in this process include the mandrel shape (originally cylindrical,

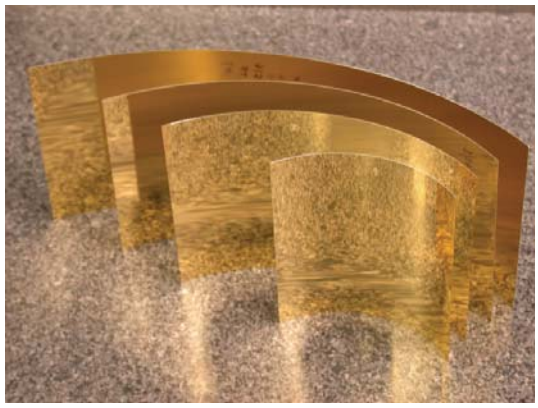

Figure 2: Finished foil mirror segments. These particular mirror segments were produced using epoxy replication, but appear identical to those produced using lacquer coating.

(a)

(b)

Figure 3: (a) Assembled conical mirror quadrant housing. Two such housings (primary and secondary) are stacked to form a complete quadrant. Mirror segments are inserted from the open side through the grooves in the radial alignment bars. (b) Magnified view of a portion of an alignment bar. The width at the base of the angled grooves is slightly larger than the segment thickness.

now conical, and with increasing radial accuracy), how the substrates are held against mandrels (originally mechanically and now using suction), and the details of the thermal cycle used for the forming.

Even aluminum sheet stock with the most mirror-like appearance has a surface structure making it an inefficient X-ray reflector. It tends to have unacceptably high roughness on spatial scales shorter than a few millimeters, which if not removed would introduce unacceptably high scattering of incident X-rays. Additionally, the X-ray reflecting surface

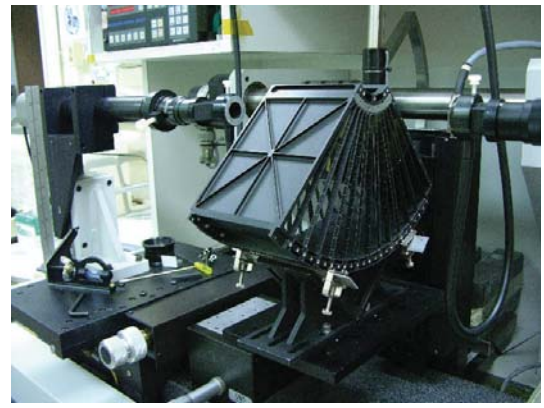

Figure 4: One reflection stage of a mirror quadrant being undergoing alignment on an optical table. Microscopes (left and right) view the edges of the mirror segments as the housing is rotated about the mirror optical axis, allowing them to be accurately positioned.

needs to be coated with a high-density metal (e.g., Ni or Au) to obtain high X-ray reflectivity.

The initial solution to the roughness problem and the one that made foil mirrors a viable technology was the use of acrylic lacquer [2]. It was found that immersing the shaped aluminum segments in a lacquer bath and slowly drawing them out left a thin, uniform, microscopically smooth surface coating. An X-ray reflective surface was applied via evaporation of a thin layer of gold (Figure 2). This was the approach used for the first conical mirrors.

Another important aspect of the foil mirror concept is modularity [2]. A complete shell is divided into equal arc lengths, initially quadrants. This eases manufacture of substrates and handling of both substrates and modules.

Mounting in a housing and aligning 100 or more pairs of mirror segments is challenging, and misalignment remains a primary source of blur. Serlemitsos [2] introduced gang alignment, whereby all of the segments in the primary or secondary housing are loaded together and are held in place front and rear by a set of accurately grooved radial alignment bars. Substantial research has gone into optimizing the number of alignment bars as well as the shape of the grooves. The grooves must be precisely located and not allow the segments to shift. At the same time they cannot be so narrow as to prevent insertion of segments or to distort them. A housing and a magnified portion of an alignment bar are shown in Figure 3.

Gang alignment offers the substantial benefit that it can be done relatively quickly (Figure 4). Its primary disadvantage is the limit it places on angular resolution—aligning all the segments to the best average focus introduces segment-to-segment variation. The need for the grooves to be wider than the segments to allow loading without damaging the segments and introducing distortions leads to the introduction of a small variation in mirror slope, in turn leading to blur. This slope error tends to be random within a quadrant and is typically an arc minute in the mirrors developed for flight.

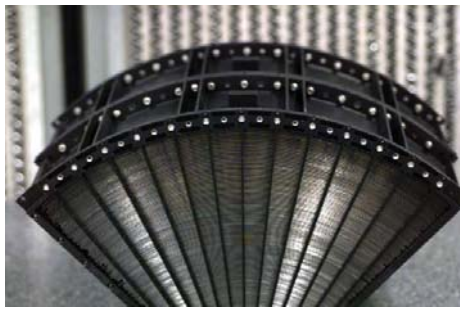

Figure 5: A completed quadrant, viewed from the front.

Primary to secondary alignment is generally performed in an optical beam, while the location of the focus and quality of the image is monitored. Figure 5 shows a completed module, in this instance a quadrant. Once all the modules comprising a mirror (primary plus secondary) have been populated and internally aligned, they are mounted on a ring. Alignment at this stage entails only shifting the foci of the respective modules via translation; since each module separately acts as a thin lens, small overall tilts can be ignored. The net effect of a slight tilt is the reduction of the on-axis effective area.

3. The First Foil Mirrors

A total of eight flight quality lacquer coated foil mirrors were produced at GSFC between 1987 and 1992. The parameters of these mirrors are summarized in Table 1. One of these was for a sounding rocket instrument, two for the Broad Band X-ray Telescope (BBXRT), and five for the Japan/US X-ray observatory ASCA (four flight plus one spare). The properties of these mirrors are listed in Table 1.

The first conical mirror to fly was constructed in 1987 for a Supernova X-ray Spectrometer sounding rocket payload, intended to search for X-ray emission from SN 1987A [2]. The mirror was adopted from the (not yet built) BBXRT design, but the focal length was reduced from 3.84 m to 2.1 m. It was launched in February 1988 with a pixilated Si(Li) detector at its focus. During its five-minute exposure above the atmosphere, it detected LMC X-1 as well as hot, diffuse emission from the LMC, but not SN 1987A, which it failed to observe due to an attitude control program error. The mirror was recovered intact. Its primary success was a demonstration that such mirrors can survive a launch environment and deliver the expected performance in space. This mirror has recently been renovated and will be used on the Micro-X sounding rocket instrument [4].

The first real application of a foil mirror was BBXRT. The objective of this instrument was to perform sensitive, moderate resolution spectroscopy of a variety of X-ray sources over the 0.3–12.0 keV band. This band contains the K line radiation of all astrophysically abundant metals (O, Ne, Mg, Si, S, Ca, Ar, Fe), plus the L lines of iron. This instrument carried a pair of coaligned foil mirrors, each illuminating a pixilated Si(Li) detector. The mirrors have a 40 cm diameter and focal length of 3.84 m; each was constructed of 118 nested shells, constructed in quadrants. The axial length of each reflection stage was 10 cm. The mirror segments were produced by lacquer coating 0.127 mm thick aluminum foil substrate and overcoating the lacquer with gold for X-ray reflection. Each mirror had a mass of 20 kg. BBXRT was flown in December 1990 for nine days as part of the Astro-1 payload on Shuttle mission STS-35, performing approximately 150 observations of 85 celestial targets. The performance of the instrument, including the mirrors, is described in detail in Weaver et al. [5].

The broadband point spread function was determined on orbit by comparing the distribution of counts from discrete cosmic sources with models based on ground calibration. It was best modeled using a pair of Gaussian profiles. The inner image core ($\sigma = 1.8$ arcmin) contained 65 percent of the source flux; the outer halo ($\sigma = 5.8$ arcmin) contained 35 percent. Some energy dependence of the point-spread function was observed; this was ascribed to residual roughness of the mirror foils. The degree of energy dependence was not quantified, but consistent with that measured for the mirrors on ASCA, which were fabricated using the same approach (see below). The effective area of each mirror was approximately 290 cm^2 at 1 keV and 125 cm^2 at 7 keV.

The Japanese-US ASCA was the first free flying, general use X-ray observatory to incorporate foil mirrors [6]. With its foil mirrors and its groundbreaking CCD detectors, ASCA made numerous important contributions to astrophysics and demonstrated the utility of both high throughput mirrors and CCD detectors.

ASCA was severely mass limited, with a total mass of ~400 kg. Thus there was a premium on the effective area-to-mass ratio of the X-ray mirrors, a situation for which foil mirrors provide the best solution. ASCA incorporated four identical coaligned foil mirrors, each with a mass of 10 kg [7]. Two mirrors illuminated imaging gas scintillation proportional counters, the other two illuminated the first CCD detectors ever used in an orbiting X-ray observatory. Each mirror had a diameter of 35 cm and a 3.5 m focal length and consisted of 120 nested shells. The foil thickness and axial length were the same as in BBXRT. Also as in BBXRT, the mirror surfaces were produced using the lacquer coating, with an evaporated gold overcoat. One of the flight mirrors is shown in Figure 6.

ASCA was launched on February 20, 1993, and operated in orbit for six years. The point-spread function had two distinct components, a sharp core plus a halo. While the full width at half maximum was ~1 arcmin, the HPD was 3.6 arcmin. While the HPD was largely constant across the 0.5–10 keV energy band, the halo did show some energy-dependent broadening. This is ascribed to small angular scale roughness on the mirror surfaces. The fractional flux in the broadened component varied from 8 percent at 1.5 keV to 17 percent at 8 keV. The broadening is consistent with the measured surface microroughness of ~3 Å. Despite the modest dimensions and mass of the mirrors, each of the four had an effective area of approximately 300 cm^2 at 1 keV and 140 cm^2 at 8 keV. There was no appreciable difference among the four mirrors. Over the six-year mission life, no degradation of the mirror performance was observed.

Table 1: Foil mirror parameters.

	SXS/Micro-X	BBXRT	SODART	ASCA	Astro-E/E2 SXT-I	Astro-E/E2 SXT-S
Number flown	1	2	0	4	8	2
Diameter (cm)	40	40	60	35	40	40
Focal length (m)	2.1	3.77	8	3.5	4.75	4.5
Number of Shells	68	118	143	120	175	168
Number of modules per mirror	4	4	4	4	4	4
Segment length (cm)	10	10	20	10	10	10
Total number of segments	544	944	1144	960	1400	1344
AI Substrate thickness (mm)	0.127	0.127	0.4	0.127	0.152	0.152
Surface production method	lacquer	lacquer	lacquer	lacquer	replication	replication
Reflective coating	gold	gold	gold	gold	gold	gold
Mass (kg)	20	20	101	9.84	19.3	19.9
Effective area at 1 keV (cm^2)	300	290	950	300	450	450
Effective area at 7 keV (cm^2)	—	125	750	150	250	250
Angular resolution (HPD-arcmin)	3	3	2.4–3.8	3.6	1.6-1.7	1.7
Year of launch	1988	1990	—	1993	2000, 2005	2000, 2005

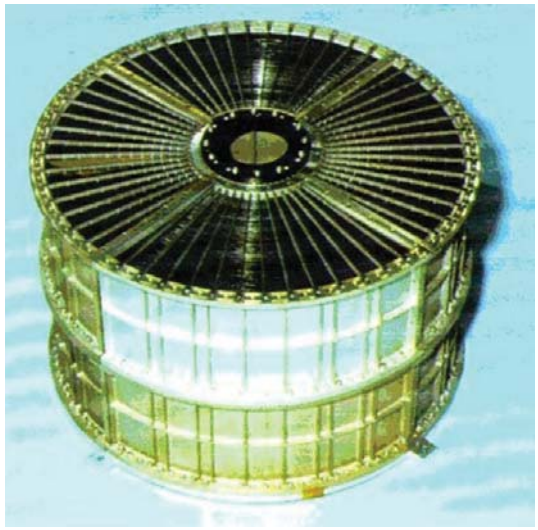

Figure 6: An ASCA flight mirror, one of five constructed. The aperture diameter is 35 cm; the height is approximately 20 cm. The mirror consists of 118 nested shells and has a mass of 10 kg.

The most ambitious application of lacquer-coated mirrors was the pair constructed for the SODART, Soviet-Danish Röntgen Telescope [8]. The SODART instrument was to have flown in the 1990s on the Russian Spectrum X-Gamma observatory, but the observatory was never launched. Each of the two mirrors had a 60 cm diameter and an 8 m focal length. It consisted of 143 nested shells divided into quadrants like the GSFC mirrors. The shells were thicker (and thus stiffer) than those used at GSFC (0.4 mm as opposed to 0.127 mm) and longer (20 cm as opposed to 10 cm). The mirror forming and mounting approaches largely duplicated those used at GSFC for BBXRT and ASCA [9]. One exception is that the segments were bonded to the housing sides after alignment of a primary and secondary quadrant. The reflecting surfaces were prepared using a similar lacquer coating technique to that developed at GSFC. Each mirror weighed 101 kg.

Extensive ground testing was performed on the SODART mirrors [10]. The measured performance was strongly dependent on the field of view of the detector, the result of large angle scattering off surface imperfections. The half power diameter ranged from 2.4 arcmin to 3.8 arcmin, depending on field of view and energy. The on-axis effective area was 765 cm^2 at 6.6 keV and was 65 percent of that expected from an ideal geometry, independent of energy.

4. Epoxy Surface Replication

One attribute of the lacquer-coated mirrors was the presence of "orange peel" on their surfaces—millimeter-scale ripples that limited their angular resolution. This surface roughness was a major source of blur and is likely to be largely responsible for the field of view and energy dependence of the angular resolution best quantified for the SODART mirrors, but common to all lacquer-coated mirrors. The quest to remove this effect led to the introduction of epoxy replication [11]. Epoxy replication is a proven technique for producing optical components. It is a standard way for instance of making gratings. For X-ray astronomy, epoxy was used to produce the mirrors for ESA's Exosat mission [12] and the reflection gratings on the XMM-Newton mission [13]. If epoxy replication was to work for thin foil mirrors without sacrifice of their reasonable cost, then it was necessary to develop a straightforward process that would consistently produce better quality mirror surfaces than lacquer coating and lend itself to mass production.

The replication process introduced by Serlemitsos and Soong [11] does just that. First, the thin reflective layer (gold or platinum) is deposited onto a glass mandrel. Then a thin,

even layer of epoxy is sprayed onto the preformed aluminum substrate and/or the coated mandrel. The mandrel and substrate are brought into contact under vacuum and then brought to atmosphere to force the two together. The epoxy is allowed to cure in air for several hours at an elevated temperature. Once the epoxy is cured, then the mirror segment is separated from the mandrel. The segment is trimmed to its final shape for installation into its housing; the mandrel is cleaned in preparation for another replication cycle.

A number of factors contribute to the success of this approach. Inexpensive, durable mandrel material needed to be found. Drawn cylindrical borosilicate glass tubing manufactured by Schott has a surface with very low microroughness that is transferred to the epoxy. Mandrels are selected by scanning the surface of a tube to find portions with minimal curvature (typically less than 1 arcmin). The smooth microsurface of the mandrels allows the deposited reflective layer to release easily, with no need for a release layer. Additionally, since the reflective layer is deposited onto the mandrel, it is possible to use sputtering instead of evaporation. Sputtering yields a layer with density closer to bulk than evaporation and thus a higher X-ray reflectivity (the gold on the ASCA and BBXRT mirrors had density ~85 percent of bulk). For the replication to be viable, it was essential to find an epoxy that could be thinned to allow uniform spraying of a thin layer. A spraying process then needed to be developed that yields a uniform coating (this was done via robotic spraying—see Figure 7). Using a sufficiently thin epoxy layer minimizes transfer of large-scale mandrel surface features onto the substrate, meaning that the substrates retain the shape imparted to them through heat forming. The thin epoxy layer is also necessary to minimize distortions due to stresses built up during curing, as well as bilayer thermal deformation. Finally an epoxy cure cycle was developed that was not too cool, lest the epoxy cure insufficiently, nor too hot, lest the epoxy intermix with the reflecting material and spoil the surface quality.

5. Epoxy-Replicated Flight Mirrors: Astro-E and Suzaku (Astro-E2)

Epoxy replication has become the baseline approach for making foil mirrors. The first epoxy-replicated mirrors were built for the Japan/US Astro-E mission. Included in the Astro-E instrumentation were five 40 cm diameter epoxy-replicated foil mirrors [14]. Four mirrors illuminated CCD detectors, which together comprise the XIS instrument. These mirrors had a focal length of 4.75 m and consisted of 175 nested shells. The fifth mirror illuminated an X-ray microcalorimeter: a unique, nondispersive imaging spectrometer with high spectral resolution, that operates at a temperature of 0.065 K. This mirror had a 4.5 m focal length and consisted of 168 shells. The reflection stages of both mirror types again had an axial length of 10 cm. Each mirror had a mass of approximately 19 kg; the reflectors comprised over half the total mass.

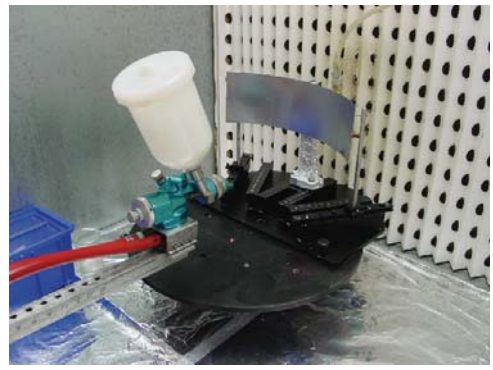

Figure 7: Epoxy coating of a foil using a robotic sprayer.

The Astro-E mirrors underwent extensive ground calibration in a pencil beam facility [15]. The HPD was found to be 1.8–2.2 arcmin for the five mirrors and was largely energy independent in the 1.5–8.0 keV range. This represents a substantial improvement over the resolution obtained by the lacquer-coated ASCA mirrors. The effective area of each mirror was 20 percent lower than the design values at all energies. Analysis of this loss ascribed 11 percent to mechanical misalignment and slope errors of the mirror segments, 6 percent to reflector surface roughness (5.1 Å rms), and 3 percent to wide-angle scattering of radiation beyond the boundary of the focal plane detector. Nevertheless the effective area of each mirror was ~450 cm^2 at 1 keV and ~250 cm^2 at 7 keV, a high throughput for such a modest diameter mirror.

Astro-E was launched on February 10, 2000. A first stage booster failure prevented the spacecraft from reaching orbit. To recover from this setback, a nearly identical Astro-E2 spacecraft was built. The foil mirrors are largely identical in design and construction to those of Astro-E [16]. The single major change was the addition of a stray light baffle, which was attached to the front of each mirror to largely eliminate the paths to the focal plane of radiation reflected only off the secondary reflector [17]. Additionally, a more restrictive screening was applied to the glass tubes used as replication mandrels in order to reduce the figure error of the mirror segments. Extensive ground calibration was performed using a pencil beam [18]; one of the five mirrors was calibrated using full illumination [19]. The minor process improvements yielded a slightly improved angular resolution over that of the Astro-E mirrors: the HPD was 1.6–1.7 arcmin. The effective area was essentially identical to that of the Astro-E mirrors. The same 20 percent reduction in effective area below the design area as for the Astro-E mirrors was found. It was shown that the loss of effective area due to misalignment between the mirror and the stray light baffle was at most 2 percent. A finished flight mirror is shown in Figure 8.

Astro-E2 was successfully launched on July 10, 2005, and renamed Suzaku upon reaching orbit. Because of the loss of cryogen from the microcalorimeter cryostat prior to the start of observations, only the mirrors illuminating the CCD detectors were calibrated in orbit. The in-flight effective

Figure 8: An Astro-E2 flight mirror, with stray light baffle attached on top. The aperture diameter is 40 cm; the height is approximately 22 cm. The mirror consists of 168 nested shells and has a mass of 20 kg. Between Astro-E and Astro-E2 (Suzaku) a total of 10 such mirrors were constructed.

area was found to be consistent with ground calibration. A slight degradation of the angular resolution was noted immediately after launch: the on-orbit HPD of the four mirrors is 1.8–2.3 arcmin. The reduction is thought to be the consequence of mechanical relaxation of the foil segments in their housings stimulated by launch vibrations (the segments are not bonded in place). Over nearly five years since launch there has been no detectable change in the performance of the mirrors.

6. Future Foil Mirrors: The Astro-H Soft X-ray Telescope, GEMS, and Astrosat

Astro-H is the next major Japan/US X-ray observatory, currently under development in Japan for a 2014 launch. Its instrumentation includes four X-ray mirrors: two Soft X-ray Telescopes (SXTs) for imaging in the 0.3–10 keV band and two Hard X-ray Telescopes (HXTs) for imaging in the 10–50 keV band. All are foil mirrors. One of the SXTs will illuminate a microcalorimeter detector, the other a CCD detector. The HXTs are described below; the key parameters of both are listed in Table 2

The SXT design is a scaled up and improved version of Suzaku's [20]. The mirror has a 45 cm diameter and a 5.6 m focal length. As with Suzaku and the other foil mirrors, the SXT is constructed in quadrants. The segment length will again be 10 cm. The total number of nested shells is 203. The required angular resolution is 1.7 arcmin HPD. The expected effective area of the mirror will be about 510 cm^2 at 1 keV and 390 cm^2 at 7 keV. An exploded view of the mechanical design is shown in Figure 9. Most of the components shown in this figure are common to all foil mirrors.

Several process improvements are being incorporated into the SXT fabrication process in order to improve the angular resolution, toward achieving 1.3 arcmin HPD or better [20].

(i) Closer attention is being paid to the shape of the substrates. More accurate forming mandrels are being fabricated. Fewer mirror substrates will be stacked onto a forming mandrel during each forming run. This reduces figure errors introduced by forcing a segment into a radius for which it has an incorrect cone angle.

(ii) Three different substrate thicknesses are being used: 0.125, 0.229, and 0.305 mm, with thicker substrates at larger radii. The use of thicker, thus stiffer, substrates should yield mirrors with final shape closer to the ideal one.

(iii) A thinner epoxy layer will be used ($\sim 12\,\mu$m versus $\sim 25\,\mu$m on Suzaku). There is a mismatch between the conical shape of the raw substrate material and the cylindrical replication mandrels. Use of a thicker, stiffer epoxy layer, which conforms to the shape of the replication mandrel, therefore introduces stresses on the substrate and can deform it. Use of the thinner layer will allow replication of the very smooth mandrel surface, but allow the substrate to retain the shape imposed upon it during forming.

(iv) A modified alignment and mounting scheme will be used, incorporating two distinct sets of radial bars. One set of reference bars, with precisely located and shaped grooves, will be used as in the past to perform gang alignment of the mirror segments. A second set of support bars, with larger grooves, will be interspersed with the reference bars, and the aligned segments will be bonded to them. After bonding, the accurate reference bars will be removed; only the second set will fly. Experiments using this approach on groups of 40–80 segments indicate improvement of the HPD to ≤ 1.2 arcmin.

(v) The mirror has a substantially higher mass allowance (44 kg, compared with the 20 kg per Suzaku mirror). While the total mass of the mirror substrates is considerably larger than Suzaku (due to both the larger number of substrates and the use of thicker aluminum), the housing will comprise a larger fraction of the mirror mass (41 percent, compared with 25 percent for Suzaku). The resulting stiffer housing will reduce blur.

Foil mirrors also are being utilized on the Gravity and Extreme Magnetism Small Explorer (GEMS), a mission devoted to X-ray polarimetry scheduled for a 2014 launch. GEMS has three identical telescopes, each consisting of a foil mirror and a novel, time projection chamber X-ray polarimeter. The instrument operates in the 2–10 keV band. While the polarimeter is not an imaging instrument, use of an imaging mirror allows accurate placement of a concentrated beam at its small entrance aperture, thus substantially increasing instrument sensitivity. The mirror design is based on the Suzaku design, with the same 4.5 m focal length. Fitting three coaligned telescopes in the SMEX fairing constrains the diameter of each mirror to be 32 cm.

Table 2: The foil mirrors being developed for Astro-H.

	SXT	HXT
Diameter (cm)	45	45
Focal length (m)	5.6	12
Number of shells	203	213
Number of modules per mirror	4	3
Segment length (cm)	10	20
Total number of segments	1624	1278
AI Substrate thickness (mm)	0.152, 0.229, 0.305 mm	0.2 mm
Surface production method	replication	replication
Reflective coating	gold	Pt/C multilayer
Mass (kg)	56	80
Effective Area (cm^2)	510 @ 1 keV	800 @ 6 keV
	390 @ 7 keV	200 @ 40 keV
Angular resolution (arcmin)	1.7 (goal <1.3)	2 (goal <1. 7)

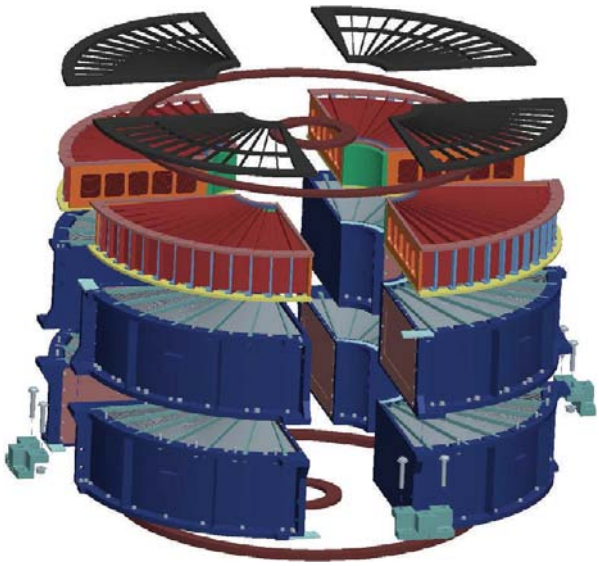

Figure 9: Exploded view of the Astro-H Soft X-ray Telescope. The mirror is segmented into quadrants. The main components, from the bottom, are inner and outer lower mounting rings, the two reflection stages, the stray light baffle, the inner and outer upper mounting rings, and the thermal shield. The overall dimensions of the assembled mirror are 47 cm in diameter and 25 cm high.

The GEMS mirrors are thus basically a smaller diameter version of the Suzaku mirrors, with 110 nested shells. The same forming and replication mandrels will be used to produce the segments, and the same lightweight housing design will be used, scaled to the smaller diameter. The resulting difference in effective area from the Suzaku mirrors primarily affects the band below 2 keV where the detectors are not sensitive. The angular resolution requirement is 1.3 arcmin, better than that achieved on Suzaku, but achievable given the smaller size and number of shells and taking advantage of some of the process improvements developed for Astro-H. Each mirror will have a mass of 10 kg.

The Indian observatory Astrosat, to be launched around 2012, will include in its instrumentation a modest X-ray imaging system consisting of a foil mirror and a CCD detector [21]. The mirror will have a focal length of 2.0 m and a diameter of 26 cm. The angular resolution is estimated to be about 3 arcmin. The effective area will be about 200 cm^2 at 2 keV and 25 cm^2 at 6 keV. The mirror segments will be fabricated using the same replication process as for Astro-E/E2 and subsequent foil mirrors. The mirror is being constructed at the Tata Institute of Fundamental Research, where the facility used for constructing the Astro-E/E2 mirrors was duplicated.

7. Multilayers

Imaging in the hard X-ray band, above 10 keV, is a true experimental challenge. Because the fluxes of all cosmic X-ray sources decline with increasing energy, performing detailed imaging observations requires substantial collecting area. At the same time, the critical angle of even the highest density metallic coatings becomes very small, leading to very large focal ratio mirrors. (Typically, for a given coating, the maximum energy that can be imaged $E_{\max}$ is proportional to the ratio of the focal length F to the mirror diameter d: $E_{\max} \propto F/d$.) However, shorter focal ratios that can realistically be implemented into instruments can be obtained by the use of multilayer coatings.

A multilayer consists of alternating layers of high and low Z material, with typical bilayer thicknesses of a few nm. The thickness of the two layers is controlled during deposition to produce efficient Bragg scattering at reasonable grazing angles for energies of interest. A uniform multilayer has efficient response only over a narrow range of energies. The invention of graded multilayers has made possible mirrors with a broadband response [22]. The layers have increasing thickness according to some prescription as a function of distance from the substrate. The thicker, outer layers reflect X-rays from the lower end of the band of interest, while the higher energy X-rays that penetrate more deeply into the layer are reflected by the deeper, more closely spaced layers. The original concept for graded multilayers introduced a power law layer variation with distance. Yamashita et al. [23] introduced the "supermirror" concept wherein the continuous gradation is replaced by a series of groups of identical thickness layers. They showed that the X-ray reflectivity of such a multilayer is comparable to that expected from an optimum grading.

Foil mirrors are attractive as high-energy mirrors because of their large geometric filling factor. With multilayers applied to the surfaces, they become efficient mirrors above 10 keV. Table 3 lists segmented multilayer mirrors that have either flown or are under construction.

The initial means for applying multilayers onto substrates was to coat the multilayers on top of the gold surface of an epoxy replicated segment [23]. This is an inherently slow and low yield approach because of the great

Table 3: Multilayer coated foil mirrors.

	InFOCμS	HEFT	SUMIT	NuSTAR
Diameter (cm)	40	24	36	38
Focal length (m)	8	6	8	10
Number of shells	255	72	90	130
Number of modules per mirror	4	1*	3	1*
Segment length (cm)	10	2×10**	13	22.5
Total number of segments	2040	700	540	2340
Substrate material	aluminum	glass	aluminum	glass
Substrate thickness (mm)	0.17	0.3	0.22	0.21
Surface production method	replication	thermal forming	replication	thermal forming
Multilayer coating	Pt/C	W/Si	Pt/C	Pt/C, W/Si
Effective area (cm^2)	51	50@40		150
Angular resolution (arcmin)	2.7	1.3	2.06	<60
Year of launch	2001, 2004	2005	2006	2012

*HEFT and NuSTAR mirrors consist of one module, but shells are composed of multiple segments.
**Each reflecting stage consists of a pair of segments.

care that must be taken to not damage the epoxy surface by overheating during deposition (the epoxy surfaces will be damaged if heated about ~40°C). It was subsequently demonstrated that multilayers could be replicated the same way as a gold monolayer: the multilayer is grown on a glass mandrel and then transferred to the aluminum substrate using epoxy replication. This introduced a major advance in production speed and yield.

This approach was used to produce the first multilayer imaging mirror for hard X-rays [24, 25]. This mirror was used on the International Focusing Optics for MicroCrab Sensitivity (InFOCμS) balloon instrument, flown for the first time in 2001 (and an upgraded version flown twice subsequently), and has produced the first images of cosmic sources in the 20–40 keV band using multilayers. This mirror used the same fabrication, mounting, and alignment techniques as used for Astro-E/E2, the only difference being the use of replicated multilayers for the reflecting surface instead of a gold monolayer. Like the Astro-E mirrors, it has a diameter of 40 cm, but it has a focal length of 8 m. A total of 255 nested shells are required. A graded Pt/C multilayer was transferred via epoxy replication onto each substrate. In the most recent mirror upgrade, the substrates were divided into 12 groups by radius, with the same multilayer prescription applied to each substrate in a group [26]. The block prescription introduced by Yamashita et al. [23] was used to determine the number of layers and the thickness of each [27]. Each mirror segment had between 28 and 78 layers, with layer thickness between 2.61 nm and 12.64 nm. This mirror has an angular resolution of 2.1–2.4 arcmin in the 20–60 keV band and an effective area of 51 cm^2 at 30 keV [28].

A mirror of similar design was constructed using the InFOCμS approach for the Supermirror Imaging Telescope (SUMIT) balloon instrument [29, 30]. Design differences were introduced in order to improve the angular resolution and the effective area (through the reduction of misalignments). The key differences were the use of thicker and longer foils (to increase stiffness and reduce the number), subdividing shells into thirds rather than quadrants (to reduce end effects), and using single housing unit instead of separate modules (to increase overall structural stiffness). These changes did lead to improved angular resolution and effective area over InFOCμS. The angular resolution measured on the ground was 2.06 arcmin. Despite the fact that only the inner 36 cm of the 40 cm aperture was populated with segments, the effective area at 30 keV was virtually the same as the 40 cm diameter InFOCμS mirror. This indicates that coupled with the higher angular resolution, less light was lost due to misalignment or internal blockage. SUMIT was launched from Brazil in late 2006, but unfortunately was lost at sea.

The combined experience of the InFOCμS and SUMIT mirrors has been employed in the design of the Hard X-ray Telescopes (HXTs) that will fly on Astro-H [31]. These mirrors are being constructed by a consortium of Japanese institutions led by Nagoya University. The HXTs are the most ambitious hard X-ray mirrors under development. Each has a diameter of 45 cm and a 12 m focal length. As was the case for SUMIT, each shell is divided azimuthally into only three segments, and an integral housing is used. The mirror consists of 213 nested shells. Aluminum substrates 0.2 mm thick will be used. The mirror segments are 20 cm long in order to reduce the number of nested shells and increase the clear aperture. Another innovation is that the housings will be considerably more massive, to minimize distortions. Each mirror has a total mass of 80 kg, four times more massive than the Suzaku mirrors. The required angular resolution is 2 arcmin (HPD), but the expected angular resolution is <1.7 arcmin. Graded Pt/C multilayers, designed using the supermirror approach, are transferred to the segments. The expected effective area of each mirror is 800 cm^2 at 6 keV and 420 cm^2 at 40 keV.

8. Limiting Factors to Angular Resolution in Foil Mirrors

Over the 30 years of development, there has been substantial improvement in foil mirror performance. The angular resolution has improved incrementally with each new generation of mirror. The introduction of epoxy replication removed the energy dependence of the point-spread function. More accurately machined and stiffer housings have reduced misalignments. Better substrates and forming mandrels have reduced figure errors on individual segments. Nevertheless, no foil mirror has attained an angular resolution better than one arc minute.

A number of error budget analyses for various foil mirror implementations have been presented (e.g., [30–32]). The key contributors to blur include misalignment of segments within the housing, misalignment of primary and secondary segments, macroscopic axial figure errors on the foil surfaces, and distortions introduced by the mismatch between the segment shape and its location in the housing (effectively delta-delta-R errors). The intrinsic angular resolution due to the conical approximation is generally small compared with any of these terms. These analyses universally conclude that several terms contribute approximately equally. Thus all must be addressed if significant improvement is to be achieved. From the discussion above about the Astro-H SXT design, it can been seen both that incremental improvements are still being made and, more importantly, that addressing errors across a broad front can potentially lead to a considerably better mirror. Still it is unlikely that an aluminum foil mirror will ever achieve angular resolution substantially better than one arc minute. As we describe below, however, use of a different substrate material allows for construction of a high angular resolution mirror that preserves many of the desirable attributes of the foil mirror.

9. Glass as a Substrate

Aluminum has numerous desirable attributes as a substrate material for foil mirrors: low density, easy to form, moderate cost, good surface properties. Nevertheless it is not ideal; it is flimsy, cannot be formed in three dimensions (i.e., cannot impart the axial curvature of a true Wolter mirror), and most importantly the surface quality of even the best material limits the attainable resolution to about an arc minute, considerably worse than the intrinsic resolution of the conical approximation for typical designs. Hailey et al. [33] performed a careful characterization of the surface properties of Al and concluded that the surface properties limit the angular resolution of even a perfectly aligned aluminum foil mirror to 25 arcsec. Hailey was especially interested in a substrate to which multilayers could be applied. For a W/Si multilayer, Mao et al. [34] found that the interfacial roughness on glass (3.5–4.0 Å) was lower than that on an epoxy replicated foil (4.5–5.0 Å) (they did not try multilayer replication).

A number of alternative materials have been proposed: different metallic foil, silicon, carbon fiber-reinforced plastic. Each of these materials introduces a new set of challenges. The most promising alternative material, and one that has produced a revolution in thin substrate mirrors, is glass. In searching for an alternative substrate for aluminum for hard X-ray mirror for a balloon instrument, Hailey et al. [33] showed that the intrinsic surface quality of commercially available borosilicate glass is far superior to that of aluminum. Moreover, the glass he investigated, commercially available Schott Desag D263 and AF45, has good mechanical properties, even at thicknesses of 200–400 μm. Hailey developed a thermal slumping approach to form the glass to its approximate shape. Multilayers could be directly deposited onto the glass substrate without a microroughness increase.

The slumping approach introduced by Hailey et al. [33] entails suspending a flat piece of glass substrate across a concave mandrel, and slowly thermally cycling it so that the glass assumes the form of the mandrel. While the figure of the substrate is not precise (Hailey et al. use cylindrical molds), the excellent microroughness of the surface is preserved. A slow thermal cycle in which the glass is annealed as it cools allows the glass to largely retain its mechanical properties.

The first use of glass substrates in a full mirror was for the High Energy Focusing Telescope, a balloon instrument led by CalTech with mirrors supplied by Columbia University. HEFT was designed to be sensitive in the 20–70 keV band. The mirror surfaces were therefore coated with a graded multilayer, in this case composed of tungsten and silicon. The mirror consists of 70 shells, with an outer diameter of 24 cm and a 6 m focal length. Each shell was conical approximation of a Wolter 1 and was comprised of 20 elements. The primary and secondary each consisted of two 10 cm long, end-to-end sets of five azimuthal segments. Each segment was 0.2 mm thick.

The HEFT mirror introduced a novel mounting and alignment scheme. The mirror was built outward from a central core. A set of carbon spacers was attached to the existing outermost shell (or the central core). The outer surfaces of these spacers were then machined in situ to the proper diameter and slope for the next shell. Then the 20 glass segments comprising the next shell were epoxied to the spacers, while the image formed by the shell was monitored optically. Once the epoxy set, the next layer was attached the same way. This mounting scheme is illustrated in Figure 10 and the mounting fixture in Figure 11. This mounting approach has three significant advantages over the approach used for foil segments. Mechanically it yields a rigid structure, which is unlikely to experience changes due to vibration or shock. The in situ machining eliminates stack up error and ensures confocality. The forcing of the stiff glass substrates into contact with the accurately machined spacers forces them to maintain a conical shape to high accuracy. The performance of a mirror constructed using this approach therefore has the potential for better angular resolution than foil mirrors mounted in the traditional way, with the blur dominated by substrate misalignments and figure errors.

Three HEFT mirrors were constructed. Two are shown in Figure 12. The angular resolution of the best mirror was ~1.3 arcmin at 8 keV [35, 36]. There was a clear angular

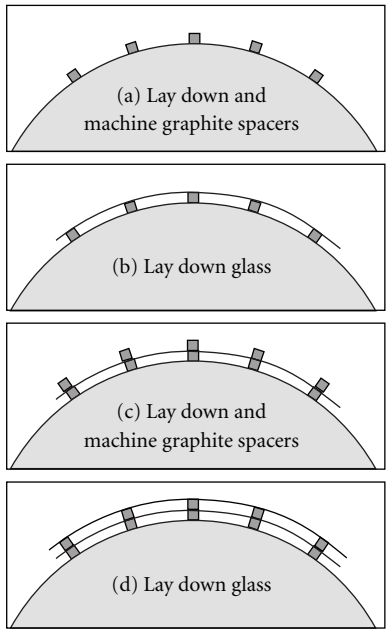

Figure 10: The mounting scheme for thermally formed glass mirrors invented for HEFT.

resolution improvement from the inner shells to the middle ones, across the boundary where the spacer density doubled. This is likely due to the fact that the larger number of spacers forces the glass substrates to conform more closely to the ideal conical surface. The effective area was within 20 percent of expectations from modeling, approximately 20 cm^2 at 25 keV. HEFT was flown in May 2005, but no report of its performance has been published.

10. Future Application of Glass Substrates: NuSTAR

The HEFT balloon mirror serves as the prototype of the Nuclear Spectroscopy Telescope Array (NuSTAR), a Small Explorer expected to be launched in 2012. NuSTAR features a pair of conical slumped glass mirrors. Each mirror has a 38 cm diameter and a 10 m focal length. It consists of 133 nested glass shells with segment length of 22.5 cm. The outer 65 shells consist of 12 pairs of azimuthal segments, the inner 65 of 6 pairs. The angular resolution requirement is 60 arcsec (HPD); the goal is 40 arcsec. Each mirror is expected to have a mass of 24.5 kilograms [37].

The mirror substrates are 210 μm thick D263 glass. They are heat formed into a cylindrical shape. In contrast to the substrates for HEFT, these are thermally formed using convex mandrels incorporating slumping technique developed for IXO (described below). The mandrels are polished commercial grade fused silica. Adopting the approach under development for IXO has resulted in formed glass substrates with excellent figure: the typical two-reflection HPD for the uncoated substrates is 40 arcsec, with many around 30 arcsec. Thus the possibility exists that the integrated mirrors will attain the angular resolution goal.

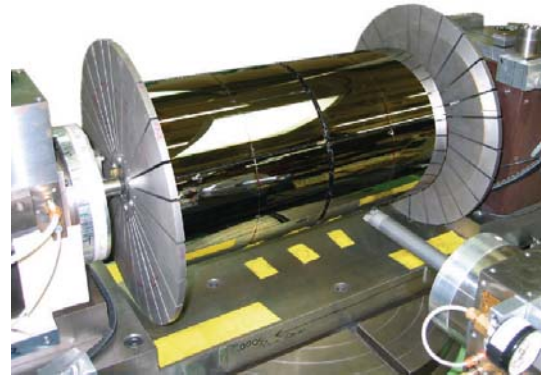

Figure 11: Fixture used to align and mount HEFT.

Figure 12: Two HEFT mirrors. Each mirror is 24 cm in diameter and 40 cm long and consists of 70 nested formed glass shells.

The mirrors are mounted and aligned using the approach developed for HEFT. Improved alignment machines have been fabricated.

11. Slumped Glass Mirrors for Constellation-X/XEUS/IXO

The introduction of slumped glass substrates stimulated work by a number of investigators seeking a means of forming thin substrates capable of providing high angular resolution. The motivation for this work comes from the consensus need for the next major X-ray astronomy mission—a substantial increase in collecting area combined with high angular resolution, to facilitate spatially resolved spectroscopy of distant (and hence faint) objects. The high angular resolution is driven by the need to perform spatially resolved spectroscopy of extended objects (clusters of galaxies, supernova remnants) as well as measure the spectrum of extremely faint objects without source confusion. The original NASA implementation was Constellation-X; the ESA implementation was the X-ray Evolving Universe Spectroscopy (XEUS). In 2007, these missions were merged into the International X-ray Observatory (IXO). For Constellation-X, the baseline implementation utilized slumped glass, with technology development led by GSFC. For XEUS, the baseline mirror was a Silicon Pore Optic

(SPO). Slumped glass was considered a backup technology for XEUS, with technology development at the Max Planck Institut für Extraterrestrische Physik (MPE) and at the *Osservatorio Astronomico di Brera* (OAB). All three institutions are participating in the glass technology development for IXO.

The fundamental differences between Constellation-X and XEUS on one hand, and IXO on the other, are the size and performance specifications of the mirror. Constellation-X incorporated an array of four identical mirrors, each with a 1.3 m diameter and a 10 m focal length. The angular resolution was to be 15 arcsec HPD, with a goal of 5 arcsec. XEUS was to have a single mirror, with 5 m^2 of collecting area and a 50 m focal length. The angular resolution was to be 5 arcsec HPD, with a goal of 2 arcsec. IXO incorporates a single, large diameter mirror with 20 m focal length, 3.3 m diameter, and mass of 1750 kg. The effective area at 1.25 keV is to be at least 2.5 m^2 with a 3.0 m^2 goal and 0.6 m^2 at 6 keV. The angular resolution of the entire observatory is to be 5 arcsec; to achieve this, the mirror angular resolution must be ~3-4 arcsec. Two approaches to the mirror are being pursued. ESA is developing a mirror based on silicon pore optics (SPO), wherein commercially available 0.773 mm thick Si wafers are stacked to form a conical approximation of a Wolter I mirror [38–40]. Careful stacking and alignment of the wafers lead to a mirror in which the dominant component of the angular resolution error budget is the conical approximation. The second approach, under study by NASA and independently in Europe at MPE and OAB, uses segmented glass substrates, slumped into a Wolter shape, and mounted accurately into groups of identical modules [41–43]. Note that unlike previous implementations in which a conical approximation sufficed, true Wolter surfaces are required if the angular resolution requirement is to be met for IXO. But as for previous foil mirrors, a key design parameter in the IXO design is the effective area per unit mass.

A possible slumped glass design for the IXO mirror (Figure 13) consists of 361 nested Wolter I shells [44]. The mirror is divided into three rings of modules. The intent of the modular design is that all the precision alignment and mounting (and thus all technology development) are contained within a module; aligning the modules to each other is straightforward. The inner ring has 12 identical modules, and the middle and outer rings each have 24. Each mirror segment is 20 cm in axial length; no segment has an arc length longer than 40 cm. The inner module contains 143 segment pairs, the middle 115, and the outer 103. Thus a total of 13,986 segments are incorporated into the full mirror. The module structure must be carefully CTE matched to the glass to minimize the introduction of blur due to thermal gradients. The modules vary in mass between 16 and 23 kg.

Thin slumped glass is the substrate of choice because of its combination of desirable mechanical and optical properties. The fundamental technical challenges associated with using slumped glass are (i) how to introduce via thermal forming a surface with a contribution of <1.5 arcsec to the angular resolution error budget; (ii) how to mount and align these flimsy substrates without introducing stresses

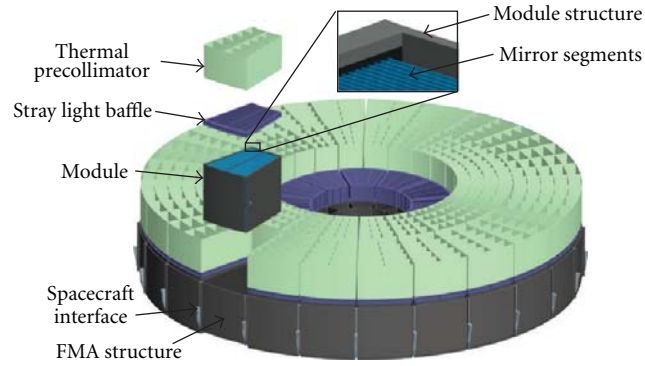

Figure 13: Schematic of the NASA reference design of the IXO mirror. The mirror consists of 361 nested shells, in 60 modules. The overall diameter of the aperture is 3.3 m.

or distortions. While neither goal has been accomplished, substantial progress has been made towards them.

In the NASA approach, the glass is slumped onto a convex mandrel (the European glass mirror development partly retains concave mandrels). The primary reason for using a convex mandrel is because in a concave mold, thickness variations in the substrate, even if they are fractions of a micron, would introduce figure errors even in a substrate that conforms exactly to the mold. In the IXO design, a 1 μm error in the mirror curvature corresponds to a blur of 8 arcsec. Mandrels and formed substrates are shown in Figure 14.

Use of a convex mold means that the X-ray reflecting surface comes into contact with the mandrel. The Columbia group used concave mandrels to avoid this contact, to ensure preservation of the excellent microroughness of the raw material. Zhang et al. have found that use of a suitable release layer on a convex mold preserves the microsurface quality [41]. The microroughness degradation is measured to be a most 1 Å. The challenges faced in forming precise mirror segments are threefold. (i) Mandrels with sufficiently high quality figure need to be mass produced. (ii) Distortions introduced into the glass from the slumping must be controlled. The most destructive distortions are those with spatial frequencies in the millimeter to centimeter range, the so-called midfrequency errors. (iii) Any X-ray reflective coating deposited onto the substrate must not distort it via bimorphic stresses.

Of the three challenges, the most formidable is the control of the midfrequency errors. Several optics manufacturers have the capability for producing mandrels of the required quality and quantity. Experiments have demonstrated that the bimorphic stresses imparted by iridium, the reflective coating of choice, can be compensated by the use of an undercoating material (such as chromium) that imparts opposite stress,. Control of the midfrequency errors depends on the release layer surface quality. Current experiments are concentrated on a boron nitride coating. Once the coating is applied, it must be conditioned through a series of buffing and thermal cycling steps.

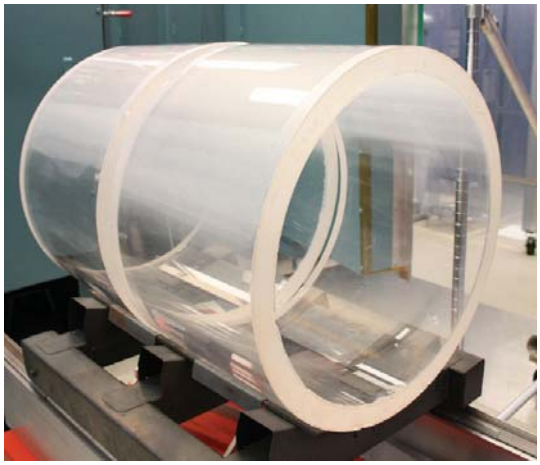

(a)

(b)

Figure 14: Two views of thermally formed glass substrates for IXO on mandrels. The mandrels are fused silica; each is approximately 50 cm in diameter. The two mandrels shown represent the primary and secondary reflection stages for a particular shell.

Results to date are promising. It has been shown that the formed substrates conform to the mandrel figure with very high fidelity. For a number of reasons, the required figure quality has not yet been attained. In order for the full mirror to have 3 arcsec resolution, the error budget requires each segment to have figure errors less than 2.3 arcsec. This is subdivided into error ascribed to the forming mandrel (1.5 arcsec) and error due to the forming process of 1.7 arcsec; dominating this 1.7 arcsec is the midfrequency error due to the release layer. Mandrels with the required 1.5 arcsec HPD are only now available. Individual segments with figure of ~5 arcsec have been fabricated, and refinement of the process could make the requirement reachable within a few months.

The coated substrates must next be mounted accurately in a module without distorting the optical figure. Bending moments applied at mounting points propagate across the entire substrate, compromising the figure. What makes the mounting extremely challenging is that the substrates are

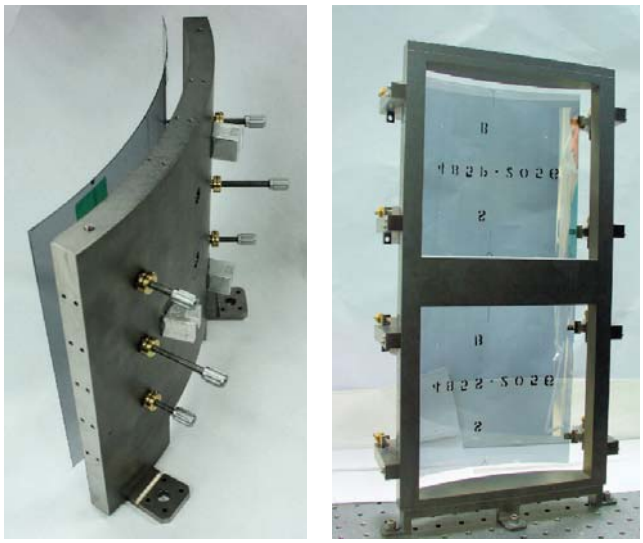

(a) (b)

Figure 15: (a) Rear view of an IXO mirror on a strongback for transfer to a permanent mount. The six actuators provide the mounting points. (b) A pair of uncoated IXO mirror segments mounted in a prototype permanent mount.

flimsy, bending under their own weight. At the same time, alignment tolerances are a fraction of a micron. To accurately align and mount the substrates, they need to be rigidized, but in such a way that the intrinsic shape is preserved. Alternatively, advantage can be taken of the segments' flimsiness, and the capability for correcting first-order figure errors (like out of roundness or cone angle variations with azimuth) can be incorporated into the alignment scheme. Both approaches are under study and are referred to as the "passive" and "active" approaches, respectively.

In the passive approach, the first step is to mount and bond the mirror segment temporarily onto a strongback, converting the flexible mirror segment into a *de facto* rigid body that can be handled, characterized, transported, and aligned (Figure 15). The mirror segment is next located and aligned properly in position and orientation using precision stages under the monitoring of an optical beam with grazing incidence Hartmann tests (i.e., sequential illumination of small angular portions of the mirror pair). Once the segment is aligned, it is bonded at several locations permanently to the module housing structure. The bonding process must not introduce stress or displace the segment. After the permanent bonds have cured, the transfer mount is removed.

In the active approach, radial displacements produced by actuators at the mirror segments' forward and aft ends are used to correct the mirror segments' tilt errors (pitch and yaw) and adjust cone angle to minimize the alignment aberrations of focus error and coma. After achieving the best possible focus, the mirror segment is permanently bonded to the module housing structure. After the permanent bonds have cured, the actuators are disengaged and removed.

X-ray measurements using a single mirror pair were most recently performed in 2007, using a different mounting

approach. The measured HPD was ~15 arcsec, consistent with performance predictions based on optical metrology of the mirror surfaces and the accuracy of the alignment [45]. Since that measurement, both mounting approaches have been shown to produce higher accuracy alignment, and the quality of the mirror segments has improved substantially [41].

Yet another approach would be slumped segments containing both the parabolic and hyperbolic surfaces on a single piece. The feasibility of doing this has been demonstrated at MPE [42]. Although mandrel fabrication for this approach is more challenging, the complexity of aligning the primary and secondary surfaces is avoided, and alignment errors thereby reduced.

12. The Future of Segmented Mirrors

The evolution of thin, segmented X-ray mirrors since their introduction 30 years ago has been remarkable. No longer are they merely considered as concentrators for enhancement of focal instrument sensitivity (although they still play that role on, e.g., GEMS). Through the introduction of new surface deposition methods (multilayers) and substrates (glass), they have evolved into the mirror of choice for high energy imaging (NuSTAR, the Astro-H HXT, and the hard X-ray capability on IXO). With the introduction of accurate substrate forming and precision mounting, they also now have the potential to provide high angular resolution. At the same time, their key advantages—high filling factor, low mass per unit collecting area, suitability for mass production, to name a few—remain attractive features of the design. With two upcoming space missions using (aluminum) foil mirrors (Astro-H and GEMS) and one using glass (NuSTAR), segmented X-ray mirrors play an essential role in the near-term future of X-ray astronomy. Owing to these factors and their scalability to large areas, segmented optics have become the de facto baseline for future X-ray missions.

One realm segmented mirrors opens to future exploration is imaging in very hard X-rays. New material combinations and manufacturing capabilities for multilayer coatings promise to extend the energy band accessible with direct imaging well beyond 100 keV for reasonable focal lengths (10–15 m) [46, 47]. A telescope using such multilayers would be able to detect astrophysically important nuclear transitions such as ^{56}Ni at 158 keV and ^{57}Co at 122 and 136 keV.

As discussed above, the proposed NASA implementation of IXO, which carries X-ray astronomy well into the 2020's, relies on segmented glass. Beyond that, NASA's vision mission Generation-X (Gen-X) calls for a single focal plane mirror system with 50 m^2 at 1 keV, which is unattainable unless a segmented approach is implemented [48]. It also calls for extremely high angular resolution (0.1 arcsec HPD). The starting point toward achieving such high resolution is a successful IXO development program leading to a ~3 arcsec HPD mirror. The angular resolution of this mirror would be further improved by making the mirror surfaces active, through, for example coating the back side of each glass segment with thin-film pixilated electrodes over a thin layer of piezoelectric material and then applying voltage to improve a segment's figure [49]. Segmented X-ray mirrors will continue to play a key role in X-ray astronomy instrumentation for the foreseeable future.

References

[1] P. J. Serlemitsos, "The Broad-Band X-Ray Telescope," in *X-ray Astronomy in the 1980's*, S. S. Holt, Ed., NASA TM 83848, 1981.

[2] P. J. Serlemitsos, "Conical foil x-ray mirrors: performance and projections," *Applied Optics*, vol. 27, no. 8, pp. 1447–1452, 1988.

[3] R. Petre and P. J. Serlemitsos, "Conical imaging mirrors for high-speed X-ray telescopes," *Applied Optics*, vol. 24, no. 12, pp. 1833–1843, 1985.

[4] E. Figueroa-Feliciano, P. Wikus, J. S. Adams et al., "Progress on the Micro-X rocket payload," in *Space Telescopes and Instrumentation 2008: Ultraviolet to Gamma Ray*, vol. 7011 of *Proceedings of SPIE*, June 2008.

[5] K. A. Weaver, K. A. Arnaud, E. A. Boldt et al., "Calibrating the broad band X-Ray telescope," *Astrophysical Journal, Supplement Series*, vol. 96, no. 1, pp. 303–324, 1995.

[6] Y. Tanaka, H. Inoue, and S. S. Holt, "The X-ray astronomy satellite ASCA," *Publications of the Astronomical Society of Japan*, vol. 46, no. 3, pp. L37–L41, 1994.

[7] P. J. Serlemitsos et al., "The X-ray telescope on board ASCA," *Publications of the Astronomical Society of Japan*, vol. 47, no. 1, pp. 105–114, 1995.

[8] H. W. Schnopper, "SODART telescopes on the Spectrum X-Gamma (SRG) and their complement of instruments," in *Advances in Multilayer and Grazing Incidence X-Ray/EUV/FUV Optics*, Proceedings of SPIE, pp. 412–423, July 1994.

[9] J. Polny, N. J. Westergaard, F. E. Christensen, H. U. N. Nielsen, and H. W. Schnopper, "Production, assembly and alignment of the XSPECT mirror modules for the SODART X-ray telescope on the spectrum röntgen gamma satellite," in *Grazing Incidence and Multilayer X-Ray Optical Systems*, vol. 3113 of *Proceedings of SPIE*, pp. 349–359, July 1997.

[10] F. E. Christensen, B. Madsen, A. Hornstrup et al., "X-ray calibration of the SODART flight telescopes," in *Grazing Incidence and Multilayer X-Ray Optical Systems*, vol. 3113 of *Proceedings of SPIE*, pp. 294–306, July 1997.

[11] P. J. Serlemitsos and Y. Soong, "Foil X-ray mirrors," *Astrophysics and Space Science*, vol. 239, no. 2, pp. 177–196, 1996.

[12] R. Laine, R. Giralt, R. Zobl, P. A. J. de Korte, and J. A. M. Bleeker, "X-ray imaging telescope on EXOSAT," in *Space Opt, Imaging X-Ray Opt Workshop*, vol. 184 of *Proceedings of SPIE*, pp. 181–188, 1979.

[13] A. Rasmussen, J. Cottam, T. Decker et al., "Performance characterization of the reflection grating arrays (RGA) for the RGS experiment aboard XMM," in *X-Ray Optics, Instruments, and Missions*, Proceeding of SPIE, pp. 327–337, July 1998.

[14] H. Kunieda, M. Ishida, T. Endo et al., "X-ray telescope onboard Astro-E: optical design and fabrication of thin foil mirrors," *Applied Optics*, vol. 40, no. 4, pp. 553–564, 2001.

[15] R. Shibata, M. Ishida, H. Kunieda et al., "X-ray telescope onboard Astro-E. II. Ground-based x-ray characterization," *Applied Optics*, vol. 40, no. 22, pp. 3762–3783, 2001.

[16] P. J. Serlemitsos, Y. Soong, K. W. Chan et al., "The X-ray telescope onboard Suzaku," *Publications of the Astronomical Society of Japan*, vol. 59, no. 1, pp. S9–S21, 2007.

[17] H. Mori, R. Iizuka, R. Shibata et al., "Pre-collimator of the astro-E2 X-Ray telescopes for stray-light reduction," *Publications of the Astronomical Society of Japan*, vol. 57, no. 1, pp. 245–257, 2005.

[18] K. Misaki, H. Kunieda, Y. Maeda et al., "Ground-based X-ray calibration of the telescopes onboard Astro-E2 satellite," in *Optics for EUV, X-Ray, and Gamma-Ray Astronomy*, Proceedings of SPIE, pp. 294–305, August 2003.

[19] K. Itoh, H. Kunieda, Y. Maeda et al., "Ground-based X-ray calibration of the Astro-E2 X-ray telescope II. With diverging beam at PANTER," in *UV and Gamma-Ray Space Telescope Systems*, Proceedings of SPIE, pp. 85–92, June 2004.

[20] T. Okajima, P. J. Serlemitsos, Y. Soong et al., "Soft x-ray mirrors onboard the NeXT satellite," in *Space Telescopes and Instrumentation 2008: Ultraviolet to Gamma Ray*, vol. 7011 of *Proceedings of SPIE*, June 2008.

[21] P. C. Agrawal, "A broad spectral band Indian Astronomy satellite 'Astrosat'," *Advances in Space Research*, vol. 38, no. 12, pp. 2989–2994, 2006.

[22] F. E. Christensen, A. Hornstrup, N. J. Westergaard, H. W. Schnopper, J. Wood, and K. Parker, "Graded d-spacing multilayer telescope for high-energy x-ray astronomy," in *Multilayer and Grazing Incidence X-Ray/EUV Optics*, vol. 1546 of *Proceedings of SPIE*, pp. 160–167, San Diego, Calif, USA, July 1991.

[23] K. Yamashita, "Supermirror hard-x-ray telescope," *Applied Optics*, vol. 37, no. 34, pp. 8067–8073, 1998.

[24] F. Berendse, S. M. Owens, P. J. Serlemitsos et al., "Production and performance of the InFOCμS 20-40-keV graded multilayer mirror," *Applied Optics*, vol. 42, no. 10, pp. 1856–1866, 2003.

[25] Y. Ogasaka, K. Tamura, T. Okajima et al., "Development of supermirror hard X-ray telescope and the results of the first InFOCuS flight observation," in *X-ray and Gamma-Ray telescopes and Instruments for Astronomy*, Proceedings of SPIE, pp. 619–630, August 2002.

[26] R. Shibata, Y. Ogasaka, K. Tamura et al., "Upgraded hard X-ray telescope with multilayer supermirror for the InFOCμS balloon experiment," in *UV and Gamma-Ray Space Telescope Systems*, Proceedings of SPIE, pp. 313–324, June 2004.

[27] T. Okajima, K. Tamura, Y. Ogasaka et al., "Characterization of the supermirror hard-x-ray telescope for the InFOCμS balloon experiment," *Applied Optics*, vol. 41, no. 25, pp. 5417–5426, 2002.

[28] R. Shibata, Y. Ogasaka, K. Tamura et al., "Development of hard X-ray telescope for InFOCμS balloon experiment," in *Optics for EUV, X-Ray, and Gamma-Ray Astronomy II*, Proceedings of SPIE, pp. 1–12, August 2005.

[29] T. Miyazawa, R. Shibata, Y. Ogasaka et al., "Development and performance of the advanced hard x-ray telescope for the balloon experiment," in *Space Telescopes and Instrumentation II: Ultraviolet to Gamma Ray*, Proceedings of SPIE, May 2006.

[30] Y. Ogasaka, K. Tamura, T. Miyazawa et al., "Thin-foil multilayer-supermirror hard X-ray telescope for InFOC S/SUMIT balloon exeriments and NeXT satellite program," in *Optics for EUV, X-Ray, and Gamma-Ray Astronomy III*, Proceedings of SPIE, August 2007.

[31] H. Awaki, Y. Ogasaka, H. Kunieda et al., "Current status of the Astro-H X-ray telescope system," in *Optics for EUV, X-Ray, and Gamma-Ray Astronomy IV*, Proceedings of SPIE, August 2009.

[32] H. Kunieda and P. J. Serlemitsos, "X-ray mirror assessment with optical light," *Applied Optics*, vol. 27, no. 8, pp. 1544–1547, 1988.

[33] C. J. Hailey, S. Abdali, F. E. Christensen et al., "Investigation of substrates and mounting techniques for the High Energy Focusing Telescope (HEFT)," in *EUV, X-Ray, and Gamma-Ray Instrumentation for Astronomy VIII*, vol. 3114 of *Proceedings of SPIE*, pp. 535–543, July 1997.

[34] P. H. Mao, F. A. Harrison, Y. Y. Platonov et al., "Development of grazing incidence multilayer mirrors for hard X-ray focusing telescopes," in *EUV, X-Ray, and Gamma-Ray Instrumentation for Astronomy VIII*, vol. 3114 of *Proceedings of SPIE*, pp. 526–534, July 1997.

[35] J. E. Koglin, C. M.H. Chen, J. C. Chonko et al., "Hard X-ray optics: from HEFT to NuSTAR," in *UV and Gamma-Ray Space Telescope Systems*, vol. 5488 of *Proceedings of SPIE*, pp. 856–867, June 2004.

[36] J. E. Koglin, W. H. Baumgartner, C. M. H. Chen et al., "Calibration of heft hard X-ray optics," in *X-Ray Universe 2005*, A. Wilson, Ed., vol. 2 of *ESA SP-604*, pp. 955–960, September 2006.

[37] J. E. Koglin, H. An, K. L. Blaedel et al., "NuSTAR Hard X-ray Optics Design and Performance," in *Optics for EUV, X-Ray, and Gamma-Ray Astronomy IV*, Proceedings of SPIE, August 2009.

[38] M. Bavdaza, PH. Gondoina, K. Wallaceb et al., "IXO system studies and technology preparation," in *Optics for EUV, X-Ray, and Gamma-Ray Astronomy IV*, Proceedings of SPIE, August 2009.

[39] M. J. Collon, R. Günther, M. Ackermann et al., "Stacking of silicon pore optics for IXO," in *Optics for EUV, X-Ray, and Gamma-Ray Astronomy IV*, Proceedings of SPIE, August 2009.

[40] M. Bavdaz, M. Collon, M. Beijersbergen, K. Wallace, and E. Wille, "X-ray pore optics technologies and their application in space telescopes," *X-Ray Optics and Instrumentation*, vol. 2010, Article ID 295095, 15 pages, 2010.

[41] W. W. Zhang, J. Bolognese, G. Byron et al., "Mirror technology development for the international x-ray observatory (IXO) mission," in *EUV and X-Ray Optics: Synergy between Laboratory and Space*, Proceedings of SPIE, April 2009.

[42] M. Vongehr, P. Friedrich, H. Bräuninger et al., "Experimental results on slumped glass x-ray mirror segments," in *Optics for EUV, X-Ray, and Gamma-Ray Astronomy III*, vol. 6688 of *Proceedings of SPIE*, August 2007.

[43] M. Ghigo, S. Basso, R. Canestrari et al., "Hot slumping glass technology and integration process to manufacture a grazing incidence scaled prototype for the ixo telescope modules," in *Optics for EUV, X-Ray, and Gamma-Ray Astronomy IV*, vol. 7437 of *Proceedings of SPIE*, August 2009.

[44] R. S. Mcclelland, T. M. Carnahan, M. K. Choi, D. W. Robinson, and T. T. Saha, "Preliminary design of the international X-ray observatory flight mirror assembly," in *Optics for EUV, X-Ray, and Gamma-Ray Astronomy IV*, Proceedings of SPIE, August 2009.

[45] W. W. Zhang, J. Bolognese, G. Byron et al., "Constellation-X mirror technology development," in *Space Telescopes and Instrumentation 2008: Ultraviolet to Gamma Ray*, Proceedings of SPIE, June 2008.

[46] F. E. Christensen, C. P. Jensen, K. K. Madsen et al., "Novel multilayer designs for future hard X-ray missions," in *Space Telescopes and Instrumentation II: Ultraviolet to Gamma Ray*, Proceedings of SPIE, May 2006.

[47] C. P. Jensen, F. E. Christensen, S. Romaine, R. Bruni, and Z. Zhong, "Stacked depth graded multilayer for hard X-rays, measured up to 130 keV," in *Optics for EUV, X-Ray, and Gamma-Ray Astronomy III*, Proceedings of SPIE, August 2007.

[48] S. J. Wolk, R. J. Brissenden, M. Elvis et al., "Science with generation-X," in *Space Telescopes and Instrumentation 2008: Ultraviolet to Gamma Ray*, Proceedings of SPIE, June 2008.

[49] D. A. Schwartz, R. J. Brissenden, M. Elvis et al., "On-orbit adjustment calculation for the Generation-X X-ray mirror figure," in *Space Telescopes and Instrumentation 2008: Ultraviolet to Gamma Ray*, Proceedings of SPIE, June 2008.

Hindawi Publishing Corporation
X-Ray Optics and Instrumentation
Volume 2010, Article ID 295095, 15 pages
doi:10.1155/2010/295095

Review Article

X-Ray Pore Optics Technologies and Their Application in Space Telescopes

Marcos Bavdaz,[1] Max Collon,[2] Marco Beijersbergen,[2] Kotska Wallace,[1] and Eric Wille[1]

[1] *European Space Agency, Keplerlaan 1, 2200 AG Noordwijk, The Netherlands*
[2] *Cosine Research B.V., Niels Bohrweg 11, 2333 CA Leiden, The Netherlands*

Correspondence should be addressed to Marcos Bavdaz, marcos.bavdaz@esa.int

Received 12 March 2010; Accepted 25 August 2010

Academic Editor: Stephen L. O'Dell

Silicon Pore Optics (SPO) is a new X-ray optics technology under development in Europe, forming the ESA baseline technology for the International X-ray Observatory candidate mission studied jointly by ESA, NASA, and JAXA. With its matrix-like structure, made of monocrystalline-bonded Silicon mirrors, it can achieve the required angular resolution and low mass density required for future large X-ray observatories. Glass-based Micro Pore Optics (MPO) achieve modest angular resolution compared to SPO, but are even lighter and have achieved sufficient maturity level to be accepted as the X-ray optic technology for instruments on board the Bepi-Colombo mission, due to visit the planet Mercury. Opportunities for technology transfer to ground-based applications include material science, security and scanning equipment, and medical diagnostics. Pore X-ray optics combine high performance with modularity and economic industrial production processes, ensuring cost effective implementation.

1. Introduction

With two powerful observatories already in space, X-ray astrophysics is enjoying a time of discoveries and exciting new science. XMM-Newton [1] and Chandra [2] were launched by ESA and NASA, respectively, more than a decade ago, and there is good hope that they will continue serving the science community well for another decade before consumables are exhausted or their support systems fail.

X-ray astrophysics has crucially contributed to our current understanding of the structure and history of the universe. The next generation X-ray astrophysics observatory [3] needs to employ a new X-ray optics technology, enabling a greater X-ray aperture size without sacrificing angular resolution in order to explore the Universe in even deeper detail and provide answers to the questions raised by Chandra and Newton.

High performance X-ray optics are regarded as the core enabling technology for the next-generation X-ray astrophysics observatories to follow the currently operating missions. The scientific importance of such a new space telescope is evident from the priorities expressed by the scientific communities in Europe, the USA, and Japan. In the ESA Science Programme, Cosmic Visions 2015–2025 [4, 5], the International X-ray Observatory (IXO) is one of three selected large class (L) mission candidates for a launch slot in 2020. IXO is also a high priority in the NASA and JAXA programmes and is being studied jointly by all three agencies.

European X-ray astrophysics has an impressive heritage, with a large number of missions from the early phases [6] with Exosat to the currently operating Newton [7, 8] observatory. Since such space missions have always been driving X-ray optics technology, each of them has advanced the state-of-the-art. For example, the Newton spacecraft carries three large area telescopes made from electroformed nickel shells. This technology was developed under ESA leadership in collaboration with European industry and research institutions. With this nickel optics, Newton provides a much larger collecting area (and therefore many more photons from the cosmological sources are delivered to the detector instruments) than the Chandra telescope operated by NASA (albeit at a reduced angular resolution to Chandra). It is largely due to its telescope technology that Newton is one the most productive ESA astrophysics missions to date (in terms of published papers).

The IXO mission, a merger of the XEUS [3, 9–11] and Constellation-X [12] mission concepts, has demanding requirements on the X-ray optics, which cannot be fulfilled with current state-of-the-art technologies. The Newton optics provide an angular resolution of about 12 arc seconds (″) half-energy-width (HEW), while IXO requires 5″. The effective area of the three Newton telescopes together is about 0.45 m^2 at 1 keV, while IXO requires an effective area of 3 m^2 to be provided, with the mass allocation to the optics only about 35% larger than that of Newton. The Chandra optics has a superb angular resolution of about 0.5″, but a prohibitive mass when applying the same optics technology to IXO.

A number of different X-ray optics technologies have been developed to maturity, optimised, and refined for space missions, and significant investments have been made to develop each of those. Despite the fact that these missions were designed and built to achieve a range of goals, requiring diverse effective areas and angular resolutions, their performances show a clear correlation. The areal density of the optics, that is, the effective area provided by a given mass of optics, appears to be linearly dependent on the resolving power of the optics, expressed as resolution elements per angular unit; see Figure 1. The requirements for IXO, however, clearly deviate from this line; IXO needs an optics technology that can offer a much more demanding combination of mass, effective area, and angular resolution.

Additionally, the IXO aperture is large and, therefore, a timely and cost-effective production of the required optics modules must be possible.

With the invention of Silicon Pore Optics [13, 14], a solution to the challenge to meet the IXO optics technology requirements was found. The required stiffness is achieved due to the monolithic pore structure of the optic modules that are individually aligned into the optical bench, replacing the mounting approach for individual shells used in more traditional X-ray optic technologies [12, 15, 16]. The span over which mirror elements must be self-supporting is drastically reduced in the pore optic due to the rib structure between shells, as opposed to the use of a few fixed mounting points in the traditional approach. This allows the mirror substrate thickness to be drastically reduced, allowing a much denser packing of mirror shells, thereby increasing the effective aperture without compromising the optics stiffness and figure accuracy. Compared to the replicated nickel shell X-ray optics technology the mass is reduced by an order of magnitude.

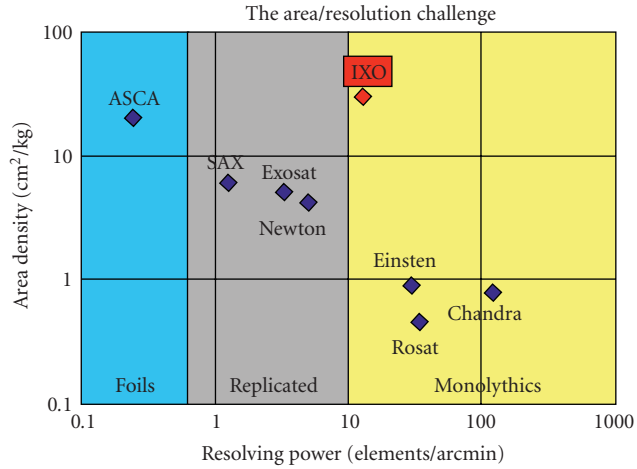

Figure 1: The effective area versus angular resolution challenge: A clear correlation is noted, when plotting the mass required to provide a given effective area as a function of the angular resolving power, expressed as resolution elements per angular unit. The X-ray optics flown to date can be separated into three groups: foil based optics, replicated shells and polished monolithic optics. Although these are very different from each other, the same area/resolution correlation is valid for all of them. The optics for each of the flown missions has been carefully optimised and raised to a high level of maturity. IXO requires a truly novel optics technology, clearly off the correlation line. The IXO optics technology has to be able to provide much more effective area per given mass, whilst maintaining the angular resolution performance than any of the preceding missions to date.

2. Silicon Pore Optics (SPO)

2.1. A Novel Approach to Making X-Ray Optics. The mounting concepts of the X-ray optics technologies used by the missions flown to date and plotted in Figure 1 share one common aspect. The optical mirror elements, be it closed shells or shell segments, are attached to the support structure on individual points. In most cases, a spider structure is used, to which the optical mirror element is attached at the intersection points. These mounting interfaces are rather localised and involve mechanical clamping or glue-spots to form the connection. In Figure 2, images A and B, the mounting concept for closed shells and sectors, respectively, is sketched.

The Silicon Pore Optics relies on a different mounting concept [13, 14, 17, 18]. The X-ray mirror elements are mounted along densely spaced lines, via ribs, which attach to the back of the mirror element; see Figure 2, image C. These mounting elements (ribs) have two functions: (1) they provide stiffness to the mirror element in the decisive longitudinal direction (parallel to the optical axis), and (2) they distribute the load over a line and not a point. The mirror element becomes much stiffer, and its figure much less distorted by the mounting elements.

The pore structure is obtained when mirror elements are stacked, attached to each other front-to-back, as illustrated in Figure 2, image D. The ribs on adjacent mirror elements are coaligned, jointly generating very strong structural walls. These radial walls, each of their extensions containing the optical axis, provide strength in the direction normal to the optical surface. Due to their dense packing, the required thickness of these walls is very small and the overall loss in geometric area is, therefore, comparable with that of the classical spider obscuration.

In the SPO technology, the mounting ribs are made of the same material as the mirror elements. Actually, the mirror element and the ribs are manufactured from a single

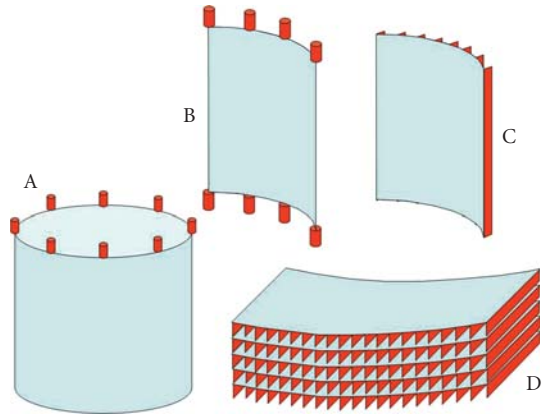

Figure 2: The mounting concept of traditional X-ray optics technologies is illustrated in images A and B. The closed mirror shells or sectors are mounted to the support structure at individual points. In the Silicon Pore Optics technology ribs attached to the back of the mirror elements form the mounting elements (image C). These ribs dramatically increase the stiffness of the mirror elements in the critical longitudinal direction. Mirror elements are stacked upon each other in the SPO approach, forming a stiff, monolithic structure containing many mounted mirror elements (image D).

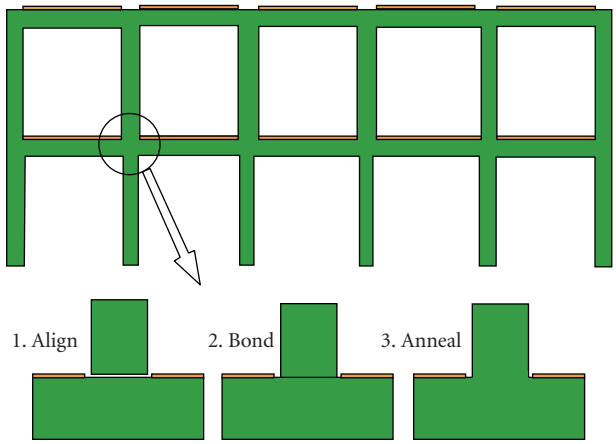

Figure 3: The mirror elements are joined using optical bonding, avoiding the use of glue or cement with its associated shrinkage and CTE mismatch problems. The mirror element stack is, therefore, a monolithic silicon crystal. If required, the mirror elements can be coated before the stacking process.

piece of silicon crystal. Therefore, the thermal expansion coefficient (CTE) of the mirror elements and ribs is identical. Individual, ribbed mirror elements are attached to each other using optical bonding. The surface of the rib tops, as well as the optical surfaces, must be of sufficient quality to ensure that the surfaces of adjacent plates bond to form a single monolithic structure. No glue is required, which would cause shrinkage and CTE mismatch problems. The stacking process and the merging of adjacent optical mirror elements is shown schematically in Figure 3. The mirror elements are first accurately aligned, then contacted to form a bond, and finally annealed to improve the strength of the joint. In Figure 3, it is also indicated by the orange lines, that the mirror elements can be coated as required before the stacking process, in order to increase the X-ray reflectivity. Note also that the unavoidable residual stress introduced by the coating (with its different CTE) is easily handled by the stiffness of the mirror element stack.

Considering the large number of required optics modules for a mission like IXO, it was very important to take into account mass production aspects right from the beginning of the technology development. Due to the small size of the SPO modules the production equipment can be kept compact, ensuring the cost-effective implementation of a production line, including the associated cleanroom infrastructure.

The production of the telescope optics for a large mission like IXO can be split into two streams, as indicated in Figure 4: (1) the production of SPO modules and (2) the integration and assembly of the SPO modules into the complete telescope. These two streams can be established at different geographic locations and assigned to different management structures if required.

2.2. Production of Silicon Pore Optics. X-ray optics require superpolished mirror surfaces. Similar requirements are imposed on the surface finish of the latest generation silicon wafers for the electronics industry. These are already commercially mass produced and very substantial investments have been made by the semiconductor industry to achieve the high quality surface finish. The surface roughness corresponds to that required for X-ray optics and the figure errors are within the error budget for a few arc second angular resolution optic [19, 20]. In addition, the surfaces of such double-sided polished wafers are very parallel, with very small thickness variations.

As illustrated in Figure 5, the starting material is procured and then processed for use in an SPO, relying largely on existing and modified processes available in the semiconductor industry. New processes and associated tools are developed only where required. The silicon pore optics production can be grouped as follows:

(a) production of ribbed and wedged silicon plates,

(b) coating of the plates,

(c) assembly into stacks of tens of plates,

(d) assembly of two stacks to form a mirror module.

The production of silicon mirror plates [21] starts with dicing SEMI standard ⟨100⟩ 300 mm silicon wafers, which are double sided polished and 0.775 mm thick, into square plates. The diced plates are then coated with a protective layer to prevent damage to the superpolished surface during the subsequent production steps (see Figure 6). The ribbing process dices grooves into the silicon substrate, thereby creating

(i) the pores forming the channels for the X-rays to pass through,

(ii) the ribs providing the required structural stiffness when bonded in a stack, and

(iii) a thin membrane.

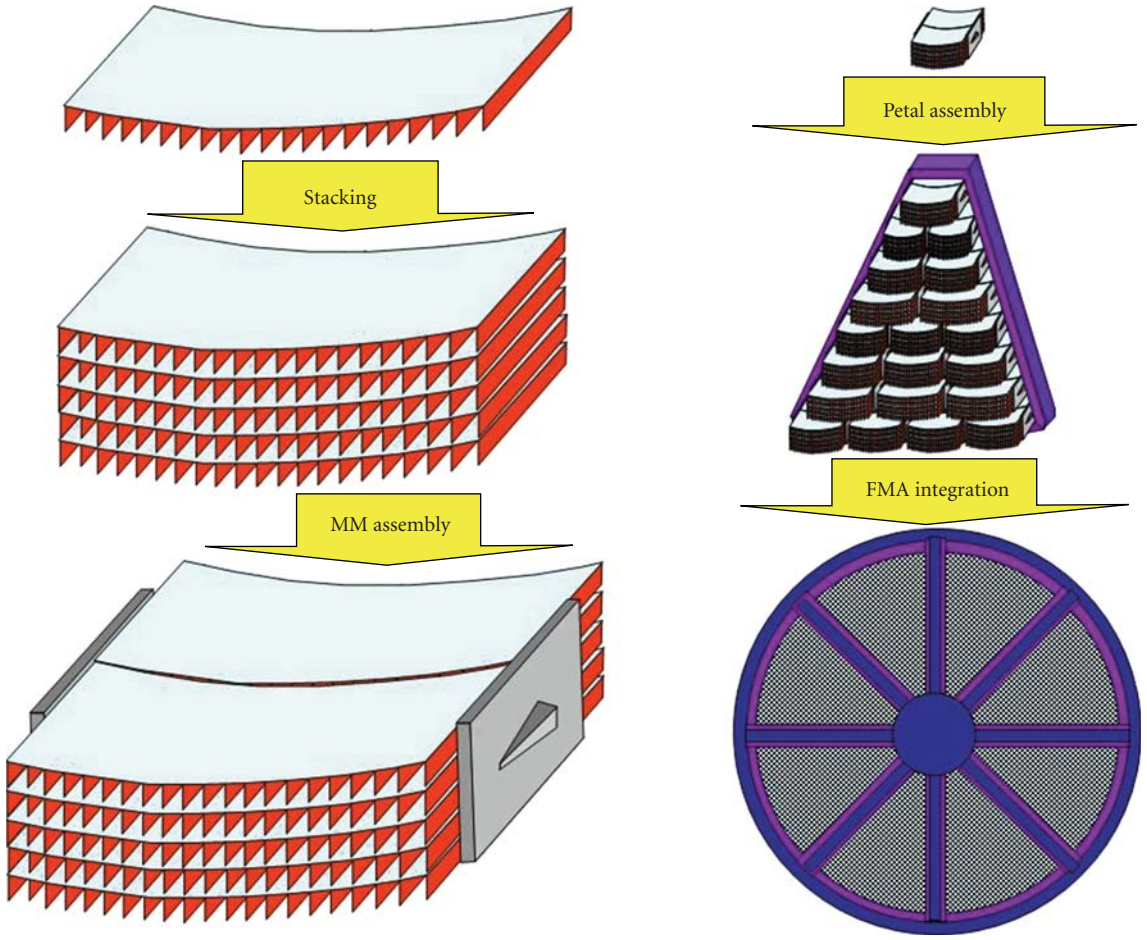

Figure 4: The production streams for a telescope using SPO technology.

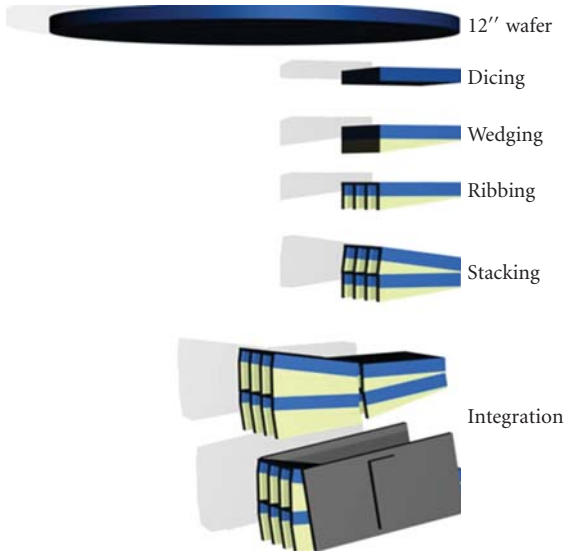

Figure 5: The production of SPO modules starts with commercial silicon wafers and utilises, as far as possible, existing methods and processes. The stacking is done automatically using a stacking robot.

Parameters such as rib width, pitch, number of ribs, and membrane thickness can be optimised for the specific application. Typically the ribs are 0.17 mm wide with a 1 mm pitch and a membrane thickness of 0.17 mm. A slightly modified standard semiconductor dicing saw is used for cutting the channels.

During stacking the plates will be elastically deformed [22] to create approximations of the curved surfaces of a Wolter-I optic [23]. To minimise the strain energy, one reduces the membrane thickness to a level sufficient to meet the figure requirements of the final optic. Although the plate ribbing process results in a well-defined pore geometry, a known side effect of dicing is the generation of microcracks in the material. Therefore, a second step in the shaping of the required rib geometry has to be applied to remove any residual microcracks, a so-called damage etch. A potassium hydroxide (KOH) solution is used to anisotropically and selectively etch damaged silicon material inside the diced grooves, while a protective coating is preventing the top surface of the ribs from being etched (see also Figure 6). Although the surface of the diced grooves remains rough after damage etching, this will not affect the optical performance of the telescope. In contrast, surface

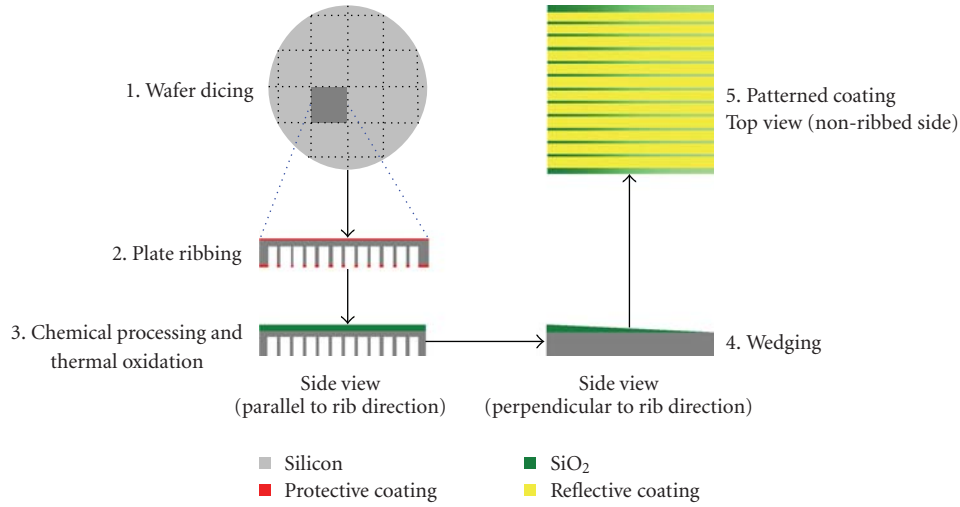

Figure 6: Schematic overview of process flow for production of Si mirror plates (Reproduced from [20]).

roughness within the grooves helps to absorb or at least scatter unwanted X-rays. Since in the SPO manufacturing one has full access to the pores during manufacturing of the plates, one could also apply other surface roughening techniques to further reduce stray light.

The goal of the wedging process is to taper plates along the optical axis so as to create, when they are elastically bent and stacked, a conical approximation to a Wolter I Optic (Figure 7). The wedge angle is proportional to the pore height, inverse proportional to the focal length of the optic and, therefore, independent from the radial position of the plate. Typically the wedge angle is a few 10 μrad, resulting on plate lengths of 66 mm in a wedge layer with a maximum thickness of a few 100 nm. The tapered wedge of the plates is applied by controlled etching of the plates in an isotropic etchant solution using custom-built equipment. The wedge angle accuracy directly influences the optical performance and has, therefore, to be controlled to 10 microarcsecond level. Dedicated equipment has been developed and reliably produces wedges well within this tight tolerance.

After wedging, a final processing step is necessary for optimization of the reflectivity of the mirror plates. High-Z metallic coatings such as platinum, tungsten, gold, or iridium are typically used to increase the reflectivity [24]. Patterning of the coated surface by metallic masks [25] or lithographic processes [21] is necessary to ensure bondability of the silicon mirror plates during the stacking process.

The silicon plate surfaces can be bonded either by hydrophilic or by hydrophobic bonding. Hydrophobic bonding occurs between two silicon layers which are typically made by removing the native oxide. Hydrophilic bonding occurs between two oxide layers, which can be native oxide layers of a few angstroms in thickness or thermal oxide layers of hundreds of nanometers. The bond strength of room temperature direct bonded wafers is highest for native oxide (83 mJ/cm^2) and thermal oxide (52 mJ/cm^2) and lowest for hydrophobic Si (10–20 mJ/cm^2) [26]. Note that the bond strength can be increased by a factor 10–20 if the bonded stacks are annealed.

The wedged mirror plates are then cleaned and elastically bent, using a fully automated stacking robot, into a conical shape. A flexible die is used to set the appropriate radius of curvature. The Wolter-I geometry of a parabolic and a hyperbolic mirror can, for long focal lengths, be approximated by two cones ("conical approximation"). When stacked the mirrors remain flat along the pores. The achievable angular resolution is then limited by the height of a single pore [27]. In the case of IXO with a focal length of 20 m and using pores with a height of 0.6 mm, this results in a lower limit to the half-energy width (HEW) of about 3″. To reduce the lower limit, we explore shaping the mirrors also in longitudinal direction.

The fully automated assembly robot (Figure 8) is specifically developed [28, 29] to stack silicon pore optics and is a combination of standard semiconductor systems and newly developed tools. The complete system has a footprint of a few m^2 only and is installed in a class 100 clean area. The robot selects a plate for stacking and inspects it for particles. The plate is then handed over to the actual stacking tool, which will elastically bend it into a cylindrical or conical shape. This tool, called a die, is then lowered onto the mandrel, where it will deposit the plate, or stack it, onto already existing ones. The die and the mandrel are supervised by metrology systems based on autocollimators, cameras and force sensors. Note that only the figure of the mandrel is replicated, not its roughness. The stacking is done from outer radii inwards, thus always exposing the last integrated mirror surface to the metrology tools.

Multiple mirrors stacked on top of each other form together a stack, in which the X-rays are reflected off the reflective membrane inside each pore. Due to the inherent stiffness of the stacks, the figure of the individual mirrors remains preserved during further mounting and integration. Two of such stacks are coaligned and integrated into brackets to form a so-called mirror module.

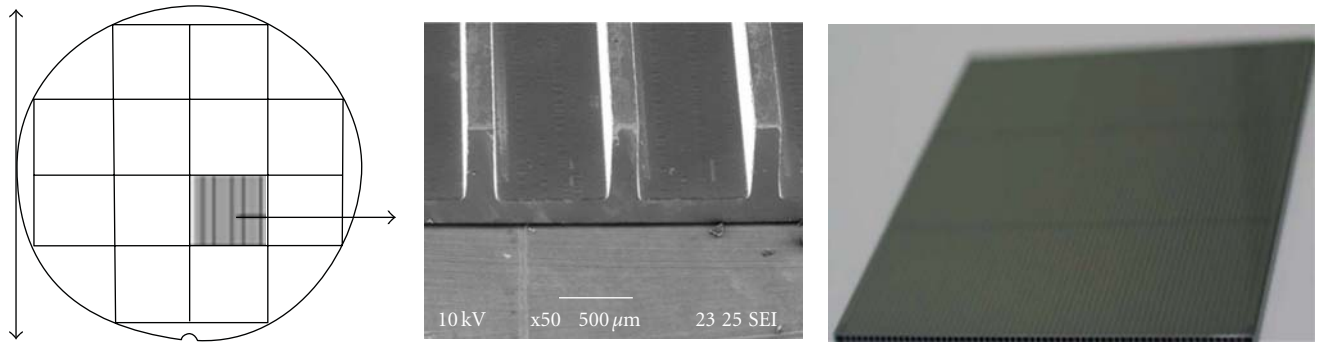

(a) (b) (c)

Figure 7: (a) Silicon Pore Optics are made from commercial high-quality 12″ silicon wafers which are diced into plates. (b) The plates are ribbed (reflecting surface pointing downwards). The 0.17 mm wide ribs have a pitch of 1 mm and the membrane is 0.17 mm thick. The plates are then wedged along the rib direction (not shown) and a patterned iridium coating is applied on the reflective surface (c). The pattern keeps the areas free where the next plate will be bonded. The plate shown has dimensions of $66 \times 66\,\text{mm}^2$ and a thickness of 0.775 mm. Photographs courtesy of Micronit (b) and DNSC (c).

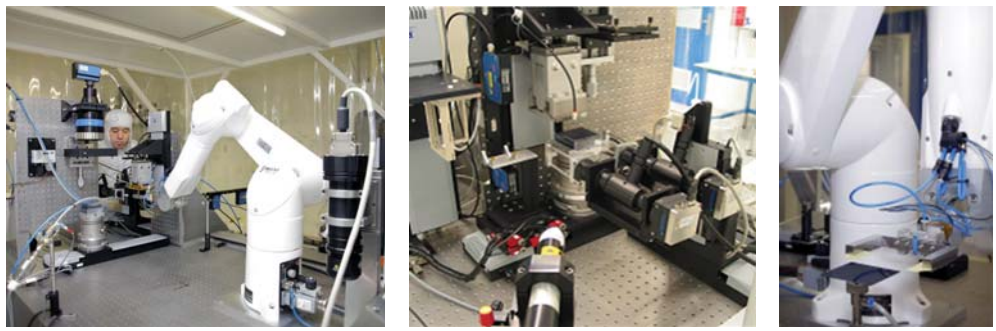

(a) (b) (c)

Figure 8: Stacking robot inside the class 100 clean area at cosine. The system is installed on a vibration isolated table, consists of more than 16 axes, is fully automated, and is designed to build stacks up to 100 plates high. The plates can be positioned with μm accuracy and automatically be bent into the required shape. Photographs courtesy of cosine Research BV.

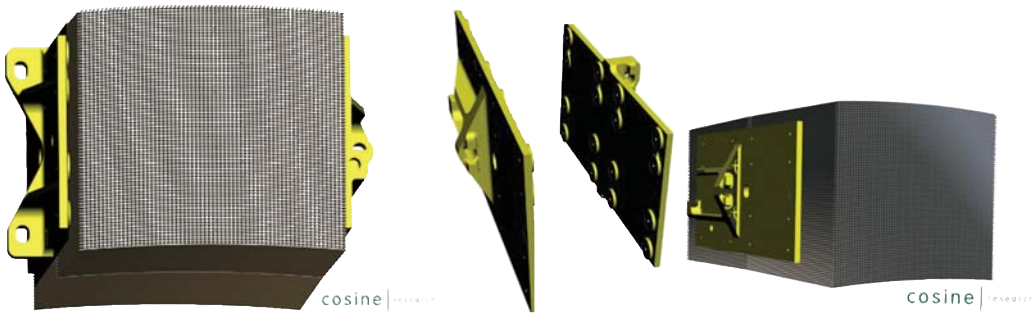

(a) (b)

Figure 9: A mirror module, consisting of two mirror stacks, coaligned to form a Wolter-I optics, is fixed by two CeSiC brackets. These brackets provide glue pads, petal interfaces, and integration interfaces. The area covered by the bracket is $92 \times 47\,\text{mm}^2$ and both brackets together have a weight of 56 g.

Several concepts on how to fix two stacks together, and thereby maintain particularly the tight tolerance on the kink-angle required for the Wolter 1 configuration, have been evaluated and traded [19]. The outcome was a simple design (Figure 9) consisting of two brackets, which are glued onto the two stacks, once these are coaligned. This very lightweight solution uses the intrinsic stiffness of a pore structure to form a rigid X-ray lens. The brackets have in total three interface points to the optical bench, which allow for radial translation and rotation around the optical axis. The bracket material of

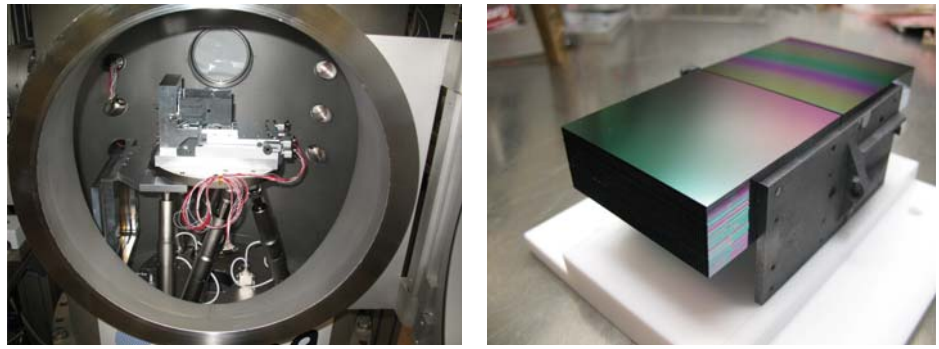

(a) (b)

Figure 10: (a) A mirror module inside the vacuum tank of the PTB X-ray test facility at the BESSY synchrotron in Berlin. (b) A mirror module consisting of two wedged stacks coaligned to arc-second level and fixated together by two silicon carbide mounting brackets. Photographs courtesy of ESA/PTB (a) and cosine Research BV (b).

choice is CeSiC, a silicon carbite ceramics, because it matches the CTE of silicon, has a high thermal conductivity, can be easily machined, and has excellent mechanical properties.

Several integration concepts were analysed in order to achieve the challenging requirement of 1″ for coalignment of two stacks. The simplest solution found was to align the optics under active X-ray illumination, since it simultaneously tests the optics at the wavelength under which it will operate and allows to determine the optical axis for integration into the optical bench [29, 30]. For this purpose, full beam illumination can be used; however, the required integration times can be quite long and an image is obtained that convolves alignment errors and possible figure errors. Pencil beam testing using a synchrotron source has been already successfully used to characterise silicon pore optics and has also been found to be well suited for measuring the coalignment of a mirror module. It yields a higher spatial resolution and the integration time on the CCD is only a few seconds (Figure 10).

A dedicated beamline has been set up in the laboratory of the Physikalisch-Technische Bundesanstalt (PTB) at the synchrotron radiation facility of BESSY [31]. A 2.8 keV pencil beam of dimension ranging from 1 mm down to 50 μm is used to scan the sample. After double reflection of the beam an image is recorded by the CCD, which is located at 5 m distance from the sample, providing arcsecond pixel resolution. The beam is used to probe the sample and the information thereby obtained is correlated with results obtained from interferometry during assembly of the stacks. Since the mirror module is then essentially an X-ray lenslet, residual integration errors can be partially corrected during integration into the optical bench [32] (see Figure 11), namely, by radial translation and rotation around the optical axis.

Currently, conical approximations to the Wolter 1 geometry are the baseline for the technology development, since metrology and the associated data analysis is somewhat simplified. In the case of IXO, the conical approximation contributes about 3″ to the HEW budget. Once the angular resolution performance of the SPO modules produced will approach closely the IXO requirements, the technology developments will start to use true Wolter geometries. The implication on the SPO production of moving to true Wolter 1 optics are fully understood, and the required equipment modifications have already been considered. Preliminary tests have demonstrated the required elastic bending of the mirror plates.

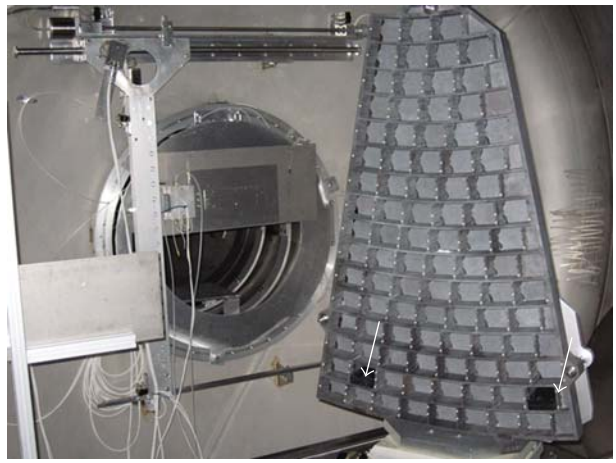

Figure 11: Cesic optical bench ("petal") with a height of 1.1 m inside the PANTER X-ray test facility, with two silicon pore optics mirror modules mounted (marked by white arrows) in flight representative configuration. Photograph courtesy of MPE/Kayser-Threde.

2.3. Performance of Silicon Pore Optics. The quality of silicon pore optics is measured throughout the production process [19]. After the plate has been stacked, its figure is measured using an interferometer equipped with a computer-generated hologram acting as nulling lens. Figure errors can be measured to $\lambda/20$, and the surface deviation measurements indicate whether residual particles have been trapped and what size they had. From these interferograms, it is possible to predict the X-ray performance of the mirrors.

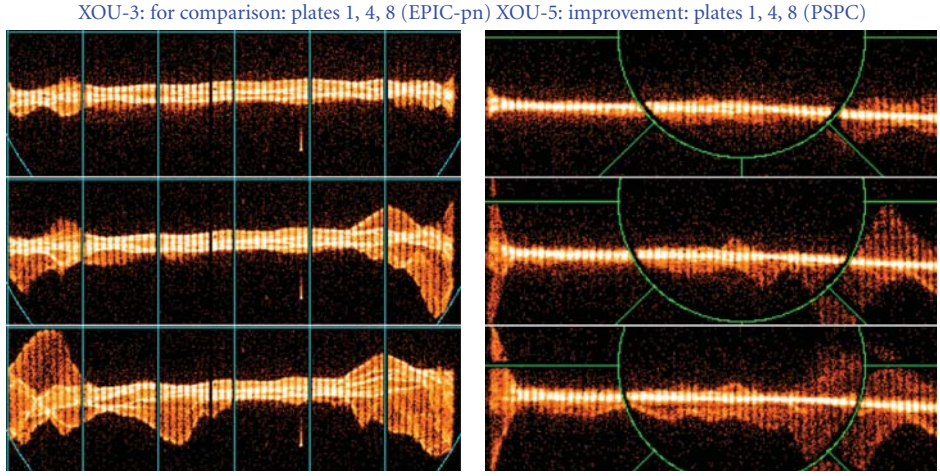

Figure 12: Examples of intrafocal measurements (camera was positioned 8 meters behind the optics) of the two mirror modules at the PANTER facility. The mirror module on the left was produced in 2007, the one in the right in 2009. From top to bottom plates 1, 4, and 8 are shown. The measurements have been taken at an energy of 3 keV. Such measurements allow to estimate the alignment of the individual mirror plates and to identify the location and magnitude of figure errors.

Full area illumination is used to characterise the optics, to measure scattering off the ribs, and to perform reflectivity as function of energy measurements.

Figure 12 shows a comparison of two different mirror modules, assembled between 2007 and 2009, and measured using 3 keV X-rays at the PANTER facility [33] of the Max Planck Institute für extraterrestrische Forschung (MPE). The figure shows a comparison of plates 1, 4, and 8. The significant improvement in quality is clearly visible from the direct comparison of the double reflected image measured under an incidence angle of 0.5 deg at a distance of 8 m.

Pencil beam X-ray measurements, measured at PTB, are used during alignment and integration of a mirror module and are then used to predict its optical performance by reflecting a small X-ray beam at grazing incidence of the surface of every plate/pore. These measurements allow determining the angular deviation of the mirror surface in each pore of a mirror module. Using raytracing algorithms [34], this allows us then to predict the PSF and HEW of the optic in the focal plane. In combination with the data taken from the individual stacks (see Figure 13), this gives additional information on how stack up errors propagate.

In November 2009, a mirror module (XOU5) was then measured in double reflection, mounted in flight representative configuration (i.e., the mirror module was mounted in a petal structure as required for IXO). From the results measured at 5 m, one can extrapolate an estimate for the PSF expected in the focal plane, shown in Figure 14 for the first 4 and for 20 plates.

Figure 15 shows the measured performance of the first assembled mirror modules made from silicon pore optics and an estimate for the further evolution. The quality of the optics has drastically improved with increased cleanliness of all involved process steps. The technological issues of cleanliness and bonding are being addressed by improved assembly hardware, developed in the course of the ongoing technology research program and during the steep learning curve in assembling pore optics. It shall be noted that so far no show stopper has been identified that would impede improving the performance of silicon pore optics beyond 5″.

2.4. International X-Ray Observatory. Silicon Pore Optics technology enables future X-ray telescopes with a large effective area and high angular resolution. The International X-ray Observatory (IXO) is an L-class mission candidate within ESA's Cosmic Vision 2015–2025 programme [5]. IXO is developed with the joint efforts of NASA, ESA, and JAXA and launch is planned for around 2021.

The key requirements of the IXO X-ray mirror are an effective area of 3 m^2 at 1.25 keV and an angular resolution of 5 arcsec HEW. Multilayer coatings on the inner part of the mirror will provide enhanced reflectivity for the 10–40 keV range, with an effective area of 150 cm^2 at 30 keV and 30 arcsec angular resolution. The available launchers limit the mass of the mirror assembly to 2000 kg, including mounting structure and thermal control. This requires a mirror technology with a very high area-to-mass ratio of 20 cm^2/kg, being 50 (8) times larger than for Chandra [2] (XMM Newton [1]). Two different approaches are studied by IXO: Silicon Pore Optics by ESA and Segmented Glass Optics by NASA.

The mirror diameter is 4 m, limited by the size of the fairing. To allow small grazing angles of incidence, a large focal length between 20–25 m is required. This is realized by connecting the mirror and the instrument modules by a deployable structure (see Figure 16). The spacecraft is folded to fit into the launcher fairing and deployed once in space.

IXO will contain five different instruments for imaging, spectroscopy, polarimetry, and timing measurements.

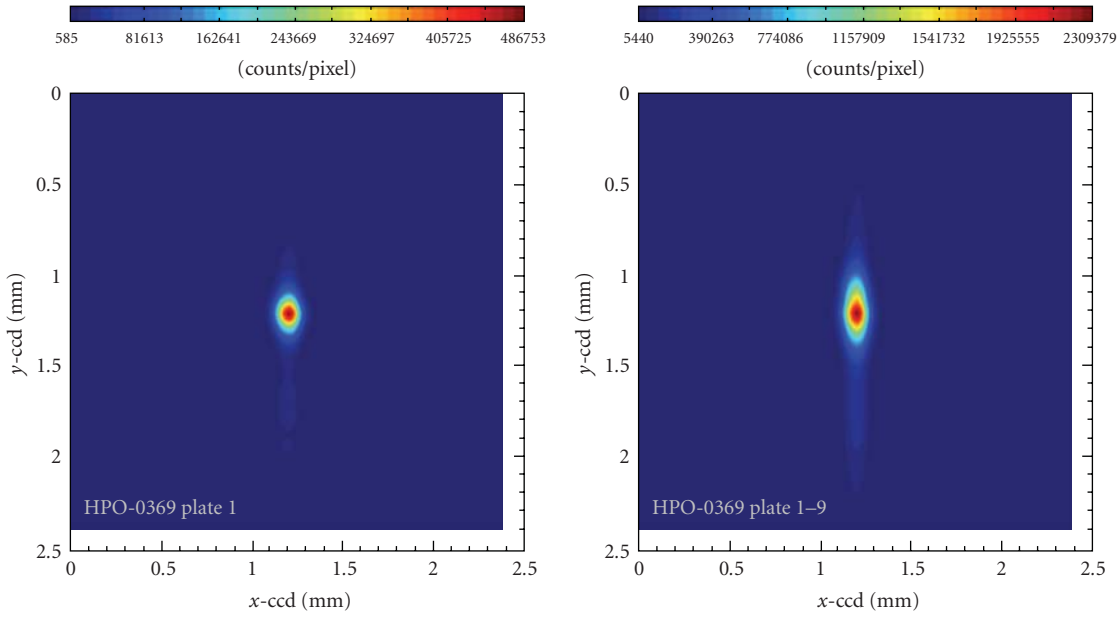

Figure 13: (a) PSF of the first plate (bottom) of a stack of 9 wedged plates measured using established procedures in single reflection at 2.8 keV at the FEM beamline in the PTB lab at the BESSY synchrotron radiation facility. The full length of the plate was scanned using a 100 μm pencil beam with an intrinsic HEW of 4″. The scans where repeated every 2 mm over the full width of the plate. The resulting PSF, excluding the direct beam, has a HEW of 4.2″. (b) The same measurement repeated on the entire stack of 9 plates. The HEW of the PSF, excluding the direct beam, is 7″. In double reflection this would result in a HEW of a mirror module of 10″.

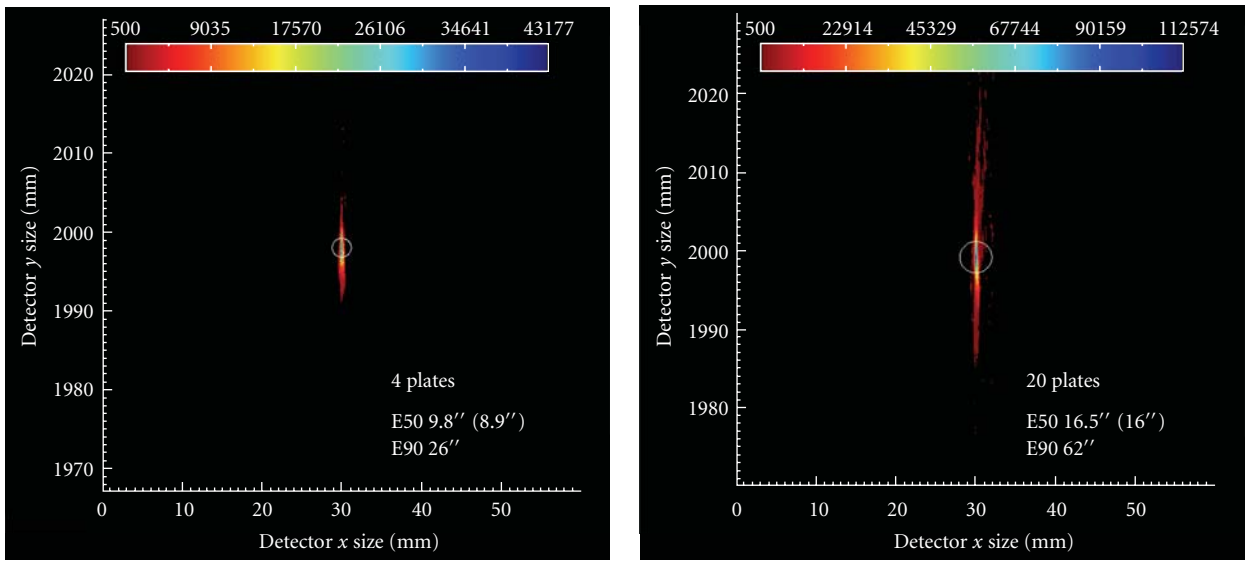

Figure 14: PSF of the first 4 (a) and 20 (b) plates of a mirror module consisting of 20 wedged plates measured using established procedures in double reflection at 2.8 keV at the FEM beamline in the PTB lab at the BESSY synchrotron radiation facility. The full length of the plate was scanned using a 100 μm pencil beam with an intrinsic HEW of 4″. The scans where repeated every 2 mm over the full width of the plate. The resulting PSF, excluding the direct beam, has a HEW of 8.9″ (4 plates) and 16″ (20 plates).

Their details can be found in [35, 36]. The large effective area of the telescope will enable observations that are not possible with Chandra or XMM Newton, but are crucial for a quantitative understanding of the X-ray universe.

3. Glass Micropore Optics (MPO)

This optic type is less performing in terms of angular resolution but extremely efficient with regard to the mass allocation, making it of particular interest for applications on

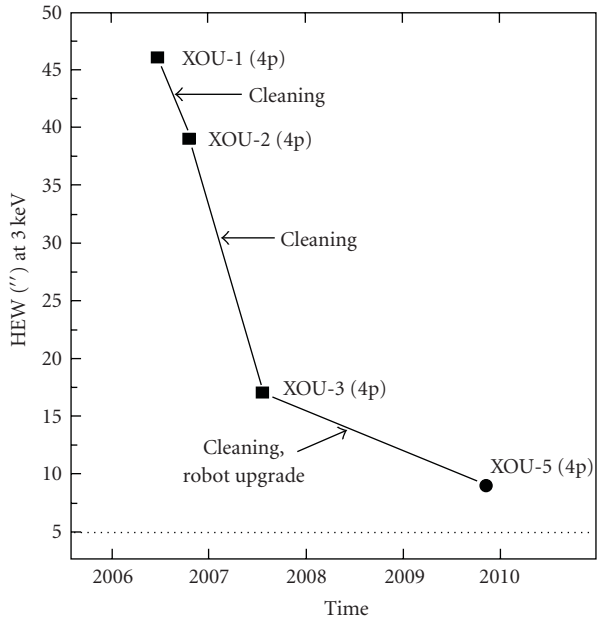

Figure 15: Performance of mirror modules of silicon pore optics measured (solid blocks) in mounted configuration, measured with X-rays at 3 keV.

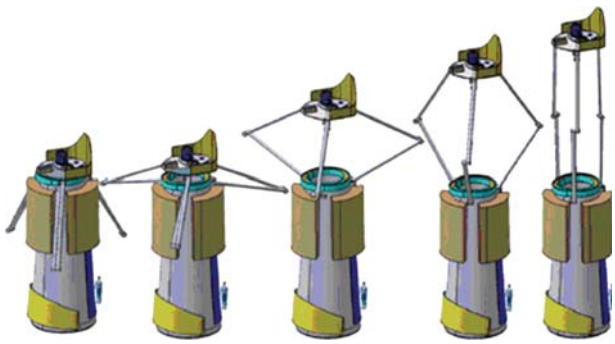

Figure 16: Schematic diagram of IXO showing the articulated arm deployment system (shroud not shown) [35].

planetary missions. Collimating elements still form the backbone of X-ray instrumentation for planetary exploration and science. With the development of coated, square pore micropore optics for X-ray imaging optics, this situation changed.

3.1. Building on Night Vision. Glass micropore optics (as opposed to silicon micropore optics [37], which is produced by micromachining silicon) are based on the Microchannel Plate (MCP) technology that has been developed for many decades for image intensifiers and photon and particle detectors. One method to produce microchannel plates is to cut thin slices off fused bundles of thin round glass fibres and etch out the fibre cores. The glass fibres have a cladding of a different type of glass than the core, and the fibre bundle is fused at a temperature where the cladding glass melts together but the core glass is unmodified. The slices are etched such that the core glass of all fibres is etched away, leaving behind the cladding glass. The result is a glass plate, of about 0.5 to a few mm thick, with a high density of cylindrical holes with diameters between 3 and 100 μm. The surface of the pores in the plate can be treated or coated to become able to produce photo and secondary electrons, and an electric field is placed over the two sides of the plate. A photon that is absorbed by a wall inside one of the pores may generate a free electron through the photoelectric effect. This electron is then accelerated by the electric field towards the anode. When it hits the wall of the pore again, it may generate several secondary electrons, resulting in an amplified cascade of electrons. The resulting charge pulse can be measured to determine the energy of the photon and the position where it was absorbed on the plate, resulting in a microchannel plate detector that can be used to measure energy and position of incoming visible to gamma ray photons and particles such as electrons, protons, neutrons and ions. The electron pulse can also be converted into several photons using a fluorescent screen, resulting in an image intensifier as for example used in night vision equipment.

The walls of these pores will also reflect X-rays under grazing incidence and can be used to focus X-rays into a spot. However, because the original direction of the photons is lost upon one or more reflections on the round walls, it cannot be used to produce an imaging optics. This problem is overcome by using square fibres, which results in pores with flat, aligned walls. These walls can be used as reflecting surfaces to produce an imaging optics. Because of the extreme extension of the glass in the fibre production process, the roughness of the interface between square and cladding glass is reduced from that of a typical optical polish to the few nm roughness required for X-ray reflection.

The fibres can be placed in different geometries, each resulting in a different type of optic. For example, when the square fibres are placed in a circular geometry, the pore walls will reflect the X-rays from a point source towards a single focus. When the plate is also curved to a spherical shape, this will also happen for a source at a large distance.

However, proper imaging requires two reflections. This occurs with some of the X-rays that are reflected by a square array of fibres, namely, those rays that reflect from two adjacent orthogonal walls (i.e., an X-ray is reflected on one surface of the pore, and then hits the perpendicular surface of the adjacent wall of the same pore, where it is once more reflected). This results in a cross-shaped focus. When the plate is also curved to a spherical shape, the geometry resembles that of the eye of a lobster and images over a large field of view [38–44]. This technology can even be used to mimic the two surfaces of revolution that constitute a Wolter-I geometry for X-ray imaging [45, 46]. This requires two plates, each with the fibres aligned in circles around the optical axis. The plates are curved to a spherical shape, where the radius of curvature of the second plate is 1/3 of that of the first plate, and the plates are placed directly behind each other. X-rays from a source at a large distance, and that are reflected by the first and second plate consecutively, are imaged to a proper focus at a focal distance that is 1/4 of the radius of curvature of the first plate. This also holds for

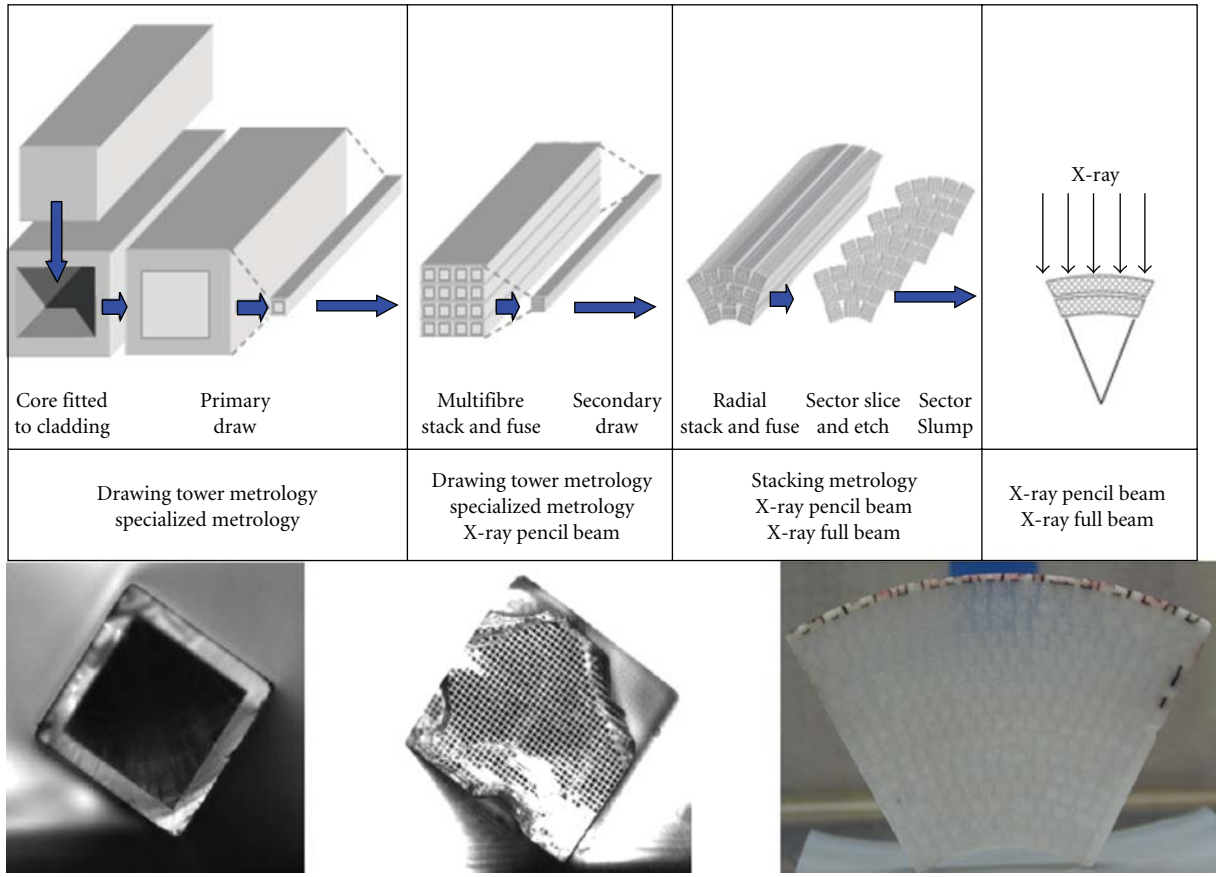

Figure 17: Manufacturing steps for micropore optics, reproduced from [47].

sources that are not on the optical axis, and therefore the two plates together form the equivalent of an X-ray "lens".

Larger MPOs can be tiled using MPO units, which themselves are limited in size (typically to less than 100 mm diameter) due to the manufacturing process. The angular resolution is currently limited to a few arc minutes.

3.2. Production of MPOs. The production of MPOs is derived from well established manufacturing methods of microchannel plates using drawing and stacking of glass fibres. But while microchannel plates contain cylindrical holes, X-ray optics need flat surfaces and consequently pores with a square profile. The required manufacturing steps are illustrated in Figure 17.

The base material is a polished glass block with a square profile that is surrounded with a cladding of a different glass type. Note that while the outer cladding forms the pore walls, its surface quality is mainly determined by the core glass block. A primary draw is performed in a draw tower, where the glass block is partially melted and drawn into a fibre by a traction system. The fibre is broken in regular pieces and stored. The geometry of the fibres is measured by dedicated optical metrology devices [47] during the drawing. Starting with a block size of approximately $20 \times 20 \times 300\,\text{mm}^3$, the resulting fibres have a size of about $1 \times 1 \times 40\,\text{mm}^3$.

A second drawing step is required to reach pore sizes in the order of a few $10\,\mu$m. Therefore, about 35×35 fibres are fused together, forming a multifibre stack. The second drawing results in multifibres with a pore size of $20 \times 20\,\mu$m and a wall thickness of $3\,\mu$m. These multifibres are the basic building blocks for larger X-ray pore optics.

The multifibre stacks are again stacked and fused to form X-ray optics with larger apertures, including the possibility to form a geometry of radial segments. Micropore optics plates with the desired geometry can be sliced from this block. The glass fibre cores are removed by selective etching of the glass type. The glass fibre cladding material forms the walls of a large number of holes with a square profile. Due to the high number of fused pores, the resulting element is of high structural stability.

The shape of a Wolter optic is approximated by thermally slumping separate micropore optic plates to form approximations to the hyperbolic and parabolic elements. In order to increase the reflectivity, metallic coatings such as nickel or iridium can be applied using an electroless deposition method. Two plates placed in front of each other form a focusing, micropore, X-ray optics.

3.3. Performance of Micropore Optics. The optical performance of the micropore optics strongly depends on the deformation of the individual fibres during the drawing,

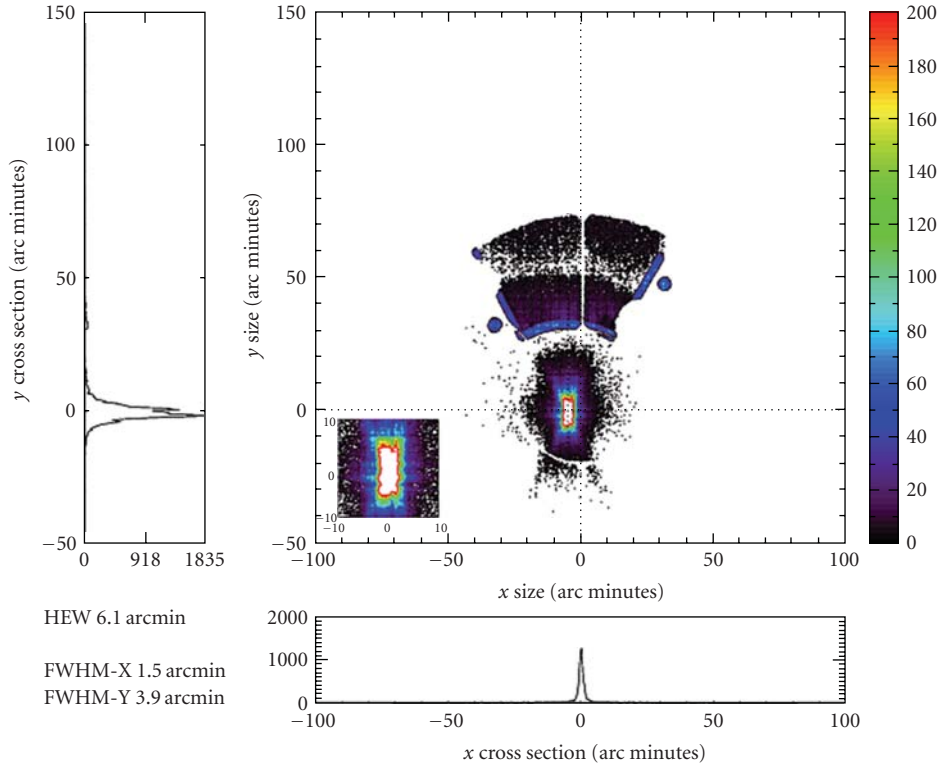

Figure 18: Full beam illumination measurement of a slumped sector, measured at 1.48 keV. The focus was found at the expected distance of 2 m. The measured HEW of the focal spot is 6.1 arcmin. Even reflections and openings in the sample holder generate an image of the radial sector on the detector (visible above the focal spot).

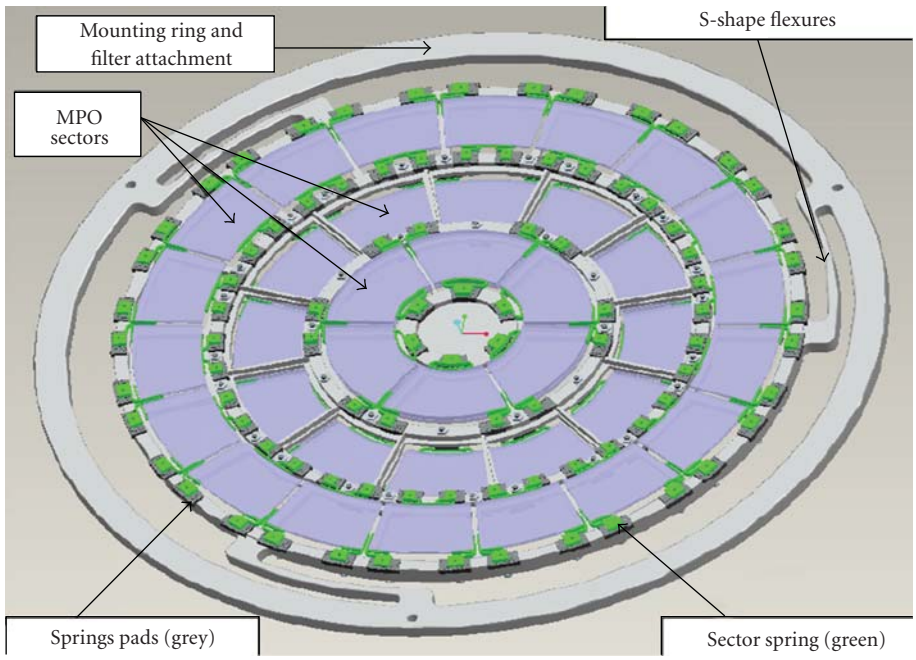

Figure 19: An early concept for assembling MPO sectors into an X-ray optics unit. The support structure is made of Titanium and must provide the correct and stable alignment of the sectors, while protecting them from thermal and mechanical loads. Three s-shaped flexures at the optic mount absorb mechanical loads, which would otherwise pass directly to the optic from the optical bench; they also provide a possible mount point for a filter. MPO sectors can be individually removed and replaced by unscrewing the bolts to the pads. The diameter of the optics is 200 mm.

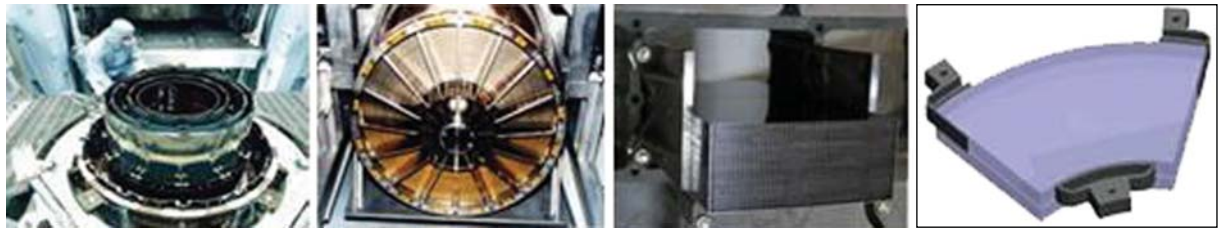

CHANDRA	XMM-NEWTON	IXO-SPO	Glass-MPO
0.5″	14″	5″	30″
18500 kg/m^2	2300 kg/m^2	200 kg/m^2	25 kg/m^2
A_{eff} at 1 keV	A_{eff} at 1 keV	A_{eff} at 1 keV	A_{eff} at 1 keV

Figure 20: Comparison of X-ray optics technologies.

stacking and slumping processes. In order to understand and improve the production process, X-ray measurements of the optics are performed after the different manufacturing steps [46–48]. Pencil beam measurements performed at the BESSY II beamlines of the Physikalisch-Technische Bundesanstalt (PTB) in Berlin are used for characterizing local properties of the micropore optics, using a 50 μm beam size. Full beam illumination is done at the PANTER facility of the MPE in Munich.

Figure 18 shows a full beam illumination measurement from the first generation of slumped micropore optics sectors, about $50 \times 30\,\text{mm}^2$ in size. At the design focal distance of 2 m, the focal spot with a HEW of 6.1 arcmin was measured. The focal position demonstrates the successful slumping of the 2.5 mm thick plate to a radius of curvature of 4 m. The HEW of 6.1 arcmin indicates that not all multifibres have been slumped correctly. Single reflection measurements on single multifibres have a typical HEW of 120 arcsec, where individual fibres within the multifibre are as good as 30 arc seconds [47], demonstrating the potential of the technology. In Figure 19, an early design is shown for assembling MPO sectors into complete optics.

An early concept for mounting of MPOs into an optics assembly is shown in Figure 19 [49].

3.4. Bepi-Colombo. In 2007, the MPO technology was chosen for implementation in the Mercury Imaging X-ray Spectrometer (MIXS). MIXS is an instrument of the Mercury Planetary Orbiter of the Bepi Colombo Mission [50, 51] planned to launch in 2014. The imaging spectrometer will measure X-ray fluorescence from Mercury within an energy range of 0.5–7.5 keV. It consists of two instruments [52]: one collimator (MIXS-C) and one telescope (MIXS-T) which uses a conical approximation of the Wolter-I configuration. The latter has a diameter of 210 mm and a focal length of 1 m and is required to yield a field of view of 1 degree with an angular resolution below 9 arcmin.

4. Summary

Pore Optics technology allows the production of high performance X-ray optics. The mass density required to achieve a given angular resolution is much lower than the established X-ray optics technologies. In Figure 20, the established optics technologies currently operating in orbit, on board Chandra and Newton, are compared with the SPO and the MPO technologies.

SPO technology has already demonstrated the required mass density for use on IXO and has shown very promising performance measured at X-ray facilities. A technology programme is being implemented, addressing further improvement of the angular resolution to reach the requirement of IXO, the predevelopment of mass production equipment necessary for large telescope implementations and, finally, the environmental qualification of SPO modules [35, 53–56].

MPO technology has achieved a maturity level adequate for adoption into a flight programme. This technology is the lightest, albeit with reduced angular resolution performance, and is suitable to meet the reduced mass and envelope requirements for planetary mission instrumentation.

The transfer of these technologies to ground applications is possible and attractive, in a wide range of fields, ranging from material science to medical diagnostics and security equipment.

Acknowledgments

The authors would like to acknowledge the work done by the industrial and institutional entities and the people involved in the technology preparation activities. Their work forms the basis onto which the future science missions are built. Without their efforts, the next generation X-ray astrophysics observatory, IXO, could not be realised, and planetary X-ray optics would not be possible. The MPO section of this paper is dedicated to the memory of Sven-Olof Flyckt. His genuine kindness, his passion, and his expertise were not only vital for the technical but also for the human aspects of such projects.

References

[1] F. Jansen, D. Lumb, B. Altieri et al., "XMM-Newton observatory. I. The spacecraft and operations," *Astronomy and Astrophysics*, vol. 365, no. 1, pp. L1–L6, 2001.

[2] S. L. O'Dell and M. C. Weisskopf, "Advanced X-ray astrophysics facility (AXAF):calibration overview," in *X-Ray Optics, Instruments, and Missions*, vol. 3444 of *Proceedings of SPIE*, pp. 2–18, San Diego, Calif, USA, July 1998.

[3] M. J. L. Turner, G. G. C. Palumbo, J. A. M. Bleeker, G. Hasinger, A. Peacock, and J. Trumper, "Xeus: an X-ray observatory for the post-XMM era," in *The Next Generation of X-Ray Observatories: Workshop Proceedings Leicester X-ray Astronomy Group Special Report XRA 97/02*, M. J. L. Turner and M. G. Watson, Eds., p. 165, 1997.

[4] A. Parmar, G. Hasinger, and M. Turner, "XEUS—the X-ray evolving universe spectroscopy mission," in *Proceedings of the 34th Cospar Assembly*, p. 2368, 2004.

[5] G. Bignami et al., "Cosmic vision," ESA BR-247, 2005.

[6] B. Aschenbach, "X-ray telescopes," *Reports on Progress in Physics*, vol. 48, no. 5, pp. 579–629, 1985.

[7] A. Peacock, B. G. Taylor, and J. Ellwood, "The high throughput X-ray spectroscopy mission: XMM," *Advances in Space Research*, vol. 10, no. 2, pp. 273–285, 1990.

[8] P. Gondoin, B. R. Aschenbach, H. Brauninger et al., "X-ray performance of a qualification model of an XMM mirror module," in *EUV, X-Ray, and Gamma-Ray Instrumentation for Astronomy VII*, vol. 2808 of *Proceedings of SPIE*, pp. 390–401, Denver, Colo, USA, August 1996.

[9] M. Bavdaz, J. A. M. Bleeker, G. Hasinger et al., "X-ray evolving universe spectroscopy mission (XEUS): narrow-field imaging high-resolution spectrometer: II (1 to 10 keV)," in *X-Ray Optics, Instruments, and Missions II*, vol. 3766 of *Proceedings of SPIE*, pp. 82–93, Denver, Colo, USA, July 1999.

[10] M. Bavdaz, A. J. Peacock, A. N. Parmar, M. Beijersbergen, and J. Schiemann, "The X-ray evolving universe spectroscopy mission (XEUS)," in *The Role of the International Space Station. ESA SP-433: Utilisation of the International Space Station 2*, p. 621, 1999.

[11] M. Bavdaz, M. Beijersbergen, A. J. Peacock, R. Willingale, B. R. Aschenbach, and H. W. Braeuninger, "X-ray evolving universe spectroscopy mission (XEUS): X-ray mirror design and technology," in *X-Ray Optics, Instruments, and Missions II*, R. B. Hoover and A. B. Walker, Eds., vol. 3766 of *Proceedings of SPIE*, pp. 94–102, Denver, Colo, USA, July 1999.

[12] W. W. Zhang, K.-W. Chan, T. Hajimichael et al., "Development of lightweight X-ray mirrors for the constellation-X mission," in *Optics for EUV, X-Ray, and Gamma-Ray Astronomy III*, vol. 6688 of *Proceedings of SPIE*, San Diego, Calif, USA, August 2007.

[13] M. Bavdaz, A. Peacock, E. Tomaselli et al., "Progress at ESA on high energy optics technologies," in *Optics for EUV, X-Ray, and Gamma-Ray Astronomy*, vol. 5168 of *Proceedings of SPIE*, pp. 136–147, San Diego, Calif, USA, August 2003.

[14] M. Beijersbergen, S. Kraft, M. Bavdaz et al., "Development of X-ray pore optics: novel high-resolution silicon millipore optics for XEUS and ultra-low mass glass micropore optics for imaging and timing," in *Design and Microfabrication of Novel X-Ray Optics II*, vol. 5539 of *Proceedings of SPIE*, pp. 104–115, Denver, Colo, USA, August 2004.

[15] P. Friedrich, B. Aschenbach, C. Braig et al., "Manufacturing of Wolter-I mirror segments with slumped glass," in *Space Telescopes and Instrumentation II: Ultraviolet to Gamma Ray*, vol. 6266 of *Proceedings of SPIE*, Orlando, Fla, USA, May 2006.

[16] M. Ghigo, O. Citterio, F. Mazzoleni et al., "The manufacturing of the XEUS X-ray glass segmented mirrors: status of the investigation and last results," in *Optics for EUV, X-Ray, and Gamma-Ray Astronomy*, vol. 5168, pp. 180–195, San Diego, Calif, USA, August 2003.

[17] M. Beijersbergen, S. Kraft, R. Günther et al., "Silicon pore optics: novel lightweight high-resolution X-ray optics developed for XEUS," in *UV and Gamma-Ray Space Telescope Systems*, vol. 5488 of *Proceedings of SPIE*, pp. 868–874, Glasgow, UK, June 2004.

[18] S. Kraft, M. Collon, R. Guenther et al., "Development of modular High-performance pore optics for the XEUS X-ray telescope," in *Optics for EUV, X-Ray, and Gamma-Ray Astronomy II*, vol. 5900 of *Proceedings of SPIE*, pp. 297–308, San Diego, Calif, USA, August 2005.

[19] M. J. Collon, S. Kraff, R. Günther et al., "Metrology, integration and performance verification of silicon pore optics in Wolter-I configuration," in *Space Telescopes and Instrumentation II: Ultraviolet to Gamma Ray*, vol. 6266 of *Proceedings of SPIE*, Orlando, Fla, USA, May 2006.

[20] Q. Wang, U. Griesmann, and R. Polvani, "Interferometric thickness calibration of 300 mm silicon wafers," in *ASPE Summer Topical Meeting on Precision Interferometric Metrology*, July 2005.

[21] M. B. O. Riekerink, B. Lansdorp, L. J. de Vreede et al., "Production of silicon mirror plates," in *Optics for EUV, X-Ray, and Gamma-Ray Astronomy IV*, vol. 7437 of *Proceedings of SPIE*, p. 27, San Diego, Calif, USA, August 2009.

[22] M. D. Ackermann, M. J. Collon, R. Günther et al., "Performance prediction and measurement of silicon pore optics," in *Optics for EUV, X-Ray, and Gamma-Ray Astronomy IV*, vol. 7437 of *Proceedings of SPIE*, San Diego, Calif, USA, August 2009.

[23] H. Wolter, "Spiegelsysteme streifenden Einfalls als abbildende Optiken fur Rontgenstrahlen," *Annalen der Physik*, vol. 445, pp. 94–114, 1952.

[24] D. H. Lumb, F. E. Christensen, C. P. Jensen, and M. Krumrey, "Influence of a carbon over-coat on the X-ray reflectance of XEUS mirrors," *Optics Communications*, vol. 279, no. 1, pp. 101–105, 2007.

[25] C. P. Jensen, M. Ackermann, F. E. Christensen, M. J. Collon, and M. Krumrey, "Coating of silicon pore optics," in *Optics for EUV, X-Ray, and Gamma-Ray Astronomy IV*, vol. 7437 of *Proceedings of SPIE*, San Diego, Calif, USA, August 2009.

[26] Q.-Y. Tong and U. Gösele, *Semiconductor Wafer Bonding: Science and Technology*, John Wiley & Sons, New York, NY, USA, 1999.

[27] A. L. Mieremet and M. W. Beijersbergen, "Fundamental spatial resolution of an X-ray pore optic," *Applied Optics*, vol. 44, no. 33, pp. 7098–7105, 2005.

[28] R. Günther, M. Collon, S. Kraft et al., "Production of silicon pore optics," in *Space Telescopes and Instrumentation II: Ultraviolet to Gamma Ray*, vol. 6266 of *Proceedings of SPIE*, Orlando, Fla, USA, May 2006.

[29] M. J. Collon, R. Günther, S. Kraft et al., "Silicon pore optics for astrophysical X-ray missions," in *Optics for EUV, X-Ray, and Gamma-Ray Astronomy III*, vol. 6688 of *Proceedings of SPIE*, San Diego, Calif, USA, August 2007.

[30] M. J. Collon, S. Kraft, R. Günther et al., "Performance characterization of silicon pore optics," in *Space Telescopes and Instrumentation II: Ultraviolet to Gamma Ray*, vol. 6266 of *Proceedings of SPIE*, Orlando, Fla, USA, May 2006.

[31] M. Krumrey and G. Ulm, "High-accuracy detector calibration at the PTB four-crystal monochromator beamline," *Nuclear Instruments and Methods in Physics Research, Section A*, vol. 467-468, pp. 1175–1178, 2001.

[32] R. Graue, D. Kampf, S. Kraft et al., "Assembling silicon pore optics into a modular structure," in *Space Telescopes and Instrumentation II: Ultraviolet to Gamma Ray*, vol. 6266 of *Proceedings of SPIE*, Orlando, Fla, USA, May 2006.

[33] M. Freyberg, B. Budau, W. Burkert et al., "Potential of the PANTER X-ray test facility for calibration of instrumentation for XEUS," in *Space Telescopes and Instrumentation II: Ultraviolet to Gamma Ray*, vol. 6266 of *Proceedings of SPIE*, Orlando, Fla, USA, May 2006.

[34] E. J. Buis and G. Vacanti, "X-ray tracing using Geant4," *Nuclear Instruments and Methods in Physics Research, Section A*, vol. 599, no. 2-3, pp. 260–263, 2009.

[35] M. Bavdaz, PH. Gondoin, K. Wallace et al., "IXO system studies and technology preparation," in *Optics for EUV, X-Ray, and Gamma-Ray Astronomy IV*, vol. 7437 of *Proceedings of SPIE*, San Diego, Calif, USA, August 2009.

[36] D. Martin, N. Rando, D. Lumb et al., "Payload study activities on the international X-ray observatory," in *Space Telescopes and Instrumentation: Ultraviolet to Gamma Ray*, vol. 7732 of *Proceedings of SPIE*, San Diego, Calif, USA, June 2010.

[37] Y. Ezoe, M. Koshiishi, M. Mita et al., "Micropore X-ray optics using anisotropic wet etching of (110) silicon wafers," *Applied Optics*, vol. 45, no. 35, pp. 8932–8938, 2006.

[38] W. K. H. Schmidt, "A proposed X-ray focusing device with wide field of view for use in X-ray astronomy," *Nuclear Instruments and Methods*, vol. 127, no. 2, pp. 285–292, 1975.

[39] J. R. P. Angel, "Lobster eyes as X-ray telescopes," *Astrophysical Journal*, vol. 233, pp. 364–373, 1979.

[40] S. W. Wilkins, A. W. Stevenson, K. A. Nugent, H. Chapman, and S. Steenstrup, "On the concentration, focusing, and collimation of X-rays and neutrons using microchannel plates and configurations of holes," *Review of Scientific Instruments*, vol. 60, no. 6, pp. 1026–1036, 1989.

[41] G. W. Fraser, J. E. Lees, J. F. Pearson, M. R. Sims, and K. Roxburgh, "X-ray focusing using microchannel plates," in *Multilayer and Grazing Incidence X-Ray/EUV Optics*, R. B. Hoover, Ed., vol. 1546 of *Proceedings of SPIE*, pp. 41–52, San Diego, Calif, USA, 1992.

[42] G. W. Fraser, A. N. Brunton, J. E. Lees, and D. L. Emberson, "Production of quasi-parallel X-ray beams using microchannel plate "X-ray lenses"," *Nuclear Instruments and Methods in Physics Research A*, vol. 334, no. 2-3, pp. 579–588, 1993.

[43] A. G. Peele, B. E. Allman, and V. Cucevic, "Square capillary X-ray optics," in *Applications of Laser Plasma Radiation*, vol. 2015 of *Proceedings of SPIE*, pp. 118–127, San Diego, Calif, USA, July 1993.

[44] A. N. Brunton, G. W. Fraser, J. E. Lees, and I. C. E. Turcu, "Metrology and modeling of microchannel plate X-ray optics," *Applied Optics*, vol. 36, no. 22, pp. 5461–5470, 1997.

[45] R. Willingale, G. W. Fraser, A. N. Brunton, and A. P. Martin, "Hard X-ray imaging with microchannel plate optics," *Experimental Astronomy*, vol. 8, no. 4, pp. 281–296, 1998.

[46] M. Beijersbergen, M. Bavdaz, A. Peacock et al., "Microchannel plate based X-ray optics," in *EUV, X-Ray, and Gamma-Ray Instrumentation for Astronomy X*, vol. 3765 of *Proceedings of SPIE*, pp. 452–459, Denver, Colo, USA, July 1999.

[47] M. J. Collon, M. W. Beijersbergen, K. Wallace et al., "X-ray imaging glass micro-pore optics," in *Optics for EUV, X-Ray, and Gamma-Ray Astronomy III*, vol. 6688 of *Proceedings of SPIE*, San Diego, Calif, USA, August 2007.

[48] K. Wallace, M. Collon, M. Bavdaz, R. Fairbend, J. Séguy, and M. Krumrey, "Developments in glass micro pore optics for X-ray applications," in *Space Telescopes and Instrumentation II: Ultraviolet to Gamma Ray*, vol. 6266 of *Proceedings of SPIE*, p. 37, Orlando, Fla, USA, May 2006.

[49] K. Wallace, M. J. Collon, M. W. Beijersbergen, S. Oemrawsingh, M. Bavdaz, and E. Schyns, "Breadboard micro-pore optic development for X-ray imaging," in *Optics for EUV, X-Ray, and Gamma-Ray Astronomy III*, vol. 6688 of *Proceedings of SPIE*, p. 44, San Diego, Calif, USA, August 2007.

[50] A. Owens, M. Bavdaz, M. Beijersbergen et al., "HERMES: an imaging X-ray fluorescence spectrometer for the Bepi-Colombo mission to Mercury," in *Soft X-Ray and EUV Imaging Systems II*, vol. 4506 of *Proceedings of SPIE*, pp. 136–145, San Diego, Calif, USA, August 2001.

[51] M. Collon, E. J. Buis, M. Beijersbergen et al., "Design and performance of the payload instrumentation of the BepiColombo Mercury planetary orbiter," *Acta Astronautica*, vol. 59, no. 8-11, pp. 1052–1061, 2006.

[52] G. W. Fraser, J. D. Carpenter, D. A. Rothery et al., "The mercury imaging X-ray spectrometer (MIXS) on bepicolombo," *Planetary and Space Science*, vol. 58, no. 1-2, pp. 79–95, 2009.

[53] M. D. Ackermann, M. J. Collon, C. P. Jensen et al., "Performance of multilayer coated silicon pore optics," in *Space Telescopes and Instrumentation: Ultraviolet to Gamma Ray*, vol. 7732 of *Proceedings of SPIE*, San Diego, Calif, USA, June 2010.

[54] M. Bavdaz, E. Wille, K. Wallace et al., "ESA optics technology preparation for IXO," in *Space Telescopes and Instrumentation: Ultraviolet to Gamma Ray*, vol. 7732 of *Proceedings of SPIE*, San Diego, Calif, USA, June 2010.

[55] M. J. Collon, R. Günther, M. Ackermann et al., "Stacking of silicon pore optics for IXO," in *Optics for EUV, X-Ray, and Gamma-Ray Astronomy IV*, vol. 7437 of *Proceedings of SPIE*, San Diego, Calif, USA, August 2009.

[56] N. Rando, D. Martin, D. Lumb et al., "ESA assessment study activities on the International X-ray observatory," in *Space Telescopes and Instrumentation: Ultraviolet to Gamma Ray*, vol. 7732 of *Proceedings of SPIE*, San Diego, Calif, USA, June 2010.

Hindawi Publishing Corporation
X-Ray Optics and Instrumentation
Volume 2010, Article ID 856836, 15 pages
doi:10.1155/2010/856836

Research Article

Active Microstructured Optical Arrays of Grazing Incidence Reflectors

Richard Willingale,[1] Charlotte Feldman,[1] Alan Michette,[2] Tim Button,[3] Camelia Dunare,[4] Melvyn Folkard,[5] David Hart,[2] Chris McFaul,[2] Graeme R. Morrison,[2] William Parkes,[4] Sławka Pfauntsch,[2] A. Keith Powell,[2] Daniel Rodriguez-Sanmartin,[3] Shahin Sahraei,[2] Matthew T. Shand,[2] Tom Stevenson,[4] Boris Vojnovic,[5,6] and Dou Zhang[3]

[1] *Department of Physics and Astronomy, University of Leicester, Leicester LE1 7RH, UK*
[2] *Department of Physics, Kings College London, Strand, London WC2R 2LS, UK*
[3] *Department of Metallurgy and Materials, University of Birmingham, Birmingham B15 2TT, UK*
[4] *Scottish Microelectronics Centre, University of Edinburgh, The Kings Buildings, West Mains Road, Edinburgh EH9 3JF, UK*
[5] *Gray Cancer Institute, Old Road Campus, Roosevelt Drive, Headington, Oxford, Oxfordshire OX3 7DQ, UK*
[6] *Randall Division of Cell and Molecular Biophysics, Randall Institute, New Hunt's House, King's College London, Guy's Campus, London, SE1 1UL, UK*

Correspondence should be addressed to Richard Willingale, rw@star.le.ac.uk

Received 22 September 2009; Accepted 16 June 2010

Academic Editor: Ali Khounsary

The UK Smart X-Ray Optics (SXO) programme is developing active/adaptive optics for terrestrial applications. One of the technologies proposed is microstructured optical arrays (MOAs), which focus X-rays using grazing incidence reflection through consecutive aligned arrays of microscopic channels. Although such arrays are similar in concept to polycapillary and microchannel plate optics, they can be bent and adjusted using piezoelectric actuators providing control over the focusing and inherent aberrations. Custom configurations can be designed, using ray tracing and finite element analysis, for applications from sub-keV to several-keV X-rays, and the channels of appropriate aspect ratios can be made using deep silicon etching. An exemplar application will be in the microprobing of biological cells and tissue samples using Ti K_α radiation (4.5 keV) in studies related to radiation-induced cancers. This paper discusses the optical design, modelling, and manufacture of such optics.

1. Introduction

Microoptical arrays (MOAs) is the generic name for optical systems consisting of a very large number of small (microscopic) elements. Such elements can be refractive (lenses), diffractive (gratings), or reflective (mirrors). The idea of MOAs of grazing incidence reflectors was first discussed at a SPIE meeting in 2001 [1] and subsequently at the international X-ray Microscopy conference in Grenoble in 2002 [2]. Some further development has been reported since then [3, 4], and the UK Smart X-ray Optics consortium (SXO) has received funds initially for a pilot study (2004) and a full programme of research (starting 2006) under the Council UKs' Basic Technology scheme [5, 6]. Initial work on X-ray MOAs in the SXO programme was reported at SPIE in 2007 [7] and in 2009 [8–10].

The MOA concept is similar to polycapillary [11] and microchannel plate [12] optics, in which X-rays are guided by multiple grazing incidence reflections along a large number of small channels. The arrays can be manufactured by etching a periodic array of narrow channels in silicon wafers as illustrated in Figure 1. In this sample, the channels are parallel, $\approx 10\,\mu$m wide, with a pitch of $\approx 20\,\mu$m. The sides of the channels act as mirrors at grazing incidence to provide point-to-point or line-to-line imaging/focusing as shown in Figure 2. If the channels are planar then we can get line-to-line focusing via just 1 reflection or spot-to-spot focusing using two successive orthogonal reflections.

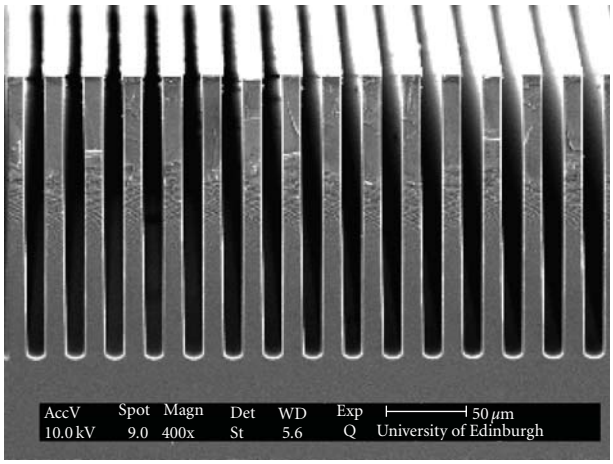

Figure 1: MOA channels etched in Si (SMC UoE).

If a more ambitious circular/radial slot geometry is adopted and 2 reflections are employed, then we can get point-to-point imaging as illustrated in Figure 3. The use of two reflections means that the Abbe sine condition can be approximately satisfied, thereby greatly reducing aberrations (in particular coma). A central stop prevents unreflected X-rays from reaching the focus. In practice many more channels would be used than those illustrated. Through actively varying the radius of curvature of one of the reflection arrays by actuating piezoelectric material fixed to the radial spoke the focal length can be changed.

In Section 2, we consider the geometric optics of several possible MOA arrangements suitable for focusing X-rays. The manufacturing of the channels by etching and the actuators attachment are discussed in Section 3 and X-ray scattering from the surface roughness and profile errors on the channel walls are discussed in Section 4. Ray-tracing and finite element analysis of a 1-D MOA structure are presented in Section 5, and finally, Section 6 describes the application of X-ray focusing by MOAs in microprobing of biological cells.

2. The Geometric Optics of Grazing Incidence Microstructured Optical Arrays

We will start by considering line-to-line focusing using a single-reflection MOA consisting of planar channels, as shown schematically in Figure 2. We will then discuss tandem systems which use two reflections; firstly in the same plane to provide line-to-line focusing and secondly in perpendicular crossed planes to provide spot-to-spot focusing. Finally, we will look at the generalisation to spot-to-spot focusing using channels with a circular geometry (as shown in Figure 3) which is obvious via symmetry arguments.

2.1. Line-to-Line MOA Focusing. For an unbent component the object and image distances are equal, or more generally, using a bent component such that the channel walls are tilted, we have the geometry shown in Figure 4. The combined reflections from many channels only provide an approximate line focus because the reflecting surfaces are assumed to be planar rather than curved. If the length of the channels is l and the grazing angle is θ_g, then the focused line width will be $\simeq l\theta_g$. The geometry of a single-reflection from a channel wall is shown in Figure 4; the source to MOA distance is s_1 and the MOA to image distance is s_2. The channel is tilted by an angle φ with respect to the optical axis. If the distance of the channel wall from the axis is h, then, using the small angle approximation ($h \ll s_1, s_2$),

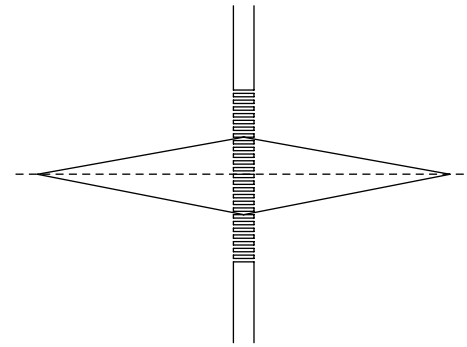

Figure 2: Grazing incidence reflections from the slot walls provide line-to-line focusing.

$$\frac{h}{s_1} = \theta_g - \varphi,$$
$$\frac{h}{s_2} = \theta_g + \varphi. \tag{1}$$

Eliminating φ leads to

$$\frac{1}{s_1} + \frac{1}{s_2} = \frac{2\theta_g}{h} = \frac{1}{f} \tag{2}$$

which is the standard Gaussian imaging equation with a focal length $f = h/2\theta_g$. Eliminating θ_g between (1) gives

$$\frac{1}{s_2} - \frac{1}{s_1} = \frac{2\varphi}{h} \tag{3}$$

which gives the MOA radius of curvature, $R = h/\varphi$,

$$R = \frac{2s_1 s_2}{s_1 - s_2}. \tag{4}$$

Note that if $s_2 = s_1$, the radius of curvature is infinite and the MOA is unbent. If the channel width is w, then there is a maximum grazing angle of operation, $\theta_{g\max} = 2w/l$, assuming parallel walls (see Figure 5). This, in turn, sets an upper limit to the separation from the optical axis, $h_{\max} = 2s_1 w/l$ and hence, assuming no channel curvature, defines the effective f-ratio of the optic, $2h_{\max}/f = 8w/l$.

The aperture can be increased by employing a pair of MOAs so that the focusing is accomplished by two reflections. The grazing angles on each component are then reduced by a factor of approximately two for a given value of h. The increase in the effective aperture depends on the ratio of the grazing angles in the two-components. Such an arrangement is shown schematically in Figure 6.

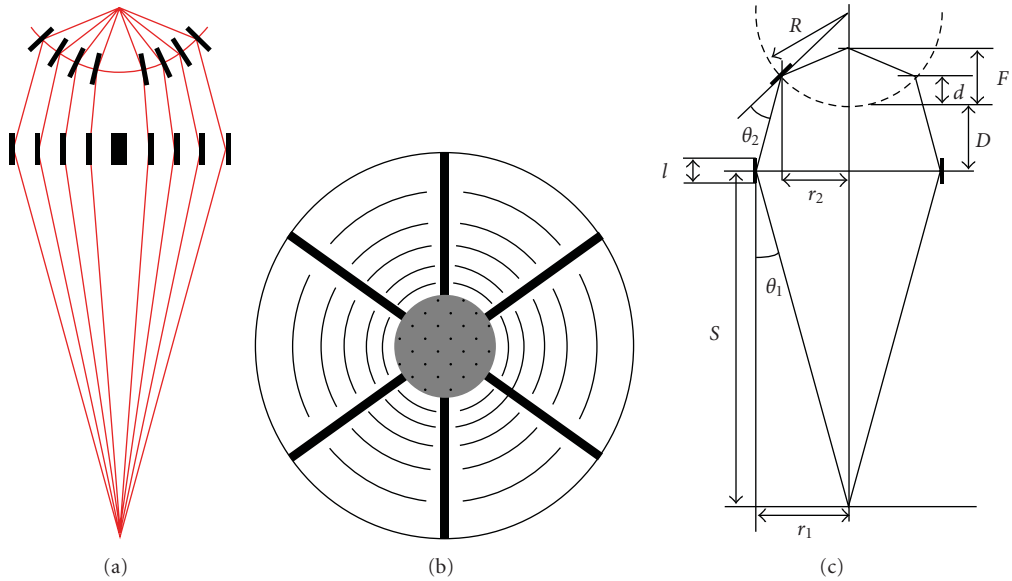

Figure 3: (a) Schematic of a two-reflection MOA. (b) Possible channel layout of one of the components. (c) Definition of the geometry of a two-reflection MOA.

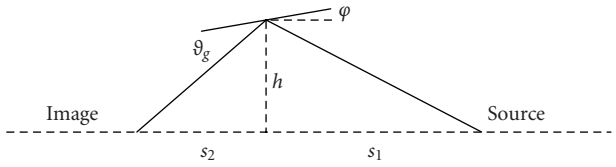

Figure 4: Geometry of a single-reflection.

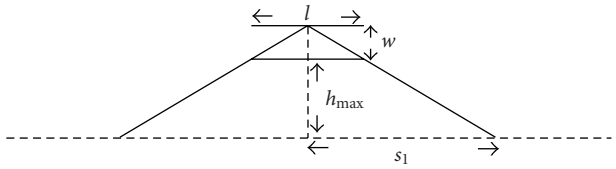

Figure 5: The maximum grazing angle for a channel of length l and width w.

Three cases of a two component (2-reflection) MOA are considered below:

(i) The grazing angle is the same in each of the components, which are bent in opposite directions (defined to be negative curvature for the first component and positive for the second). This is likely to yield close-to-maximum efficiency for the double-reflections which, for linear arrays, produce a line image. The effective aperture will be double that obtained with a single MOA, $2h_{max}/f = 16w/l$.

(ii) One component is flat and the other is curved.

(iii) The focal length of the first component is set to the object distance s_1 and that of the second component to the image distance s_2.

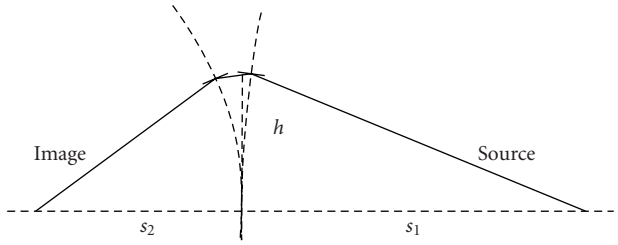

Figure 6: In-plane reflection from a two-component MOA.

In the third case, the pair of plates forms a collimator-telescope combination; rays passing from the first to the second component are parallel to the optical axis (planar wave fronts). If the channel sizes and spacings are identical for both components then all rays reflected from the first will intersect with the reflecting surfaces of the second. However, in the first two cases, the rays are converging or diverging and the fraction of rays reflected by the second component will depend on the separation between the plates.

For the reflections from the two components

$$\frac{h_1}{s_1} = \theta_{g1} + \varphi_1, \qquad \frac{h_2}{s_2} = \theta_{g2} + \varphi_2. \tag{5}$$

2.1.1. Equal Grazing Angle Double-Reflection MOAs. Setting the grazing angles to be equal ($\theta_{g1} = \theta_{g2} = \theta_g$), eliminating them from (5), using $\varphi_1 = -h_1/R_1$ and $\varphi_2 = h_2/R_2$, and assuming that the component separation $D \ll s_1, s_2$ so that $h_2 \approx h_1 \approx h$, then

$$\frac{1}{R_1} + \frac{1}{R_2} = \frac{1}{s_2} - \frac{1}{s_1}. \tag{6}$$

The included angle between the two components is equal to $\Pi - \varphi_1 - \varphi_2$ and to $\Pi - 2\theta_g$. It then follows that

$$\frac{1}{R_2} - \frac{3}{R_1} = \frac{2}{s_1}, \tag{7}$$

and solving (6) and (7) for the radii of curvature R_1 and R_2 gives

$$R_1 = \frac{4s_1s_2}{s_1 - 3s_2}, \qquad R_2 = \frac{4s_1s_2}{3s_1 - s_2}. \tag{8}$$

It can be seen that if $s_1 = s_2 = s$, then $R_1 = -R_2 = -2s$, so that the radii of curvature are equal but with different signs, as expected. The angle between the optical axis and the rays between the two components is $\theta_a = \theta_{g1} + \varphi_1 = 2h/R_1 + |h/s_1|$. Substituting for R_1 from (8) gives

$$\theta_a = \frac{h(s_1 - s_2)}{2s_1s_2}. \tag{9}$$

Eliminating φ_1 and φ_2 from (5), with equal grazing incidence angles, gives the grazing angle for this configuration

$$\theta_g = \frac{h}{4}\frac{s_1 + s_2}{s_1s_2}, \tag{10}$$

and the width b of the transmitted beam is

$$b = l\theta_g = \frac{lh}{4}\frac{s_1 + s_2}{s_1s_2}, \tag{11}$$

noting that the latter result neglects reflections from the opposite sidewalls, that is, a nondiverging beam and $s_1, s_2 \gg h$.

So that the rays reflected from the first component are reflected by the second, the gap D between them must be small enough such that the rays intersect the width b in the second component, that is,

$$D \ll \frac{lh}{4\theta_a}\frac{s_1 + s_2}{s_1s_2}, \tag{12}$$

which gives, by substituting for θ_a,

$$D \ll \frac{l}{2}\frac{s_1 + s_2}{s_1 - s_2}. \tag{13}$$

If $s_1 = s_2$, then the rays between the components are nominally parallel, and there is no limitation on the gap D given by (13). In this case, the divergence of the rays set by the source distance s_1 becomes important, and we require $D \ll s_1$ so that rays which reflect from channels in the first component intersect with channel walls of the seconds component.

2.1.2. Flat-Curved Double-Reflection MOAs. With the first component unbent, and the second component bent, (5) are still valid, but now $\varphi_1 = 0$, corresponding to the required infinite radius of curvature. In addition, $\varphi_2 = \theta_{g1} + \theta_{g2} = h/R_2$, so that

$$R_2 = \frac{2s_1s_2}{s_1 + s_2}, \tag{14}$$

noting that $s_1 = 3s_2$ gives $R_1 = \infty$ for the equal grazing angle case, (8), and $R_2 = s_1/2$ for the flat-curved combination (14). Satisfying these two requirements simultaneously is a special case for which the first component is flat and the grazing angles are equal in the two components. For the flat-curved combination, $\theta_a = \theta_{g1}$ and (13) are reduced to the simpler criterion that $D \ll l$ to avoid heavy losses.

2.1.3. Collimator-Telescope Double-Reflection MOAs. A collimator-telescope configuration requires $R_1 = -2s_1$ and $R_2 = 2s_2$, where the negative sign indicates that the first component is curved with the centre of curvature on the object side so the two components curve in opposite directions. If R_1 is set correctly and the reflecting surfaces are flat and introduce negligible scatter, then rays in the gap between the components will be parallel to the axis and the gap can be widened to accommodate other optical elements, such as a grating, filters, and/or support structure without loss in performance.

2.2. Spot-to-Spot MOA Focusing Using Planar Channels. We can achieve spot-to-spot focusing with two-planar channel MOAs using the geometry described in Section 2.1, but setting the channels in the second component (aligned to, for example, the y axis) are set perpendicular to those in the first (aligned to the x axis). If there is a gap between the components (which there must be in any practical system), then the object and image distances, s_1 and s_2, will be slightly different for the first and second component, and hence the magnification will be slightly different in the x and y axes on the image plane, but otherwise the system will provide true imaging limited only by the resolution set by the width of the channels (see Section 2.3). The radii of curvature of the components can be set independently using (4) and the effective f-ratio of the optic will be as given in Section 2.1. In such an arrangement, there is no need for accurate alignment of the channels in the first component with those in the second, and the size of the gap D is not critical and has little impact on the efficiency.

2.3. Efficiency and Resolution

2.3.1. Line-To-Line Focusing. The width b of the beam transmitted through the channels increases linearly with axial offset h until $b = w$, the width of the channel. At this offset, the opposite wall of the channel starts to block the inner edge of the beam. As h is increased further, the beam width drops linearly until it reaches zero at the edge of the useful aperture which is given by (for a single-reflection MOA in the equal grazing angle case)

$$h_{\max} = \frac{4w}{l}\frac{s_1s_2}{s_1 + s_2}. \tag{15}$$

Note that $h_{\max}$ will be twice this value for a double-reflection MOA; using two reflections doubles the width of the available aperture. The mean beam width across the aperture is $b_{\text{mean}} = w/2$.

The geometric area of the single-reflection aperture which provides the line-to-line focusing is given by the sum of all the channels over a square aperture of size $W = 2h_{\max}$. If the channels are evenly spaced with a period p, the geometric area is

$$A_{\text{geom}} = \frac{32w^3}{pl^2}\left(\frac{s_1 s_2}{s_1 + s_2}\right)^2. \tag{16}$$

The effective area is limited by the grazing incidence reflectivity of X-rays from the channel walls. For a given X-ray energy, there is a critical angle θ_c for reflection, that is, the grazing angle below which the reflectivity is high. Efficient use of the channels thus requires $w/l \approx \theta_c$, so that

$$h_{\max} = 4\theta_c \frac{s_1 s_2}{s_1 + s_2}. \tag{17}$$

So long as channels can be manufactured with this aspect ratio (l/w) and over an area of $2h_{\max} \times 2h_{\max}$ then the maximum effective area which can be achieved at the X-ray energy corresponding to the critical angle is

$$A_{\text{eff}} \approx 32\theta_c^2 \frac{w}{p}\left(\frac{s_1 s_2}{s_1 + s_2}\right)^2, \tag{18}$$

assuming that the reflectivity is 100% for $\theta_g < \theta c$. This represents an idealised upper limit to the effective area for a single-reflection MOA. If we use a double-reflection MOA, $h_{\max}$ is increased by a factor of two because the grazing angles are reduced by a factor of two, and the areas A_{geom} and A_{eff} will be increased by a factor of four. In practice absorption and scattering will reduce the reflectivity, and the aspect ratio corresponding to this effective aperture will be hard to achieve; a silicon surface reflecting titanium K_α X-rays would require $l/w \approx 140$ while in the current work only ≈ 30 has been achieved.

Planar channel walls provide no focusing. If the source line is very narrow, the width of the on-axis line from a single channel is

$$\delta = \frac{lhs_2}{4}\left(\frac{s_1 + s_2}{s_1 s_2}\right)^2, \tag{19}$$

so that the best resolution (minimum δ) will result from short channels close to the optical axis but these channels provide very little effective area. If the aperture is constructed to give the maximum area as described above then the resolution from the combination of channels across the aperture is determined by the average effective beam width $w/2$. A finite source size χ will increase the line focus width by $\chi s_2/s_1$ so that the overall line focus width for a single-reflection configuration Δ_1 is the combination of two terms,

$$\Delta_1 \sim \left(\frac{w}{2}\frac{s_1 + s_2}{s_1}, \chi\frac{s_2}{s_1}\right); \tag{20}$$

if the profiles are Gaussian, Δ_1 is given by adding the two terms in quadrature but for other profiles the combination will have a different form.

The centre of the line-spread distribution corresponds to rays which reflect from half way down the channel walls while the extremities correspond to rays which reflect from the ends. Because the channel walls are planar and not curved, the reflections from the ends introduce a small angular reflection error $\Delta\theta_{\max} \approx w/s_1$. This maximum reflection angle error occurs for $h = h_{\max}/2$. For a double-reflection configuration the maximum reflection angle error is given by the same expression but this now occurs at twice the axial offset, $h = h_{\max}$, because the radii of curvature of the plates is twice as large. However, each ray in the double-reflection case suffers two reflection errors so the line-spread function contribution from the length of the channels will be twice as wide.

$$\Delta_2 \sim \left(w\frac{s_1 + s_2}{s_1}, \chi\frac{s_2}{s_1}\right). \tag{21}$$

For many applications, it is useful to express the performance of a device in terms of a gain given by the ratio of the geometric (or effective) aperture area to the area of the line (or spot) focus. If we use the first term in (20) for the focus width and the total length of the line focus as $4h_{\max}$ (this length is twice the width of the MOA aperture) then the geometric gain of a single-reflection device is

$$G_{\text{geom}} = \frac{4w}{pl}\frac{s_1 s_2^2}{(s_1 + s_2)^2}. \tag{22}$$

The gain of a double-reflection configuration will be twice this because the aperture area is increased by a factor of four while the line-spread width is increased by a factor of two. Of course, the true gain will be limited by the X-ray reflectivity and scattering losses, so G_{geom} represents an idealised upper limit.

In summary, the maximum aperture half width, geometric area, and width of the line-spread function for a single-reflection MOA are given by (15), (16), and (20), respectively. For a double-reflection MOA, the maximum aperture width is twice that of a single-reflection MOA. This increases the geometric area by a factor of four and the line-spread width by a factor of two. Therefore the flux per unit area in the line-spread function from a double-reflection MOA could be twice that of a single-reflection MOA. That is, the double-reflection system has twice the gain. However, it is likely that channel alignment, figure errors in the channel walls and surface roughness of the channel walls will limit the performance of a double-reflection device, and this potential advantage over a single-reflection MOA may not be realised.

Adjustment of the curvature of the plates gives us potential control over the focused line width and, for a double-reflection MOA, the flux level in the focused line. For a single-reflection device, we can tweak the curvature, R, using piezoelectric actuators, so that it matches the requirement given by (4). In principle, an array of actuators could be employed such that any error in the bending or deviations away from the cylindrical (circular) form could be reduced or eliminated. For a double-reflection configuration tweaking the curvature of the first plate will alter the convergence or divergence of the beam (rays) in the gap between the plates. This will provide control over the flux that intersects with the channels in the second plate and hence the flux in the focused

line/spot. Tweaking of the curvature of the second plate then gives us control of the size of the focused line, but this has only a very small effect on the efficiency.

For the double-reflection configuration, the lateral and rotational alignment of the two elements is also critical in achieving the highest efficiency. It is envisaged that these alignments would have to be adjusted in conjunction with the curvature of the first plate to realise the highest flux level in the focused line. The potential flux advantage of the double-reflection device would only be achieved if such adjustment was possible/successful.

2.3.2. Spot-to-Spot Focusing. For a crossed pair of planar channel MOAs in the arrangement described in Section 2.2 the geometric area is a factor of $w/2p$ less than a single-reflection MOA because only that fraction of the flux focused by the first component is intercepted by the channels of the second. The geometric aperture area is therefore

$$A_{\text{geom}} = \frac{16w^4}{p^2 l^2}\left(\frac{s_1 s_2}{s_1 + s_2}\right)^2, \tag{23}$$

where we have assumed that the gap between the components is small such that s_1 and s_2 are the same for both. Two reflections give focusing in two axes so the area of the focused spot (assuming a point source) is

$$\Delta_1^2 = \frac{w^2}{4}\left(\frac{s_1 + s_2}{s_1}\right)^2. \tag{24}$$

Therefore the geometric gain is given by

$$G_{\text{geom}} = \frac{64w^2}{p^2 l^2}\frac{s_1^4 s_2^2}{(s_1 + s_2)^4}, \tag{25}$$

and the ratio of the gain for the spot-to-spot focusing using a crossed pair compared with line-to-line focusing using just one MOA is $2ws_1/(pl)$.

In order to achieve the optimum (minimum spread) focus in a crossed pair configuration, we required adjustment of either both the radii of curvature of the components or the adjustment of the radius of one component and the position of the detector or source along the axis (tweak of s_1 or s_2). These adjustments could be provided using piezoelectric actuators and would give independent control of the focus in x and y directions on the image plane.

2.4. Circular-Channel MOAs. A schematic of the geometry of a two-reflection MOA with circular channels is shown in Figure 3. This is similar to the flat-curved configuration with planar channels considered above except that the two components are set with separation (of the centres along the axis) D; the grazing angles on the first and second components are θ_1 and θ_2; distances h_1 and h_2 now become radii of the reflecting surface walls, r_1 and r_2; S is the distance from the source to the first component; d is the axial distance between the centre and edges of the second component (introduced by the curvature); F is the focal distance measured from the centre of the second component which is bent to a radius R. We have

$$\begin{aligned} \tan\theta_1 &= \frac{r_1}{S}, \\ r_2 &= r_1 - (D + d)\tan\theta_1, \\ (R - d)^2 + r_2^2 &= R^2. \end{aligned} \tag{26}$$

Assuming that D and R are set by the user, we can solve (26) giving d and r_2 for a given r_1. Then, θ_2 can be calculated from

$$\begin{aligned} \tan(\theta_1 + \theta_2) &= \frac{r_2}{(R - d)}, \\ \tan(\theta_1 + 2\theta_2) &= \frac{r_2}{F - d}, \end{aligned} \tag{27}$$

These equations hold for rays which come from a point source on axis and reflect from the centres of the channels. In practice, radiation incident on the first component before (after) the centre will have a larger (smaller) grazing incidence angle and will therefore hit the second component channel after (before) the centre. The result is a broadening of the focal spot. The system provides point-to-point imaging with a resolution limited by the length of the channel wall, l. The rays diverging from the source intersect the rays converging to the focus at a principal surface which is approximately planar and lies between the first and second components, perpendicular to the optical axis. Thus a source spot of finite size will be imaged to a focal spot of finite size with demagnification $\approx F/S$.

The geometric aperture area and gain of a two-reflection MOA with circular channels could be comparable to or larger than a crossed pair of planar channel devices as described in Section 2.3.2 but it would be critically dependent on the manufacture tolerances of the channels and the co-alignment of the two components. Circular channel MOAs can be aligned and adjusted for optimum performance in the same way as planar channel devices. The spot flux and spot size produced by the flat-curved configuration illustrated in Figure 3 could be controlled by changing both the separation, D, and curvature, R, using piezo actuators.

3. Manufacture of MOAs

There are two stages in the manufacture of the types of optics discussed in the previous section: first, to produce the channel structures and second, to bond the actuators. To date, only the 1-D planar channel components have been made.

3.1. Deep Silicon Etching of the Channel Structures. The channel structures of the MOAs can be formed by silicon etching via the Bosch process [13], using a pattern mask and a cycle of etching/passivation. The gases used are SF_6 for etching and C_4F_8 for passivation; the latter prevents sidewall etching and so allows deep channels with parallel walls to be made. However, the cyclic etch process results in quasi periodic "terracing" or "scalloping" of the sidewalls as the

etch proceeds down into the silicon. Also, line edge roughness on the mask—which is random but not periodic—is replicated on the etched sidewalls as vertical striations, the "curtain effect". Both of the surface roughness features are illustrated by the SEM pictures shown in Figure 8. They must be minimised to prevent excessive X-ray scattering. A root-mean-square roughness of around 2 nm is required as discussed in the next section. Early etching attempts did not provide roughnesses much better than 1 μm, but a succession of changes to the process cycle has led to values within an order of magnitude or so of those required, coupled with deep channels and relatively straight walls. The changes include the following:

(i) shortening of the etch/passivate cycle time to reduce both the amplitude and the spacing (wavelength) of the scallops,

(ii) the use of "over-run", that is, overlapping the etch and passivate stages, to smooth the peaks and troughs of the scallops,

(iii) varying the gas flow rates and pressure,

(iv) following etching, the channel walls are subject to oxidisation followed by removal, which has the effect of "snapping off" the peaks.

Using such improvements, other authors have achieved sidewall roughnesses of ~10 nm [14]; although this is still several times larger than that required, it is likely that further changes to the processes can provide further improvements. An alternative to the "dry" etching process is "wet" etching whereby the silicon is immersed in a chemical solution and is dissolved to achieve the desired shape by the use of a mask. This preferentially etches along the ⟨111⟩ or ⟨110⟩ silicon crystal planes, creating very smooth, straight walls. Initial testing indicates that the surface roughness achieved is much lower than that for the dry etching process, providing that the mask edges are accurately aligned to the crystal lattice, but this technique cannot be used to produce cylindrical geometry because the etch follows the crystal planes. A full analysis of the manufacturing process will be given in subsequent publications.

3.2. Actuator Control. Several 2 × 1 cm silicon chips with 2 × 2 mm active areas have been epoxy-bonded to piezo actuators with the general arrangement shown in Figure 7, and these are awaiting testing. Issues that are being addressed include piezo thickness, and width, bonding agent thickness and the use of low-shrinkage glues (to prevent shrinking itself causing bending). Different types of actuators, including unimorph (as discussed here), bimorph, and piezo fibres are also being considered. These aspects will also be discussed in future publications.

4. X-Ray Scattering from the MOA Walls

Surface roughness in the axial direction (across the scallops) will cause in-plane scattering while the curtain profile will give either out-of-plane reflection errors and/or out-of-plane scattering in which the curtain behaves like a ruled grating in a conical diffraction configuration.

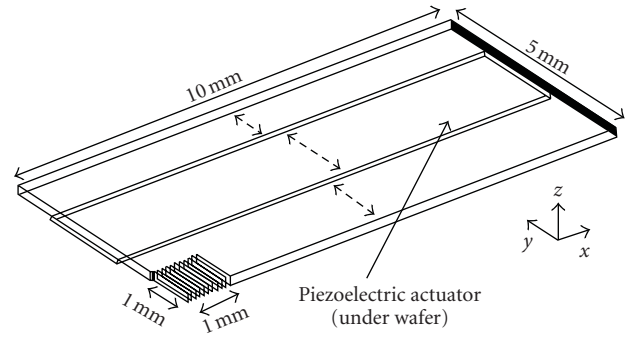

Figure 7: Schematic of the piezo actuator bonded to silicon wafer. A quarter of a 1-D chip is shown. The bottom left corner contains the etched channels which cover $2 \times 2\,\text{mm}^2$ in the centre of the chip. The dashed line indicates dimensions which were varied in the FEA modelling.

4.1. In-Plane Scattering. Figure 9 shows the geometry of in-plane scattering from the axial surface roughness across the scallops. This scattering is conventionally calculated using first-order theory which gives the Total Integrated Scatter (TIS),

$$\text{TIS} \simeq \left(\frac{4\pi\theta_g\sigma}{\lambda}\right)^2, \tag{28}$$

where σ is the rms surface roughness; λ is the X-ray wavelength; θ_g is the grazing angle. This will be a good approximation provided that $\theta_g\sigma/\lambda \ll 1$ and the TIS is a few percent. Rearranging gives

$$\sigma \simeq \frac{\lambda(\text{TIS})^{1/2}}{4\pi\theta_g}. \tag{29}$$

If we take $\lambda = 10\,\text{Å}$ (1.24 keV), $\theta_g = 2 \times 10^{-2}$ radians (1.14 degrees) then $\sigma = 4(\text{TIS})^{1/2}$ nm, and we require $\sigma \simeq 2$ nm to keep the TIS small (<0.25) as already stated above. The scattering angles will be given by the grating equation

$$\frac{n\lambda}{d\sin\theta_g} = \sin\beta, \tag{30}$$

where d is the correlation length of the surface roughness along the axial direction down the scallop. If the surface is much rougher than this, then higher-order scattering and/or shadowing (absorption) will become important and TIS → 1. The higher orders can, in principle, be calculated but we require detailed knowledge of the statistical properties of the surface height distribution over and above σ and d.

4.2. Out-Of-Plane Reflection/Scattering. The walls of an MOA will act as a diffraction grating with the grating spacing given by the width of the curtain features b as shown in

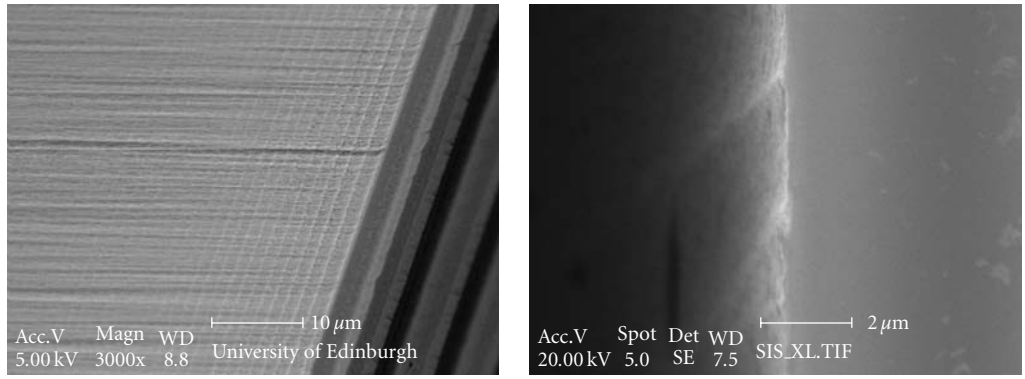

(a) (b)

Figure 8: (a) Scalloping on the etched channel walls. (b) Details of the curtain effect caused by rough edges of the etching mask.

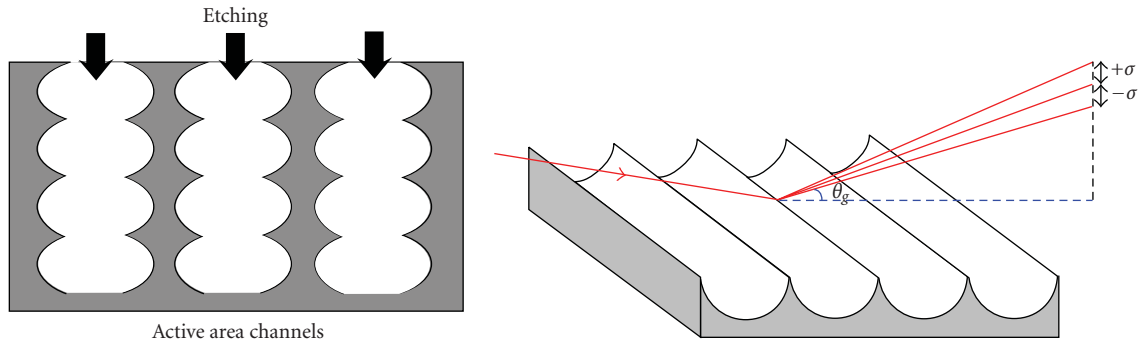

(a) (b)

Figure 9: In-plane scattering from the MOA wall with scallops of width b, height h, and radius T.

Figure 10. The grating equation gives a diffraction angle out-of-plane

$$\sin\beta_d = \frac{\lambda}{b\sin\theta_g}, \tag{31}$$

which for small angles reduces to

$$\beta_d = \frac{\lambda}{b\theta_g}. \tag{32}$$

Taking the curtain profile to be a sector of a circle, the radius of the profile can be calculated using the height of the curtain features, h, and the width, b,

$$T \simeq \frac{b^2}{8h}. \tag{33}$$

Using the radius of the curtain profile T and the spacing between the cusps b, the maximum out-of-plane gradient error is then given by

$$\Delta g_{\max} = \frac{b}{2T}, \tag{34}$$

and the average gradient error is then

$$\overline{\Delta g} = \frac{b}{4T}. \tag{35}$$

Therefore, the average out-of-plane deflection error (twice the gradient error) from the curtain is

$$\beta_r = \frac{2b}{4T} = \frac{b}{2T}. \tag{36}$$

The dividing line between geometric optics (figure error dominated) and wave optics (scattering and/or diffraction dominated) is given by equating the two angles, β_d and β_r, giving

$$\frac{b}{2T} = \frac{\lambda}{b\theta_g}, \tag{37}$$

and rearranging to give

$$\frac{b^2}{T} = \frac{2\lambda}{\theta_g}. \tag{38}$$

If b^2/T is larger than this (i.e., T is small or b is large) then the geometric out-of-plane reflection errors dominate. If b^2/T is smaller than this (i.e., T is large or b is small) then the diffraction from the scallops dominates. b and T (and therefore h) will be fixed by the channel manufacture, and λ will be restricted to a given range so the dominant varying factor will be θ_g. This will be small for the channels

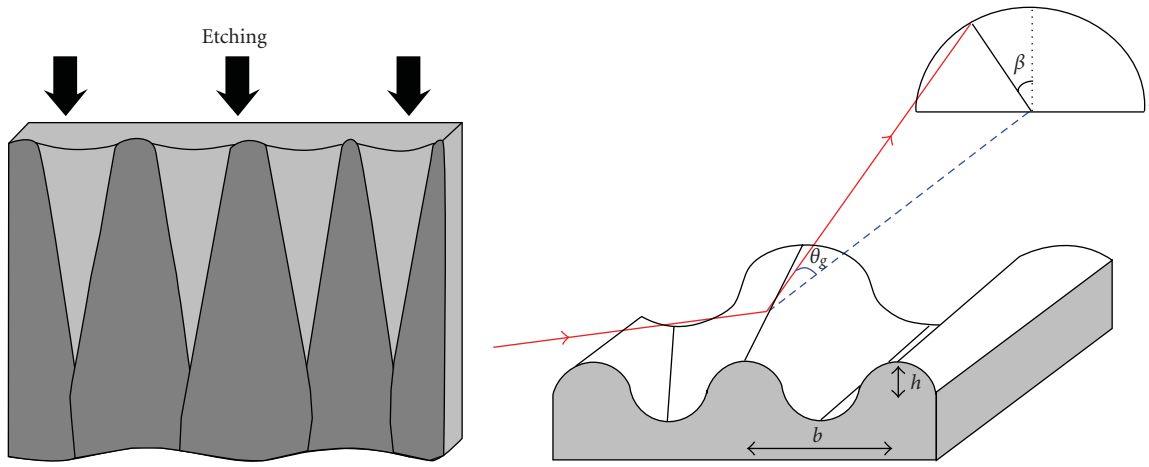

Figure 10: Out-of-plane scattering of an MOA wall with the curtain effect.

at the centre of the MOA plates and large at the edges. Again rearranging and using (33), (37) becomes

$$\theta_g = \frac{\lambda}{4h} \tag{39}$$

thus giving us the dividing line between geometric reflection errors and diffraction over the MOA aperture.

We can look at this from the point of view of the 1st-order scattering theory. For the out-of-plane diffraction, the TIS is dependent on the height of the scallops, h, just as the in-plane TIS is dependent on the rms surface roughness, σ. The out-of-plane TIS from the scallops is given by

$$\mathrm{TIS} = \left(\frac{4\pi\theta_g\sigma_h}{\lambda}\right)^2, \tag{40}$$

where σ_h is the rms height of the scallops. If $h \ll T$, then we can we can estimate this rms height

$$\sigma_h = \sqrt{\overline{h^2} - \overline{h}^2}, \tag{41}$$

giving

$$\sigma_h = \frac{2h}{3\sqrt{5}}, \tag{42}$$

Substituting this into (44), setting TIS = 1, and rearranging, we get

$$\theta_g = c\frac{\lambda}{4h}, \tag{43}$$

where

$$c = \frac{3\sqrt{5}}{2\pi} = 1.068. \tag{44}$$

This is comparable to the result produced in (39)and again gives the dividing line between geometric reflection errors and scattering/diffraction. At small grazing angles the phase errors introduced by the height error of the scallops are small, so scattering drops and geometry take over. As θ_g increases, the height errors become important and at some point scattering takes over. This also means that diffraction dominates when the projected area of the channel walls is large.

The typical curtain width is $b = 800$ nm. Assuming $\lambda = 10$ Å and $\theta_g = 2\times10^{-2}$ radians, (32) gives a diffraction angle of $\beta_d = 0.63$ radians or 35 degrees. When the depth of the curtain, h, is given by (39) (or (44)), the deflection error β_r, given by (36), will also be 35 degrees. If we are using planar channels to produce a line focus, this out-of-plane deflection will simply shift rays out-of-plane, and there should be little effect on the focus but there will be a marked decrease in the efficiency. Using the same wavelength and grazing angle we require a curtain depth $h \ll 50$ nm to prevent excessive losses due to out-of-plane scattering/reflection. For a crossed planar or circular-channel double-reflection configuration which can produce a focused spot rather than a line focus, the out-of-plane scattering by the curtain is a more serious problem. The curtain depth must be reduced to $h \approx 6.7$ nm so that $\sigma_h \approx 2$ nm and out-of-plane scattering is reduced to the same level as the in-plane scattering.

5. Finite Element Analysis and Ray-tracing

The MOA channels are made in flat silicon and then bent using piezo actuation to give the required focusing and active control. We are using finite element analysis (FEA) to model the effects of the bending on the channel walls, and the results from this will be fed into ray-tracing analysis in order to determine the properties of the MOA focus. Section 5.1 describes the progress to date on the FEA, and Section 5.2 discusses the results of ray-tracing. The latter uses in-house software as commercial packages are not well suited to MOA structures (Zemax was used for the same initial ray-tracing

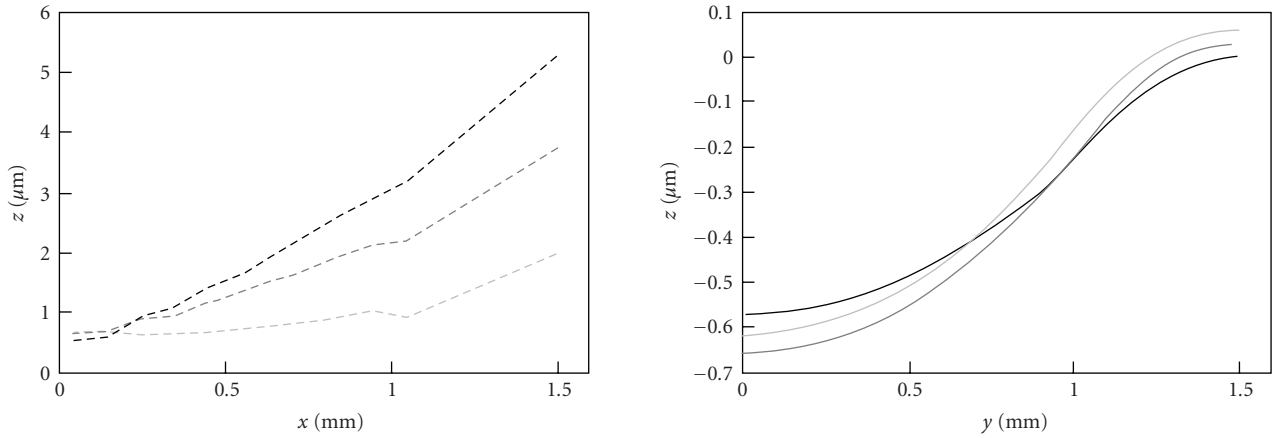

Figure 11: FEA results for bending of a 1-D MOA using two strips of 150 μm thick PZT-5H. See text for details.

analysis but this was very cumbersome and time consuming). The FEA results have not yet been incorporated in the ray-tracing.

5.1. Finite Element Analysis. The FEA was carried out using the commercial package COMSOL Multiphysics [15]. The aim was to study the stress and displacement of a 1-D MOA when bent by a unimorph piezoelectric actuator in different configurations. Only a quarter of the silicon wafer was modelled to take advantage of the symmetry, thus reducing the processing time and allowing finer FEA meshing. The geometry is shown in Figure 7. Figure 11 shows the bending produced by two strips of 150 μm thick PZT-5H placed adjacent to the active area. The dark curve is for strips 4 mm wide, that is, covering the whole area between the active area and the edge of the silicon chip (see Figure 7). The grey curve is for 2 mm wide strips and the light curve for 1 mm wide strips. In these calculations, the effect of glue used to bond the actuators was neglected. The applied voltages were the maximum that the piezos are expected to withstand, namely $\sim$2.5 V/μm of thickness. The curvature required is along the X-axis. Note that there is a small step at $x = 1$ mm which corresponds to the edge of the etched area which contains the channels. Clearly, the bending results in very complex shapes, and more detailed analyses are ongoing. The smallest radius of curvature, produced by the 4 mm wide strips of PZT-5H, is $\approx$200 mm. Similar curves produced using piezo thicknesses of 50 μm and 100 μm indicate that this is the smallest radius of curvature which can be produced with PZT-5H. The typical radius of curvature required for optimum 1-D single-reflection designs is $\sim$50 mm and for double-reflection configurations $\sim$100 mm although some configurations in which $s_1 \approx s_2$ utilize flat plates or very large radii. Further work is required to find the optimum piezo material and geometry which can generate and give adequate adjustment of these curvatures.

5.2. Ray-tracing. For the ray-tracing described in this section, the software "Q", developed at the University of Leicester specifically for grazing incidence [16], was used. This is much better suited to optics such as MOAs than commercial packages are and has the flexibility to allow future add-ons, for example, to take diffraction into account. In the examples given here the rays travel from right to left. In all the simulations presented, the same channel dimensions were assumed; channel width $w = 10\,\mu$m, channel pitch $p = 20\,\mu$m, and channel depth (axial length) $l = 200\,\mu$m. In the first four cases, the total distance between the source and image plane ($s_1 + s_2$) was set to 40 mm, and the aperture dimension was set to the appropriate value of $2h_{\max}$ depending on the configuration. As a first example, line-to-line focusing by a single-reflection MOA with $s_1 = 25$ mm, $s_2 = 10$ mm, and bending radius $R = 33$ mm is shown in Figure 12. The rays which suffer from one reflection and are brought to a line focus are shown in green. Rays which are not reflected but penetrate the channels near the axis and rays, towards the edge of the aperture, which suffer from two reflections are shown in red and blue, respectively. The width and integral of the focused line profile shown in the right-hand panel are in good agreement with the predictions given by (20) and (16). The Full Width Half Maximum (FWHM) of the line profile is 16 μm and the geometric area of the utilized aperture is 3.5 mm^2.

Ray-tracing of a double-reflection equal grazing angle MOA is shown in Figure 13. This has $s_1 = s_2 = 20$ mm so that it is also a special case of the collimator-telescope configuration. The gap between the components is set to 2 mm so that rays in the gap, parallel to the axis, are clearly visible. The bending radii are $R_1 = R_2 = 40$ mm, with opposite curvatures. Near the axis a few rays miss both components. Further out rays which reflect from the 1st component but miss the 2nd are clearly visible as rays running parallel to the axis on the left. There are also a few rays which miss the 1st and reflect from the 2nd being brought to a focus half way between the 2nd component and the image plane. The focused line profile in the right-hand panel is much broader than the single-reflection configuration shown in Figure 12. This is partly because there are two reflections

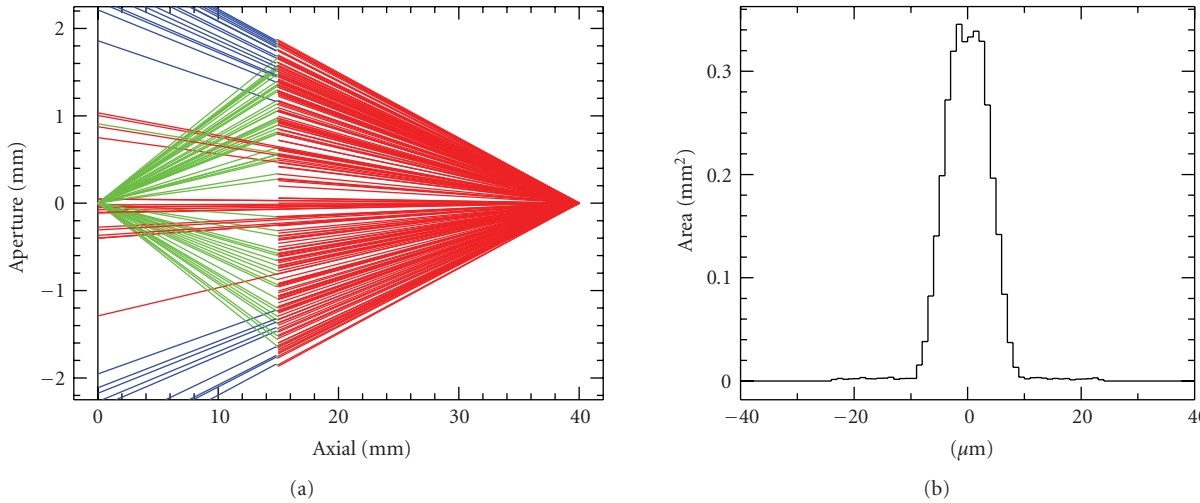

FIGURE 12: Line focusing by a single-reflection MOA (a) traced rays; red: no reflection, green: 1 reflection, blue: 2 reflections, (b) the focused line profile.

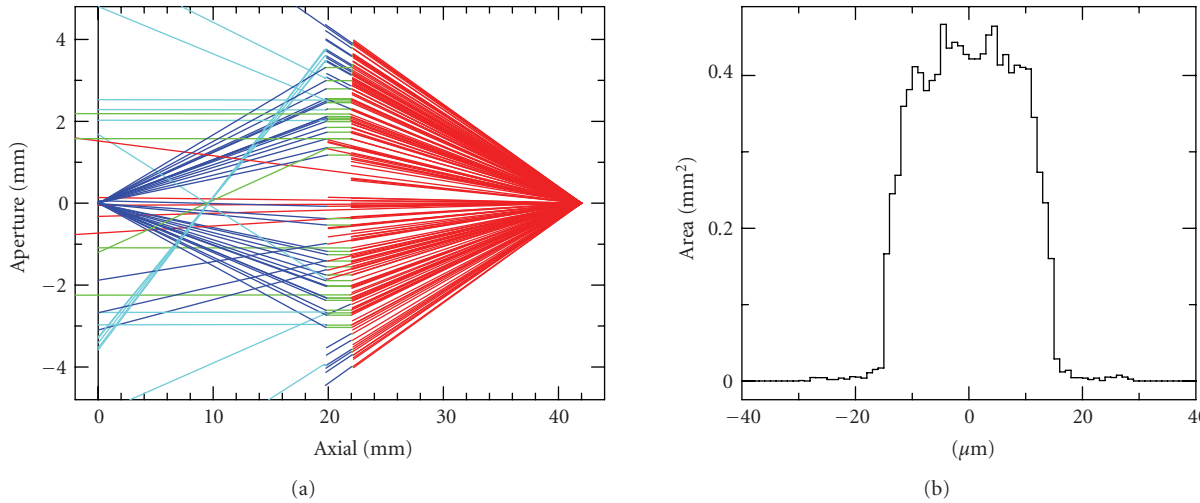

FIGURE 13: Line focusing by a double-reflection MOA with equal grazing angles. (a) Traced rays; red: no reflection, green: 1 reflection, blue: 2 reflections, (b) The focused line profile.

but also because $(s_1 + s_2)/s_1 = 2$ whereas this ratio was set to 1.6 in the single-reflection case. The FWHM of the line profile is 30 μm. The effective aperture width and hence the integrated flux in the line-spread distribution is a factor 3.2 larger for the double-reflection configuration as expected; the geometric area of the utilized aperture is 11.1 mm^2. In this configuration the double-reflection MOA provides a flux advantage but degrades focusing.

Figure 14 shows the ray-tracing results for a double-reflection flat-curved configuration with equal grazing angles. The structure in the focused line profile seen outside the central peak is due to rays which have penitrated both components without reflection. These could be eliminated using a small central aperture stop. As explained in Section 2.1.2 $s_1 = 3\ s_2 = 30$ mm and the curvature of the second plate must be $R_2 = s_1/2 = 15$ mm. In order to maximise the throughput, the gap was adjusted until the integral in the line-spread function was maximised. This corresponded to $D = 0.45$ mm. The position of the source and the image plane were then tweaked to minimize the width of the line-spread function. The geometric area and line-spread function width for this configuration are very similar to the single-reflection case shown in Figure 12. The FWHM of the line profile is 9 μm, and the geometric area of the utilized aperture is 2.9 mm^2 so, surprisingly, the ray-tracing simulation indicates that using two reflections in a flat-curved configuration gives very little performance benefit over the single-reflection configuration. This is because some flux reflected from the first plate is not intercepted by the channels in the second plate even when the gap has been optimised. Furthermore, experience in setting up the ray-tracing and optimizing the simulation performance indicates that the double-reflection configuration would be more difficult to align and adjust in reality.

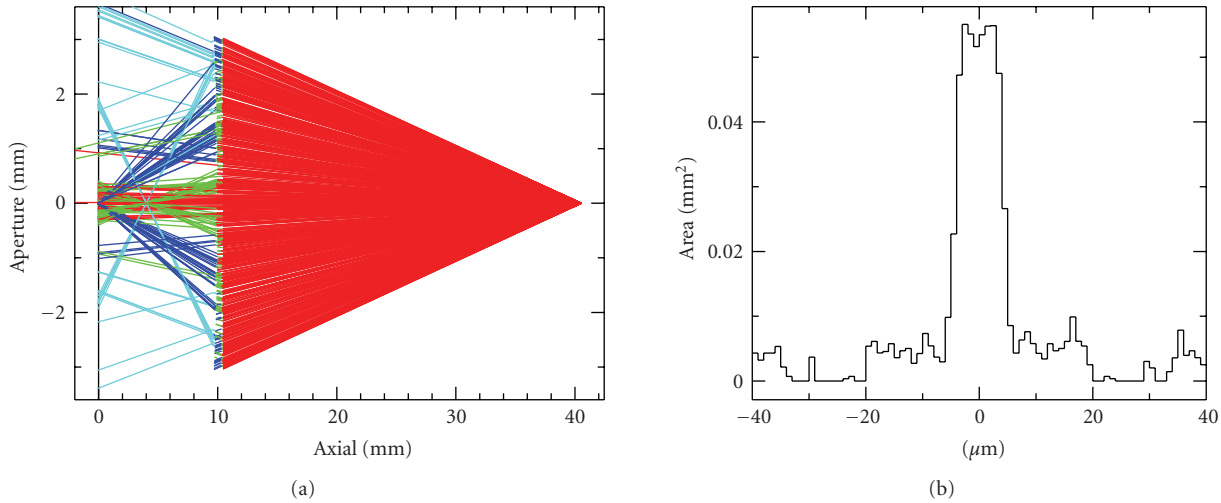

FIGURE 14: Line focusing by a double-reflection MOA with a plane-curved equal grazing angle configuration. (a) Traced rays; red: no reflection, green: 1 reflection, blue: 2 reflections, (b) The focused line profile.

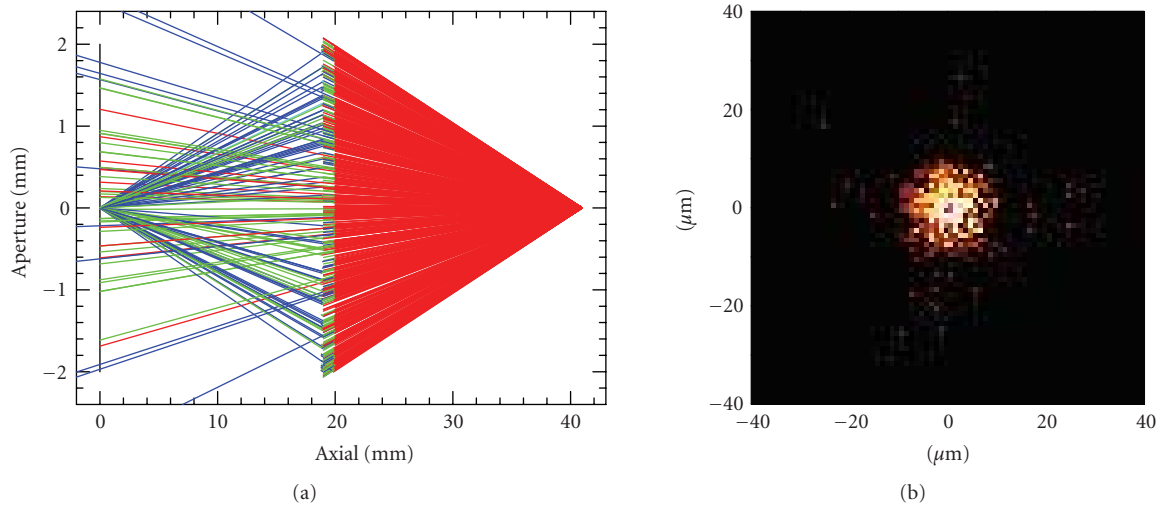

FIGURE 15: Spot focusing by a double-reflection crossed pair. (a) Traced rays; red: no reflection, green: 1 reflection, blue: 2 reflections. (b) Image of the focused spot.

Figure 15 shows a ray-tracing of a crossed double-reflection configuration. The first component is placed with $s_1 = 20\,\text{mm}$ and the second with $s_1 = 21\,\text{mm}$ so the gap is $D = 1\,\text{mm}$. The radii of curvature were adjusted in an iterative process to find the minimum spot Half Energy Width (HEW); $R_1 = 691\,\text{mm}$ and $R_2 = 262\,\text{mm}$. Thus the ray-tracing software was used to simulate the active adjustment of the components to optimise the performance. The geometric aperture area was $0.8\,\text{mm}^2$, and the minimum HEW found was $10.1\,\mu\text{m}$. The FWHM of the spot was $9.1\,\mu\text{m}$.

Table 1 Summarises the ray-tracing results for the four configurations tested. The ray-tracing was run with perfect reflectivities to give the geometric area A_{trace} mm^2 and the line/spot width FWHM μm. It was then rerun using theoretical reflectivities as a function of grazing angle for 1 keV X-rays from a Silicon surface and Gold surface so that gains, G_{Si} and G_{Au}, could be calculated. These represent the best estimates of the gains which could be achieved if the channel walls were perfectly smooth. The gains calculated using the simple formula, A_{geom}, and the ray-tracing, A_{trace}, are in reasonable agreement. The differences are due to a combination of losses not included in the formulae for double-reflectivity MOAs and a better estimate of the true width of the focused distribution is provided by the ray-tracing. The G_{Si} values are all much lower because the critical angle from Silicon at 1 keV is much smaller than that required to utilise the edges of the aperture. The G_{Au} values are significantly better because the high-Z material provides a much higher soft X-ray reflectivity than bare Silicon. For applications where the flux per unit area in the focused line/spot is paramount the crossed spot-to-spot

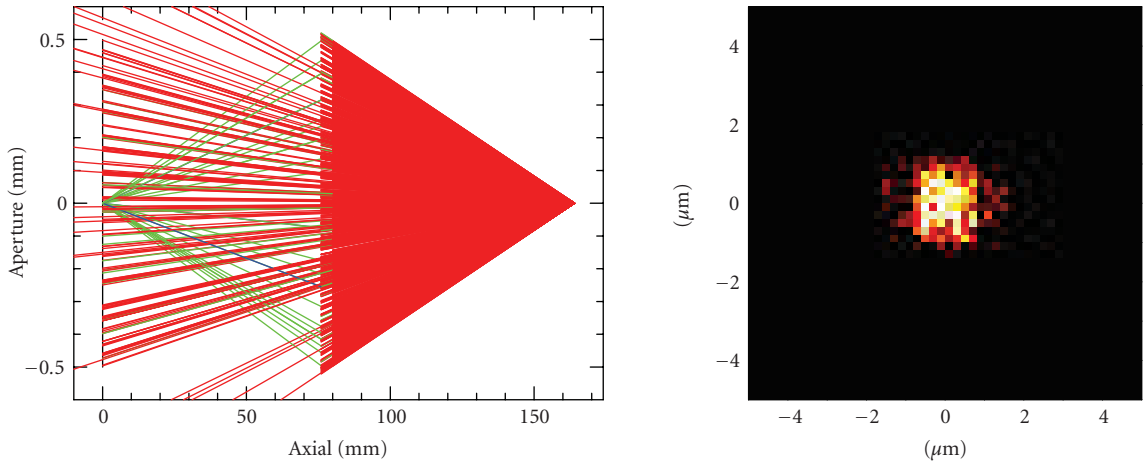

Figure 16: A small aperture double-reflection crossed pair system. (a) Traced rays; red: no reflection, green: 1 reflection, blue: 2 reflections, (b) Image of the focused spot.

Table 1: Summary of ray-tracing results. G_{geom} is the gain calculated using the formula (22) or (25). A_{trace} (mm^2) and G_{trace} are the geometric area and gain calculated from the ray-tracing. FWHM (μm) is the width of the line-spread or point-spread function. G_{Si} is the gain calculated including the reflectivity of 1 keV X-rays from a Silicon surface (uncoated). G_{Au} is the gain calculated including the reflectivity of 1 keV X-rays from a Gold surface (channel walls coated).

Configuration	G_{geom}	A_{trace}	FWHM	G_{trace}	G_{Si}	G_{Au}
Single Figure 12	58	3.5	16	58	9.0	23
Double Figure 13	100	11.1	30	70	8.2	16
Flat-curved Figure 14	56	2.5	9.0	40	0.06	6.9
Crossed Figure 15	6400	0.80	9.1	9660	326	1690

focusing configuration is by far the best, despite the fact that the geometric aperture area is rather small. However, gain values of 100s to 1000s will only be achievable if the channel walls can be manufactured with low-surface roughness, <2 nm rms, so that the TIS is kept low.

The results in Table 1 are for configurations in which the aperture (f-ratio) was set to maximise the geometric collecting area. In these configurations, the width of the line-or point-spread functions is determined by the channel width p which is why the FWHM values are $\sim 10\,\mu$m or bigger. Instead of trying to maximize the aperture area we can choose to minimize the width of the focus while also providing a useful gain. At the same time we can look for configurations which are optimized for X-rays, including the X-ray reflectivity, rather than considering just the geometric response. We can reduce the focus size by shrinking the aperture, increasing the object and image distance and increasing the demagnification by making s_2/s_1 smaller. Figure 16 shows the ray-tracing results for a double-reflection crossed pair system with $s_1 = s_2 = 80$ mm, gap between the components $D = 1$ mm, and aperture width 1 mm. The simulation was run using X-ray reflectivities calculated for Silicon at 4.51 keV. The spot size and effective area are therefore representative of the idealised X-ray performance at this energy. The radii of curvature were adjusted to give the minimum spot size FWHM = $1.27\,\mu$m and HEW = $1.28\,\mu$m; $R_1 = 3180$ mm and $R_2 = 1077$ mm. The effective area was $A_{\text{eff}} = 6.15 \times 10^{-4}$ mm^{-2}. This is tiny because the grazing angles are very small, and most of the radiation goes straight through the channels without reflecting from the walls. A much larger area could be achieved if the channels were much narrower but such channels would be difficult to manufacture. Despite the low area, the gain is $G_{Si} = 380$ which is comparable to the value obtained for the crossed system given in Table 1. Using a larger f-ratio, we can decrease the spot size, shift the response to higher X-ray energies, and suffer a large decrease in effective area, but retain a high gain.

6. Microprobing of Biological Cells

A potential application of the MOAs described above is in the microprobing of biological cells. Research into radiation-induced cancers involves measuring the response of biological material—cells, subcellular components, and ultimately, tissue samples—to hard radiation. To do this, we need to focus X-rays down to micrometre scale and to date this has been carried out using (primarily) carbon K X-rays (wavelength 44 Å, energy 284 eV) and zone plate optics [17, 18]. These initial investigations are limited because carbon K X-rays are almost totally absorbed by single cells, so that tissue samples, of more relevance to living organisms,

cannot be studied. For every ~104 cells killed by irradiation only one will mutate, so very many cells must be irradiated to track mutations, and in order to irradiate smaller cellular components, very small focal spot sizes are necessary. What is required is a focusing optic capable of delivering more flux per unit time (intensity) than a zone plate (which is limited by its aperture, typically a few hundred micrometres), while providing a focal spot of similar size. To facilitate tissue irradiation, higher X-ray energies are also needed but a zone plate focal length is proportional to energy, so a zone plate system is inherently achromatic and provides less demagnification of the source and hence larger spot sizes at higher energies. The fundamental equation which describes a zone plate is [19]

$$r_n^2 = n\lambda f + r_0^2, \tag{45}$$

where λ is the wavelength of the X-rays being focused; f is the focal length; r_0 is the radius of the first zone. The width of the nth zone can be calculated using

$$d_n \approx \frac{\lambda f}{2r_n} = \frac{r_n}{2n}. \tag{46}$$

In Section 5.2, we showed that an MOA system with a geometric aperture of ≈2 mm, a channel aspect ratio (length : width) of ≈20 : 1, and a constant period of 20 μm in 200 μm thick silicon can produce small spot size and high gains provided that sidewall roughness is no more than a few nanometres. In particular, the double-reflection crossed system, Figure 16, was shown to provide a spot size of ~1 μm and gain of ~380 for an energy of 4.51 keV (Ti K_α X-rays). Ultimately, a double-reflection circular MOA configuration may be able to provide a performance better than this if the components can be manufactured and aligned.

For example, using the system illustrated in Figure 3 with $S = 160$ mm, $D = 1$ mm, $R = 100$ mm, and $l = 100\,\mu$m, gives $d \approx 10\,\mu$m and $F = 72.9$ mm, the same as the focal length of a zone plate (using (45) and (46)) of diameter 200 μm and outer zone width 100 nm for Ti K_α X-rays. For a point source of Ti K_α X-rays, the ray-tracing package Zemax [20] predicts an MOA focal spot diameter of ≈0.2 μm while for a 5 μm source, the focal spot diameter is ≈2 μm; the latter is dominated by the demagnified source size, and so it is the same for the zone plate and the MOA. With a smaller bending radius R the value of F for the MOA would be reduced, resulting in a smaller focal spot size. The only way to do this with a zone plate is to use a different optic with either a smaller diameter or a smaller outer zone width. With a sidewall roughness of ≈2 nm, the MOA provides around two orders of magnitude more focused flux (higher gain) than the corresponding zone plate, primarily due to the larger aperture—the effective aperture diameter is ≈1 mm as towards the edge of the optic, the grazing angle is larger than the critical angle, so that the reflectivity decreases.

7. Conclusion

Active MOAs manufactured by etching Silicon have a great potential for the focusing of soft X-rays, 0.1–5 keV, into very small spot sizes. We have presented a comprehensive analysis of the various geometrical configurations that can be employed and simulation results which demonstrate this potential. The SXO consortium is currently working on refining the manufacturing process which produces the arrays of slots and optimising the way in which piezoelectric actuators can provide the necessary curvature and active adjustment of the focusing properties. Progress in these areas will be reported in subsequent publications.

Acknowledgments

The Smart X-Ray Optics consortium is funded by the UK Research Councils' Basic Technology programme, Grant code D04880X. The members of the consortium are University College London (including the Mullard Space Science Laboratory), King's College London (KCL), the Gray Cancer Institute (GCI), the University of Leicester, the Scottish Microelectronics Centre at the University of Edinburgh, the University of Birmingham, and STFC Daresbury Ltd. Silson Ltd. is an associate member. KCL has also received support from the European Science Foundation COST Action P7 "X-Ray and Neutron Optics", while KCL and GCI are supported by the COST Action MP0601 "Short Wavelength Laboratory Sources".

References

[1] P. D. Prewett and A. G. Michette, "MOXI: a novel microfabricated zoom lens for x-ray imaging," in *Advances in X-Ray Optics*, Proceedings of SPIE, pp. 180–187, August 2000.

[2] A. G. Michette, P. D. Prewett, A. K. Powell, S. J. Pfauntsch, K. D. Atkinson, and B. Boonliang, "Novel microstructured adaptive X-ray optics," *Journal de Physique IV*, vol. 104, pp. 277–280, 2003.

[3] M. Y. Al Aioubi, P. D. Prewett, S. E. Huq, V. Djakov, and A. G. Michette, "Design and fabrication of micro optical system for x-ray analysis of biological cells," in *Opto-Ireland 2005: Optoelectronics, Photonic Devices, and Optical Networks*, vol. 5825 of *Proceedings of SPIE*, pp. 640–646, Dublin, Ireland, 2005.

[4] M. Y. Al Aioubi, P. D. Prewett, S. E. Huq, V. Djakov, and A. G. Michette, "A novel MOEMS based adaptive optics for X-ray focusing," *Microelectronic Engineering*, vol. 83, no. 4-9, pp. 1321–1325, 2006.

[5] July 2007, http://SmartXrayOptics.org.

[6] July 2007, http://www.rcuk.ac.uk/basictech/default.htm.

[7] A. Michette, T. Button, C. Dunare et al., "Active microstructured arrays for X-ray optics," in *Advances in X-Ray/EUV Optics and Components II*, vol. 6705 of *Proceedings of SPIE*, August 2007.

[8] A. G. Michette, S. J. Pfauntscha, S. Sahraeia et al., "Active microstructured X-ray optical arrays," in *EUV and X-Ray Optics: Synergy between Laboratory and Space*, vol. 7360 of *Proceedings of SPIE*, April 2009.

[9] C. Dunare, W. Parkes, T. Stevenson et al., "Microstructured optical arrays for smart x-ray optics," in *EUV and X-Ray Optics: Synergy between Laboratory and Space*, vol. 7360 of *Proceedings of SPIE*, April 2009.

[10] D. R. Sanmartin, D. Zhang, T. Button et al., "Progress on the development of active micro-structured optical arrays for X-ray optics," in *Advances in X-Ray/EUV Optics and Components IV*, vol. 7448 of *Proceedings of SPIE*, August 2009.

[11] C. A. MacDonald and W. M. Gibson, "Applications and advances in polycapillary optics," *X-Ray Spectrometry*, vol. 32, no. 3, pp. 258–268, 2003.

[12] G. J. Price, A. N. Brunton, G. W. Fraser et al., "Hard X-ray imaging with microchannel plate optics," *Nuclear Instruments and Methods in Physics Research. Section A*, vol. 490, no. 1-2, pp. 290–298, 2002.

[13] A. A. Ayn, X. Zhang, and R. Khanna, "Anisotropic silicon trenches 300–500m deep employing time multiplexed deep etching (TMDE)," *Sensors and Actuators A*, vol. 91, pp. 381–385, 2001.

[14] H.-C. Liu, Y.-H. Lin, and W. Hsu, "Sidewall roughness control in advanced silicon etch process," *Microsystem Technologies*, vol. 10, no. 1, pp. 29–34, 2003.

[15] July 2007, http://www.comsol.com/.

[16] July 2007, http://www.star.le.ac.uk/~rw/q_v6/index.html.

[17] M. Folkard, K. M. Prise, C. Shao et al., "Understanding radiation damage to cells using microbeams," *Acta Physica Polonica A*, vol. 109, no. 3, pp. 257–264, 2006.

[18] A. G. Michette, "X-ray optics," in *The Optics Encyclopedia*, Th. G. Brown, K. Creath, H. Kogelnik, M. A. Kriss, J. Schmit, and M. J. Weber, Eds., pp. 3305–3371, John Wiley & Sons, Berlin, Germany, 2003.

[19] G. R. Morrison, "Diffractive X-ray optics," in *X-Ray Science and Technology*, A. G. Michette and C. J. Buckley, Eds., p. 335, chapter 8, Institute of Physics Publishing, Bristol, UK, 1993.

[20] July 2007, http://www.zemax.com/.

Hindawi Publishing Corporation
X-Ray Optics and Instrumentation
Volume 2010, Article ID 867049, 17 pages
doi:10.1155/2010/867049

Review Article

Focusing Polycapillary Optics and Their Applications

Carolyn A. MacDonald

Center for X-Ray Optics, University at Albany, SUNY, Albany, NY 12222, USA

Correspondence should be addressed to Carolyn A. MacDonald, c.macdonald@albany.edu

Received 23 April 2010; Revised 26 August 2010; Accepted 18 October 2010

Academic Editor: Ali Khounsary

A summary of focusing X ray polycapillary optics is presented including history, theory, modeling, and applications development. The focusing effects of polycapillary optics come from the overlap of the beams from thousands of small hollow glass tubes. Modeling efforts accurately describe optics performance to allow for system development in a wide variety of geometries. The focusing of X ray beams with polycapillary optics yields high gains in intensity and increased spatial resolution for a variety of clinical, lab-based, synchrotron or in situ analysis applications.

1. Introduction

Polycapillary optics are arrays of small hollow glass tubes. X rays are guided down these curved and tapered tubes by multiple reflections in a manner analogous to the way fiber optics guide light. They differ from single-bore capillaries and X ray mirrors in that the focusing or collecting effects come from the overlap of the beams from thousands of channels, rather than from a few surfaces. Generally, this results in relatively efficient collection, especially from large divergent sources such as conventional X ray tubes, but does not produce submicron beam spot sizes.

The potential for guiding X rays down single-capillary tubes by total reflection was noted in the 1950s [1, 2] and measured in the 1960s [3] and 70s [4–6]. The invention of polycapillary optics by Kumakhov was built on this work [7–10] and inspiration from ion channeling and channeling radiation [11]. A theoretical review of the potential for polycapillary optics and prototype testing was published in 1990 [12].

In November of 1990, the Center for X Ray Optics (CXO) at the University at Albany was jointly founded with the Institute for Roentgen Optical Systems (IROS) in Moscow as part of an agreement between Kumakhov and the late Gibson to jointly develop the technology [13–15] both at these institutes and at a jointly founded company, X Ray Optical Systems (XOS). Early work at CXO [16–21] and IROS [22–25] was concerned with developing techniques for systematic measurements and of investigating the potential for application development. In 2001, Gibson retired from the university and moved to XOS. Kumakhov also worked in commercialization of the optics with other companies, especially with Unisantis. Over the years, many more groups have contributed to the worldwide development of the optics. Not every group can be mentioned here, but more than two dozen are cited in this paper. In addition, while in the discussion of the behavior of the optics, example data has largely been drawn from CXO, in many cases similar data could have been obtained from almost any of the other groups.

Polycapillary optics are well suited for clinical, *in situ*, or laboratory-based applications such as X ray fluorescence and X ray diffraction, especially on small samples [26, 27]. Because they are based on reflection, not diffraction, they are achromatic, appropriate for broadband applications, including white beam synchrotron focusing and collection of astronomical signals for spectroscopy.

X rays can be transmitted down a curved hollow tube as long as the tube is small enough, and bent gently enough, to keep the angles of incidence less than the critical angle for total reflection, θ_c. The critical angle for borosilicate glass is approximately

$$\theta_c \approx \frac{30\,\text{keV}}{E}\text{mrad}, \tag{1}$$

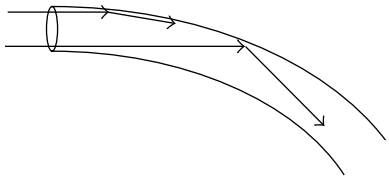

Figure 1: X rays traveling in a bent capillary tube. The trajectory of the ray entering at the top at grazing incidence is projected onto the page, but in three dimensions will "toboggan" in a constant radius spiral. The X ray entering at the bottom (closest to the center of curvature) strikes at a larger angle.

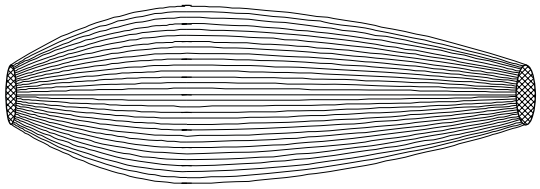

Figure 2: Sketch of the interior channels of a monolithic polycapillary optic with a short input and longer output focal length.

which is approximately 1.7° for 1 keV photons and 0.086° for 20 keV photons. The angles are somewhat larger for leaded glass.

As shown in Figure 1, the angle of incidence for rays entering a bent tube increases with tube diameter. The requirement that the incident angles remain less than the critical angle necessitates the use of small channel sizes, typically between 2 and 50 μm, although research for submicron channel sizes is reported in Section 5.6. The optics are produced by pulling large diameter glass tubes to create small diameter tubes, stacking and pulling them together, and repeating. The final pull is designed to create a section with the desired shape, from which the ends are cut away, as shown in Figure 2.

2. Alignment and Transmission with Tube Sources

Standard techniques have been developed for aligning and characterizing polycapillary optics with tube sources [17–19, 24, 28–30]. The optic is typically first rough aligned by determining the location and direction of the most intense part of the X ray cone emitted from the tube source. This can be accomplished by placing two washers in the path, as shown in Figure 3. The first washer is translated until the image of the washer is centered in the most intense part of the beam. The second washer is then translated until the two images are concentric, as shown in Figure 4. Lasers can then be aligned to the two washers to provide a rough beam axis.

To begin alignment, the optic is placed near the source, as shown in Figure 5. Then, depending on the source geometry, either the source or the optic is translated in the two dimensions perpendicular to the optic axis in small steps, producing a measurement of intensity versus relative source position, as shown in Figure 6 [29]. Alternatively, the optic

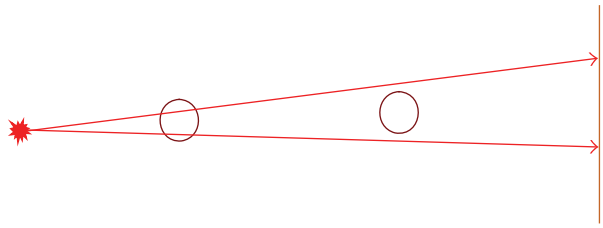

Figure 3: Alignment of washers.

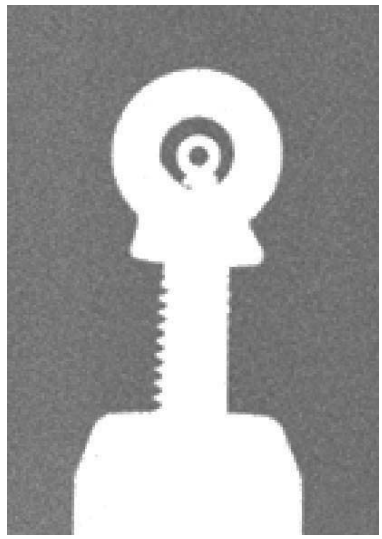

Figure 4: Image of two washers of the same size [31].

may be rotated in two dimensions [28]. In order to determine the focal length of the optic, scans are repeated at increasing distances from the source. When the source is away from the focal point, the intensity is low and the scan is broad. Near the focal point, the plots are symmetric and Gaussian, which indicates good alignment of the source, optic, and detector. At the focal distance, the ratio of the width of the scan curve to the optic-to-source distance, called the source scan angle,

$$\varepsilon = \frac{\Delta x}{z}, \tag{2}$$

should be a minimum, as shown in Figure 7. At the focal point, the maximum source size that is captured by the optic is approximately

$$D_{\text{source}} \sim f\ \theta_c, \tag{3}$$

where f is the input focal length of the optic and θ_c is the critical angle for reflection. Rays originating from outside this range are incident on the optic channels at too high an angle to be reflected. Smaller sources allow for smaller input focal lengths and hence higher beam intensity.

Transmission is the ratio of the number of photons passing along the channels to the number incident on the front face of the optic. Transmission with respect to the source-optic distance is also shown in Figure 7. The highest transmission and the lowest source angle occur at

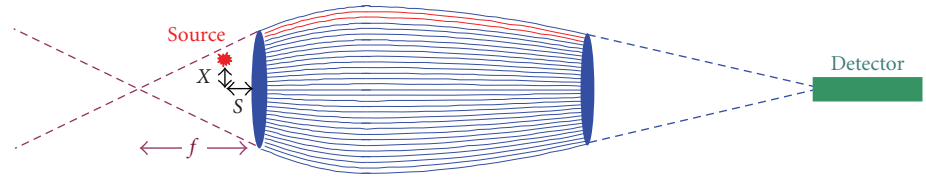

Figure 5: Geometry for source scans. With the source at a distance S which is less than the input focal length f, only a few channels of the optic transmit.

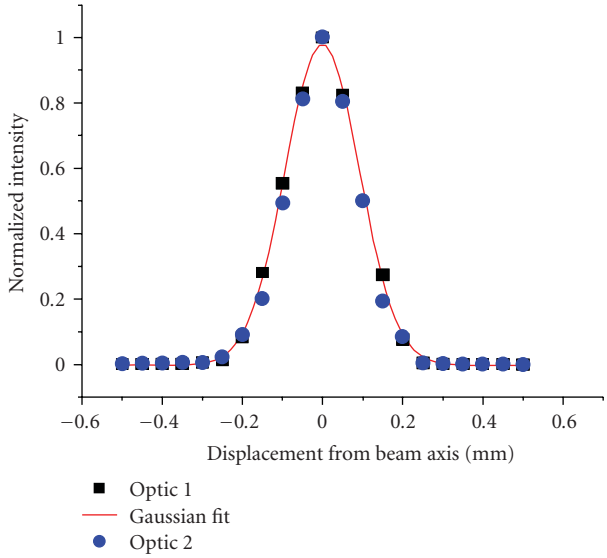

Figure 6: Source scan with the source near the focal point, taken at 17.5 keV for two different optics with input focal lengths ranging from 48–56 mm.

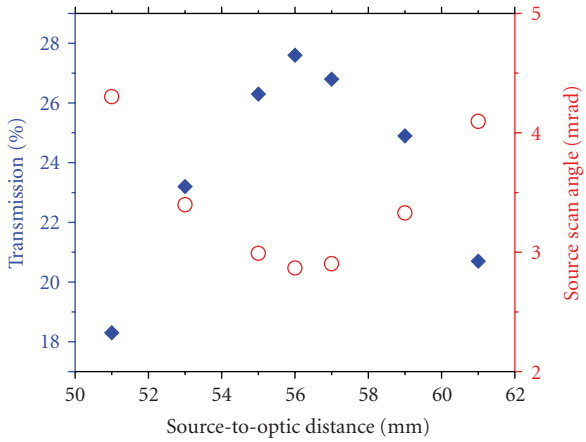

Figure 7: Transmission (♦) and source angle (O) versus source distance. The transmission is the highest at the design focal length of 56 mm.

the focal distance. Transmission at the focal distance as a function of photon energy can be measured with an energy sensitive detector, with a typical result shown in Figure 8. The transmission falls with photon energy because of the energy dependence of the critical angle given in (1). The maximum

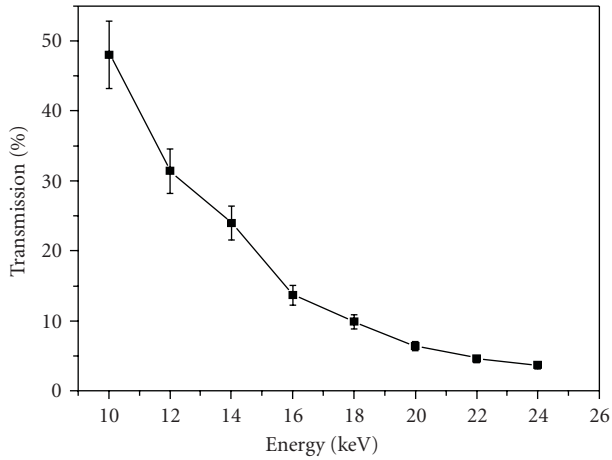

Figure 8: Transmission versus energy for a focusing optic with a 58 mm input focal length and 119 mm output focal length.

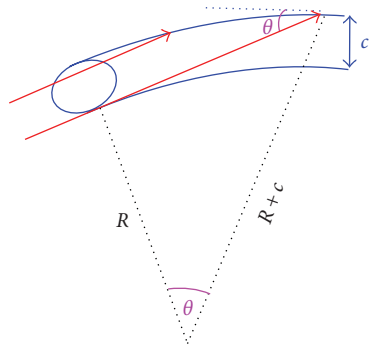

Figure 9: Estimating the maximum incident angle, θ.

incident angle for a input beam can be estimated from the channel size and bending radius, as shown in Figure 9, using

$$\cos(\theta) = \frac{R}{R+c} \Longrightarrow 1 - \frac{\theta^2}{2} \approx \frac{1}{1+(c/R)} \approx 1 - \frac{c}{R} \Longrightarrow \theta \approx \sqrt{\frac{2c}{R}}, \tag{4}$$

where R is the radius of curvature of the channel and c is the channel diameter. R can be estimated from the length of the optic as in Figure 10 by

$$L \approx 2\frac{R}{2}\phi \Longrightarrow R \approx \frac{L}{\phi}, \tag{5}$$

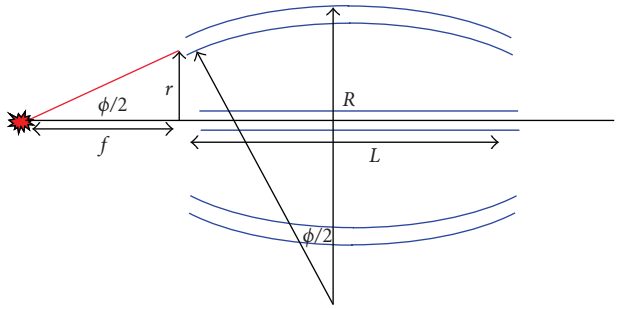

Figure 10: Estimation of channel bending radius, R.

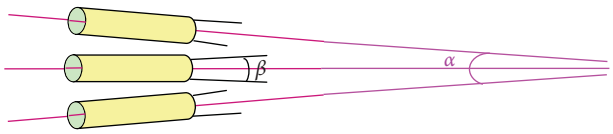

Figure 11: Global divergence, α.

where L is the length of the optic and ϕ is the capture angle, found from the radius of the optic, r, and the focal length, f,

$$\phi = 2\,\mathrm{atan}\left(\frac{r}{f}\right). \tag{6}$$

For the optic measured in Figure 8, $c = 10\,\mu$m, and $R \approx 2.7$ m, giving a maximum incident angle of 2.7 mrad, equal to the critical angle for 11 keV photons. At 10 keV, the transmission is 50%, nearly the full fraction of the front face not filled by glass walls, but the transmission drops rapidly with energy as the critical angle decreases below the maximum incident angle.

3. Divergence and Focal Spot Size

As shown in Figure 11, the output from a polycapillary focusing optic has both global divergence, α, and local divergence, β. Even for a collimating optic, where the channels are parallel on output ($\alpha = 0$), the output divergence, β, is not zero, but is approximately given by the critical angle and therefore is dependent on the X ray energy [32]. The local divergence and transmission losses will result in a beam spot which is less intense than the emission spot on the anode. This is consistent with the second law of thermodynamics, which requires that the photon state density in phase space cannot increase, as sketched in Figure 12.

The total divergence, $\alpha + \beta$, at a energy of a Bragg peak can be estimated by rotating a high quality crystal in the beam and measuring the angular width of the peak, as shown in Figure 13 [33]. The inherent width of the Bragg peak is typically a few eV [34, 35], so that the angular width, given by Bragg's law, is

$$\Delta\theta = -\tan\theta\frac{\Delta E}{E} \tag{7}$$

usually less than 100 μrad. Since the Darwin width and mosaicity of the crystal are typically also much smaller

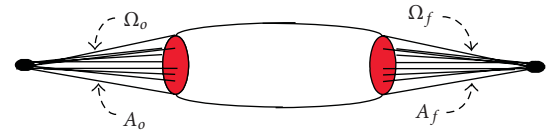

Figure 12: Liouville's Theorem requires that $A_o\Omega_o \le A_f\Omega_f$ for each photon energy transmitted by any optic.

than the exit divergence from the optic, the measurement yields the divergence directly. Using collimating optics, the local divergence, β, has been measured and typically is $\sim 1.3\theta_c$. The factor 1.3 is an experimentally determined parameter that arises from the fact that most of the beam has a divergence less than the maximum divergence of $2\theta_c$ produced by reflection at the critical angle. Unlike the case for pinhole collimation, the local divergence of the beam does not depend on the source size, although it should be remembered, as noted in (3), that large sources may not be efficiently captured by the optic.

The global divergence can be found separately from the slope of a plot of the beam size versus distance from the optic, as shown in Figure 14. In that instance, an imaging detector was used. However, near the focal point, the spot size can be small compared to the resolution of the imaging detector. The spot can be measured using a knife edge technique as shown in Figures 15, 16, and 17, or by scanning a small pinhole across the beam. Better accuracy in determining the focal spot size requires insuring that the knife edge or detector plane is perpendicular to the beam axis [30].

Assuming perfect overlap, the spot size at the focal point is determined by the spot size from each individual capillary channel, which depends on channel size, c, output focal length, f, and local divergence, β, as shown in Figure 18, as

$$d_{\mathrm{spot}} \approx \sqrt{c^2 + (f_{\mathrm{out}} \cdot \beta)^2}. \tag{8}$$

The critical angle, θ_c, at 20 keV is 1.5 mrad. Using $\beta \sim 1.3\theta_c$, an optic with $c = 3.4\,\mu$m and $f_{\mathrm{out}} = 9$ mm has a predicted spot size of 18 μm. An intensity distribution measurement, by the pinhole technique, gave an FWHM of 21 μm [37]. Because of the divergence from each channel, optics with smaller focal lengths have smaller spot sizes, as do measurements at higher photon energies.

Focusing the beam increases the intensity, for example, onto a small sample, compared to pinhole collimation. While for some systems higher intensity could be achieved by simply moving the sample closer to the source, there are generally geometric constraints which limit the minimum distance. If a comparison is made between a pinhole with a diameter σ constrained to be at a distance L from a conventional source, and an optic with focal spot size σ focused at the pinhole location L, the gain is given by

$$\mathrm{Gain} = \left(\frac{d_{\mathrm{optic}}^2}{f_{\mathrm{in}}^2}\right) T \left(\frac{L}{\sigma}\right)^2, \tag{9}$$

where d_{optic} is input diameter of the optic, T is the transmission, and f_{in} is the input focal length. Measured gains are in good agreement with this computation [32].

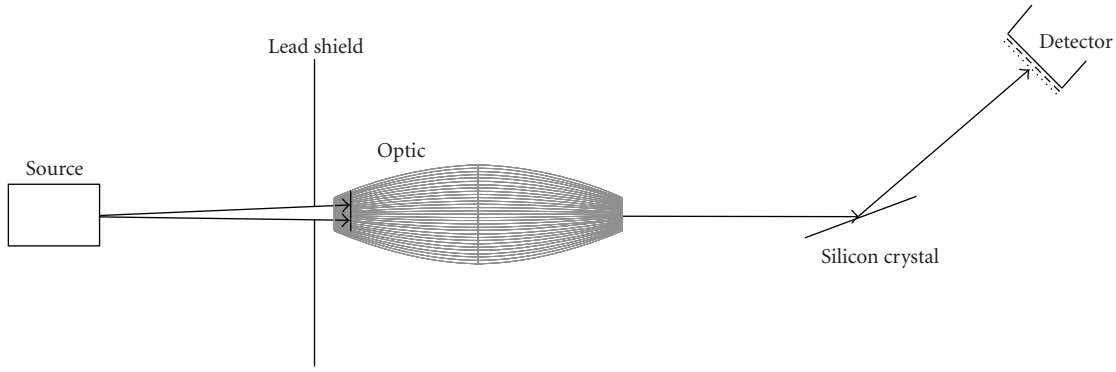

Figure 13: Rocking curve geometry for focusing optic.

Table 1: Results for monolithic focusing optic in a synchrotron beam [38]. The spot size was measured using the knife edge technique. The gain was calculated as for (9) taking $f_{in} \sim L$, given the low divergence of the synchrotron beam.

X ray energy (keV)	Spot size (mm)	Transmission (%)	Measured Gain 350 μm pinhole	Calculated Gain 350 μm pinhole
6	0.09	36	78	81
8	0.08	49	96	110
10	0.09	39	83	87
12	0.09	39	74	87
white	0.17	42	11	89

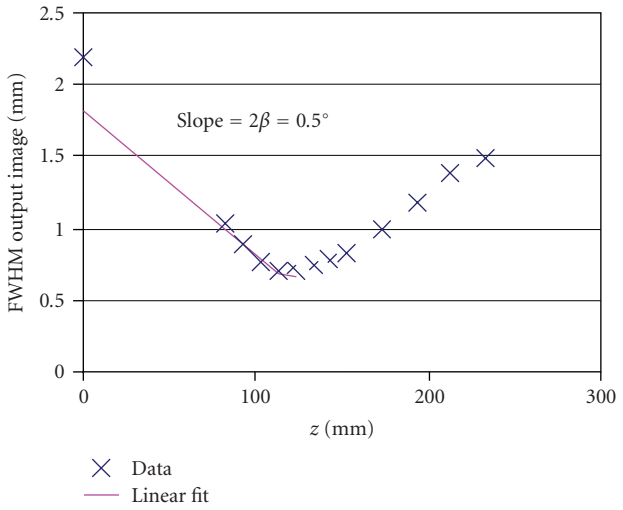

Figure 14: Global divergence of focusing optic found by a linear fit to the beam size on an imaging detector versus optic-to-detector distance [33].

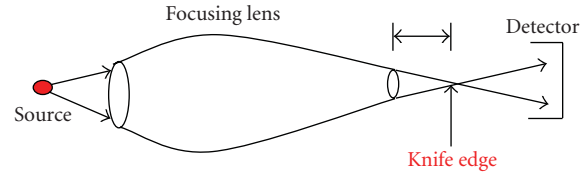

Figure 15: Geometry for knife edge measurement.

Similarly, polycapillary optics can be used to focus synchrotron beams. For example, Table 1 shows the result of focusing white beam bending magnet radiation using a 5 mm diameter optic with a 17 mm focal length. The measured gain for a 350 μm sample was ~100x, and the calculated gain through a 10 μm pinhole for this optic was more than 1000 [38]. Polycapillary optics have been installed on beamlines at BESSY [39], Hasylab [40–42], and ESRF [43], generally for micro X ray Fluorescence (μXRF) but also for a variety of other applications, including spectroscopy. More discussion of applications is included in Section 6.

4. Energy Filtering

The dependence of the critical angle for reflection on photon energy results in an energy-dependent transmission, as shown in Figure 8. Thus, capillary optics can be used as a low pass filter, using the same principle as for the mirrors commonly used for synchrotron and plasma facilities. With this low pass filter, higher-order harmonics can be removed from the output of a crystal monochromator [44] or from conventional sources for energy-dispersive X ray diffractometry and reflectometry [45]. With the optics, high anode voltages can be used to increase the intensity of the characteristic lines without increasing the high energy background. An example of the effect of a polycapillary optic designed to pass 8 keV Cu $K\alpha$ radiation is shown in Figure 19 [32]. The optic slightly reduces the Cu $K\beta$ 9 keV peak and suppresses the high energy bremsstrahlung. For low resolution diffraction applications, the energy filtration provided by the optic allowed the monochromator to be

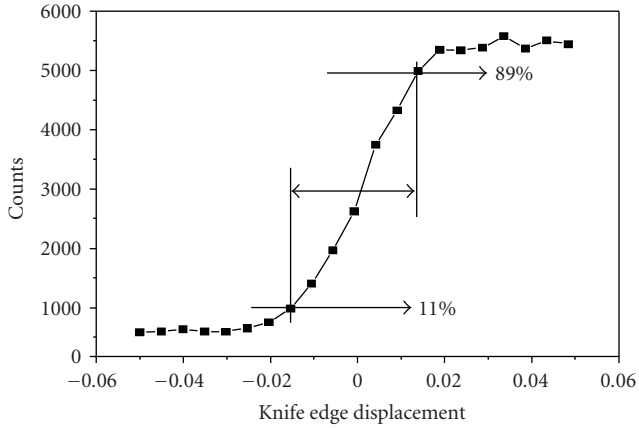

FIGURE 16: Results of a knife edge measurement. The width can be found by numerical differentiation or by assuming a Gaussian intensity distribution and directly determining the FWHM from the scan. In this case the width was 39 μm [36].

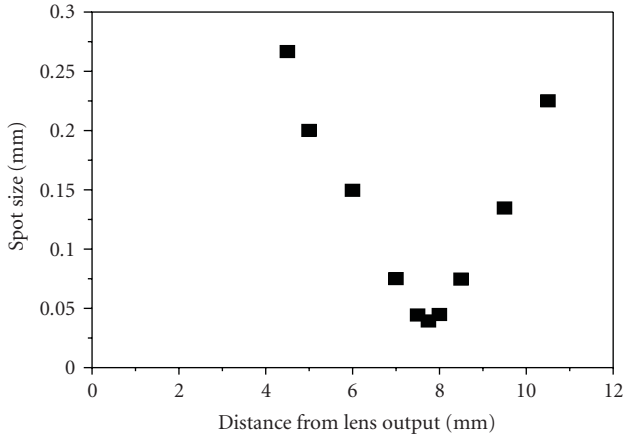

FIGURE 17: Spot size versus distance from optic.

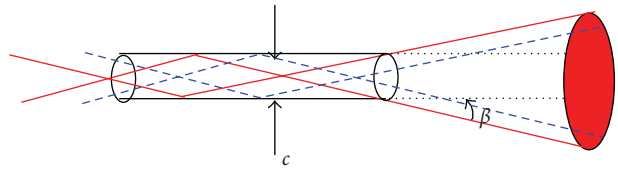

FIGURE 18: The spot size is enlarged from the channel diameter c because of the local divergence which arises from reflections at angles up to the critical angle.

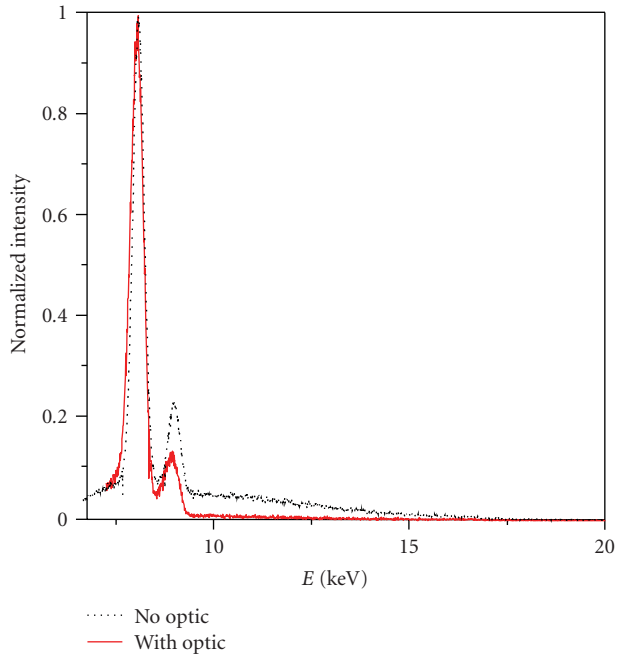

FIGURE 19: Spectrum of a copper tube source with and without a slightly focusing optic. The optic suppresses the high energy Bremsstrahlung [32].

replaced with a simple nickel absorption filter to remove the $K\beta$ peak.

5. Simulations and Defect Analysis

In order to assess optics defects and also to predict performance in a variety of geometries for applications development, a number of computer codes have been developed to simulate X ray transport in polycapillary optics. Modeling of polycapillary optics requires manipulation of relatively complex geometries compared to one or two bounce mirror optics. Further, because of the multiple reflections, the total throughput, the transmission, is more sensitive to roughness and other optics defects. Early modeling was based on an algorithm developed for ion channeling [46], and included a projection of the three-dimensional geometry onto a moving planar cross-section of the optic channel [17]. Very good agreement was found between simulation and experimental results [47–49] for transmission, absorption, and exit divergence, a wide range of X ray energies, source geometries, and optics lengths, channel sizes, and bend radii.

The realization of numerous applications has been advanced by the development of simulation analyses which allow for increasingly accurate assessment of optics defects. These computer codes, like Shadow [50] are generally based on Monte Carlo simulations of geometrical optics trajectories and provide essential information on performance, design and potential applications of polycapillary optics [51–53]. Generally, a point is selected on the source and the optic face, the ray is propagated until it hits the channel wall surface, a computation is performed of the angle of incidence and hence reflectivity, and the ray, if reflected, is propagated along the channel. If the capillary channel has a complex shape versus distance along the optic axis, the computation of the point of incidence is usually performed by iteration or approximation, and the computation of the surface normal can be complicated.

Some simulations allow for optics defects, discussed below, including roughness, waviness of the capillary walls, channel blockage and profile error to be taken into account.

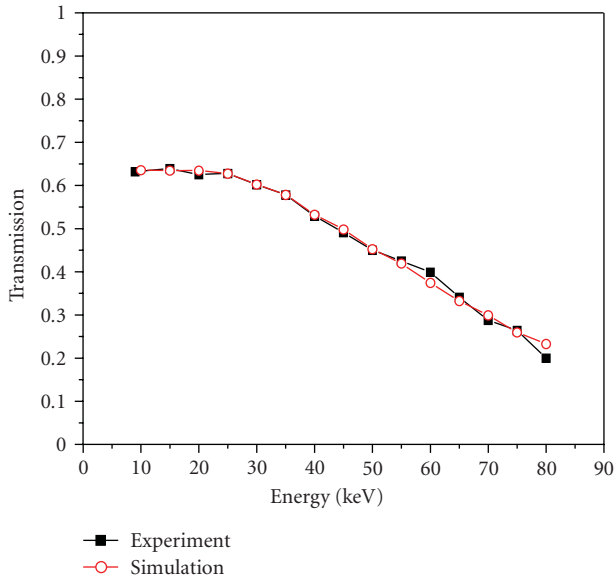

Figure 20: Transmission of a 0.5 mm diameter straight polycapillary optic, compared to a simulation with two fitting parameters, waviness = 0.15 mrad, and unintentional central axis bending radius $R = 120$ m [54]. The fiber had a measured open area of 64.5%, 10 μm channel diameter, and a length of 200 mm.

While characterizing these defects could introduce a large number of fitting parameters, the defects create different signatures in different energy and source geometry regimes, and so can be assessed almost independently. Optics performance over a range of energy from 10 to 80 keV, including multiple datasets of transmission as a function of source position and energy, can often be matched with one or two fitting parameters, as shown in Figures 20 and 21 [55, 56]. For submicron channels, wave effects become significant, as discussed in Section 5.6.

5.1. Open Area. The fractional open area of a polycapillary optic is defined as the fraction of the area of the front face of the optic which is not taken up with the glass walls of the channels. Both the channel diameter and the open area can be measured from microscope images of the front face of the optics. Alternatively, it is simplest to estimate open area for fiber stock by measuring the X ray transmission as a function of energy for short pieces. The transmission maximum is generally equal to the fractional open area.

However, since most optics are sealed to prevent etching by water vapor and avoid other contamination, values of both the channel size and open area must be obtained from the manufacturer. Typical values are 50–70% open area and channel sizes of 5–25 μm. The open area tends to decrease with channel size because of surface tension effects during the drawing of the glass. If it is not known, it can be used as an overall multiplicative fitting parameter independent of photon energy and source location.

5.2. Bending and Profile Error. Bending the channels increases the X ray incidence angles, as shown in Figure 1. Because the critical angle, θ_c, is inversely proportional to the X ray photon energy, bending the channels decreases the X ray transmission down the channels most significantly at higher photon energies. Experimental data taken on a nominally straight fiber (i.e. a thin, straight polycapillary optic) are shown in Figure 22 compared to a CXO simulation [55, 56] which includes otherwise perfect channels with a slight bending. A bending radius smaller than 100 m would underestimate the high energy transmission. Thus the limit on unintentional bending can be estimated solely from the transmission at the highest photon energies. Unintentional bending is consequently unimportant for lower photon energies or channels of an optic which have smaller deliberate bending radii. Simulations with smaller deliberate bending in different shapes also show good agreement to measurements [17].

5.3. Waviness. Midrange spatial frequency slope errors, that is surface oscillations with wavelengths shorter than the capillary length and longer than the wavelength of the roughness, are often called waviness, ripple, or surface oscillations. The detailed shape of the channel walls is unknown, but waviness can be modeled as a random tilt of the glass wall. Waviness is then implemented by changing the surface normal after the point of impact of the ray has been determined. For the CXO simulation, the distribution of surface angles in the glass is assumed to be Gaussian with width w [55, 56]. For high quality glass and photon energies less than 200 keV, w is much smaller than the critical angle, θ_c. Most borosilicate and lead glass optics have simulation fitting parameters which give a Gaussian width for the waviness of 0.12–0.15 mrad. This is in agreement with the directly measured slope variance of the Cornell group [57].

Consideration should be taken in the simulation of the fact that rays are more likely to impact a surface that is tilted toward the ray rather then tilted away [55]. The effect of waviness on fiber transmission is shown in Figure 23. Waviness decreases the transmission a midrange energies, where bending has little effect. The value of the waviness can be estimated from the midrange transmission data alone. Waviness also causes a reduction in the width of source scans at those energies. A simulation fit including waviness and bending for a single 0.5 mm diameter fiber with 10 μm channels is shown in Figure 20 [54].

If the input X ray beam has small local divergence, for example, from a very small spot source, the waviness increases the average angle of reflection and thus the average angle at which X rays exit the fiber. For example, for the case of a small source with a local divergence of 2.4 mrad, a simulation at 8 keV with no channel wall defects produces a divergence less than the critical angle. For a simulation including a typical waviness of 0.15 mrad, the divergence grows to 3.9 mrad, which matches the measured value [56]. In a geometry in which the number of bounces per photon is small, the output divergence can remain smaller than the critical angle.

5.4. Roughness. Roughness is small-scale fluctuations of the glass surface [58, 59]. If the surface can be described as

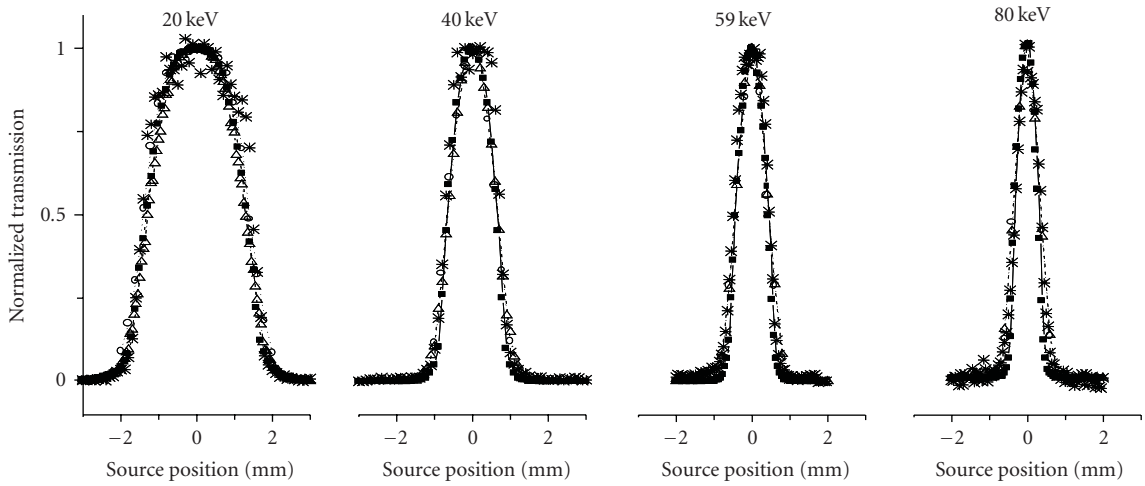

FIGURE 21: Source scan data from the fiber of Figure 20, and simulation (solid line) using the same two fitting parameters, $R = 120$ m, $w = 0.15$ mrad, and also roughness = 0.5 nm.

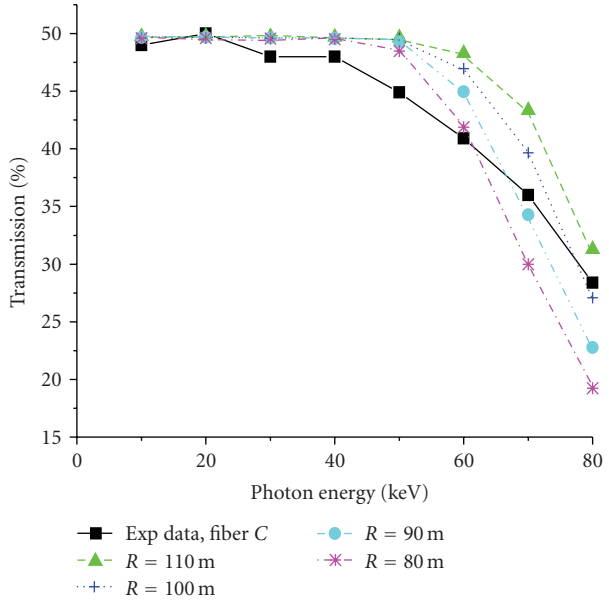

FIGURE 22: Transmission spectra of a thin fiber similar to that of Figure 20, compared to simulations with different bending curvature alone [55]. At the highest energies, a radius of less 100 m will not fit the data. The best fit bending radius will be slightly larger and should be determined after the simulation fitting for waviness is determined.

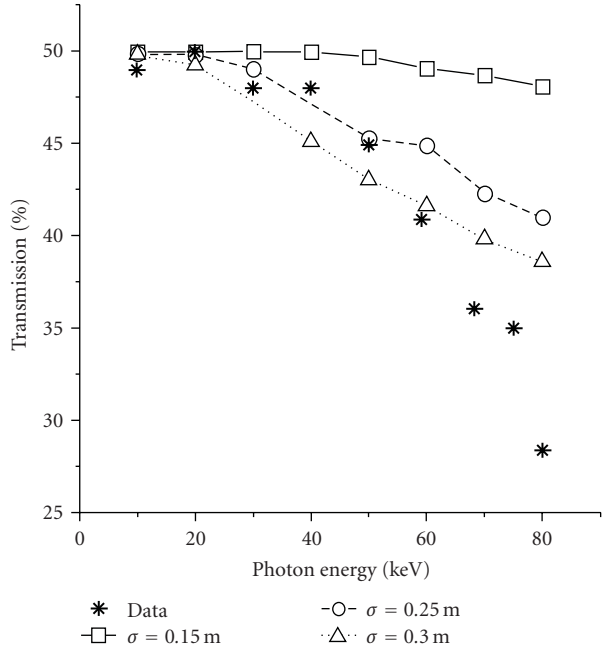

FIGURE 23: Simulations [56] of transmission spectra for a fiber with waviness values from 0.15 to 0.3 mrad compared with the experimental data. A waviness of 0.15 mrad fits the midrange energy data well. That value of waviness should be included with the best fit bending radius [55].

deviating locally from some average smooth surface by an amount $Z(x)$, then the effects are described in terms of roughness correlations which are given in terms of the correlation function $g(x)$,

$$g(x) = \frac{1}{L}\int_0^L Z(x')Z(x'+x)dx' \doteq \overline{Z}^2 e^{-(|x|/s)}, \qquad (10)$$

which has an rms amplitude $\overline{Z}$ and correlation length s. Roughness causes a decrease in reflectivity which depends on both parameters, but becomes relatively insensitive to changes in correlation length for large lengths [58]. Simulations typically use a value for s in the long length range and fit the roughness amplitude alone. For example, the correlation length for the data in Figure 24 was chosen as 6 μm to bring the roughness height into an agreement with atomic force microscopy (AFM) data of similar fibers. Roughness only slightly decreases the specular reflectivity at low angles and so has almost no impact on the transmission spectra of the optics. However, roughness becomes increasingly important

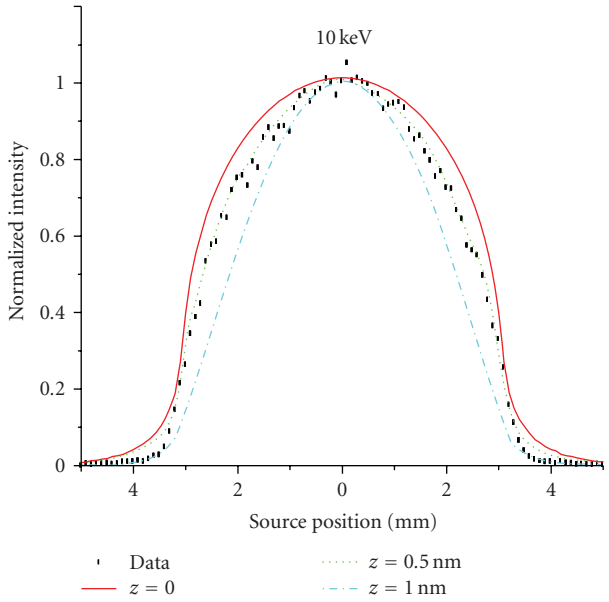

Figure 24: Roughness has little effect on the transmission of an aligned fiber, but decreases the width of the source scans in the simulation (solid colored lines) [55, 56]. For the data at 10 keV, a roughness height of 0.5 nm fits the data well.

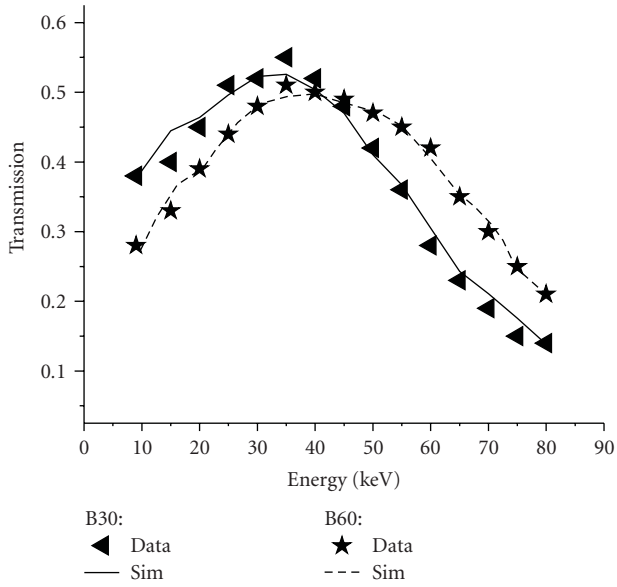

Figure 25: Transmission of two similar lead glass fibers, 30 and 60 mm in length. The simulation [55, 56] fits include 17 and 33 μm of glass layer, respectively, or 0.55 μm of blockage per mm of length [48].

under circumstances in which the angle and number of reflections increases, for example in source scans, as shown in Figure 24. Thus, it is often only necessary to include roughness in the model if the application is one for which off axis photons are important.

5.5. Absorption: Blockage and Halo. Another defect that is seen occasionally in borosilicate glass optics, and more prevalently in lead glass fibers, [47, 60] is a drop in transmission at low energies, as shown in Figure 25. Reasonable agreement is obtained over the whole range of photon energies by assuming that a layer of glass of the same composition as the channel walls blocks the channels. This glass could be dust left from the cutting process or from crystallites which have formed in the channels during drawing [61]. An increase in required layer thickness with fiber length is consistent with a stochastic random model of glass inclusions. This random probability of glass inclusions would cause the transmission to drop exponentially with optic length, as shown in Figure 26 [47]. Because of the increased processing at high temperatures, and the dust which can be induced into the channels due to the process of cutting a shaped optic, the transmission decrease at low energies is also occasionally observed for finished borosilicate optics, as shown in Figure 27.

Conversely, for a focusing optic it can be important that the halo of the unfocussed beam be removed completely by absorption in the glass walls of the optic [62]. Typically the optics are packaged in housings which contain absorptive materials, but unless care is taken in design, the focal spot may be surrounded by a "cut through" halo approximately

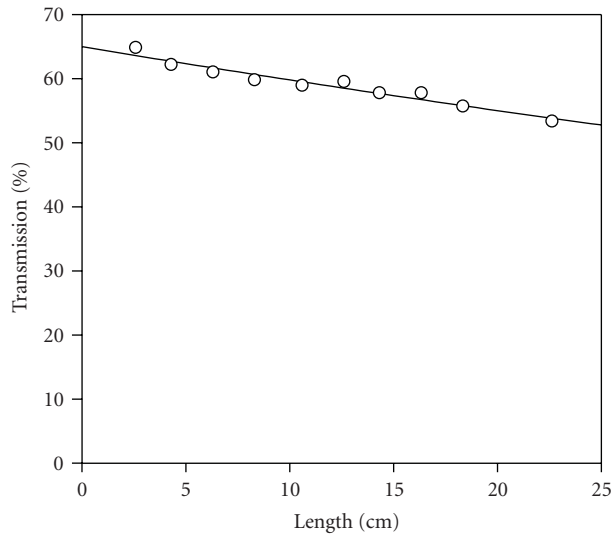

Figure 26: Measured transmission at 8 keV, as a function of length, for identical borosilicate polycapillary fibers with 17 μm channels. The solid line is an exponential fit with decay length = 120 cm.

equal to the diameter of the housing aperture [63–65]. In such cases the spot size from the optic is generally larger than predicted by (8) and does not decrease with photon energy. The expected transmission of the walls of the optic is

$$T_w = e^{-(1-f)\mu\rho x}, \tag{11}$$

where f is the fractional open area, $(1 - f)$ is the fraction filled with glass, $\mu\rho$ is the absorption coefficient of the glass, and x is the path length across the optic [66].

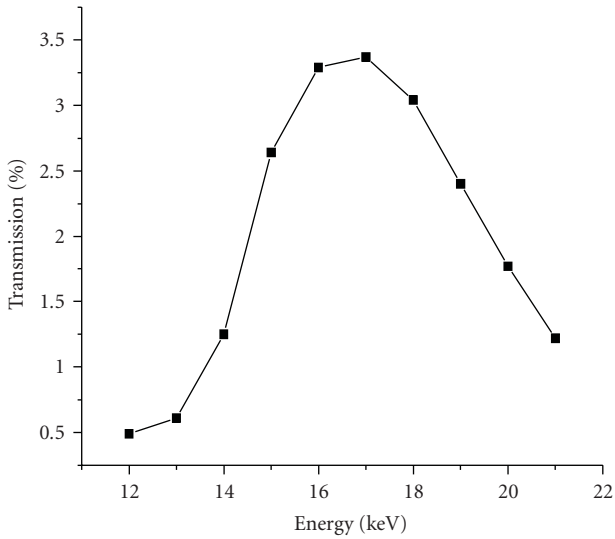

Figure 27: Drop in transmission at low energy of a sharply bent focusing polycapillary optic, possibly due to blockage by glass inclusions.

5.6. Wave Modeling and Nanocapillaries. Most simulations of polycapillary optics use simple geometric ray tracing. For coherence and wave effects to be important, the wavefront must be partially coherent over the capillary channel diameter. The transverse coherence width from a source of diameter s at a distance D for a wavelength λ is

$$L_T = \frac{\lambda}{s} D. \tag{12}$$

For a conventional source with $\lambda = 0.16\,\text{nm}$ (8 keV), $s = 200\,\mu\text{m}$, and $D = 50\,\text{mm}$, the coherence width is only about 40 nm and the typical criterion for the use of geometrical optics is well satisfied. Certain effects due to the capillary structure of the optics can still be seen in this regime [67, 68]. Coherence effects could be seen from a small part of an area of array of capillaries, even if each acts as an incoherent source, if the propagation distance is large enough to satisfy (12). For example, if two neighboring capillaries act as a source of size $s = 2d_c$, the transverse coherence of the combined source for two 5 μm capillaries will be 100 μm at a distance of 8 m for 10 keV X rays.

For a 5 μm source at 1 m, the coherence width of the source is 30 μm, and interference effects might be observed between neighboring channels. To use waveguide modeling for transport down a capillary channel, the number of waveguide modes excited by the beam must be small. The number of modes is approximately [69]

$$N_{\text{modes}} = \frac{d_c}{\lambda_{\text{eff}}}, \tag{13}$$

where d_c is the diameter of a channel. For a channel size of 5 μm, and a wavelength of 0.16 nm, the number of modes is in the tens of thousands. However, this is reduced if consideration is made of the fact that only incident angles less than the critical angle are important, so the effective transverse wavelength is

$$\lambda_{\text{eff}} = \frac{\lambda}{\theta_c}. \tag{14}$$

Because both the critical angle and the wavelength increase inversely with photon energy, the effective wavelength is roughly independent of X ray photon energy and is about 40 nm. For a 5 μm channel, this still results in hundreds of modes, but a small number of modes are present for capillaries with diameters in the submicron regime. Waveguide theory has been developed for coherent sources [69], partially coherent sources and short pulse sources [70]. Measurements for coherent sources and small channels have been performed and are consistent with wave-based calculations [71–75].

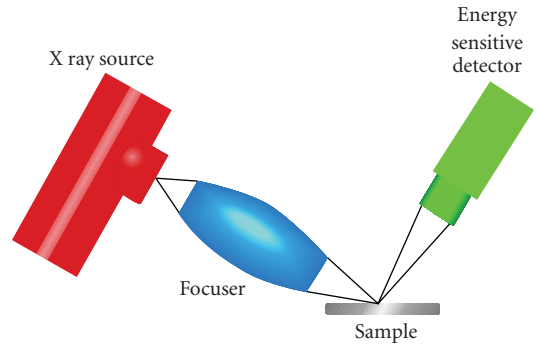

Figure 28: Geometry for XRF mapping. Courtesy of XOS.

6. Applications

6.1. X Ray Fluorescence and Spectrometry. Focusing polycapillary optics are widely used [76–79] in X ray fluorescence (XRF) and spectrometry (XRS) because of the large intensity increase compared to pinhole collimation and the resulting more flexible system design. These allow for in situ and rapid throughput systems [80, 81] as well as medical [82], and portable monitoring systems [83–85]. The smooth beam shape potentially allows for easier analysis. A large body of current work is concentrated on the issues of quantitative analysis, especially for irregularly shaped objects [86–88]. A typical geometry for conventional sources is shown in Figure 28. Rastering the sample then allows for spatial mapping. An example of the results from a volcanic inclusion is shown in Figure 29. Polycapillary focusing optics are also used on several synchrotron beam lines [39–41] for XRF, absorption spectroscopy [43], and micro XRF tomography [89, 90].

Instead of using the focusing optic on the excitation side, many groups use a focusing optic to collect the fluorescence radiation from the sample in conventional, synchrotron beam [91], proton beam [92], and particle-induced X ray emission (PIXE) [93, 94] systems.

Confocal systems such as that sketched in Figure 30 [15] provide the double benefit of enhanced signal intensity and

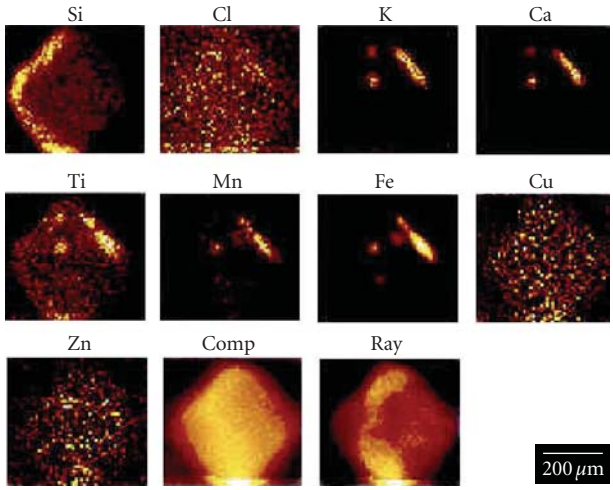

Figure 29: MXRF maps of a quartz phenocryst with small volcanic glass inclusions. Courtesy of Ning Gao, XOS.

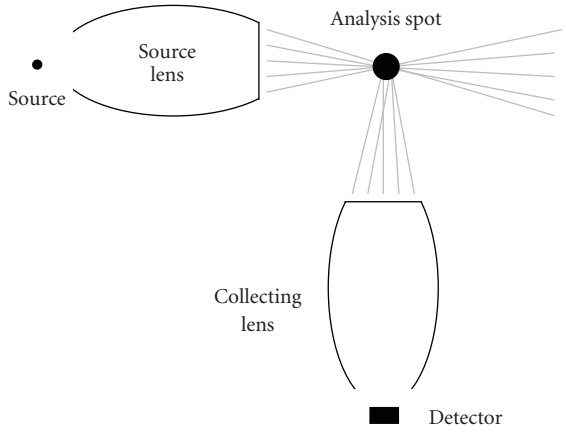

Figure 30: Sketch of microfluorescence experiment, showing that overlap of irradiation and collection volumes yield three-dimensional spatial resolution [15].

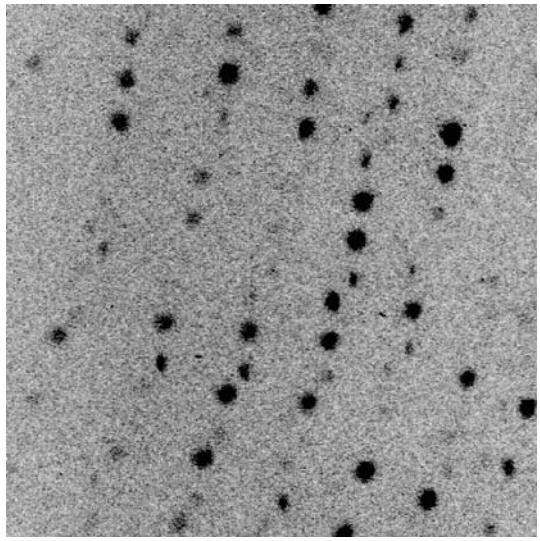

Figure 31: Lysozyme pattern taken in 20 s with 2.8 kW rotating anode, comparable to 30–35 min. without the optic. The linear R factor (a measure of the deviation from the expected intensity for all indexed reflections) was 6.4% without the optic compared to 6.9% with the optic on the same sample.

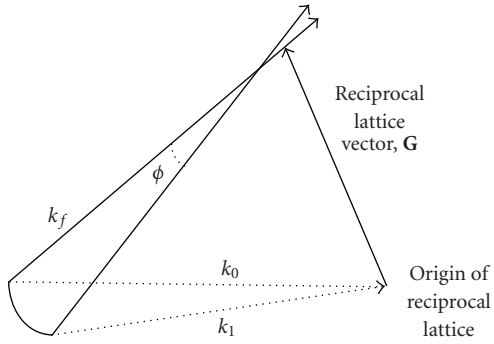

Figure 32: Ewald sphere description of focused beam diffraction on a single crystal.

three-dimensional spatial resolution. There are a growing number of confocal systems, [42, 95, 96] including multiple beam confocal systems [97].

There are also a rising number of multiple optics combinations [98], including pairing polycapillary optics with Kirkpatrick-Baez mirrors for XRF and a toroidal mirror for EXAFS [99].

6.2. Single Crystal Diffraction. Significant reduction in data collection times for single crystal diffraction can be achieved with polycapillary optics [100–103]. An image recorded in just 20 seconds is shown in Figure 31 [100]. For focused beam diffraction, the volume of reciprocal space that is accessed in a single measurement is greatly increased compared to parallel beam geometries. The local divergence from the optic, for example, 0.19° at 8 keV, is less than the ω crystal oscillations typically employed to increase the density of reflections captured in a single image in protein crystallography, so a gentle focus does not significantly broaden the spots.

Figure 32 displays a sketch of the diffraction condition for a single crystal with a monochromatic convergent beam. Diffraction conditions are satisfied for the two incident beam directions, k_0 and k_1, when they make the same angle with the reciprocal lattice vector, **G**. Thus, changing from k_0 to k_1 rotates the diffraction triangle of k_0, **G,** and k_f about the vector **G** by an angle ϕ [100]. This results in the diffracted beam, k_f, moving to trace out a tangential line on the detector as shown in Figure 33. The maximum value of ϕ is the convergence angle. There is no broadening in the transverse direction.

The effects of the one-dimensional streaking are shown in Figure 34 for a lysozyme diffraction pattern taken with a 2.1° focusing angle [103]. Serious overlap problems were not encountered except in low index directions. However, for cell dimensions >200 Å, the diffraction spots are not completely

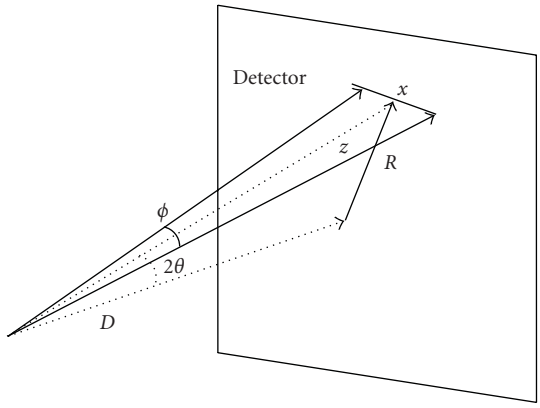

Figure 33: Diffraction streak due to beam focusing.

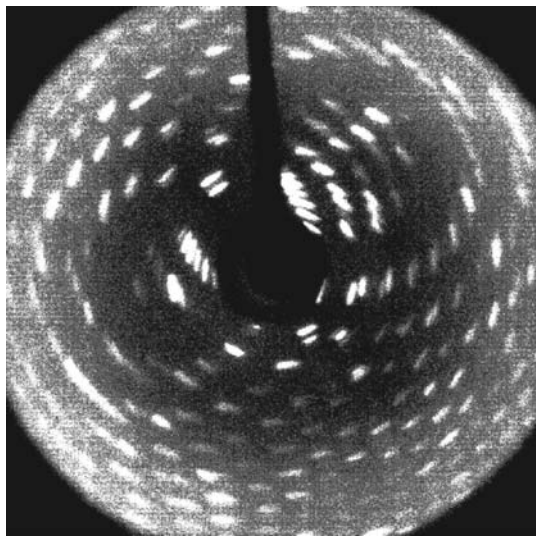

Figure 34: Lysozyme diffraction image taken in 5 minutes with a 1 mA tube source and a focusing polycapillary optic [103].

separated. Patterns with smaller convergence angles can be analyzed with conventional software and give good results [100, 104].

6.3. Powder Diffraction. Reductions in data collection time can also be obtained for powder diffraction. The symmetric beam profile and enhanced flux give improved particle and measurement statistics. While powder diffraction measurements are most commonly performed with collimating optics to reduce beam divergence, the nearly Gaussian peaks produced by the polycapillary optics provide uncertainties in peak center localization which is much less than the peak widths [33]. Thus the peak location uncertainty for powder diffraction are much smaller than the beam angle, even for highly convergent beams [36]. Polycapillary optics are also used in synchrotron systems, for example, to evaluate stresses in steel [105] and in other confocal geometries [106].

6.4. Medical Therapy and Small Animal Imaging. Polycapillary optics have been tested to provide beam shaping and

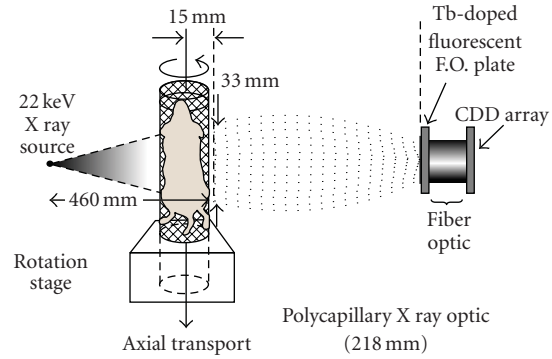

Figure 35: Focusing optic used to collect both the external beam used for computed tomography and the emission from the internal radiation emitted from the radioactively tagged pharmaceutical to produce registered images.

scatter rejection in radiography [14, 28, 47]. Beam shaping is particularly intriguing for small animal imaging. An example of a focusing optic used to collect combined computed tomography (CT) and micro Single Particle Emission CT (SPECT) images is shown in Figure 35 [107, 108]. Collecting both the external CT beam and the scintigraphy image with a single optic decreases registration error when combining scintigraphy images from a conventional γ camera with CT data.

Polycapillary optics could also be used to shape focused beams with the potential for orthovoltage therapy. Conventional X ray radiation therapy is performed with high energy X ray or gamma radiation. High-energy photons are chosen to minimize the absorbed skin dose relative to the dose at the tumor, although energies as low as 100 keV are employed in orthovoltage modalities. The choice of high energies to reduce skin dose is necessary because, in an unfocused beam, the intensity is highest near the point of entry. As an alternative method, polycapillary optics have been tested for their potential to provide a beam of lower energy X rays focused at the tumor site [109].

Neutron beams can also be focused by polycapillary optics [110–112]. A focused neutron beam could be used in boron neutron capture therapy (BNCT), based on the selective delivery of a boronated pharmaceutical to cancerous tissue followed by irradiation with thermal neutrons [113–115]. This procedure could be useful in treating near surface regions such as ocular melanomas.

6.5. Astronomy. Polycapillary optics can also be used to focus parallel beam radiation for astrophysical applications. The transmission of a 3 cm square multifiber optic developed for astrophysical applications is shown as a function of photon energy in Figure 36 [116, 117]. Polycapillary optics could be used to collect broadband radiation and redirect it to a spectroscopic detector.

6.6. Radiation Resistance. Because the X ray optical properties of materials depend on total electron density, the optical constants are insensitive to changes in electronic state.

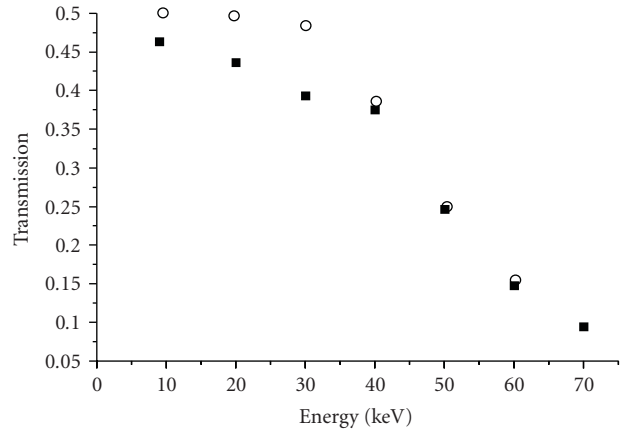

Figure 36: Simulated [116] (circles) and measured [117] (squares) transmission of a 3 cm square optic with 2 m focal length.

While color centers form rapidly in glass during exposure to intense radiation, the blackening of the glass is not indicative of a change in the X ray transmission of a polycapillary optic. Thin fibers exposed to intense beams do undergo reversible deformation due to nonuniform densification in the radiation beam. In addition, radiation-enhanced diffusion causes crystallites to grow into the channels and cause a decrease in low energy performance similar to that of Figure 27. However, rigid optics annealed *in situ* at 100 C, were shown to withstand in excess of 2 MJ/cm^2 of white beam bending magnet radiation without measurable change in performance at 8 keV [61, 118].

7. Summary

The focusing of X ray beams with polycapillary optics yields high gains in intensity and increased spatial resolution for a variety of clinical, lab-based, synchrotron, or *in situ* analysis applications. Modeling efforts accurately describe optics performance to allow for system modeling in a wide variety of geometries.

Acknowledgments

The author wishes to indicate her appreciation for data and ideas from many people, including Carmen Abreu Bittel, David Aloisi, Simon Bates, Henning Von Berlischpe, Ayhan Bingolbali, David Bittel, Cari, Dan Carter, Heather Chen, Patrick Conlon, Sonja Dittrich, Greg Downing, Sarah Formica, Christi Freinberg-Trufas, Ning Gao, David Gibson, Walter Gibson, Mikhail Gubarev, Joseph Ho, Frank Hoffman, Huapeng Huang, Huimin Hu, Abrar Hussein, Chris Jezewski, Marshall Joy, Kardiawarman, Andrei Karnaukhov, John Kimball, Ira Klotzko, David Kruger, Susanne Lee, Danhong Li, Jan Lohbreier, Dip Mahato, Kevin Matney, David Mildner, Johanna Mitchell, Charles Mistretta, Robin Moresi, Noor Mail, Scott Owens Rohrbach, Wally Peppler, Sushil Padiyar, Igor Ponomarev, Bimal Rath, Christine Russell, Robert Schmitz, Francisca Sugiro, Suparmi, Christi Trufus-Feinberg, Johannes Ullrich, Hui Wang, Lei Wang, Russel Youngman, Brian York, Qi Fan Xiao, and Wei Zhou, and for grant support from the U.S. Department of Commerce, NASA, NIH, and the Breast Cancer Research Program.

References

[1] P. B. Hirsch and J. N. Kellar, "An X ray micro-beam technique: I—collimation," *Proceedings of the Physical Society B*, vol. 64, no. 5, pp. 369–374, 1951.

[2] R. V. Pound and G. A. Rebka, "Gravitational red-shift in nuclear resonance," *Physical Review Letters*, vol. 3, no. 9, pp. 439–441, 1959.

[3] L. Marton, "X ray fiber optics," *Applied Physics Letters*, vol. 9, no. 5, pp. 194–195, 1966.

[4] P. J. Mallozzi, H. M. Epstein, R. G. Jung et al., "Laser-generated plasmas as a source of X ray for medical applications," *Journal of Applied Physics*, vol. 45, no. 4, pp. 1891–1895, 1974.

[5] W. T. Vetterling and R. V. Pound, "Measurements on an X ray light pipe at 5.9 and 14.4 keV," *Journal of the Optical Society of America*, vol. 66, no. 10, pp. 1084–1089, 1976.

[6] D. Mosher and S. J. Stephanakis, "X ray light pipes," *Applied Physics Letters*, vol. 29, no. 2, pp. 105–107, 1976.

[7] Y. M. Aleksandrov, K. A. Valiev, L. V. Velikov et al., "Transport of soft X radiation along an optical waveguide," *Soviet Technical Physics Letters*, vol. 13, no. 3, pp. 105–106, 1987.

[8] V. A. Arkad'ev, M. A. Kumakhov, and L. I. Ognev, "Total external reflection of γ rays from a surface," *Soviet Technical Physics Letters*, vol. 12, no. 11, pp. 540–542, 1986.

[9] V. A. Arkad'ev, M. A. Kumakhov, and R. F. Fayazov, "Theoretical capabilities of grazing-incidence X ray optics," *Soviet Technical Physics Letters*, vol. 14, no. 2, pp. 101–102, 1988.

[10] V. A. Arkd'ev, A. I. Kolomitsev, M. A. Kumakhov, V. V. Labuzov, and I. Y. Ponomarev, "Focusing system using multiple reflection of radiation from curved surfaces," *Soviet Technical Physics Letters*, vol. 14, no. 1, p. 42, 1988.

[11] V. A. Arkd'ev, A. I. Kolomitsev, M. A. Kumakhov et al., "Wide-band X ray optics with a large angular aperture," *Soviet Physics Uspekhi*, vol. 32, no. 3, p. 271, 1989.

[12] M. A. Kumakhov and F. F. Komarov, "Multiple reflection from surface X ray optics," *Physics Report*, vol. 191, no. 5, pp. 290–350, 1990.

[13] W. M. Gibson and C. A. MacDonald, "Polycapillary Kumakhov optics: a status report," in *X Ray and UV Detectors*, vol. 2278 of *Proceedings of SPIE*, pp. 156–167, July 1994.

[14] W. M. Gibson, C. A. MacDonald, and M. S. Kumakhov, "The Kumakhov lens; a new X ray and neutron optics with potential for medical applications," in *Technology Requirements for Biomedical Imaging*, S. K. Mun, Ed., vol. 2580, pp. 164–169, IEEE Press, New York, NY, USA, 1991.

[15] W. M. Gibson and M. A. Kumakhov, "Applications of X ray and neutron capillary optics," in *X Ray Detector Physics Applications*, vol. 1736 of *Proceedings of SPIE*, p. 172, 1992.

[16] C. A. MacDonald, C. C. Abreu, S. Budkov et al., "Quantitative measurements of the performance of capillary X ray optics," in *Multilayer and Grazing Incidence X Ray/EUV Optics II*, R. B. Hoover and A. Walker, Eds., vol. 2011 of *Proceedings of SPIE*, pp. 275–286, 1993.

[17] J. B. Ullrich, V. Kovantsev, and C. A. MacDonald, "Measurements of polycapillary X ray optics," *Journal of Applied Physics*, vol. 74, no. 10, pp. 5933–5939, 1993.

[18] B. Rath, R Youngman, and C. A. MacDonald, "An automated test system for measuring polycapillary X ray optics," *Review of Scientific Instrumentation*, vol. 65, pp. 3393–3398, 1994.

[19] J. B. Ullrich, I. Y. Ponomarev, M. V. Gubarev, N. Gao, Q. F. Xiao, and W. M. Gibson, "Development of monolithic capillary optics for X ray diffraction applications," in *X Ray and UV Detectors*, R. B. Hoover and R. B. Tate, Eds., vol. 2278 of *Proceedings of SPIE*, pp. 148–155, 1994.

[20] C. A. Macdonald, "Applications and measurements of polycapillary X ray optics," *Journal of X Ray Science and Technology*, vol. 6, no. 1, pp. 32–47, 1996.

[21] C. C. Abreu and C. A. MacDonald, "Beam collimation, focusing, filtering and imaging with polycapillary X ray and neutron optics," *Physica Medica*, vol. 13, no. 3, pp. 79–89, 1997.

[22] V. A. Arkadiev and D. I. Gruev, "Principal possibilities of Kumakhov lenses," in *X Ray and UV Detectors*, vol. 2278 of *Proceedings of SPIE*, pp. 200–209, July 1994.

[23] M. A. Kumakhov, "Status of X ray capillary optics," in *X Ray and Extreme Ultraviolet Optics*, R. B. Hoover and A. B. C. Walker Jr., Eds., vol. 2515 of *Proceedings of SPIE*, pp. 86–102, 1995.

[24] V. A. Arkadiev, A. A. Bzhaumikhov, H. E. Gorny, and N. S. Ibraimov, "Experimental investigation of Kumakhov lenses," in *X Ray and Extreme Ultraviolet Optics*, R. B. Hoover and A. B. C. Walker Jr., Eds., vol. 2515 of *Proceedings of SPIE*, pp. 103–113, 1995.

[25] M. A. Kumakhov, "Development of X ray and neutron capillary optics," in *Grazing Incidence and Multilayer X Ray Optical Systems*, R. B. Hoover and A. B. C. Walker Jr., Eds., vol. 3113 of *Proceedings of SPIE*, pp. 362–368, 1997.

[26] M. A. Kumakhov, "X ray capillary optics: history of development and present status," in *Kumakhov Optics and Application: Selected Research Papers on Kumakhov Optics and Application of 1998–2000*, M. A. Kumakhov, Ed., vol. 4155 of *Proceedings of SPIE*, pp. 2–12, 2000.

[27] C. A. MacDonald and W. M. Gibson, "Polycapillary optics," in *Handbook of Optics*, M. Bass, C. DeCusatis, J. Enoch et al., Eds., vol. 5 of *Atmospheric Optics, Modulators, Fiber Optics, X Ray and Neutron Optics*, McGraw-Hill, New York, NY, USA, 3rd edition, 2010.

[28] G. Cappuccio and S. B. Dabagov, "Capillary optics as an X ray condensing lens: an alignment procedure," in *Kumakhov Optics and Application: Selected Research Papers on Kumakhov Optics and Application 1998–2000*, M. A. Kumakhov, Ed., vol. 4155 of *Proceedings of SPIE*, pp. 40–47, 2000.

[29] D. Li, F. R. Sugiro, and C. A. MacDonald, "Source-optic optimization for compact monochromatic imaging," in *X Ray Sources and Optics*, C. A. MacDonald, A. T. Macrander, T. Ishikawa, C. Morawe, and J. L. Woo, Eds., vol. 5537 of *Proceedings of SPIE*, pp. 105–114, 2004.

[30] T. Sun and X. Ding, "Study on the measurement of properties of polycapillary X ray lens," *Nuclear Instruments and Methods*, vol. 226, no. 4, pp. 651–658, 2004.

[31] A. Bingölbali and C. A. MacDonald, "Quality assessment system for curved crystal X ray optics," *Nuclear Instruments and Methods*, vol. 267, no. 5, pp. 832–841, 2009.

[32] S. M. Owens, J. B. Ullrich, I. Y. Ponomarev et al., "Polycapillary X ray optics for macromolecular crystallography," in *Hard X Ray/Gamma-Ray and Neutron Optics, Sensors, and Applications*, R. B. Hoover and F. B. Doty, Eds., vol. 2859, pp. 200–209, 1996.

[33] W. Zhou, D. N. Mahato, and C. A. MacDonald, "Analysis of powder X ray diffraction resolution using collimating and focusing polycapillary optics," *Thin Solid Films*, vol. 518, no. 18, pp. 5047–5056, 2010.

[34] R. E. Ban Gridken and A. A. Markowicz, *Handbook of X Ray Spectrometry*, Marcel Dekker, New York, NY, USA, 1993.

[35] A. Thompson, D. Atlword, E. Gullikson et al., *X Ray Data Booklet*, CXRO, Berkeley, Calif, USA, 2002.

[36] A. Bingölbali, W. Zhou, D. N. Mahato, and C. A. MacDonald, "Focused beam powder diffraction with polycapillary and curved crystal optics," in *Advances in X Ray/EUV Optics and Components III*, A. M. Khounsary, C. Morawe, and S. Goto, Eds., vol. 7077 of *Proceedings of SPIE*, 2008.

[37] F. A. Hoffman, N. Gao, S. M. Owens, W. M. Gibson, C. A. MacDonald, and S. M. Lee, "Polycapillary optics for in-situ process diagnotstics," in *In Situ Process Diagnostics and Intelligent Materials Processing, Materials Research Society Proceedings*, P. A. Rosenthal, W. M. Duncan, and J. A. Woollam, Eds., vol. 502, pp. 133–138, 1998.

[38] F. A. Hofmann, C. A. Freinberg-Trufas, S. M. Owens, S. D. Padiyar, and C. A. MacDonald, "Focusing of synchrotron radiation with polycapillary optics," *Nuclear Instruments and Methods*, vol. 133, no. 1-4, pp. 145–150, 1997.

[39] A. Erko, F. Schäfers, A. Firsov, W. B. Peatman, W. Eberhardt, and R. Signorato, "The BESSY X ray microfocus beamline project," *Spectrochimica Acta B*, vol. 59, no. 10-11, pp. 1543–1548, 2004.

[40] A. Al-Ebraheem, A. Mersov, K. Gurusamy, and M. J. Farquharson, "Distribution of Ca, Fe, Cu and Zn in primary colorectal cancer and secondary colorectal liver metastases," *Nuclear Instruments and Methods A*, vol. 619, no. 1–3, pp. 338–343, 2010.

[41] V. G. Mihucz, G. Silversmit, I. Szalóki et al., "Removal of some elements from washed and cooked rice studied by inductively coupled plasma mass spectrometry and synchrotron based confocal micro-X ray fluorescence," *Food Chemistry*, vol. 121, no. 1, pp. 290–297, 2010.

[42] K. Janssens, K. Proost, and G. Falkenberg, "Confocal microscopic X ray fluorescence at the HASYLAB microfocus beamline: characteristics and possibilities," *Spectrochimica Acta B*, vol. 59, no. 10-11, pp. 1637–1645, 2004.

[43] G. Silversmit, B. Vekemans, S. Nikitenko et al., "Polycaillary based μ-XAS and confocal μ-XANES at a bending magnet source of the ESRF," *Journal of Physics: Conference Series*, vol. 190, Article ID 012036, 2009.

[44] A. Erko, N. Langhoff, A. A. Bjeoumikhov, and V. I. Beloglasov, "High-order harmonic suppression by a glass capillary array," *Nuclear Instruments and Methods*, vol. 467-468, pp. 832–835, 2001.

[45] V. Rossi Albertini, B. Paci, A. Generosi, S. B. Dabagov, O. Mikhin, and M. A. Kumakhov, "On the use of polycapillary structures to improve laboratory Energy-Dispersive X ray Diffractometry and Reflectometry," *Spectrochimica Acta B*, vol. 62, no. 11, pp. 1203–1207, 2007.

[46] Q. F. Xiao, I. Y. Ponomarev, A. I. Kolomitsev, and J. C. Kimball, "Numerical simulations for capillary-based X ray optics," in *X Ray Detector Physics and Applications*, R. B. Hoover, Ed., Proceedings of SPIE, 1992.

[47] C. C. Abreu, D. G. Kruger, C. A. MacDonald, C. A. Mistretta, W. W. Peppler, and Q. F. Xiao, "Measurements of capillary X ray optics with potential for use in mammographic imaging," *Medical Physics*, vol. 22, no. 11, part 1, pp. 1793–1801, 1995.

[48] Suparmi, Cari, L. Wang, H. Wang, W. M. Gibson, and C. A. MacDonald, "Measurement and analysis of leaded glass capillary optic performance for hard X ray applications," *Journal of Applied Physics*, vol. 90, no. 10, pp. 5363–5368, 2001.

[49] C. A. MacDonald and W. M. Gibson, "Applications and advances in polycapillary optics," *X Ray Spectrometry*, vol. 32, no. 3, pp. 258–268, 2003.

[50] A. Liu, "The X ray distribution after a focussing polycapillary—a shadow simulation," *Nuclear Instruments and Methods B*, vol. 243, no. 1, pp. 223–226, 2006.

[51] D. Hampai, G. Cappuccio, G. Cibin, S. B. Dabagov, and V. Sessa, "Modeling of X ray transport through polycapillary optics," *Nuclear Instruments and Methods A*, vol. 580, no. 1, pp. 85–89, 2007.

[52] D. Hampai, S. B. Dabagov, G. Cappuccio, and G. Cibin, "X ray propagation through polycapillary optics studied through a ray tracing approach," *Spectrochimica Acta B*, vol. 62, no. 6-7, pp. 608–614, 2007.

[53] L. Xiaoyan, LI. Yude, T. Guotai, and S. Tianxi, "Evaluation of transmitting performance of cylindrical polycapillary," *Nuclear Instruments and Methods*, vol. 572, no. 2, pp. 729–733, 2007.

[54] F. R. Sugiro, S. D. Padiyar, C. A. MacDonald, and C. A. MacDonald, "Characterization of pre- and post-patient X ray polycapillary optics for mammographic imaging," in *Advances in Laboratory-Based X Ray Sources and Optics*, R. B. Hoover, A. B. C. Walker II, and S. Goto, Eds., vol. 4144 of *Proceedings of SPIE*, pp. 204–215, 2000.

[55] L. Wang, B. K. Rath, W. M. Gibson, J. C. Kimball, and C. A. MacDonald, "Performance study of polycapillary optics for hard X rays," *Journal of Applied Physics*, vol. 80, no. 7, pp. 3628–3638, 1996.

[56] H. Wang, L. Wang, W. M. Gibson, and C. A. MacDonald, "Focused beam powder diffraction with polycapillary and curved crystal optics," in *X Ray Optics, Instruments, and Missions*, R. B. Hoover, A. B. C. Walker II, and S. Goto, Eds., vol. 3444 of *Proceedings of SPIE*, pp. 643–651, July 1998.

[57] D. H. Bilderback, "Review of capillary X ray optics from the 2nd international capillary optics meeting," *X Ray Spectrometry*, vol. 32, no. 3, pp. 195–207, 2003.

[58] D. Bittel and J. C. Kimball, "Surface roughness and the scattering of glancing-angle X rays: application to X ray lenses," *Journal of Applied Physics*, vol. 74, no. 2, pp. 877–883, 1993.

[59] J. Harvey, "X ray optics," in *Handbook of Optics*, M. Bass, Ed., vol. 2, chapter 11, McGraw-Hill, New York, NY, USA, 1st edition, 1996.

[60] Cari, C. A. MacDonald, W. M. Gibson et al., "Characterization of a long focal length polycapillary optic for high energy X rays," in *Advances in Laboratory-Based X Ray Sources and Optics*, C. A. MacDonald and A. M. Khounsary, Eds., vol. 4144 of *Proceedings of SPIE*, pp. 183–192, 2000.

[61] B. K. Rath, L. Wang, B. E. Homan, F. Hofmann, W. M. Gibson, and C. A. MacDonald, "Measurements and analysis of radiation effects in polycapillary X ray optics," *Journal of Applied Physics*, vol. 83, no. 12, pp. 7424–7435, 1998.

[62] A. Bjeoumikhov, N. Langhoff, S. Bjeoumikhova, and R. Wedell, "Capillary optics for micro X ray fluorescence analysis," *Review of Scientific Instruments*, vol. 76, no. 6, Article ID 063115, 2005.

[63] S. Dittrich, *Energy sensitive measurements of X Ray beam focusing with polycapillary optics*, M.S. thesis, University at Albany, 2006.

[64] H. von Berlischpe, *Focused beam applications polycapillary X ray optics*, M.S. thesis, University at Albany, 2005.

[65] J. Lohbreier, *Fluorescence and diffraction measurements with polycapillary X ray optics*, M.S. thesis, University at Albany, 2004.

[66] L. Wang, W. M. Gibson, C. A. MacDonald et al., "Potential of polycapillary X ray optics in medical imaging applications," in *EUV, X Ray, and Neutron Optics and Sources*, C. A. MacDonald, K. A. Goldberg, J. R. Maldonado, A. J. Marker III, and S. P. Vernon, Eds., vol. 3767 of *Proceedings of SPIE*, pp. 102–112, 1999.

[67] M. A. Kumakhov, "Status of experimental works in the field of X ray capillary optics," in *X Ray and UV Detectors*, vol. 2278 of *Proceedings of SPIE*, pp. 180–190, July 1994.

[68] S. B. Dabagov, A. Marcelli, V. A. Murashova, N. L. Svyatoslavsky, R. V. Fedorchuk, and M. N. Yakimenko, "Coherent and incoherent components of a synchrotron radiation spot produced by separate capillaries," *Applied Optics*, vol. 39, no. 19, pp. 3338–3343, 2000.

[69] S. B. Dabagov and H. Uberall, "On X ray channeling in narrow guides," *Nuclear Instruments and Methods*, vol. 266, no. 17, pp. 3881–3887, 2008.

[70] S. V. Kukhlevsky, G. Nyitray, V. L. Kantsyrev, and J. Kaiser, "Detailed structure of fs pulses passing through straight and tapered optical waveguides," *Optics Communications*, vol. 192, no. 3–6, pp. 225–229, 2001.

[71] S. LaBrake, *Glass capillary X ray waveguides*, Doctoral Dissertation, University at Albany, 2003.

[72] A. Bjeoumikhov, S. Bjeoumikhova, H. Riesemeier, M. Radtke, and R. Wedell, "Propagation of synchrotron radiation through nanocapillary structures," *Physics Letters A*, vol. 366, no. 4-5, pp. 283–288, 2007.

[73] S. V. Kukhlevsky, F. Flora, A. Marinai et al., "Diffraction of X ray beams in capillary waveguides," *Nuclear Instruments and Methods B*, vol. 168, no. 2, pp. 276–282, 2000.

[74] A. Bjeoumikhov, "Observation of peculiarities in angular distributions of X ray radition after propagation through nanocapill structure," *Physics Letters A*, vol. 360, pp. 405–410, 2007.

[75] S. B. Dabagov, "Channeling of neutral particles in micro- and nanocapillaries," *Physics-Uspekhi*, vol. 46, no. 10, pp. 1053–1075, 2003.

[76] K. Janssens, W. De Nolf, G. Van Der Snickt et al., "Recent trends in quantitative aspects of microscopic X ray fluorescence analysis," *Trends in Analytical Chemistry*, vol. 29, no. 6, pp. 464–478, 2010.

[77] K. Tsuji, K. Nakano, H. Hayashi, K. Hayashi, and C. U. Ro, "X ray spectrometry," *Analytical Chemistry*, vol. 80, no. 12, pp. 4421–4454, 2008.

[78] K. H. A. Janssens, F. C. V. Adams, and A. Rindby, Eds., *Microscopic X Ray Fluorescence Analysis*, John Wiley & Sons, New York, NY, USA, 2000.

[79] Y. Yan and W. M. Gibson, "Polycapillary optics and X ray analytical techniques," *Advances in X Ray Analysis*, vol. 45, pp. 298–304, 2002.

[80] S. P. Formica and S. M. Lee, "X ray fluorescence system for thin film composition analysis during deposition," *Thin Solid Films*, vol. 491, no. 1-2, pp. 71–77, 2005.

[81] Z. Luo, B. Geng, J. Bao et al., "High-throughput X ray characterization system for combinatorial materials studies," *Review of Scientific Instruments*, vol. 76, no. 9, Article ID 095105, 2005.

[82] L. Borgese, A. Zacco, E. Bontempi et al., "Use of total reflection X ray fluorescence (TXRF) for the evaluation of heavy metal poisoning due to the improper use of a traditional ayurvedic drug," *Journal of Pharmaceutical and Biomedical Analysis*, vol. 52, no. 5, pp. 787–790, 2010.

[83] S. V. Nikitina, A. S. Shcherbakov, and N. S. Ibraimov, "X ray fluorescence analysis on the base of polycapillary Kumakhov optics," *Review of Scientific Instruments*, vol. 70, no. 7, pp. 2950–2956, 1999.

[84] G. Buzanich, P. Wobrauschek, C. Streli et al., "A portable micro-X ray fluorescence spectrometer with polycapillary optics and vacuum chamber for archaeometric and other applications," *Spectrochimica Acta B*, vol. 62, no. 11, pp. 1252–1256, 2007.

[85] G. Vittiglio, S. Bichlmeier, P. Klinger et al., "A compact μ-XRF spectrometer for (in situ) analyses of cultural heritage and forensic materials," *Nuclear Instruments and Methods B*, vol. 213, pp. 693–698, 2004, 5th Topical Meeting on Industrial Radiation andRadioisotope Measurement Applications.

[86] B. Kanngießer, N. Kemf, and W. Malzer, "Spectral and lateral resolved characterisation of X ray microbeams," *Nuclear Instruments and Methods B*, vol. 198, no. 3-4, pp. 230–237, 2002.

[87] E. Langer, S. Dabritz, W. Hauffe, and M. Haschke, "Advances in X ray excitation of Kossel patterns by a focusing polycapillary lens," *Applied Surface Science*, vol. 252, no. 1, pp. 240–244, 2005.

[88] A. G. Revenko, "Specific features of X ray fluorescence analysis techniques using capillary lenses and synchrotron radiation," *Spectrochimica Acta B*, vol. 62, no. 6-7, pp. 567–576, 2007.

[89] J. M. Feldkamp, C. G. Schroer, J. Patommel et al., "Compact X ray microtomography system for element mapping and absorption imaging," *Review of Scientific Instruments*, vol. 78, no. 7, Article ID 073702, 2007.

[90] P. Bleuet, P. Gergaud, L. Lemelle et al., "3D chemical imaging based on a third-generation synchrotron source," *Trends in Analytical Chemistry*, vol. 29, no. 6, pp. 518–527, 2010.

[91] Ž. Šmit, K. Janssens, K. Proost, and I. Langus, "Confocal μ-XRF depth analysis of paint layers," *Nuclear Instruments and Methods B*, vol. 219-220, no. 1–4, pp. 35–40, 2004.

[92] M. Žitnik, P. Pelicon, N. Grlj et al., "Three-dimensional imaging of aerosol particles with scanning proton microprobe in a confocal arrangement," *Applied Physics Letters*, vol. 93, no. 9, Article ID 094104, 2008.

[93] N. Grassi, C. Guazzoni, R. Alberti, T. Klatka, and A. Bjeoumikhov, "External scanning micro-PIXE for the characterization of a polycapillary lens: measurement of the collected X ray intensity distribution," *Nuclear Instruments and Methods B*, vol. 268, no. 11-12, pp. 1945–1948, 2010.

[94] R. Alberti, A. Bjeoumikhov, N. Grassi et al., "Use of silicon drift detectors for the detection of medium-light elements in PIXE," *Nuclear Instruments and Methods B*, vol. 266, no. 10, pp. 2296–2300, 2008.

[95] T. Sun, Z. Liu, Y. Li et al., "Quantitative analysis of single aerosl particles with confocal micro-X ray fluorescence spectrometer," *Nuclear Instruments and Methods A*, vol. 622, no. 1, pp. 295–297, 2010.

[96] A. Castoldi, C. Guazzoni, R. Hartmann, C. Ozkan, L. Strüder, and A. Visconti, "Application of controlled-drift detectors to spectroscopic X ray imaging," in *Proceedings of the IEEE Nuclear Science Symposium and Medical Imaging Conference (NSS-MIC '07)*, pp. 1003–1008, November 2007.

[97] K. Tsuji, K. Nakano, and X. Ding, "Development of confocal micro X ray fluorescence instrument using two X ray beams," *Spectrochimica Acta B*, vol. 62, no. 6-7, pp. 549–553, 2007.

[98] W. M. Gibson and C. A. MacDonald, "Summary of X ray and neutron optics," in *Handbook of Optics*, M. Bass, Ed., vol. 3, chapter 37, McGraw-Hill, New York, NY, USA, 2000.

[99] T. Sun, Y. Xie, Z. Liu, T. Liu, T. Hu, and X. Ding, "Application of a combined system of polycapillary X ray lens and toroidal mirror in micro-X ray-absorption fine-structure facility," *Journal of Applied Physics*, vol. 99, no. 9, Article ID 094907, 2006.

[100] P.-W. Li and R.-C. Bi, "Applications of polycapillary X ray optics in protein crystallography," *Journal of Applied Crystallography*, vol. 31, no. 5, pp. 806–811, 1998.

[101] F. A. Hofmann, W. M. Gibson, C. A. MacDonald, D. A. Carter, J. X. Ho, and J. R. Ruble, "Polycapillary optic-source combinations for protein crystallography," *Journal of Applied Crystallography*, vol. 34, no. 3, pp. 330–335, 2001.

[102] C. A. MacDonald, S. M. Owens, and W. M. Gibson, "Polycapillary X ray optics for microdiffraction," *Journal of Applied Crystallography*, vol. 32, no. 2, pp. 160–167, 1999.

[103] S. M.. Owens, F. A. Hoffman, C. A. MacDonald, and W. M. Gibson, "Microdiffraction using collimating and convergent beam polycapillary optics," *Advances in X Ray Analysis*, vol. 41, pp. 314–318, 1997.

[104] J. X. Ho, E. H. Snell, R. C. Sisk et al., "Stationary crystal diffraction with a monochromatic convergent X ray source and application for macromolecular crystal data collection," *Acta Crystallographica D*, vol. 54, no. 2, pp. 200–214, 1998.

[105] C. Kirchlechner, K. J. Martinschitz, R. Daniel et al., "X ray diffraction analysis of three-dimensional residual stress fields reveals origins of thermal fatigue in uncoated and coated steel," *Scripta Materialia*, vol. 62, no. 10, pp. 774–777, 2010.

[106] S. T. Misture and M. Haller, "Application of polycapillary optics for parallel beam powder diffraction," *Advances in X Ray Analysis*, vol. 43, pp. 248–253, 2000.

[107] C. A. MacDonald, N. Mail, W. M. Gibson, S. M. Jorgensen, and E. L. Ritman, "Micro gamma camera optics with high sensitivity and resolution," in *Physics of Medical Imaging*, M. J. Flynn, Ed., vol. 5745 of *Proceedings of SPIE*, pp. 1–6, 2005.

[108] S. M. Jorgensen, M. S. Chmelik, D. R. Eaker, C. A. MacDonald, and E. L. Ritman, "Polycapillary X ray optics- based integrated micro-SPECT/CT scanner," in *Developments in X Ray Tomography IV*, U. Bonse, Ed., vol. 5535 of *Proceedings of SPIE*, pp. 36–42, 2004.

[109] D. N. Mahato and C. A. MacDonald, "Potential for focused beam orthovoltage therapy," in *Penetrating Radiation Systems and Applications XI*, F. P. Doty, H. B. Barber, H. Roehrig, and R. C. Schirato, Eds., vol. 7806 of *Proceedings of SPIE*, 2010.

[110] H. Chen, R. G. Downing, D. F. R. Mildner et al., "Guiding and focusing neutron beams using capillary optics," *Nature*, vol. 357, no. 6377, pp. 391–393, 1992.

[111] Q. F. Xiao, H. Chen, V. A. Sharov et al., "Neutron focusing optic for submillimeter materials analysis," *Review of Scientific Instruments*, vol. 65, no. 11, pp. 3399–3402, 1994.

[112] D. F. R. Mildner, H. H. Chen-Mayer, and R. G. Downing, "Characteristic of a polycapillary neutron focusing lens," in *Proceedings of the International Symposium on Advanced in Neutron Optics and Related Research Facilities*, Japan, March 1996.

[113] R. F. Barth, A. H. Soloway, and R. G. Fairchild, "Boron neutron capture therapy for cancer," *Scientific American*, vol. 263, no. 4, pp. 100–106, 1990.

[114] A. J. Peurrung, "Capillary optics for neutron capture therapy," *Medical Physics*, vol. 23, no. 4, pp. 487–494, 1996.

[115] R. Mayer, J. Welsh, and H. Chen-Mayer, "Focused neutron beam dose deposition profiles in tissue equivalent materials: a pilot study of BNCT," in *Proceedings of the 5th International Conference on Neutron Techniques*, Crete, Greece, June 1996.

[116] C. H. Russell, W. M. Gibson, M. V. Gubarev et al., "Application of polycapillary optics for hard X ray astronomy," in *Grazing Incidence and Multilayer X Ray Optical Systems*, R. B. Hoover and A. B. C. Walker II, Eds., vol. 3113 of *Proceedings of SPIE*, pp. 369–377, 1997.

[117] C. H. Russell, M. Gubarev, J. Kolodziejczak, M. Joy, C. A. MacDonald, and W. M. Gibson, "Polycapillary X ray optics for X ray Astronomy," in *Advances in X Ray Analysis*, vol. 43, 1999.

[118] B. K. Rath, F. B. Hagelberg, B. E. Homan, and C. A. MacDonald, "Synchrotron white beam thermal loading on polycapillary X ray optics," *Nuclear Instruments and Methods*, vol. 401, no. 2-3, pp. 421–428, 1997.

Hindawi Publishing Corporation
X-Ray Optics and Instrumentation
Volume 2010, Article ID 421945, 7 pages
doi:10.1155/2010/421945

Research Article

Focusing X-Rays with Curved Multiplate Crystal Cavity

Ying-Yi Chang,[1] Sung-Yu Chen,[1] Shih-Chang Weng,[1] Chia-Hung Chu,[1] Mau-Tsu Tang,[2] Yuriy Stetsko,[2] Bo-Yuan Shew,[2] Makina Yabashi,[3] and Shih-Lin Chang[1]

[1] *Department of Physics, National Tsing Hua University, Hsinchu 300, Taiwan*
[2] *Experiment Facility Division, National Synchrotron Radiation Research Center, Hsinchu 300, Taiwan*
[3] *RIKEN, XFEL Project Head Office, Experimental Facility Group, Spring-8/RIKEN, Mikazuki, Hyogo 679-5148, Japan*

Correspondence should be addressed to Shih-Lin Chang, slchang@phys.nthu.edu.tw

Received 26 January 2010; Accepted 23 July 2010

Academic Editor: Gene Ice

An overview is given of the study on X-ray focusing using the Fabry-Perot type multi-plate silicon crystal cavities consisting of compound refractive lenses. Silicon (12 4 0) is used as the back reflection for cavity resonance at the photon energy of 14.4388 keV. Measurements of focal length of the transmitted beam through the crystal cavities show enhanced focusing effect due to the presence of back diffraction. Also, an incident beam with ultrahigh energy resolution can improve the focusing owing to the wider acceptance angle of the back diffraction. Considerations based on the excitation of dispersion surface within the framework of X-ray dynamical diffraction theory are also presented to reveal the origin of this enhanced focusing.

1. Introduction

Focusing X-rays is usually considered very difficult because the refractive index of X-rays is smaller than and very close to unity. The advances in technology development have led to X-ray focusing using polycapillaries [1] and zone plates [2]. In 1996, Snigirev et al. succeeded in focusing high-energy X-rays by the so-called compound refractive lenses (CRL) of spherical shape [3]. Later, the CRL of parabolic shape have been developed to eliminate the spherical aberration and other distortion and Kinoform lenses have also been used to diminish the absorption [4]. Moreover, several kinds of CRL were proposed to exceed the critical angle limit [5, 6]. Very recently, two- and multi-plate X-ray cavities of silicon have been realized using X-ray back reflection and X-ray interference fringes due to cavity resonance been observed [7, 8]. In addition, attempts to combine this Fabry-Perot type crystal cavity with CRL lenses of circular [9] and parabolic shapes [10] for X-ray focusing have been pursued. In this paper, an overview is given of this development of utilizing crystal cavities for focusing X-rays. Also, the difference in beam-focusing between the use of back diffraction and the conventional optical refraction will be addressed.

In the following, we will first briefly describe the cavity resonance in Fabry-Perot type crystal cavity via back diffraction from perfect silicon crystals.

2. X-Ray Fabry-Perot Resonator and Back Diffaction

Hard X-ray Fabry-Perot resonator is composed of two or multiple crystal plates of a monolithic Si crystal. An incident X-ray beam is reflected back and forth within the gap between the two adjacent crystal plates via a back reflection, whose Bragg angle is 90 degrees [7, 8, 11, 12]. The interaction among the forward transmitted and back reflected beams gives rise to interference fringes due to cavity resonance, provided that the required coherent condition is satisfied. That is, the longitudinal coherent length l_L is greater than two times the effective gap distance d_e, that is, $l_L > 2d_e$, where $d_e = d + t$, d is the thickness of the crystal plate and t the gap distance [7, 8]. Experimentally, interference fringes in angle and energy scans are the convincing proof for the cavity resonance effects. The distance between two adjacent maxima of the transmitted beams in an energy scan is the so-called free spectral range (E_d), defined as $E_d = hc/2d_e$

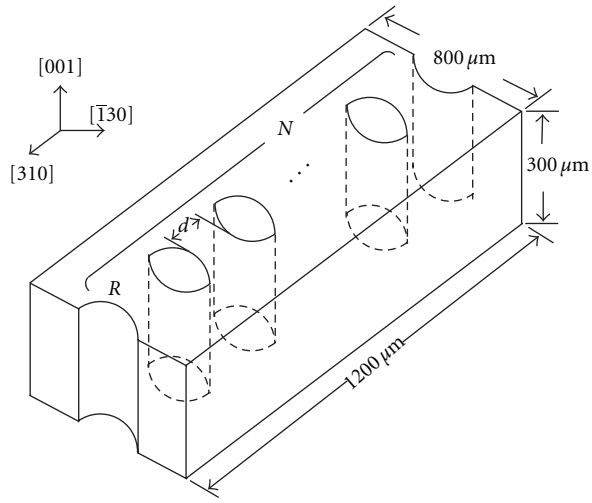

Figure 1: Schematic of focusing crystal cavity with compound parabolic lenses: Each hole also serves as a crystal cavity of the Fabry-Perot type.

Table 1: The parameters of the focusing crystal cavity devices.

Device	d (μm)	R (μm)	N	f_{optics} (mm)
No. 1	10	40	12	715
No. 2	10	50	13	800

where h is the Planck constant. This distance can be verified experimentally.

If the surface of the crystal plates of a cavity (resonator) is changed from flat to concaved surface, then the cavity could act as an X-ray lens, similar to the compound refractive lens. With this idea, the following focusing cavities and related X-ray diffraction experiments are designed.

3. Sample Preparation and Experimental Setup

Figure 1 is the schematic of a multi-plate crystal cavity for X-ray focusing. The shape of curved multiple plates is similar to the conventional parabolic refractive X-ray lenses. The crystal devices were manufactured from [001] silicon wafers using microelectronic lithography processes and dry etched with reactive ions. Several holes with parabolic cross-section were made on the wafer such that a serious of concave lenses are lined up along the [310] direction. The (12 4 0) was used as the back reflection for 14.4388 keV X-rays. The structures were 300 μm deep along the [001] direction. There were two different designs for the crystal devices, No.1 and No.2. The design parameters are listed in Table 1, where R is the radius of the parabola apex, d the distance between the two adjacent holes, and N the number of the lenses. The lens formula $f_{\text{optics}} = R/2N\delta$ was used for the design, where f_{optics} is focal length and the corresponding refractive index is $n = 1 - \delta - i\beta$. For 14.4388 keV photon energy, the real and imaginary corrections of the refractive index are $\delta = 2.33 \times 10^{-6}$ and $\beta = 1.72 \times 10^{-8}$. The ideal focal distances are 715 and 820 mm for No. 1 and No. 2 cavities, respectively.

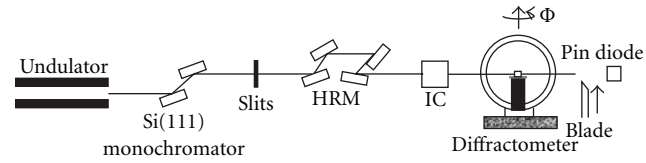

Figure 2: Experimental setup: The incident radiation was monochromatized by a Si(111) double-crystal first and then by a high-resolution monochromator (HRM) at 14.4388 keV. The focusing crystal cavity is placed at the center of an 8-circle diffractometer. An ion chamber (IC) and a pin diode were used to monitor the back-diffracted (12 4 0) and the forward-transmitted (000) beam.

Focal length measurements were carried out on the Taiwan undulator beamline BL12XU at the Spring-8 synchrotron facility in Japan. Figure 2 is the experimental layout. The storage ring was operating at 8 GeV and 100 mA. The synchrotron radiation was first monochromatized to the X-ray energy close to 14.4388 keV using a Si(111) double-crystal monochromator. The X-rays were then further tuned to have the energy resolution $\Delta E/E \sim 2.5 \times 10^{-8}$ at 14.4388 keV with a four-crystal high-resolution monochromator (HRM). The HRM was composed of two pairs of asymmetric (422) and (11 5 3) reflection planes of Si [13]. Experimentally, focal lengths were measured with and without the HRM to investigate the energy-resolution dependence of focusing. The crystal device was mounted on a goniometric head located at the center of a Huber 8-circle diffractometer. The incident beam was in the [−3 −1 0] direction normal to the device. The forward-transmitted and the back-reflected beams were monitored by an ion chamber and a pin-diode, respectively. A knife-edge of 500 Å surface roughness was used to measure the beam size of the forward-transmitted beam through the crystal cavity at several positions along the transmitted beam direction.

4. Results

The energy resolution of the incident beam without using the HRM was about $\Delta E/E \sim 1.4 \times 10^{-4}$ and $\Delta E \sim 2$ eV at 14.4388 keV. Under this condition, both the horizontal tilt, $\Delta\varphi$, around [001] and the vertical rotation, $\Delta\theta$, around [−1 3 0] of the device No. 1 gave the intensity distribution of the transmitted beam as a dip as shown in Figures 3(a) and 3(b). The high background plateau was the intensity of the (000) beam without diffraction. This means that during the back diffraction of (12 4 0) at the position, $\Delta\theta = 0°$ and $\Delta\varphi = 0°$, the intensity of the (000) beam was taken away by the (12 4 0) reflection. However, due to the insufficient energy resolution, we were sure that the diffraction condition of the (12 4 0) back reflection was not exactly fulfilled because the dip was too sharp. As will be clear, the correct profile of the (12 4 0) back reflection is a much wider dip (see Figure 4(a)). Nevertheless, it is yet worth investigating the beam-focusing effect under general diffraction conditions with modest energy resolution.

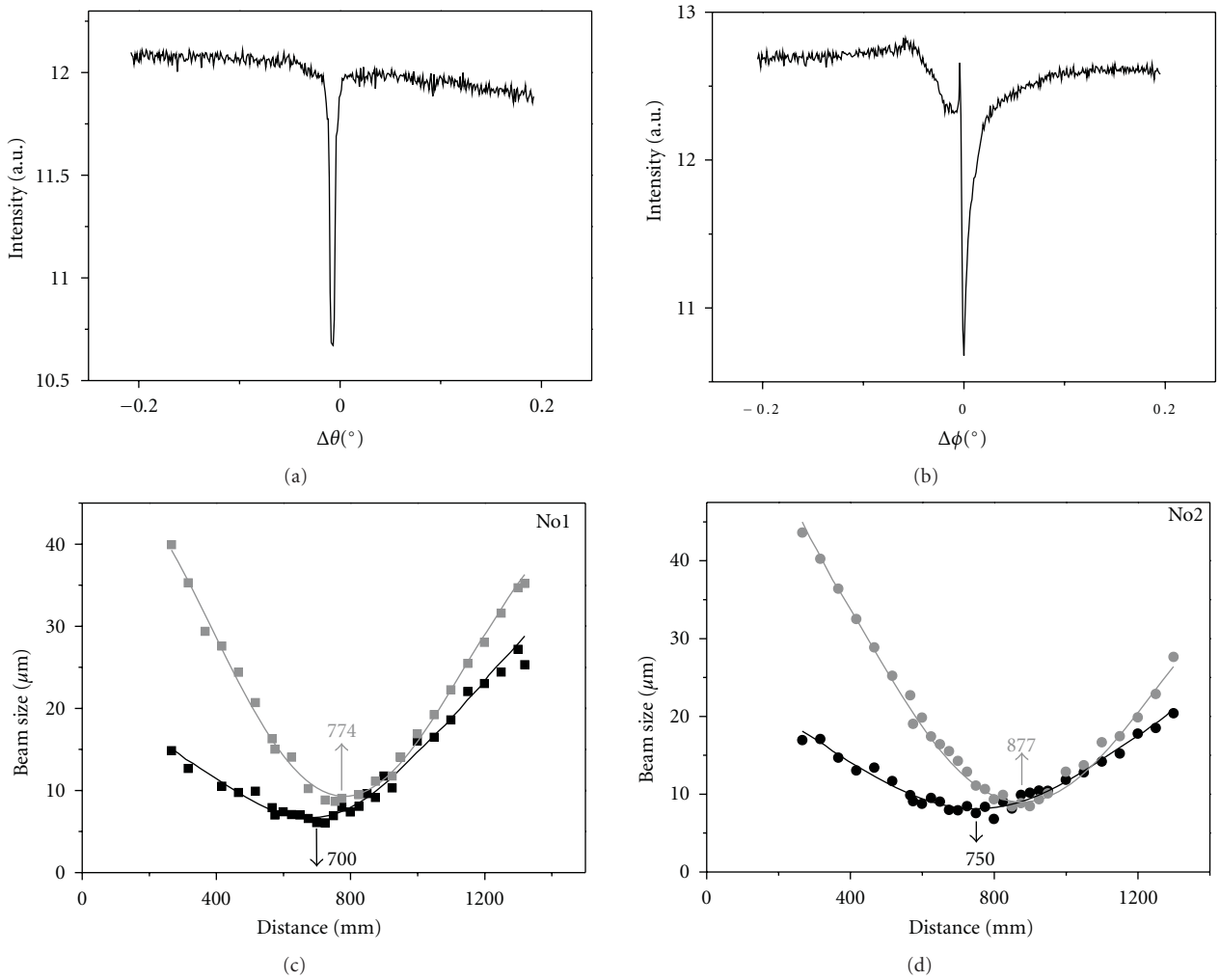

Figure 3: (a) The $\Delta\theta$ scan at $\Delta\varphi = 0$ and (b) the $\Delta\varphi$ scan at $\Delta\theta = 0$ of the transmitted beam through the crystal device No. 1. (c) and (d) The beam sizes of the transmitted beams through the crystal devices, No. 1 and No. 2, with (black dots) and without the back diffraction (gray dots) versus the distance from the exit end of the crystal devices.

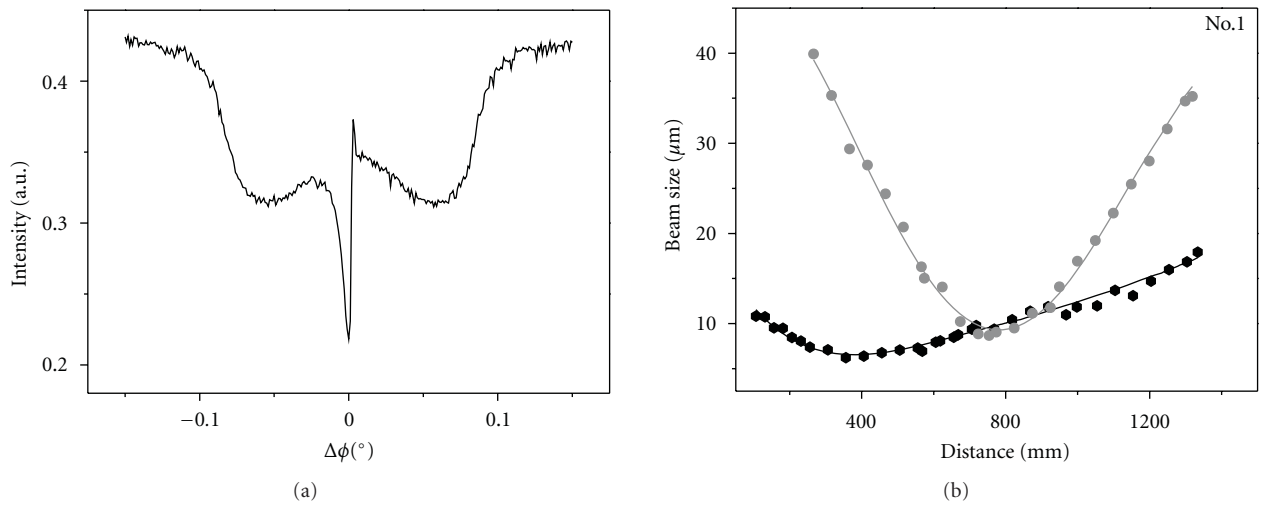

Figure 4: (a) The $\Delta\varphi$ scan at $\Delta\theta = 0$ of the (12 4 0) back diffraction for the crystal device No. 1. (b) The beam sizes of the transmitted beam through the crystal device No. 1 with (black dots) and without back diffraction (gray dots) versus the distance from the exit end of the crystal device.

Figures 3(c) and 3(d) are the measured sizes of the transmitted beam at various positions versus the distance of the measured position from the exit end of the crystal devices, No. 1 and No. 2, respectively. The gray dots and black dots show respectively the beam sizes measured at the angular position, $\Delta\theta = 0^\circ$ and $\Delta\varphi = -0.15^\circ$, at which no diffraction takes place and at the position, $\Delta\theta = 0^\circ$ and $\Delta\varphi = 0^\circ$, at which the (12 4 0) diffraction occurs. When there is no diffraction, the experimental focal lengths were around 774 and 877 mm at the position, $\Delta\theta = 0^\circ$ and $\Delta\varphi = -0.15^\circ$, for the crystal devices, No. 1 and No. 2, respectively. The results are close to the theoretical values, 715 and 820 mm. The difference probably originates from the inaccuracy in cavity manufacturing. On the other hands, when there is a diffraction, the black dotted curves give the focal distances, 700 and 750 mm, for the crystal devices, No. 1 and No. 2, respectively. The reduction in focal length is about 2~9%. This is probably because the width of the diffraction peak, about 0.01°, is too narrow to maintain the back diffraction. In other words, when the parallel incident beam passes through several crystal plates, the outer part of the beam is bent more than 0.01°. The back diffraction condition is then no longer satisfied so that this part of the beam is bent only due to optical refraction. That is why the reduction of the focal length is very small.

After inserting the HRM into the experimental setup, the energy resolution of the incident beam was about 0.36 meV. In Figure 4(a), the horizontal tilt ($\Delta\varphi$) of the crystal device at $\Delta\theta = 0^\circ$ shows the intensity profile with a wide hollow of the width about 0.2° against the (000) background. This indicates the occurrence of the (12 4 0) back diffraction at the photon energy almost exactly equal to 14.4388 keV. In addition, the sharp dip located right in the middle of the hollow at $\Delta\varphi = 0$ results from the simultaneous presence of other 22 reflections owing to the high structural symmetry Si [7, 8]. This 24-beam multiple diffraction also took away the transmitted and reflected intensities from the (12 4 0) reflection to the 22 reflected directions. Consequently the reflectivity and transmissivity of the involved X-ray beams drop considerably.

The measured beam sizes versus the distance from the end of the exit surface are shown in Figure 4(b), where the black curve was obtained at $\Delta\varphi = 0^\circ$ when the (12 4 0) back reflection and the additional 22 diffractions (24-beam diffraction) were in operation [7, 8]. And the gray curve is the measurement taken without the back reflection, namely, under a pure refraction circumstance like in the CRL situation. As can be seen, the transmitted beam was focused to the position 356 mm from the end of the device for the 24-beam diffraction at $\Delta\varphi = 0^\circ$, while the optical CRL focusing gave the focal length of about 774 mm. The beam sizes at the focal points were respectively 6.2 and 9 μm. In other words, the focal length of the CRL was reduced by nearly a factor of 2 due the 24-beam diffraction. Moreover, under the 24-beam diffraction condition, the crystal devices also preserve the characteristics of X-ray Fabry-Perot resonators. Indeed, the interference fringes were observed clearly from the device No. 1 in the photon-energy scan of the transmitted-beam (Figure 5). Since the effective gap distance is 200 μm for this crystal device, the fringe spacing, also called free spectral range (E_d), is about 3.4 meV, which agrees with the calculated value 3.1 meV.

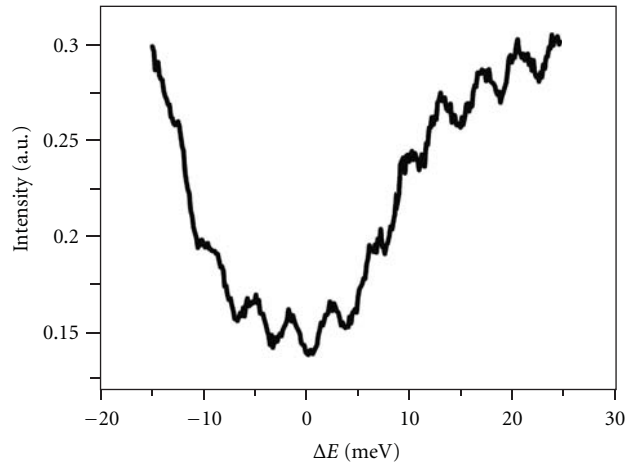

FIGURE 5: The energy ΔE scan at $E = 14.4388$ keV of the transmitted beam through the crystal device No. 1. The vertical axis is the normalized transmitted intensity.

It is estimated that for crystal No. 1 the real gain defined in [3] is about 7.6 for refraction and 11 for back diffraction. We have also measured the intensity of the focused transmitted beam by back-diffraction which is about 18% of that of the incident beam, which is comparable with that of conventional CRL.

5. Theoretical Analysis

The beam-focusing effect can be understood according to the dynamical diffraction theory of X-ray back diffraction [11, 12, 14–18].

The dynamical theory of X-ray diffraction [11, 12, 14–16] describes the interaction of X-ray waves with a crystalline material, thus forming the so-called wavefields in crystal lattice. The wavefields during the X-ray diffraction can be described by Maxwell's equations. The wavefields in the crystal are assumed to take the form of Bloch waves, which lead to the fundamental equation of wavefield [14]. The secular equation of this fundamental equation gives the dispersion relation and the dispersion surface can be constructed accordingly. Dispersion surface simply sketches the relationship of the amplitudes and wavevectors of the wavefields as a function of the angular position of the crystal in the reciprocal space. As an example, Figure 6(a) is the schematic of the dispersion surface (green color) of a two-beam Bragg reflection in a wide-angle incidence geometry, where O and G are the reciprocal lattice points representing, respectively, the (000) and (hkl) reflection. The spheres in black are the Ewald spheres outside the crystal centered at points O and G. After the X-rays enter the crystal, the Ewald sphere becomes smaller due to the fact that the index of refraction n is smaller that unity. The intersections of the two Ewald spheres (green curves) centered at O and G inside the crystal are modified approximately as hyperbola

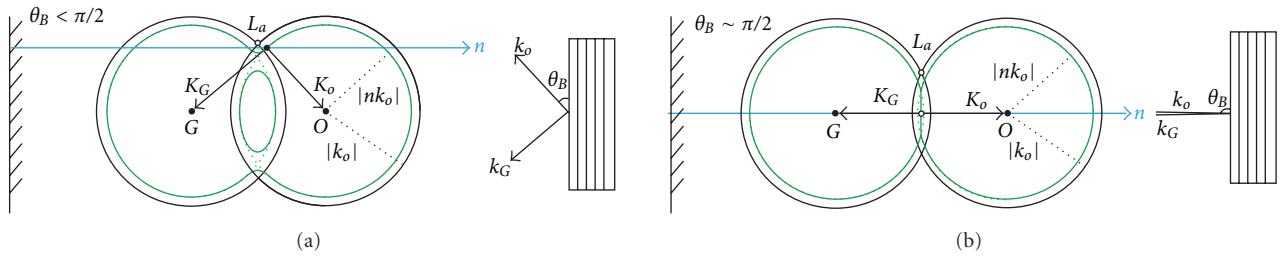

FIGURE 6: Dispersion surface projected onto the plane of incidence of a Bragg diffraction: (a) the general wide-angle incidence case with $\theta_B < \pi/2$ and (b) the back diffraction case with $\theta_B \sim \pi/2$. The green curves represent the dispersion surface inside the crystal.($\hat{n}$: the crystal surface normal; θ_B: the Bragg angle; L_a: the Laue point [14]).

(green solid curves) when the Bragg's law, $\vec{K}_G = \vec{K}_O + \vec{d}_G$ is satisfied, where $\vec{K}_O$ and $\vec{K}_G$ are the wavevectors of the (000) and (hkl) diffracted beams inside the crystal and $\vec{d}_G = \overrightarrow{OG}$. The corresponding wavevestors outside the crystal are $\vec{k}_O$ and $\vec{k}_G$. The dispersion surface is excited by an incident beam $\vec{k}_O$, whose wavevector starts from a given entrance point on the black Ewald sphere and ends at point O. This excitation generates the diffracted beams, $\vec{K}_O$ and $\vec{K}_G$, which have a common starting point, called tie point. The tie point and the entrance point lie along the surface normal direction $\hat{n}$ such that the continuity of the tangential components of the $\vec{K}_O$ and $\vec{k}_O$ at the crystal boundary is fulfilled. The same is true for $\vec{K}_G$ and $\vec{k}_G$. Hence, by taking the sample surface normal into account, the wavevectors inside the crystal can be determined.

However, when the Bragg angle is almost equal to $\pi/2$, the dispersion surface has the unusual shape represented schematically in Figure 6(b). The two Ewald spheres in green color centered at points O and G inside the crystal are just touching and tangent to each other at the only contact point, which is also the tie point for the exact back reflection. Therefore, $\vec{K}_O$ and $\vec{K}_G$ are parallel to $\hat{n}$ and opposite to each other. Since there is only one contact region, this corresponds to only one angular range of total reflection whose angular width is $w_{D,\theta_B\sim\pi/2} \sim 2\sqrt{|\chi_G|} = 0.0745°$, derived from the dynamical theory [14]. It is wider than that of the general case of wide-angle incidence, $w_{D,\theta_B<\pi/2} \sim |\chi_G| = 0.0014°$, because the value of the electric susceptibility $|\chi_G|$ is generally about 10^{-5} to 10^{-7}. Hence the acceptance angle of a back diffraction is about one order of magnitude greater than that of general cases [11, 12, 14]. This feature is useful for beam-focusing under back diffraction conditions.

We now consider the focusing effects associated with the back diffraction in the multi-plate focusing cavity based on the determination of wavevectors inside the crystal via the excitation of the dispersion surface. We will first concentrate on the back diffraction of the first crystal lens, and then extend it to the N lenses. In real space (Figure 7(a)), a parallel beam of the wavevector $\vec{k}_{o0}$ is incident on the first crystal. For simplicity, the upper part of the incident beam hits the first concave surface and generates an transmitted beam with the wavevector $\vec{K}_{O1}$ which propagates inside the first crystal. After passing through the second (exit) surface, this $\vec{K}_{O1}$ beam becomes the forward transmitted wavevector, $\vec{k}_{o1}$ and exits from the first crystal. The vector $\mathbf{n}_{i1}$ and $\mathbf{n}_{i2}$ stand for the entrance and exit surface normals of the ith crystal. Similar situation is encountered for the lower part of the incident beam. Although the scheme (Figure 7(a)) looks similar to optical refraction, the focusing mechanism is different due the presence of back diffraction.

The distinction between diffractive and optical focusing can be understood from the excitation of the dispersion surface in the reciprocal space. In Figure 7(b) the reciprocal lattice points O and G represent the incident (000) and the (12 4 0) back reflection. Because the Bragg angle θ_B is nearly equal to $\pi/2$, the wavefront, Σ_O, of the incident beam $\vec{k}_{o0}(= \overrightarrow{E_0O})$ is almost perpendicular to the reciprocal lattice vector $\overrightarrow{OG}$. E_0 is the entrance point of the beam $\vec{k}_{o0}$. Considering the continuity of the tangential components of the wavevectors inside and outside the crystal at the boundary, the incident beam $\vec{k}_{o0}$ excites the dispersion surface at the tie point T_1 along the first surface normal $\mathbf{n}_{11}$, thus generating a forward transmitted wave, $\overrightarrow{T_1O}(= \vec{K}_{O1})$inside the first crystal. When the beam $\vec{K}_{O1}$ arrives at the first exit surface, it generates the outgoing wavevector, $\overrightarrow{E_1O}(= \vec{k}_{o1})$ along the exit surface normal $\mathbf{n}_{12}$. In contrast to the back diffraction, the grey dashed line represents the dispersion surface for optical refraction, projected onto the plane of the incidence of the (12 4 0) reflection. In this case, the incident beam $\vec{k}_{o0}$ excites the (grey) dispersion surface and generates a refracted beam $\overrightarrow{g_1O}$ inside the first crystal. Subsequently, an outgoing exit beam $\overrightarrow{r_1O}$ is produced. By comparing the degree of inclination of the wavevectors involved in diffraction and refraction, it is clear that the diffracted beams $\overrightarrow{T_1O}$ hand $\overrightarrow{E_1O}$ are more focused onto point O than the refracted beams $\overrightarrow{g_1O}$ and $\overrightarrow{r_1O}$. Figure 7(c) shows the focusing effects due to diffraction and refraction in ray tracing in real space for one crystal lens. Similar situation occurs for the incident beam entering in the lower half of the crystal. Namely, the beam-bending ability of back diffraction is better than that of optical refraction. Moreover, there are more dispersion sheets (96 in total) involved in the 24-beam diffraction [18]. That implies that there are more chances for the transmitted beam to focus on to point O [10].

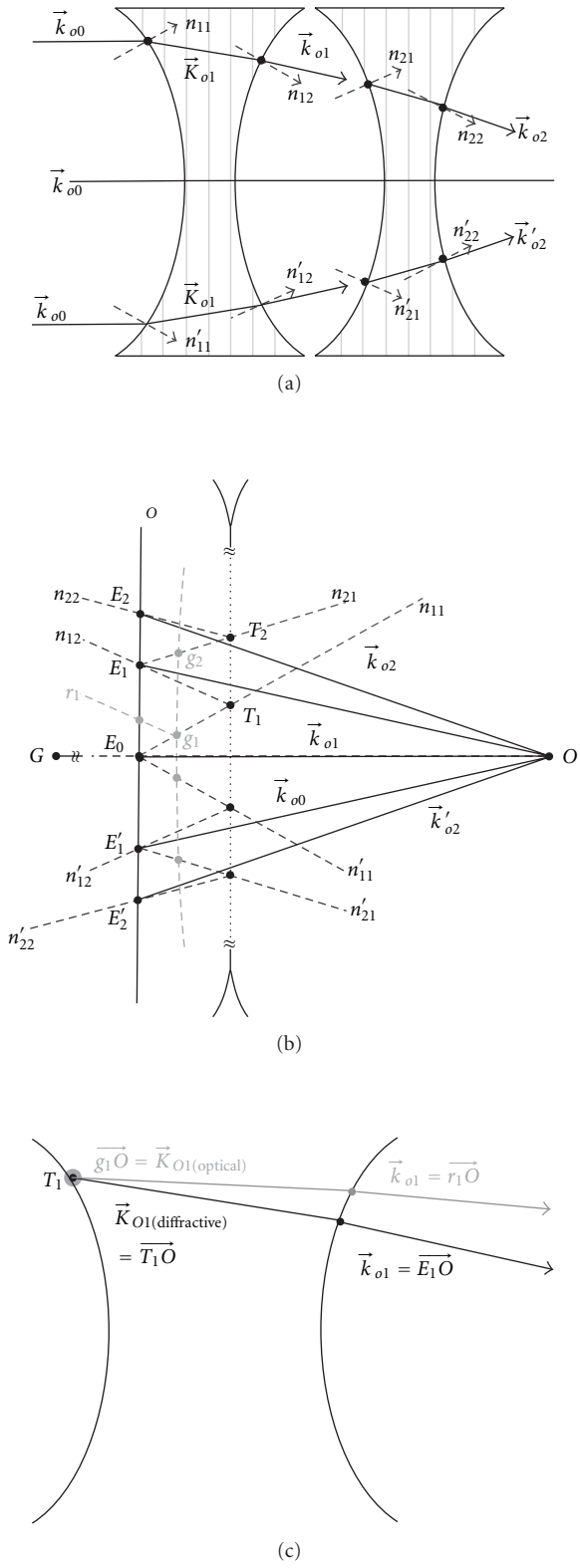

FIGURE 7: (a) Ray-tracing of a parallel incident beam in the first two crystal lenses in real space: the symbols with "prime" are for the lower part of the beam; (b) Schematic of the excitation of the dispersion surface projected onto the plane of incidence in reciprocal space for (a); (c) The ray-tracing of the diffracted beam (black) and the optical refracted beam (gray) for the first crystal according to the corresponding wavevectors.

Hence the transmitted beam will be focused further. This theoretical consideration can be continually applied to next crystal lens and up to the Nth crystal and the focusing effect due to back diffraction is expected to be much enhanced.

In summary, the dynamical effect on focusing involving back diffraction is mainly due to the excitation of the dispersion surface for curved crystal surfaces. This curved crystal boundaries make beam focusing happen. That is, this focusing effect, governed by the curvature of the curved CRL, is due to the change of the direction of the wavevector of the transmitted beam during the excitation of the dispersion surface of the diffractions involved.

6. Conclusion

In conclusion, we have shown X-ray focusing using curved crystal cavity with incident X-rays of modest and ultrahigh energy-resolution. If only a conventional double crystal monochromator is employed as the beam conditioner, the focusing is less effective than the case with an ultrahigh resolution monochromator, because the latter could easily fulfill cavity resonance conditions and provide a wider acceptance angle for the incident beam. On the other hand, this type of focusing depends on the presence of diffraction. It seems that in this particular case reported here optical refraction, the two-beam back reflection, and the 24-beam diffraction give the longest, shorter, and the shortest focal length, respectively. The reduction in focal length could be 50% compared to the refraction case. Also, according to [3], the real gain of a CRL lens depends on the absorption, real focus size, effective lens aperture, image distance, and source distance. Since the focus size for back diffraction is smaller than for refraction, the gain for back diffraction is larger than that for refraction. This distinct feature could be useful for high resolution diffraction, scattering, and imaging investigations. However, because back diffraction takes place at a specific energy and the required energy resolution is very strict, the use of this type of crystal devices as a focus tool might be limited to some specific photon energies for a given crystal used for making the devices.

Acknowledgements

The authors thank C.-C. Chen, N. Hiraoka of NSRRC for technical supports, and the Ministry of Education and National Science Council (NSC) of Taiwan, for financial supports. Special funding from the NSC Academic Summit Program is also gratefully acknowledged.

References

[1] C. A. MacDonald and W. M. Gibson, "Applications and advances in polycapillary optics," *X-Ray Spectrometry*, vol. 32, no. 3, pp. 258–268, 2003.

[2] G.-C. Yin, Y.-F. Song, M.-T. Tang et al., "30 nm resolution x-ray imaging at 8 keV using third order diffraction of a zone plate lens objective in a transmission microscope," *Applied Physics Letters*, vol. 89, no. 22, Article ID 221122, 2006.

[3] A. Snigirev, V. Kohn, I. Snigireva, and B. Lengeler, "A compound refractive lens for focusing high-energy X-rays," *Nature*, vol. 384, no. 6604, pp. 49–51, 1996.

[4] V. Aristov, M. Grigoriev, S. Kuznetsov et al., "X-ray refractive planar lens with minimized absorption," *Applied Physics Letters*, vol. 77, no. 24, pp. 4058–4060, 2000.

[5] C. G. Schroer and B. Lengeler, "Focusing hard X rays to nanometer dimensions by adiabatically focusing lenses," *Physical Review Letters*, vol. 94, no. 5, Article ID 054802, 2005.

[6] K. Evans-Lutterodt, A. Stein, J. M. Ablett, N. Bozovic, A. Taylor, and D. M. Tennant, "Using compound kinoform hard-X-ray lenses to exceed the critical angle limit," *Physical Review Letters*, vol. 99, no. 13, Article ID 134801, 2007.

[7] S.-L. Chang, YU. P. Stetsko, M.-T. Tang et al., "X-ray resonance in crystal cavities: realization of fabry-perot resonator for hard X rays," *Physical Review Letters*, vol. 94, no. 17, Article ID 174801, 2005.

[8] S.-L. Chang, Yu. P. Stetsko, M.-T. Tang, et al., "Fabry-Perot resonator for hard X rays: a diffraction experiment," *Physical Review B*, vol. 74, Article ID 134111, 7 pages, 2006.

[9] S.-Y. Chen, Y.-Y. Chang, M.-T. Tang et al., "Multi-plate crystal cavity with compound refractive lenses," in *Advances in X-Ray/EUV Optics and Components III*, vol. 7077 of *Proceedings of SPIE*, San Diego, Calif, USA, August 2008.

[10] Y.-Y. Chang, S.-Y. Chen, H.-H. Wu et al., "Diffraction-enhanced beam-focusing for X-rays in curved multi-plate crystal cavity," *Optics Express*, vol. 18, no. 8, pp. 7886–7892, 2010.

[11] A. Caticha and S. Caticha-Ellis, "Dynamical theory of x-ray diffraction at Bragg angles near $\pi/2$," *Physical Review B*, vol. 25, no. 2, pp. 971–983, 1982.

[12] V. G. Kohn, YU. V. Shvydko, and E. Gerdau, "On the theory of an X-ray Fabry-Perot interferometer," *Physica Status Solidi B*, vol. 221, no. 2, pp. 597–615, 2000.

[13] M. Yabashi, K. Tamasaku, S. Kikuta, and T. Ishikawa, "X-ray monochromator with an energy resolution of 8×10^{-9} at 14.41 keV," *Review of Scientific Instruments*, vol. 72, no. 11, pp. 4080–4083, 2001.

[14] A. Authier, *Dynamical Theory of X-Ray Diffraction*, Oxford University Press, Oxford, UK, 2001.

[15] S.-L. Chang, *X-Ray Multiple-Wave Diffraction: Theory and Application*, Spinger, Berlin, Germany, 2004.

[16] S. Kikuta, Y. Imai, T. Iizuka, Y. Yoda, X.-W. Zhang, and K. Hirano, "X-ray diffraction with a Bragg angle near $\pi/2$ and its applications," *Journal of Synchrotron Radiation*, vol. 5, no. 3, pp. 670–672, 1998.

[17] J. P. Sutter, E. E. Alp, M. Y. Hu et al., "Multiple-beam x-ray diffraction near exact backscattering in silicon," *Physical Review B*, vol. 63, no. 9, Article ID 094111, 12 pages, 2001.

[18] M.-S. Chiu, YU. P. Stetsko, and S.-L. Chang, "Dynamical calculation for X-ray 24-beam diffraction in a two-plate crystal cavity of silicon," *Acta Crystallographica Section A*, vol. 64, no. 3, pp. 394–403, 2008.

Hindawi Publishing Corporation
X-Ray Optics and Instrumentation
Volume 2010, Article ID 583626, 10 pages
doi:10.1155/2010/583626

Research Article

Measuring Curved Crystal Performance for a High-Resolution, Imaging X-Ray Spectrometer

Michael J. Haugh[1] and Richard Stewart[2]

[1] *National Security Technologies, LLC (NSTec), 161 S. Vasco Road, Livermore, CA 94550, USA*
[2] *Lawrence Livermore National Laboratory (LLNL), 7000 East Avenue, Livermore, CA 94550, USA*

Correspondence should be addressed to Michael J. Haugh, haughmj@nv.doe.gov

Received 16 December 2009; Accepted 7 June 2010

Academic Editor: Gene Ice

This paper describes the design, crystal selection, and crystal testing for a vertical Johann spectrometer operating in the 13 keV range to measure ion Doppler broadening in inertial confinement plasmas. The spectrometer is designed to use thin, curved, mica crystals to achieve a resolving power of $E/\Delta E > 2000$. A number of natural mica crystals were screened for flatness and X-ray diffraction width to find samples of sufficient perfection for use in the instrument. Procedures to select and mount high quality mica samples are discussed. A diode-type X-ray source coupled to a dual goniometer arrangement was used to measure the crystal reflectivity curve. A procedure was developed for evaluating the goniometer performance using a set of diffraction grade Si crystals. This goniometer system was invaluable for identifying the best original crystals for further use and developing the techniques to select satisfactory curved crystals for the spectrometer.

1. Introduction

The analysis of the X-ray emission line spectrum of highly ionized atoms in high temperature inertial confinement target implosions is a powerful tool for the characterization of plasma conditions in the target [1]. In principle, space and time resolved spectroscopic data can be used to determine three dimensional plasma conditions in the compressed plasma. Electron densities can be determined from Stark broadened line profiles and continuum edge shifts, and electron temperatures can be determined from line ratios and continuum distributions [2]. In most current inertial confinement experiments however, ion temperatures have been impossible to measure from X-ray spectroscopy because Stark broadening and collisional broadening of dopant ions are larger than the thermal ion Doppler broadening that could be used to measure ion temperatures. While neutron and proton emission time histories and spectra can provide some data on ion temperatures, no satisfactory technique currently exists to measure time and space resolved ion temperatures in implosion plasmas, and any viable technique for ignition targets will likely have to rely on X-ray emission rather than on neutron or proton emission because of time of flight dispersion of particle arrival times at the detectors as well as proton range effects.

Yaakobi et al. [3, 4] have shown, however, that for very highly charged Kr XXXV ions in exploding pusher implosions, which achieve ion temperatures in excess of 10 keV, ion Doppler broadening in low lying helium like 13–15 keV resonance lines may be observable if spectra can be recorded with sufficiently high spectral resolution. This is basically possible because the energy levels of the highly charged krypton ions are tightly bound, have large relativistic fine structure splitting, have low polarization in the plasma microfield, and have small collision cross sections. The observable lines least sensitive to Stark broadening are the 1s to 2p resonance transitions at 13029 eV and 13115 eV. Similar conditions are expected in experiments that will be possible when the ignition of thermonuclear burn is achieved with the next generation of megajoule class lasers like NIF, where nuclear energy released is expected to produce electron temperatures as high as 50 keV and even higher ion temperatures. The high electron temperatures will produce hydrogen and helium like ions in heavy dopant

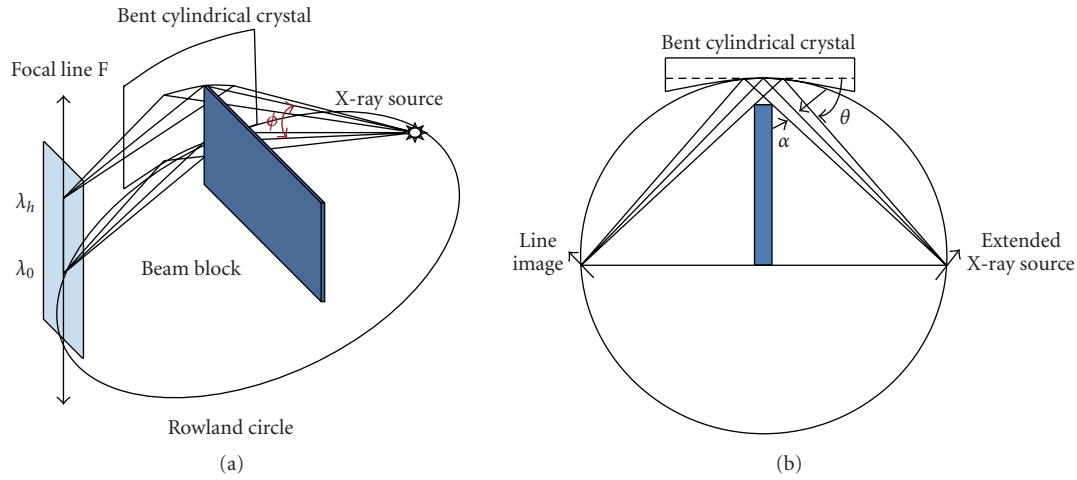

Figure 1: (a) Vertical Johann Spectrometer Scheme-Layout (b) Vertical Johann Spectrometer Scheme-Top view looking down cylinder axis.

atoms such as krypton and xenon, and the broadening of 1s to 2p resonance lines from these ions is predicted to be dominated by ion-Doppler broadening despite the very high expected plasma electron densities in excess of $10^{26}\,e^{-}/cm^{3}$. The Kr dopant can be used in exploding pusher gas, targets on NIF, or with high atomic number impurities in the solid portion of cryogenic targets.

The resolving power necessary to measure Doppler broadening in these heavy ions is expected to be $E/\Delta E \geq 2000$ or greater, depending on the ion temperature achieved and the mass of the ions being observed. This type of measurement is now standard in Tokamak experiments [5], but it is difficult to achieve on laser driven implosions due to the relatively low brightness of the source and the restricted viewing solid angle and space available for instrumentation. In this paper, we describe the design of a small one-dimensional imaging spectrometer that is compatible with the experimental space constraints for direct drive laser implosions, and that can achieve high resolving powers for helium-like krypton transitions at 13 keV. We also describe our work on the design and characterization of the curved diffraction crystals needed to provide sufficient resolving power for the spectrometer. This type of instrument could be used to make time and space resolved measurements of the ion temperature in exploding pusher krypton doped plasmas or other very high temperature plasma experiments that are expected to be possible in the future.

2. Spectrometer Design

The spectrometer we are designing is a version of a vertical Johann spectrometer (VJS). The principle of this type of spectrometer has been described in detail by Renner et al. [6, 7] and Kopecký [8].

The main element of the VJS is a cylindrically curved crystal that diffracts X-rays from a source of small spatial extent located on the Rowland circle of the crystal. In a normal Johann spectrometer, X-rays from a monochromatic point source are approximately focused to an opposing point on the Rowland circle in a plane normal to the axis of the cylinder containing the point source, as shown in Figure 1. It is easy to show that this focusing is conserved for points along the line parallel to the cylinder axis that intersects the Rowland circle above this central plane, as shown in Figure 1(a). A point source on the Rowland circle focuses to a line shown as F in Figure 1(a). The angle of incidence of lines incident on the diffraction crystal increases slowly with increasing elevation angle from the Rowland circle, so that the sine of the angle of incidence varies as

$$\sin(\theta) = \sin(\theta_0)\cos(\phi). \tag{1}$$

The wavelength of diffracted rays is determined by the Bragg relation

$$\lambda = 2d\,\sin\Theta. \tag{2}$$

This means that the wavelength of X-rays diffracted from the crystal for the point source varies with ϕ as

$$\lambda_h = \lambda_0\,\cos\phi, \tag{3}$$

where λ_0 is the wavelength focused in the plane of the Rowland circle and λ_h is the wavelength for the ray tilted at an angle ϕ to the plane.

For high resolution, the length of the crystal illuminated by the source must be limited because the angle of incidence on the crystal from a point source slowly changes as the X-rays from the source hit the crystal at increasing distances from its center. This is the familiar Johann defocusing defect. The angular size of the crystal used can be controlled with the beam block shown in Figures 1(a) and 1(b).

For extended sources, the cylindrical crystal focuses the image of the source in one dimension perpendicular to the ray diffracting from the crystal. The high vertical dispersion of the spectrum greatly reduces the effects of source size on spectral resolution in the direction of the axis. For sources displaced from the Rowland circle in the direction perpendicular the ray striking the crystal and the axis of

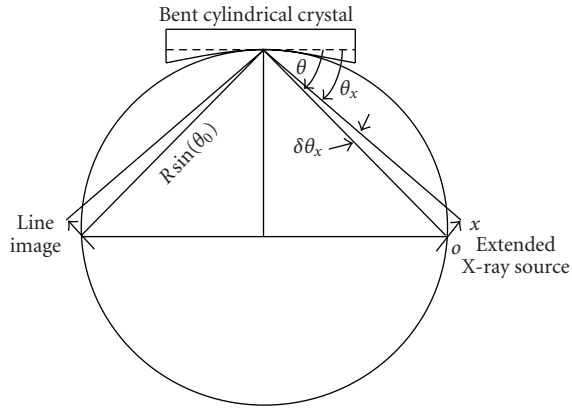

Figure 2: Spectral line formation geometry.

symmetry of the crystal, as shown in Figure 2, the spectrum is shifted spectrally relative to the point on the Rowland circle because the angles of incidence of all rays are shifted slightly. A small spatial shift in this direction gives a much larger change in Bragg angles on the surface of the crystal than an equivalent vertical translation of diffracted rays in the image plane, so the wavelength at one value of ϕ changes very rapidly with horizontal source size, leading to steeply sloped lines on the detector for a given wavelength.

The dependence of the line position on the position of the source can be calculated from the geometry of the spectrometer. For a distance x shown in Figure 2, displaced laterally from the Rowland circle, the change in Bragg angle in the plane of the Rowland circle is given by (4):

$$\delta\Theta_{0x} = \tan^{-1}\left[\frac{x}{R\,\sin\Theta_0}\right], \qquad \Theta_{0x} = \Theta_0 - \delta\Theta_{0x}, \tag{4}$$

where R is the radius of curvature of the crystal.

Then the angle of inclination of the diffracted X-rays of wavelength λ for a given point x displaced off the Rowland circle is given by

$$\phi_x = \cos^{-1}\left[\frac{\lambda}{2d\,\sin\Theta_{0x}}\right]. \tag{5}$$

The displacement of an X-ray diffracting at ϕ_x in the vertical (axial) direction of the diffracted line is then given by

$$z = \frac{2R\,\sin(\Theta_0)\,\tan(\phi_x)}{\cos(\delta\Theta_{0x})}. \tag{6}$$

The one dimensional imaging of the detector allows these spatially dependent spectral profiles to be separated. If a detector with poor or no spatial resolution in the imaging direction is used, the combined spectral effects are equivalent to the normal source size broadening for a flat crystal.

The VJS has several properties that make it useful for laser experiments. It has high collection efficiency due to having the source on the Rowland circle, where all rays at one angle of inclination phi hitting the crystal are collected and focused to a point. It has very high dispersion independent of wavelength and Bragg angle due to vertical dispersion. This means that small Bragg angles and small beam deflections can be used in a very high resolution design, which allows us to fit the spectrometer into a very small solid angle that is compatible with direct drive laser experiments. The large vertical dispersion also allows us to use detectors with relatively poor spatial resolution in one dimension. Finally, the spectrometer has a spatial resolution that can be better than 10 microns in one direction for a properly bent crystal.

For our experiments we have designed a spectrometer to look at the Kr XXXV 1s to 2p resonance lines. By using only the portion of the crystal diffracting rays at an angle near 13° angle of inclination and then rotating the source, crystal, and detector around the line normal to the center of the crystal, we can achieve the vertical Johann geometry in a small linear package that can fit in a diagnostic tube. The layout is shown in Figure 3, which shows the schematic design for a vertical Johann instrument designed to be used in a 6 inch diagnostic tube for laser implosion experiments. Bragg angles less than 10° are required in order to meet the geometric constraints of the diagnostic tube. For our design, the crystal is bent to a radius of 1644 mm, with a 13.4° angle of inclination, and a Bragg angle of 8.201° using a mica crystal in third order (006 plane).

3. Crystal Requirements

The resolution achievable with this spectrometer depends primarily on the diffraction properties of the crystal and the accuracy of its surface alignment to a cylinder. Resolving powers of 2000 to 10000 are required, with higher values allowing lower ion temperatures to be measured and increasing the potential accuracy of the measurement. A variety of bonding techniques can be used to bend the crystal into a cylindrical form with optical precision. We are using fused silica substrates ground to an accuracy of 1/4 wavelength, with a 1642 mm radius of curvature. The crystals are held between two glass forms with convex and concave curvature and glued with a thin layer of UV curing cement to the concave cylindrical substrate.

Crystal planes that could be used for the 13 keV X-rays we are measuring, with Bragg angles less than 10°, can have resolving powers $E/\Delta E \sim 10{,}000$ for flat crystals comprised of low atomic number materials like mica 006, quartz 10-10 and 10-11, and silicon 111. This isotopic approach of Taupin, which depends only on Poisson's ratio and neglects anisotropy of the crystal when bent, agrees well with the Bragg reflections measured by Uschmann et al. [9, 10]. Unfortunately the diffraction width of these planes is significantly affected by the 1.6 m radius of curvature being used. The effects of curvature are primarily due to penetration of X-rays close to the Bragg angle at the surface of the crystal far enough into the crystal that the vector normal to the curved lattice planes of the crystal can rotate enough to allow Bragg diffraction. The result of this is a decaying tail of diffraction at lower angles of incidence, dropping slowly from the peak of the pattern. Distortion of the lattice as the X-ray propagates into the crystal is a smaller effect for our conditions. Diffraction patterns for the curved

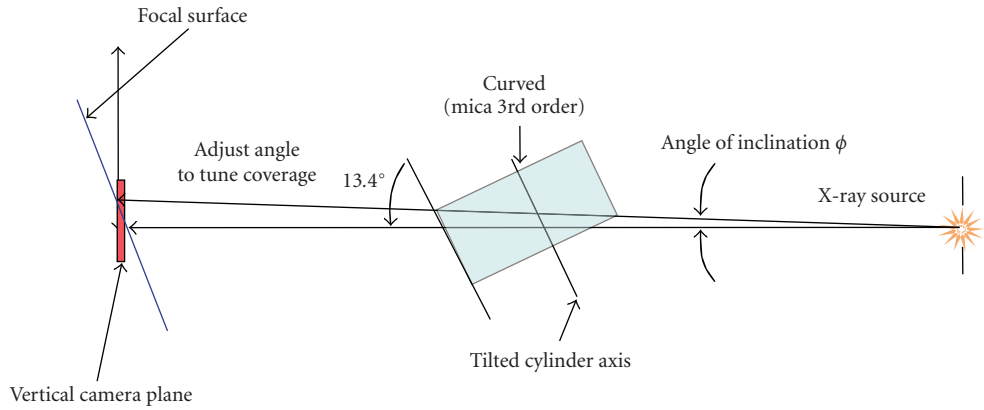

Figure 3: Side view of vertical Johann mica spectrometer. X-rays of increasing energy are diffracted at increasing angle of inclination ϕ.

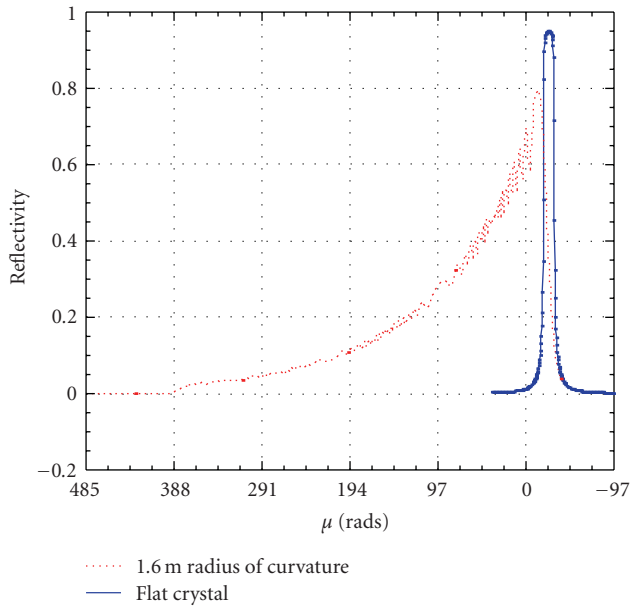

Figure 4: Comparison of reflectivity vs angle for a 100 micron thick crystal having a 1.6 m radius of curvature.

crystals can be calculated from the Takagi-Taupin equations which account for both these effects [11, 12].

Figure 4 shows how diffraction pattern calculated with the code from the Taupin equations [9] changes for a flat and 100 micron thick mica 006 (third order reflection) crystal at 13 keV. The tail increases the integrated reflection coefficient for the crystal, but increases the width of the curve. It is theoretically possible to reduce this curvature-induced broadening by using a crystal that is thinner than the propagation depth of the X-rays, as shown in Figure 5. The tail on the diffraction curve is reduced as the crystal thickness is reduced. Five micron thick crystals have curves very similar to the flat crystal. With a 5 micron thick perfect mica crystal of 1.644 m radius using 6 mm of arc, ray tracing calculations show that the resolving power possible is about 7800.

Higher atomic number crystals with higher absorption at 13 keV do not have large changes to the flat crystal diffraction widths due to crystal curvature. This is because their absorption prevents X-rays from reaching deep enough into the crystal to form large diffraction tails. Germanium 111 is an example of this type of crystal, which can have a resolving power of 3160 at 13 keV. This crystal has less resolution than a perfect thin mica crystal, but has the advantages of higher integrated reflection, consistently more perfect grown crystals, and surfaces that can be polished optically flat. Ge 111 crystals were mounted and tested in the same way as mica, so they could be used for initial testing and as a backup for the mica crystal.

4. Monochromator Crystal Selection

Mica (006) and Si (111) have nearly the same reflectivity as flat, perfect crystals. But mica has been selected as the best candidate for the VJS because it can be cleaved to the 5 micron thickness and bent to the desired curvature. This is not practical for Si (111) and quartz. Si (111) crystals are used to evaluate the dual goniometer system performance. Dicing Si or quartz crystals was considered but rejected as being too costly.

Manufacturing crystals thinner than 100 μm that have dimensions on the order of 1 cm in the crystal axis orientation needed is very difficult for most available crystals except for mica. Mica has very weak binding between planes, and is readily cleaved to thickness of 1 micron or even thinner. Mica tends to be an imperfect crystal, however, with distorted surfaces and mosaic broadening occurring in most crystals. But studies done by Uschmann et al. [10] have shown that some crystals can be flat and perfect on an atomic scale over areas of up to 20 cm^2.

Natural mica crystals vary considerably in their diffraction quality. Mica crystals were purchased from a variety of sources, and a synthetic crystal was also tested. The crystals were tested flat in the first stage. The procedure for evaluating these crystals began with optical testing, selection of those having the best quality, and measurement of the X-ray reflectivity curve for the selected crystals. We have examined several hundred crystals visually and interferometrically using Fizeau and Haidinger fringes with optical flats in

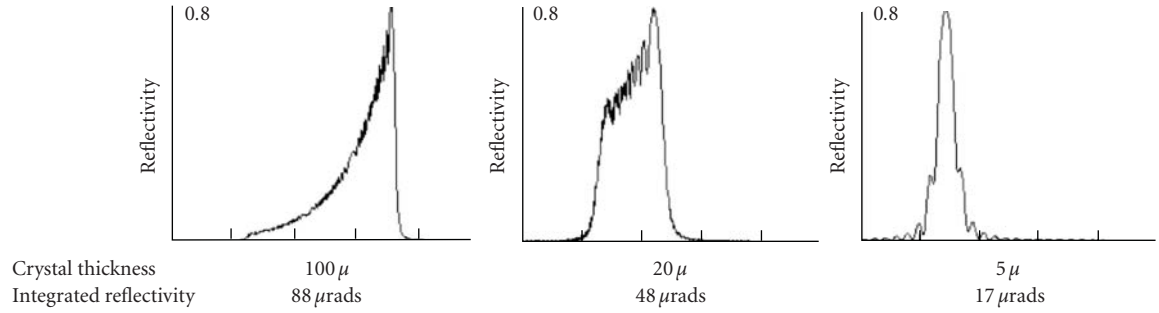

Figure 5: Broadening due to curved crystal curvature with crystals of thickness varying from 5 microns to 100 microns at 1.6 m radius of curvature, calculated with Takagi-Taupin equation.

Table 1: Crystals Used, the Miller Indices, and the Bragg Angle at 11442.3 eV.

Crystal	Silicon 111	Mica 006	Germanium 111
Bragg angle, degrees	9.950	9.347	9.547

monochromatic light to find sufficiently perfect mica crystals for our needs. The crystals were examined as 200 to 300 μm thick slabs. Relatively few were acceptable for the X-ray testing, and this became a learning process for the best sources of mica crystals.

The crystals that passed the optical evaluation were then tested using X-rays as thick flats. There were many more rejections in this phase. The best flat candidates were mounted at their original thickness with UV curing glue on fused silica curved substrates, and then cleaved in water to thicknesses of 3–10 microns while attached to the substrate. We were unable to first cleave the crystals and then mount them, as they wrinkled uncontrollably when they contacted the UV cement. The reflectivity curve for these curved crystals was then measured.

5. Characterizing the X-ray Diffraction

Measurements of X-ray reflectivity for mica and Ge crystals were done using the Au $L_{\beta 1}$ spectral line at 11442.3 eV. Measurements on the Si crystal were done using the Au $L_{\beta 1}$ spectral line and the Au $L_{\alpha 1}$ spectral line at 9713 eV. The Bragg angle at 11443 eV for these crystals is given in Table 1. The calculated dynamic diffraction properties for a mica crystal at the X-ray energy used for testing are given in Table 2 [13]. All measurements are compared to these quantities. The curve quality needed for high resolution spectroscopy is the width of the reflectivity curve. The Full Width at Half Maximum (FWHM) is an adequate measure of this quality. This width represents an energy spread of the reflected radiation for a given Bragg angle.

The energy spread can be adequately estimated using the differential form of Bragg's Law:

$$\frac{\Delta E}{E} = \Delta\Theta \cdot \cot\Theta_B, \tag{7}$$

where E is the band center of the spectral line, ΔE is the energy spread produced by the crystal reflectivity width, $\Delta\Theta$ is the FWHM for the reflectivity curve, Θ_B is the Bragg angle.

For the conditions in Table 2, and assuming an equal polarization mixture so that $\Delta\Theta = 12.373\,\mu$rad, $\Delta E = 0.860$ eV at 11442.3 eV.

5.1. The Dual Goniometer Instrumentation and Technique. The X-ray source used for measuring the mica crystal diffraction performance is a diode type with a water cooled anode. It operates in the medium X-ray energy range, 600 eV to 16 keV and is illustrated in Figure 6. The source chamber and the sample chamber have independent vacuum controls and are separated by a tubing section that includes a remotely operated valve. The source maximum operating voltage and power are 20 kV and 4000 W. The operating anode was gold for the mica measurements, and the Au $L_{\beta 1}$ spectral line was selected.

To collimate the X-ray beam, the sample chamber has a pair of slit mechanisms separated by 200 mm. Each slit mechanism has a vertical and a horizontal slit pair, with the horizontal slit pair operated manually, and the vertical slit pair operated using a computerized motion controller. Both slit opening and slit offset can be operated remotely. The slit mechanism locations are shown in Figure 6.

The dual goniometer system has four separate rotation stages, two for the monochromator crystal and two for the sample crystal stage. The sample stage has three orthogonal translation degrees. Each of these stages has an independent motion control. They are computer controlled and can be programmed for automatic scanning. Rotation precision is 1 mdeg, and the translation precision is 1 μm. The absolute rotation accuracy is determined by the actual alignment of the elements of each rotation stage. A crystal can be moved in the horizontal and vertical directions using the translation stages to produce reflectivity curves so that uniformity of the crystal across the entire surface can be verified.

The crystal arrangement for these experiments is shown in Figure 7. A vacuum compatible, solid state, energy dispersive detector is mounted on the 4th rotation stage. It provides photon counting sensitivity, and the energy

Table 2: Calculated Mica 006 Crystal Properties at 11442.3 eV.

Polarization	R_p	FWHM, mdeg	FWHM, μrad	Integrated Reflection Curve, mdeg	Integrated Reflection Curve, μrad
mica 006					
σ	0.932	0.728	12.708	0.868	15.142
π	0.928	0.690	12.037	0.820	14.308
mixed	0.930	0.704	12.37	0.844	14.716

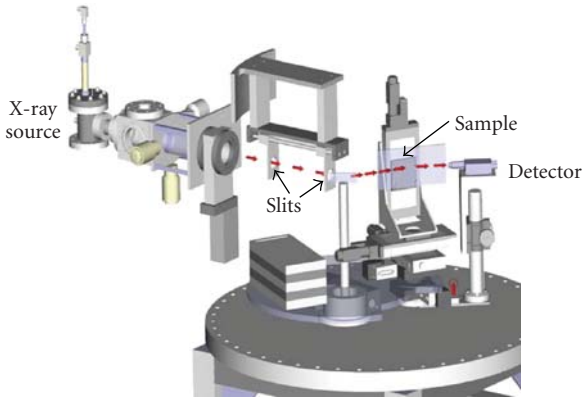

- Beam arrangement
- Dual goniometer
- Sample translation in 3 directions

Figure 6: The NSTec X-ray Source and Dual Goniometer for Crystal Measurements, showing the X-ray Beam Path.

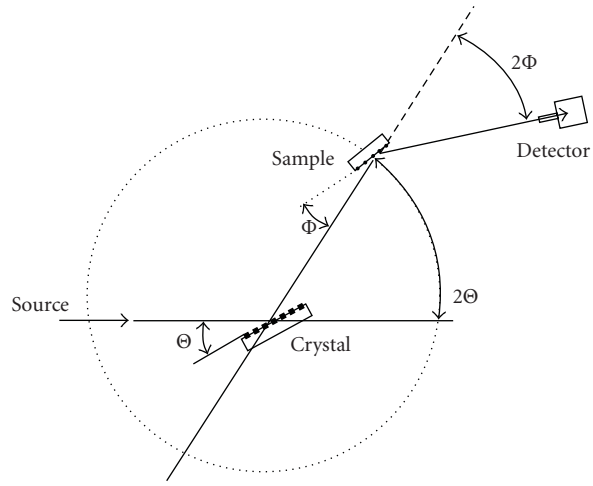

Figure 7: The NSTec X-ray Source and Goniometer for Crystal Measurements, showing Angles.

information helps to verify that the reflection being observed is in the correct spectral range (i.e., the correct spectral line from the monochromator has been selected, etc.). The X-ray source is 600 mm from the first slit. The slits are separated by 200 mm. The slit opening for all measurements given in the following sections was 200 μm. Measurements made using smaller slits did not change the measured reflectivity curve.

5.2. Alignment Procedure. For reliable reflectivity curves, the monochromator crystal and the sample crystal must be properly aligned to the X-ray axis (the rotation axis of the crystal is perpendicular to the X-ray beam axis). They must also be parallel to each other. The system is set up so that a laser beam that can be injected into the X-ray beam path and follow it exactly. The initial system alignment assures that this beam path goes directly over the rotation axis of the monochromator crystal and the sample crystal.

The crystal alignment is done using the laser beam. The monochromator crystal is removed from the system for the sample alignment, and the alignment technique utilizes retro-reflection of the laser beam. The mounting devices for the crystals provide micrometer positioners for precise vertical alignment. The sample crystal is adjusted vertically after rotating the stage so that the crystal faces the slits. Using this micro-positioner, the sample crystal is rotated until the laser beam is reflected exactly back on the slits. The rotation origin is also obtained by rotating the sample until the reflected laser beam falls unto the slit. The monochromator crystal is then put in place and the same retro-reflection procedure follows, ensuring that the two crystals are parallel.

The system is not designed or operated to measure crystal angles from the goniometer angles exactly. The absolute angle is determined from the spectral analysis and the literature values of the Bragg angle. The relative angles are determined accurately by the goniometers.

5.3. Measuring the Crystal Reflectivity Curve and Instrumental Contributions—The Integrated Reflection Curve (IRC) and FWHM R_P.* Several factors, both instrumental and spectral, influence the measurement of the crystal reflection curve. These factors include the horizontal and vertical beam divergence, spectral energy spread, alignment of the monochromator and sample crystals, and the monochromator crystal reflectivity FWHM. The system performance was evaluated using a set of three diffraction grade silicon crystals. One crystal would be used as a monochromator and the other as a sample crystal. The reflectivity curve of the sample was then measured. The three crystals were interchanged to test all combinations. The reflectivity curves for all combinations agreed within experimental uncertainty, indicating that all three crystals had similar diffraction quality. Typical reflectivity curves for two energies are shown in Figures 8 and 9.

Table 3: Calculated and measured silicon 111 crystal properties at 11442.3 eV and 9713.3 eV.

	Peak reflectivity, R_p	FWHM, mdeg	FWHM, μrad	Integrated reflection coefficient, mdeg	Integrated reflection coefficient, μrad
11443.2 eV					
Mixed polarization	0.966	1.280	22.344	1.571	27.42
Measured double crystal	0.41	4.1	71.6	2.13	37.2
Single crystal (calculated from the double crystal)		2.85	49.7		
9713.3 eV					
Mixed polarization	0.953	1.504	25.250	1.820	31.76
Measured double crystal	0.35	5.2	90.8	2.31	40.3
Single crystal (calculated from the double crystal)		3.61	63.0		

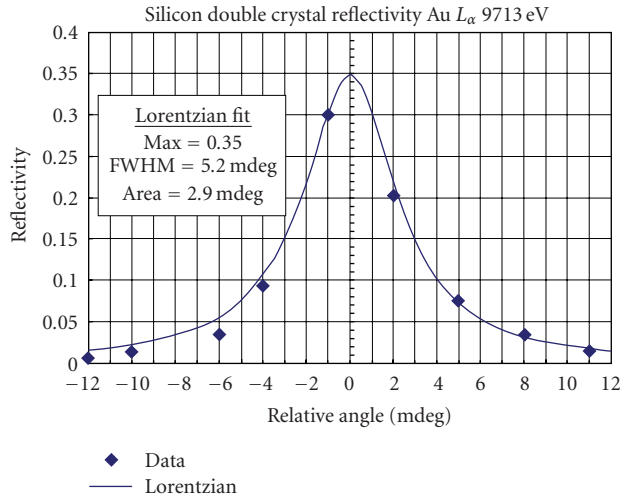

Figure 8: Reflectivity curve for Si-Si double crystal measurement at 9713 eV.

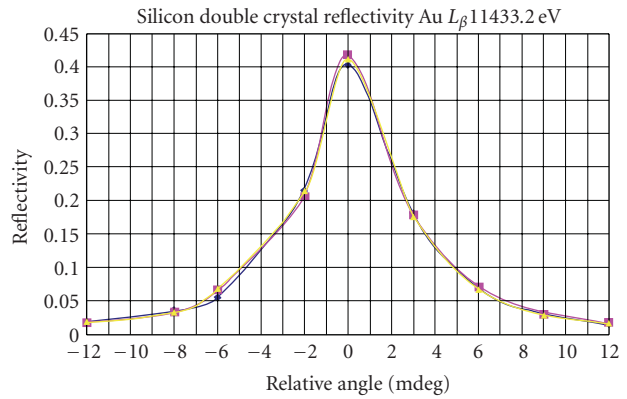

Figure 9: Silicon double crystal reflectivity curve from three measurements (shown with three different, closely overlapping, colored curves) taken using the Au $L_{\beta 1}$ spectral line, 11443.2 eV.

These figures show the typical results for all crystal combinations and quite reproducible. Measurements have been done by different instrument operators and separated by extended periods so that the full alignment procedure could be done by the different operators. The motion control system limits the step size to 3 mdeg, thus reducing the accuracy of measuring the integrated reflectivity. Figure 8 shows a Lorentzian fit to the data.

The calculated properties for Si 111 are given in Table 3. The measured values are included in the table so that they can be compared easily. A significant feature for this instrument evaluation is the measured FWHM compared to the theoretical. Since this is a two-crystal measurement, the results are increased roughly by $\sqrt{2}$ [9]. This value for FWHM is shown in the row called *Single Crystal*, and is a factor of about 2.2 larger than the value expected theoretically. The integrated reflectivity is larger than the theoretical value. The uncertainty in the FWHM is on the order of 20% and that of the integrated reflectivity is 30% based on the reproducibility of the measurements. Since the two crystals are the same, they have the same diffracting plane separation and the same Bragg angle, so the measurements should be unaffected by the Au spectral band width of 8 eV. The 4 mdeg (0.004°) reflectivity curve width calculated from (6) corresponds to 5 eV.

These results imply that there is an instrument contribution to the measurement of the FWHM. It was not deemed practical or necessary to determine the origin of this instrument contribution. It has been discussed in the literature [14, 15] that the integrated reflectivity is not sensitive to instrument parameters. The purpose of the reflectivity measurements is to select the best mica crystals. Since the integrated reflectivity is less influenced by the instrument properties than the peak reflectivity (R_P) and the FWHM, it was chosen for this comparison.

6. Measured Crystal Diffraction Properties for Mica and Germanium

As discussed in the previous section, the goniometer system produced an instrumental broadening of the Si reflectivity curve. Since the integrated reflection curve is not influenced by these instrument parameters, it was chosen to be the measure used to evaluate the mica crystal quality. All measurements were done using an Si monochromator, the same crystal that was used for the measurements shown in

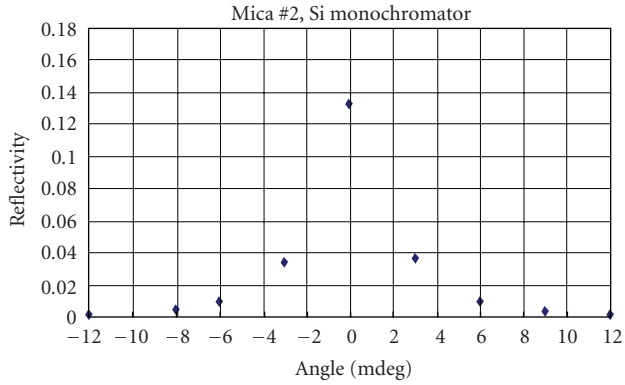

	Measured	Calculated
R_p	0.17	0.93
FWHM (mdeg)	4	0.7
Integrated reflection curve (mdeg)	0.84	0.84

Figure 10: Reflectivity curve for the best mica flat crystals, 300 μm thick.

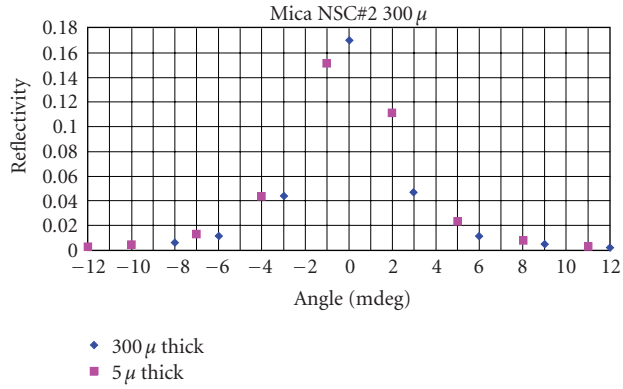

Figure 11: Comparing the crystal shown in Figure 10 when it was 300 μm thick to the same crystal after it was cleaved to 5 μm thick.

Figures 8 and 9. A round robin comparison of the three Si crystals all gave reflectivity curves similar to Figure 9. The X-ray illuminated area was near 1.5 mm high by 0.30 mm wide. For the better crystals, several points were measured in the 1 cm^2 area that would be illuminated in the VJS.

The initial measurements were done on two square centimeter mica crystals about 300 μm thick attached to an optically flat glass substrate. The first set of mica crystals fell into two categories. The majority had an integrated reflection curve (IRC) that was significantly larger than the calculated value given in Table 2. There were a few that measured an IRC that was within experimental uncertainty of the theoretical value but the FWHM was near 10 mdeg and so was larger than the instrumental contribution observed in the Si double crystal measurements. Then we came upon the first crystal that matched the theoretical IRC and the FWHM was at the instrumental limit that was obtained with the Si double crystal measurement. This is shown in Figure 10.

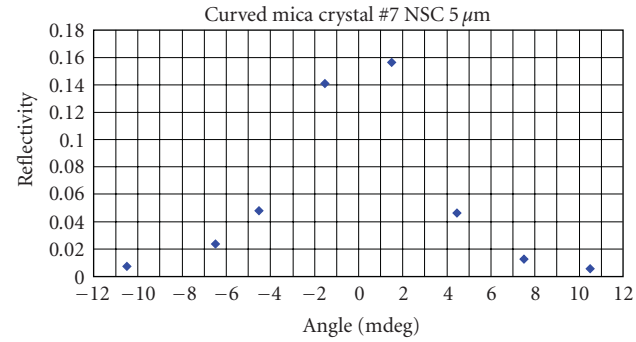

	Measured	Calculated
R_p	0.16	0.93
FWHM (mdeg)	6	0.7
Integrated reflection curve (mdeg)	1.18	0.84

Figure 12: Typical best reflectivity curve for good quality mica attached properly to a curved glass substrate.

It appears that mica IRC values can match the theoretical value with diffraction widths at the apparent instrumental limit. Therefore, the criterion for our decision that a mica crystal might have sufficient diffraction quality for the high resolution spectrometer was that the FWHM be near 4 mdeg (0.004°).

The flat crystal whose measurement is shown in Figure 10 was then cleaved to a thickness of 5 μm while still glued to the flat glass substrate, and the reflectivity curve was measured again. The result of this measurement is shown in Figure 11 along with the data from the thick crystal. Within the measurement uncertainty, these diffraction curves are identical. The cleaving did not disturb the crystal diffraction quality. At 9.4° the path through the mica is much larger than the mica extinction length (2.6 μm).

The next step was to take crystals that had come from sources that provided the satisfactory flat crystals and test them for X-ray diffraction quality. The 300 μm thick mica flat was glued to a glass substrate that was curved in one direction to a 1.6 m curvature radius and flat in the other direction. The mica was then cleaved to a thickness of 5 μm. This procedure took some practice to develop so that the mica adhered accurately to the glass surface.

The curved crystal's reflectivity was then measured on the X-ray goniometer system. The reflectivity measurement was done varying the angle of incidence in the direction with no surface curvature of the cylindrical mica crystal. The majority of crystals did not have satisfactory diffraction quality. The best crystals had a typical reflectivity curve as that shown in Figure 12. The 6 mdeg (0.006°) width apparently represents the instrumental contribution for measuring the curved mica crystal, although it is not entirely clear if this instrumental limit could not be closer to the flat crystal measured value of 0.004°. This 6 mdeg (0.006°) reflectivity curve width became the criterion for selecting spectrometer crystals.

Table 4: Calculated germanium 111 crystal properties at 11442.3 eV.

	R_p	FWHM, mdeg	FWHM, μrad	Integrated reflection curve, mdeg	Integrated reflection curve, μrad
Mixed polarization	0.724	2.743	47.87	2.297	40.06
Measured	0.27	7.5	131	2.34	40.8

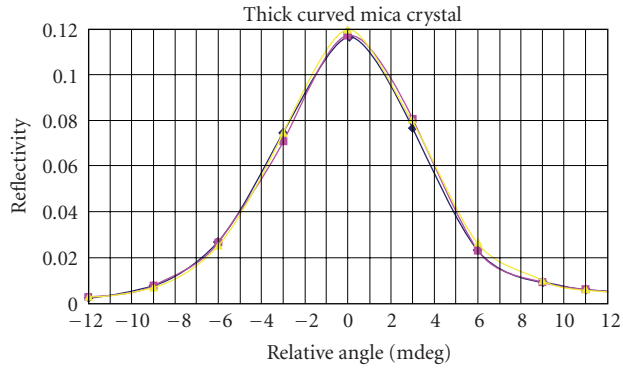

Figure 13: Typical best reflectivity curves for thick (300 μm) mica crystal from three measurements (shown with three different, closely overlapping, colored curves).

For reference, several curved 300 μm thick crystals were measured. Typical reflectivity curves for the best crystals are shown in Figure 13. The FWHM of 0.008° is larger than the 0.006° width obtained from the best thin curved crystal measurements. This is consistent with the calculated broadening of a thick mica crystal of 4 mdeg shown in Figure 5.

Germanium was chosen as a backup for the mica crystal for use in the initial testing of the spectrometer. Its reflectivity properties at 11442.3 eV are given in Table 4. Reflectivity measurements of a 500 μm thick germanium crystal bent to a 1.6 m radius of curvature are given in the last row of the table. The measured reflectivity curve width for the curved germanium crystal is slightly less than that of the thick mica crystal curved to the same radius, and this is consistent with theoretical calculations.

7. Further Experiments Using an X-ray Source

NSTec Livermore Operations also has a high energy, open beam X-ray source. It uses a 160 kV source to produce fluorescence from various materials. X-ray beams from 8 keV to 100 keV can be generated. The spectrometer can be aligned and tested using this facility. The Rb K_α and Bi L_α spectral lines will be used since they are near the Kr XXXV He like lines.

The spectrometer will be mounted and aligned to the X-ray beam. Image plates and film will be used to turn the alignment and focus the spectrometer. An upgrade to the dual goniometer system is planned for 2010. This includes a high resolution rotator stage and upgraded monochromator crystals.

8. Conclusion

The goniometer system of the NSTec Livermore Operations, although limited in resolution, is a good tool for finding satisfactory crystals for hard X-ray spectrometers like the Vertical Johann Spectrometer described in this work. Because of the instrument's construction it is not possible to measure the true crystal resolving power. It is able to differentiate crystal diffraction performance sufficiently to show when the reflectivity curve width is $\Delta\Theta \leq 2.8$ mdeg (see Table 3) so that $\Delta E \leq 5.5$ eV at 13.3 keV (6) and is usable for the Doppler width measurements. The process of selecting suitable mica crystals, curving them accurately to a precision glass substrate, and thinning them to a thickness less than 10 microns is difficult and time consuming. A tool such as the NSTec goniometer system has proved to be invaluable for evaluating the diffraction quality of the crystals needed for this work.

Acknowledgments

Significant contributions to the success of this work were made by the following colleagues. Jim Emig developed techniques to glue the mica crystal to the flat and curved glass substrates and techniques to cleave the mica. Fletcher Goldin designed a number of mechanical improvements to the alignment procedure to allow us to get the instrument contribution down to the level given in the paper. Ken Jacoby produced much of the reflectivity curve data. This manuscript has been authored by National Security Technologies, LLC, under Contract no. DE-AC52-06NA25946 with the U.S. Department of Energy. The United States Government retains and the publisher, by accepting the article for publication, acknowledges that the United States Government retains a non-exclusive, paid-up, irrevocable, world-wide license to publish or reproduce the published form of this manuscript, or allow others to do so, for United States Government purposes. DOE/NV/25946–839. This work was done under the auspices of the U.S. Department of Energy by Lawrence Livermore National Laboratory under Contract DE-AC52-07NA27344. LLNL-JRNL-420787.

References

[1] I. Golovkin, R. Mancini, S. Louis et al., "Spectroscopic determination of dynamic plasma gradients in implosion cores," *Physical Review Letters*, vol. 88, no. 4, Article ID 045002, pp. 450021–450024, 2002.

[2] J. A. Koch, N. Izumi, L. A. Welser et al., "Core temperature and density profile measurements in inertial confinement fusion implosions," *High Energy Density Physics*, vol. 4, no. 1-2, pp. 1–17, 2008.

[3] B. Yaakobi, R. Epstein, C. F. Hooper Jr., D. A. Haynes Jr., and Q. Su, "Diagnosis of high-temperature implosions using low- and high-opacity Krypton lines," *Journal of X-Ray Science and Technology*, vol. 6, no. 2, pp. 172–187, 1996.

[4] B. Yaakobi, F. J. Marshall, and R. Epstein, "High temperature of laser-compressed shells measured with Kr34+ and Kr35+ x-ray lines," *Physical Review E*, vol. 54, no. 5, pp. 5848–5850, 1996.

[5] M. Bitter, S. Von Goeler, R. Horton et al., "Doppler-broadening measurements of x-ray lines for determination of the ion temperature in tokamak plasmas," *Physical Review Letters*, vol. 42, no. 5, pp. 304–307, 1979.

[6] O. Renner, T. Missalla, P. Sondhauss et al., "High-luminosity, high-resolution, x-ray spectroscopy of laser-produced plasma by vertical-geometry Johann spectrometer," *Review of Scientific Instruments*, vol. 68, no. 6, pp. 2393–2403, 1997.

[7] O. Renner, S. G. Podorov, O. Wehrhan, and E. Förster, "Vertical dispersion Johann x-ray spectrometer with asymmetrically cut crystal," *Review of Scientific Instruments*, vol. 75, no. 11, pp. 4569–4577, 2004.

[8] M. Kopecký, "A modified scheme of Johann spectrograph," *Review of Scientific Instruments*, vol. 66, no. 10, pp. 4921–4924, 1995.

[9] I. Uschmann, E. Forster, K. Bell, and G. Holzer, "X-ray reflection properties of elastically bent perfect crystals in bragg geometry," *Journal of Applied Crystallography*, vol. 26, pp. 405–412, 1993.

[10] I. Uschmann, A. C. Malgrange, and E. Forster, "Measurement of a bent crystal rocking curve with oscillations," *Journal of Applied Crystallography*, vol. 30, pp. 1150–1151, 1997.

[11] D. Taupin, "Théorie dynamique de la diffraction des rayons X par les cristaux déformés," *Bulletin de la Société Française de Minéralogie et de Cristallographie*, vol. 84, pp. 469–511, 1964.

[12] S. G. Podorov and E. Förster, "Theory of X-ray diffraction on asymmetrically cut and bent crystals," *Physica Status Solidi A*, vol. 220, no. 2, pp. 829–836, 2000.

[13] S. G. Podorov, "X-Ray for Windows," www.podorov.de/programs.htm.

[14] S. Tolansy, *Multiple Beam Interferometry of Surfaces and Films*, Dover, New York, NY, USA, 1970.

[15] S. Stepanov, "X0h on the Web," http://sergey.gmca.aps.anl.gov/x0h.html.

Hindawi Publishing Corporation
X-Ray Optics and Instrumentation
Volume 2010, Article ID 215375, 18 pages
doi:10.1155/2010/215375

Review Article

Laue Gamma-Ray Lenses for Space Astrophysics: Status and Prospects

Filippo Frontera[1] and Peter von Ballmoos[2]

[1] *Physics Department, University of Ferrara, Via Saragat 1, 44100 Ferrara, Italy*
[2] *Centre d'Etude Spatiale des Rayonnements, 9, Avenue du Colonel Roche, 31028 Toulouse, France*

Correspondence should be addressed to Filippo Frontera, frontera@fe.infn.it

Received 21 April 2010; Accepted 4 November 2010

Academic Editor: Stephen L. O'Dell

We review feasibility studies, technological developments, and the astrophysical prospects for Laue lenses devoted to hard X-/gamma-ray astronomy observations.

1. Introduction

Hard X-/soft gamma-ray astronomy is a crucial window for the study of the most energetic and violent events in the Universe. With the ESA INTEGRAL observatory [1] and the NASA *Swift* satellite [2], unprecedented sky surveys in the band beyond 20 keV are being performed [3, 4]. As a consequence, hundreds of celestial sources have already been discovered, new classes of Galactic sources are being identified, and an overview of the extragalactic sky is available, while evidence of extended matter-antimatter annihilation emission from our Galactic center [5] and of Galactic nucleosynthesis processes have been also reported [5, 6]. However, in order to take full advantage of the extraordinary potential of soft gamma-ray astronomy, a new generation of telescopes is needed. The current instrumentation has relied on the use of direct-viewing detectors with mechanical collimators (e.g., BeppoSAX/PDS, [7]) and, in some cases, with modulating aperture systems, such as coded masks (e.g., INTEGRAL/IBIS, [8]). These telescopes are penalized by their modest sensitivities, that improve at best as the square root of the detector surface. The only solution to the limitations of the current generation of gamma-ray instruments is the use of focusing optics. To study either the continuum emission or the nuclear line emission from celestial sources, Laue lenses, based on diffraction from crystals in a transmission configuration, are particularly suited to focus photons in the hard X-/soft gamma-ray (<1 MeV) domain. As we will show, they show imaging capabilities for on-axis sources.

With these lenses, we expect a big leap in both flux sensitivity and angular resolution. As far as the sensitivity is concerned, the expected increase is by a factor of at least 10–100 with respect to the best nonfocusing instruments of the current generation, with or without coded masks. Concerning the angular resolution, the increase is expected to be more than a factor 10 (from ∼15 arcmin of the mask telescopes like INTEGRAL IBIS to less than 1 arcmin).

The astrophysical issues that are expected to be solved with the advent of these telescopes are many and of fundamental importance. A thorough discussion of the science case has been carried out in the context of the mission proposal *Gamma Ray Imager* (GRI), submitted to ESA in response to the first AO of the 'Cosmic Vision 2015–2025′ plan [9] (but see also [10–12]). We summarize here some of these issues.

(i) *Deep study of high-energy emission physics in the presence of super-strong magnetic fields (magnetars)*

The XMM and INTEGRAL observed spectra of Soft Gamma Ray Repeaters [13], and Anomalous X-ray pulsars [14] leave unsolved the question of the physical origin of the high-energy component (>100 keV). A better sensitivity at $E > 100$ keV is needed.

(ii) *Deep study of high-energy emission physics in compact galactic objects and AGNs*

A clue to the emission region and mechanism, along with the properties of the hidden black hole, can be obtained with the measurement of the high-energy cutoff and its relation with the power-law energy spectrum of the compact objects. The current observational status is far from clear (see, e.g., [15, 16]). Much more sensitive observations are needed, for both AGNs and compact Galactic sources. In the case of blazars, the gamma-ray observations are crucial for the determination of their emission properties given that their energy emission peaks at hundreds of keV [17].

(iii) *establishing the precise role of nonthermal mechanisms in extended objects like galaxy clusters*

The existence of hard tails from Galaxy Clusters (GCs) is still a matter of discussion [18], and, should they exist, their origin is also an open issue. Are they the result of a diffuse emission or are they due to AGNs in the GC? In the former case, what is the emission mechanism? What is their contribution to CXB? To answer these questions will require much more sensitive observations, like those achievable with broad band Laue lenses.

(iv) *Origin of cosmic hard X/soft gamma-ray diffuse background*

Currently, a combination of unobscured, Compton thin, and Compton thick radio-quiet AGN populations with different photon index distributions and fixed high-energy spectral cutoff (E_c) are assumed in synthesis models of the Cosmic X-ray background (CXB) [19]. Is it reasonable to assume a fixed E_c for these sources? A photon-energy-dependent contribution from radio-loud AGN to CXB, like blazars, is generally assumed. But their real contribution is still a matter of discussion. Deep spectral measurements of a significant sample of AGNs beyond 100 keV is needed to solve these issues.

(v) *Positron Astrophysics*

Positron production occurs in a variety of cosmic explosion and acceleration sites, and the observation of the characteristic 511 keV annihilation line provides a powerful tool to probe plasma composition, temperature, density, and ionization degree. The positron annihilation signature is readily observed from the galactic bulge region, yet the origin of the positrons remains mysterious. Compact objects—both galactic and extragalactic—are believed to release significant numbers of positrons leading to 511 keV gamma-ray line emission in the inevitable process of annihilation. A recent SPI/INTEGRAL all-sky map [5] of galactic e^- e^+ annihilation radiation shows an asymmetric distribution of 511 keV emission that has been interpreted as a signature of low-mass X-ray binaries with strong emission at photon energies >20 keV (hard LMXBs). A claim for an annihilation line from a compact source (Nova Muscae) was reported in the 90 s [20] but was never confirmed. Much more sensitive observations are needed to study the annihilation line origin, sources, and their nature.

(vi) *Physics of supernova explosions*

Type Ia supernovae (SNe Ia) are major contributors to the production of heavy elements and hence a critical component for the understanding of life cycles of matter in the Universe and the chemical evolution of galaxies. Because Laue lens telescopes allow the direct observation of radioactive isotopes that power the observable light curves and spectra, gamma-ray observations of SNe Ia that can be performed with this type of instrument are in a position to allow a breakthrough on the detailed physical understanding of SNe Ia. This is important for its own sake, but it is also necessary to constrain systematic errors when using high-z SNe Ia to determine cosmological parameters.

High-resolution gamma-ray spectroscopy provides a key route to answering these questions by studying the conditions in which the thermonuclear explosion starts and propagates. A sensitivity of 10^{-6} photons $cm^{-2}s^{-1}$ to broadened gamma-ray lines allows observations of supernovae out to distances of 50–100 Mpc. Within this distance, it is expected that there will always be a type Ia SN in the phase of gamma-ray line emission, starting shortly after explosion, and lasting several months.

In this paper, we review the physical principles of Laue lenses, their geometry, their optimization criteria, their optical properties, the current development status and the prospects for future missions for gamma-ray astronomy.

2. Laue Lens Concept

Diffraction lenses use the interference between the periodic nature of the electromagnetic radiation and a periodic structure such as the matter in a crystal. For a classical textbook on X-ray diffraction see, for example, [21]. In a Laue lens, the photons pass through the full crystal, using its entire volume for interacting coherently. In order to be diffracted, an incoming gamma-ray must satisfy the Bragg-condition, relating the spacing of lattice planes d_{hkl} with the energy of incident photons E and with the angle of incidence θ_B with respect to the chosen set of planes (hkl) (*The indices h, k, l, known as Miller indices, are defined as the reciprocals of the fractional intercepts which the lattice plane makes with the crystallographic axes. For example, if the Miller indices of a plane are (hkl), written in parentheses, then the plane makes fractional intercepts of* 1/*h*, 1/*k*, 1/*l with the axes, and, if the axial lengths of the unit cell are a, b, c, the plane makes actual intercepts of a/h, b/k, c/l. If a plane is parallel to a given axis, its fractional intercept on that axis is taken as infinity and the corresponding Miller index is zero. If the Miller indices [hkl] are shown in square brackets, they give the direction of the plane with the same indices.*)

$$2d_{hkl}\sin\theta_B = n\frac{hc}{E}, \tag{1}$$

where d_{hkl} (in Å) is the spacing of the lattice planes (hkl), n is the diffraction order, $hc = 12.4$ keV. Å and E is the energy (in keV) of the gamma-ray photon. An elementary illustration of the Bragg condition, in two different configurations (reflection and transmission), is given in Figure 1, where

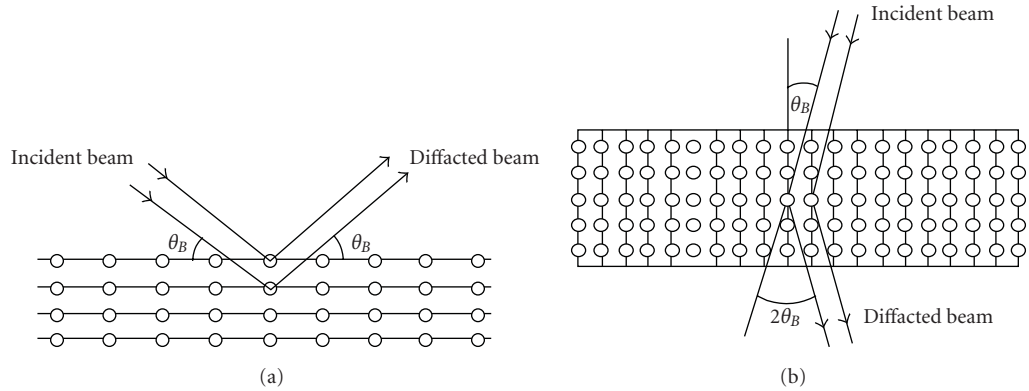

Figure 1: The Bragg condition for constructive interference of a gamma-ray photon beam with the atoms of a given crystalline plane. (a) Bragg diffraction in reflection configuration (Bragg geometry). (b) Bragg diffraction in transmission configuration (Laue geometry).

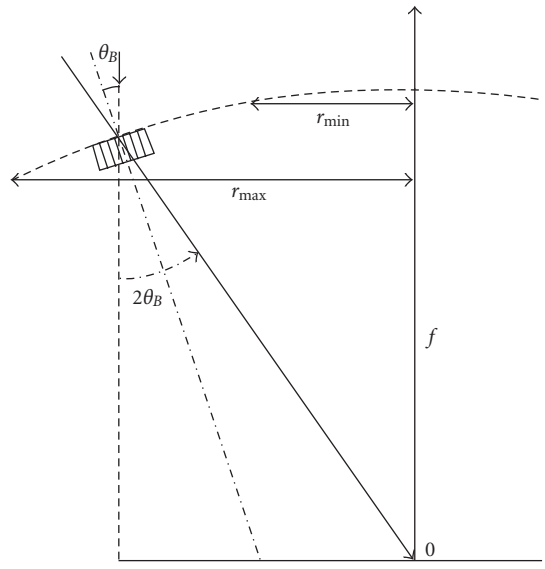

Figure 2: Geometry of a Laue lens (see text).

it can be seen that the incident waves are reflected by the parallel planes of the atoms in the crystal.

A Laue lens is made of a large number of crystals, in transmission configuration (Laue geometry), that are disposed such that they will concentrate the incident radiation onto a common focal spot. A convenient way to visualize the geometry of a crystal lens is to consider it as a spherical cup covered with crystal tiles having their diffracting planes perpendicular to the sphere (see Figure 2). The focal spot is on the symmetry axis at a distance $f = R/2$ from the cup, with R being the radius of the sphere of which the spherical cup is a part; f is called the *focal length*.

From the Bragg equation, for the first diffraction order ($n = 1$), it can be seen that the photons incident on a given crystal at distance r ($r_{\min} \le r \le r_{\max}$) from the lens axis can be reflected toward the lens focus if their energy E is given by

$$E = \frac{hc}{2d_{hkl}} \sin\left[\frac{1}{2}\arctan\left(\frac{f}{r}\right)\right] \approx \frac{hc\,f}{d_{hkl}\,r}, \tag{2}$$

where the approximated expression is valid for gamma-ray lenses, given the small diffration angles involved.

Conversely, the lens radius r (see Figure 2) at which the photon energy E is reflected in the focus is given by

$$r = f\,\tan[2\theta_B] \approx \frac{hc\,f}{d_{hkl}\,E}. \tag{3}$$

Rotation around the lens optical axis at constant r results in concentric rings of crystals (see Figure 3(a)), while a uniformly changing value of r gives rise to an Archimedes spiral (Figure 3(b)). Assuming that the chosen diffracting planes (hkl) of all the lens crystals are the same, in the first case (constant r), the energy of the diffracted photon will be centered on E for all the crystals in the ring, while in the second case (Archimedes spiral), the reflected energy E will continuously vary from one crystal to the other, as shown in Figure 4.

2.1. Energy Passband. Any Laue lens will diffract photons over a certain energy passband ($E_{\min}$,$E_{\max}$). From (2), at first-order diffraction (the most efficient), it results that

$$E_{\min} \approx \frac{hc\,f}{d_{hkl}r_{\max}}, \qquad E_{\max} \approx \frac{hc\,f}{d_{hkl}r_{\min}}. \tag{4}$$

Given that, for astronomical applications, the lens passband is desired to be covered with the highest effective area (*The effective area at energy E is defined as the geometrical area of the lens projected in the focal plane times, the total reflection efficiency at energy E.*) and in a smooth manner as a function of energy, the energy bands of the photons reflected by contiguous crystal rings or, in the case of the Archimedes structure of a lens, by contiguous crystals have to overlap each other, like in Figure 4. Since the full width at half maximum (fwhm) of the acceptance angle δ (known as *the Darwin width*) of perfect crystals is extremely narrow (fractions of an arcsec to a few arcsec, see [21]), such materials are not suitable for astrophysical Laue lenses. In order to increase

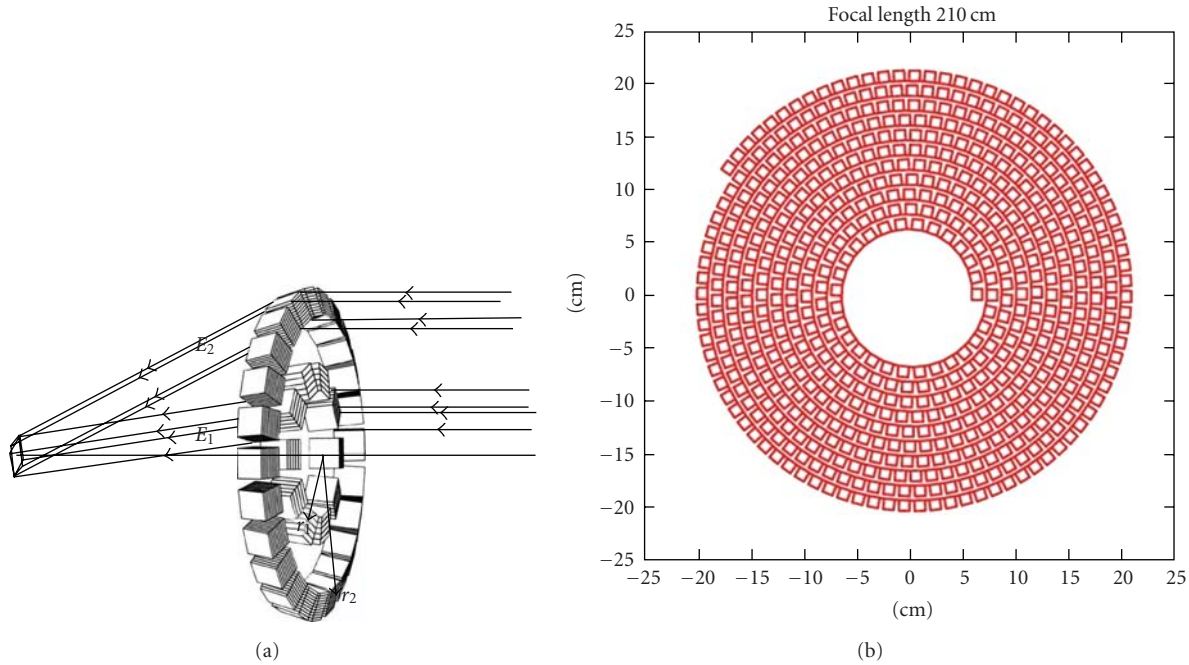

Figure 3: The basic design of a crystal diffraction lens in Laue geometry. Flat crystal tiles are assumed. (a) concentric rings of a given radius r concentrating a constant energy E. (b) crystal tiles disposed along an Archimedes' spiral result in a continuously varying energy E. Given the footprint of the crystals, the image in the focal plane has a minimum size equal to that of the crystal size.

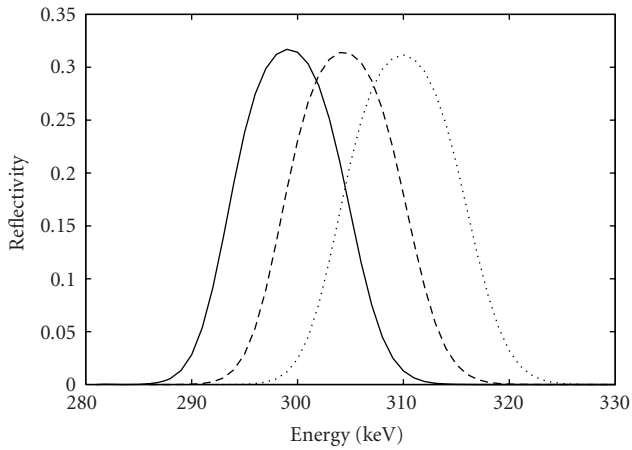

Figure 4: An example of the expected reflectivity profile of three contiguous crystals with a mosaicity of 1.5 arcmin along an Archimedes' spiral. Reprinted from [22].

the energy passband of individual crystals, one uses mosaic crystals or curved crystals (see Section 3). The *mosaicity* of mosaic crystals (see Section 3.1) and the *total bending angle* of curved crystals (see Section 3.2) govern the flux throughput, the angular resolution, and the energy passband of the Laue lenses. The diffracted flux from a continuum source increases with increasing the mosaicity of mosaic crystals or the total bending angle of curved crystals. For a crystal lens telescope, crystals with mosaicities or total bending angles ranging from a few tens of arcseconds to a few arcminutes are of interest.

The bandwidth of a lens for an on-axis source is determined by the mosaicity or total bending angle of the individual crystals and by the accuracy of the alignment of the single crystals. By forming the derivative of the Bragg relation in the small angle approximation ($2d_{hkl}\theta_B \approx nhc/E$), we get

$$\frac{\Delta\theta_B}{\theta_B} = \frac{\Delta E}{E}. \tag{5}$$

If $\Delta\theta_B$ is the mosaicity of the mosaic crystal or the total bending angle of the curved crystal, the corresponding energy passband ΔE of the crystal becomes

$$\Delta E = \frac{2d_{hkl} \cdot E^2 \cdot \Delta\theta_B}{nhc}. \tag{6}$$

It is worth pointing out that, whereas the energy passband of a crystal lens grows with the square of energy, the Doppler broadening of the astrophysical lines (e.g., in SN ejecta) increases linearly with energy for a given expansion velocity.

3. Crystal Reflectivity

Both mosaic crystals and curved crystals are suitable to be used for a Laue lens. We discuss the properties of both of them and their reflectivity.

3.1. Mosaic Crystals. Mosaic crystals are made of many microscopic perfect crystals (*crystallites*) with their lattice planes slightly misaligned with each other around a mean direction, corresponding to the mean lattice planes (*hkl*)

chosen for diffraction. In the lens configuration assumed, the mean lattice plane is normal to the surface of the crystals. The distribution function of the crystallite misalignments from the mean direction can be approximated by a Gaussian function

$$W(\Delta) = \frac{1}{\sqrt{2\pi}\eta} \exp\left(-\frac{\Delta^2}{2\eta^2}\right), \tag{7}$$

where Δ is the magnitude of the angular deviation from the mean, while $\beta_m = 2.35\eta$ is the fwhm of the mosaic spread (called *mosaicity*).

For the Laue geometry and diffracting planes perpendicular to the cross section of the crystal tile (see, e.g., Figure 2), the crystal reflectivity $R(\Delta, E)$ is given by [21]

$$\begin{aligned} R(\Delta, E) &= \frac{I_d(\Delta, E)}{I_0} \\ &= \sinh(\sigma T) \exp\left[-(\mu + \gamma_0\sigma)\frac{T}{\gamma_0}\right] \\ &= \frac{1}{2}\left(1 - e^{-2\sigma T}\right) e^{-\mu T/\gamma_0}, \end{aligned} \tag{8}$$

where I_0 is the intensity of the incident beam, μ is the absorption coefficient corresponding to that energy, γ_0 is the cosine of the angle between the direction of the photons and the normal to the crystal surface, T is the thickness of the mosaic crystal, and σ is

$$\sigma = \sigma(E, \Delta) = W(\Delta) Q(E) f(A), \tag{9}$$

where

$$Q(E) = r_e^2 \left|\frac{F_{hkl}}{V}\right|^2 \lambda^3 \frac{1 + \cos^2(2\theta_B)}{2\sin 2\theta_B}, \tag{10}$$

in which r_e is the classical electron radius, F_{hkl} is the structure factor, inclusive of the temperature effect (Debye-Waller's factor), V is the volume of the crystal unit cell, λ is the radiation wavelength, and θ_B is the Bragg angle for that particular energy, while $f(A)$ in (9) is well approximated by

$$f(A) = \frac{B_0(2A) + |\cos 2\theta_B|\ B_0(2A|\cos 2\theta_B|)}{2A(1 + \cos^2\theta_B)}. \tag{11}$$

Here, B_0 is the Bessel function of zero order integrated between 0 and $2A$, with A defined as follows:

$$A = \frac{\pi t_0}{\Lambda_0 \cos\theta_B}, \tag{12}$$

in which t_0 is the crystallite thickness, and Λ_0 (*extinction length*) is defined for the symmetrical Laue case (see e.g., [23]) as

$$\Lambda_0 = \frac{\pi V \cos\theta_B}{r_e \lambda\ |F_{hkl}|(1 + |\cos 2\theta_B|)}. \tag{13}$$

In general, $f(A) < 1$ and converges to 1 if $t_0 \ll \Lambda_0$. In this case, we get the highest reflectivity.

The quantity $\gamma_0\sigma$ is known as *secondary extinction* coefficient and T/γ_0 is the distance travelled by the direct beam inside the crystal.

3.2. Curved Crystals. Similarly to mosaic crystals, curved crystals have an angular dispersion of the lattice planes and thus a much larger energy passband (see (6)) than perfect crystals. The properties of these crystals and the methods to get them are discussed in [24]. Here, we summarize their reflection properties.

The most recent theory of the radiation diffraction in transmission geometry for such crystals, in the case of a large and homogeneous curvature, is now well fixed and has been compared with the experimental results (see [25, 26]). In this theory, the distortion of diffracting planes is described by the strain gradient β_s, that, in the case of a uniform curvature, is given by

$$\beta_s = \frac{\Omega}{T_0(\delta/2)}, \tag{14}$$

where Ω is the *total bending angle* and corresponds to the mosaicity of the mosaic crystals, T_0 is the thickness of the crystal and δ is the Darwin width.

When the strain gradient $|\beta_s|$ becomes larger than a critical value $\beta_c = \pi/(2\Lambda_0)$, it has been shown that, for a uniform curvature of planes, the peak reflectivity $R^{\max}$ of a curved crystal is given by

$$\begin{aligned} R^{\text{peak}}\left(c_p, E\right) &= \frac{I_r^{\text{peak}}\left(c_p, E\right)}{I_0} \\ &= \left(1 - e^{-(\pi^2 d_{hkl})/(c_p \Lambda_0^2)}\right) e^{-(\mu\Omega)/(c_p \cos\theta_B)}, \end{aligned} \tag{15}$$

where I_r^{peak} is the reflected peak intensity, $c_p = \Omega/T_0$ is the curvature of the lattice planes assumed to be uniform across the crystal thickness, and the extinction length $\Lambda_0 = \Lambda_0(E)$ is given by (13). The reflected intensity profile $I_r(c_p, E)$ is that of a perfect crystal with the Darwin width replaced with Ω. This profile is shown in Figure 5.

From the last equation, it can be shown that the highest peak reflectivity is obtained for a curvature of the lattice planes given by

$$c_p^{\text{opt}} = \frac{M}{\ln(1 + M/N)}, \tag{16}$$

where $M = \pi^2 d_{hkl}/\Lambda_0^2$ and $N = \mu\Omega/\cos\theta_B$.

3.3. Mosaic Crystals versus Curved Crystals. Both mosaic crystals and curved crystals can be used for a Laue lens, if they can be produced with the needed angular spread. However, in principle, curved crystals can reach a higher efficiency than mosaic crystals. Indeed, while the diffraction efficiency of mosaic crystals is limited to 50%, that of curved crystals can reach 100%. Another advantage of curved crystals is that the diffraction profile of a curved crystal is rectangular with width related to Ω, while that of mosaic crystals is Gaussian with fwhm equal to the mosaicity β_m. Given the absence of Gaussian tails, curved crystals concentrate the flux better (see Section 4). This better performance of the curved crystals with respect to the mosaic crystals for Laue lenses is discussed in depth in [27].

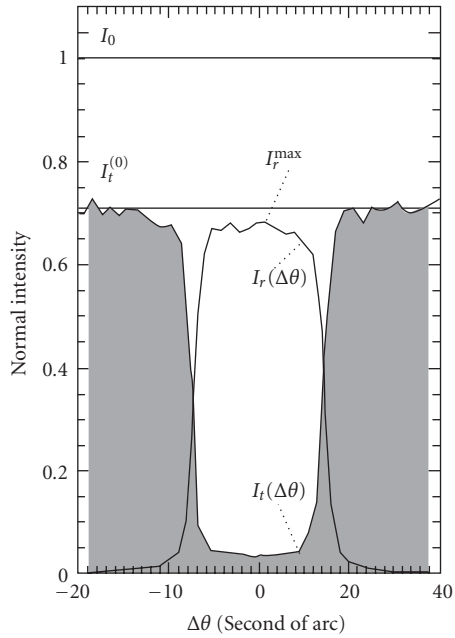

Figure 5: Reflectivity profile of a curved crystal as a function of the rocking angle $\Delta\theta$. This angle gives the difference between the incidence angle of the monochromatic photon beam and the Bragg angle. I_0 represents the incident intensity, $I_t(\Delta\theta)$ the transmitted intensity, and $I_r(\Delta\theta)$ the reflected intensity. Reprinted from [25].

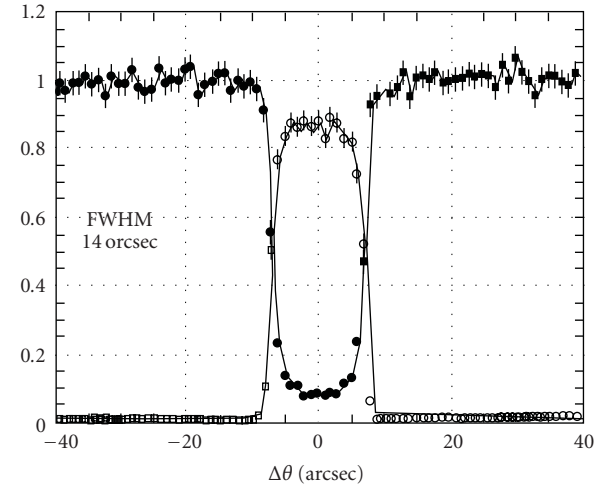

Figure 6: Measured rocking curve, in transmission geometry at 150 keV, of a Si(111) crystal curved at the University of Ferrara (see text). $\Delta\theta$ gives the difference between the incidence angle of the monochromatic photon beam and the Bragg angle. *Open circles*: ratio between measured intensity of the diffracted beam and measured intensity of the transmitted beam (also called *diffraction efficiency*). Filled circles: difference between transmitted and diffracted intensities. Note that the angle $\Delta\theta$, through the Bragg law, is related to the reflected photon energy. Thus, the figure also shows the energy bandwidth of the curved crystal. Reprinted from [28], who tested the crystal sample.

Curved crystals can be obtained in various ways [24]. The most feasible techniques to be used for Laue lenses include the elastic bending of a perfect crystal (the technique commonly adopted in synchrotron radiation facilities), the deposition of a coating on a wafer, the growing of a two-component crystal whose composition varies along the crystal growth axis (see, e.g., [25]), or the indentation of one face of a wafer. The last technique is being developed at the University of Ferrara (V. Guidi, private communication) with very satisfactory results (see Figure 6). Also the deposition of a coating on a wafer is being tested at the same university.

4. Optimization of a Laue Lens

The free parameters of a Laue lens are the crystal properties (materials, lattice planes for diffraction, microcrystal size and mosaicity in the case of mosaic crystals, total bending angle in the case of curved crystals, and crystal thickness), the lens geometry (ring-like or Archimedes' spiral), its focal length and its nominal energy passband. Many optimization studies of these parameters have been performed and tested [24, 29–31].

4.1. Crystal Material. Independently of the crystal structure (mosaic or curved), in order to optimize the crystal reflectivity it is important to maximize $Q(E)$ as defined in (10). This is the integrated crystal reflectivity per unit volume, whose normalization is the ratio $|F_{hkl}/V|^2$ between the structure factor of the chosen lattice planes F_{hkl} and the volume V of the unit cell. The inverse of V is the atomic density N. Thus, a small V (or a high N) is important for maximizing $Q(E)$. The value of N as a function of the element atomic number Z is shown in Figure 7.

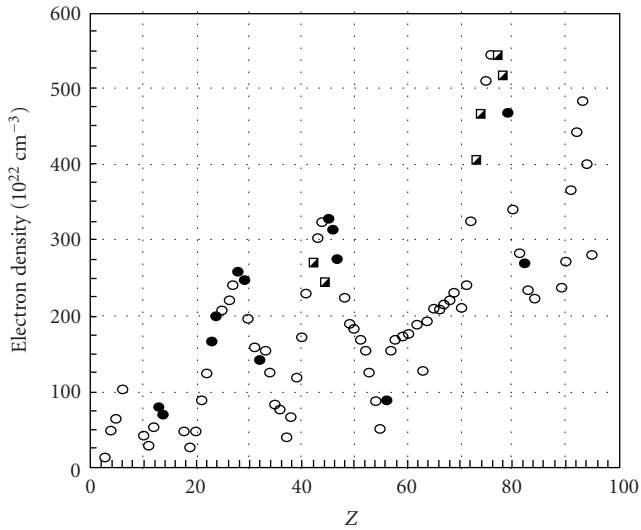

Figure 7: Density of a crystal unit cell versus element atomic number. Reprinted from [24].

As can be seen, for single-element materials, broad density peaks are apparent in correspondence of the atomic numbers 5, 13, 28, 45, and 78. Common materials like Al ($Z = 13$), Si ($Z = 14$), Ni ($Z = 28$), Cu ($Z = 29$), Zn

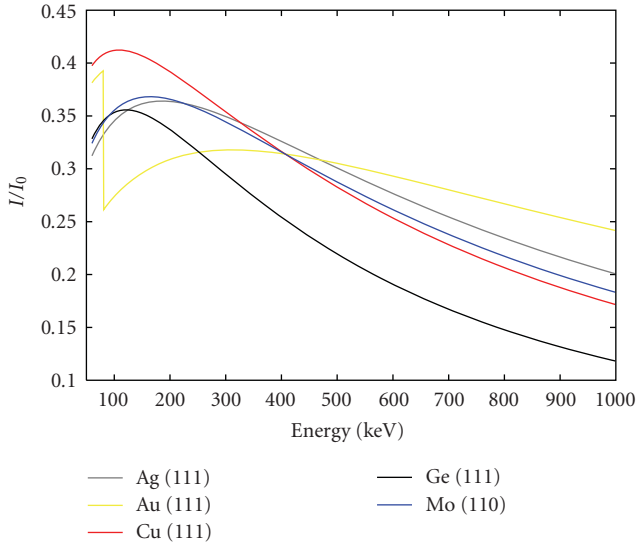

Figure 8: Peak reflectivity of 5 candidate crystal materials. The Miller indices used give the highest reflectivity. A mosaicity of 40 arcsec is assumed. The thickness has been optimized. The production technology of mosaic crystals with the required spread is already mature for Ge and Cu.

($Z = 30$), Ge ($Z = 32$), Mo ($Z = 42$), Rh ($Z = 45$), Ag ($Z = 47$), Ta ($Z = 73$), W ($Z = 74$), and Au ($Z = 42$) are good candidates to be used for Laue lenses and should be preferred to other elements if they are available as crystals with the requested properties. The peak reflectivity versus energy of few single-element mosaic crystal materials is shown in Figure 8.

Also double-element crystal materials can be used for Laue lenses. Several of them, developed for other applications, are already available, like GaAs, InAs, CdTe, and CaF_2. With some improvements, these crystal materials can be used for Laue lenses (see discussion in [24]).

Clearly the best lattice planes are those that optimize the structure factor $|F_{hkl}|$, under the condition that the corresponding d_{hkl} is consistent with lens constraints, such as energy passband, lens size, and focal length (see below).

4.2. Crystallite Size and Angular Distribution in Mosaic Crystals. From the reflectivity (8), the crystallite thickness t_0 plays an important role in the reflectivity optimization. For fixed values of the mosaicity and crystal thickness, the highest reflectivity is obtained for a crystallite thickness that satisfies the condition $t_0 \ll \Lambda_0$. In general, this implies a thickness of the order of 1 μm.

Unfortunately, this condition is still not always satisfied. From extended tests performed on Cu(111) supplied by ILL [32], it was found that the condition above is satisfied in single points [22], but not when the entire crystal cross section is irradiated (values even higher than 100 μm have been found [24]). In addition, in [24], it is found that t_0 is energy dependent, which is a surprising result that requires an interpretation (see discussion therein).

The crystal mosaicity is another crucial parameter for the optimization of the lens performance. It can be seen [11, 29–31] that, even if a higher mosaicity gives a larger lens effective area (see Figure 9), a higher spread also produces a larger defocusing of the reflected photons in the focal plane and thus a lower lens sensitivity.

This can be seen by introducing the focusing factor $G(E)$ of a Laue lens

$$G(E) = f_{\text{ph}} \frac{A_{\text{eff}}(E)}{A_d}, \tag{17}$$

in which $A_{\text{eff}}(E)$ is the effective area of the lens and A_d is the area of the focal spot which contains a fraction f_{ph} of photons reflected by the lens.

Assuming that the detector noise is Poissonian, it can be easily shown that $G(E)$ is inversely proportional to the minimum detectable continuum intensity of a lens

$$I_{\min}(E) = \frac{n_\sigma}{\eta_d G} \sqrt{\frac{2B}{A_d \Delta T \Delta E}}, \tag{18}$$

where $I_{\min}$ is given in units of photons $\text{cm}^{-2}\text{s}^{-1}\,\text{keV}^{-1}$ in the interval ΔE around E, n_σ is the significance level of the signal (typically n_σ =3–5), B is the focal plane detector background intensity (counts $\text{cm}^{-2}\,\text{s}^{-1}\,\text{keV}^{-1}$), ΔT is exposure time to a celestial source, and η_d is the focal plane detector efficiency at energy E. For a lens made of mosaic crystals of Cu(111), Figure 10 shows the dependence of G on focal length in two different energy bands, for different values of the mosaicity.

As can be seen, in spite of the fact that a higher spread gives a higher effective area, a lower spread gives a higher G and thus a higher lens sensitivity. This effect is small at short focal lengths (10–20 m), but it becomes very significant at long focal lengths (>30 m), especially at high energies (~500 keV).

4.3. Crystal Thickness. The crystal thickness is another crucial parameter for the reflectivity optimization of a mosaic crystal. The best crystal thickness is given by

$$T_{\text{best}} = \frac{1}{2\sigma} \ln\left(1 + \frac{2\sigma\gamma_0}{\mu}\right), \tag{19}$$

in the case of a mosaic crystal, and it is given by

$$T_{\text{best}} = \frac{\Omega \ln(1 + M/N)}{M}, \tag{20}$$

in the case of a curved crystal, where the involved quantities are defined in the sections above. In the case of a mosaic crystal, the optimum crystal thickness for various materials is shown in Figure 11.

As can be seen, the best crystal thickness depends on the absorption coefficient μ. A high-absorption coefficient implies a low crystal thickness for the reflectivity optimization.

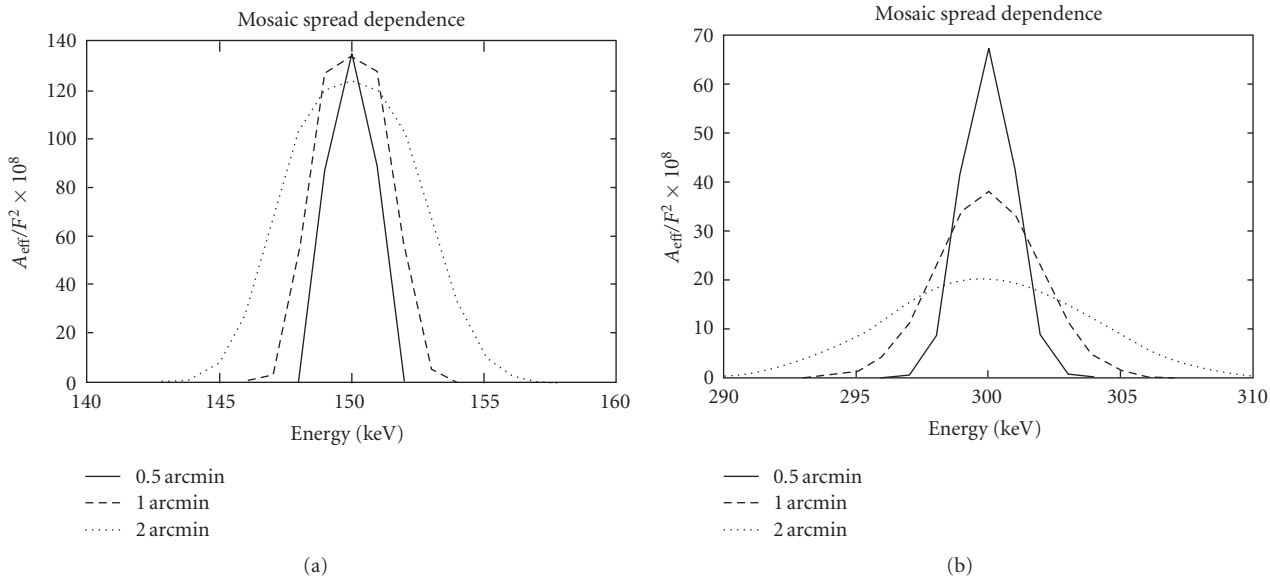

FIGURE 9: Normalized effective area for different values of the mosaicity of Cu(111). (a) First diffraction order; (b) second diffraction order. Reprinted from [31].

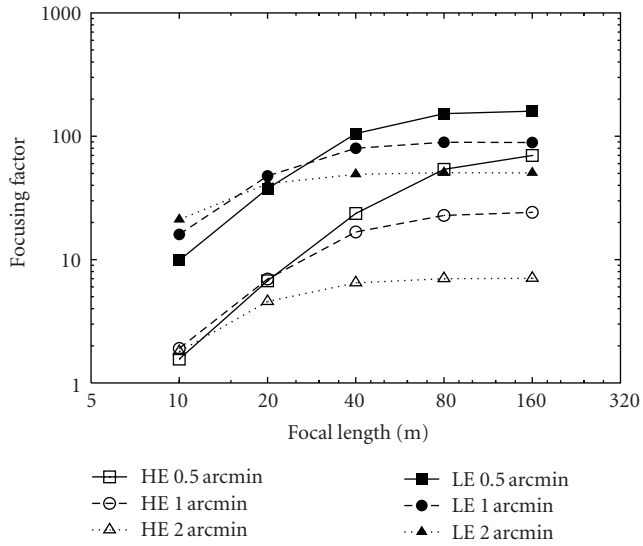

FIGURE 10: Dependence of the focusing factor G of a lens made of mosaic crystals of Cu(111) on the focal length f for three different values of the mosaicity in two different energy bands: 90–110 keV (LE) and 450–550 keV (HE). Reprinted from [11].

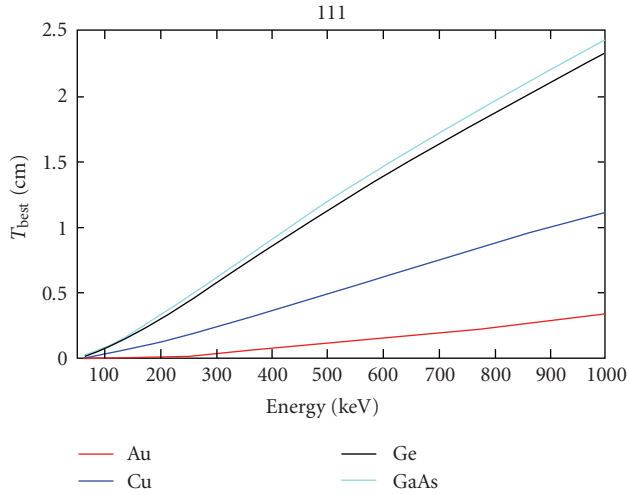

FIGURE 11: The best crystal thickness that maximizes the crystal reflectivity, for various materials. The mosaicity assumed is 1 arcmin, the crystallite thickness is 1 μm, and the crystal plane chosen for all of them is (111).

4.4. Focal Length. The focal length has a key importance in the case of Laue lenses, more than its importance in the case of traditional focusing telescopes. Indeed, given that the energy passband of a single crystal is quite narrow (see e.g., Figure 4), from the expression of nominal energy passband (E_{min}, E_{max}) of a lens (see (4)), it results that, for first-order diffraction, the lens radii (r_{min}, r_{max}), needed to get a given passband, depend linearly on f

$$r_{\text{min}} \approx \frac{hcf}{d_{hkl}E_{\text{max}}}, \qquad r_{\text{max}} \approx \frac{hcf}{d_{hkl}E_{\text{min}}}. \tag{21}$$

Given that high energy photons are focused by the innermost part of the lens, to get a given lens inner area, the focal length must be increased (the lens area approximately increases with f^2).

A gamma-ray lens with a broad continuum coverage from 300 keV to 1.5 MeV was proposed in the 90s by Lund

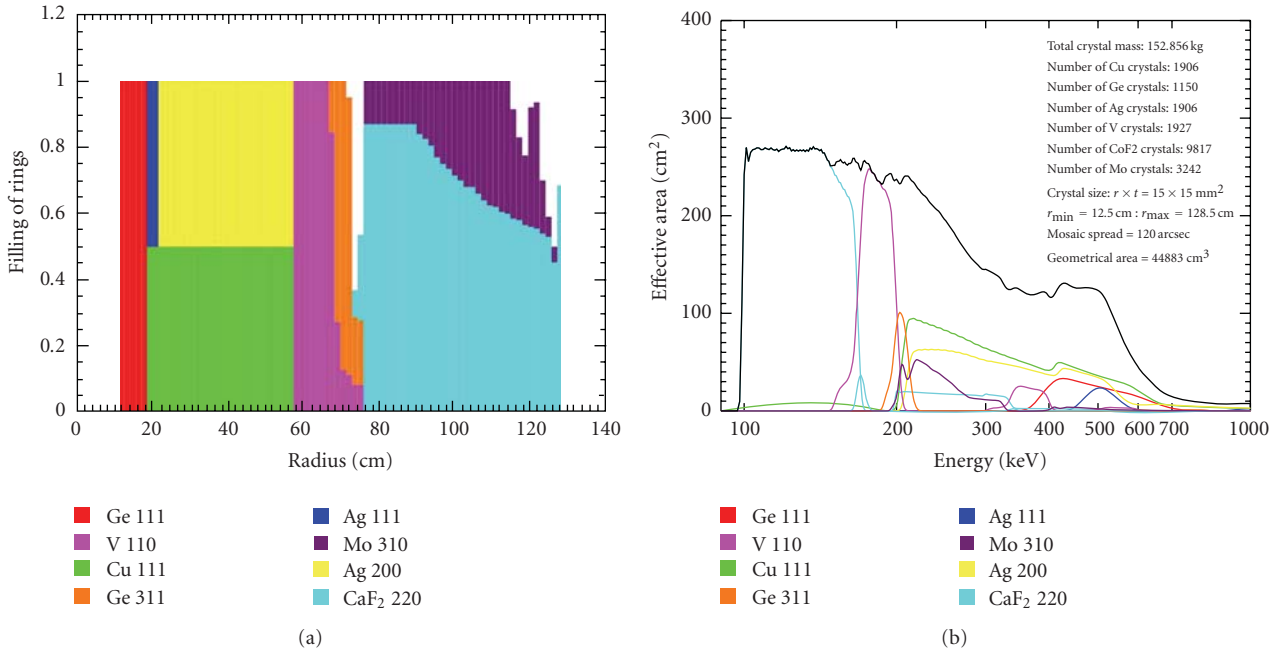

FIGURE 12: (a) Distribution of various flat mosaic crystals and chosen lattice planes in an example of a lens and focal length, as studied by Barriére et al. [28]. (b) Effective area of the studied lens. Colors show the contribution of each material.

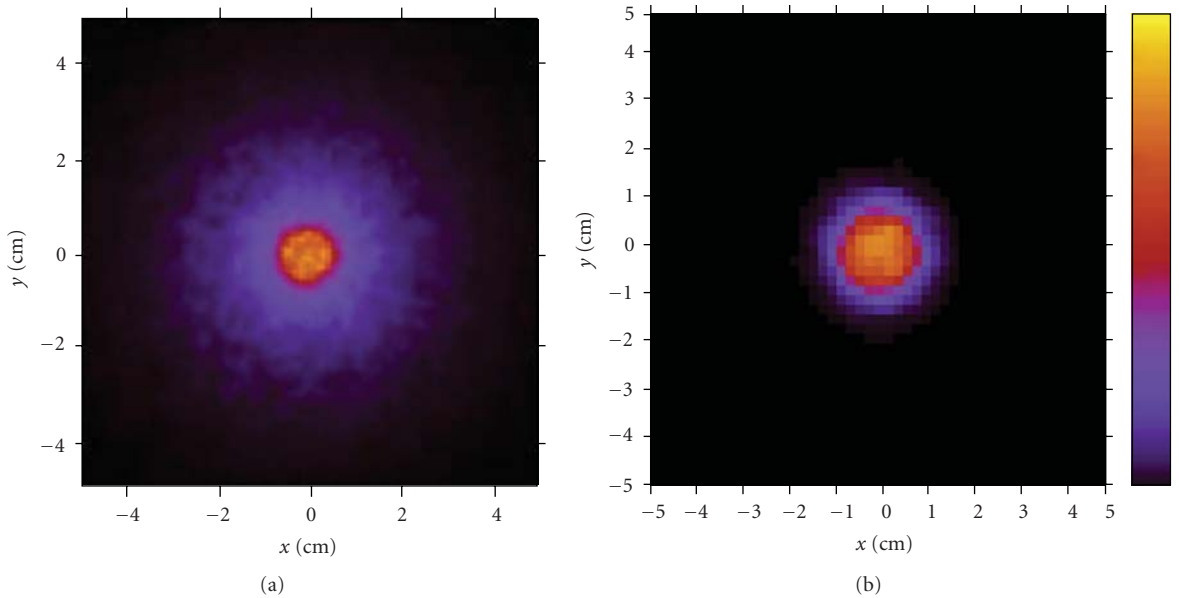

FIGURE 13: On-axis response function (PSF) of lenses made of flat mosaic crystals. (a) Lens with 40 m focal length for an on-axis source in the 150–600 keV energy band. (b) Lens with 6 m focal length for an on-axis source in the 70–300 keV energy band. See text. Reprinted from [33, 34].

[35]. He assumed mosaic crystals of Copper and Gold. In order to achieve a significant effective area at high energies (350 cm^2 at 300 keV and 25 cm^2 at 1.3 MeV), the focal length proposed was 60 m.

4.5. Broad versus Narrow Passband Laue Lenses. For the lens optimization, the selection criteria of the crystal material and lattice planes can change depending on the requested lens passband. Two classes of Laue lenses can be identified, *broad* passband and *narrow* passband. The former covers a broad energy band (e.g., 100–600 keV) for the study of continuum source spectra, while the latter achieves an optimal sensitivity in a relatively narrow energy band (e.g., 800–900 keV) for gamma-ray line spectroscopy. These two classes of lenses

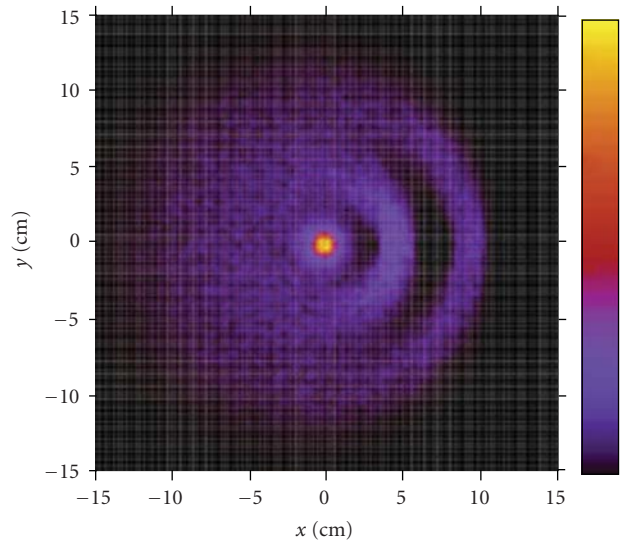

Figure 14: Off-axis expected response function (PSF) of a Laue lens made of flat mosaic crystals with 40 m focal length in the 150–600 keV energy band. Three-point sources are simulated, at 0, 2 and 4 arcmin off-axis. See text. Reprinted from [34].

require different criteria in the crystal choice and disposition in the lens for its optimization.

4.5.1. Narrow Passband Laue Lenses. Assuming a ring-like geometry, these lenses use a different crystalline plane (*hkl*) for every ring in order to diffract photons in only one energy band centered on the energy E_0. If, for a given focal length, the ring at distance r_0 from the lens axis concentrates photons centered at energy E_0 using crystals with crystalline plane spacing d_0, a ring with a radius $r_1 > r_0$, according to the Bragg law, will concentrate the same photon energies only if the crystalline plane spacing d_1 is smaller than d_0 or if a higher order is used. From (3), for materials with a cubic structure for which d_{hkl} is inversely proportional to $\sqrt{h^2 + k^2 + l^2}$, the ring radii are proportional to this quantity.

As the diffraction efficiency decreases with increasing diffraction order n, a crystal in an exterior ring will add less efficient area to the lens than a crystal on an inner ring. However, since the number of crystals increases with the ring-radius, all rings will usually contribute about the same amount of efficient area to the lens. Using larger and larger Bragg angles with increasing ring radius allows the instrument to be relatively compact, featuring a shorter focal length than required if the above criterion was not adopted. An example of a narrow passband Laue lens, the balloon telescope CLAIRE, will be discussed below.

4.5.2. Broad Passband Laue Lenses. These lenses use the best combination of crystalline planes to cover in the most efficent way the lens passband. Lowest order planes, for example, (111), are preferred because we can exploit, in addition to their optimum diffraction efficiency, also the higher order diffraction of the same planes. The principle used for covering a broad energy band is the following. In the simple assumption that a single crystal material and crystal plane (*hkl*) are used, assuming a ring-like geometry of the lens, different concentric rings focus slightly different energies because of the varying Bragg angle, and thus with several rings a broad energy band can be covered with the first-order diffraction (lens nominal energy passband). But, in addition to the first-order diffraction, higher order diffraction can be exploited that increases the effective area at higher energies, while also extending the passband. An example of the distribution of the various crystals and lattice planes in different rings for a broad passband lens (100–600 keV) made of mosaic crystals with 20 m focal length, is studied in [28] and it is shown in Figure 12.

Diffraction lenses with broad energy passbands were also developed and tested for low-energy X-rays since the sixties (e.g., Lindquist and Webber [36]). Today, photons up to 80 keV can be efficiently focused thanks to the development of grazing incidence based on multilayer mirrors (see other papers in this issue). Above this upper threshold, the development of Laue lens telescopes becomes crucial for photon focusing.

5. Optical Properties of a Lens

The optical properties of a lens, for both on-axis and off-axis incident photons, have been investigated by means of Monte Carlo (MC) simulations [11, 31]. For flat crystal tiles, the Point Spread Function (PSF) depends on the crystal size, on their mosaicity and on the accuracy of their positioning in the lens.

In Figure 13, we show the calculated on-axis Point Spread Functions for two cases: a ring-shaped lens of 40 m focal length and a spiral-shaped lens of 6 m focal length. In the first case, the lens has a 150–600 keV energy passband and a crystal tile cross section of $10 \times 10\,\text{mm}^2$, while in the second case it has a 70–300 keV passband and a crystal tile cross section of $15 \times 15\,\text{mm}^2$. In both cases it is supposed that the crystals made of Cu(111), have a mosaic structure with 1 arcmin spread and they are perfectly oriented in the lens. The 6 m focal length lens has been proposed for a balloon experiment [33].

In the case of curved crystals, whose development is giving very satisfactory results (see Section 3.3), the expected PSF becomes very sharp, with a great advantage in terms of angular resolution and sensitivity. Assuming a lens of 15 m focal length made of crystals with a mosaic spread of 30 arcsec, the PSF obtained in the case of $15 \times 15\,\text{mm}^2$ flat mosaic crystals and that obtained in the case of curved crystals with a curvature radius of 30 m (2 times the focal length) are shown in Figure 15. The difference between the two PSFs is outstanding. In the case of curved crystals we expect an angular resolution of 20 arcsec and a sensitivity higher than the corresponding lens with flat crystals by a factor of about 10.

In Figure 14, for flat crystal tiles of $15 \times 15\,\text{mm}^2$, we show the expected PSF of the 40 m focal length lens when three sources are in the Field of View (FOV), with one of the sources on-axis and the other two off-axis. As can

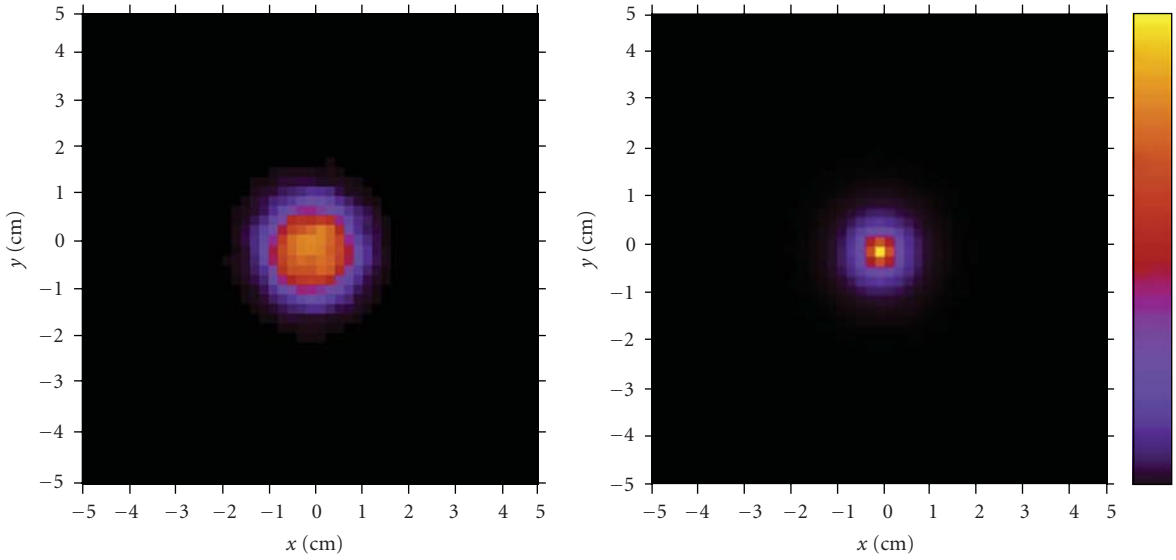

FIGURE 15: On-axis response function (PSF) of a lens of 15 m focal length made of mosaic crystals with 30 arcsec spread, for an on-axis source. (a) Flat crystals with cross section of 15 × 15 mm^2. (b) Curved crystals with a curvature radius of 30 m.

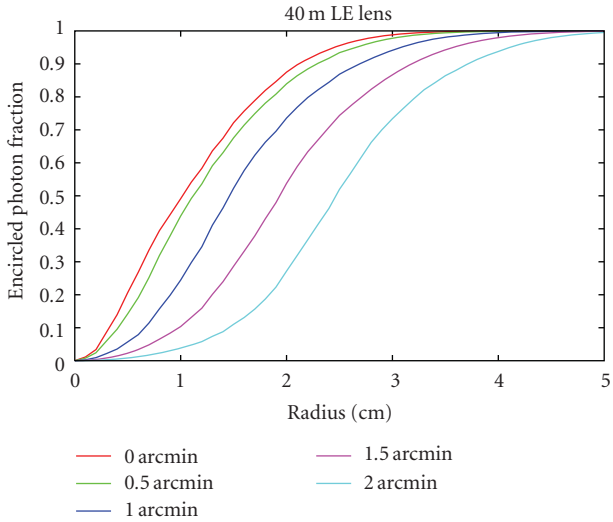

FIGURE 16: Cumulative distribution of photons with the distance from the lens focus, for different values of the mosaic spread, 40 m focal length lens, at about 100 keV.

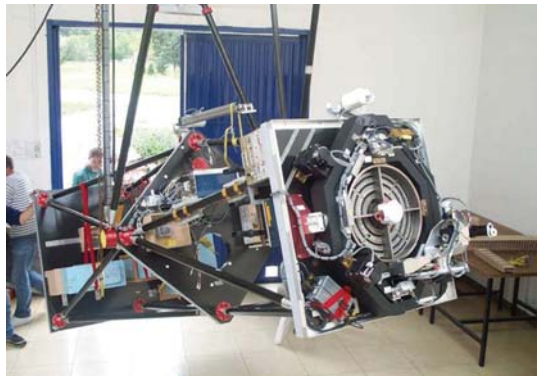

FIGURE 17: The CLAIRE telescope at the Gap-Tallard balloon base during the 2001 balloon campaign. On the first platform, the gamma-ray lens in its two-axes gimbal.

be seen, in the case of off-axis sources the image has a ring shape centered in the on-axis source image, with inner radius that increases with the offset angle, and a nonuniform distribution of the reflected photons with azimuth. It is found that the integrated number of photons focused by the lens does not significantly vary from an on-axis source to an off-axis source, but they are spread over an increasing area. As a consequence, in principle the FOV of the lens is determined by the detector radius, but, taking into account that the focused photons from sources at increasing offset spread over an increasing area, the lens sensitivity decreases with the source offset. The azimuthal nonuniformity of the PSF for off-axis sources can be usefully exploited, because it gives information on the azimuthal source direction. The angular resolution, in addition to the size of the flat crystal tiles, depends on the mosaic spread and on the misalignments of the lens crystal tiles. For the lens image shown in Figure 14, the angular resolution is of the order of, or even better than, 1 arcmin.

Figure 16 shows the cumulative distribution of the on-axis photons with the distance from the lens focus, for different values of the mosaic spread, in the case of a 40 m focal length lens made of mosaic crystals of Cu(111) with 15 × 15 mm^2 flat crystal tile cross section. As can be seen, for a low mosaic spread, the distribution is driven by the crystal size, while for large spreads, it is mainly driven by this spread.

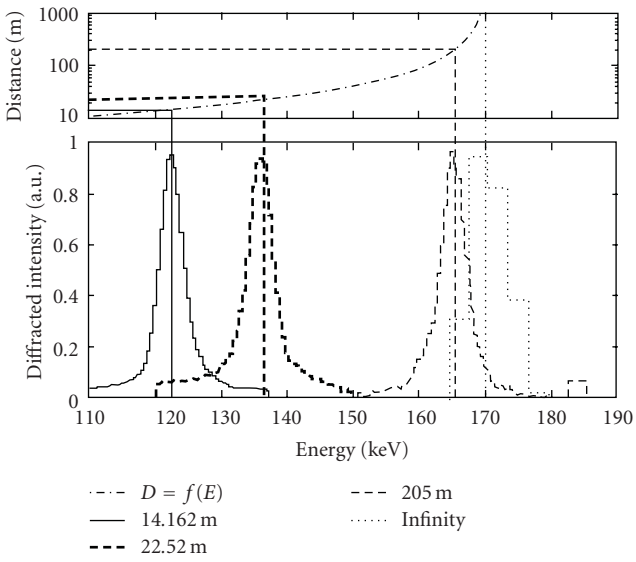

Figure 18: Recorded spectra for various source distances (lower graph). The upper graph represents the distance of the source as a function of diffracted energy. The vertical lines show the theoretical corresponding energies. 14.162 m corresponds to the tuning distance (E_{th} = 122.29 keV). The measurement at 22.52 m (E_{th} = 136.5 keV) was performed on the optical bench at CESR with a partially tuned lens. 205 m is the distance of the generator on the long distance test range (E_{th} = 165.5 keV). The peak for an infinite distance is taken from the stratospheric flight of June 2001.

Figure 19: A view of the current configuration of the apparatus for the lens assembling. The apparatus is located in the LARIX lab of the University of Ferrara.

6. The Development of Laue Lenses

Two key issues have to be faced in order build a Laue lens:

(i) Development of technologies for the mass production of suitable crystals (mosaic and/or curved crystals) in a reasonable time, consistent with that of preparation of a space mission.

(ii) Development of a technology for assembling, in an equally reasonable time, thousands of crystal tiles in a lens with the proper orientation accuracy, that largely depends on the focal length.

Laue lens developments are being carried out in different institutions. We summarize here the major results obtained in our institutes.

6.1. CLAIRE—a Narrow Passband Laue Lens Experiment. The objective of the R & D (Research and Development) project CLAIRE (French word that means "clear") [37] was to demonstrate that a prototype Laue lens can work under space conditions, measuring its performance by observing an astrophysical target. The CLAIRE telescope was flown twice (2000, 2001) on a stratospheric balloon by the French Space Agency CNES. CLAIRE's Laue lens was further tested on a 205 m long optical bench in 2003 [38]. The project involved research groups from CESR (Centre d'Etude Spatiale des Rayonnements) Toulouse, University of Birmingham, Institute Laue-Langevin (ILL) Grenoble, IEEC (Institut d'Estudis Espacials de Catalunya) Barcelona, and Argonne National Laboratory Chicago. CLAIRE's *narrow passband* lens consisted of 556 crystals (see Table 1) mounted on eight rings of a 45 cm diameter Titanium frame. In each ring i, the combination of the crystal plane spacing d_i and the Bragg angle θ_{Bi} results in the concentration of 170 keV photons onto a common focal spot of 1.5 cm diameter at 279 cm behind the lens.

CLAIRE's crystals were produced by *N.* Abrosimov at the Institut für Kristallzüchtung (IKZ) in Berlin. The Germanium-rich Ge_{1-x} Si_x crystals ($x \approx 0.02$) were grown by a modified Czochralski technique using Silicon feeding rods to replenish the loss of Si in the melt during the growth. The mosaicities of the Ge_{1-x} Si_x crystals range between roughly 30 arcsec and 2 arcmin, leading to a field of view of about 1.5 arcmin and a diffracted energy bandwidth of about 3 keV at 170 keV. A correlative study between crystal structure, mosaicity and diffraction efficiency of the CLAIRE crystals is presented in Abrosimov et al. [39]. After cutting the crystal ingots at IKZ Berlin, most of the crystal tiles were characterized (mosaicity) at the Hard X-Ray Diffractometer of ILL Grenoble.

At CESR Toulouse, the individual crystal tiles were mounted on flexible aluminium supports, which in turn are mounted on the lens frame. The reinforced 45 cm diameter titanium frame that holds up to 576 crystals on 8 rings was designed and manufactured at the Argonne National Laboratory, Argonne, USA. The tuning of the lens consisted of tilting each crystal tile to the appropriate Bragg angle so that the diffracting energy was 170 keV for a source at infinity. Instead of directly calibrating the lens for a parallel beam of 170 keV photons, crystal tuning on the 20 m optical bench at CESR used a 150 kV X-ray generator situated on the lens optical axis at a distance of 14.16 m. At this

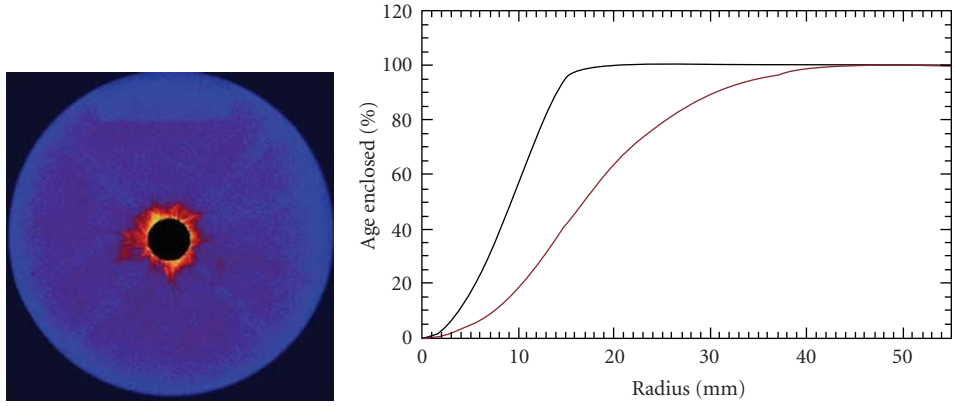

FIGURE 20: (a) Difference between the PSF measured and that obtained with a Monte Carlo code by assuming a perfect positioning of the crystal tiles in the lens. (b) Cumulative distribution of the focused photons as a function of radial distance from the focal point. *Black line:* expected distribution in the case of a perfect positioning of the crystal tiles in the lens. *Red line:* measured distribution. Reprinted from [34].

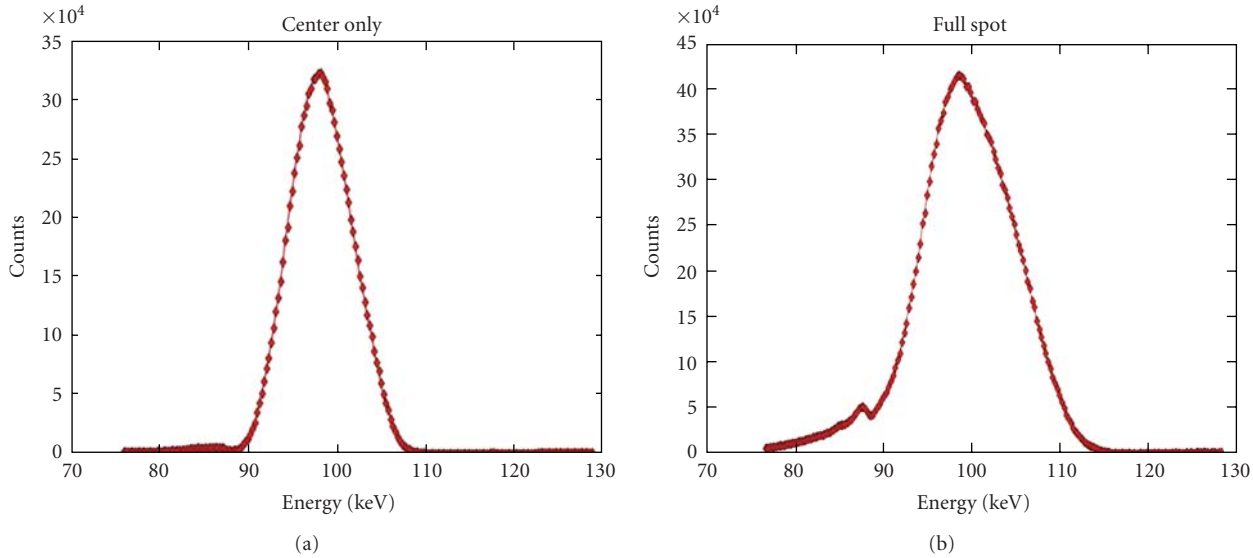

FIGURE 21: (a) Photon spectrum of the region (see left panel of Figure 20) in which all the reflected photons are expected to be found in the case of a perfect mounting of the crystal tiles in the lens. (b) Spectrum of all reflected photons. Reprinted from [34].

distance, a crystal was correctly tuned (170 keV at infinity) if it diffracted 122.28 keV photons. A coaligned mask (brass-lead sandwich) of the size of the entire lens, placed on the optical axis just in front of the lens, was used to select an individual crystal for tuning, while shielding already tuned crystals.

The resulting geometric area of the CLAIRE lens was 511 cm^2, the FOV and the passband were 90″ and ∼3 keV, respectively. The photons were focused onto a small 3 × 3 array of high-purity Germanium detectors, housed in a single cylindrical aluminum cryostat. Each of the single Ge bars was an *n*-type coaxial detector with dimensions of 1.5 cm × 1.5 cm × 4 cm. Focusing onto such a small detector volume already results in very low background noise. The CLAIRE stabilization and pointing system was developed by the balloon division of the French space agency CNES.

CLAIRE's First Light. On June 14 2001, CLAIRE was launched by the balloon division of French Space Agency CNES from its base at Gap-Tallard in the French Alps (see Figure 17). The astrophysical target was the Crab Nebula. (While nuclear lines are the perfect astrophysical targets for narrow passband Laue lenses, the balloon test flight ironically required the observation of a continuum spectrum.) With a mere 72 minutes of the flight having satisfactory pointing, CLAIRE nevertheless collected 33 photons from the Crab Nebula. This 3σ detection has been validated by ground tests conducted at distances of 14.16 m, 22.52 m (CESR optical bench), and 205 m (long distance test, Ordis, Catalunia). Figure 18 shows the recorded spectra for these experiments. The energies of the centroids are in very good agreement with theory, slight departures from theoretical values (less than 0.5 keV) being the consequence of the incident spectrum

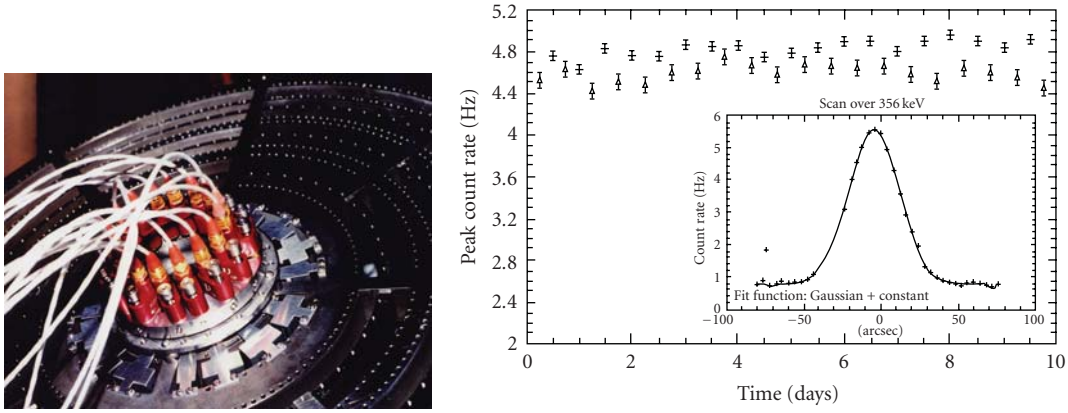

(a) (b)

FIGURE 22: (a) Prototype tunable lens. (b) The evolution in time of the peak count rate when alternatively focusing 303 keV (circles) and 356 keV (crosses) γ-rays demonstrates the stability and reproducibility of the lens tuning.

TABLE 1: The crystalline plane, the crystal size, the number of crystals per ring as well as the ring radius, and the Bragg angle at 170 keV are listed for each ring of the prototype crystal lens.

ring	Reflection [*hkl*]	d [*hkl*] [A]	Size [mm]	Number of crystals	Radius [cm]	Bragg angle at 170 keV
0	111	3.27	10×10	28	6.17	0.64
1	220	2.00	10×10	52	10.08	1.04
2	311	1.71	10×10	56	11.82	1.22
3	400	1.41	10×10	72	14.26	1.48
4	331	1.30	10×7	80	15.62	1.61
5	422	1.15	10×10	96	17.47	1.81
6	333	1.09	10×7	96	18.82	1.92
7	440	1	10×10	104	20.17	2.09

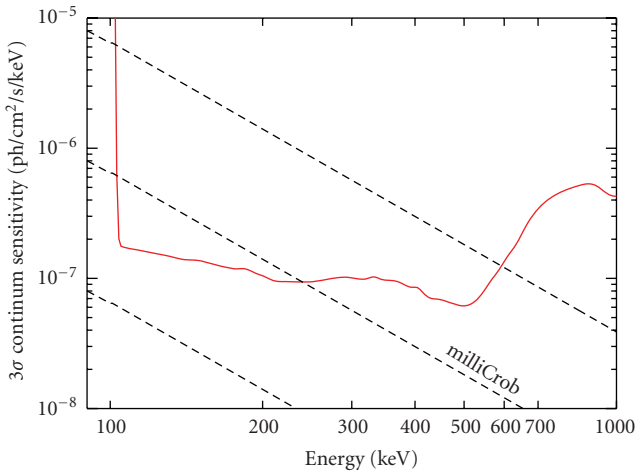

FIGURE 23: 3σ continuum sensitivity ($\Delta E = E/2$) of the lens discussed in Section 4.5.2 for 100 ks observation time. Reprinted from [28].

shape, and/or the detector calibration drifts. The measured peak efficiencies of the ground experiments are in fairly good agreement with the Crab observation; when their efficiencies are rescaled for a polychromatic source at infinity, a peak efficiency of $9 \pm 1\%$ is obtained. At first glance, this figure may seem rather modest; however, when considering the constraints on a compact balloon instrument, the result is actually very positive. The short focal length leads to a lens with the outermost rings occupied by crystals with high reflection orders n (see (1)); the outermost rings ((333) and (440) crystals) are roughly 4 times less efficient than the innermost rings ((111) and (220) crystals). Note that the largest numbers of crystals are situated in the outer rings where efficiencies are unfortunately lowest. A future space instrument will allow longer focal lengths and hence only low-order crystalline planes with the highest efficiencies would be used. Also, the quality of the CLAIRE crystals was quite heterogeneous the efficiency of the individual crystals within a ring varied by factors of 2 to 10, depending on the ring! However, the CLAIRE lens contained crystals as efficient as the Darwin model predicts: the best crystals of the lens showed peak efficiencies well above 20%.

CLAIRE's balloon flight provided the first observation of an astrophysical source with a gamma-ray lens. In combination with the long-distance test on the ground, these results validate the theoretical models and demonstrate the principle of Laue lens. Moreover, CLAIRE's stratospheric

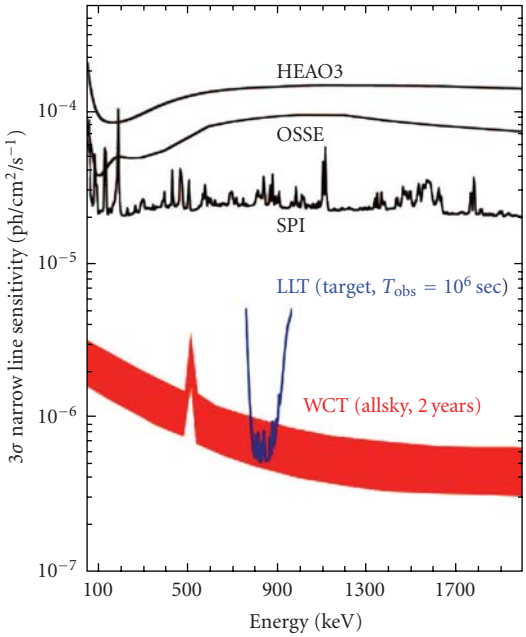

FIGURE 24: Sensitivity estimation of DUAL's Laue Lens Telescope (LLT, blue curve), enabling study of SNe Ia out to 50–80 Mpc, for dozens of potential targets each year. Also shown is the estimated survey sensitivity (two years) of the Wide Field Compton Telescope (WCT, red curve) which serves as a focal plane detector of the LLT.

flight represents a first demonstration of the Laue lens technology in a space environment.

6.2. Current Crystal Development. The crystal development status is discussed in detail in [24, 40]. Mosaic crystals of Copper are developed and produced at ILL [32]; gradient composition crystals of $Si_{1-x}Ge_x$ alloy with x increasing along the crystal growth axis (curved crystal) are produced at IKZ [39]. Crystal developments for Laue lenses are being undertaken in Italy: mosaic crystals at the CNR-IMEM Institute and curved crystals at the Physics Department, University of Ferrara (see Figure 6).

6.3. Current Lens Assembly Technology Development. Currently new lens assembly technologies are being developed at the University of Ferrara, for building broad passband (70/100–600 keV) Laue lenses, and at CESR for building high-energy narrow passband (800–900 keV) Laue lenses.

The crystal tile positioning accuracy in the lens is the most critical issue. It depends on the mosaic spread and the focal length. Longer focal lengths require better positioning accuracies, thus the development is more challenging for lenses working at the highest energies.

6.3.1. Assembly Technology Status for Broad Passband Laue Lenses. A technology for assembling crystal tiles for a moderately short (≤10–15 m) focal length lens is at an advanced stage of development at the University of Ferrara [34, 41, 42]. It does not require any mechanism for a fine adjustment of the crystal orientation once the crystal is positioned in the lens frame. Using this technology, a first lens prototype with 6 m focal length has already been developed and tested. It makes use of mosaic crystals of Cu(111).

The technique adopted is described in detail in [34, 41]. It makes use of a countermask provided with holes, two for each crystal tile. Each tile is positioned on the countermask by means of two cylindrical pins, rigidly glued to the crystal tile, that are inserted in the countermask holes. The pin direction and the axis of the average lattice plane of each crystal tile have to be exactly orthogonal. The hole axis direction constrains the energy of the photons diffracted by the tile, while the relative position of the two holes in the countermask establishes the azimuthal orientation of the axis of the crystal lattice plane. This axis has to cross the lens axis.

Depending on the direction of the hole axes in the countermask, the desired geometry of lens can be obtained. In the case of a lens for space astronomy, the hole axes have to be directed toward the center of curvature of the lens. In the case of the developed prototype, the hole axes were set parallel to the lens axis for the quick test of the lens with an X-ray tube, that provides a divergent X-ray beam.

Once all the crystal tiles are placed on the counter-mask, a frame is glued to the entire set of the crystals. Then the lens frame, along with the crystals, is separated from the counter-mask and from the pins. In the case of the first prototype, instead of using a chemical attack in order to separate the countermask from the lens as foreseen in the project, a mechanical separation was attempted.

The first developed prototype is made of a 36 cm diameter ring of 20 mosaic crystal tiles. The mosaic spread of the used crystals ranges from ~2.5 to ~3.5 arcmin. The tile cross-section is 15×15 mm^2 while its thickness is 2 mm. The lens frame is made of carbon fiber composite with a total thickness of 1 mm.

The X-ray beam used, first to assemble the crystals and then to test the complete lens, is that available in the LARIX (LArge Italian hard X-ray) facility of the University of Ferrara. For an LARIX description see [43]. A view of the experimental apparatus in the current configuration is shown in Figure 19.

The prototype was thoroughly tested using the polychromatic X-ray beam described above, as reported in [34]. Figure 20 shows the difference between the measured PSF and that obtained from a simulation, in which a perfect positioning of the crystals in the lens was assumed. As can be seen, only the center part of the measured image (i.e., the black region) is subtracted by the simulated image. The corona still visible in the difference image is the result of the cumulative error (mainly that due to the mechanical separation of the lens from the countermask) during the lens assembly process.

The disagreement between the measured and the expected PSF is also apparent by comparing the cumulative distribution of the photons with the distance from the lens focus (see Figure 20(b)). As can be seen, the PSF radius at which the expected fraction of focused photons reach the saturation (16 mm) corresponds to ~60% of the measured fraction.

The spectrum of the photons focused by the developed prototype is shown in Figure 21, where we compare the measured spectrum of the central region (i.e., photons in the black region of the left panel of Figure 20) with the spectrum of all reflected photons. As can also be seen from this figure, the centroid of the spectrum of the central region achieves an intensity level 0.8 times that of the peak spectrum of all reflected photons.

A new prototype is being developed that takes into account the experience gained constructing the first one [42].

6.4. R & D for a Tunable Narrow Passband Lens. Observing in *only one* narrow energy band might be considered too much of a handicap for a space instrument. In the framework of an R & D project for the French Space Agency CNES, a tunable γ-ray lens prototype (Figure 22(a)) was developed and demonstrated [44]. The capability to observe more than one astrophysical line with a narrow passband Laue lens requires the tuning of two parameters: the Bragg angle θ_B and the focal length f. While the length f will have to be controlled to within $\sim$1 cm, the precision of the crystal inclination has to be better than the mosaic structure of the crystals. In the setup of [44], each crystal was tuned by using piezo-driven actuators to change the crystal inclination, and an eddy-current sensor to determine the current position (Figure 22(a)). The resolution of the control-loop permitted an angular resolution of 0.1 − 0.4 arcsec. The stability was found to be better than 0.8 arcsec per day and the reproducibility of a particular tuning better than 5 arcsec over a 10-day period (Figure 22(b)).

7. Prospects and Conclusions

A big effort has already been invested in the development of focusing Laue lenses for gamma-ray astronomy (>70/100 keV). Thanks to the most recent developments, Laue lenses with short focal length (10–15 m) are already feasible. The major task now in progress is the development of the crystals needed to optimize the lens effective area. A project "LAUE," supported by the Italian Space Agency, has just started in Italy (main contractor DTM, Modena) for the development of both suitable Laue lens crystals and an advanced assembly technology for long focal length lenses (up to 100 m).

Thus far, the major limit to the launch of a Laue lens gamma-ray telescope has been the need of long focal lengths (20–100 m), that implies the use of two satellites in formation flying, one for the lens and the other for the focal plane detector. The development of extendable booms up to 20 m, the optimization of the lens effective area and the limitation of the lens passband to lower energies, all make realistic the prospect of broad band satellite missions that could join together multilayer mirrors and Laue lenses to extend the focusing band up to several hundreds of keV.

As an example, the 10^5 s continuum sensitivity of a Laue lens made of mosaic crystals, that was investigated in [28] and mentioned above (see Section 4.5.2), is shown in Figure 23. The use of curved crystals can further increase the lens sensitivity.

In the framework of formation flying missions, the mission concept DUAL [45] is currently under study by a consortium of institutes from Europe, Japan and the USA. The DUAL mission is composed of a Wide-field Compton telescope (WCT) which carries out all-sky surveys, and a narrow band (800–900 keV) Laue-Lens Telescope (LLT) that simultaneously performs very deep observations of selected narrow-field targets. Combining a small Compton telescope with a Laue lens will permit the resolution of the apparently contradictory needs for a future gamma-ray mission: to map out large-scale distributions, monitor extreme accelerators, and measure the polarization of gamma-ray bursts with a small medium-sensitivity Compton Camera and simultaneously accomplish the stringent performance requirements for the specific science goal of SN1a thanks to the Laue Lens. A compact, wide field (2-3 π steradian) Compton telescope with a modest geometric area (400–1600 cm^2) resulting in a effective area of 40–160 cm^2 can fulfill the needs for the "all-sky science" and simultaneously serve as a focal plane detector for the LLT. A Laue lens that, in 10^6 s, can achieve sensitivities of 10^{-6} photons cm^{-2}s^{-1} for a 3% broadened line at 847 keV can be made from Au, Ag, and Cu crystals, similar to those presently available. The model lens used for the sensitivity shown in Figure 24 would have a focal length of the order of 68 m, a radius of 40–58 cm, and a total mass of 40 kg.

We expect that future broad band X-/gamma-ray missions for the deep study of nonthermal astrophysical processes above 100 keV, antimatter annihilation signatures, and nuclear lines from SN explosions will include Laue lenses.

Acknowledgments

F. Frontera acknowledges the financial support by the Italian Space Agency ASI. P. v. Ballmoos acknowledges continuing support from the French Space Agency CNES and is particularly grateful to the Balloon Division of CNES which built the pointing system and operated the CLAIRE flights from the launch to the gondola recovery. The authors also would like to thank the anonymous referees who have given valuable contributions to improve this paper.

References

[1] C. Winkler, N. Gehrels, V. Schönfelder et al., "First results from the INTEGRAL galactic plane scans," *Astronomy & Astrophysics*, vol. 411, no. 1, pp. L349–L355, 2003.

[2] N. Gehrels, G. Chincarini, P. Giommi et al., "The Swift gamma-ray burst mission," *Astrophysical Journal*, vol. 611, no. 2 I, pp. 1005–1020, 2004.

[3] A. J. Bird, A. Bazzano, L. Bassani et al., "The fourth IBIS/ISGRI soft gamma-ray survey catalog," *Astrophysical Journal Supplement Series*, vol. 186, no. 1, pp. 1–9, 2010.

[4] G. Cusumano, V. La Parola, A. Segreto et al., "The Palermo Swift-BAT hard X-ray catalogue. II—results after 39 months

of sky survey," *Astronomy & Astrophysics*, vol. 510, article A48, 2010.

[5] G. Weidenspointner, G. Skinner, P. Jean et al., "An asymmetric distribution of positrons in the Galactic disk revealed by γ-rays," *Nature*, vol. 451, no. 7175, pp. 159–162, 2008.

[6] R. Diehl, H. Halloin, K. Kretschmer et al., "Radioactive ^{26}Al from massive stars in the Galaxy," *Nature*, vol. 439, no. 7072, pp. 45–47, 2006.

[7] F. Frontera, E. Costa, D. dal Fiume et al., "PDS experiment on board the BeppoSAX satellite: design and in-flight performance results," in *EUV, X-ray, and Gamma-Ray Instrumentation for Astronomy VIII*, O. H. Siegmund and M. A. Gummin, Eds., vol. 3114 of *Proceedings of SPIE*, pp. 206–215, San Diego, Calif, USA, July 1997.

[8] P. Ubertini, F. Lebrun, G. Di Cocco et al., "IBIS: the Imager on-board INTEGRAL," *Astronomy & Astrophysics*, vol. 411, no. 1, pp. L131–L139, 2003.

[9] J. Knödlseder, P. von Ballmoos, F. Frontera et al., "GRI: focusing on the evolving violent Universe," in *Optics for EUV, X-ray, and Gamma-Ray Astronomy III*, S. L. O'Dell and G. Pareschi, Eds., vol. 6688 of *Proceedings of SPIE*, San Diego, Calif, USA, August 2007.

[10] F. Frontera, A. Pisa, P. de Chiara et al., "Exploring the hard X-/soft gamma-ray continuum spectra with Laue lenses," in *Proceedings of the 39th ESLAB Symposium*, F. Favata, J. Sanz-Forcada, A. Giménez, and B. Battrick, Eds., no. 588, pp. 323–326, Noordwijk, The Netherlands, April 2005.

[11] F. Frontera, A. Pisa, V. Carassiti et al., "Gamma-ray lens development status for a European gamma-ray imager," in *Space Telescopes and Instrumentation II: Ultraviolet to Gamma Ray*, M. J. L. Turner and G. Hasinger, Eds., vol. 6266 of *Proceedings of SPIE*, May 2006.

[12] J. Knödlseder, "GRI: the gamma-ray imager mission," in *Space Telescopes and Instrumentation II: Ultraviolet to Gamma Ray*, M. J. L. Turner and G. Hasinger, Eds., vol. 6266 of *Proceedings of SPIE*, Orlando, Fla, USA, May 2006.

[13] D. Götz, S. Mereghetti, A. Tiengo, and P. Esposito, "Magnetars as persistent hard X-ray sources: INTEGRAL discovery of a hard tail in SGR 1900+14," *Astronomy & Astrophysics*, vol. 449, no. 2, pp. L31–L34, 2006.

[14] L. Kuiper, W. Hermsen, P. R. den Hartog, and W. Collmar, "Discovery of luminous pulsed hard X-ray emission from anomalous X-ray pulsars 1RXS J1708-4009, 4U 0142+61, and 1E 2259+586 by INTEGRAL and RXTE," *Astrophysical Journal*, vol. 645, no. 1, pp. 556–575, 2006.

[15] G. C. Perola, G. Matt, M. Cappi et al., "Compton reflection and iron fluorescence in BeppoSAX observations of Seyfert type 1 galaxies," *Astronomy & Astrophysics*, vol. 389, no. 3, pp. 802–811, 2002.

[16] G. Risaliti, "The BeppoSAX view of bright compton-thin Seyfert 2 galaxies," *Astronomy & Astrophysics*, vol. 386, no. 2, pp. 379–398, 2002.

[17] G. Ghisellini, R. D. Ceca, M. Volonteri et al., "Chasing the heaviest black holes of jetted active galactic nuclei," *Monthly Notices of the Royal Astronomical Society*, vol. 405, no. 1, pp. 387–400, 2010.

[18] Y. Rephaeli, J. Nevalainen, T. Ohashi, and A. M. Bykov, "Nonthermal phenomena in clusters of galaxies," *Space Science Reviews*, vol. 134, no. 1–4, pp. 71–92, 2008.

[19] R. Gilli, A. Comastri, and G. Hasinger, "The synthesis of the cosmic X-ray background in the Chandra and XMM-Newton era," *Astronomy & Astrophysics*, vol. 463, no. 1, pp. 79–96, 2007.

[20] A. Goldwurm, J. Ballet, B. Cordier et al., "Sigma/GRANAT soft gamma-ray observations of the X-ray nova in Musca—discovery of positron annihilation emission line," *Astrophysical Journal*, vol. 389, pp. L79–L82, 1992.

[21] W. H. Zachariasen, *Theory of X-rays Diffraction in Crystals*, John Wiley & Sons, New York, NY, USA, 1945.

[22] D. Pellicciotta, F. Frontera, G. Loffredo et al., "Laue lens development for hard X-rays (>60 keV)," *IEEE Transactions on Nuclear Science*, vol. 53, no. 1, pp. 253–258, 2006.

[23] A. Authier, *Dynamical Theory of X-ray Diffraction*, Oxford University Press, Oxford, UK, 2001.

[24] N. Barriére, J. Rousselle, P. von Ballmoos et al., "Experimental and theoretical study of the diffraction properties of various crystals for the realization of a soft gamma-ray Laue lens," *Journal of Applied Crystallography*, vol. 42, no. 5, pp. 834–845, 2009.

[25] S. Keitel, C. Malgrange, T. Niemöller, and J. R. Schneider, "Diffraction of 100 to 200 keV X-rays from an $Si_{1-x}Ge_x$ gradient crystal: comparison with results from dynamical theory," *Acta Crystallographica A*, vol. 55, no. 5, pp. 855–863, 1999.

[26] C. Malgrange, "X-ray propagation in distorted crystals: from dynamical to kinematical theory," *Crystal Research and Technology*, vol. 37, no. 7, pp. 654–662, 2002.

[27] N. Barriere, *Developpement d'une lentille de Laue pour l'astrophysique nucleaire*, Ph.D. thesis, University of Toulouse, Toulouse, France, 2008.

[28] N. M. Barrière, L. Natalucci, N. Abrosimov et al., "Soft gamma-ray optics: new Laue lens design and performance estimates," in *Optics for EUV, X-ray, and Gamma-Ray Astronomy IV*, vol. 7437 of *Proceedings of SPIE*, San Diego, Calif, USA, August 2009.

[29] A. Pisa, F. Frontera, P. de Chiara et al., "Feasibility study of a Laue lens for hard X-rays for space astronomy," in *Advances in Computational Methods for X-ray and Neutron Optics*, M. Sanchez del Rio, Ed., vol. 5536 of *Proceedings of SPIE*, pp. 39–48, Denver, Colo, USA, August 2004.

[30] A. Pisa, F. Frontera, P. de Chiara et al., "Development status of a Laue lens for high energy X-rays (>60 keV)," in *Optics for EUV, X-ray, and Gamma-Ray Astronomy II*, O. Citterio, S. L. O'Dell et al., Eds., vol. 5900 of *Proceedings of SPIE*, pp. 1–10, San Diego, Calif, USA, August 2005.

[31] A. Pisa, F. Frontera, G. Loffredo, D. Pellicciotta, and N. Auricchio, "Optical properties of Laue lenses for hard X-rays (>60 keV)," *Experimental Astronomy*, vol. 20, no. 1–3, pp. 219–228, 2005.

[32] P. Courtois, K. H. Andersen, and P. Bastie, "Copper mosaic crystals for Laue lenses," *Experimental Astronomy*, vol. 20, no. 1–3, pp. 195–200, 2005.

[33] F. Frontera, G. Loffredo, A. Pisa et al., "A gamma-ray Laue lens focusing telescope aboard a balloon experiment," *Memorie della Societa Astronomica Italiana*, vol. 79, pp. 807–811, 2008.

[34] F. Frontera, G. Loffredo, A. Pisa et al., "Focusing of gamma-rays with Laue lenses: first results," in *Space Telescopes and Instrumentation 2008: Ultraviolet to Gamma Ray*, vol. 7011 of *Proceedings of SPIE*, Marseille, France, June 2008.

[35] N. Lund, "A study of focusing telescopes for soft gamma rays," *Experimental Astronomy*, vol. 2, no. 5, pp. 259–273, 1992.

[36] T. R. Lindquist and W. R. Webber, "A focusing X-ray telescope for use in the study of extraterrestrial X-ray sources in the energy range 20-140 keV," *Canadian Journal of Physics*, vol. 46, p. 1103, 1968.

[37] P. von Ballmoos, H. Halloin, J. Evrard et al., "CLAIRE: first light for a gamma-ray lens," *Experimental Astronomy*, vol. 20, no. 1–3, pp. 253–267, 2005.

[38] J. M. Alvarez, H. Halloin, M. Hernanz et al., "Long distance test of the CLAIRE gamma-ray lens," in *Proceedings of the 5th INTEGRAL Workshop on The INTEGRAL Universe*, pp. 757–760, Munich, Germany, February 2004.

[39] N. V. Abrosimov, "Mosaic and gradient SiGe single crystals for gamma ray Laue lenses," *Experimental Astronomy*, vol. 20, no. 1–3, pp. 185–194, 2005.

[40] J. Rousselle, P. V. Ballmoos, N. Barrière et al., "High-Z crystals for gamma-ray optics," in *Optics for EUV, X-ray, and Gamma-Ray Astronomy IV*, vol. 7437 of *Proceedings of SPIE*, San Diego, Calif, USA, August 2009.

[41] F. Frontera, G. Loffredo, A. Pisa et al., "Development status of a Laue lens project for gamma-ray astronomy," in *Optics for EUV, X-ray, and Gamma-Ray Astronomy III*, S. L. O'Dell, G. Pareschi et al., Eds., vol. 6688 of *Proceedings of SPIE*, San Diego, Calif, USA, August 2007.

[42] F. Ferrari, F. Frontera, G. Loffredo et al., "New results on focusing of gamma-rays with Laue lenses," in *Optics for EUV, X-ray, and Gamma-Ray Astronomy IV*, vol. 7437 of *Proceedings of SPIE*, San Diego, Calif, USA, August 2009.

[43] G. Loffredo, F. Frontera, D. Pellicciotta et al., "The Ferrara hard X-ray facility for testing/calibrating hard X-ray focusing telescopes," *Experimental Astronomy*, vol. 20, no. 1–3, pp. 413–420, 2005.

[44] A. Kohnle, R. Smither, T. Graber, P. von Ballmoos, P. Laporte, and J. F. Olive, "Realization of a tunable crystal lens as an instrument to focus gamma rays," *Nuclear Instruments and Methods in Physics Research A*, vol. 408, no. 2-3, pp. 553–561, 1998.

[45] P. von Ballmoos, T. Takahashi, and S. E. Boggs, "A DUAL mission for nuclear astrophysics," *Nuclear Instruments and Methods in Physics Research A*, vol. 623, no. 1, pp. 431–433, 2010.

Hindawi Publishing Corporation
X-Ray Optics and Instrumentation
Volume 2010, Article ID 401854, 10 pages
doi:10.1155/2010/401854

Review Article

Multilayer Laue Lens: A Path Toward One Nanometer X-Ray Focusing

Hanfei Yan,[1,2] Hyon Chol Kang,[3,4] Ray Conley,[2,5] Chian Liu,[5] Albert T. Macrander,[5] G. Brian Stephenson,[1,3] and Jörg Maser[1,4]

[1] *Center for Nanoscale Materials, Argonne National Laboratory, Argonne, IL 60439, USA*
[2] *National Synchrotron Light Source II, Brookhaven National Laboratory, Upton, NY 11973, USA*
[3] *Materials Science Division, Argonne National Laboratory, Argonne, IL 60439, USA*
[4] *Department of Advanced Materials Engineering and BK21 Education Center of Mould Technology for Advanced Materials and Parts, Chosun University, Gwangju 501–759, Republic of Korea*
[5] *Advanced Photon Source, Argonne National Laboratory, Argonne, IL 60439, USA*

Correspondence should be addressed to Hanfei Yan, hyan@bnl.gov

Received 12 May 2010; Accepted 13 September 2010

Academic Editor: Gene Ice

The multilayer Laue lens (MLL) is a novel diffractive optic for hard X-ray nanofocusing, which is fabricated by thin film deposition techniques and takes advantage of the dynamical diffraction effect to achieve a high numerical aperture and efficiency. It overcomes two difficulties encountered in diffractive optics fabrication for focusing hard X-rays: (1) small outmost zone width and (2) high aspect ratio. Here, we will give a review on types, modeling approaches, properties, fabrication, and characterization methods of MLL optics. We show that a full-wave dynamical diffraction theory has been developed to describe the dynamical diffraction property of the MLL and has been employed to design the optimal shapes for nanofocusing. We also show a 16 nm line focus obtained by a partial MLL and several characterization methods. Experimental results show a good agreement with the theoretical calculations. With the continuing development of MLL optics, we believe that an MLL-based hard x-ray microscope with true nanometer resolution is on the horizon.

1. Introduction

X-ray techniques have found numerous applications in life science, materials science, chemistry, medicine, and environmental science utilizing the unique properties of X-rays, such as penetration capability and sensitivity to structural and chemical information. The rapid growth of nanoscience in the last decade gives rise to a strong demand for X-ray microscopy tools capable of providing information at the nanoscale. Many of the grand challenges we are facing today may be tackled only when such tools become available. For example, chemical imaging of spatial heterogeneities at nanoscale in real catalysts is essential to understand the diffusion of reactants and reaction products within the porous catalyst crystals or grains of submicrometer dimensions [1]. However, because of the weak refractive interaction of materials for X-rays (the difference of the refractive index from unity is typically 10^{-5}–10^{-6} for hard X-rays), it is very difficult to fabricate X-ray nanofocusing optics. This difficulty is the major obstacle preventing current X-ray microscopy from achieving nanometer resolution.

There have been significant efforts devoted to the development of X-ray focusing optics utilizing the refraction, reflection and diffraction properties of X-rays. Recent progress in mirrors [2], zone plates (ZPs) [3], and refractive lenses [4] has pushed the frontiers of X-ray nanofocusing well below 50 nm. However, many of these optics may be close to their practical limits for focusing. The fabrication of zone plates is limited by lithographic methods; it is hard to fabricate zone plate with below 15 nm outmost zone width, a requirement for a small focus, and with an adequately high aspect ratio required for high efficiency at hard X-ray energies. Refractive lens have achieved ~50 nm [2] in two dimension (2D) [4], but a further reduction

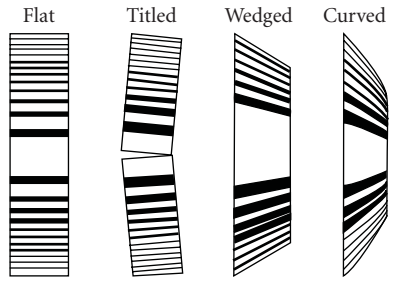

Figure 1: Types of multilayer Laue lens arrangements: flat, tilted, wedged, and curved. Reprinted from [18]. Copyright 2007, with permission from the American Physical Society.

of the focal size is very challenging, again because of the fabrication difficulty. Kirkpatrick–Baez (K-B) mirrors have made tremendous progress. Very recently, a line focus of 7 nm in one dimension (1D) has been achieved by multilayer K-B mirrors [5].

The multilayer Laue lens (MLL) [6, 7], a novel diffractive optic, has been shown in theory to be able to focus X-rays to well below 1 nm with very high efficiency. MLL is a special type of linear ZP which consists of thousands of alternating layers grown by the magnetron sputter deposition technique [8]. The thin film deposition method allows the growth of very thin zones with an almost limitless aspect ratio, overcoming the two difficulties encountered in the fabrication of lithographically produced ZP. MLL is a 1D focusing optic. To date a line focus of 16 nm with a focusing efficiency over 30% has been achieved by a partial MLL structure at an energy of 19.5 keV [9]. However, for real applications, two MLLs focusing in orthogonal directions have to be assembled to produce a 2D focus[10], similar to K-B mirrors. Because an MLL is operated in transmission geometry and the size of the lens is on the order of tens of microns, assembling two MLLs to produce a 2D focus is feasible.

2. Types of MLLs

MLLs can be treated as special 1D zone plates with structures optimized for dynamical diffraction. They may be divided into four different types: the flat, tilted, wedged, and curved MLLs as shown in Figure 1. The MLL possessing flat zones is no different from a 1D ZP. It consists of thousands of alternating layers (zones) with alternating optical constants. The position of the jth zone follows the zone plate law

$$x_j^2 = j\lambda f + \frac{j^2\lambda^2}{4}, \tag{1}$$

where λ is the wavelength of the incident X-ray and f is the focal length. According to the Rayleigh criterion, the diffraction-limited focus of a 1D lens is determined by

$$s = \frac{0.5\lambda}{NA}. \tag{2}$$

Here, s is the focus size and NA is the numerical aperture of the lens, approximately equal to $x_{\max}/f$. If one utilizes the full-width-at-half-maximum as the focus size, a smaller factor 0.44 in (2) should be used. By combining (1) with (2), one obtains

$$s = \Delta x_{\min}, \quad \Delta x_{\min} = \frac{\lambda f}{2x_{\max}}\sqrt{1 + \frac{x_{\max}^2}{f^2}}, \tag{3}$$

where $\Delta x_{\min}$ is the outmost zone width of the lens. Thus, one has to fabricate a thinner outmost zone in order to achieve a smaller focus.

Conventionally, the focusing performance of a ZP is calculated by the geometric-optical theory, which neglects the X-ray diffraction effect inside the optic. The focusing efficiency for the hth focusing order is given by [11]

$$c_h = \begin{cases} \dfrac{2\exp(-2kw\overline{\eta})}{h^2\pi^2}\left[\cosh(kw\Delta\eta) - \cos(kw\Delta\delta)\right], & \\ \qquad\qquad h = \pm 1, \pm 3, \pm 5, \ldots, & \\ 0 \qquad\qquad h = \pm 2, \pm 4, \pm 6, \ldots, & \end{cases} \tag{4}$$

where $k = 2\pi/\lambda$, $\Delta\delta = \delta_A - \delta_B$, $\Delta\eta = \eta_A - \eta_B$ and $\overline{\eta} = (\eta_A + \eta_B)/2$. Here, $n_A = 1 - \delta_A + i\eta_A$ and $n_B = 1 - \delta_B + i\eta_B$ are the refractive indexes of the lens materials A and B and w is the section depth of the lens along its optical axis. For high efficiency, the phase change, $kw\Delta\delta$, associated with the optical path difference in zones made of materials A and B has to be close to (or equal to if there is no absorption) π for maximum efficiency. However, this simple calculation is valid only when the lens is "optically thin"; that is, the section depth w is less than $(2\Delta x_{\min})^2/\lambda$. At the optimum section depth, this condition is usually satisfied for zones with widths no smaller than 10 nm. For thinner zones, the dynamical diffraction effect becomes dominant and the zones diffract X-rays more like crystals. Studies on a thick-sectioned multilayer have shown clearly the dynamical diffraction effect [12]. Therefore, an MLL that can focus X-rays to below 10 nm and with reasonable efficiency is operating in the dynamical diffraction regime, akin to Laue diffraction in the transmission geometry. This property is very different from a conventional ZP. In such cases, the MLL performance is dependent on the titling angle because of the diffraction effect; an improvement is expected when the MLL is tilted by a small angle to satisfy the Bragg condition at one particular region within the MLL stack. This consideration leads to the tilted MLL.

For a tilted MLL, the Bragg condition is only fulfilled at a specific location of the lens because the zone width varies gradually from the center to the outmost region of the lens, limiting the maximum improvement that can be obtained by tilting alone. A further improvement can be achieved by a wedged MLL, in which zones are tilted progressively to the incident radiation. The approximate Bragg condition is satisfied everywhere if the numerical aperture (NA) of the lens is moderate. To achieve a focus size close to the wave length, a parabolic (plane wave illumination) or elliptical (spherical wave illumination) zone profile is required to exactly fulfill the Bragg condition. We will have a detailed discussion on the properties of different types of MLLs in the following sections.

3. Simulation Methods

As has been discussed in the preceding section, the geometrical theory becomes invalid for an MLL with a high NA. For this type of volume diffractive optic, the transmission function at the exit surface of the lens cannot be obtained by a simple ray tracing calculation of the flight path of the incident X-rays. One has to employ a full-wave diffraction theory to study the propagation and diffraction of X-ray waves inside the lens. This was initially done by Maser and Schmahl [13], who applied locally a 1D approach of the coupled-wave theory (CWT) to study the variation of the local diffraction with respect to the thickness and slant of the zones. With the assumption that the MLL can be locally decomposed into periodic gratings, their approach is limited to cases of $w \ll f$ with a relatively small NA corresponding to a resolution of 2 nm. Later on and using similar assumptions, Levashov and Vinogradov studied the variation of the total diffraction efficiency with thickness [14]. A numerical approach based on a parabolic wave equation with the paraxial approximation was developed by Kurokhtin and Popov [15]. More recent methods of solving the parabolic wave equation using eigenfunctions have been reported [16, 17]. The validity of these approaches is limited to a relatively small NA due to the paraxial approximation. To overcome the limitation of these approaches and to provide a model that is valid to a spatial resolution on the order of the wavelength of radiation used, we developed a modeling method that is analogous to Takagi-Taupin equations in crystallography by realizing the similarities of X-ray diffraction between an MLL and a single crystal [18].

The scalar wave equation describing the electric field variation of a monochromatic X-ray wave in a medium with susceptibility function $\chi(\mathbf{r})$ is given by

$$\nabla^2\mathbf{E}(\mathbf{r}) + k^2\Big[1+\chi(\mathbf{r})\Big]\mathbf{E}(\mathbf{r}) = 0. \tag{5}$$

We begin by considering an MLL with flat zones whose positions satisfy (1). After a variable transform,

$$x' = \sqrt{x^2+f^2} - f, \tag{6}$$

the structure of the MLL becomes periodic in terms of x' so that the susceptibility function can be expanded into a puesdo-Fourier series in terms of x

$$\chi(x) = \sum_{h=-\infty}^{\infty} \chi_h \exp[i\phi_h(x)], \qquad \chi_0 = \frac{\chi_A+\chi_B}{2},$$
$$\chi_{h\neq 0} = \frac{\chi_A-\chi_B}{2ih\pi}\left[1-(-1)^{|h|}\right], \qquad \phi_h = hk\left(\sqrt{x^2+f^2}-f\right). \tag{7}$$

For an incident wave, $\mathbf{E}_0^{(a)}(\mathbf{r})\exp(i\mathbf{k_0}\cdot\mathbf{r})$, we assume that a trial solution to the wave equation can be written as

$$\mathbf{E}(\mathbf{r}) = \sum_{h=-\infty}^{\infty} \mathbf{E}_h(\mathbf{r})\exp[i(\mathbf{k_0}\cdot\mathbf{r}+\phi_h)]. \tag{8}$$

Substituting (7) and (8) into (5) and equating terms with the same order h yield an infinite set of differential equations. We further simplify the system by neglecting second-order derivatives on $\mathbf{E}_h(\mathbf{r})$ and limiting the number of excited orders. The validity of these approximations is discussed in [18]. Eventually, we arrive at a set of differential equations

$$\frac{2i}{k}\nabla E_h\cdot\left(\mathbf{s}_0+\frac{\nabla\phi_h}{k}\right)+\beta_h(\mathbf{r})E_h+\sum_l \chi_{h-l}E_l\cos\vartheta_{hl}=0,$$
$$\beta_h \approx \frac{k^2-(k_0+\nabla\phi_h)^2}{k^2}, \qquad h,l=0,\pm1,\pm2,..., \tag{9}$$

with the boundary conditions

$$\mathbf{E}_0(\mathbf{r})\big|_{\text{entrance}} = \mathbf{E}_0^{(a)}(\mathbf{r})\Big|_{\text{entrance}}, \mathbf{E}_{h\neq0}(\mathbf{r})\big|_{\text{entrance}} = 0. \tag{10}$$

Here, $\mathbf{s}_0$ is a unit vector along the incident direction and ϑ_{hl} is the angle between the polarization direction of the hth and lth diffraction orders. The quantity, β_h, represents the deviation from the Bragg condition for the hth diffraction order. For other types of MLLs, (9) still holds but ϕ_h will possess a different functional form.

4. Properties of MLL

We have mentioned in the preceding section that the geometric theory is no longer valid for thick MLLs. In the following, we will employ the theoretical model in Section 3 to study the wave propagation and diffraction inside a thick MLL.

We start by considering a MLL with flat zones and a radius, $x_{\max}$, of 30 μm. At 19.5 keV (= 0.634λÅ), it has a focal length f of 4.72 mm and an outmost zone width of 5 nm. The lens is made of WSi_2 and Si. An incident plane wave with σ polarization impinges on the MLL with an angle θ to its surface normal, as shown in Figure 2. A θ angle of zero degree corresponds to the normal incidence. Because $x_{\max}$ is much smaller than f, one can neglect the second term on the right hand side of (1) and arrive at

$$\phi_h \approx \frac{h\pi}{\lambda f}x^2, \qquad \beta_h \approx -2\frac{hx}{f}\sin\theta-\left(\frac{hx}{f}\right)^2. \tag{11}$$

Substituting this into (9) and limiting the calculation to only consider a finite number of diffraction orders, we can numerically solve the exit wave front for different diffraction orders. In our definition, a diffraction order with a negative sign corresponds to a converging wave, so that the negative first order is the primary focusing order and is of most interest.

To begin, we will study the dependence of the local diffraction intensity at the exit surface of the lens, $|E_{-1}(x, w)|^2$, on the section depth, w, under the condition of normal incidence ($\theta = 0$). Two values, $w = 1.5$ and $w = 10\,\mu$m, are considered. These two cases correspond to a thin and thick lens, respectively. In the latter case, the phase change in two adjacent zones is π. The geometrical theory is invalid for a thick lens, and the dynamical diffraction model has to be employed. In the top panel of Figure 3(a), we plot the variation of the local diffraction intensity of the negative

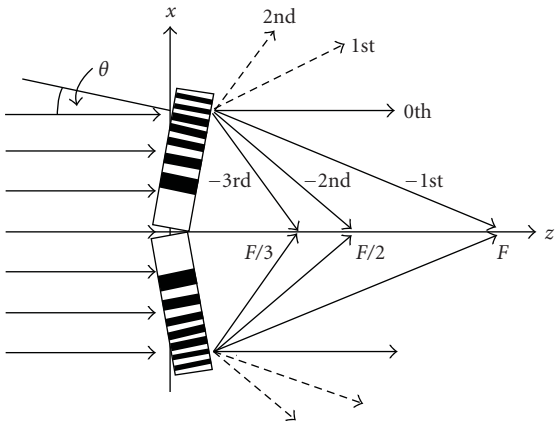

Figure 2: Schematic representation of a plane wave diffracted with a tilted MLL containing flat zones, in which many diffraction orders are excited. Reprinted from [18]. Copyright 2007, with permission from the American Physical Society.

first order calculated by the dynamical diffraction model (9) and the geometric model (4). One can clearly see that for the thin lens, both models yield almost identical results, but for the thick lens, they differ significantly in most regions except in the vicinity of the center where the thin lens approximation is still valid. For the thin lens, although the local diffraction intensity is low, it is nearly a constant across the lens. Therefore, all parts of the lens contribute equally to focusing and are effective. As a result, the thin lens' effective NA is equal to its physical NA, $x_{\max}/f$, as predicted by the geometric theory. In contrast, the local diffraction intensity of a thick lens drops down quickly to almost zero in the outer region. Lens positions beyond $x = 15\,\mu$m do not contribute to focusing as strongly as the inner parts. As a result, the effective NA of a thick MLL with flat zones is limited by the dynamical diffraction effect. A further increase in the physical NA of such a thick lens will not lead to a smaller focus in contrast to what happens for a thin lens.

Next, we will study the dependence of the lens' performance on the tilting angle. In the bottom panel of Figure 3(a), we plot the variation of the local diffraction intensity at a tilting angle θ of 1.6 milliradian. For the thick lens, a diffraction peak is observed around the position $x = 15\,\mu$m, where the Bragg condition is satisfied. The diffraction intensity drops down to zero around $x = 25\,\mu$m, much larger than that under the condition of normal incidence. Due to this tilting, one can see that not only is the efficiency enhanced, but also the effective NA is increased. For the thin lens, tilting has very little effect on its performance, as expected. We also plot the focusing efficiency of the negative first order (the normalized integrated diffraction intensity) as a function of both the depth and the tilting angle (Figure 3(b)). It can be seen that at a section depth of $13.5\,\mu$m and tilting angle of 2.1 milliradian a maximum focusing efficiency of 33% is reached. This efficiency is much higher than that in the conventional geometry (normal incidence, $\theta = 0$), which is about 9.2%. In addition, the focus size is reduced by tilting because the effective NA is increased. Figure 4 depicts the focus profiles at four different tilting angles at the same section depth of $13.5\,\mu$m. This plot clearly shows the effect of tilting. At the angle of 2.1 milliradian, one achieves the smallest focus with the highest efficiency.

We have shown that for an MLL with flat zones, the effective NA may be limited, depending on whether the dynamical diffraction effect becomes dominant. For an MLL with a very small outmost zone width, one can always achieve a diffraction-limited focus size if the section depth of the lens is small enough so that the thin lens approximation is valid. However, the efficiency has to be sacrificed. There is a tradeoff between the effective NA and the efficiency for this type of MLL. For instance, for an MLL with 1 nm outmost zone width, the achievable focus size and the efficiency vary with the depth w (Figure 5). In order to achieve a diffraction-limited focus size of 1 nm, the lens has to be thinner than $0.5\,\mu$m but its efficiency will decrease below 0.1%. Because of the extremely low efficiency, such a lens may not be useful in practice.

The conflict between the effective NA and the efficiency can be overcome by optimizing the MLL structure for dynamical diffraction; that is, each zone is progressively tilted to satisfy the Bragg condition. This consideration results in a wedged zone structure as shown in Figure 1. The Bragg condition is approximately fulfilled everywhere in a wedged MLL satisfying the modified zone plate law

$$x_j^2 = \left(j\lambda f + \frac{j^2\lambda^2}{4}\right)a(z)^2, \quad a(z) = 1 - \frac{z}{2f}. \tag{12}$$

Accordingly, the phase function, ϕ_h, is changed to

$$\phi_h = hk\left[\sqrt{x^2/a(z)^2 + f^2} - f\right]. \tag{13}$$

For a wedged MLL with 1 nm outmost zone width and with a focal length of 2.6 mm, we plot the local diffraction intensity of the zeroth, negative first, negative second, and negative third orders in Figure 6(a). The section depth is $16\,\mu$m, equal to the Pendellösung thickness for the maximum diffraction in the Laue geometry, $w = \lambda/2\sqrt{|\chi_{-1}\chi_1|}$. Within a close vicinity of the center, a low diffraction intensity of about 0.13 is observed and is in good agreement with the geometric calculation. This is because the lens in this region can still be considered thin. Around the position with a zone width of 20 nm ($x = 4\,\mu$m), the diffraction intensity jumps to about 0.7 and remains nearly a constant across the lens. The enhancement of the diffraction is due to the fulfillment of the Bragg condition so that strong dynamical diffraction is excited. Except in the region near the center, all other orders including the zeroth order (directly transmitted wave) are significantly suppressed. This is one of the great advantages of the wedged MLL because an order sorting aperture that blocks high orders may not be necessary. We obtain a diffraction-limited focus size (full-width-at-half-maximum) of 0.86 nm (Figure 6(b)), and a very high efficiency of 63% for the negative first order, which is much higher than the maximum efficiency achievable even by a conventional phase ZP.

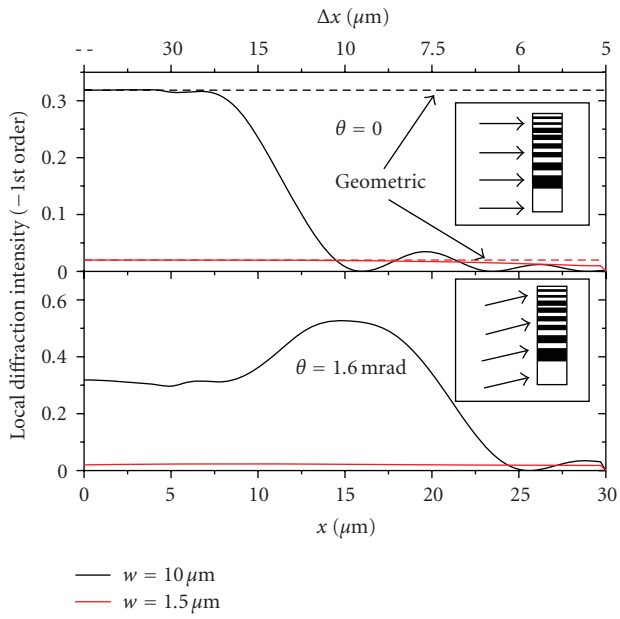

(a)

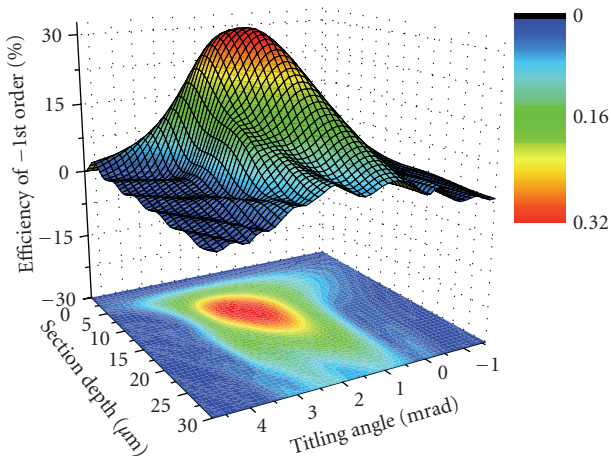

(b)

Figure 3: (a) The local diffraction intensity of the negative first order at the exit surface of the MLL with a section depth of 1.5 and 10 μm in the normal incidence and tilted geometries. The dashed lines are calculated by the geometrical theory (4) in the cases of thick section (black) and thin section (red), assuming a normal incidence. (b) Efficiency of the negative first order as a function of the tilting angle and the section depth.

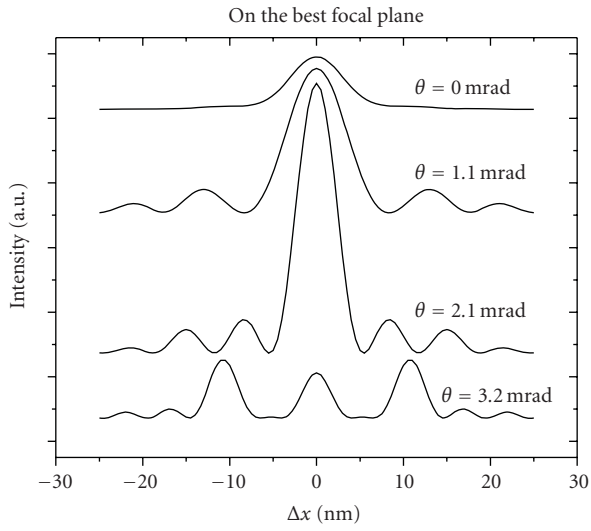

Figure 4: Focus profiles at four different tilting angles. Reprinted from [18]. Copyright 2007, with permission from the American Physical Society.

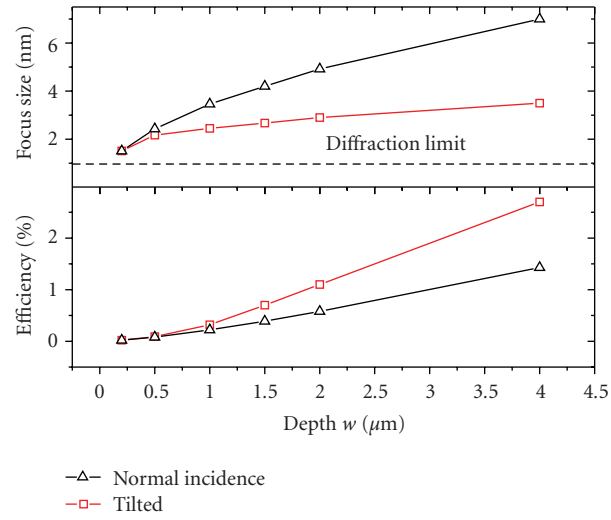

Figure 5: The efficiency and the focus size of an MLL with 1 nm outmost zone width at different section depths.

The wedged structure is still an approximation to the ideal MLL. In order to achieve a focus close to the wave length, elliptical (spherical wave illumination) or parabolic (plane wave illumination) zone profiles are needed. In such an MLL, the Bragg condition is satisfied exactly everywhere and the diffracted waves from each zone are in phase at the focus. Although the parabolic and elliptical profiles for multilayer focusing optics are well known and can be obtained from holography [19], the rigorous dynamical diffraction simulation shows that they are ideal as well for volume diffractive optics [18].

Real MLLs always possess imperfections. For example, a small growth error can result in a systematic deviation of the zone position from the zone plate law. This kind of error can be described by a zone plate equation with additional error terms [20] and can be incorporated into the simulation

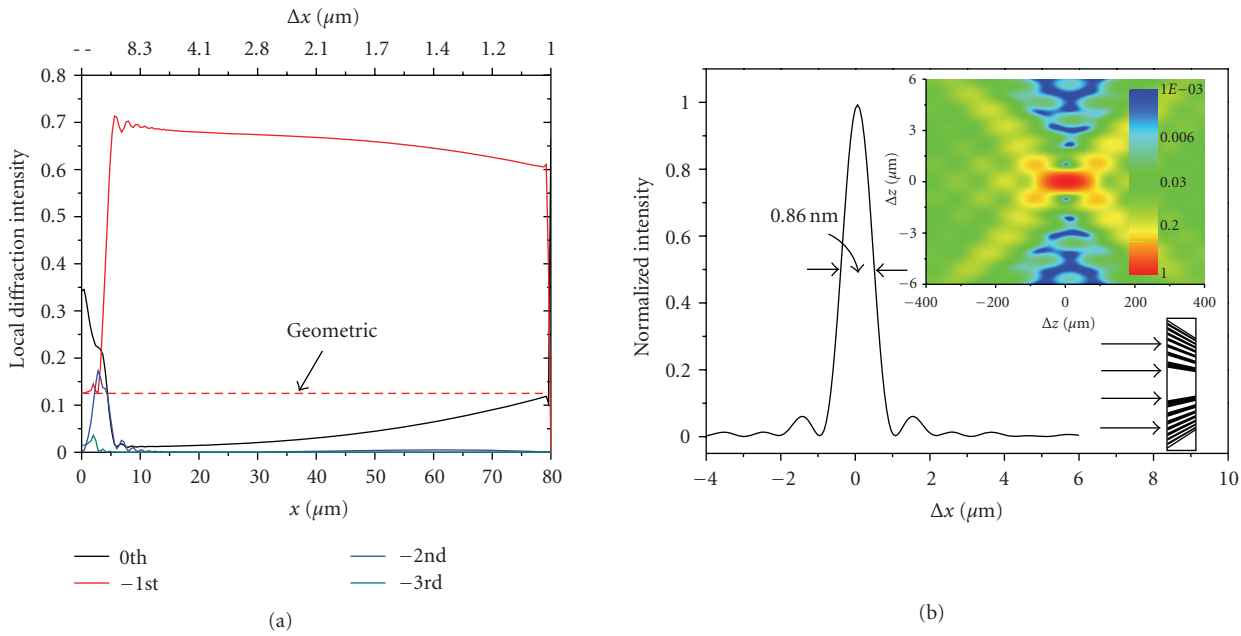

FIGURE 6: (a) The local diffraction intensity of the zeroth, negative first, second, and third orders of a wedged MLL with 1 nm outmost zone width. The dashed line is calculated by (4) and is for the negative first order. (b) The focus profile shows a diffraction-limited size of 0.86 nm. The inset on top is the isophote pattern near the focus (in logarithmic scale).

model by changing the phase function, ϕ_h, accordingly. With this type of imperfection, the focusing efficiency is usually nearly unchanged, but the focus is greatly distorted. Another type of imperfection is due to interfacial roughness, which is inevitable with layer thicknesses approaching atomic dimensions. If the roughness is uncorrelated, its effect is accounted for by a roughness factor similar to "Debye-Waller factor", $\exp(-M_h) = \langle \exp(i\boldsymbol{\rho}_h \cdot \mathbf{u}) \rangle$, where $\boldsymbol{\rho}_h = \nabla\phi_h$ is the hth local reciprocal-lattice vector, $\mathbf{u}$ is the random displacement vector of the interface, and the angle bracket denotes the statistical average [21]. The pseudo-Fourier coefficient of the susceptibility function, χ_h, has to be multiplied by this factor. Uncorrelated roughness usually results in a decrease of the focusing efficiency but has little effect on the focus profile, unless the RMS roughness becomes comparable with the zone width.

5. Fabrication Methods

The MLL growth was performed using DC magnetron sputtering systems located in the deposition laboratories of both the Advanced Photon Source (APS) [22] and the National Synchrotron Light Source-II (NSLS-II). To ensure the accuracy of the layer position, the thinnest layer is deposited first, which lessens the impact of any buildup in the thickness error during the growth. The multilayer structures were deposited on both diced Si (100) semiconductor-grade substrates and superpolished Si (100) substrates. The selection of substrate doping concentration was not closely controlled beyond a preference for low resistivity in order to assist with electron dissipation during postsectioning SEM analysis.

MLL deposition employed standard 3 inch MAK and Onyx-3 cathodes at the APS, and modified Polaris [23] 3 inch direct-gas injection cathodes at the NSLS-II. We chose the Si/WSi_2 materials system for several reasons. We have found that there is a compensation of compressive stresses in Si layers by tensile stresses in WSi_2 layers, with very little net accumulation [24]. The low buildup stress avoids the occurrence of delamination. In-situ X-ray reflectivity study also revealed that the noticeably rough Si layer can be sharpened by the WSi_2 layer [25], leading to interfaces with very small roughness. The speed of sputtering is another concern. The Si film growth rate is 10 Å to 13 Å·sec^{-1}, and the WSi_2 film growth rate is 30 Å to 40 Å·sec^{-1}, which are reasonably fast. Other than this system, other systems are being explored actively elsewhere for the MLL growth [26, 27].

For our MLL deposition, the WSi_2 targets used are 99.5% pure powder-hot-pressed with a nominal bulk density of 8.10 g·cm^{-3}, and the Si targets used are 99.999% pure and Boron-doped to allow for DC sputtering. No electrical bias or active temperature control is presently applied to the substrates; however, the substrate temperature does rise somewhat above ambient due to the presence of the plasma and energetic ion bombardment. The target to sample distance used varied from 70 mm to 110 mm. A base pressure of 10^{-8} Torr is reached before the commencement of pump throttling and Ar process gas injection. Ar gas pressure is held at a constant 2.3 milliTorr (with later growths using 4 milliTorr) by upstream MFC feedback control. Deposition was carried out using a constant cathode power of 215 watts for both guns, and each gun is turned on for 7 seconds before the start of each layer growth to stabilize. Uniform deposition

thickness is affected by raster-scanning the substrate over figured apertures by varying both the number of passes over this aperture and the translational velocity. Custom software controls design each pass over the sputtering gun to deposit as close as possible to 5 Å of film growth, or 10 Å per loop. The individual layer thickness requirement is then divided by the calculated number of loops, and the translational velocity is adjusted as needed. As the required thickness changes, additional passes over the appropriate sputtering gun and translational velocity adjustments are handled automatically.

Wedged MLL growth uses the same deposition process as described above but with sharply tapered masks to produce steep laterally graded layers [28]. Due to the inherent nature of magnetron deposition growth rate to decay over time, a compensation factor is included during the growth which adjusts the velocity appropriately. An initial MLL growth is characterized by extracting an inverse d-spacing line profile from SEM images [29] which is then used as feedback for a revised compensation factor for a second, accurate MLL growth.

Subsequent to growth, the multilayer must be sectioned and thinned to the requisite optical depth to form the halves of the MLL. A series of steps akin to that for making cross-section transmission electron microscopy samples has been found to be successful in making sections of sufficient perfection [30].

The physical aperture of the MLL is determined by the total deposition thickness. Currently, it is in the range of 10–40 μm and is mainly limited by two factors: (1) the accumulated interfacial stress as the deposition thickness increases and (2) the maximum deposition allowed by the consumable sputtering target. The former can be controlled by properly setting the growth parameters so that the stresses generated in two adjacent layers have opposite sign and cancel each other. The latter can be addressed by adding more sputtering targets. A new sputtering deposition machine with eight guns has been built at NSLS-II to grow MLLs with sizes over 100 μm [31], which will be comparable to the diameter of the high-resolution ZP that is currently available. This size is also in the same order of the coherence length of the third-generation synchrotron source so that the lens will be able to fully utilize the coherent flux delivered to it.

6. Characterization Methods

A typical setup of the line focus measurement for MLLs is shown in Figure 7. A beam-defining aperture is used to reduce the size of the incident plane wave to match the size of the lens. A fluorescence detector is used to record the excited fluorescence signal from the scanning object, and a scintillation detector with narrow slits in front is placed at a downstream position to record the transmission and diffraction signals. The lens tested has a focal length of 2.6 mm at 19.5 keV, an outmost zone width of 5 nm and a deposited thickness of 13.5 μm, corresponding to about 40% of the full structure. Figure 8 is a scanning electron microscopy image of the lens, showing 1588 zones with zone widths varying from 25 to 5 nm. Because the line focus is formed at the real optical axis through the center of the lens

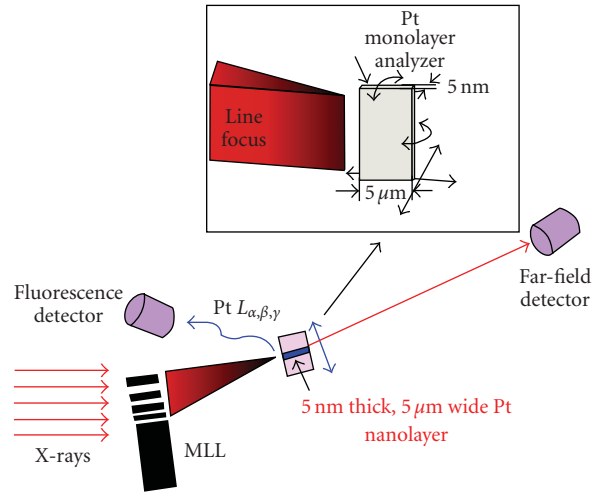

Figure 7: The experimental setup for the line focus measurement. The nanolayer has to be aligned parallel to the line focus in x and z directions.

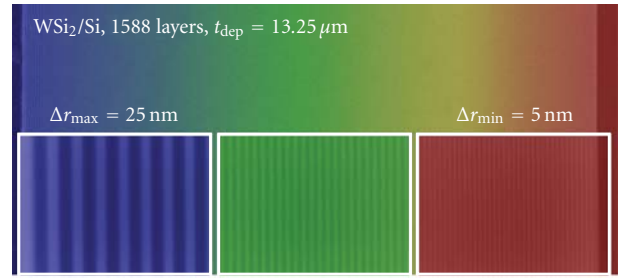

Figure 8: A scanning electron microscopy image of the MLL under test. The color is for aid to view and has no physical meanings. The white boxes on the bottom show the zoom-in images of the multilayer at three different locations. Reprinted from [9]. Copyright 2008, with permission from the American Institute of Physics.

and is several microns away from the directly transmitted wave, a beam-stop and an order sorting aperture are not required if the scanning object is smaller than this separation distance.

We first need to tilt the lens to the right angle for an optimum performance. This can be done by monitoring the variation of the transmission intensity as a function of the tilting angle. The top panel of Figure 9 depicts the transmission rocking curve, which has two symmetric attenuation dips around $\pm 0.1^\circ$. These two dips are ascribed to both the photoelectric absorption and the diffraction extinction effect. A theoretical simulation is also presented. One needs to make sure that the lens is tilted to the right direction so that the diffraction order for focusing, not for diverging, is enhanced. When the tilting angle becomes too large, significantly dissimilar from the Bragg condition for any d-spacing of the lens, the diffraction extinction becomes negligible. The difference of the attenuation at and off the Bragg condition is approximately equal to the focusing efficiency of the negative first order, since most of

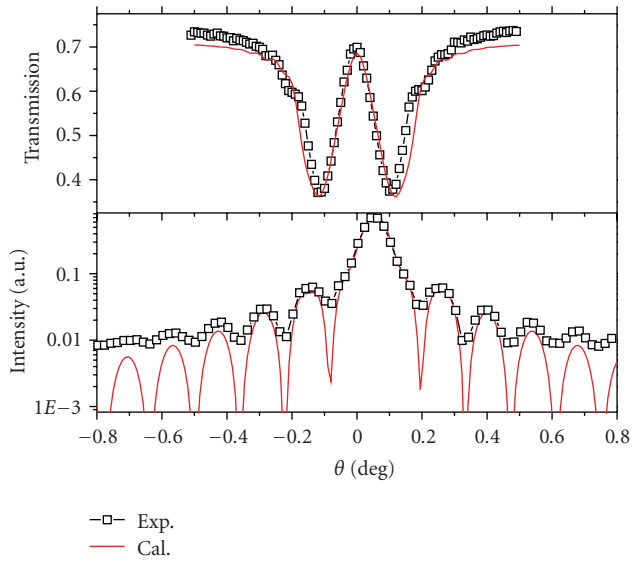

FIGURE 9: The transmission (top) and the diffraction (bottom) rocking curves.

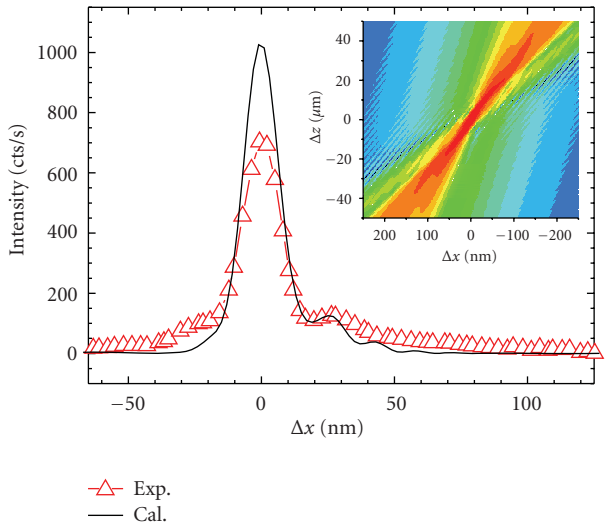

FIGURE 10: The measured line focus profile compared to the theoretical calculation. The inset shows the simulated isophote pattern near the focus. Reprinted from [9]. Copyright 2008, with permission from the American Institute of Physics.

the diffracted photons are focused to this order. From the measurement, an efficiency of 37% is observed.

We then move the scintillation detector along the x-axis to a position a few millimeters away from the optical axis to measure the variation of the diffraction intensity at a specific 2θ angle as the lens is rocked. The bottom panel of Figure 9 shows one of these diffraction rocking curves, together with the theoretical simulation. At a fixed 2θ angle, rocking the lens results in a change of the scattering vector, $\Delta\mathbf{Q}$, perpendicular to the reciprocal lattice vector. Because the lens diffracts X-rays in the transmission geometry (Laue case), its reciprocal lattice vector is perpendicular to its depth direction (z-axis). As a result, the scanned $\mathbf{Q}$ direction ($\Delta\mathbf{Q}$) is along the z-axis and the period of the intensity oscillation is determined by the section depth. Such a phenomenon is known as thickness fringes in crystal diffraction [32]. From this curve, we obtain a section depth of 13.4 μm.

A Platinum nanolayer with 5 nm thickness and 5 μm depth along the optical axis is used as the scanning object to measure the line focus profile. This depth is chosen to maximize the fluorescence signal; however, it also has to be smaller than the depth of focus, which is 9.4 μm in this case. The nanolayer needs to be well aligned with respect to the line focus so as to obtain the correct focus profile. In addition to the requirement of having a spatial placement exactly at the focal plane, the nanolayer also has to be aligned parallel to the line focus in both x and z directions (see Figure 7). The experimental result is shown in Figure 10, and is compared to the theoretical calculation. Although the diffraction-limited focus size is 12.5 nm for this lens, a 15 nm focus is expected from the simulation due to the dynamical diffraction effect at this section depth, which limits the effective NA. The measured focus is 16 nm, very close to the theoretical prediction.

7. Conclusion

Hard X-ray imaging with nanometer resolution has been identified as one of the key objectives for making full use of the continuing investment in major synchrotron facilities [33]. The key to realizing this challenging goal is the successful development of nanofocusing optics for hard X-rays. We provide a review on types, modeling approaches, properties, and fabrication and characterization methods of MLL optics and show that MLLs are well suited for hard X-ray nanofocusing with high efficiency. Sputtering deposition has demonstrated the capability of growing multilayers with layer thicknesses below 1 nm and with small interface roughness, making the fabrication of 1 nm MLL optics possible [22].

To date, a line focus of 16 nm with very high focusing efficiency has been obtained by MLL optics. For most real applications, however, a 2D focus is required. This can be achieved by placing two MLLs orthogonally [10], but the performance of the crossed pair is sensitive to many misalignments [34]. There has been great progress in the effort of 2D focusing by two crossed MLLs as well. An apparatus with eight degrees of freedom required for a full alignment of two MLLs has been designed and constructed [35, 36]. A 2D imaging resolution of sub-30 nm has been demonstrated using the MLL microscope [37]. With the continued development of MLL optics, we believe that hard X-ray microscopy with true nanometer resolution is on the horizon.

Acknowledgments

Work at Argonne, including use of the Advanced Photon Source and Center for Nanoscale Materials, was supported by the Department of Energy, Office of Basic Energy Sciences under Contract no. DE-AC-02-06CH11357.

Work at Brookhaven was supported by the Department of Energy, Office of Basic Energy Sciences under Contract no. DE-AC-02-98CH10886. One of the authors (H. C. Kang) would like to acknowledge the support by Basic Science Research Program through the National Research Foundation of Korea (NRF) funded by the Ministry of Education, Science, and Technology (MEST no. R15-2008-006-01000-0 and no. 2010-0023604).

References

[1] B. M. Weckhuysen, "Chemical imaging of spatial heterogeneities in catalytic solids at different length and time scales," *Angewandte Chemie - International Edition*, vol. 48, no. 27, pp. 4910–4943, 2009.

[2] H. Mimura, H. Yumoto, S. Matsuyama et al., "Efficient focusing of hard x rays to 25 nm by a total reflection mirror," *Applied Physics Letters*, vol. 90, no. 5, Article ID 051903, 3 pages, 2007.

[3] W. Chao, B. D. Harteneck, J. A. Liddle, E. H. Anderson, and D. T. Attwood, "Soft X-Ray microscopy at a spatial resolution better than 15 nm," *Nature*, vol. 435, no. 7046, pp. 1210–1213, 2005.

[4] C. G. Schroer, O. Kurapova, J. Patommel et al., "Hard X-Ray nanoprobe based on refractive X-Ray lenses," *Applied Physics Letters*, vol. 87, no. 12, Article ID 124103, 3 pages, 2005.

[5] H. Mimura, S. Handa, T. Kimura et al., "Breaking the 10 nm barrier in hard-X-Ray focusing," *Nature Physics*, vol. 6, no. 2, pp. 122–125, 2010.

[6] H. C. Kang, J. Maser, G. B. Stephenson et al., "Nanometer linear focusing of hard X Rays by a multilayer laue lens," *Physical Review Letters*, vol. 96, no. 12, Article ID 127401, 4 pages, 2006.

[7] A. T. Macrander, H. Yan, and H. C. Kang, "Nanofocusing of hard X-Rays with multilayer Laue lenses," in *Hand Book of Optics*, vol. 5, McGraw–Hill, New York, NY, USA, 2009.

[8] C. Liu, R. Conley, A. T. MacRander et al., "Depth-graded multilayers for application in transmission geometry as linear zone plates," *Journal of Applied Physics*, vol. 98, no. 11, Article ID 113519, 6 pages, 2005.

[9] H. C. Kang, H. Yan, R. P. Winarski et al., "Focusing of hard X-Rays to 16 nanometers with a multilayer Laue lens," *Applied Physics Letters*, vol. 92, no. 22, Article ID 221114, 3 pages, 2008.

[10] J. Maser, G. B. Stephenson, S. Vogt et al., "Multilayer Laue lenses as high-resolution X-Ray optics," in *Design and Microfabrication of Novel X-Ray Optics II*, vol. 5539 of *Proceedings of SPIE*, Denver, Colo, USA, August 2004.

[11] J. Kirz, "Phase zone plates for X Rays and the extreme uv," *Journal of the Optical Society of America*, vol. 64, no. 3, pp. 301–309, 1974.

[12] H. C. Kang, G. B. Stephenson, C. Liu et al., "High-efficiency diffractive X-Ray optics from sectioned multilayers," *Applied Physics Letters*, vol. 86, no. 15, Article ID 151109, 3 pages, 2005.

[13] J. Maser and G. Schmahl, "Coupled wave description of the diffraction by zone plates with high aspect ratios," *Optics Communications*, vol. 89, no. 2–4, pp. 355–362, 1992.

[14] V. E. Levashov and A. V. Vinogradov, "Analytical theory of zone plate efficiency," *Physical Review E*, vol. 49, no. 6, pp. 5797–5803, 1994.

[15] A. N. Kurokhtin and A. V. Popov, "Simulation of high-resolution X-Ray zone plates," *Journal of the Optical Society of America A*, vol. 19, no. 2, pp. 315–324, 2002.

[16] C. G. Schroer, "Focusing hard X Rays to nanometer dimensions using Fresnel zone plates," *Physical Review B*, vol. 74, no. 3, Article ID , 4 pages, 2006.

[17] F. Pfeiffer, C. David, J. F. van der Veen, and C. Bergemann, "Nanometer focusing properties of Fresnel zone plates described by dynamical diffraction theory," *Physical Review B*, vol. 73, no. 24, Article ID 245331, 2006.

[18] H. Yan, J. Maser, A. Macrander et al., "Takagi-Taupin description of X-Ray dynamical diffraction from diffractive optics with large numerical aperture," *Physical Review B*, vol. 76, no. 11, Article ID 115438, 13 pages, 2007.

[19] E. Spiller, *Soft X-Ray Optics*, SPIE Optical Engineering Press, Bellingham, Wash, USA, 1994.

[20] H. Yan, H. C. Kang, J. Maser et al., "Characterization of a multilayer Laue lens with imperfections," *Nuclear Instruments and Methods in Physics Research, Section A: Accelerators, Spectrometers, Detectors and Associated Equipment*, vol. 582, no. 1, pp. 126–128, 2007.

[21] H. Yan, "X-Ray dynamical diffraction from multilayer Laue lenses with rough interfaces," *Physical Review B*, vol. 79, no. 16, Article ID 165410, 12 pages, 2009.

[22] R. Conley, C. Liu, C. M. Kewish, A. T. Macrander, and C. Morawe, "Multilayer growth in the APS rotary deposition system," in *Advances in X-Ray/EUV Optics and Components II*, vol. 6705 of *Proceedings of SPIE*, San Diego, Calif, USA, September 2007.

[23] http://www.msi-pse.com/Polaris.htm.

[24] C. Liu, R. Conley, and A. T. Macrander, "Film stress studies and the multilayer Laue lens project," in *Advances in X-Ray/EUV Optics, Components, and Applications*, vol. 6317 of *Proceedings of SPIE*, San Diego, Calif, USA, August 2006.

[25] Y. P. Wang, H. Zhou, L. Zhou, R.L. Headrick, A.T. Macrander, and A.S. Ozcan, "Interface roughness evolution in sputtered WSi_2/Si multilayers," *Journal of Applied Physics*, vol. 101, no. 2, Article ID 023503, 6 pages, 2007.

[26] T. Koyama, T. Tsuji, H. Takano et al., "Performance test of Mo/Si and $Mosi_2$/Si multilayer Laue lenses," *Journal of Physics: Conference Series*, vol. 186, no. 1, Article ID 012066, 2009.

[27] T. Koyama, S. Ichimaru, T. Tsuji et al., "Optical properties of MoSi2/Si multilayer laue lens as nanometer X-Ray focusing device," *Applied Physics Express*, vol. 1, no. 11, Article ID 117003, 3 pages, 2008.

[28] R. Conley, C. Liu, J. Qian et al., "Wedged multilayer Laue lens," *Review of Scientific Instruments*, vol. 79, no. 5, Article ID 053104, 4 pages, 2008.

[29] N. Jahedi, R. Conley, B. Shi, J. Qian, K. Lauer, and A. Macrander, "Metrology of multilayer Laue lens structures by means of scanning electron microscope imaging," *Nuclear Instruments and Methods in Physics Research, Section A: Accelerators, Spectrometers, Detectors and Associated Equipment*, vol. 616, no. 2-3, pp. 89–92, 2010.

[30] H. C. Kang, G. B. Stephenson, C. Liu et al., "Sectioning of multilayers to make a multilayer Laue lens," *Review of Scientific Instruments*, vol. 78, no. 4, Article ID 046103, 3 pages, 2007.

[31] R. Conley, N. Boueta, J. Biancarosaa et al., "The NSLS-II multilayer laue lens deposition system," in *Advances in X-Ray/EUV Optics and Components IV*, vol. 7448 of *Proceedings of SPIE*, San Diego, Calif, USA, August 2009.

[32] A. Authier, *Dynamical Theory of X-ray Diffraction*, Oxford University Press, Oxford, UK, 2002.

[33] NSLS-II conceptual report, http://www.bnl.gov/nsls2/project/.

[34] H. Yan, J. Maser, H. C. Kang, A. Macrander, and B. Stephenson, "A theoretical study of two-dimensional point focusing by two multilayer Laue lenses," in *Advances in X-Ray/EUV Optics and Components III*, vol. 7077 of *Proceedings of SPIE*, San Diego, Calif, USA, August 2008.

[35] D. Shu, H. Yan, and J. M. Maser, in Proceedings of SRI-2008 (to be published in Nucl. Instrum. Methods A).

[36] D. Shu, H. Yan, and J. M. Maser, USA Patent No. 7597475.

[37] H. Yan, V. Rose, D. Shu et al., submitted.

Hindawi Publishing Corporation
X-Ray Optics and Instrumentation
Volume 2010, Article ID 743485, 17 pages
doi:10.1155/2010/743485

Review Article

Diffractive X-Ray Telescopes

Gerald K. Skinner[1,2]

[1] *CRESST and NASA-GSFC, Greenbelt, MD 20771, USA*
[2] *Department of Astronomy, University of Maryland, College Park, MD 20742, USA*

Correspondence should be addressed to Gerald K. Skinner, skinner@milkyway.gsfc.nasa.gov

Received 25 February 2010; Accepted 17 August 2010

Academic Editor: Stephen L. O'Dell

Diffractive X-ray telescopes using zone plates, phase Fresnel lenses, or related optical elements have the potential to provide astronomers with true imaging capability with resolution several orders of magnitude better than available in any other waveband. Lenses that would be relatively easy to fabricate could have an angular resolution of the order of microarcseconds or even better, that would allow, for example, imaging of the distorted spacetime in the immediate vicinity of the supermassive black holes in the center of active galaxies What then is precluding their immediate adoption? Extremely long focal lengths, very limited bandwidth, and difficulty stabilizing the image are the main problems. The history and status of the development of such lenses is reviewed here and the prospects for managing the challenges that they present are discussed.

1. Introduction

Diffractive optics, in the form of zone plates and various forms of Fresnel lenses and kineforms, already play a major role in the manipulation of X-ray beams at synchrotron facilities and in X-ray microscopy. Diffractive X-ray telescopes, in contrast, exist almost entirely as concepts on paper and as proposals and suggestions, though as will be seen demonstrations of scaled systems have been made. Because of atmospheric absorption, their potential application is almost certainly limited to astronomy (and specifically to astronomy from space), perhaps including solar and planetary studies. However, for certain objectives within that field they present the prospect of enormous advances over current instrumentation, which relies largely on grazing incidence reflective optics (reviewed elsewhere in this series [1–3]). The most notable prospect that diffractive telescopes offer is that of superb angular resolution, with improvements of perhaps six orders of magnitude on the current state of the art. But even neglecting benefits from the imaging properties, their capability of concentrating the flux received over a large effective area onto a small, and hence low background, detector may also offer unique advantages in some circumstances.

This paper will consider the various concepts that have been proposed and discuss the current state of development of the technologies necessary to turn the ideas into a real system. For simplicity the term X-rays will often be used to apply to both X-rays and gamma rays, there being no clear distinction or borderline between the two. The paper will be limited to techniques exploiting the wave nature of X-ray (and gamma ray) radiation, so excluding, for example, the use of screens with zone-plate-like patterns singly as coded masks [4] or in pairs to produce Moiré fringes [5, 6]. Within wave optics, systems based on multilayer optics or on crystal diffraction are not addressed (the latter are reviewed elsewhere in this series [7]).

2. History

The basic diffractive optics imaging element can be considered to be the zone plate (ZP) in which an aperture is divided into transparent and opaque regions according to whether radiation passing through them would arrive at some selected focal point with a phase such as to interfere constructively or destructively. The resulting pattern is shown in Figure 1(a). The first zone plate was made by Lord Rayleigh in 1871 though this work was never published (see [8, 9]) and it was Soret [10] who first described them in print in 1875. Already in 1888 Rayleigh [11] realized that problems of high background due to undiffracted light and

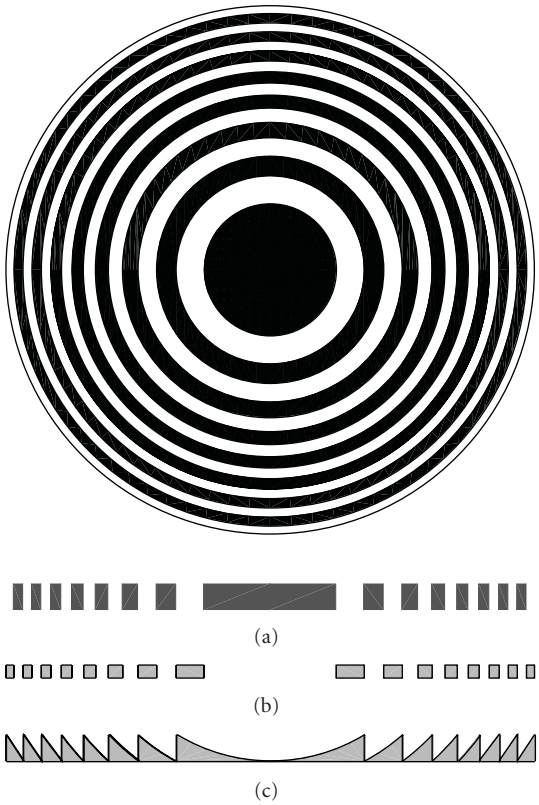

Figure 1: Three basic forms of diffractive optics for X-ray telescopes. (a) A zone plate (ZP), with opaque and transparent regions, (b) A phase zone plate (PZP), in which the shaded zones transmit radiation with a phase shift of π, (c) A phase Fresnel lens (PFL), in which the thickness is everywhere such that the phase is shifted by the optimum angle. The profile in (c) is drawn for a converging lens assuming the refractive index is less than unity.

low efficiency could be overcome by using phase-reversal zone plates (PZPs) in which the opaque regions are replaced by ones whose thickness is chosen to introduce a phase shift of π (Figure 1(b)). Wood demonstrated the operation of PZPs ten years later [12]. Miyamoto [13] further extended the concept, introducing the term phase Fresnel lens (PFL below) for an optic in which the phase shift is at each radius the same as that for an ideal conventional lens (Figure 1(c)).

The possibility of using ZPs for X-ray imaging seems first to have been seriously considered in the 1950s by Myers [14] and by Baez [15], who were concerned with X-ray microscopy. In 1974 Kirz [9] pointed out that the relative transparency of materials in the X-ray band and the fact that X-ray refractive indices differ slightly from unity would allow PZPs to be constructed even for high energy photons, so obtaining much higher efficiency.

Remarkably, as early as the 1960s simple zone plates were used for solar (soft) X-ray astronomy. Elwert [16] obtained the agreement of Friedmann to replace the pinholes in two of the pinhole cameras on a 1966 NRL solar-viewing sounding rocket flight with small zone plates designed to operate in lines at 51 Å (0.246 keV) and 34 Å (0.367 keV). Although the attitude control malfunctioned, blurred images were obtained. Over the next few years the technique was used, in particular by the Tübingen and Utrecht groups, for solar imagery from sounding rockets at energies up to 0.8 keV (e.g., [17, 18]). One of the disadvantages of zone plates proved to be the halo due to zero-order diffraction surrounding the focal point of a simple zone plate. Ways were found of alleviating this problem by using only the zones within an annular region [19, 20].

At much the same time Wolter I grazing incidence telescopes were becoming available for soft X-ray solar imaging—the first was flown on a sounding rocket in 1965 [21] and two were used on the Apollo Telescope mount on Skylab [22]. With the size of instrumentation that was feasible at that epoch, the grazing incidence technology proved superior. For cosmic observations as well as solar, it has become the imaging technique of choice except where the need for very wide fields of view or operation at high energies precludes its use, in which case nonfocussing devices such as coded mask or Compton telescopes are used.

As a result of the success of grazing angle reflective optics, diffractive X-ray optics for astronomical applications tended to be forgotten. In a 1974 PhD thesis Niemann [23] did discuss the possible use of diffractive optics for extra-solar astronomy and in 1996 Dewey et al. [24] proposed a mission concept in which patched blazed diffraction gratings based on the technology developed for the AXAF mission (now Chandra) would approximate a PZP. But it is only comparatively recently that there has been a revival of interest in the possibility of using diffractive optics for X-ray and gamma-ray astronomy in particular circumstances where it may offer unique advantages. Several authors (e.g., [25–30]) have pointed out that the angular resolution potentially available with diffractive X-ray telescopes exceeds by many orders of magnitude the practical limits of reflective optics.

Meanwhile there have been major advances in diffractive X-ray optics for nonastronomical applications, driven in particular by the availability of synchrotron sources and interest in X-ray microscopy with the best possible spatial resolution. For reasons discussed below, most of the effort has been towards lenses with structures on an extremely small scale, even if the diameter is also small. For astronomical telescopes on the other hand fineness of structure would be of secondary importance, but large apertures are essential.

3. Theory

3.1. Basic Parameters. A zone plate such as illustrated in Figure 1(a) can be conveniently characterized by the outside diameter, d, and the pitch, $p_{\min}$ of one cycle of the opaque/transparent pattern at the periphery where it is smallest (the number of cycles is assumed to be large so that a local characteristic period can be defined). The focal length for radiation of wavelength λ is then given by

$$f = \frac{p_{\min} d}{2\lambda}, \tag{1}$$

a relationship that applies equally to PZPs and PFLs. In terms of photon energy E and physical units this becomes

$$f = 403.3\left(\frac{p_{\min}}{1\,\mu\text{m}}\right)\left(\frac{d}{1\,\text{m}}\right)\left(\frac{E}{1\,\text{keV}}\right)\text{m}, \tag{2}$$

making clear that focal lengths of systems of interest for X-ray astronomy are likely to be long.

Diffractive X-ray optics has so far been employed almost exclusively for microscopy and for other applications for which *spatial* resolution is all important, but for telescopes, it is the *angular* resolution that counts. For ideal PFLs one can use the usual rule that the diffraction-limited angular resolution expressed as half-power diameter (HPD) is

$$\begin{aligned}\Delta\theta_d &= 1.03\,\frac{\lambda}{d} \\ &= 263\left(\frac{E}{1\,\text{keV}}\right)^{-1}\left(\frac{d}{1\,\text{m}}\right)^{-1}\ \text{micro-arcseconds}\ (\mu'') \qquad (3)\\ &= 0.501\left(\frac{p_{\min}}{f}\right), \qquad (4)\end{aligned}$$

(using the Rayleigh criterin, the numerical factor 1.03 would be the familiar 1.22). The same expression can in practice be used for ZPs and PZPs with a large number of cycles (Stigliani et al. [31] present an exact solution). Assuming a simple single lens system, the corresponding dimension in the image plane is then

$$\Delta x = f\Delta\theta_d = 0.501\,p_{\min}. \tag{5}$$

This is also approximately the spatial resolution of a microscope with a diffractive lens, explaining why the main drive in X-ray diffractive optics technology has so far been towards reducing $p_{\min}$. ZPs with zones of less than 15 nm, corresponding to $p_{\min} < 30$ nm, have been reported [32]. If the angular resolution of a telescope is to be limited only by diffraction, then it is important that the distance Δx be larger than the spatial resolution of the detector. Equation (5) then implies that $p_{\min}$ should *not* be too small. Current state of the art detectors have pixel sizes from 5–10 μm (CCDs at X-ray energies) to a fraction of a millimeter (pixelized CZT or Ge detectors for hard X-rays and gamma-rays). Although the centroid of the released charge can in some circumstances be localized to better than one pixel, the range of the electron which receives energy from the incoming photon sets a limit on the spatial resolution that can be obtained. So $p_{\min}$ for diffraction-limited X-ray telescopes is likely to be at least of the order of tens to hundreds of microns.

3.2. Lens Profile. A simple zone plate is inefficient because it is only 50% transmitting and because much of the radiation is not diffracted into the primary focus (order $n = 1$) but is undiffracted ($n = 0$) or diffracted into secondary focii ($n < 0$, $n > 1$). Table 1 shows that even if it is perfect the efficiency of a ZP is only ~10%.

For a ZP the depth of the profile is simply dictated by the requirement that the material be adequately opaque; the only upper limit is that imposed by manufacturing considerations. High density, high atomic number, materials are generally to be preferred. Taking Tungsten as an example and assuming 45% open area to provide for support structures, 90% opacity implies 130 gm^{-2} at 10 keV or 2.9 kg m^{-2} at 100 keV.

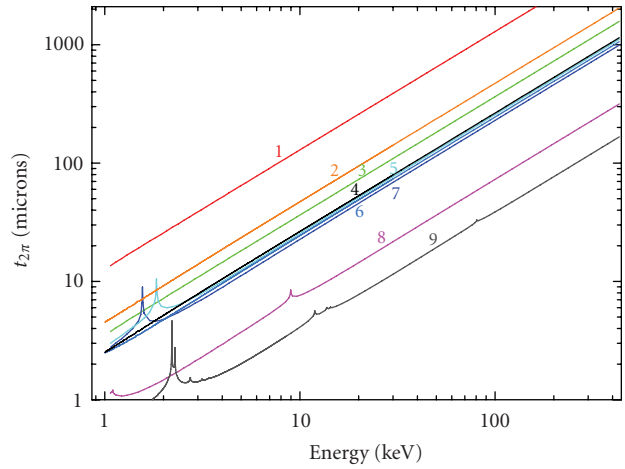

FIGURE 2: The thickness, $t_{2\pi}$, necessary to shift the phase of X-rays by 2π for some example materials. From top to bottom Li (1, red) Li, Polycarbonate (2, orange), Be (3, green), B_4C (4, light blue), Si (5, cyan), LiF (6, light blue), Al (7, dark blue), Cu (8, violet), and Au (9, grey).

For PZPs and PFLs on the other hand, the thickness of the profile and the transparency of the material are critical. The nominal thickness of a PZP is that which produces a phase shift of π. The complex refractive index of the material may be written

$$\mu = 1 - \frac{r_e\lambda^2}{2\pi}n_0(f_1 + if_2) = 1 - \delta - i\beta, \tag{6}$$

where r_e is the classical electron radius, n_0 is the number of atoms per unit volume, and $f = f_1 + if_2$ is the atomic scattering factor. The required thickness is then $(1/2)t_{2\pi}$, where $t_{2\pi}$ is λ/δ. Well above the energy of any absorption edges f_1 approaches the atomic number, so δ is proportional to λ^2 and $t_{2\pi}$ to λ^{-1}, or to E.

The practicability of X-ray PZPs relies on the fact that although the wavelengths λ are extremely short, δ is also very small. Consequently $t_{2\pi}$ is in a range, from microns to millimeters, where fabrication is practicable and where the absorption losses in traversing the required thickness of material are not too serious. Figure 2 shows some values of $t_{2\pi}$ as a function of photon energy for some materials of interest.

In the case of PFLs, the surface of each ring is ideally part of a paraboloid. This is evident if the lens is regarded as a thick refractive lens with the thickness reduced by multiples of $t_{2\pi}$. Usually the maximum height is $t_{2\pi}$ though $t_{4\pi}t_{6\pi}\cdots$ lenses can be made, with a correspondingly reduced number of rings. At large radii the small sections of paraboloids are almost straight and the cross-section is close to a triangular sawtooth. With some fabrication techniques it is convenient

Table 1: Comparison of the efficiency of ideal zone plates (ZPs), phase zone plates (PZPs), and phase Fresnel lenses (PFLs).

	Efficiency (primary focus) $n = 1$	Lost to absorption	Undiffracted $n = 0$	Secondary foci $n = -1, \pm 3, \pm 5 \cdots$
ZP	$1/\pi^2 = 10.1\%$	50%	25%	14.9%
PZP	$4/\pi^2 = 40.5\%$	0	0	59.5%
PFL	100%	0	0	0

Table 2: The primary focus efficiency, in the absence of absorption, of a stepped approximation to a PFL (see [34]).

Levels	2 (PZP)	3	4	8	16	n
Efficiency	40.5%	68.4%	81.1%	95.0%	98.7%	$\mathrm{sinc}^2(\pi/n)$

to use a stepped approximation to the ideal profile (e.g., [33]). High efficiency can be obtained with a relatively small number of levels (Table 2). Fabrication "errors" in the form of rounding of corners will actually tend to *improve* efficiency.

In contrast to ZPs, because of their lower absorption (see Section 3.5) low atomic numbers materials will generally be preferred for the fabrication of PZPs and PFLs. The low density that tends to be associated with low atomic number can however be something of a disadvantage as it implies larger $t_{2\pi}$ and so higher aspect ratio for the profile. In fact for a given photon energy the areal density of the active part of such devices is relatively independent of the material chosen. Typical values are only 30 gm^{-2} at 10 keV or 300 gm^{-2} at 100 keV. The additional mass of a substrate and/or support structure must be taken into account, but diffractive X-ray optics are intrinsically *very* light weight.

3.3. Field of View. Young [35] has discussed the off-axis aberrations of ZPs and the same conclusions can be applied to PZPs and in practice to PFLs. The expressions that he derives imply that in circumstances of interest for astronomy the most important Seidel aberration is coma, which only becomes important at off-axis angles greater than $4\lambda f^2/d^3$. In other terms, this implies that the number of diffraction-limited resolution elements across the coma-free field of view is $\sim 8(f/d)^2$. With the very large focal ratios that seem to be inevitable for diffractive X-ray telescopes, aberrations are entirely negligible over a field of view far larger than any practicable detector.

3.4. Chromatic Aberration and Other Limits to Angular Resolution. As well as the limit imposed by diffraction, given in (4), two other considerations are important for the angular resolution. The most important is the limit imposed by chromatic aberration. It is apparent from (2) that the focal length of a diffractive lens varies in proportional to the photon energy. At an energy E' away from the nominal energy E, radiation will converge in a cone towards a displaced focus (Figure 4). In the absence of diffraction, purely geometric considerations imply that this would lead to a focal spot corresponding to an angular size

$$\left|\frac{E' - E}{E}\right|\left(\frac{d}{f}\right). \tag{7}$$

Unless the spectrum of the radiation being imaged is a very narrow line with negligible continuum emission, blurring due to photons with energy other than the nominal energy has to be taken into account. Fortunately modern X-ray detectors of interest for the low flux levels that are encountered in astronomy are photon counting and energy resolving. Thus photons of energy outside a defined bandwidth can be disregarded when analyzing the data. Consequently in the most common case of a broad line and/or continuum spectrum it is the energy resolution of the detector that has to be used for ΔE in (7) and that dictates the degree of chromatic aberration.

At X-ray energies the most widely used imaging detectors are CCDs, that typically have an energy resolution of $\sim$150 eV at 6 keV, corresponding to $\Delta E/E = 2.5\%$, or active pixel sensors with similar capability [36]. In the 100–1000 keV region Germanium detectors can achieve $\Delta E/E \sim 0.25\%$–1%, though the (fractional) resolution is not as good at lower energies. Position-sensitive Germanium detectors are now becoming available (see e.g., [37], where the possibility of their use in a "Compton" configuration to reduce background by selecting only those events that are consistent with photons that may have passed through a lens is also discussed). Pixelated CZT arrays are approaching the performance of Germanium detectors and do not need cooling (Li et al. [38] report 0.61%–1.64% at 662 keV for a variety of single pixel detectors and small arrays). Microcalorimeter detectors are reaching energy resolutions of 2.5–5 eV at 6 keV [39, 40], corresponding to $\Delta E/E \sim 0.05\%$, but this performance is currently only achieved in single detector elements or small arrays. Braig and Predehl [30] have even suggested that a Bragg crystal monochromator might be used in the focal plane of a diffractive telescope and that $\Delta E/E \sim 0.01\%$ might be achieved in this way.

As discussed in Section 3.1, the spatial resolution of the detector can be important as well. The net resolution is thus in general a combination of three components

Diffraction. Rewriting the expression in (4) in terms of energy for consistency

$$\Delta\theta_d = \frac{1.03}{d}\frac{hc}{E}. \tag{8}$$

Chromatic Aberration. Equation (7) allows the *maximum* extent of the spread due to chromatic aberration, and in the absence of effects due to diffraction, to be written

$$\Delta\hat{\theta}_c = \frac{1}{2}\frac{d}{f}\frac{\Delta E}{E}. \tag{9}$$

Detector Resolution. Characterizing this by a pixel size, one has

$$\Delta\theta_p = \frac{\Delta x}{f}. \tag{10}$$

Diffraction limited performance will only be obtainable if the second and third components are negligible compared to the first. The energy bandwidth could be estimated by comparing $\Delta\theta_d$ and $\Delta\hat{\theta}_c$, but as these are different measures of the widths of very different PSF profiles a better approach is to consider the range of energies for which the wavefront error at the edge of the lens remains below some value. It is usual to place the comparatively strict limit of $\lambda/4$ corresponding to a Strehl ratio (the ratio between the peak brightness and that for an ideal, diffraction-limited system) of $8/\pi^2 \sim 80\%$. Yang [41] use a limit twice as large and other criteria lead to even wider bandwidths. For $\lambda/4$ it is found [35] that

$$\frac{\Delta E}{E} = 4\frac{f}{d^2}\frac{hc}{E} = \frac{1}{N_F}, \tag{11}$$

where N_F is the number of Fresnel zone in the PFL (twice the number of periods for a $t_{2\pi}$ lens).

3.5. Absorption. The efficiencies discussed so far ignore absorption. In evaluating such effects a key parameter is the critical Fresnel number defined by Yang [41]

$$N_0 = \frac{\delta}{2\pi\beta} = \frac{2}{t_{2\pi}\mu_{\text{abs}}}, \tag{12}$$

where $\mu_{\text{abs}} = 4\pi\beta/\lambda$ is the linear absorption coefficient. N_0 measures the relative importance of refraction and absorption. It can be thought of as the number of Fresnel zones in a refractive lens whose maximum thickness is equal to the absorption length. Example values are shown in Figure 3.

Kirz [9] has shown how in the presence of significant absorption the optimum thickness of a PZP is somewhat lower than $t_{2\pi}/2$. For $\beta/\delta = 1$ the (primary focus) efficiency is maximized if the thickness is reduced to 0.73 of this value. Similarly it can be shown that the efficiency of a PFL made from a material in which the absorption is important is maximized if the profile is modified as shown in Figure 5. Nöhammer et al. [42] discuss this issue in more detail. Efficiencies with and without this adjustment are shown as a function of N_0 in Figure 6. The improvement is not large, but the modified profile is actually likely to be lighter and easier to fabricate. Note that the optimum form would be different if the objective were to minimize either the undiffracted (zero-order) flux or that in higher orders, rather than maximize the flux diffracted into the prime focus.

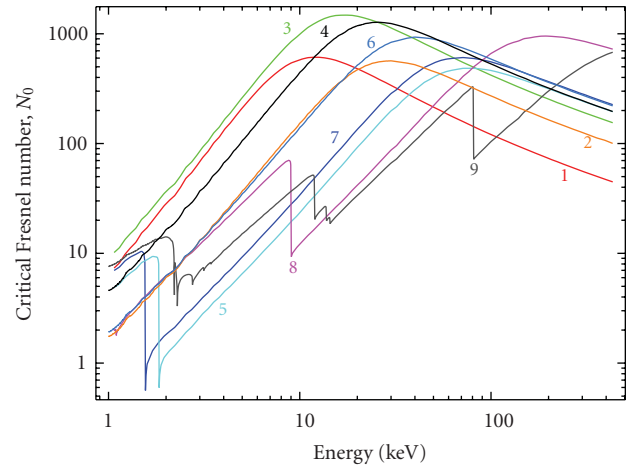

Figure 3: The critical Fresnel number, N_0, for some example materials. Numbers, colors, and materials as in Figure 2.

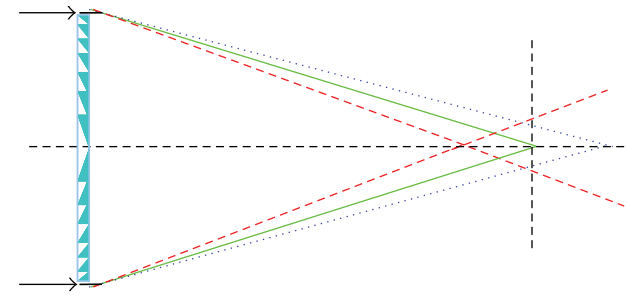

Figure 4: The effect of chromatic aberration. As the focal length of a diffractive lens is proportional to photon energy, ignoring diffraction, at energies differing by δE from the nominal energy E radiation converges in a cone and intercepts the detector plane in a disc of size given by (7).

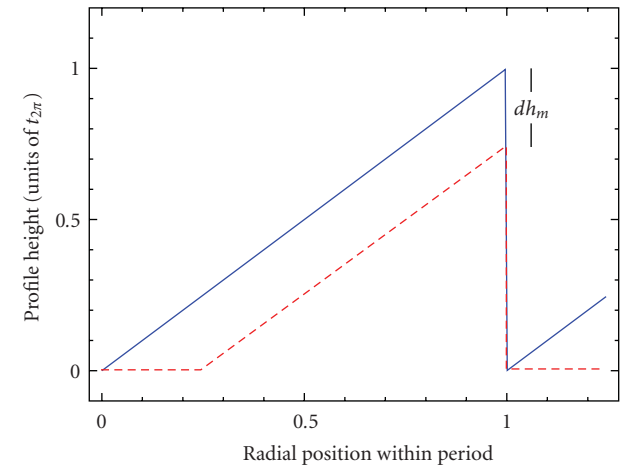

Figure 5: If significant absorption is taken into account the efficiency of a PFL can be improved by modifying the profile because improved throughput can be obtained at the expense of some phase error. The shape of the profile of a PFL that gives maximum efficiency for diffraction into the primary focus is shown by the dashed line.

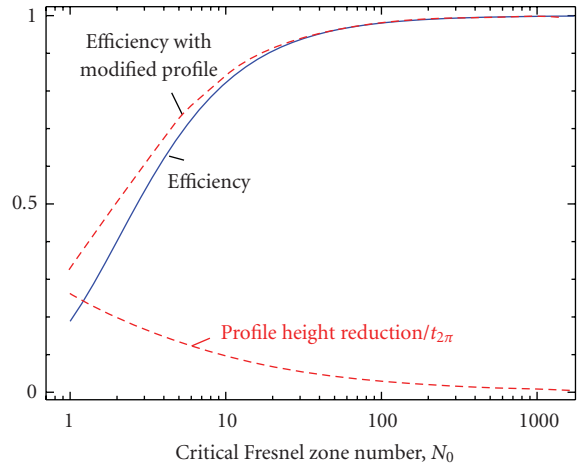

FIGURE 6: The efficiency of a PFL with significant absorption as a function of the critical fresnel number, N_0, of the material from which it is made. Also shown are the fractional amount, dh_m, by which the nominal profile height of $t_{2\pi}$ should be reduced as in Figure 5 to optimize the performance and the resulting efficiency.

4. The Advantages and Potential

4.1. Fabrication and Tolerances. Compared with grazing incidence optics of a comparable aperture, diffractive optics for X-ray astronomy are expected to be relatively simple to fabricate. As noted in Section 3, diffraction limited diffractive telescopes are likely to have profiles with a minimum period of microns to mm—well within the capabilities of current micro-electro-mechanical systems (MEMS) or single point diamond turning (SPDT) technologies. Because the refractive index of the lens is so close to unity, the tolerances on the profile are comparatively relaxed. Even for the sub-nm wavelengths involved, lens figuring to $\lambda/10$ optical precision requires only $t_{2\pi}/10$ tolerances, where $t_{2\pi}$ is ~10–1000 μm (Figure 2). Radial tolerances for the same precision are no tighter than $p_{\min}/10$ and will usually be of a similar order of magnitude to the vertical tolerance.

Figure 3 shows that at energies greater than a few keV it is possible to select materials with N_0 greater than a few, meaning that not only is absorption of X-rays in the material forming the active part of a PZP or PFL small, but the profile can be etched or machined into a somewhat thicker substrate (or deposited onto one) without serious absorption losses.

Thus the profile can be close to ideal and losses can be small so, at least at their design energy, diffractive X-ray telescope lenses can have an effective area that is very close to their geometric area, which may easily be several square meters.

A great advantage of optical elements used in transmission rather than reflection is their relative insusceptibility to tilt errors and out-of-plane distortions. Multiple reflection mirror systems in which the radiation undergoes an even number of reflections, such as Wolter grazing incidence optics, are better in this respect than single reflection systems (provided the relative alignment of the mirrors does not change). However they still act as "thick" lenses and if the optic (or a part of it) is tilted by angle $\delta\psi$ the resulting transverse displacement of rays passing through it leads to an aberration in the image on angular scale $\sim (t/f)\delta\psi$, where t is the distance between the principal planes, a measure of the thickness of the "lens". For Wolter optics t is the axial distance between the centers of the two mirrors. For the Chandra optics $(t/f) = 0.08$. Diffractive telescope lenses are very close to ideal "thin" lenses, having (t/f) ratios of 10^{-6}–10^{-9} or even smaller.

4.2. Applications of High Angular Resolution Diffractive Telescopes. The most obvious attraction of diffractive optics for X-ray telescopes for astronomy is the potential they offer for superb angular resolution. From (3) it is apparent that angular resolution better than a milli-arcsecond should be readily obtainable in the X-ray band. With optics a few meters in size working with hard X-rays, sub-micro-arcsecond resolution should be possible.

One of the original incentives for the recent reconsideration of diffractive optics for high energy astronomy was indeed the possibility that it offers of sub-micro-arcsecond resolution. As has been discussed in proposals to use X-ray interferometry for astronomy [43, 44], this is the angular resolution that would be needed to image space-time around the supermassive black holes believed to exist at the centers of many galaxies. Even our own Galaxy, the Milky Way, apparently harbors a black hole, Sgr A*, with a mass of $4.3 \times 10^6\,\mathrm{M}_\odot$ (where $\mathrm{M}_\odot$ is the mass of the sun) [45].

The Schwarzschild radius of a black hole of mass M is

$$R_s = \frac{2GM}{c^2} = 2.9\frac{M}{\mathrm{M}_\odot}km, \tag{13}$$

where G is the gravitational constant and c the vacuum velocity of light. The radius of the "event horizon" is R_s in the case of a nonrotating black hole or somewhat larger for one with angular momentum. For Sgr A* R_s corresponds to an angular scale of 10 μ''. The black holes at the centers of "active" galaxies (Seyfert galaxies, Quasars and giant radio sources) can be much more massive—for example that in M87 may be as much as 2000 times the mass of Sgr A* [46]. Their Schwarzschild radii will be correspondingly bigger, so despite their much greater distances (also by a factor of 2000 in the case of M87), R_S in many cases still corresponds to angular scales of 0.1–10 μ''.

Of course one does not expect to detect radiation from the black hole itself, but the gravitational energy released by matter as it approaches the event horizon is the origin of the extremely high luminosity of some of these objects. Simulations have been made showing how such radiation originating near to the event horizon, even from behind the black hole itself, should appear after being bent by the gravitational field (Figure 7). The distribution expected depends not only on the mass of the black hole but on its angular momentum and inclination angle.

Figure 8 indicates the angular resolution available to astronomers with the current state of the art. At present the best angular resolution is obtained at mm wavelength by VLBI (very long baseline interferometry, see [47] for a recent review). Current technologies, with transatlantic

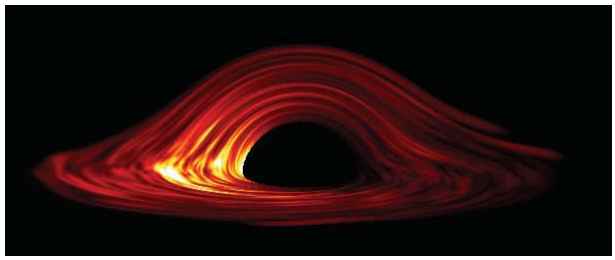

Figure 7: Simulation of X-ray radiation from the region surrounding a black hole. A Schwarzschild black hole is assumed to be seen at an inclination angle of 80°. For other details see Armitage and Reynolds [51].

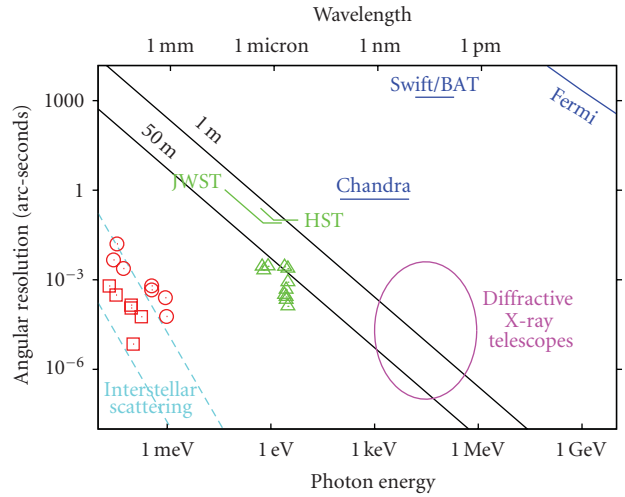

Figure 8: The angular resolution obtainable with different techniques and across the electromagnetic spectrum. The approximate domain in which diffractive X-ray optics are potentially of interest is indicated by an ellipse. Shown for comparison are (i) the Rayleigh limit for diffraction limited optics of 1 m and 50 m diameter (black lines), (ii) the angular resolution of current X-ray instruments (blues lines) and of the Hubble and James Webb Space Telescopes (green lines), (iii) the best resolution of some example optical interferometer systems (green triangles) and of some typical radio VLBI measurements (red circles), (iv) the diffraction-limited angular resolution possible with space VLBI (actual and near future; red squares), and (v) dashed lines (cyan) roughly indicating the region in which interstellar scattering becomes dominant at high galactic latitudes (left) and towards the galactic center (right). Note that while continuous lines refer to imaging instruments, the various symbols indicate the finest fringe spacing of interferometers which are not truly imaging.

baselines and wavelengths as short as 1 mm lead to angular resolutions down to 30–40 μ'', though so far only with a limited number of stations [48, 49], so a characteristic size is measured rather than forming an image. The Russian RadioAstron space VLBI mission, following in the footsteps of HALCA/VSOP, is due to be launched in 2011 and will extend baselines to 350,000 km, but the shortest wavelength is 13.5 mm. Although this should allow an angular resolution of 8 μ'', the actual resolution will be limited by interstellar scattering except at high galactic latitude. Consequently Sgr A* cannot be observed with the highest resolution. The Japanese-led Astro-G/VSOP-2 mission will go down to 7 mm in wavelength [50] and so be less affected by interstellar scattering (which is proportional to λ^2, as indicated by the dashed line in Figure 8), but with the maximum baseline limited by an apogee of only 25,000 km the best resolution will be 38 μ''. Astro-G launch has been delayed until at least 2013 due to technical problems with the deployable dish.

A useful basis of comparison across wavebands is the maximum baseline (or, for filled aperture instruments, the aperture diameter) in units of wavelength. Optical and infrared interferometers are pushing to higher and higher angular resolution, though as for VLBI, a limited number baselines provide sparse u–v plane coverage and allow model fitting, but only an approximation to true imaging. The 640 m and 330 m baselines of the SUSI and CHARA optical interferometers correspond to about 1.5 Gλ and 0.7 Gλ, respectively, while with radio VLBI fringes have been obtained with baseline as long as 6 Gλ [52]. A modest 1 m diameter lens working with 6 keV X-rays would have a size of 50 Gλ, and larger lenses and those working at higher energies have corresponding greater values. In addition such lenses would provide full u–v plane coverage up to this scale.

It is ironical that in the X-ray and gamma-ray bands, where the wavelengths are shortest and diffraction least limiting, the angular resolution at present obtainable is actually inferior to that possible at longer wavelengths. No currently planned X-ray mission will improve on, or even equal, the 0.5″ resolution of the Chandra grazing incidence mirror. While being subject to some constraints and limitations, discussed below, in appropriate circumstances diffractive optics offer the opportunity of improvements by up to 6 order of magnitude. X-ray imaging may then move from the present arc-second domain to the milli-arcsecond one, where stellar surfaces can be imaged and the formation of astrophysical jets examined in detail, and to micro-arcseconds, the resolution needed for black hole imaging.

4.3. Applications of Diffractive Optics for Light Buckets. Even if one does not take advantage of the imaging capabilities of diffractive X-ray optics, they may prove useful as flux concentrators. X-ray and gamma-ray astronomy is limited both by the small number of photons often detected and by background in the detector, mostly due to particles. The background is typically proportional to the detector area from which events are accepted. Catching photons requires large collecting area, whereas reducing background implies that the detector should be as small as possible. Applications of X-ray "light buckets" optimized for these purposes include high-resolution spectroscopy and fast timing measurements with moderate energy resolution such as studies of quasi-periodic oscillations, allowing the observation of certain general relativity effects such as frame dragging in compact black hole binaries.

At the energies where they can be used, grazing incidence reflective optics offer a solution to the problem of how to concentrate the flux from a large collecting area onto a small

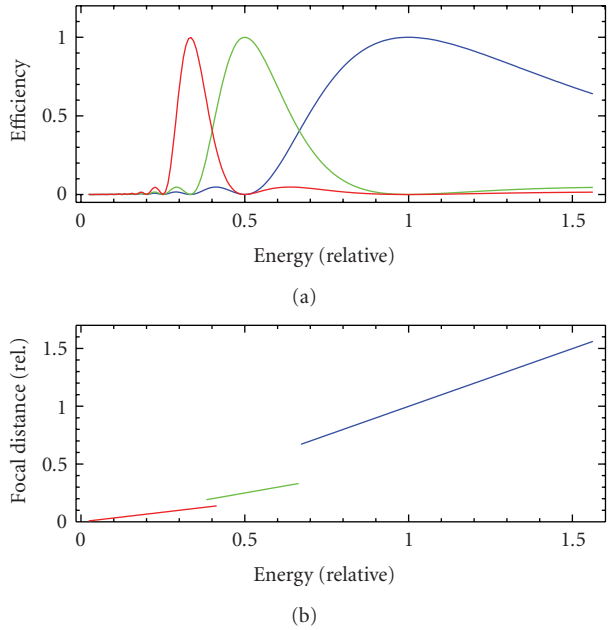

FIGURE 9: A PFL will work with relatively high efficiency over a broad band of energies provided that the detector plane is moved to the appropriate distance. The blue curve corresponds to the lens operating in the nominal mode. For the green and red curves the detector is assumed to be placed at the distances for the focii of the lens treated as a $t_{4\pi}$ and $t_{6\pi}$ one. Higher-order responses are not shown. Absorption effects are not taken into account in the plots based on [30].

detector area. Diffractive optics provide an alternative to grazing incidence mirrors—one that can be used even for high energies, and indeed whose performance is in many respects best at high energies.

For a concentrator one can drop the requirement of being able to resolve with the detector a spot size corresponding to the diffraction-limited angular resolution of which the optic might be capable. Smaller $p_{\min}$ may be used and so the focal length reduced. From the same geometric considerations that lead to (7), the bandwidth will be

$$\frac{\Delta E}{E} = 2\left(\frac{d_{\text{det}}}{d}\right), \tag{14}$$

whereas, assuming ideal efficiency for the optic and the detector, the flux is concentrated by a factor

$$C = \frac{A_{\text{eff}}}{A_{\text{det}}} \approx \left(\frac{d}{d_{\text{det}}}\right)^2 \approx 4\left(\frac{E}{\Delta E}\right)^2. \tag{15}$$

Thus where narrow spectral lines, or groups of lines, from a compact source are to be studied, significant advantages are available.

5. Overcoming the Difficulties

5.1. Minimizing Chromatic Aberration. Minimizing the effects of chromatic aberration is one of the biggest challenges to overcome in developing diffractive X-ray telescopes. The various measures that can be taken are discussed below.

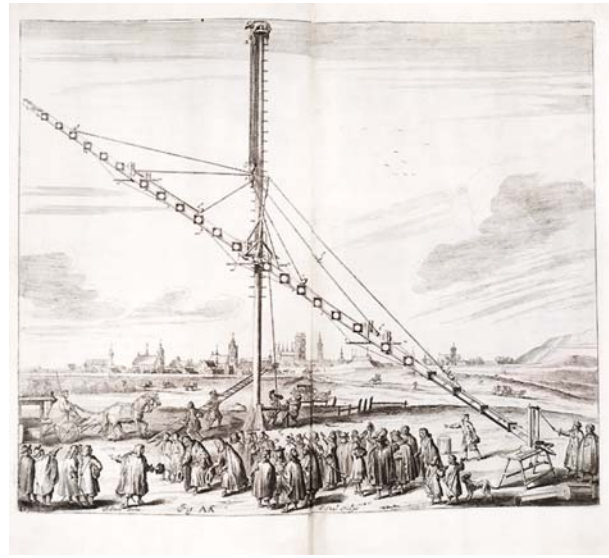

FIGURE 10: It has long been known that chromatic aberration is minimized by adopting a long focal length. Before the invention of the achromatic lens Hevelius built telescopes with 60 and (shown here) 140 foot focal lengths [53].

5.1.1. Refocusing. The first thing to note is that a diffractive X-ray lenses can work well over a broad range of energies provided the detector position is adjusted for each energy. Figure 9 shows the effective area of a PFL as a function of energy *if the telescope is refocused by adjusting the detector plane to the optimum position for each energy*. Braig and Predehl have pointed out [29] that, as indicated in the figure, well below the energy, E_0 for which a PFL was designed one can take advantage of the high efficiency near $E_0/2$, $E_0/3, \ldots$ because the lens acts like a $t_{4\pi}$, $t_{6\pi} \ldots$ one in the sense described in Section 3.2. As only one energy can be observed at a time this is not a very practical way of making broadband observations, but the approach could be useful in studying, for example, lines whose energy may be red-shifted to different extents in different sources. Note that at energies where the efficiency is less than unity, the lost flux appears in focii of other orders. The resulting halo to the PSF will have low surface brightness compared with the peak, but if it is troublesome it is possible to imagine blanking off the inner part of the lens area [29].

5.1.2. Improving Chromatic Aberration with Long Focal Lengths. From (7) it is clear that the effect of chromatic aberration on angular resolution is reduced if the focal ratio is large. For a given lens size, this means that the focal length should be as long as is consistent with other constraints. This is a long-known effect; before the invention of the (visible-light) achromatic doublet, astronomical telescopes were built with very long focal lengths in order to minimize chromatic aberration. Figure 10 shows an extreme example. Long focal lengths lead to a limited field of view (Section 5.4) and tend to have severe implications for the logistics of

maintaining the telescope in space (Section 5.2), but the bandwidth increases in proportion to f.

5.1.3. Segmenting Lenses for Multienergy Operation. Given that PFLs of large surface area are not too difficult to make but wide bandwidth is hard to achieve, it has been pointed out on a number of occasions (e.g., [26, 28, 29]) that the surface of a diffractive lens can be divided into regions tuned to different energies, thus providing information over a wider bandpass. The division may be into a few zones or into many, and an aperture may be divided radially or azimuthally, or both. The "subtelescopes" so formed may be either concentric, or parallel but offset.

An important consideration is the interference fringes that are produced when radiation of the same energy arrives in the same part of the detector after passing through the different regions of the diffractive optic, including those designed for quite different energies. In some of the work of Braig and Predehl [30, 54, 55] this issue is avoided by assuming, explicitly or implicitly, that the lens is made from many small segments that are subject to random position deviations such that their outputs add incoherently rather than coherently. In this case the resolution is of course that associated with the characteristic size of a segment (e.g., a few centimeters) rather than the lens as a whole (e.g., a few meters).

5.1.4. Diffractive-Diffractive Correction. In some circumstances the dispersion of a diffractive optical element can be corrected using that of a second diffractive optical element. However, as shown formally by Bennett [56] no optical system consisting of only two diffractive lenses can form a real image, free from longitudinal dispersion, from a real object. Buralli and Rogers [57] generalized this result to any number of diffractive elements. Michette et al. [58] has described some schemes that get around this constraint, but they do so only by allowing diffraction into multiple orders with a consequent loss in efficiency and they only provide correction at two disparate energies. Other optical systems that do correct one dispersive element with another either involve virtual images (or objects), or depend on reflective (or refractive) relay optics. The space-based visible light diffractive imager proposed by Koechlin et al. [59] is an example of the use of reflective relay optics.

X-ray telescopes that depend on both diffractive and reflective optics risk suffering the disadvantages of both, so correction schemes that depend on reflective relay optics do not seem very attractive. On the other hand, as will be noted below (Section 5.2), there are perhaps other reasons for considering incorporating a reflective component, so perhaps a feasible diffractive-reflective-diffractive design may eventually evolve.

5.1.5. Diffractive-Refractive Correction. Given the constraints that apply to diffractive-diffractive correction for telescopes forming real images, the possibility of correction using refractive optics has been widely considered. The constraints

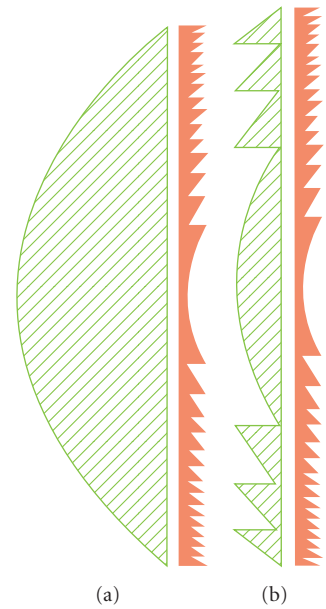

Figure 11: (a) the use of a refractive X-ray lens to chromatically correct a diffractive one. (b) A more practical configuration in which the refractive component is stepped to reduce absorption.

that preclude achromatic correction of one diffractive element with another arise because the dispersion of the two elements would be the same. Correction of a diffractive lens with a glass one is used in the visible part of the spectrum where glasses have a dispersion that differs from the E^{-1} dependence of the power of diffractive elements (e.g., [62]). The same principle can be applied to X-rays—purely refractive lenses can be made [63] and are widely used in X-ray microscopy and beam manipulation, often stacked to provide adequate power. Figure 2 shows that for most materials over most of the X-ray band $t_{2\pi}$ is proportional to E, implying that the power of a refractive lens, which depends on δ, is proportional to E^{-2}.

Figure 11, shows how in principle first-order correction of longitudinal chromatic aberration of a PFL (or ZP, PZP) is possible with a diffractive/refractive X-ray doublet [26, 27, 60]. Because the lens remains a "thin" one, there is almost no lateral color aberration. In the common situation where $t_{2\pi}$ is proportional to E, the focal length of the refractive component should be $-2f_d$, where f_d is that of the diffractive one, and the combined focal length is $2f_d$. In this case the number of Fresnel zones in the refractive component is half the number in the PFL. In the absence of absorption the bandpass is increased from $\Delta E/E = 1/N_F$ (11) to $\Delta E/E = 1/\sqrt{N_F}$ (e.g., [64]) (here N_F is the number of Fresnel zones in a single lens having the focal length of the combination).

It has already been noted (Section 3.5) that absorption becomes important in a refractive lens if N_z exceeds the critical Fresnel number N_0 for the material. As in practice N_0 is usually a few tens up to a few hundred (Figure 3), this sets a limit on the size of diffractive lens that can be corrected this way. Wang et al. [65] have suggested using the rapid energy dependence of δ just above absorption

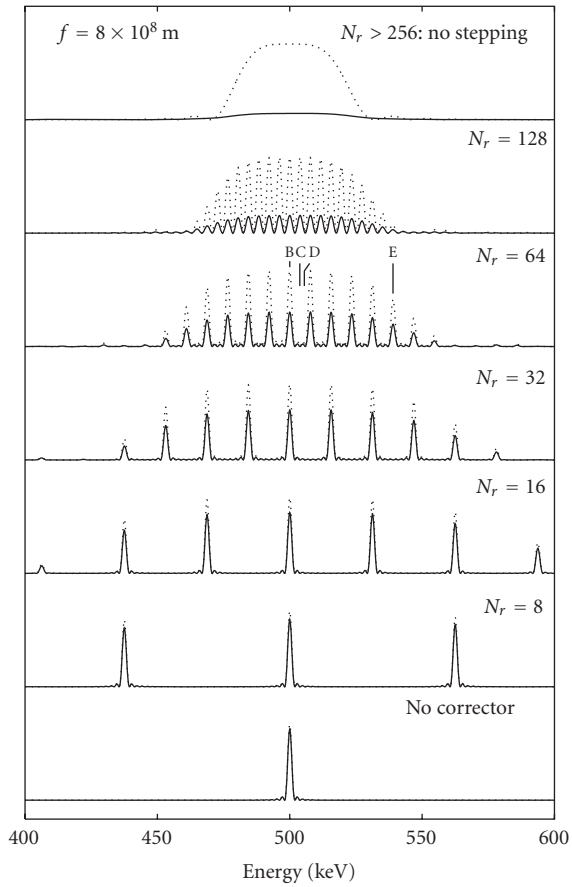

FIGURE 12: Simulated response of a refractive/diffractive achromatic doublet with different degrees of stepping of the refractive component. N_r corresponds to m in the text. The dotted lines indicate the response if there were no absorption. As the step size is made smaller, the density of coverage within the bandpass becomes worse but the effects of absorption become less serious and the band covered becomes wider, details in [60], from which this figure is taken.

edges to reduce the thickness of the refractive component needed. This approach only works at very specific energies, but it could make possible achromatic diffractive-refractive doublets several millimeters in diameter for microscopy and microlithography.

A PFL can be considered as a refractive lens in which the thickness is reduced Modulo($t_{2\pi}$). Thus it is natural to consider reducing the absorption in a refractive correcting lens by stepping it back, not Modulo($t_{2\pi}$) which simply would make it another PFL, but Modulo($m\ t_{2\pi}$) for some large integer m as in Figure 11. $t_{2\pi}$ varies with energy, so the value at some particular energy, E_0, must be chosen. Coherence is then maintained across the steps at this energy and at any other for which $m'[t_{2\pi}(E)] = m\ [t_{2\pi}(E_0)]$ for some other integer m'. This occurs at a comb of energies. In the regime where $t_{2\pi}$ is proportional to E, they occur at intervals such that $\Delta E/E \sim 1/m$. Detailed analyses of the response of PFLs with stepped achromatic correctors have been published [55, 60]. Examples are shown in Figure 12. As the step size is made smaller and the number of zones N_Z within the refractive component increases, the density of coverage within the bandpass decreases as N_Z^{-1} and the band covered becomes wider (improving approximately as $N_Z^{1/2}$) and the effects of absorption become less serious.

If one is willing to consider configurations involving the alignment of not just two widely spaced components, but three, then the configuration indicated in Figure 13 offers an even wider bandpass (see [28] and references therein; more details are provided in [60]). With the extra degree of freedom introduced by the separation between the two lenses it is possible to set to zero not just dz/dE (z being the axial position of the image), but also d^2z/dE^2. The bandwidth is increased as indicated in Table 3. The fact that the image is somewhat magnified compared with a single lens system of the same overall length could be advantageous. However as the magnification is energy dependent, care must be taken that lateral chromatic aberration does not limit the useful field of view (this will not be a problem if the detector has adequate energy resolution to allow post-facto scale-factor correction).

5.1.6. Axicons, Axilenses, and Other Wideband Variants. Variations of the ZP have been proposed in which the shape of the PSF is modified to (slightly) improve the angular resolution (e.g., [68]) or in the case of "photon sieves" to improve the resolution available with a given minimum feature size in the fabrication [69]. One such variant, the "fractal photon sieve" has been shown to have an extended spectral response [70], achieved because some of the power from the prime focus is diverted into focii at other distances. As will be seen below, this can be accomplished in other more controlled and efficient ways.

A diffractive lens can be considered as a circular diffraction grating in which the pitch varies inversely with radius so that radiation of a particular wavelength is always diffracted towards the same focal point. Regarded in this way, a PFL is a variable pitch phase grating, blazed in such a way that all of the energy goes into the +1 order. Skinner [66, 71] has discussed the application to X-ray telescopes of designs in which the pitch varies radially according to laws other than r^{-1}. They can be considered as forms of radially segmented lenses in which the pitch varies smoothly rather than in steps.

In an extreme case the pitch is constant and one has the diffractive X-ray axicon. Interestingly, to a first approximation the point source response function of an axicon is independent of energy. According to the Rayleigh criterion, the angular resolution is similar to that of a PFL of the same diameter working at the lowest energy, but the secondary diffraction rings are stronger so the HPD is larger. Indeed over a wide range of radii the PSF shape is such that the enclosed power simply increases, approximately linearly, with radius. In some respects the system should be regarded as an (achromatic) interferometer in which the information is contained more in the fringes than in the central response.

Intermediate designs are possible in which the bandpass is tailored to particular requirements based on the ideas of Sochacki [72] and of Cao and Chi [73]. This leads to the diffractive X-ray axilens discussed in [66]. The bandwidth

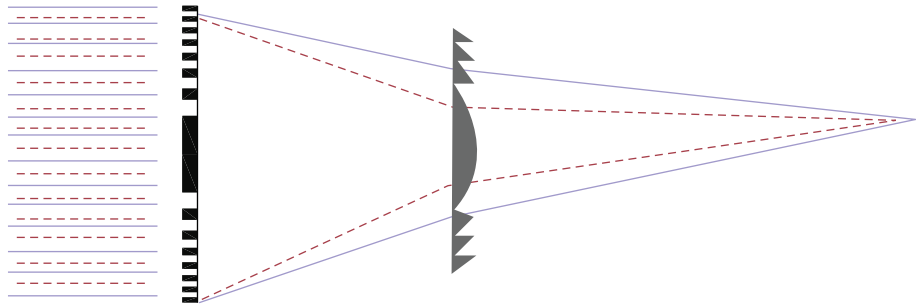

Figure 13: A variation on the refractive/diffractive achromatic doublet shown in Figure 11 in which the components are separated, allowing second-order correction of longitudinal color (Figure from [61]). A stepped version of the refractive component is shown.

Table 3: Achromatic correction of PFLs. Parameters are given for systems with the same overall length, f, at the nominal design energy, E_0, and for the case when $t_{2\pi}$ is proportional to energy, E. In the table ΔE is specified relative to E_0, and d is the diameter of the refractive component.

	Simple PFL	Doublet	Separated pair
Diffractive focal length	f	$f/2$	$f/3$
Separation	—	0	$f/9$
Refractive focal length	—	$-f$	$-8/27f$
Image plane distance	$f(1+\Delta E)$	$f(1+\Delta E^2+\cdots)$	$f(1+1.35\Delta E^3+\cdots)$
Image scale	f	f	$\frac{4}{3}f(1-(1/2)\Delta E+\cdots)$
Diffraction-limited bandwidth (fractional)	$4((f/d^2)(hc/E))$	$4((f/d^2)(hc/E))^{1/2}$	$((16/3)(f/d^2)(hc/E))^{1/3}$

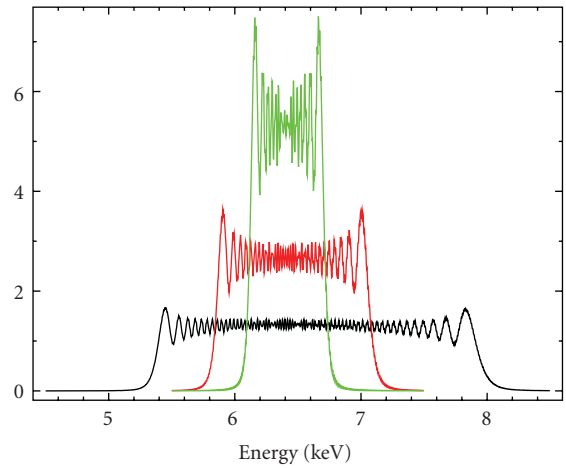

Figure 14: The on-axis response as a function of photon energy at a fixed distance of 100 m for Axilenses with different parameters [66].

can be selected at will; Figure 14 shows the response of some examples. For diffraction-limited operation, the area-bandwidth product tends to be no greater than that of a narrow band PFL. As the later has the advantage that the detector noise within a narrow band is small, devices of the axicon/axilens family are most likely to find application where an extended bandpass is essential, for example in order to include the whole of a broadened line or a group of lines.

5.1.7. Figures of Merit. Braig and Predehl [64] define an "Achromatic Gain" parameter $\mathcal{G}$ to measure the advantage that an achromatic system has over a simple lens. It is essentially the ratio of the effective areas, integrated over the energy range in the two cases.

The achromatic gain $\mathcal{G}$ may be generalized to quantify the advantage compared to a simple PFL of other variants as well as of achromatic combinations. As neither the resolution nor the image scale are necessarily the same in all cases, it is best to base the effective area on the flux within a diffraction-limited focal spot rather than peak brightness. Such a figure of merit was used in [71] where it was shown that axicons and axilenses have a "$\mathcal{G}$" close to unity—the extra bandwidth is obtained at the expense of effective area. The same is obviously true if a lens is segmented into areas devoted to different energies. On the other hand increasing the focal length is accompanied by an increase in bandwidth (11) and of $\mathcal{G}$.

Care must be used in interpreting this parameter. It measures the (square of) the improvement in signal-to-noise ratio on the assumption that the noise is dominated by photon statistics from the source. If the observation is dominated by detector background that is not source related, such as that due to particles, then a dependence on the square root of the bandwidth would be more appropriate. This assumes that the passband of the optic is wider than the energy resolution of the detector. In the detector background limited case, the background will also depend on the detector area over which the signal is spread, or on the area of a spot size dictated by the detector resolution if that is larger. Furthermore, by considering only the central spot, the information carried by the flux in high amplitude sidelobes such as occur in the PSF of axicons and axilenses, is ignored.

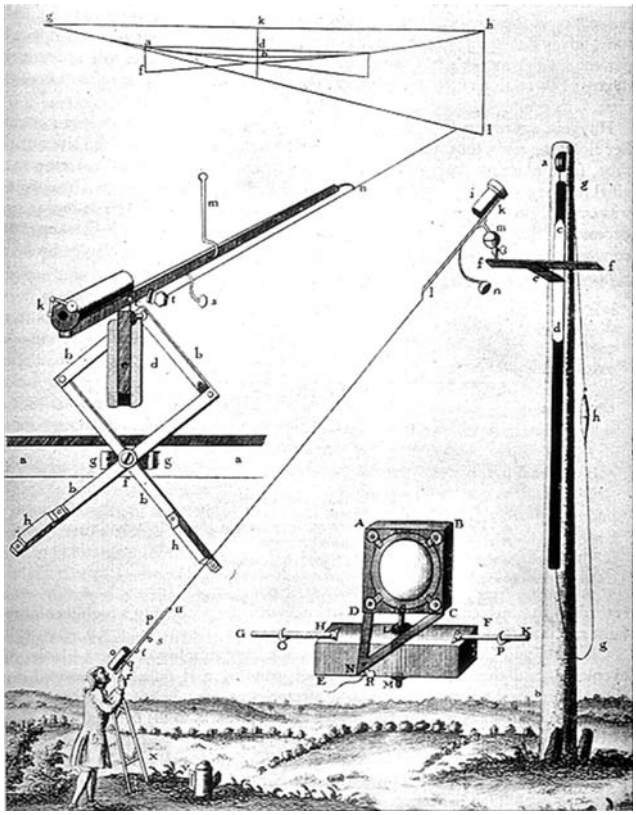

Figure 15: The concept of a telescope in which the objective of a telescope and the detector are not rigidly connected is not new. Christian Huygens (1629–1687) used this 210 foot focal length telescope [67]. Note that the design takes advantage of the relative immunity of a thin lens to tilt errors.

5.2. Focal Length: Formation Flying. Equation (2) makes it clear that the focal length, f, of any practical system is likely to be long, particularly at high energies. In addition in various respects discussed above, *very* large f will often give the best performance.

First, in Section 3.1 it was seen that a minimum focal length is required if spatial resolution of a detector at the prime focus is not to be a limiting factor. For example, even if the detector pixels are as small as 10 μm a resolution of 1 μ'' implies $f > 2000$ km. Gorenstein [74] has suggested that this problem might be alleviated if a grazing incidence reflecting telescope were used to reimage the prime focus, perhaps with a magnification by a factor of 20. Radiation from a particular sky pixel would in practice illuminate a very small part of the telescope surface because the latter would be very close to the focal plane. The reflecting surface would in effect remap positions over its aperture to pixels in a detector plane.

A second reason that long f may give the best performance is that as noted in Section 5.1 chromatic aberration is minimized if f is long.

Finally, based on (2), unless f is large diffractive lenses of a reasonable size will have a very small period $p_{\min}$ and fabrication will be more difficult and perhaps less precise.

For focal lengths of up to ~100 m, it is perhaps possible to consider telescopes with a boom connecting the lens and the detector assembly. Deployable booms of up to 60 m have been flown in space [75]; the record for the largest rigid structure in space is now held by ISS at over 100 m. On the other hand even for a focal length of 50 m, ESA studies for the proposed XEUS grazing incidence mirror X-ray mission concluded that a boom was unnecessary and that formation flying of separate spacecraft carrying the optic and the detector assemble offered a more viable solution [76]. It is interesting that a telescope without a rigid connection between objective and detector is not a new concept—see Figure 15.

Formation flying for a long focal length telescope mission implies maintaining two spacecraft such that the line joining them has a fixed direction in inertial space. Because of gravity gradients within the solar system, as well as disturbances such as those due to differences in solar radiation pressure, a continuous thrust will be needed on at least one spacecraft. Another consideration is that a major repointing of the telescope will require maneuvering one of the spacecraft by a distance $\sim f$.

Some of the issues associated with formation flying of two spacecraft for a diffractive X-ray telescope mission have been briefly discussed in the literature [25, 29]. Internal studies at NASA-GSFC's Integrated Mission Design Center of possible missions based on this technique have considered the issues more deeply. Krizmanic et al. [77] has reported on one of these and updated some of the conclusions. The missions studied were considered ambitious, but possible. A single launcher would launch both lens and detector spacecraft either to the vicinity of the L2 Lagrangian point or into a "drift-away" orbit around the sun. Existing ion thrusters can provide the necessary forces both to maintain the pointing direction against gravity gradient forces and disturbances and for reorienting the formation. The fuel and power needed for the thrusters are acceptable. In short, no "show stoppers" were identified.

5.3. Pointing Knowledge. Although precise control of the *distance* between lens and detector is not needed, the knowledge of the *direction* in celestial space of their vector separation is crucial. As information about every photon detected can be time tagged, *control* is needed "only" to the extent necessary to ensure that the image of the region to be studied falls on the detector area (Section 5.4). *Knowledge* of the orientation is needed, however, to a level corresponding to the angular resolution required. This amounts to a need to establish the transverse position of the detector with respect to a line passing from the source through the center of the lens, and to do so with a precision that can be from a millimeter down to a few microns.

The problem of precise attitude determination in celestial coordinates is one common to all missions attempting to work at the milli-/micro-arcsecond level. It has already been considered in the context of the studies of MAXIM, a proposed mission to address the problem of imaging space-time around black holes using X-ray interferometry. Gendreau et al. reviewed a number of approaches to the problem [78]. If a laser beacon is placed on the lens spacecraft and viewed against background stars, a "super-startracker"

on the detector spacecraft can in principle provide the necessary information. Obtaining measurements with the necessary precision is not out of the question—astrometry is already in an era where milli-arcsecond accuracy is the norm and micro-arc-second the target. The problem is obtaining that precision with faint stars on short enough time scales. Fortunately various technologies discussed by Gendreau et al. offer the prospect of gyroscopic systems that would have sufficient precision to allow interpolation between absolute fixes from the stellar observations. To further alleviate the difficulties, Luquette and Sanner [79] have discussed how knowledge of the dynamics dictating the spacecraft displacements can help with determining short term changes to the alignment.

5.4. Field of View. The fields of view of ultrahigh angular resolution telescopes such as those possible using diffractive optics are necessarily limited. With a single lens configuration, or with a contact achromatic doublet, the field of view will simply be the detector size divided by the focal length. With long focal lengths, reasonable detector sizes imply small fields of view. Although optical systems with separated lenses (Section 5.1.5) or with relay mirrors (Section 5.2) can change the image scale, this would probably be in the sense of increasing it, so reducing the field of view.

There is, anyway, a basic limitation. If for example micro-arc-second resolution was wanted over a 1" field of view, a detector with $>10^{12}$ pixels would be needed. The present state of the art for X-ray detectors in space is indicated by a few examples. The EPIC camera on XMM-Newton has an array of 7 CCDs with a total of 2.5×10^6 pixels. The imaging array of the ACIS focal plane instrument on Chandra has 4×10^6 pixels in 4 CCDs. Although the e-Rosita telescopes will have a total area of CCDs about an order of magnitude greater than present generation X-ray instruments, the pixel size will be larger to match the telescopes and the number of pixels will be only just over 10^6 [80]. Instruments planned for the IXO X-ray observatory are also in the few megapixel range, though a single monolithic device will cover 100 cm^2 [81].

Larger arrays of larger format CCDs are possible. Although the requirements are a little different for visible radiation, ESA's Gaia astrometry mission will have an array of 106 CCDs covering about half a square meter, with $\sim 9 \times 10^8$ pixels [82]. The Gaia pixels are rectangular 20×30 μm. Taking 20 μm as a typical dimension, a similar array would provide a field of view 30 milli-arc-seconds across with 1 μ'' pixels at a focal distance of just over 4000 km.

Of course, even where a 10^{12} pixel detector is available, it would require an extremely strong source to produce a significant signal in even a small fraction of the pixels. Sources of interest for study at the resolution possible with diffractive X-ray optics are necessarily rather compact.

6. Alternatives to Simple Lenses

Equation (3) implies that sub-micro-arcsecond angular resolution should be possible with modest sized lenses working at a few hundred keV. There is a special interest, though, in such measurements in the X-ray band. Not only are the photons more numerous, but the emission spectra of AGN typically show strong emission lines in the region of 6.7 keV associated with highly ionized Fe. These lines carry important diagnostic information because they are shifted in energy both by gravitational redshifts and by the Doppler effect. Ultra-high angular resolution mapping at energies in this band would be particularly valuable but would require lenses 50 m or more in diameter.

Although membrane/unfoldable Fresnel lenses of 25–100 m diameter for visible light have been proposed [83] and even been demonstrated on the ground on scales of up to 5 m [84], X-ray lenses of this size would not be easy to engineer and would actually have an effective area larger than needed from the point of view of photon flux.

A PFL with a partially filled aperture can be envisioned. It could comprise subsections of a PFL mounted on multiple spacecraft distributed over a plane [66, 85]. The system then becomes somewhat similar to that proposed within the studies of the proposed MAXIM (Micro-Arcsecond-X-ray IMager) mission in which mirror assemblies on spacecraft distributed over a plane would divert radiation to form fringes on a detector situated at a large distance [86]. In both cases tight control of the distances of the spacecraft from the center of the array would be needed (to a fraction of $p_{\min}$ for the partially filled PFL; similar for a MAXIM formation of the same size). The differences are (1) that the subsections of a partially filled aperture PFL would concentrate flux, whereas the plane mirrors proposed for MAXIM would not and (2) mirror reflection is achromatic, whereas the PFL subsections would divert radiation by a wavelength-dependent angle and fringes would only be formed where the concentrated, deflected, beams cross. The bandwidth over which fringes appear can be improved by altering the radial dependence of the pattern pitch in the PFL in ways analogous to X-ray axicons and axilenses. In the constant pitch (axicon) case one has a MAXIM-like interferometer in which the beam diverters are blazed diffraction gratings, and the borderline between imaging and interferometry becomes blurred.

7. Conclusions: Status and Prospects

As mentioned in the introduction, diffractive X-ray telescopes presently exist almost entirely as concepts and proposals on paper. Some work has been conducted on verifying that no problems exist and on demonstrating feasibility using scaled systems [87] fabricated by gray scale lithography [88]. By scaling down in radius (but not in thickness) the form of a large PFL that might be used for astronomy, the focal length is reduced. Lenses a few mm in diameter and with a focal length of ~100 m can act as models of ones, say, a few meters in diameter for which $f \sim 100$ km. With this reduced focal length testing is possible using existing ground-based facilities such as the 600 m long X-ray interferometry testbed at NASA-GSFC [89, 90]. Ironically the smaller lenses are *more* difficult to make than a flight lens would be, because the period of the profile is correspondingly reduced.

Tests and developments of small-scale PFLs, using various fabrication techniques and including achromatic combinations are continuing [91]. Progress to a micro-arcsecond mission would probably be through an intermediate level "pathfinder mission". Braig and Predehl [55] have suggested a concept in which a 3.5 m lens is divided radially into two regions operating, respectively, at 5 and 10 keV. Each would be made from many small achromatic segments whose outputs are assumed to add incoherently so the angular resolution is ~1 milli-arcsecond. Note that the proposed use of Lithium for the 5 keV component is unlikely to be practicable due to fabrication difficulties and to oxidation.

A specific proposal for a pathfinder mission, MASSIM [92], operating in the milli-arcsecond regime has been made in the context of NASA's "Advanced Mission Concept Studies". With a focal length of 1000 km, MASSIM would provide sub-milli-arc-second resolution with an effective area of 2000–4000 cm^2 over a pseudo-continuous 5–11 keV band using five 1 meter diameter achromatic lenses. MASSIM would allow important scientific objectives to be achieved, in particular allowing the imaging of the inner regions of jets where the acceleration takes place, while at the same time providing a stepping stone to an eventual micro-arc-second mission. It requires two spacecraft, one station keeping with respect to the other another to a fraction of a meter. A major technology driver would be the determination of direction of the actual line of sight with an accuracy corresponding to the target resolution. The proposed pointing determination method involves a state-of-the-art startracker on the detector spacecraft viewing the sky and simultaneously a beacon on the spacecraft carrying the lenses.

Another possible route forward is through solar imagery where even small diffractive lenses, little larger than those already demonstrated and having modest focal lengths (<100 m), could provide images of Fe line emission ~6.7 keV from active regions with an angular resolution many times better than any yet achieved.

In conclusion, diffractive optics offer a new family of possibilities for telescopes. Despite drawbacks in terms of inconvenient focal lengths and limited field of view and bandwidth, the potential that they have for flux concentration even at high energies and, in particular, for superb angular resolution suggests that in due course they will find their place in the range of techniques available to X-ray and gamma-ray astronomy.

Acknowledgments

The author wishes to thank colleagues for helpful discussions and in particular John Krizmanic for a careful reading of the paper and for useful suggestions.

References

[1] P. Gorenstein, "Focusing X-ray optics for astronomy," *X-Ray Optics and Instrumentation*, vol. 2010, Article ID 109740, 2010.

[2] R. Petre, "Thin shell, segmented X-ray mirrors," *X-Ray Optics and Instrumentation*, vol. 2010, Article ID 412323, 2010.

[3] M. Bavdas, M. Collon, M. Beijersbergen, K. Wallace, and E. Wille, "X-ray pore optics technologies and their application in

space telescopes," *X-Ray Optics and Instrumentation*, vol. 2010, Article ID 295095, 2010.

[4] L. Mertz, *Transformations in Optics*, John Wiley & Sons, New York, NY, USA, 1965.

[5] D. T. Wilson, G. D. DeMeester, H. H. Barrett, and E. Barsack, "A new configuration for coded aperture imaging," *Optics Communications*, vol. 8, no. 4, pp. 384–386, 1973.

[6] U. D. Desai, J. P. Norris, and R. J. Nemiroff, "Soft gamma-ray telescope for space flight use," in *Astroparticle Physics and Novel Gamma-Ray Telescopes*, D. B. Cline, Ed., vol. 1948 of *Proceedings of SPIE*, pp. 75–81, Orlando, Fla, USA, April 1993.

[7] F. Frontera and P. von Ballmoos, "Laue gamma-ray lenses for space astrophysics: status and prospects," *X-Ray Optics and Instrumentation*, vol. 2010, Article ID 215375, 2010.

[8] R. W. Wood, *Physical Optics*, Macmillan, New York, NY, USA, 3rd edition, 1934.

[9] J. Kirz, "Phase zone plates for X rays and the extreme UV," *Journal ofthe Optical Society of America*, vol. 64, no. 3, pp. 301–309, 1974.

[10] J. L. Soret, "Ueber die durch Kreisgitter erzeugten Diffractions phanomene," *Annalen der Physik*, vol. 232, pp. 99–113, 1875.

[11] L. Rayleigh, "Encyclopedia Britannica".

[12] R. W. Wood, "Phase reversal zone plates and diffraction telescope," *Philosophical Magazine*, vol. 45, p. 511, 1898.

[13] K. Miyamoto, "The phase Fresnel lens," *Journal of the Optical Society of America*, vol. 51, no. 1, pp. 17–20, 1961.

[14] O. E. Myers, "Studies of transmission zone plates," *American Journal of Physics*, vol. 19, pp. 359–365, 1951.

[15] A. V. Baez, "A study in diffraction microscopy with special reference to X-rays," *Journal of the Optical Society of America*, vol. 42, no. 10, p. 756, 1952.

[16] G. Elwert, "X-ray picture of the sun taken with fresnel zone plates," in *Structure and Development of Solar Active Regions*, K. O. Kiepenheuer, Ed., vol. 35 of *IAU Symposium*, pp. 439–443, 1968.

[17] H. Bräuninger, H. J. Einighammer, J. V. Feitzinger et al., "EUV and soft X-ray images of the sun on March 11th, 1971," *Solar Physics*, vol. 20, no. 1, pp. 81–84, 1971.

[18] M. Burger and J. H. Dijkstra, "Photographs of the Sun in the XUV-region," *Solar Physics*, vol. 24, no. 2, pp. 395–404, 1972.

[19] J. H. Dijkstra, W. de Graaff, and L. J. Lantwaard, "Construction of apodised zone plates for solar X-ray image formation," in *New Techniques in Space Astronomy*, F. Labuhn and R. Lust, Eds., vol. 41 of *IAU Symposium*, pp. 207–210, 1971.

[20] G. Elwert and F. Feitzinger, "The image improvement of field-sources with zone plates, especially of the sun in the XUV and soft X-region," *Optik*, vol. 6, pp. 600–612, 1970.

[21] R. Giacconi, W. P. Reidy, T. Zehnpfennig, J. C. Lindsay, and W. S. Muney, "Solar X-ray image obtained using grazing-incidence optics," *The Astrophysical Journal*, vol. 142, pp. 1274–1278, 1965.

[22] G. S. Vaiana, L. van Speybroeck, M. V. Zombeck, A. S. Krieger, J. K. Silk, and A. Timothy, "The S-054 X-ray telescope experiment on SKYLAB," *Space Science Instrumentation*, vol. 3, no. 1, pp. 19–76, 1977.

[23] B. Niemann, *Investigations of zone plate telescopes for the use of non-solar sources in the range of soft X-radiation*, Ph.D. thesis, Mathematisch-Naturwissenschaftliche Fakultät, Gottingen University, Germany, 1974.

[24] D. Dewey, T. H. Markert, and M. L. Schattenburg, "Diffractive-optic telescope for x-ray astronomy," in *Multilayer and Grazing Incidence X-Ray/EUV Optics III*, vol. 2805 of *Proceedings of SPIE*, pp. 224–235, Denver, Colo, USA, August 1996.

[25] G. K. Skinner, "Diffractive/refractive optics for high energy astronomy. I. Gamma-ray phase Fresnel lenses," *Astronomy and Astrophysics*, vol. 375, no. 2, pp. 691–700, 2001.

[26] G. K. Skinner, "Diffractive-refractive optics for high energy astronomy II. Variations on the theme," *Astronomy and Astrophysics*, vol. 383, no. 1, pp. 352–359, 2002.

[27] P. Gorenstein, "Concepts: X-ray telescopes with high angular resolution and high throughput," in *X-ray and Gamma-Ray Telescopes and Instruments for Astronomy*, J. E. Truemper and H. D. Tananbaum, Eds., vol. 4851 of *Proceedings of SPIE*, pp. 599–606, Waikoloa, Hawaii, USA, August 2002.

[28] P. Gorenstein, "Role of diffractive and refractive optics in x-ray astronomy," in *Optics for EUV, X-Ray, and Gamma-Ray Astronomy*, O. Citterio and S. L. O'Dell, Eds., vol. 5168 of *Proceedings of SPIE*, pp. 411–419, San Diego, Calif, USA, August 2004.

[29] C. Braig and P. Predehl, "X-ray astronomy with ultra-high angular resolution," in *UV and Gamma-Ray Space Telescope Systems*, G. Hasinger and M. J. L. Turner, Eds., vol. 5488 of *Proceedings of SPIE*, pp. 601–612, Glasgow, UK, June 2004.

[30] C. Braig and P. Predehl, "Large-scale diffractive X-ray telescopes," *Experimental Astronomy*, vol. 21, no. 2, pp. 101–123, 2006.

[31] D. J. Stigliani Jr., R. Mittra, and R. G. Semonin, "Resolving power of a zone plate," *Journal of the Optical Society of America*, vol. 57, pp. 610–611, 1967.

[32] W. Chao, E. H. Anderson, P. Fischer, and D. -H. Kim, "Towards sub-10 nm resolution zone plates using the overlay nanofabrication processes," in *Advanced Fabrication Technologies for Micro/Nano Optics and Photonics*, vol. 6883 of *Proceedings of SPIE*, San Jose, Calif, USA, January 2008.

[33] E. di Fabrizio, F. Romanato, M. Gentill et al., "High-efficiency multilevel zone plates for keV X-rays," *Nature*, vol. 401, no. 6756, pp. 895–898, 1999.

[34] H. Dammann, "Blazed synthetic phase-only holograms," *Optik*, vol. 31, no. 1, pp. 95–104, 1970.

[35] M. Young, "Zone plates and their aberrations," *Journal of the Optical Society of America*, vol. 62, no. 8, pp. 972–976, 1972.

[36] M. Bautz, "Active pixel X-ray sensor technology development for the generation-X wide-field imager," in *White paper, Astro2010: The Astronomyand Astrophysics Decadal Survey*, EOS Discipline Program Panel, 2009.

[37] C. B. Wunderer, G. Weidenspointner, A. Zoglauer et al., "Germanium (compton) focal plane detectors for gamma-ray lenses," in *Space Telescopes and Instrumentation II: Ultraviolet to Gamma Ray*, vol. 6266 of *Proceedings of SPIE*, Orlando, Fla, USA, May 2006.

[38] Q. Li, A. Garson, P. Dowkontt et al., "Fabrication and test of pixelated CZT detectors with different pixel pitches and thicknesses," in *Proceedings of IEEE Nuclear Science Symposium (NSS '08)*, pp. 484–489, Dresden, Germany, October 2008.

[39] C. K. Stahle, D. McCammon, and K. D. Irwin, "Quantum calorimetry," *Physics Today*, vol. 52, no. 8, pp. 32–37, 1999.

[40] R. L. Kelley, S. R. Bandler, W. B. Doriese et al., "The X-ray microcalorimeter spectrometer for the international X-ray observatory," in *Proceedings of the 13th International Workshop on Low Temperature Detectors (LTD '09)*, B. Young, B. Cabrera, and A. Miller, Eds., vol. 1185 of *AIP Conference Series*, pp. 757–760, December 2009.

[41] B. X. Yang, "Fresnel and refractive lenses for X-rays," *Nuclear Instruments and Methods in Physics Research A*, vol. 328, no. 3, pp. 578–587, 1993.

[42] B. Nöhammer, C. David, J. Gobrecht, and H. P. Herzig, "Optimized staircase profiles for diffractive optical devices made from absorbing materials," *Optics Letters*, vol. 28, no. 13, pp. 1087–1089, 2003.

[43] N. White, "X-ray astronomy: imaging black holes," *Nature*, vol. 407, no. 6801, pp. 146–147, 2000.

[44] W. Cash, "Imaging a black hole: MAXIM," *Advances in Space Research*, vol. 35, no. 1, pp. 122–129, 2005.

[45] S. Gillessen, F. Eisenhauer, S. Trippe et al., "Monitoring stellar orbits around the massive black hole in the galactic center," *The Astrophysical Journal*, vol. 692, pp. 1075–1109, 2009.

[46] K. Gebhardt and J. Thomas, "The black hole mass, stellar mass-to-light ratio, and Dark Halo in m87," *Astrophysical Journal*, vol. 700, no. 2, pp. 1690–1701, 2009.

[47] E. Middelberg and U. Bach, "High resolution radio astronomy using very long baseline interferometry," *Reports on Progress in Physics*, vol. 71, no. 6, Article ID 066901, 2008.

[48] T. P. Krichbaum, D. A. Graham, M. Bremer et al., "Sub-milliarcsecond imaging of Sgr A* and M 87," *Journal of Physics: Conference Series*, vol. 54, no. 1, pp. 328–334, 2006.

[49] S. S. Doeleman, J. Weintroub, A. E. E. Rogers et al., "Event-horizon-scale structure in the supermassive black hole candidate at the Galactic Centre," *Nature*, vol. 455, no. 7209, pp. 78–80, 2008.

[50] Y. Murata, N. Mochizuki, H. Saito et al., "The next generation space VLBI project: VSOP-2," in *Proceedings of the International Astronomical Union*, J. M. Chapman and W. A. Baan, Eds., vol. 242 of *IAU Symposium*, pp. 517–521, 2007.

[51] P. J. Armitage and C. S. Reynolds, "The variability of accretion on to Schwarzschild black holes from turbulent magnetized discs," *Monthly Notices of the Royal Astronomical Society*, vol. 341, no. 3, pp. 1041–1050, 2003.

[52] T. P. Krichbaum, I. Agudo, U. Bach, A. Witzel, and J. A. Zensus, "VLBI at the highest frequencies—AGN studies with micro-arcsecond resolution," in *Proceedings of the 8th European VLBI Network Symposium*, 2006.

[53] J. Hevelius, "Machinae coelestis," vol. 2, p. 353, 1738.

[54] C. Braig and P. Predehl, "Efficient Fresnel x-ray optics made simple," *Applied Optics*, vol. 46, no. 14, pp. 2586–2599, 2007.

[55] C. Braig and P. Predehl, "A diffraction-limited dual-band X-ray telescope," in *Optics for EUV, X-Ray, and Gamma-Ray Astronomy III*, vol. 6688 of *Proceedings of SPIE*, San Diego, Calif, USA, August 2007.

[56] S. J. Bennett, "Achromatic combinations of hologram optical elements," *Applied Optics*, vol. 15, no. 2, pp. 542–545, 1976.

[57] D. A. Buralli and J. R. Rogers, "Some fundamental limitations of achromatic holographic systems," *Journal of the Optical Society of America A*, vol. 6, pp. 1863–1868, 1989.

[58] A. Michette, C. Buckley, F. Gallo, K. Powell, and S. Pfauntsch, "Zone plate achromatic doublets," in *Advances in X-Ray Optics*, A. K. Freund, T. Ishikawa, A. M. Khounsary, D. C. Mancini, A. G. Michette, and S. Oestreich, Eds., vol. 4145 of *Proceedings of SPIE*, pp. 303–310, San Diego, Calif, USA, August 2001.

[59] L. Koechlin, D. Serre, and P. Deba, "The Fresnel interferometric imager," *Astrophysics and Space Science*, vol. 320, no. 1–3, pp. 225–230, 2009.

[60] G. K. Skinner, "Design and imaging performance of achromatic diffractive-refractive x-ray and gamma-ray Fresnel lenses," *Applied Optics*, vol. 43, no. 25, pp. 4845–4853, 2004.

[61] P. Gorenstein, W. Cash, N. Gehrels et al., "The future of high angular resolution X-ray astronomy," in *Space Telescopes and Instrumentation 2008: Ultraviolet to Gamma Ray*, vol. 7011 of *Proceedings of SPIE*, Marseille, France, June 2008.

[62] T. Stone and N. George, "Hybrid diffractive-refractive lenses and achromats," *Applied Optics*, vol. 27, pp. 2960–2971, 1988.

[63] B. Lengeler, C. G. Schroer, M. Kuhlmann et al., "Refractive x-ray lenses," *Journal of Physics D*, vol. 38, no. 10, pp. A218–A222, 2005.

[64] C. Braig and P. Predehl, "Advanced Fresnel X-ray telescopes for spectroscopic imaging," *Experimental Astronomy*, vol. 27, no. 3, pp. 131–155, 2010.

[65] Y. Wang, W. Yun, and C. Jacobsen, "Achromatic fresnel optics for wideband extreme-ultraviolet and X-ray imaging," *Nature*, vol. 424, no. 6944, pp. 50–53, 2003.

[66] G. K. Skinner, "X-ray and gamma-ray focusing and interferometry," in *Optics for EUV, X-Ray, and Gamma-Ray Astronomy IV*, vol. 7437 of *Proceedings of SPIE*, San Diego, Calif, USA, August 2009.

[67] R. Smith, *A Compleat System of Optiks*, Gedani, 1673.

[68] M. J. Simpson and A. G. Michette, "Imaging properties of modified fresnel zone plates," *Optica Acta*, vol. 31, pp. 403–413, 1984.

[69] L. Kipp, M. Skibowski, R. L. Johnson et al., "Sharper images by focusing soft X-rays with photon sieves," *Nature*, vol. 414, no. 6860, pp. 184–188, 2001.

[70] F. Giménez, J. A. Monsoriu, W. D. Furlan, and A. Pons, "Fractal photon sieve," *Optics Express*, vol. 14, no. 25, pp. 11958–11963, 2006.

[71] G. Skinner, "Development of optics for sub-micro-arc-second angular resolution in the X-ray and gamma-ray domains," in *White paper, Astro2010: The Astronomy and Astrophysics Decadal Survey*, pp. 1–10, 2009.

[72] J. Sochacki, A. Klodziejczyk, Z. Jaroszewicz, and S. Bara, "Nonparaxial design of generalized axicons," *Applied Optics*, vol. 31, pp. 5326–5330, 1992.

[73] Q. Cao and S. Chi, "Axially symmetric on-axis flat-top beam," *Journal of the Optical Society of America A*, vol. 17, no. 3, pp. 447–455, 2000.

[74] P. Gorenstein, J. D. Phillips, and R. D. Reasenberg, "Refractive/diffractive telescope with very high angular resolution for X-ray astronomy," in *Optics for EUV, X-Ray, and Gamma-Ray Astronomy II*, O. Citterio and S. L. O'Dell, Eds., vol. 5900 of *Proceedings of SPIE*, pp. 1–8, San Diego, Calif, USA, August 2005.

[75] T. G. Farr, P. A. Rosen, E. Caro et al., "The shuttle radar topography mission," *Reviews of Geophysics*, vol. 45, no. 2, Article ID RG2004, 2007.

[76] A. N. Parmar, M. Arnaud, X. Barcons et al., "XEUS—the X-ray evolving universe spectroscopy mission," in *Space Telescopes and Instrumentation II: Ultraviolet to Gamma Ray*, vol. 6266 of *Proceedings of SPIE*, Orlando, Fla, USA, May 2006.

[77] J. Krizmanic, G. Skinner, and N. Gehrels, "Formation flying for a Fresnel lens observatory mission," *Experimental Astronomy*, vol. 20, no. 1–3, pp. 497–503, 2005.

[78] K. C. Gendreau, J. Leitner, L. Markley, W. C. Cash, and A. F. Shipley, "Requirements and options for a stable inertial reference frame for a 100-micro-arcsecond imaging telescope," in *Interferometry in Space*, M. Shao, Ed., vol. 4852 of *Proceedings of SPIE*, pp. 685–694, Waikoloa, Hawaii, USA, August 2002.

[79] R. J. Luquette and R. M. Sanner, "Spacecraft formation control: Managing line-of-sight drift based on the dynamics of relative motion," in *Proceedings of the 3rd International Symposium on Formation Flying, Missions and Technologies (ESA-ESTEC '08)*, Noordwijk, The Netherlands, April 2008.

[80] N. Meidinger, R. Andritschke, S. Ebermayer et al., "CCD detectors for spectroscopy and imaging of x-rays with the

eROSITA space telescope," in *UV, X-Ray, and Gamma-Ray Space Instrumentation for Astronomy XVI*, vol. 7435 of *Proceeding of SPIE*, San Diego, Calif, USA, August 2009.

[81] J. Treis, R. Andritschke, R. Hartmann et al., "Pixel detectors for x-ray imaging spectroscopy in space," *Journal of Instrumentation*, vol. 4, no. 3, Article ID P03012, 2009.

[82] A. Laborie, R. Davancens, P. Pouny et al., "The Gaia focal plane," in *Focal Plane Arrays for Space Telescopes III*, vol. 6690 of *Proceedings of SPIE*, San Diego, Calif, USA, August 2007.

[83] R. Hyde, S. Dixit, A. Weisberg, and M. Rushford, "Eyeglass: a very large aperture diffractive space telescope," in *Highly Innovative Space Telescope Concepts*, H. A. MacEwen, Ed., vol. 4849 of *Proceedings of SPIE*, pp. 28–39, Waikoloa, Hawaii, USA, 2002.

[84] R. Hyde and S. Dixit, "A giant leap for space telescopes," LNL Science and Technology Review, https://www.llnl.gov/str/March03/Hyde.html.

[85] G. K. Skinner and J. F. Krizmanic, "X-ray interferometry with transmissive beam combiners for ultra-high angular resolution astronomy," *Experimental Astronomy*, vol. 27, no. 1-2, pp. 61–76, 2009.

[86] W. Cash, "Maxim: micro-arcsecond x-ray imaging mission," in *Interferometry in Space*, M. Shao, Ed., vol. 4852 of *Proceedings of SPIE*, pp. 196–209, Waikoloa, Hawaii, USA, August 2003.

[87] J. Krizmanic, B. Morgan, R. Streitmatter et al., "Development of ground-testable phase fresnel lenses in silicon," *Experimental Astronomy*, vol. 20, no. 1–3, pp. 299–306, 2005.

[88] B. Morgan, C. M. Waits, J. Krizmanic, and R. Ghodssi, "Development of a deep silicon phase fresnel lens using gray-scale lithography and deep reactive ion etching," *Journal of Microelectromechanical Systems*, vol. 13, no. 1, pp. 113–120, 2004.

[89] Z. Arzoumanian, K. C. Gendreau, W. C. Cash, A. F. Shipley, and S. Z. Queen, "Laboratory testbeds for broadband X-ray interferometry," in *UV and Gamma-Ray Space Telescope Systems*, G. Hasinger and M. J. L. Turner, Eds., vol. 5488 of *Proceedings of SPIE*, pp. 623–629, Glasgow, UK, June 2004.

[90] G. Gendreau, "GSFC X-ray Interferometry Testbed," http://xraybeamline.gsfc.nasa.gov/.

[91] J. Krizmanic, In preparation.

[92] G. K. Skinner, Z. Arzoumanian, W. C. Cash et al., "The milli-arc-second structure imager (MASSIM): a new concept for a high angular resolution x-ray telescope," in *Space Telescopes and Instrumentation 2008: Ultraviolet to Gamma Ray*, vol. 7011 of *Proceedings of SPIE*, Marseille, France, June 2008.

Hindawi Publishing Corporation
X-Ray Optics and Instrumentation
Volume 2010, Article ID 824387, 6 pages
doi:10.1155/2010/824387

Research Article

Fabrication and Performance Test of Fresnel Zone Plate with 35 nm Outermost Zone Width in Hard X-Ray Region

Yoshio Suzuki,[1] Akihisa Takeuchi,[1] Hisataka Takenaka,[2] and Ikuo Okada[2]

[1] *Japan Synchrotron Radiation Research Insitute (JASRI)/SPring-8, Sayo Hyogo 679-5198, Japan*
[2] *NTT-AT Nanofabrication Corporation, Atsugi, Kanagawa 243-0018, Japan*

Correspondence should be addressed to Yoshio Suzuki, yoshio@spring8.or.jp

Received 29 October 2009; Accepted 17 June 2010

Academic Editor: Ali Khounsary

A Fresnel zone plate (FZP) with 35 nm outermost zone width has been fabricated and tested in the hard X-ray region. The FZP was made by electron beam lithography and reactive ion etching technique. The performance test of the FZP was carried out by measuring the focused beam profile for coherent hard X-ray beam at the beamline 20XU of SPring-8. The full width at half maximum of the focused beam profile measured by knife-edge scan method is 34.9 ± 2.7 nm, that agrees well with the theoretical value of diffraction-limited resolution. Applications to scanning microscopy were also carried out.

1. Introduction

Many types of optical elements for X-ray microfocusing and microimaging in the hard X-ray regions have been developed. Fresnel zone plates [1], total reflection mirrors [2], multilayer mirrors [3], refractive lenses [4], and multilayer Laue lenses [5] were fabricated and applied to microfocusing of synchrotron radiation X-rays. At present, the Fresnel zone plate (FZP) manufactured by electron beam lithography is one of the best optical elements for X-ray microscopy because of its high spatial resolution (better than 50 nm), negligibly small coma and small field distortion. The chromatic aberrations of FZP are usually ignorable in the hard X-ray region, because the crystal monochromators used in the synchrotron radiation beamlines produce sufficient monochromaticity for hard X-rays ($\lambda/\Delta\lambda \sim 10000$). Thus, the spatial resolution of FZP optics is simply determined by the numerical aperture and by the accuracy of zone structure.

Spatial resolution of about 30 nm is already achieved with conventional FZPs. However, these results are carried out using third-order diffraction of FZP with an outermost zone width of 50 nm [1, 6]. Although a gold zone plate with 24 nm outermost zone width is also fabricated and tested in hard X-ray region [7], its spatial resolution has not been reported. Some X-ray focusing optics of spatial resolution better than 30 nm is already reported [2, 5]. However, they are still one-dimensional focusing, and these optical elements, the multilayer Laue lenses, or the aspherical Kirkpatrick-Baez mirrors are not image-forming optics. The Fresnel zone plate in the hard X-ray region is an almost ideal image-forming optical devise up to a spatial resolution of around 10 nm [8, 9]. Therefore, the conventional FZP is still indispensable for hard X-ray microscopy. In this report, recent development of FZP with an outermost zone width of 35 nm is presented, and characterization of the FZP in the hard X-ray region is described.

2. Fresnel Zone Plate Fabrication

The FZP was fabricated at NTT-AT Nanofabrication by electron beam lithography and reactive ion etching technique. The fabrication process of FZP is shown in Figure 1. The substrate is composed of 2 μm silicon nitride (SiN) membrane deposited on a Si wafer by low pressure chemical vapor deposition (CVD) method. Tantalum film with a thickness of 0.175 μm was deposited by rf-sputtering method, and SiO_2 film was deposited by electron cyclotron resonance (ECR) plasma CVD method on the Ta layer as an etching mask of Ta. The FZP patterns were written by point electron-beam exposure method. The SiO_2 film was etched with resist mask by the reactive ion etching, and the Ta film was dry-etched with SiO_2 mask by an ECR ion-stream etching. Finally, the

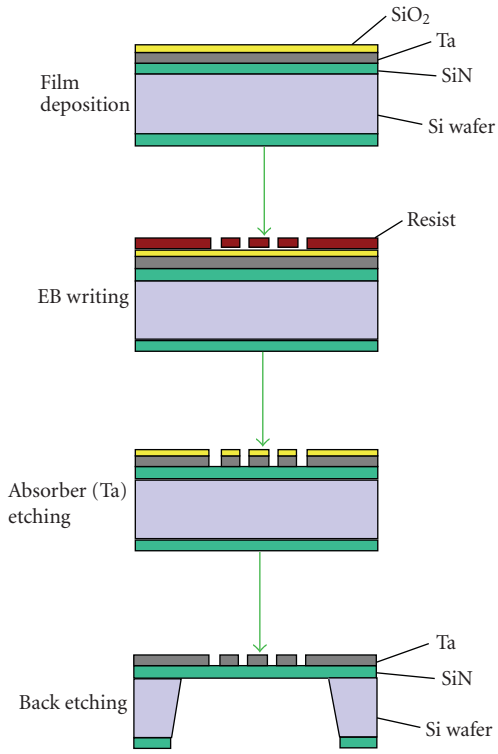

Figure 1: Processing step of Fresnel zone plate manufacturing.

Si wafer was back etched with KOH solution for windowing. The details of fabrication method of tantalum zone plates at the NTT-AT Nanofabrication are already reported elsewhere [10, 11].

Schematic drawing of the FZP structure and its SEM image is shown in Figure 2. The design width of outermost zone that determines the diffraction-limited resolution is 35 nm. The SEM image shows a cross section of outermost zone structure that was prepared from the duplicated FZP. Fine zone structures of 35 nm width are precisely formed as shown in the figure. The zone pattern is designed by the simple formula of FZP as

$$r_n^2 = n\lambda f, \tag{1}$$

where n is integer of zone number, λ is an X-ray wave length, and f is focal length. We used a parameter set of λ = 0.155 nm ($h\nu$ = 8 keV) and f = 40 mm. Comparing with the spherical-aberration-corrected exact equation of zone pattern for focusing a plane wave,

$$r_n^2 = n\lambda f + \frac{n^2\lambda^2}{4}, \tag{2}$$

it is required that f is much greater than $n\lambda/4$ for the ignorable spherical aberrations [12]. According to the Rayleigh's quarter wavelength rule [13], the spherical aberration can be ignored, when the following condition is satisfied [8]:

$$\frac{N^2}{2} < \frac{f}{\lambda}. \tag{3}$$

Here, N is total number of zone. In order to satisfy the Rayleigh's $\lambda/4$ rule, we chose N = 1265, that is, r_N = 88.56 μm (diameter of 177.12 μm). Then, the outermost zone width becomes 35.00 nm. The $\lambda/4$ rule is satisfied in the wavelength region shorter than 2.8 nm. Thus, the spherical aberration can be ignored in the hard X-ray region.

The theoretical spatial resolution (Rayleigh resolution limit) for the first-order diffraction of FZP is known to be $1.22d_N$, where d_N is the width of outermost zone [12]. Therefore, if the zone structure is ideal, spatial resolution of the FZP could be 43 nm. It should be noted that the knife-edge scan method, which is generally used for measuring the focused beam shape, gives a line spread function of beam profile. The line-spread-function, LSF(x), of a diffraction-limited focal spot for circular aperture lens is given by one-dimensional integral of point spread function as

$$\mathrm{LSF}(x) = \int_{-\infty}^{\infty} \frac{\left(2J_1\left(\sqrt{x^2+y^2}\right)\right)^2}{x^2+y^2}\,dy, \tag{4}$$

where $J_1(x)$ is a Bessel function of the first kind. The Rayleigh's criterion for spatial resolution is defined by the first minimum of the Bessel function as $J_1(x_1) = 0$, and the solution of $x_1 = 1.220\pi$ is usually used as a definition of diffraction-limited resolution [13], while the full width at half maximum (FWHM) of point-spread-function, $\{2J_1(x)/x\}^2$, is 1.0290π. It is shown by the numerical calculation of the above formula that the FWHM of line-spread-function is given by $x = 1.0016\pi$. Therefore, the FWHM of line-spread-function is nearly equal to the outermost zone width of ideal FZP, and the theoretical FWHM of knife-edge scan profile for the diffraction-limited micro focus beam is $1.0016d_N$.

The calculated diffraction efficiency for the 0.175 μm-thick tantalum FZP is only 0.8% for 8 keV X-rays. This low efficiency may sometimes be a problem for nanobeam applications or for imaging microscopy because of low signal intensity. However, the low diffraction efficiency can be compensated by high brilliance X-ray sources. Some scanning microscopy experiments can be carried out with this zone plate, and the application to the imaging microscopy would also be capable at the expense of relatively long exposure time and high radiation dose to specimen. This low diffraction efficiency is not a problem for characterization of FZP.

The thickness of FZP (0.175 μm) is, however, not optimized for 8 keV X-rays. The optimum thickness of Ta zone plate for 8 keV is 1.9 μm. Therefore, higher aspect ratio of zone structure is required for improvement of diffraction efficiency. The aspect ratio of tantalum one-to-one zone structure is presently limited by technological reason, mainly for reactive dry-etching process. The present limit of aspect ratio is about 10. The aspect ratio doubling by stacking two zone plates [7] would be a promising method for higher diffraction efficiency. Zone material of high electron density is adequate for X-ray zone plates, because the optimized thickness is in proportion to the reciprocal of electron density. Gold is generally chosen as the zone material for its high density and fabrication technology, for example, electroplating of gold. The density of tantalum is less than

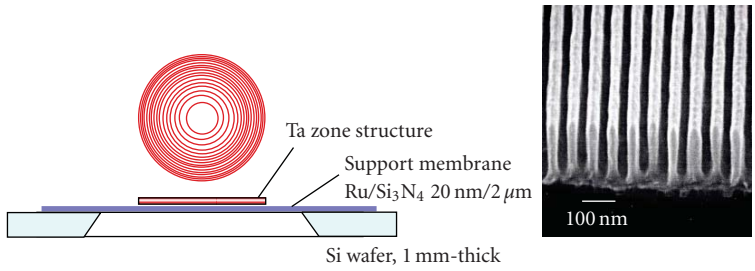

Figure 2: Schematic drawing and cross-sectional SEM image of Fresnel zone plate fabricated by electron beam lithography method. Width of outermost zone is 35 nm.

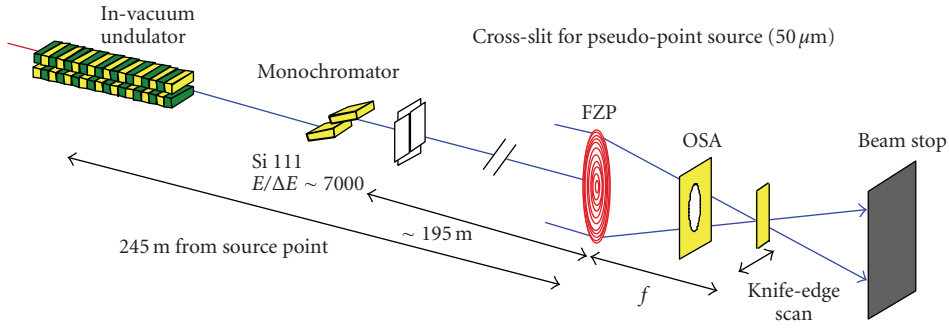

Figure 3: Experimental setup for X-ray nanofocusing at the beamline 20XU of SPring-8. FZP: Fresnel zone plate. OSA: order selecting aperture, a pinhole with 20 μm-diameter made of 0.3 mm-thick platinum plate. Beam Stop: direct beam stop for dark-field edge-scan, tantalum 3 mm-thick plate.

that of gold by about 14%. Therefore, the zone plate made of Ta usually gives lower efficiency than that made of Au in the case of same zone thickness. However, we consider that the difference of diffraction efficiency is not significant, and the tantalum is also one of the best materials for hard X-ray zone plates. In some cases, for example, near the absorption edge of gold, tantalum zone plate with the same thickness can give slightly higher efficiency than gold zone plate.

3. Performance Test of FZP

Performance test of the FZP as a nanofocusing optics has been carried out at the beamline 20XU [14] of SPring-8. A schematic view of the experimental setup is shown in Figure 3. An X-ray energy of 8 keV was chosen in the experiment. The energy resolution of monochromator is about 1.1 eV for 8 keV X-rays. To avoid the chromatic aberration of FZP optics, the relative spectral bandwidth of incident X-ray beam, $\Delta\lambda/\lambda$, must be less than or equal to the inverse of total number of zone [12], as

$$\frac{\Delta\lambda}{\lambda} \leq \frac{1}{N}. \tag{5}$$

Comparing with the zone number of the FZP, $N = 1265$, the monochromaticity of $\Delta E/E \sim 1/7000$ is sufficient for testing the performance of FZP.

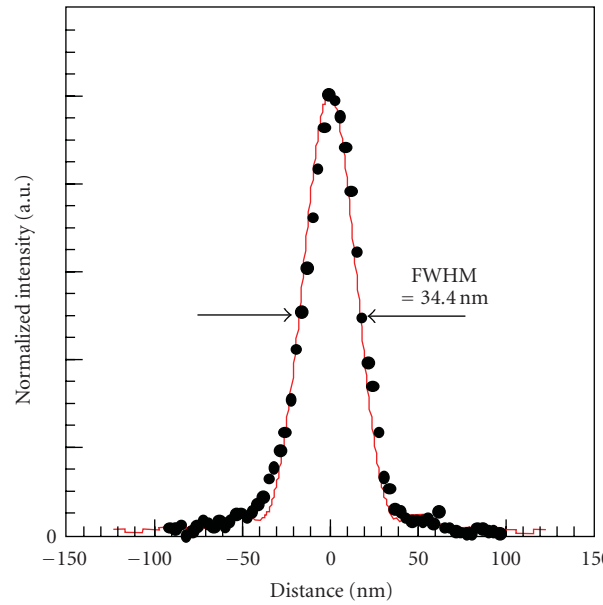

Figure 4: Focused beam profile measured by dark-field edge scan. Edge scan was carried out with 3.125 nm step and 1 s integration time per point. X-ray energy is 8 keV. An edge of tantalum thin film (0.5 μm-thick) is used as a knife-edge. Solid circles are measured data, and the red line represents theoretical profile for ideal circular aperture lens. Signal current of ionization chamber is about 2 pA at the peak.

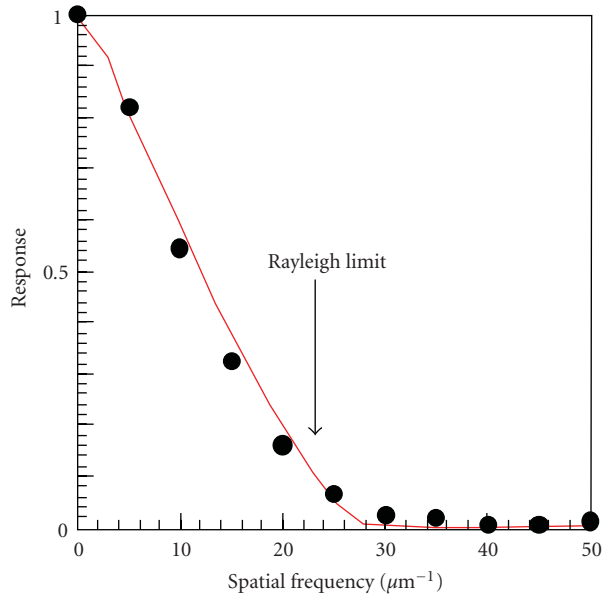

Figure 5: Modulation transfer function. Solid circles are MFT calculated from the measured beam profile shown in Figure 4. Red line is theoretical MTF obtained by numerical calculation of line-spread function.

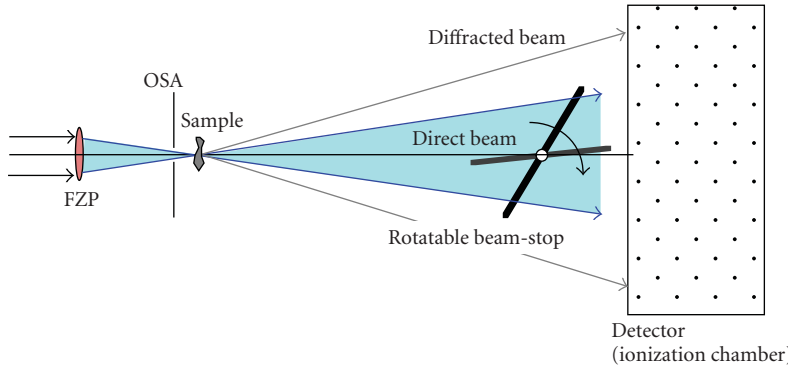

Figure 6: Schematic view of scanning microscopy setup for bright and dark field method. A lead thin plate (0.5 mm) beam stop is mounted on a rotating stage, and bright-field and dark-field imaging can be exchanged by rotating the beam stop.

The monochromatic beam is transported through the 200-m-long vacuum duct and is extracted in to the air at an end experimental station located at approximately 245 m from the light source. A precise cross slit located 49 m from the source is used as a pseudopoint source for determining the spatial coherence at the end station. The cross slit with an opening of 50 μm $\times$ 50 μm was used in the present experiment. Therefore, the geometrical spot size for an FZP with a focal length of 40 mm becomes 10 nm that is much less than the diffraction-limited resolution of the FZP. There are no optical elements between the cross-slit virtual source and the experimental station, except for a beamline X-ray window made of 125 μm-thick polyimide.

The focus spot profile is evaluated by knife-edge scan method. However, it is difficult to fabricate precise knife-edge for characterization of nano-focusing beam, because of high transmissivity of hard X-ray beam. So, the conventional knife-edge test cannot be used for the present experiment. We employed dark-field method for the knife-edge test [1]. A pattern edge of tantalum resolution test chart is used as a knife-edge. The thickness of tantalum test pattern is 0.5 μm, which corresponds to an optical path difference of about $\lambda/8$ at an X-ray wavelength of 0.155 nm. The intensity of the diffracted wave takes its maximum at an optical thickness of $\lambda/2$ for phase edge. Therefore, from point of view of signal intensity, the optimum thickness of knife-edge for dark-field method is $\lambda/2$. However, the thickness of $\lambda/8$ is still sufficient for the beam profile measurement. The thicker knife-edge may give higher dark-field signal, but the thickness must be much less than the depth of focus that is 7.9 μm in the present experimental condition. The test pattern edge was set parallel to the optical axis in order to avoid broadening of edge-scan profiles. The misalignment of substrate of test pattern was within an angle of about 0.3 degree.

The knife-edge scanning was carried out using a conventional mechanical stage driven by an open-loop-controlled

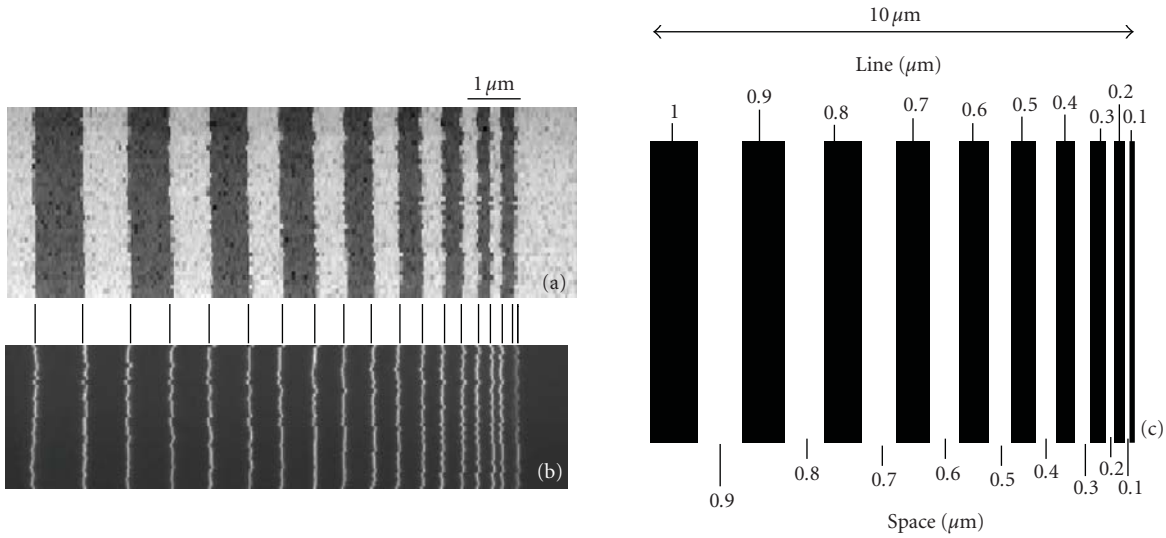

Figure 7: Scanning microscopy images of line and space test patterns. X-ray energy is 8 keV. (a) Bright field image, 50 nm pixel size and 0.2 s dwell time. (b) Dark field image, 12.5 nm pixel size and 0.2 s dwell time. (c) Schematic drawing of line and space patterns. Black area corresponds to tantalum-deposited regions.

step motor. The accuracy of the translation stage is measured to be better than 10 nm [15]. The X-ray beam intensity was measured with ionization chamber detectors with 14 cm electrode length. One is an air-flowed ionization chamber placed in front of the FZP, and the other is an argon-flowed ionization chamber behind the knife-edge. A beam stop is placed in front of the argon-flowed ionization chamber for the purpose of dark-field edge scan.

A typical example of measured beam profiles is shown in Figure 4. The FWHM of the focused beam profile shown in Figure 4 is 34.4 nm. The accuracy of beam size measurement was estimated from repeatability of measured beam size. The average of thirteen measurements around the focus is 34.9 nm, and the error of beam size measurement is 2.7 nm in standard deviation. Therefore, it is concluded that the focused beam size is 34.9 nm ± 2.7 nm in FWHM. As shown in the figure, the measured beam profile agrees well with the theoretical one. It is concluded that nanometer-resolution imaging is capable in the hard X-ray region by using the FZP as a beam-focusing device or as an objective lens for imaging microscopy. The measured diffraction efficiency of the FZP is 0.7% for 8 keV X-rays. This value agrees well with the theoretical efficiency (0.8%) of 0.175 μm-thick Ta zone plate. Modulation transfer function (MTF) obtained from the measured beam profile in Figure 4 is shown in Figure 5. The Rayleigh's resolution limit ($1.22d_N$) for 35 nm outermost zone width that corresponds to a spatial frequency of 23.4 μm^{-1} is indicated by an arrow in the figure. The measured MTF at 23.4 cycle/μm is about 10%.

4. Scanning Microscopy Experiments

Experimental setup for scanning microscopy experiment is shown in Figure 6. Bright field imaging and dark-field imaging [16] can be exchanged by rotating the beam stop in front of the detector. The beam stop is made of a lead plate with a thickness of 0.5 mm. Scanning microscopy images of a test object are shown in Figures 7(a) and 7(b). The specimen is resolution test patterns made of 0.5 μm-thick tantalum that were also fabricated at NTT-AT Nanofabrication by the same process as that of the FZP. The design feature of line and space patterns is shown in Figure 7(c). The fine patterns up to 0.2 μm were clearly seen in the measured images. The beam flux at the sample position was about 4×10^6 photons/s, and signal intensity in dark field mode was 2×10^5 photons/s.

Although the design of test pattern has the 0.1 μm-wide line and space patterns, the 0.1 μm wide patterns are not observed in the measure images, and a weak line is recognized at the right edge of pattern in the dark-field image where the 0.1 μm-wide line should be seen. The right edge of the 0.2 μm-line pattern is not observed in the dark-field image. In addition, in the bright-field image, there is a faint contrast pattern at the right side of the 0.2 μm-line pattern. From these results, we consider that the 0.1 μm-wide pattern is provably collapsed or slanted and contacts to the neighboring 0.2 μm-wide line pattern. The 0.1 μm-wide line and space patterns are unfortunately imperfect in the measured portion of large test patterns.

Acknowledgment

The experiments were performed at the BL20XU in SPring-8 under the approval of the Japan Synchrotron Radiation Research Institute (JASRI) (Proposal no. 2006A1562).

References

[1] Y. Suzuki, A. Takeuchi, H. Takano, and H. Takenaka, "Performance test of fresnel zone plate with 50 nm outermost zone width in hard X-ray region," *Japanese Journal of Applied Physics. Part 1*, vol. 44, no. 4 A, pp. 1994–1998, 2005.

[2] H. Mimura, H. Yumoto, S. Matsuyama et al., "Efficient focusing of hard x rays to 25 nm by a total reflection mirror," *Applied Physics Letters*, vol. 90, no. 5, Article ID 051903, 3 pages, 2007.

[3] O. Hignette, P. Cloetens, C. Morawe et al., "Nanofocusing at ESRF using graded multilayer mirrors," in *Synchrotron Radiation Instrumentation: 9th International Conference on Synchrotron Radiation Instrumentation*, vol. 879 of *AIP Conference Proceedings*, pp. 792–795, June 2006.

[4] C. G. Schroer, O. Kurapova, J. Patommel et al., "Hard x-ray nanoprobe based on refractive x-ray lenses," *Applied Physics Letters*, vol. 87, no. 12, Article ID 124103, pp. 1–3, 2005.

[5] H. C. Kang, H. Yan, R. P. Winarski et al., "Focusing of hard x-rays to 16 nanometers with a multilayer Laue lens," *Applied Physics Letters*, vol. 92, no. 22, Article ID 221114, 3 pages, 2008.

[6] G.-C. Yin, Y.-F. Song, M.-T. Tang et al., "30 nm resolution x-ray imaging at 8 keV using third order diffraction of a zone plate lens objective in a transmission microscope," *Applied Physics Letters*, vol. 89, no. 22, Article ID 221122, 3 pages, 2006.

[7] Y. Feng, M. Feser, A. Lyon et al., "Nanofabrication of high aspect ratio 24 nm x-ray zone plates for x-ray imaging applications," *Journal of Vacuum Science and Technology B*, vol. 25, no. 6, pp. 2004–2007, 2007.

[8] Y. Suzuki and H. Toda, *Advanced Tomographic Methods in Materials Research and Engineering*, Oxford University Press, Oxford, UK, 2008, Section 7.1.

[9] Y. Suzuki, "Resolution limit of refractive lens and fresnel lens in X-ray region," *Japanese Journal of Applied Physics. Part 1*, vol. 43, no. 10, pp. 7311–7314, 2004.

[10] M. Sekimoto, A. Ozawa, T. Ohkubo, H. Yoshihira, M. Kakuchi, and T. Tamura, *X-Ray Microscopy II*, Springer, Berlin, Germany, 1988.

[11] A. Ozawa, T. Tamamura, T. Ishii, H. Yoshihara, and T. Kagoshima, "Application of X-ray mask fabrication technologies to high resolution, large diameter Ta Fresnel zone plates," *Microelectronic Engineering*, vol. 35, no. 1–4, pp. 525–529, 1997.

[12] D. Attwood, *Soft X-Rays and Extreme Ultraviolet Radiation*, Cambridge University Press, Cambridge, UK, 1999, Section 9.

[13] M. Born and E. Wolf, *Principles of Optics*, Cambridge University Press, Cambridge, UK, 1999.

[14] Y. Suzuki, K. Uesugi, N. Takimoto, et al., "Construction and commissioning of a 248 m-long beamline with x-ray undulator light source," in *Synchrotron Radiation Instrumentation: 8th International Conference on Synchrotron Radiation Instrumentation*, vol. 705 of *AIP Conference Proceedings*, pp. 344–347, 2004.

[15] Y. Suzuki, A. Takeuchi, H. Takano, T. Ohigashi, and H. Takenaka, "Diffraction-limited microbeam with Fresnel zone plate optics in hard X-ray regions," in *X-Ray Micro- and Nano-Focusing: Applications and Techniques II*, Proceedings of the SPIE, pp. 74–84, San Diego, Calif, USA, July 2001.

[16] Y. Suzuki and F. Uchida, "Dark-field imaging in hard x-ray scanning microscopy," *Review of Scientific Instruments*, vol. 66, no. 2, pp. 1468–1470, 1995.